

This item is held in Loughborough University's Institutional Repository (<https://dspace.lboro.ac.uk/>) and was harvested from the British Library's EThOS service (<http://www.ethos.bl.uk/>). It is made available under the following Creative Commons Licence conditions.



For the full text of this licence, please go to:
<http://creativecommons.org/licenses/by-nc-nd/2.5/>

Microstructural Evolution in Grade 91 (9Cr-1MoVNb) Power Plant Steels

By

Juan Javier Sanchez-Hanton

Institute of Polymer Technology and Materials Engineering
Loughborough University

A doctoral thesis submitted in partial fulfilment of the requirements for the
award of Doctor of Philosophy

October 2007

© J. J. Sanchez-Hanton, 2007

ACKNOWLEDGEMENTS

My profuse gratitude is extended to my project supervisor, Professor Rachel Thomson, who, in addition to providing her intellectual input, has been a constant source of encouragement, inspiration and friendship throughout this research period.

Funding for this work from the Engineering and Physical Science Research Council (EPSRC) under grant number GR/S86334/01 and the support of the following companies: Alstom, Chromalloy, E.On UK, Howmet (Alcoa), Doosan Babcock, National Physical Laboratory, QinetiQ, RWE npower, Rolls Royce and Siemens is also gratefully acknowledged.

Grateful thanks to my peers from the SUPERGEN II Lifetime Extension of Conventional Power Plant programme, in particular Professor T.H. Hyde, Dr W. Sun and Dr. A. Yaghi, from the University of Nottingham, Dr S.J. Steve Brett from RWE npower, and Dr D.J. Allen from E.On UK for their helpful suggestions during numerous valuable discussions. I would also like to thank Dr. G.D. West and Mr J.S. Bates for technical assistance with electron microscopy, and Dr. S. Hogg for help with X-ray diffraction throughout this research program.

I acknowledge and thank, with great pleasure, all of the members of the IPTME Metals Research Group who have both helped me and provided an enjoyable working environment; in particular Michael Pace, Geoff West, Kate Burke and Chun-Liang Chen.

Finally, I am eternally grateful to Patricia Hernandez de los Reyes, for her constant encouragement and patience, my parents, Elio Sanchez-Marte and Mary Hanton, and the rest of my family, for their enthusiasm and support.

ABSTRACT

The aim of this research project was to gain a complete, quantified, understanding of microstructural changes in high Cr ferritic-martensitic power plant steels, as a function of pre-service heat treatment, stress, time and temperature. The creep strength, which is the main design criteria for this class of alloys, depends on the stability of the microstructure, which consists of tempered martensite and a fine dispersion of carbide precipitates. An understanding of the changes of these two features forms an essential process towards the creation of a physically or microstructural-based model, which may improve the current approaches towards the prediction of remanent operational lifetime of these materials in service in conventional fossil-fired power plant.

In order to compare the rate of microstructural change, two Grade 91 (9Cr-1MoVNb) alloys of similar composition have been investigated. One alloy exhibited a 'conventional' cast composition and possessed desirable mechanical properties, and another was a 'weak' cast with known poor creep properties and a high Al content. The materials were subjected to controlled normalizing heat treatments in a dilatometer, which were subsequently cooled at varying cooling rates and then tempered. Following this, the specimens have been subjected to long-term isothermal aging heat treatments. The microstructural changes occurring at these various time and temperature conditions were studied using scanning and transmission electron microscopy (SEM and TEM), energy dispersive x-ray spectroscopy (EDS), electron backscatter diffraction (EBSD), x-ray diffraction (XRD) and thermodynamic equilibrium calculations.

Significant changes were observed in all of the investigated Grade 91 specimens, and it was shown that the rate of microstructural change occurred more rapidly in the 'weak' cast, which was shown to be more sensitive to varying heat treatments. Analysis of the chemical composition of MX precipitates showed that the main observed change was the gradual partitioning of the composition of MX precipitates, from a linear composition distribution of V and Nb in (V,Nb)(N,C), into two distinct particle compositions, VN and NbC, with increasing aging times. It was postulated that such changes in the composition of MX carbides occur rather slowly, raising the possibility that the chemical composition changes of MX may be used to make an informed judgment on the thermal history of Grade 91 components. The

other main change of minor phase precipitation was the gradual coarsening of intergranular $M_{23}C_6$ carbides.

Electron backscatter diffraction has been used to quantify the changes in the ratio of low to high-angle boundaries and the total grain boundary line length, both of which have been shown to increase with increasing aging times at 650°C. X-ray diffraction has been used to quantify the free dislocation density of the investigated specimens, and it has been shown that this parameter decreased with prolonged high temperature exposure. Both techniques confirmed that the recovery of the matrix microstructure occurred more rapidly in the 'weak' material.

The microstructure of ex-service Grade 91 components, that have experienced typical power plant operating conditions, have also been extensively characterized and it has been shown that striking similarities between the microstructures of the ex-service materials and the long-term aged materials were found, which enabled the ex-service materials to be ranked according to the level of microstructure evolution undergone by the long-term aged specimens.

The experimental data obtained from the microstructural characterization were subsequently used to validate existing microstructural evolution models, which may be fed into a physically based continuum damage mechanics (CDM) creep model in order to assess the remaining creep life of high Cr ferritic-martensitic steels. Good agreement was found between model predictions and experimental measurements in predicting the volume fraction, type and size of minor phase precipitates in Grade 91 steel.

PUBLICATIONS

Parts of this work are published as detailed below:

- 1) Sanchez-Hanton J.J. and Thomson R.C., The Effect of Initial Heat Treatment on Creep Behaviour of P91 Steels, in *Proceedings of the EPRI International Conference on the Advances in Condition and Remaining Life Assessment for Fossil Power Plants*, 16-18th October 2006, Louisville KY, USA, pp. 1-10 (2006)
- 2) Sanchez-Hanton, J.J. and Thomson, R.C., Microstructural Characterization of Power Plant Grade 91 (9Cr-1Mo-Nb-V) Steel Welds, in *Proceedings of the 3rd International Conference on the Integrity of High Temperature Welds*, 24-26th April 2007, IOM Communications Ltd, London, pp. 361-372 (2007)
- 3) Sanchez-Hanton, J.J. and Thomson, R.C., Characterization of Isothermally Aged Grade 91 (9Cr-1Mo-Nb-V) Steel by Electron Backscatter Diffraction, *Materials Science and Engineering A*, 460-461, pp. 261-267 (2007)
- 4) Sanchez-Hanton, J.J. and Thomson, R.C., Effect of Initial Heat Treatment on Minor Phase Precipitation in Grade 91 Steel (9Cr-1Mo-V-Nb) Upon Aging, To be submitted to *Materials Science and Engineering A* (2007)

CONTENTS

	Page
Acknowledgements	i
Abstract	ii
Publications	iv
Contents	v
1. Introduction	1
1.1 Project Overview	1
1.2 Background	2
1.2.1 9-12 wt.% Ferritic-Martensitic Steels	2
1.3 Organization of the Thesis	4
2. Literature Review	6
2.1 Introduction	6
2.2 Phases Present in P91	6
2.2.1 The Fe-C System	6
2.2.2 The Fe-Cr-C System	7
2.2.3 Martensite	8
2.2.4 Alloying Additions	13
2.2.5 Carbide and Nitride Precipitates	15
2.2.5.1 M_3C	16
2.2.5.2 M_7C_3	17
2.2.5.3 $M_{23}C_6$	17
2.2.5.4 M_2C	18
2.2.5.5 M_6C	19
2.2.5.6 MX	19
2.2.5.7 AlN	22
2.2.5.8 <i>Z-phase</i>	25
2.2.5.9 <i>Laves Phase</i>	25
2.2.6 Summary of Phases Present in 9-12 wt.% Cr Steels	26
2.3 Typical Heat Treatments	27

2.3.1	Normalizing	27
2.3.2	Tempering	30
2.3.3	Summary of the Pre-service Heat Treatments Applied to 9-12 wt.% Cr Steels	33
2.4	Microstructural Evolution during Long-term Aging and Creep	33
2.4.1	Lath/Subgrain Size and Shape	33
2.4.2	Particle Size, Interparticle Spacing and Morphology	40
2.4.3	Summary of Microstructural Evolution in P91 Steel	44
2.5	Microstructure Modelling for Creep Life Prediction	44
2.6	Summary	46
3.	Experimental Procedures	48
3.1	Introduction	48
3.2	Materials	48
3.2.1	Materials Supplied in the As-received Condition	49
3.2.2	Ex-Service Materials	50
3.2.3	Materials Supplied After Accelerated Creep Testing	50
3.3	Heat Treatment	51
3.3.1	Normalizing	52
3.3.2	Tempering	54
3.3.3	Aging	54
3.4	Thermodynamic Calculations	55
3.5	Optical Microscopy	58
3.6	Metallography	58
3.7	Scanning Electron Microscopy	59
3.8	Electron Backscatter Diffraction	60
3.8.1	Sample preparation for EBSD analysis	61
3.8.2	EBSD Analysis	61
3.9	Transmission Electron Microscopy (TEM)	62
3.9.1	Specimen Preparation	63
3.9.1.1	Carbon Extraction Replicas	63
3.9.1.2	Thin-foil Preparation	64
3.9.2	Microstructure Characterization with TEM	64

3.9.2.1	<i>Imaging Modes Used</i>	64
3.9.2.2	<i>Identification of Composition: Energy Dispersive X-ray Analysis (EDX)</i>	64
3.9.2.3	<i>Identification of Composition: Parallel Electron Energy Loss Spectroscopy (PEELS)</i>	65
3.9.2.4	<i>Identification of Structure: Electron Diffraction</i>	65
3.10	Focussed Ion Beam	66
3.11	X-Ray Diffraction	67
3.11.1	X-Ray Diffraction from Electrolytically Extracted Precipitates	68
3.11.2	X-Ray Diffraction Line Profile Analysis from Tempered Martensite	69
3.12	Hardness Testing	70
3.13	Summary	70
4.	Effect of Initial Heat Treatments on the Microstructure of Grade 91 Steel	71
4.1	Introduction	71
4.2	As-received Specimens	72
4.2.1	Microstructure	72
4.3	Equilibrium Predictions of the Phases in Grade 91 Steel	73
4.3.1	Overview of Predicted Phases	73
4.3.2	Equilibrium Prediction of MX Precipitates in Grade 91 Steel	74
4.3.3	Discussion of Equilibrium Predictions	77
4.3.4	Summary of Thermodynamic Equilibrium Predictions	78
4.4	Creation of Starting Microstructures	79
4.4.1	Results from Dilatometry Experiments	79
4.4.2	Discussion of Dilatometry Results	84
4.5	Analysis of As-normalized Microstructures	85
4.5.1	Martensitic Lath and Subgrain Structure	86
4.5.1.1	<i>Results</i>	86
4.5.1.2	<i>Discussion</i>	94
4.5.2	Minor Phase Precipitation	96
4.5.2.1	<i>Results</i>	96
4.5.2.1	<i>Discussion</i>	100
4.5.3	Effect of Normalizing Treatment on the Hardness	102

4.5.3.1	<i>Results</i>	102
4.5.3.2	<i>Discussion</i>	103
4.6	Analysis of the As-tempered Microstructures	104
4.6.1	Minor Phase Precipitation Induced by Tempering	104
4.6.1.1	<i>The Particle Size Distribution of $M_{23}C_6$ Particles</i>	107
4.6.1.2	<i>Results of Particle Size Distribution of $M_{23}C_6$ Precipitates</i>	110
4.6.1.3	<i>The Effect of Aluminium Nitride on the Precipitation of $M_{23}C_6$</i>	111
4.6.2	The Lath/Subgrain Structure of As-tempered Grade 91 Steel	113
4.6.3	Effect of Subsequent Tempering on the Hardness	114
4.6.4	Discussion on the Effect of Normalizing Condition on Subsequent Tempering	116
4.7	Summary of Initial Heat Treatments	117
5.	Effects of Long-Term Aging and Creep on Minor Phase Precipitation	119
5.1	Introduction	119
5.2	Materials	119
5.3	Experimental Procedures	120
5.4	Analysis of the Chemical Composition of MX Precipitates	120
5.4.1	Chemical Composition of MX in As-received Condition P91	121
5.4.2	Chemical Composition of MX in As-normalized Specimens	122
5.4.2.1	<i>Results</i>	122
5.4.2.1	<i>Discussion</i>	124
5.4.3	Chemical Composition of MX in Aged Specimens	125
5.4.4	Chemical Composition of MX in Accelerated Creep Test Specimens	131
5.5	Discussion Concerning MX Composition	131
5.6	Particle Size Analysis of Minor Phase Precipitates	135
5.6.1	Particle size distribution of MX precipitates	136
5.6.2	Particle Size Distribution of $M_{23}C_6$ Precipitates	139
5.6.2.1	<i>As-received Materials</i>	139
5.6.2.2	<i>Long-term Aged Specimens</i>	140
5.6.2.3	<i>Creep Specimens</i>	149
5.6.2.4	<i>Comparison of $M_{23}C_6$ Particle Size</i>	150

5.6.2.5	<i>Discussion</i>	151
5.6.3	Particle Size Distribution of AlN and Laves Phase	152
5.7	Summary	155
6.	Effects of Long-Term Aging and Creep on the Matrix Microstructure	157
6.1	Introduction	157
6.2	EBSD for the Assessment of Material Microstructure	158
6.2.1	The Microstructure of As-received P91 Steel	159
6.2.2	The Effect of Long-Term Aging on the Microstructure of P91 Steel	161
6.2.2.1	<i>The Effect of Long-term Aging on the Hardness</i>	161
6.2.2.2	<i>EBSD Analyses of Long-term Aged Microstructures</i>	163
6.2.2.3	<i>Discussion on the Effect of Long-term Aging on the Microstructure Evolution</i>	170
6.2.3	Effect of Accelerated Creep Testing on the Microstructure of P91 Steel	171
6.2.3.1	<i>The Effect of Creep Stress on the Hardness of P91</i>	172
6.2.3.2	<i>EBSD Analyses of Accelerated Creep Tested Microstructures</i>	173
6.2.3.3	<i>Discussion on the Effect of Creep Testing on the Microstructure Evolution</i>	178
6.2.4	Boundary length as a method of assessing material microstructure	178
6.2.5	Image Quality Parameter as a Method of Assessing Material Condition	183
6.3	X-Ray Diffraction (XRD) Line Profile Analysis for the Assessment of Material Microstructure	185
6.3.1	Review of the Application of XRD for the Quantification of Dislocations	185
6.3.2	Some Considerations for Dislocation Density Measurements with XRD	187
6.3.3	XRD Analysis of the As-received P91 Steel Specimens	188
6.3.4	XRD Line Profile Analysis of Long-Term Aged Materials	190
6.3.4.1	<i>Results</i>	190
6.3.4.2	<i>Discussion</i>	196
6.3.5	XRD Line Profile Analysis of Accelerated Creep Test Specimens	196
6.3.6	XRD Analysis of Dislocation Densities in P91 Steel	198
6.3.6.1	<i>Results</i>	200
6.3.6.2	<i>Discussion</i>	201

6.4	Summary	202
7.	Microstructure of Ex-Service Materials	203
7.1	Introduction	203
7.2	Materials and Experimental Techniques	203
7.3	Results from Microstructural Characterization	204
7.3.1	Thermodynamic Modelling of Minor Phase Precipitates	204
7.3.2	Chemical Composition of MX Precipitates in Ex-Service Materials	206
7.3.3	Hardness Testing	208
7.3.4	$M_{23}C_6$ Size Distribution	209
7.3.5	Precipitation of Laves Phase	212
7.3.6	The Effect of Service Exposure on the Subgrain Structure of P91	212
7.3.7	Subgrain Size	217
7.3.8	The Effect of Service Exposure on the Dislocation Structure of P91	218
7.4	Discussion Concerning the Microstructure of Ex-service Materials	221
7.5	Summary	222
8.	Microstructural Characterization of P91 Steel Welds	223
8.1	Introduction	223
8.2	Experimental Procedure	224
8.3	Results from the Microstructural Characterization of P91 Steel Welds	225
8.3.1	The Matrix Microstructure	225
8.3.2	$M_{23}C_6$ Precipitate Size Distribution	233
8.3.3	Chemical Composition of MX Precipitates	235
8.3.4	Aluminium Nitride	237
8.4	Discussion Concerning the Effect of Heat Treatment on the Creep Strength of P91 Steel Welds	238
8.5	Summary	241
9.	A Model for the Prediction of Creep Strength in Grade 91 Steel	243
9.1	Introduction	243
9.2	Physically Based Continuum Damage Mechanics (CDM) Modelling	244

9.2.1	Primary Creep	247
9.2.2	<i>'Damage' Due to the Dislocation Substructure</i>	248
9.2.2.1	<i>Review of Dislocation and Subgrain Evolution Parameters</i>	248
9.2.2.2	<i>Comparison Between Experimental and Modelled Subgrain Size and Dislocation Density Results</i>	251
9.2.2.3	<i>Discussion Concerning the 'Damage' Due to the Dislocation Substructure</i>	253
9.2.3	<i>'Damage' Due to Particle Coarsening</i>	255
9.2.3.1	<i>Review of Particle Coarsening Equations</i>	255
9.2.3.2	<i>Comparison Between Experimental and Modelled Particle Coarsening Results</i>	260
9.2.3.3	<i>Discussion Concerning the 'Damage' Due to Particle Coarsening</i>	268
9.3	Summary	269
10.	Conclusions and Future Work	270
11.	References	274

Chapter 1

INTRODUCTION

1.1 Project Overview

The present study forms a part of a programme of research funded by Engineering and Physical Sciences Research Council (EPSRC) within its entitled SUPERGEN, or Sustainable Power Generation and Supply, programme. This particular research project was entitled “Lifetime Extension of Conventional Fossil-Fired Power Plant”. This programme is divided into four main areas of research, called “work packages”, each being lead by a particular UK university. Work package 1, called “Condition Monitoring”, led by the University of Bristol, is at present developing miniaturised condition monitoring tools in order to assess the on-line (*in situ*) state of power plant components. The aims of work package 2, called “Environmental Degradation and Protection” led by Cranfield University, is to characterize the environmental degradation of critical power plant materials under specific operating environments. The University of Nottingham leads work package 4, called “Modelling of Mechanical Behaviour”, whose aims are to improve life prediction and failure assessment methods for power plant components. Finally, work package 3, called “Microstructural Degradation”, is led by Loughborough University, and its contribution to the research programme is the characterisation and modelling of the microstructural evolution of power plant materials. Although each university leads a specific package, the fundamental aim of the research programme is to combine the activities from each work package to form an ‘integrated toolbox’ of plant lifetime extension monitoring and modelling tools for the power generation industry.

The aim of this research project was to gain a complete, quantified, understanding of microstructural changes in high Cr tempered martensitic power plant steels, as a function of pre-service heat treatment, stress, and time and temperature. Indeed, this is an essential process towards the creation of a physically or microstructural-based model, which may improve the current approaches towards the prediction of remnant operational lifetime of these materials in service in conventional fossil-fired power plant.

1.2 Background

There has been an increasing motivation to reduce both the operating costs and the environmental effects of the process of electrical power generation by conventional burning of fossil fuels ^[1-5]. Therefore, in recent times, there has been an increase in the movement of world economies towards more sustainable methods of satisfying their energy requirements, and the main focus has been to increase the contribution to electricity generation from renewable sources. A major disadvantage of these methods is the variability of supply, which in turn has led to the increased cycling of existing conventional power plant. As a consequence, system reliability and availability, due to the demands of flexible plant operation, are becoming increasingly important. In addition, there is also an increasing trend towards the co-firing of coal with biomass, which places additional demands on the materials performance, particularly the corrosion resistance. It is therefore, at present, evermore necessary to be able to predict material performance and component life, and also to safely extend plant life beyond their original design lives, given that fossil fuels are expected to maintain a dominant share of the electricity generation market as newer renewable sources are being introduced.

1.2.1 9-12% Cr Ferritic-Martensitic Steels

The Rankine cycle is the most widely used cycle for electrical power generation, and a schematic diagram is shown in Figure 1.1. In steam power plant, a fuel (coal) is burned to produce heat, which is used to produce steam to drive a turbine and thus produce mechanical energy. This is subsequently converted to electrical energy by an alternator.

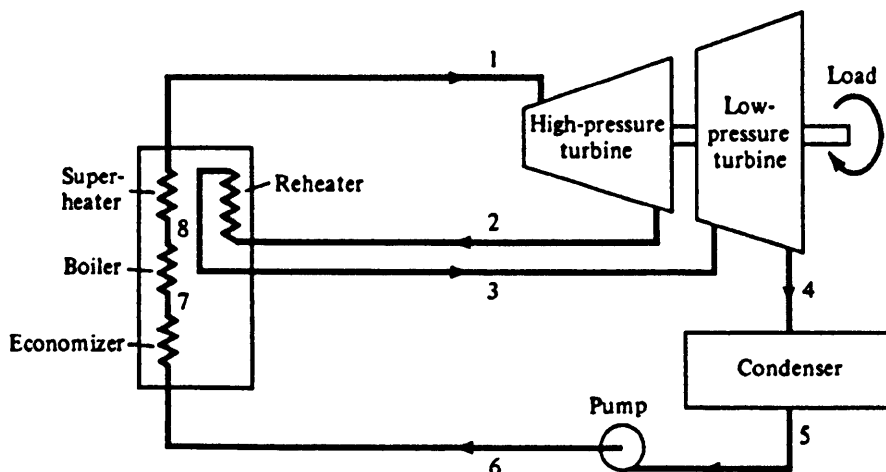


Figure 1.1: Schematic diagram of a Rankine cycle with superheat and reheat stages. After Kiameh ^[6].

Most coal-fired power plants operate at a nominal steam temperature of 568°C at a pressure of approximately 160 MPa ^[7]. Components are expected to operate for several years under these conditions, and must therefore offer good resistance to both creep and corrosion. Advanced 9-12 wt.% Cr ferritic-martensitic steels, in particular modified 9Cr steels with additions of Mo, V and Nb such as grade 91 (9Cr-1MoVNb steel), have become indispensable in the electrical power generation industry where they are used in the construction of headers (pictured in Figure 1.2) and steam piping, and boiler super-heater and re-heater tubes in both advanced coal- and gas fired power plants ^[8]. This is due to the fact that these materials possess desirable properties, such as excellent elevated temperature strength and creep resistance, high corrosion-oxidation resistance, good thermal conductivity, low coefficient of thermal expansion and a high resistance to thermal shock ^[8,9].

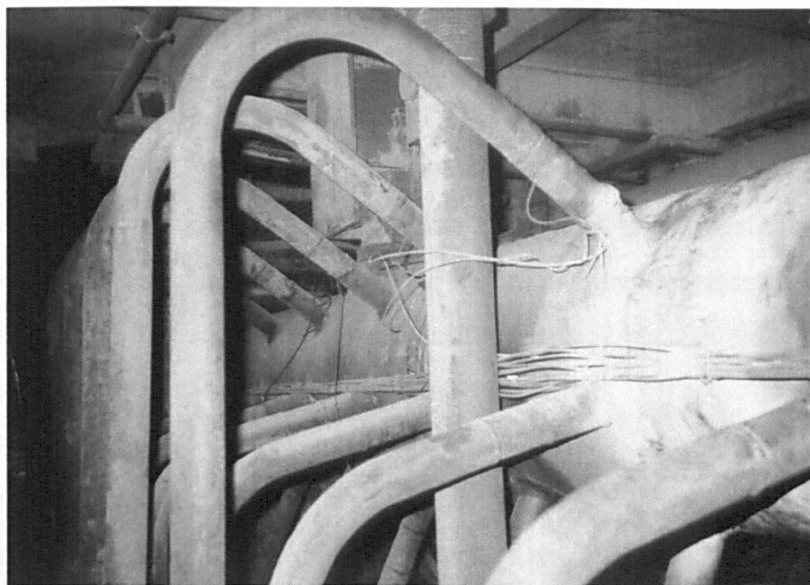


Figure 1.2: Photograph of a P91 header and superheater steam pipes. Courtesy of Dr Steve Brett, RWE npower.

High chromium ferritic-martensitic steels used for high temperature power plant applications have a complex microstructure as a result of the alloying elements present in the steel and also because of the heat treatment to which they are subjected. For instance, prior to service these steels are typically given a two stage heat treatment that consists of normalizing and tempering to produce a tempered martensitic structure. The martensitic matrix has a high dislocation density. Alloying additions such as Nb, V, Mo and Cr are all strong carbide formers, and on tempering complex carbide and nitride precipitate particles are formed and become distributed in the microstructure. These various particles precipitate in different parts of the martensitic microstructure. For example, chromium rich $M_{23}C_6$ particles are usually

found in the prior austenite and lath boundaries, while VN and NbC can be found dispersed within the martensite laths.

It is the resultant microstructure, with a high dislocation density, a fine dispersion of particles, and the presence of solid solution strengthening elements, that provides an increased resistance dislocation motion. This factor makes 9-12 wt.% Cr ferritic-martensitic steels suitable candidate materials for applications that require good creep resistance and which operate in relatively severe conditions requiring good corrosion and oxidation resistance, such as high temperature steam piping. However, long-term thermal exposure and the occurrence of creep strain in the material causes the reduction of the mechanical integrity of such components and provokes the microstructure to constantly evolve during service, which is the stimulus for the present project.

1.3 Organization of the Thesis

This thesis is organised into eleven chapters as follows. Chapter 2 presents a review of the physical metallurgy of 9-12 wt.% Cr ferritic-martensitic steels from the literature, which includes phase transformations and characteristics of precipitate particles, together with experimental findings regarding the effect of heat treatments and the microstructure evolution. A brief section describing some of the modelling techniques developed to predict the remanent lifetime of power plant components is also included.

Chapter 3 discusses the experimental techniques used for this research. It begins with a detailed description of the materials that were used, identifying chemical compositions and conditions in which the investigated materials were processed. It subsequently presents in detail the heat treatments that were carried out in the present investigation. The rest of the chapter describes sample preparation techniques and a brief explanation of the different microstructure characterization techniques used, in addition to a description of the instrument parameters used.

In Chapter 4, the effects of pre-service normalizing and tempering heat treatment on the microstructure and mechanical properties of P91 steel are discussed. The chapter begins with an overview of the generation of different starting microstructures, by varying normalizing

and tempering parameters, followed by a discussion of the results obtained using a variety of microscopy techniques and from hardness testing.

Chapter 5 investigates the effect of varying initial thermal histories, from the previous chapter, and subsequent aging and stress on minor phase precipitation, and in Chapter 6, an attempt is made to quantify changes in the martensitic matrix microstructure with respect to changes in the same parameters, using techniques such as electron backscatter diffraction (ESBD) and X-ray line profile analysis. The microstructure of ex-service P91 materials is discussed in Chapter 7, and compared with those created and studied in the laboratory in this investigation. Continuing the theme of microstructure evolution as a function of heat treatment, Chapter 8 discusses the effect pre-weld heat treatment on the microstructure and creep properties of P91 steel welds, and investigates the microstructure along the intercritical heat-affected zone (ICHAZ), whereby Type IV cracking, an important mechanism responsible for the untimely failure of these materials, occurs. These results are set in the context of those obtained in this work on parent material microstructural evolution.

Chapter 9 discusses possible methods of incorporating microstructural parameters, determined in the preceding chapters, into a model suitable for the creep life assessment of grade 91 steel. Chapter 10 presents the conclusions obtained from this research and further work.

Chapter 2

LITERATURE REVIEW

2.1 Introduction

The present chapter reviews the literature relevant to the various factors which affect the microstructure, and in turn, mechanical properties of 9-12 wt.% Cr power plant steels. These factors include the physical metallurgy of this class of alloys, the different phases present, the effects of pre-service heat treatments, and the evolution of the microstructure under creep loading conditions. In addition, a section has been dedicated to reviewing some of the existing creep life prediction techniques.

2.2 Phases Present in 9-12 wt.% Cr Steels

2.2.1 The Fe-C system

Plain carbon steel without any alloying additions can exist in a range of different crystal structures. These crystal structures can change as a function of both temperature and carbon concentration. The iron-carbon binary phase system shown in Figure 2.1 describes how on heating above 723°C iron changes from ferrite (α), which is a body-centred cubic structure (hereafter referred to as bcc), to austenite (γ), which is a face-centred cubic structure (hereafter referred to as fcc).

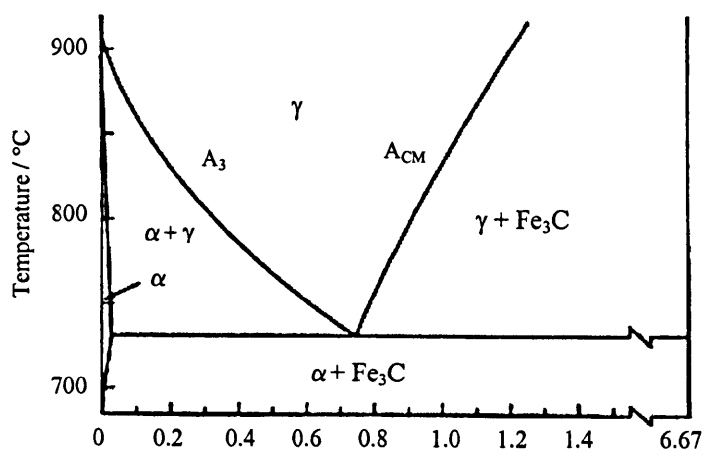


Figure 2.1: Iron-carbon phase diagram. After Askeland ^[10].

By heating a pure hypoeutectoid iron-carbon alloy (<0.8 wt.% C) to the austenite temperature range, cementite (Fe_3C) disappears because the solid solubility of carbon in iron increases with the creation of larger octahedral sites in the resulting fcc structure, even though this structure is more closely-packed than the bcc structure of ferrite (Figure 2.2). The approximate increase in the solubility of carbon from bcc ferrite to fcc austenite is hundredfold, i.e. from 0.02 to 2.14 weight percent carbon in iron.

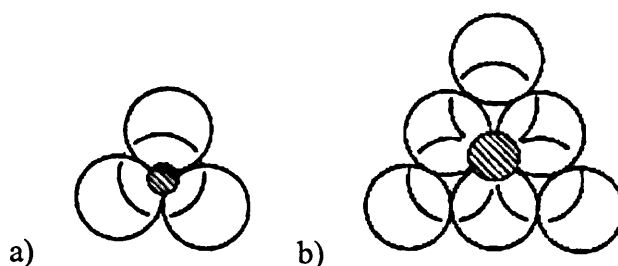


Figure 2.2: Possible sites for interstitial atoms in an fcc structure; a) tetrahedral and b) octahedral. After Porter and Easterling ^[11].

2.2.2 The Fe-Cr-C System

The addition of Cr into steel produces a complex Fe-Cr-C system, in which many different equilibrium phases, depending on the composition and temperature, can be present in the microstructure. Figure 2.3 shows a vertical section through the Fe-Cr-C phase diagram at 0.1 wt.% C. It is shown that Cr is a ferrite stabilizing element, and that there is the possibility that a range of Cr-based carbides may form in the microstructure. For 9 to 12 wt.% Cr power plant steels, the equilibrium microstructure at $\sim 750^\circ\text{C}$, the approximate tempering temperature, and below 600°C , the approximate service temperature, the equilibrium microstructure consists of ferrite and carbides. The process of normalizing at $\sim 1050^\circ\text{C}$ causes the Cr-based carbides to dissolve and produces the transformation of Fe from α to γ , with the possibility of some delta ferrite being present. Other alloying additions are added to this class of steels for a variety of purposes, which may also improve the stability of austenite or ferrite, and reduce the possibility of delta ferrite formation upon normalizing. These alloying additions, as well as the phases present in high Cr power plant steels, are discussed in detail in the following sections.

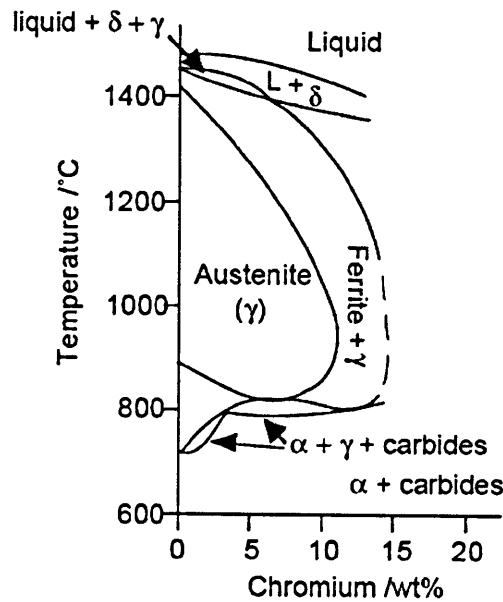


Figure 2.3: Phase diagram for the Fe-xCr-0.1C system. After Sanderson ^[12].

2.2.3 Martensite

9-12 wt.% Cr ferritic steels are subjected to a complex heat treatment prior to exposure to typical operating conditions in power plant. This is discussed further in section 2.3. The matrix phase that is most widely encountered in service in 9-12 wt.% Cr steel is martensite, or more accurately tempered martensite. The presence of martensite is the result of a diffusionless transformation which occurs when steel is rapidly cooled from a temperature high enough such that austenite is present in the microstructure. Under equilibrium conditions, the crystal structure of iron changes from bcc ferrite to fcc austenite during a normalizing heat treatment, which also causes cementite (Fe_3C) particles dissolve, thus the carbon present in the steel must move, by diffusion, to different interstitial sites in the newly created fcc lattice. When carbon occupies an interstitial site in the parent austenite phase, a strain is exerted on the surrounding atoms, as the carbon atoms of $1.54 \times 10^{-10} \text{ m}$ in diameter are larger than the octahedral interstice of $1.044 \times 10^{-10} \text{ m}$ diameter that they occupy ^[13].

Similarly, if the steel is cooled slowly from the austenite phase, the carbon in the fcc austenite matrix can diffuse out to produce cementite in order to relieve the deformation of the austenite lattice. Under slow cooling conditions, there is also sufficient time available for substitutional alloying elements to become redistributed in ferrite, or to form equilibrium carbides. However, on rapid cooling (quenching) from the normalizing temperature, the carbon becomes trapped inside the lattice as there is little time for diffusion to occur, thus producing a supersaturated solution of carbon in the matrix. As a result, a body-centred tetragonal

structure (hereafter referred to as bct) is produced, along with very high strain and residual stresses as by-products of the transformation. Carbon atoms are preferentially situated in (001/2) type sites, which give rise to tetragonal distortion ^[14]. This bct crystal structure is not a closed-packed cell, so in effect it has fewer active slip planes resulting in a greater resistance to dislocation motion, which in turn produces higher strength, hardness and indeed creep-resistance, whilst at the same time inducing brittleness. Tempering treatments are therefore applied to relieve some of the internal residual stresses of as-quenched steels and in turn increase toughness (see section 2.3.2).

The lattice parameters a and c , as shown in Figure 2.4, vary as a function of the carbon content in the steel. It can be seen that the bct lattice becomes more distorted with an increase in carbon concentration. The lattice correspondence for the formation of martensite from austenite is shown in Figure 2.5, which illustrates how the martensitic bct cell is produced from the austenitic fcc cell without rearrangement of the atoms.

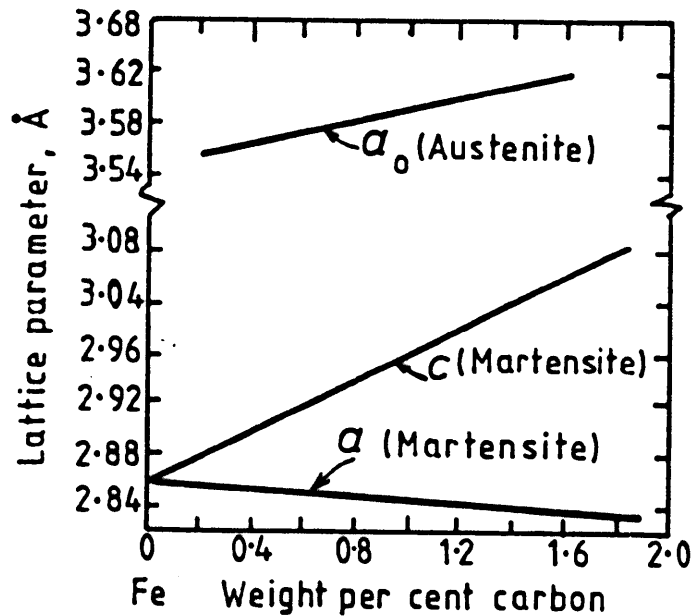


Figure 2.4: The changes of the lattice parameters of ferrous martensite as a function of carbon composition. After Porter and Easterling ^[11].

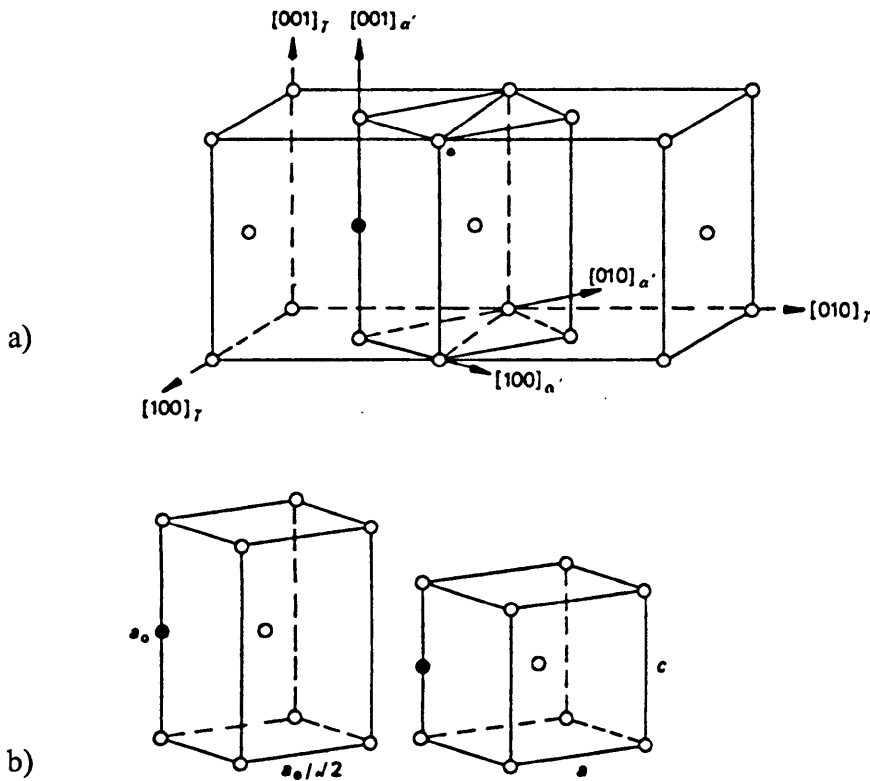


Figure 2.5: Lattice correspondence for the formation of martensite from austenite. a) A body-centred tetragonal cell highlighted within two face-centred cubic cells, b) Lattice deformation that comprises of compression along the c -axis to form martensite of correct c/a ratio Bain strain. After Honeycombe and Bhadeshia ^[13].

Figure 2.6 shows that the microstructure of martensite is sensitive to carbon concentration. High Cr power plant steels fall into the category of low C steel, thus the martensitic microstructure is expected to consist of fine needle-like laths, the substructure of which consists of a high density of dislocations ^[15]. Lath martensite exists as individual lath packets inside a prior austenite grain.

Martensite is a metastable phase, thus on subsequent reheating, carbon will diffuse out of the lattice and form carbides with iron and/or other carbide forming elements, which is beneficial as it gives rise to precipitation strengthening, and hence yields an improvement in creep strength. Conversely, the high dislocation density present in virgin martensite gives rise to a high level of stored energy, which promotes the process of recovery under typical operating conditions. Recovery of the high energy dislocation structure is manifested in subgrain formation and growth, which is discussed in more detail in section 2.4.

The temperature at which martensite forms (M_s) in P91 steel upon cooling from the normalizing temperature is approximately 386°C ^[8]. In many low carbon steels with a high M_s ,

(Figure 2.6) there is a brief period in which carbon redistribution occurs, segregating to lattice defects during quenching through the martensite temperature range ^[14,16]. This process is called auto-tempering and occurs because the stress fields around individual dislocations and cell walls in lath martensite cause certain interstitial lattice sites near such defects to have a lower energy for carbon than the interstitial lattice positions. This redistribution is the first step of the tempering process. Evidence of the segregation of C in high- M_s Fe-C martensites to dislocations and to sub-boundaries in rapidly quenched samples has been given by Speich ^[17] using electrical resistivity results, and Thomson and Miller ^[18] observed, using atom probe field ion microscopy, significant carbon enrichment in the lath boundaries of a 2.25Cr-1Mo steel that had been rapidly quenched from an normalizing temperature of 1050°C, although the latter was attributed to the formation of retained austenite films on the lath boundaries. A relatively small amount of retained austenite is expected in low carbon steels, as illustrated in Figure 2.7.

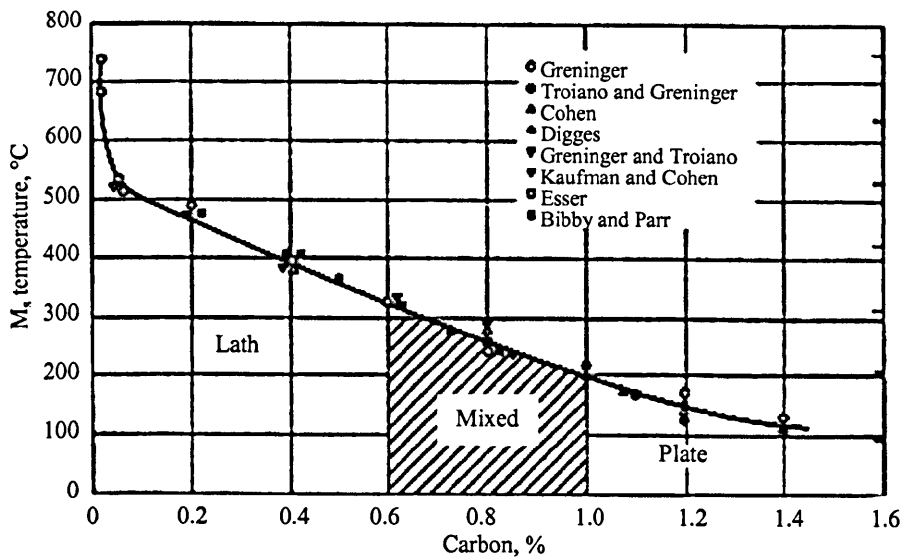


Figure 2.6: Martensite start temperatures as a function of carbon content and composition ranges of lath and plate martensite in a simple iron-carbon alloy. After Speich and Leslis ^[16].

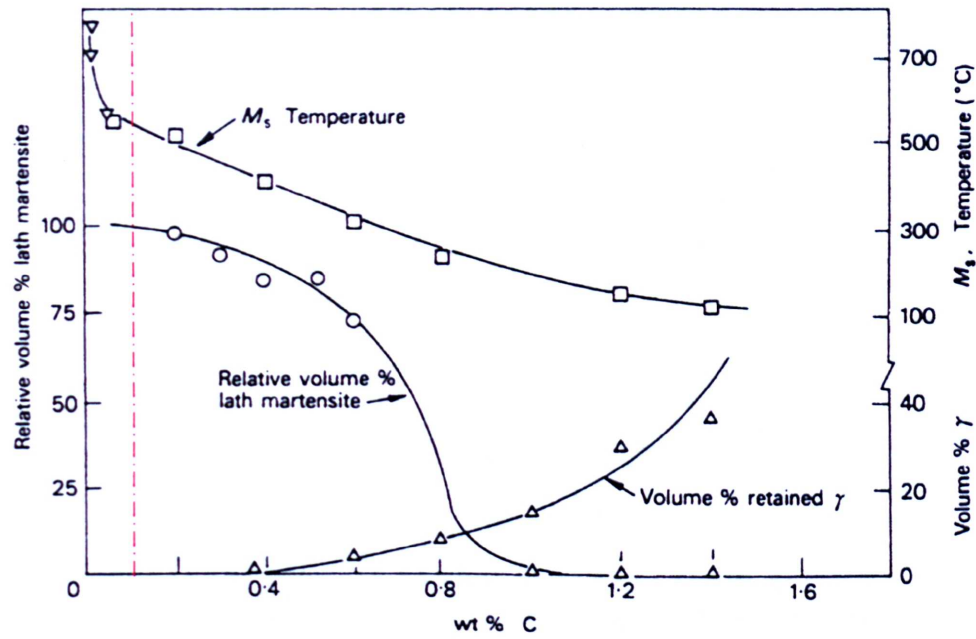


Figure 2.7: Effect of carbon content on the amount of retained austenite in Fe-C alloys. The red line indicates the approximate carbon content of P91 steel. It is shown that the possibility of finding retained austenite is low because the curve begins at ~0.4 wt.% C. After Honeycombe and Bhadeshia ^[13].

Other phases such as bainite and delta ferrite may also exist in P91 steel. However, these phases are rarely found following the typical heat treatments applied given to this class of alloys prior to service, due primarily to the very high hardenability associated with the high chromium concentration. 9-12 wt.% Cr steels are known to produce a fully martensitic structure even when the time interval for cooling between 800 and 500°C is as long as 3000 to 4000 seconds ^[19], which is illustrated in Figure 2.8.

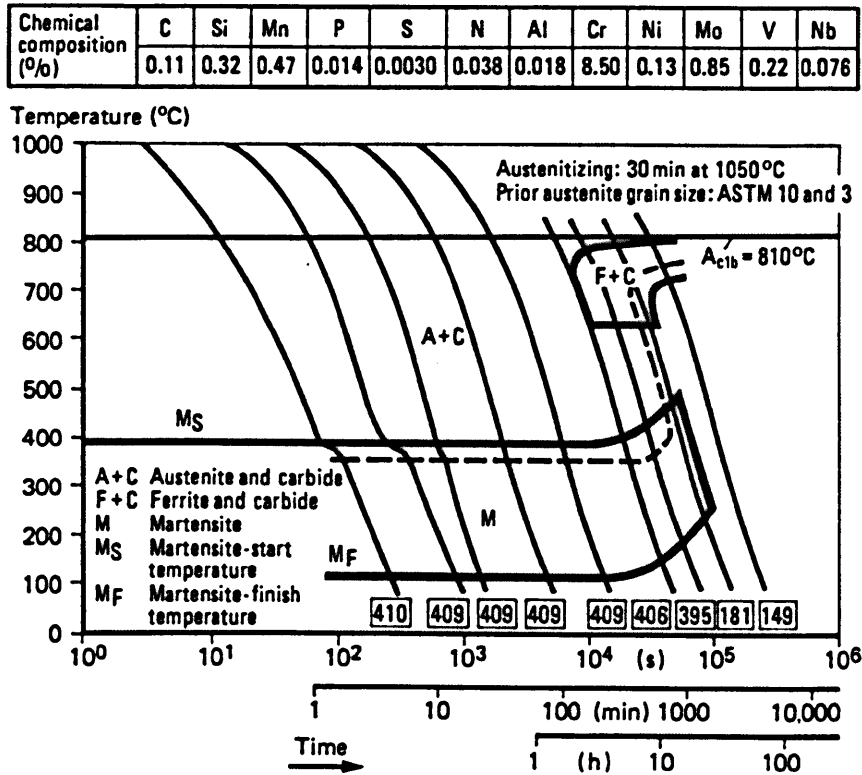


Figure 2.8: CCT diagram of a P91 steel sample. After Haarmann *et al* ^[8]

2.2.4 Alloying Additions

Table 2.1 shows the chemical composition range of grade 91 steel. Chromium is the major alloying element in this steel, which has several interesting effects. For instance, chromium greatly improves the hardenability of the steel to a point where 9-12 wt.% Cr steels become air hardenable to achieve a fully martensitic structure. It is a strong ferrite stabiliser, evident from Figure 2.3, and it is also a very strong carbide former, which encourages the strengthening of steels by precipitation hardening. It also forms the basis for the corrosion resistance of stainless steels, as it forms a protective oxide on the surface of steel, which self-repairs in the presence of oxygen if the steel is damaged mechanically or chemically, and thus retards the effects of high temperature oxidation and corrosion.

Grades		C	Mn	P	S	Si	Cr	Mo	V	Nb	N	Al	Ni
T/P91	Min.	0.08	0.30	-	-	0.20	8.00	0.85	0.18	0.06	0.03	-	-
	Max	0.12	0.60	0.02	0.01	0.50	9.50	1.05	0.25	0.10	0.07	0.04	0.4

Table 2.1: Composition range of P91 in weight %, the balance is Fe. Reproduced from Haarmann *et al*. ^[8].

Molybdenum is also a ferrite stabilizing element and carbide former. It increases the hardenability of steel and reduces the risk of temper embrittlement. It is present in 9-12 wt.% Cr steels primarily to increase strength by solid solution strengthening. Molybdenum also forms carbide precipitates that are stable at temperatures higher than those used in service and thus tends to yield a fine grain structure. Molybdenum is a favoured alloying element because it increases the strength at a relatively low cost ^[20].

Vanadium is one of the most widely used precipitation strengthening additives in steel, and like other microalloying elements, it has a strong affinity for carbon and nitrogen while at the same time it exhibits a high solubility in austenite at temperatures as high as 1150°C. This is important because it must remain in solution at normalizing temperatures, until it precipitates as carbonitride particles in during tempering, in order to maximise its contribution to precipitation strengthening. As it is a very expensive alloying element, its presence in the steel must be utilised effectively. Vanadium may precipitate as a carbide, a carbo-nitride or as a nitride, depending on the carbon and nitrogen concentration, and the heat treatment. Another important characteristic of vanadium is that its presence slows the rate at which grain growth occurs ^[21]. Vanadium is also a ferrite stabilizing element.

Niobium, in small quantities, can significantly increase the yield strength and, to a lesser degree, the tensile strength of carbon steel. This element can also have a moderate precipitation strengthening effect. Its main contributions are to form carbide precipitates above the transformation temperature, and to retard the recrystallization of austenite, thus promoting a fine-grain microstructure. Niobium is a ferrite stabilizing element.

Nitrogen is found in relatively high quantities and initially exists as an interstitial element like carbon. Its main purpose is to combine with certain elements such as vanadium and niobium to form nitrides, which strengthen the steel by precipitation hardening. Nitrogen is an austenite stabilizing element.

Nickel is also an austenite stabilizing element and, unlike the other metallic additions added to 9-12 wt.% Cr steels, it does not tend to form carbides. It suppresses the formation of δ -ferrite at the high normalizing temperatures employed. Strang and Vodarek ^[22] found that an increasing nickel content caused an increase in the coarsening rate of $M_{23}C_6$ particles in

12CrMoVNB steel. It was also found by the same authors that higher nickel contents favour the precipitation of Z-phase, to the detriment of fine MX precipitates.

Carbon, as previously discussed, occupies interstitial sites in ferrite and austenite, with a much greater solubility in the latter. Increasing the carbon content strongly encourages the precipitation of carbide phases. In general, the higher the content of carbon in steel, the more difficulties arise when it comes to welding as it tends to promote cracking in the heat affected zone region. This is an important issue for 9-12 wt.% Cr power plant steel components.

2.2.5 Carbide and Nitride Precipitates

Generally for steels, pure binary carbides do not tend to occur due to the fact that there is always some solubility of the alloying elements in the various carbide phases^[23], and in many cases, the degree of solubility of alloying elements can be very high indeed. Also, there are many sites in the microstructure where carbide nucleation and growth can occur. These include dislocations in the martensite matrix or intra-lath regions, lath boundaries, prior-austenite grain boundaries and even at pre-existing carbide particles (due to incomplete dissolution during normalizing), all of which are high energy sites that are energetically favourable for the formation of carbides, as they provide high diffusivity paths for the rapid diffusion of interstitial atoms such as carbon and nitrogen. Another peculiarity with carbides in steels is that they may not be thermodynamically stable^[24], and so are referred to as metastable. As a consequence, during the initial stages of tempering the first carbides to form are not necessarily the most stable or equilibrium carbide, as on further heating, these may be gradually replaced by more stable ones at higher temperatures either at the same location of the less stable carbide (In Situ) or separately away from the dissolving carbide^[23]. Table 2.2 shows the carbides in the Fe-Cr-C system.

Carbide	Structure	Lattice Parameters /Å	Formula Units /Cell	Density /gcm ⁻³
M ₃ C	Orthorhombic	a = 4.5241 b = 5.0883 c = 6.7416	4	7.704
M ₇ C ₃	Trigonal	a = 13.982 c = 4.506	8	6.965
M ₂₃ C ₆	Cubic F	a = 10.638	4	6.996
M ₆ C	Cubic F	a = 11.082	16	6.325
M ₂ X	Hexagonal	a = 3.002 c = 4.724	1	9.188

Table 2.2: Carbides in the Fe-Cr-C system. The composition of the metal portion, M, of the carbide is left unspecified. The density and the lattice parameter of each carbide will vary with respect to chemical composition. After Andrews *et al.* [25].

2.2.5.1 M₃C

M₃C in steel is better known as cementite or Fe₃C. It has an orthorhombic structure with lattice parameters of a = 0.4510 nm, b = 0.5040 nm and c = 0.6730 nm [23]. This precipitate is only present in the initial stages of tempering as it tends to form at low temperatures. Nutting [26] showed that carbon precipitates in the form of fine carbides, with a composition believed to be Fe_{2.4-2.8}C. These tend to have a Widmanstätten distribution, and are present in martensite laths as a result of auto-tempering in low alloy steels. On tempering in the range of 200-400°C, these become cementite precipitates which are found in the lath boundaries.

Jones *et al.* [27] found that air cooling P91 steel from a normalizing temperature of around 1045°C results in the precipitation of fine (Fe,Cr)₃C particles within the martensite laths. Kuo [23] argues that as chromium has a higher affinity for carbon than iron, this phase tends to be replaced by more stable ones at higher temperatures such as M₂C, M₇C₃ and M₂₃C₆. Chromium in steels tends to concentrate itself in Fe₃C in preference to ferrite and austenite. The solubility of chromium in cementite is fairly high at around 18 wt.% [23].

The dissolution of cementite occurs in two stages. Firstly, the concentration of Cr in Fe₃C proceeds until a saturation value of approximately 20 at.% is reached. Secondly, Fe₃C becomes replaced by Cr₇C₃ or Cr₂₃C₆, which is accompanied by a large increase of Cr in the carbide. Fe₃C is only usually present at temperatures of up to 500°C.

2.2.5.2 M_7C_3

M_7C_3 is a Cr-rich precipitate with a trigonal crystal structure with lattice parameters $a = 0.1398$ nm and $c = 0.4523$ nm, where iron can replace chromium in equilibrium with ferritic iron from 30 to 50 wt.% [28]. As mentioned previously, this phase gradually replaces M_3C at higher tempering temperatures due to the ready supply of chromium and carbon. Cr_7C_3 is formed by the reaction of M_3C with the matrix [23,28]. It must be noted that it is difficult to observe the presence of M_7C_3 in high chromium steels, because the precipitation kinetics of $M_{23}C_6$ formation are very fast. Therefore, in order to find a significant proportion of M_7C_3 the diffusion rates need to be slowed considerably. Beech and Warrington [28] are in favour of separate competitive nucleation for the M_7C_3 to $M_{23}C_6$ transformation as opposed to an *in situ* mechanism.

2.2.5.3 $M_{23}C_6$

$M_{23}C_6$ forms at higher tempering temperatures than M_7C_3 and was found by Kuo [23] to be the only carbide phase (out of Fe_3C and Cr_7C_3) to be present in a 12 wt.% Cr steel at tempering temperatures greater than 700°C. $M_{23}C_6$ precipitates have an fcc structure and may vary in chemical composition depending on the proportion of alloying elements in the steel, and are more commonly found in high chromium containing steels. These carbides contain Cr, although they may also contain Fe, V, Mo and Ni and require tempering temperatures in excess of 500°C in order to form [17].

$M_{23}C_6$ precipitates may contribute to an improvement in creep strength by the prevention of subgrain boundary motion, by impeding knitting reactions between free dislocations and subgrain boundaries, and also by pinning sub-boundary dislocations [15]. In addition to acting as pinning sites, $M_{23}C_6$ particles inhibit subgrain growth as they precipitate on martensite lath boundaries, prior austenite grain boundaries, and sub-boundaries (Figure 2.9).

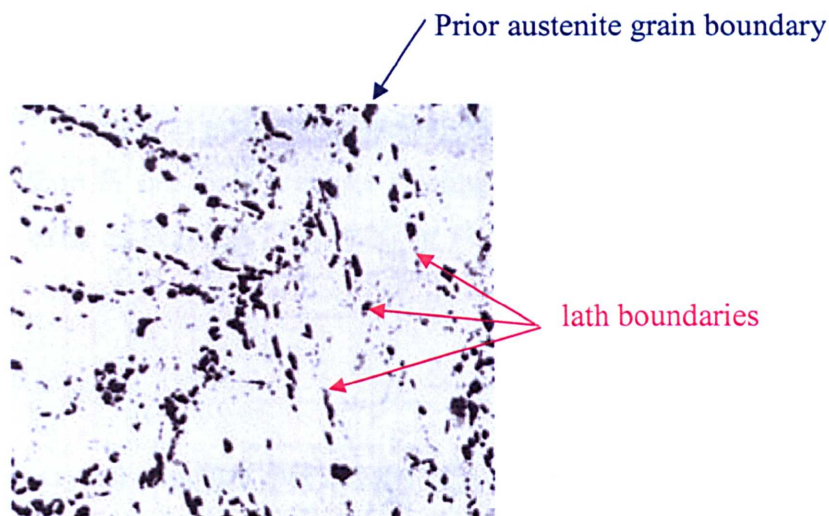


Figure 2.9: Bright field TEM micrograph of a carbon extraction replica of $M_{23}C_6$ precipitation at lath boundaries and prior austenite grain boundaries of steel 91 that was normalised at 1100°C followed by tempering at 750°C . After Orr *et al* ^[29].

The carbide does not form initially, but instead tends to replace less stable carbides such as M_2X and M_3C . Strang and Vodarek ^[22] have shown in their experiments on 12 wt.% Cr steels that with increasing high temperature exposure and creep strain, the coarsening of $M_{23}C_6$ precipitates occurs by Ostwald ripening. Therefore, as this process advances, the grain boundary pinning ability of these particles is reduced, which may reduce the mechanical integrity of high temperature power plant components in service. Indeed, the mobility of the lath interfaces is expected to increase as the coarsening and spheroidisation of the $M_{23}C_6$ particles proceeds, as these particles are primarily responsible for the pinning of lath boundaries ^[30]. A number of studies reveal that $M_{23}C_6$ carbides represent the majority of the dispersed phases situated in the subgrain boundaries ^[5].

2.2.5.4 M_2C

M_2C , or Mo_2C as it is commonly denoted, is a molybdenum-rich carbide with a close-packed hexagonal (cph) structure. It has a lattice parameter of $a = 3.002 \text{ \AA}$ and $c = 4.724 \text{ \AA}$ ^[25]. It is believed that the precipitation of this phase leads to a decrease in creep resistance, possibly because it removes molybdenum from within the subgrain regions, which would otherwise act as a solid solution strengthening element ^[30].

2.2.5.5 M_6C

Like M_2C , M_6C is an fcc structured carbide that has molybdenum-rich content. It has a lattice parameter of $a = 11.08 \text{ \AA}$ ^[23]. It tends to nucleate in ferrite grain boundaries, which would suggest that it does not transform *in situ* from previous existing carbides. Depending on the Mo content, the carbide can exist as Fe_4Mo_2C , Fe_2Mo_4C or Fe_3Mo_3C in a simple Fe-Mo-C ternary system ^[23,24].

2.2.5.6 MX

MX precipitates have an fcc crystal structure and consist of a complex mixture of carbide and/or nitride forming elements such as chromium, vanadium and niobium, which are denoted as “M”, and carbon and nitrogen denoted as “X”. Precipitation of MX particles occurs during tempering and is very important for the long-term creep strength of these steels, as MX particles tend to dissolve at much higher temperatures than those experienced under typical power plant operating conditions. These particles stabilise the subgrain boundary network and also impede knitting and absorption reactions, which involve free dislocations and subgrain boundaries ^[31].

Niobium and vanadium rich MX particles are known to exist in 9-12 wt.% Cr steels such as grade 91, but the chemical composition depends on the composition of the steel and the applied heat treatment cycles. MX precipitates are thus referred to as (V,Nb)(N,C). In its simplest form, MX particles can exist as VN and NbC. VN has a lattice parameter of $a = 0.4139 \text{ nm}$ (35-0768 in ICDD-JCPDS ^[32] catalogue) and NbC has a lattice parameter of $a = 0.4469 \text{ nm}$ (38-1364 in ICDD-JCPDS ^[32] catalogue). As well as forming during a typical pre-service tempering treatment, MX particles also tend to form during the exposure to service conditions, a phenomenon known as secondary precipitation ^[26].

The nitrogen content of the steel greatly affects the amount of vanadium that is precipitated ^[27]. This is very important because it correlates with a marked increase in creep rupture strength of 9-12 wt.% Cr steels. Tokuno *et al* ^[33] showed that the creep rupture strength was greater in a 9Cr steel with a high N content than another with a lower N content, as illustrated in Figure 2.10. The work of Zajac *et al* ^[34] on V-micro-alloyed steels has shown that an increase in N content results in finer VN precipitates with a smaller interparticle spacing. Taneike *et al* ^[35] have shown that MX particles tend to precipitate dispersed within the

martensite laths in high chromium steels. Orr and Di Gianfrancesco ^[36] stated that VN is probably the most important dispersion strengthening precipitate in grade 91 steel, as their results from creep strength experiments were greatly influenced by vanadium to nitrogen ratio, and the precipitation strengthening component was shown to optimise at a ratio approaching stoichiometry for VN (Figure 2.11).

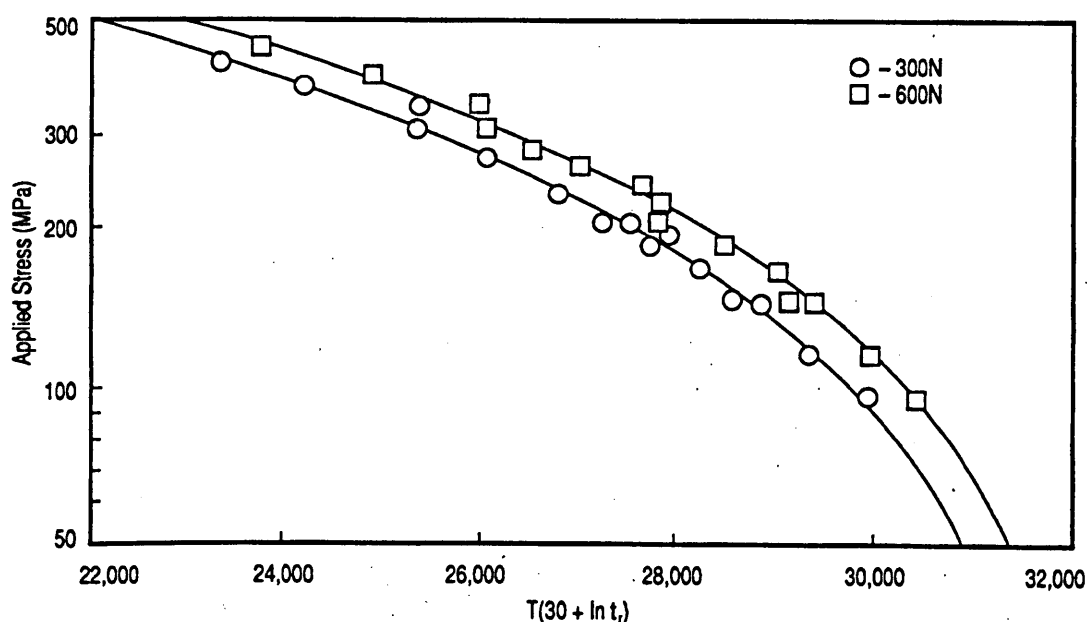


Figure 2.10: Relation between the creep rupture stresses and the parameters $T(30 + \ln t_r)$, of 9Cr-1Mo-Nb-V steels with 0.0593wt% N (600N) and 0.0312wt% N (300N). After Tokuno *et al.* ^[33].

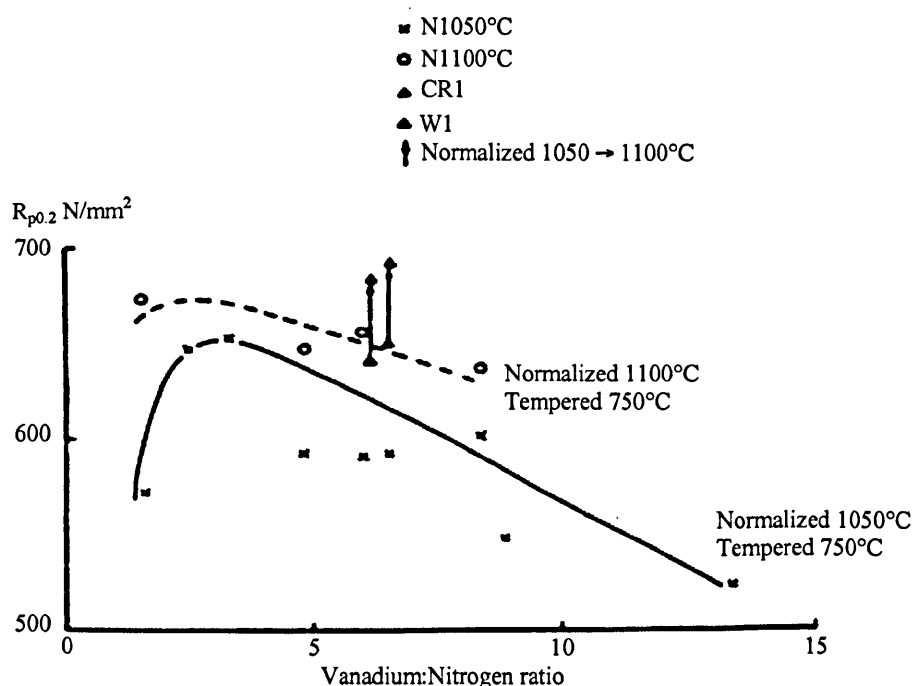


Figure 2.11: Relation between the Vanadium:Nitrogen ratio and the 0.2% proof stress of P91 steels. After Orr and Di Gianfrancesco ^[36].

Another aspect of MX carbonitrides, making them very effective against creep deformation, is that they tend to form complex irregular shaped particles, such that the local climb of dislocations may occur with more difficulty. These shapes include the formation of V-wings during tempering above 600°C, where plate-like vanadium carbonitride particles attach themselves to spherical Nb(C,N) particles. Examples of such particles were highlighted by the work of Tokuno *et al.* ^[37] and can be seen in Figure 2.12.

Hamada *et al.* ^[38] suggested that V-wing shaped precipitates have two main effects on the microstructure. The first of these being that these particles can restrain local climb from occurring, even in conditions where dislocation climb can occur over spherical precipitates. The second is that the probability of the trapping of dislocations at V-wings is larger than at spherical Nb(C,N) particles. Yamada *et al.* ^[39], however, reported that the adherence of VN to Nb(C,N) seems to be unfavourable to long-term creep resistance, because it decreases the distribution density of fine VN precipitates. Therefore, there is disagreement on the effect of such particles on the creep properties of 9-12 wt.% Cr steels.

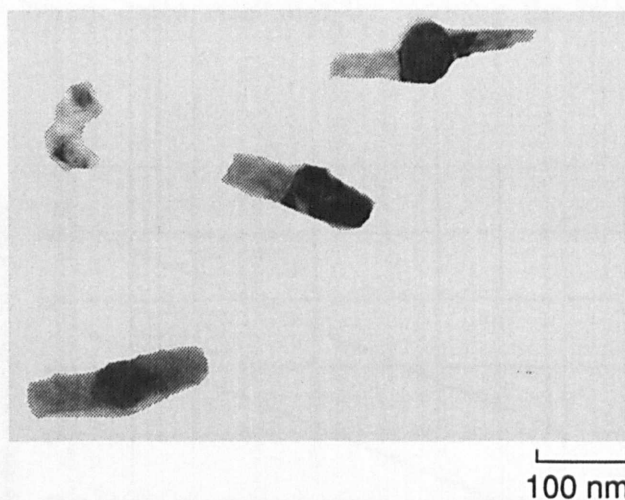


Figure 2.12: TEM images of V-wings in 9 wt.% Cr chromium steel showing a NbC core with VN ‘wings’. After Tokuno *et al.* ^[37].

Tamura *et al.* ^[40] reported an unusual re-dissolution of VN during tempering of a 0.0032%C-7.2%Cr-0.3%Mo-0.41%V-0.091%N-0.15%Si-0.51%Mn (units in wt.%) steel. According to the authors, VN particles precipitate on dislocations during the initial stages of tempering, which then dissolve temporarily causing a decrease in hardness. Interestingly, it was found that after additional tempering VN particles ultimately re-precipitate. Tempering was carried out between 740 and 800°C for up to a maximum time of 500 h, where it was found that the

amount of dissolved V reaches a peak after tempering for ~100 h. Typical 9-12 wt.% Cr steels such as P91 are tempered in this temperature range, nevertheless, the tempering time is much shorter (~2 h) and service temperatures rarely exceed 600°C, so this phenomena remains to be observed during typical service conditions.

2.2.5.7 AlN

Aluminium nitride is a phase that is also associated with 9-12 wt.% Cr steels. It may exist either as a hexagonal structure, $a = 0.311114$ nm and $c = 0.49792$ nm ([25-1133] in ICDD-JCPDS ^[32] catalogue), or a cubic structure, $a = 0.7913$ nm ([34-0697] in ICDD-JCPDS ^[32] catalogue). It has been suggested by various scholars that the presence of Al in these materials is detrimental for two main reasons. Firstly, it has been observed that AlN tends to precipitate as coarse particles, and secondly, because the available nitrogen might preferentially combine with aluminium at the expense of the V, which may reduce the volume fraction of VN precipitates which, as previously discussed, are important for the long term creep strength of the steel ^[41-43]. Indeed, Kubon and Foldyna ^[44] found that increasing aluminium contents in the steel considerably lowers creep resistance by reducing the level of nitrogen in solid solution (Figure 2.13).

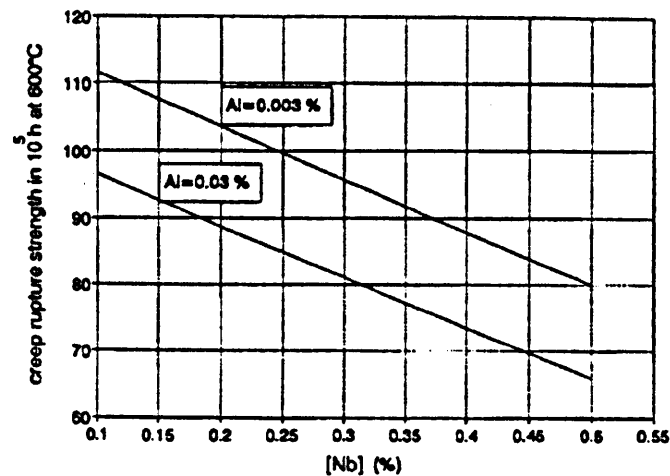


Figure 2.13: Graph showing the dependence of creep rupture strength of steel X19CrMoVNbN at 600°C for 100,000 h on the aluminium and niobium contents. After Kubon and Foldyna ^[44].

Michel *et al.* ^[45] found that the precipitation of AlN on dislocations during deformation leads to a significant increase in the peak strain, which according to the authors, is a measure of how effective a fine dispersion of such particles are at inhibiting recrystallization. They also reasoned that the rapid coarsening of these particles promotes rather than hinders

recrystallization. On the contrary, Cheng *et al.* [46] found that AlN precipitates inhibit grain growth in a low carbon steel because, even though they appear to coarsen rapidly during initial tempering, slow coarsening occurs during further aging.

AlN apparently tends to be present in grain boundaries [46] and has been proven to refine the grain structure of P91 steel [47-48]. Contrary to belief that a fine grain structure improves the mechanical properties of steel, Naoi *et al.* [42] argued that the main strengthening method of 9Cr steels was by precipitation hardening. As a result, it was postulated that finer grains meant that more precipitates were located at the grain boundaries, which resulted in the presence of fewer intragranular precipitates. As a consequence, lower tensile strength values were achieved. Figure 2.14 shows the typical form of an aluminium-rich particle found in 9Cr steels.

It has been demonstrated that AlN in steel can assume various shapes, including dendritic, large plates, rods, needles, rectangles/cuboids and/or prismatic shapes depending on the heat treatment and processing conditions applied to the steel [47]. According to Yamanaka and Ohmori [48], the preferential growth of AlN occurs along the direction $[0001]\text{AlN} // [-110]\gamma\text{-Fe}$, where the degree of misfit between the AlN and austenite is very small.

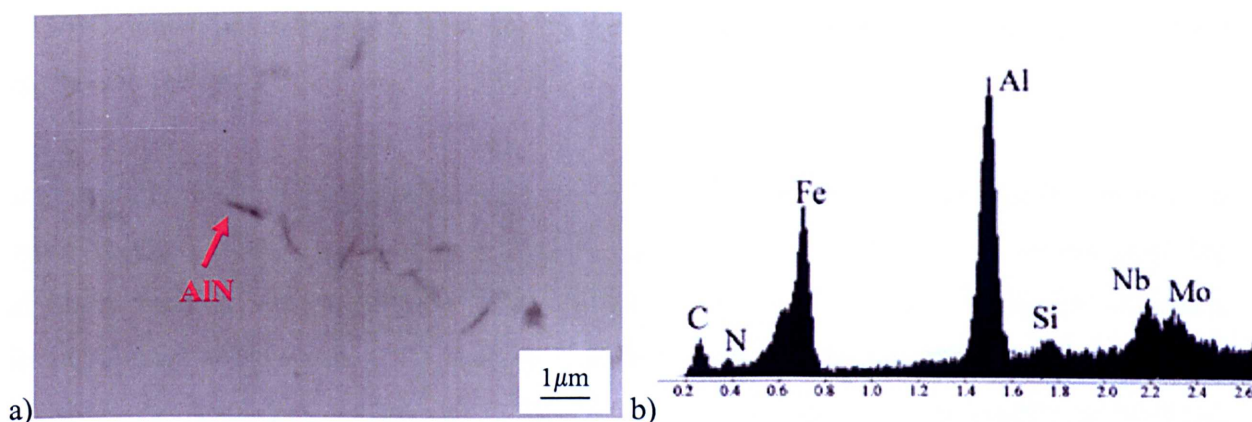


Figure 2.14: a) Backscattered SEM image from a P91 steel showing darkly imaging particles with an Al-rich signature and b) a typical EDX spectra detected in the SEM from an Al-rich particle. After Brett *et al.* [41].

It was found by Edwards [49], who used Auger electron spectroscopy, that one of the likely reasons why AlN nucleates easily is that aluminium, nitrogen and silicon show significant segregation to austenite grain boundaries. AlN can nucleate on dislocation substructures, austenite grain boundaries and second-phase particles [47]. Hall and Bennett [50] observed that significant grain coarsening occurred above 1050°C in steels containing Fe-0.4C-0.8Mn with

varying Al and N contents, which corresponded with the AlN solution temperature. They found that on heating above this temperature, the diminishing fraction of fine particles accompanies an agglomeration process, which cause a few large AlN particles to be present at the grain boundaries, but which do not satisfy the Zener criterion (Figure 2.15).

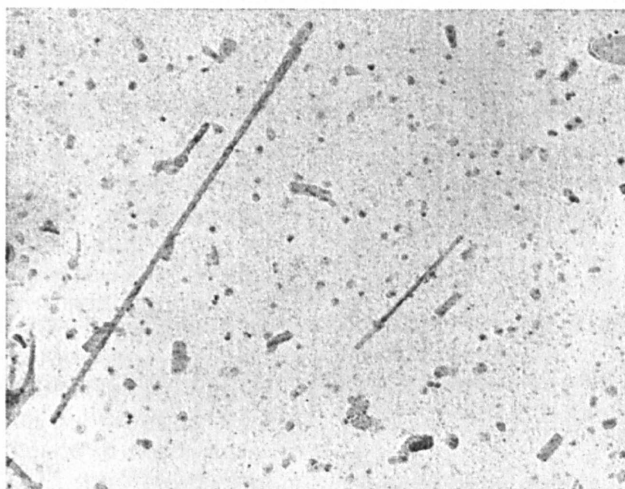


Figure 2.15: Carbon extraction replica image showing large, needle-like AlN particles which have coarsened during a solution treatment above 1050°C. The steel composition was Fe-0.4C-0.8Mn (wt.%), the Al and N content are unreported. After Hall and Bennett ^[50].

Another important characteristic of AlN is that it can be stable at high temperatures. Cheng *et al.* ^[46] reported that AlN precipitates in a low carbon steel do not completely dissolve below 1150°C, which is much higher than the standard normalizing temperatures applied to high Cr steels (see section 2.3.1).

Interestingly, aluminium nitride precipitates have been observed to form duplex precipitates with Nb(C,N) in low carbon micro-alloyed steels. Leap and Brown ^[51] investigated the crystallography of duplex AlN-Nb(C,N) precipitates in a 0.21%C-0.04%Nb-0.028%Al (units in wt.%) steel and found that there exists a high-energy incoherent interface between the two components. According to the authors, this is an indication that the precipitation of Nb(C,N) particles is heterogeneous and occurs on pre-existing AlN particles in such steels. Another interesting finding was that Nb(C,N) precipitation on AlN is controlled by the spatial orientation of these pre-existing AlN particles in the steel matrix. Therefore, in order for this duplex precipitate to form, the AlN precipitate must be oriented such that the interfacial energy between the two precipitates is lower than that of AlN and the matrix, whilst at the same time Nb(C,N) maintains an orientation relationship with the matrix, which in principle would restrict the number of Nb(C,N) precipitates found attached to AlN precipitates.

2.2.5.8 Z-phase

Z-phase is a precipitate that is frequently detected in stainless steels that contain both niobium and nitrogen. It has a tetragonal unit cell of $a = 6.784 \text{ \AA}$, $c = 7.387 \text{ \AA}$, as illustrated in Figure 2.16a), with a chemical composition of $(\text{Cr, Fe, Mn})_8 (\text{Nb, Mo})_6 \text{N}_6$ [52]. A study by Strang and Vodarek [52] showed that after long-term exposure of a 12 wt.% Cr-Mo-V-Nb steel at 600°C , a modified Z-phase was the equilibrium nitride phase in the steel. This precipitate was found to form at the expense of fine $(\text{V,Nb})\text{X}$, M_2X and primary NbX precipitates. It is believed that the progressive dissolution of $(\text{V,Nb})\text{X}$ and primary NbX , in addition to the corresponding reduction in creep rupture strength as a function of time, are directly related to the precipitation of this phase [53-55]. Figure 2.16b) shows a micrograph of a coarse Z-phase precipitate. The formation of Z-Phase was observed by Sawada *et al.* [53] to accelerate when the nitrogen content increases in low carbon bearing 9Cr-3W-MoVNb steel.

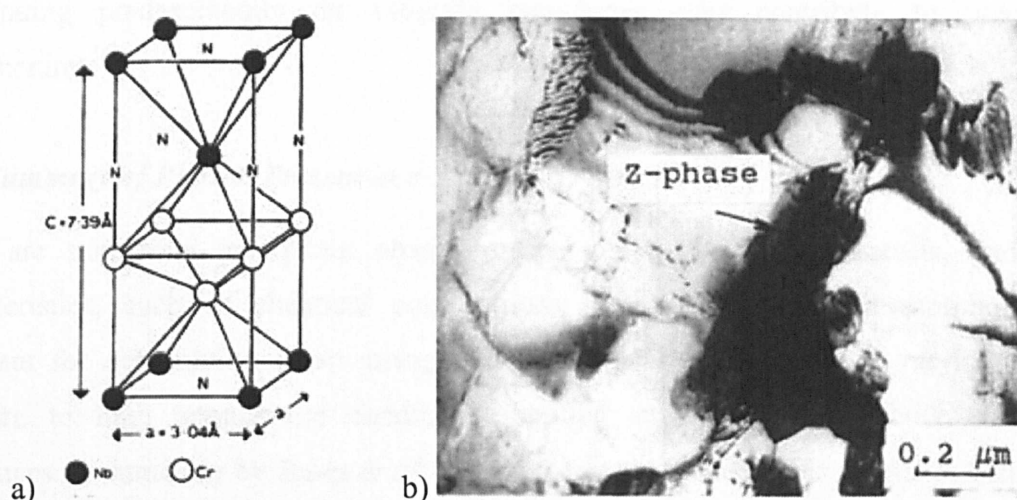


Figure 2.16: a) Structure of Z phase. After Jack and Jack [55]. b) Thin-foil micrograph showing a modified Z phase particle in a 12CrMoVNb steels after 30 800 h at 600°C . After Strang and Vodarek [55].

2.2.5.9 Laves Phase

Laves phase is an intermediate intermetallic phase that has been found to precipitate most commonly in prior-austenite and subgrain boundaries, and also in the vicinity of Cr-rich M_{23}C_6 precipitates [56,57]. It has the general composition of Fe_2M , where the “M” portion can be either molybdenum, tungsten or both. It is apparent that Laves phase tends to form during high temperature creep conditions, such as those experienced in service, and has been observed to reach up to 1,000 nm in size [2,3,58]. Dimmler *et al.* [56] found that Laves-phase precipitates appear to both nucleate and grow very quickly during the first 2,000 h, and on further high temperature exposure, the equivalent diameter stabilises. Interestingly, it has been

observed that no significant differences are seen when comparing the size of Laves particles in aged (unstressed) and the size in crept (stressed) high chromium steels ^[56]. Ryu *et al* ^[59] found that the precipitation of Laves phase in a P92 steel is reduced by 20% on increasing the carbon content from 0.1 to 0.2 wt.%. However, 0.2 wt.% C exceeds the chemical composition range for these steels. Other elements that have been reported to affect Laves phase precipitation are nickel and silicon.

Laves phase can have either a beneficial or detrimental effect on the creep rupture properties of ferritic heat resistant steels ^[44,59]. On the one hand, it can be interpreted as being detrimental because the formation of Laves phase draws out elements such as Mo and W, which are effective solid solution strengtheners, from the lattice. This acts as a softening process, and Laves phase particles tend to be large and widely spaced which can make them too weak to offset the softening process ^[60]. On the other hand, small particles of $\text{Fe}_2(\text{Mo},\text{W})$ precipitating predominantly on subgrain boundaries may contribute to precipitation strengthening ^[44].

2.2.6 Summary of Phases Present in 9-12 wt.% Cr Steels

There are numerous precipitate phases present in 9-12 wt.% Cr steels, and certain characteristics, such as chemical composition, size, distribution and morphology, are important for determining creep strength, are very much dependent on varying levels of exposure to high temperature conditions, applied stress and minor bulk composition differences. A summary by Jones *et al.* ^[27] states that the first carbide phases to form during the tempering of martensite in high Cr steels are not usually the equilibrium carbides, but primarily those that can form without extensive diffusion of the substitutional alloy elements. Hence, the constant evolution of the microstructure of 9-12 wt.% Cr steels occurs during elevated temperature service conditions as the phases reach their equilibrium state. A summary of the precipitates found in high-Cr creep resistant steels and the stages of thermal history at which they form are shown in Table 2.3.

Steel	Precipitate	Formula	Remark
X22	$M_{23}C_6$	$(Cr,Fe,Mo)_{23}C_6$	Precipitates during tempering
P91	$M_{23}C_6$	$(Cr,Fe,Mo)_{23}C_6$	Precipitates during tempering
	MX	$(Nb,V)(C,N)$	Undissolved during normalizing
	MX	$(V,Nb)(N,C)$	Precipitates during tempering
	Laves Phase	$(Fe,Cr)_2Mo$	Precipitates during creep ($T < 650^\circ C$)
P92	$M_{23}C_6$	$(Cr,Fe,Mo)_{23}C_6$	Precipitates during tempering
	MX	$(Nb,V)(C,N)$	Undissolved during normalizing
	MX	$(V,Nb)(N,C)$	Precipitates during tempering
	Laves Phase	$(Fe,Cr)_2(Mo,W)$	Precipitates during creep ($T < 720^\circ C$)

Table 2.3: Precipitates found in 9-12% Cr steels and remarks on their formation characteristics. After Hald *et al.* [61].

2.3 Typical Heat Treatments

9-12 wt.% Cr steel components for use in high temperature power plant applications can be produced as castings or forgings. After these initial forming processes, such steels are typically subjected to a two-stage heat treatment cycle in order to optimise creep strength. The two stage process involves a normalizing treatment followed by rapid cooling to martensite, and a subsequent tempering treatment. Heat treatment process variables such as temperature and duration can have an important influence on the microstructure of 9-12 wt.% Cr steels. These are described in the following sections.

2.3.1 Normalizing

The normalizing treatment is applied in order to dissolve all of the precipitates that are present in the matrix from prior forming operations, and also to produce a fully hardened martensitic structure, which is usually achieved by air cooling. The high hardenability of this class of alloys, as a result of the high chromium and molybdenum content, allow this microstructure to be achieved. Normalizing is carried out above the A_{c3} temperature, which for P91 steel can range between $890^\circ C$ and $940^\circ C$ [8]. The suggested normalizing temperature has been established by many authors to be approximately between 1050 and $1100^\circ C$ [29,36,62]. After air-cooling, a hardness range of 400 HV to 420 HV is expected [29]. Depending on the precise composition of the steel and the normalizing temperature, the structure may also comprise of varying proportions of retained austenite, undissolved carbides and δ -ferrite. The latter two may cause fluctuations in the prior austenite grain size and may also result in the partitioning of alloying elements between these phases [10]. In addition, the cooling cycle from the solution heat treatment may affect minor phase precipitation. Indeed, cooling commonly produces evidence of Fe_3C precipitation, which is a result of auto-tempering [63].

The resulting microstructure that is produced from normalizing is very sensitive to temperature, and in turn, both under- and over-normalizing can drastically affect the creep properties, and indeed the useful service life of power plant components. It has been shown by Orr and Burton ^[62] that increasing the normalizing temperature from 1050 to 1100°C results in a 10-15% increase in strength. It was concluded that this increase was a result of the increased degree of carbide and nitride dissolution at the higher temperature. Figure 2.17 shows how the normalizing temperature affects the as-tempered hardness. Under-normalizing can result in precipitates not dissolving, which may have detrimental effects on the creep behaviour of the steel in service, such as shorter life in service. The effects of under-normalizing are difficult to detect, as they are not easily distinguishable in the hardness values or the microstructure of the as-normalized sample.

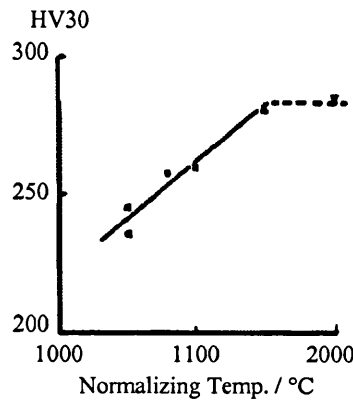


Figure 2.17: As-tempered (1h/750°C) hardness as a function of normalizing temperature. After Orr and Burton ^[62]

Over normalizing can also have a detrimental effect on the mechanical properties of the steel as it may result in grain growth, heterogeneous grain sizes and the formation of delta ferrite, which are considered unacceptable for pressure vessel steels ^[4]. The effects of over-normalizing are thus very easy to detect using an optical microscope. Grain growth occurs more slowly in V and Nb strengthened 9-12 wt.% Cr steel alloys due to the effectiveness of the fine MX particles at inhibiting this process.

Results from Pickering and Vassiliou's work ^[64] on the effect of normalizing temperature on the constitution, hardness and prior-austenite grain size of 9Cr-1Mo steel are summarised in Table 2.4. It is shown that the grain size increases with temperature, but at 1200°C the average grain size decreases slightly, due to 35% of the microstructure containing δ -ferrite. A

similar study undertaken by Borggreen ^[65] on P91 steel revealed that the relationship between ASTM grain size and normalizing temperature is almost linear (Figure 2.18). The normalizing temperature has also been found to affect the width of martensite laths. Ennis *et al.* ^[2] showed in their experiment on P92 steel that normalizing temperatures of 970°C, 1070°C and 1145°C produced lath widths of 0.38 μm , 0.42 μm and 0.58 μm respectively.

Solution-treatment temperature / °C	Water-quenched hardness / HV	Austenite grain size / μm	Constitution at solution temperature	Ferrite (α or δ) content
800	302	10	$\alpha + \gamma + \text{M}_{23}\text{C}_6$	75%
850	408	10	$\alpha + \gamma + \text{M}_{23}\text{C}_6$	25%
900	440	18	$\alpha + \gamma + \text{M}_{23}\text{C}_6$	Trace α
950	459	27	$\gamma + \text{M}_{23}\text{C}_6$	0%
1000	480	30	$\gamma + \text{M}_{23}\text{C}_6$	0%
1050	470	52	γ	0%
1100	461	80	γ	0%
1150	415	120	γ	0%
1200	420	85	$\gamma + \delta$	35% δ
1280	305	75	$\gamma + \delta$	45% δ
1320	350	Fully ferritic	δ	100% δ
1380	370	Fully ferritic	δ	100% δ

Table 2.4: Effect of solution-treatment temperature on constitution, hardness, and austenite grain size of 9Cr-1Mo steel. After Pickering and Vassiliou ^[65].

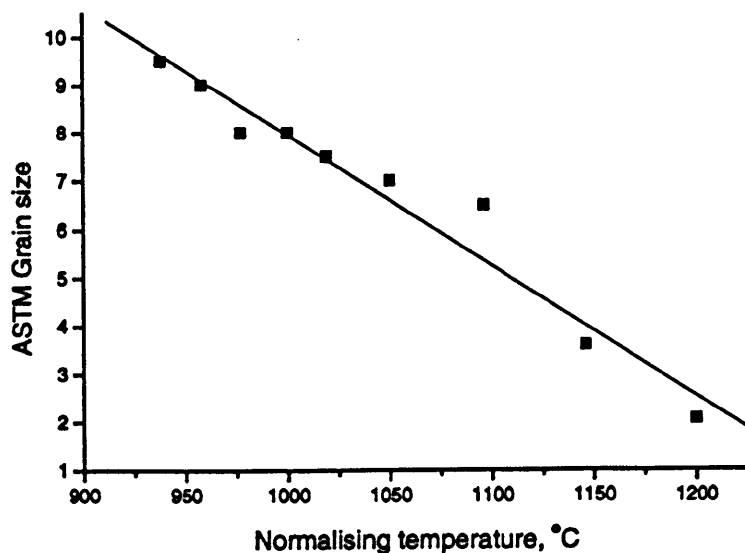


Figure 2.18: Effect of normalizing temperature on the ASTM grain size of P91 steel. After Borggreen ^[66]. Note that a decreasing value of ASTM grain size indicates an increase in grain diameter.

The cooling rate from the normalizing temperature may also affect the microstructure and properties of 9-12 wt.% Cr steels. Yamada *et al.* ^[66] studied the effects of cooling rate on the creep properties of 9CrW steels and found that both creep rate and creep strain are smaller in quenched and tempered steels than for air-cooled and tempered steels (Figure 2.19). This was

attributed to the fact that the rapid formation of Nb(C,N) during cooling was suppressed at the faster cooling rate (quenched), thus, this precipitate did not become a preferential nucleation site for fine VN, which would otherwise result in a coarse complex MX particle such as V-wings. Therefore, a finer distribution of MX particles can be expected by cooling at faster rates. The precipitation of AlN in steel has also been found to be suppressed by applying more rapid cooling rates ^[47].

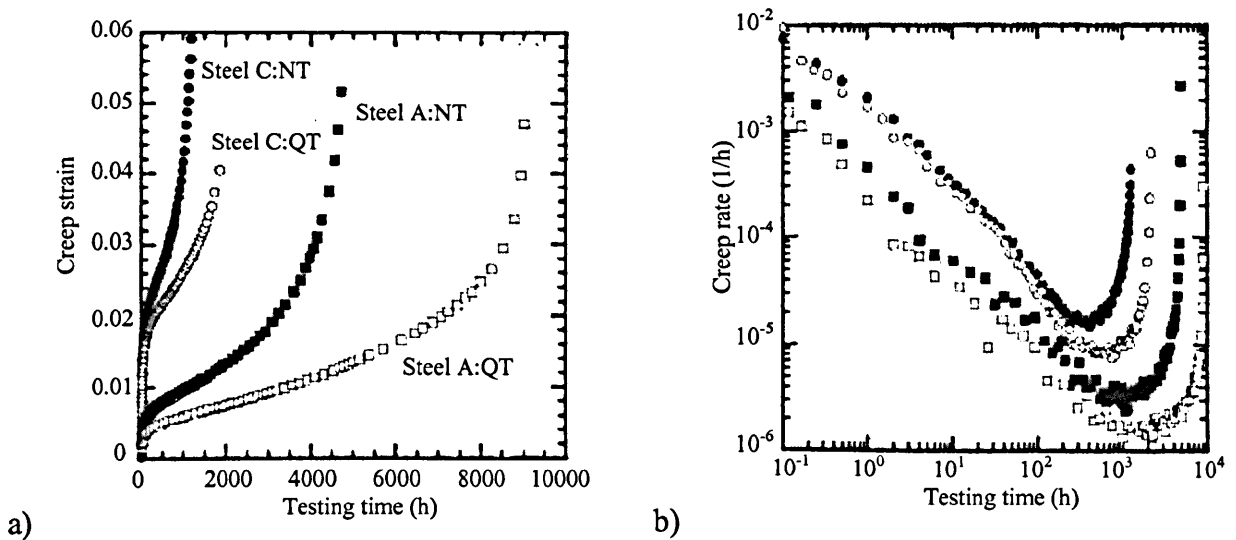


Figure 2.19: Changes in the a) the creep strain and b) the creep rate with respect to time at 923K and 120MPa for air-cooled and tempered and quenched and tempered steels. After Yamada *et al.* ^[66]. NT represents the steel that was air cooled from the normalizing heat treatment and QT represents the steel that was quenched from the normalizing treatment.

2.3.2 Tempering

Tempering is the second stage of the heat treatment cycle and similar to normalizing, the microstructure of the steel is very sensitive to the temperature at which it is carried out. This process has two main functions. The first is to relieve internal residual stresses that are present in the material by diffusing out the carbon that is trapped in a super saturated solid solution in the iron matrix, which improves the ductility and toughness of the steel. The second function is to promote the precipitation of carbide and nitride particles with alloying elements such as chromium, vanadium and niobium.

9-12 wt.% Cr steels are typically reheated to a recommended temperature of approximately 750-800°C ^[8,29,62] in order to promote precipitation strengthening. As virgin martensite is reheated, the carbon that was supersaturated in the lattice diffuses and forms carbides that are thermodynamically more stable than cementite ^[4]. Cementite forms and coarsens at

comparatively low tempering temperatures. Between the temperature range of 500-700°C carbide forming elements such as Cr, V, Nb and Mo that form fine particles that eventually replace the thermodynamically less stable cementite particles.

The result of the tempering process is the formation of a tempered martensitic structure, barely recognisable to the as-normalized microstructure, which is strengthened by $M_{23}C_6$ carbides present at the lath and grain boundaries and also by niobium and vanadium rich carbonitrides that tend to precipitate within the laths and subgrains ^[27,36], along with a high density of dislocations within the subgrains. A typical microstructure of a tempered 9 wt.% Cr steel illustrating these features is shown in Figure 2.20.

Orr and Burton ^[62] found that tempering P91 at temperatures greater than 800°C produces a hardness reversion (Figure 2.21), due to the relatively low A_{c1} temperature of this type of steel that may have caused the retransformation and hardening of the martensitic microstructure. Indeed, Haarmann *et al.* ^[8] state that the A_{c1} temperature of P91 can vary from 800-830°C, hence the retransformation of martensite above this temperature is plausible.

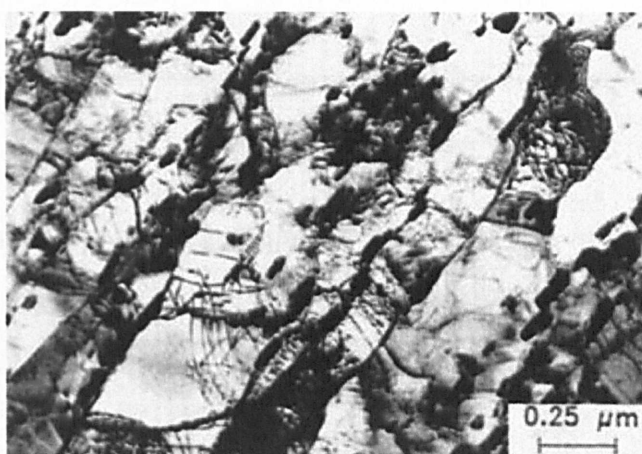


Figure 2.20: Bright Field TEM micrograph of a thin foil illustrating the typical microstructure of tempered martensite in a 9 wt.% Cr steel. A high number of carbides are shown to be present predominantly on the martensite lath boundaries. A high dislocation density is also shown within the subgrains. After Ennis *et al.* ^[2].

Ennis *et al.* ^[2] found that increasing the tempering temperature of P92 steel between the range of 750-800°C leads to enhanced martensite recovery processes, which decreases the dislocation density and reduces the creep rupture strength. Orr *et al.* ^[29] show that varying tempering times also has a significant effect on the properties of P91 steel (Figure 2.22). However, the authors commented that the toughness of P91 is high even at tempering times as

short as one hour. Therefore, they speculate that the preferred tempering procedure is to restrict it to short tempering times so that the maximum strength levels can be maximised. This is in agreement with results reported by Jones *et al.* [27], who also investigated the effect of tempering times on the microstructure of P91 steel. They found that when tempered at 760°C, 9Cr-1Mo steel exhibited a more severe degree of rearrangement of transformation dislocations and the initiation of martensite lath break-up with the increase in tempering time from 16 minutes up to 1 hour.

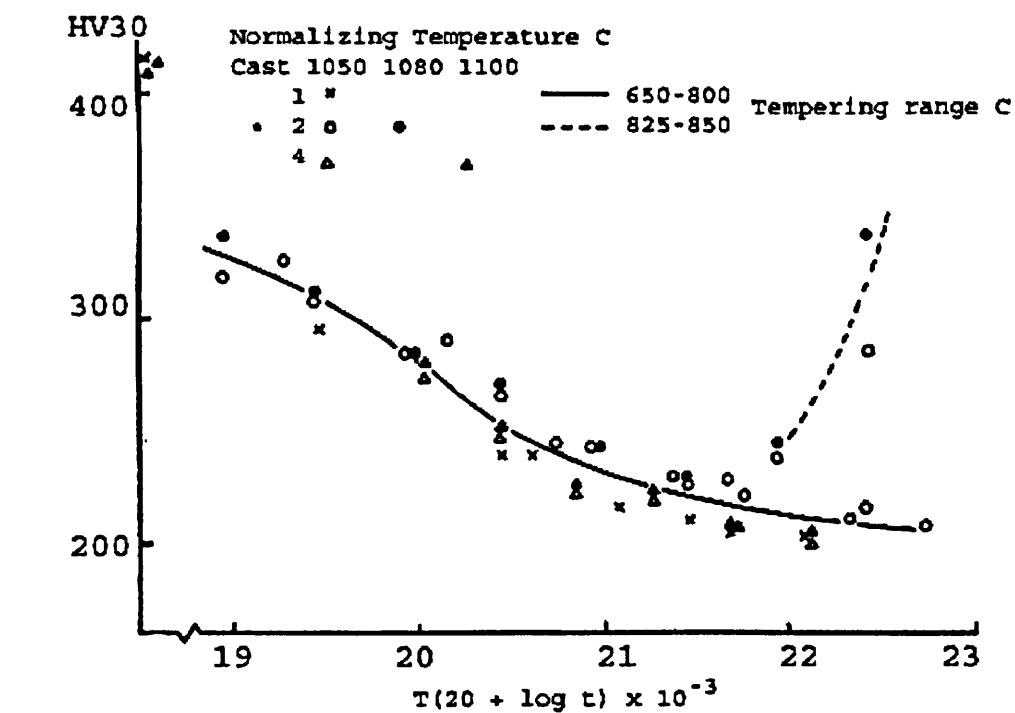


Figure 2.21: Graph illustrating the tempering curve data for steel 91. After Orr and Burton [62].

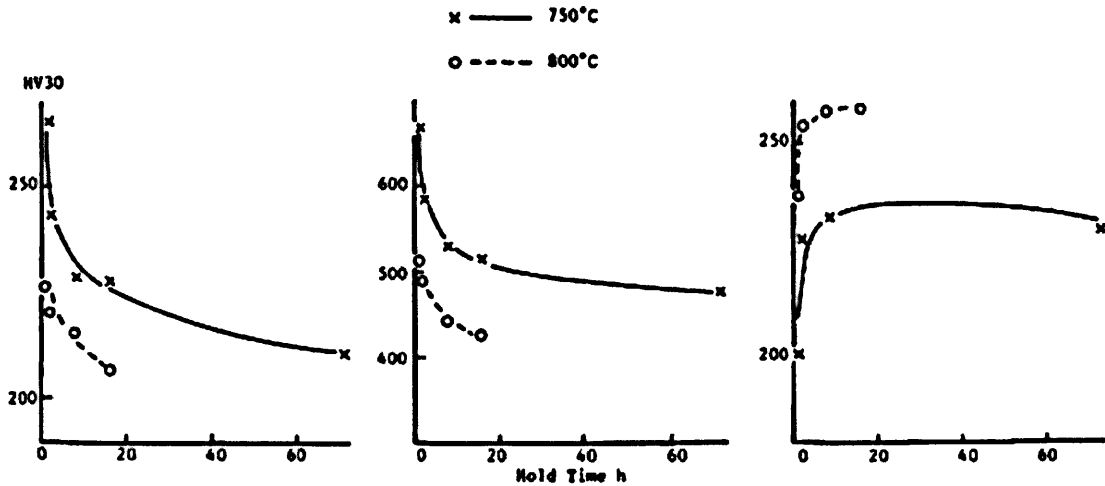


Figure 2.22: Graph illustrating the effect of tempering time on a selection of mechanical properties: a) hardness (HV30), b) 0.2% proof stress (N/mm²) and c) Charpy impact (J). After Orr *et al.* [29].

2.3.3 Summary of the Pre-service Heat Treatments Applied to 9-12 wt.% Cr Steels

9-12 wt.% Cr steels have been shown to be very sensitive to pre-service heat treatments, which are applied to control important factors such as grain size, to ensure the homogeneity of the microstructure, to achieve an adequate hardness and also to ensure the fine distribution of small creep-resisting second-phase particles.

2.4 Microstructural Evolution During Long-term Aging and Creep

The microstructure of high chromium ferritic steels is very complex, as its formation can be strongly influenced by slight adjustments of various parameters, such as pre-service heat treatments and minor composition differences. For example, it has been shown in the previous section that microstructural parameters such as lath width, grain size, particle identity and distribution, and the dislocation structure can all change with respect to applying different heat treatment parameters. In this section, the effects of long-term aging and stress on the microstructure evolution of high chromium steels will be reviewed.

The microstructural stability of 9-12 wt.% Cr ferritic-martensitic steels is the key factor that needs to be understood in order to predict the remaining lifetime of such safety critical and reliability dependent components as high temperature tubing in power plant applications. It is, therefore, necessary to have a fundamental understanding of the conditions that are encountered by these materials in service, such as varying operating temperature, time at temperature and stress.

Numerous studies have investigated the effects of prolonged aging and creep in order to quantify microstructural evolution, by methods such as lath width measurement, particle size distribution and interparticle spacing, and the presence of deleterious phases with respect to changes in the aforementioned parameters. A review of each of these aspects will follow. The effects of deleterious phases have already been discussed in section 2.2.5.

2.4.1 Lath/Subgrain Size and Shape

It has often been found that during creep testing, the subgrains in the gauge (stressed) portion of a creep specimen coarsen significantly compared to those observed in the head (unstressed) portion with respect to the initial pre-service microstructure^[67,68]. Qin *et al.*^[69] have claimed

that the coarsening of subgrains is negligible during annealing. Figure 2.23 shows the change in mean lath width of martensite during creep and during unstressed aging.

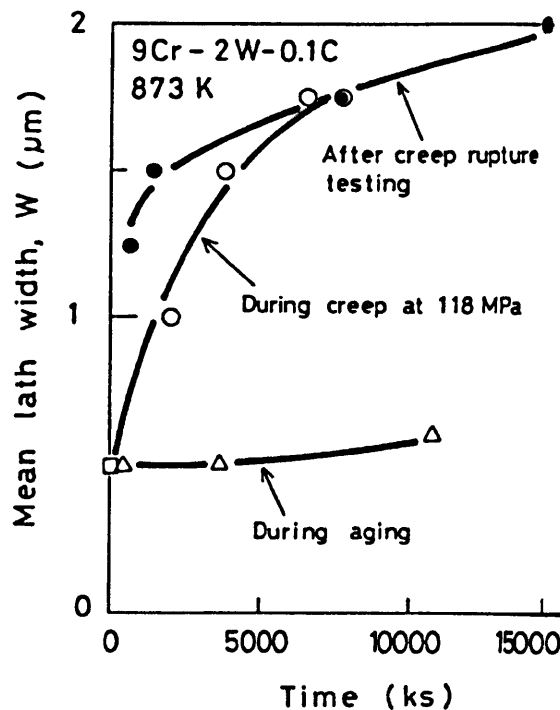


Figure 2.23: Change in mean width of martensite lath during creep at 118MPa, after creep rupture testing, and during aging. The test temperature is 873K. After Abe *et al.* [70].

Another factor that appears to be closely related to the increase of subgrain size is the coarsening of $M_{23}C_6$ particles that are present on the lath and prior austenite grain boundaries. These particles are believed to act as pinning points for subgrain boundaries [15,71]. Indeed, recrystallization was found to be hindered in higher carbon martensites because the pinning action of a higher density of cementite particles, in an Fe-C system, prevents the migration of high angle boundaries required for recrystallization [17]. It is not entirely certain whether particle coarsening is the cause of subgrain growth. However, Cerri *et al.* [15] observed some subgrain boundaries to disappear as subgrains grow, which left some of the particles that generally try to pin down subgrain boundaries in the subgrain interior. As a consequence, the fraction of $M_{23}C_6$ carbides attached to the grain boundaries may decrease during creep.

One possible explanation for the occurrence of these phenomena being more pronounced in conditions of applied stress has been offered by Eggeler [31]. He reasoned that higher densities of subgrain boundary dislocations can be expected to be maintained when a stress (creep) is present as compared to the absence of a stress (aging). This can then be related to higher

effective subgrain boundary pipe diffusion fluxes, which can result in faster particle coarsening during long-term creep compared to long-term aging ^[31]. This concurs with the work of Hattestrand and Andren ^[72], who reported the strain accelerated coarsening of $M_{23}C_6$ particles in 9 wt.% Cr steels. In addition, Spigarelli *et al.* ^[73] found that the subgrain size, or the degradation of the microstructure expressed in terms of recovery of the initial high dislocation density, can be directly related to coarsening of the strengthening secondary phases, in this case $M_{23}C_6$ particles found on subgrain boundaries (Figure 2.24). Correspondingly, Orlova *et al.* ^[68] have shown that the number of particles per subgrain can have an inverse correlation with the creep rate (Figure 2.25).

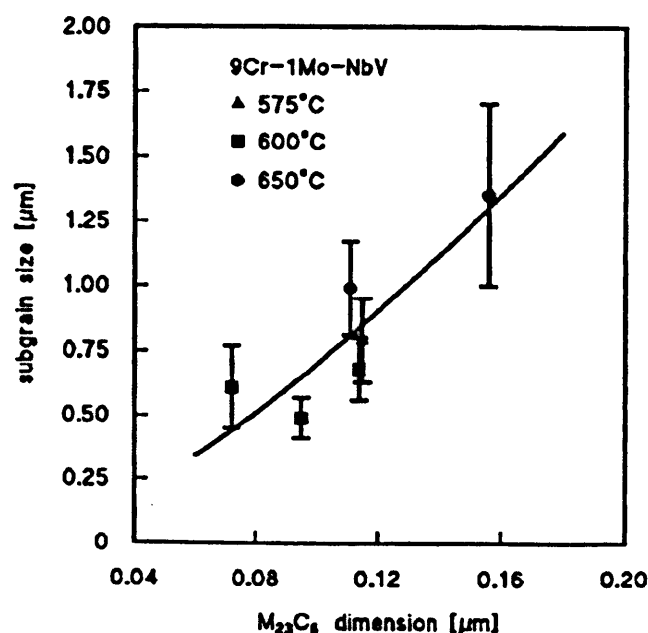


Figure 2.24: Relationship between interparticle spacing and subgrain size under different testing conditions. After Spigarelli *et al.* ^[73].

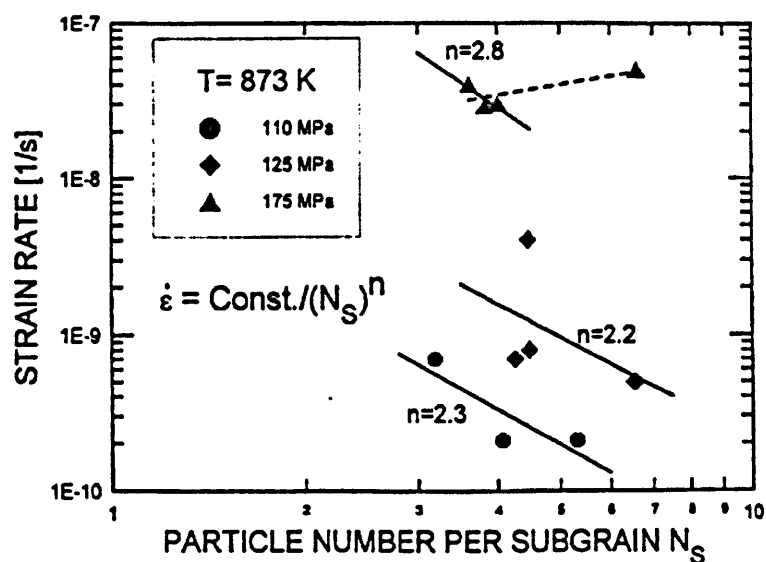


Figure 2.25: Correlation of strain rate with particle number per subgrain. After Orlova *et al.* ^[68].

A dispersion of particles will exert a force on a boundary which could have a profound effect on coarsening processes, because once a boundary has intersected with a particle, some of the boundary area is removed from the system. Therefore, in order for the particle and the boundary to separate, the removed area must be recreated and this requires an increase in energy ^[74]. This effect is known as Zener drag. The Zener pinning pressure (P_z) i.e. the pinning pressure exerted by boundary particles on the unit area of a grain boundary is given by:

$$P_z = 3f_v\gamma_s/2r \quad [2.1]$$

where f_v is the volume fraction of randomly distributed spherical particles of radius r and γ_s is the boundary energy. The driving force (P_D) for subgrain growth exists when there is a stored energy loss as subgrain growth occurs.

$$P_D = \alpha \gamma_s / R \quad [2.2]$$

Where α is a shape factor and R is the radius of the subgrains. Therefore, grain growth will ideally halt when the driving force for grain growth equals the Zener pinning pressure.

$$P = P_D - P_z \quad [2.3]$$

From the Zener pinning pressure equation, it can be seen that a larger volume fraction of precipitates and a small precipitate size are both effective at slowing down subgrain growth.

An interesting suggestion from Sawada *et al.* ^[75] was that at present it is unclear whether the increase in lath width is caused by either the migration of lath boundaries or the unknitting of the dislocations that form lath boundaries. Another microstructural process that occurs in 9-12 wt.% Cr steels is the gradual the reduction of dislocation density with increasing creep time. Many authors have found that creep strain accumulation strongly promotes the rapid decrease in dislocation density due to dynamic recovery ^[76,77]. The decrease in dislocation density is also a thermally activated process. Speich ^[17] emphasised that during the third stage of the tempering of martensite, the dislocation substructure is effectively becomes annealed out, which generally results in a dislocation-free ferritic structure. Sawada *et al.* ^[75], reported a relationship between lath width increase and dislocation density decrease in the lath interior in a modified 9Cr-1Mo steel (Figure 2.26). However, such a general statement may not be

accurate as Pešićka *et al.* ^[76], who have shown that even though there is an observed reduction in dislocation density, the resultant microstructure after creep is very heterogeneous, where the dislocation densities vary within one subgrain that can have regions with and without dislocations, which is illustrated well in Figure 2.27.

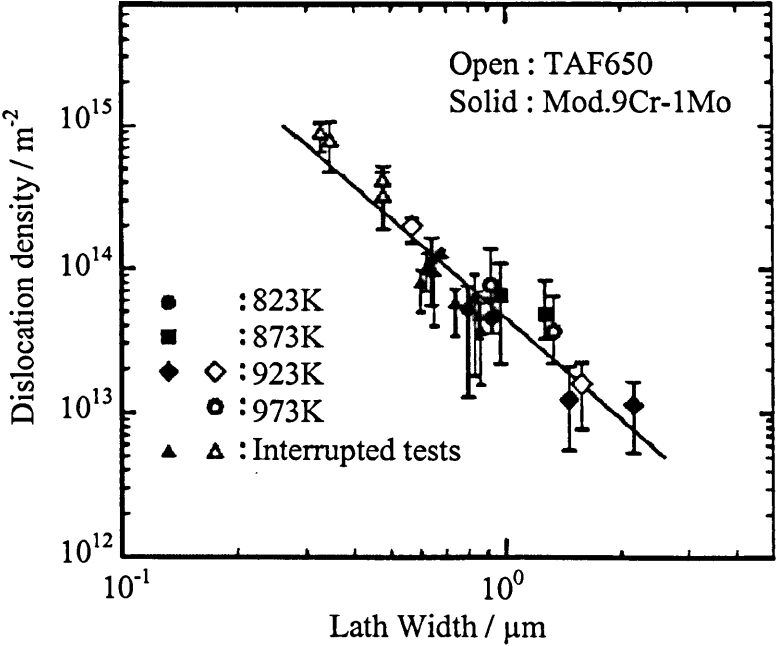


Figure 2.26: Relationship between lath width and dislocation density in lath interior during creep. After Sawada *et al.* ^[75].

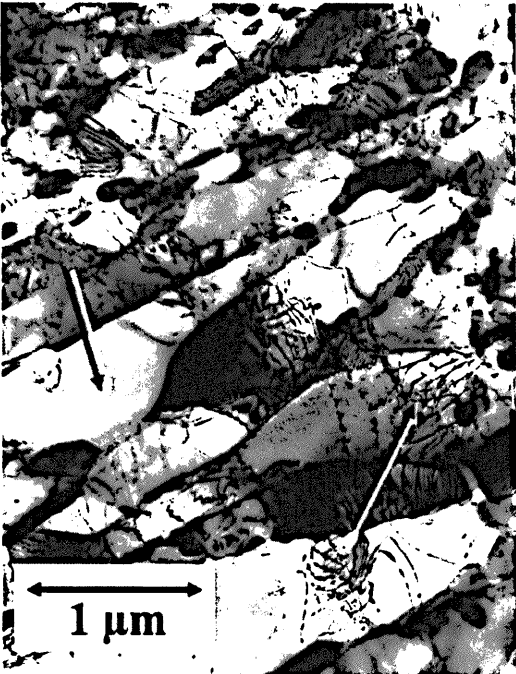


Figure 2.27: Overview TEM micrograph showing the tempered X20 after 1.2% creep (X20-5 in Table 3). About half of the micro grains are free of dislocations. One arrow pointing down shows a micro grain with no dislocations while one arrow pointing up shows a micro grain with dislocations. After Pešićka *et al.* ^[76].

It has been suggested by Pešićka *et al.* [77] that the density of free dislocations and also subgrain boundary dislocations remains constant during secondary, or steady state creep. Thus, they did not expect that the evolution of the dislocation substructure strongly affects the creep rate, since the glide and climb of free dislocations and grain boundary migration contribute to creep deformation.

In addition to the observations concerning martensite lath and subgrain growth, it has also been reported that the microstructure becomes more equiaxed with increasing time under creep loading conditions [68,78,79]. For example, Orlova *et al.* [68] have observed that simultaneous mean lath width increase corresponds to a change in the subgrain shape factor (the ratio of the minimum and maximum subgrain dimensions), which was also found to increase. This finding is indicative of the fact that subgrains tend to approach an equiaxed shape as the material is crept for increasing time periods. According to Speich [80], when recrystallization is inhibited due to the pinning action of boundary particles, the martensite structure then contains an array of stable low angle dislocation cell walls formed by recovery. Here, the equiaxed grain structure is only achieved by preferential growth of some of the low angle boundaries.

During creep at high temperatures, work hardening, which takes place with increasing creep strain in the material, occurs simultaneously with recovery, a process in which the material gradually softens with time at high temperature [81]. Therefore, as creep proceeds at elevated temperatures, the dislocation motion and the creation of dislocations results in strain (work) hardening, while climb and cross-slip, both of which are recovery processes, results in the annihilation or rearrangement of dislocations into low energy configurations.

Figure 2.28 provides a schematic representation of the changes of subgrain structure during different stages creep. This is representative of the findings of previous authors who reported a change in the martensitic lath structure after severe tempering or creep stress in high Cr ferritic-martensitic steels [68,73,75,76]. Indeed, Humphries and Hatherly [74], referring to general particle-strengthened alloys, state that the factors which tend to promote the formation of a subgrain structure during deformation, in this case creep, are low solute content, large strain and high temperature of deformation. The latter two are a consequence of the operating conditions of the steel in critical power plant applications. The solute content has been reported to decrease in high Cr ferritic-martensitic steels [56-58] due to the formation and

significant coarsening of deleterious phases such as Laves phase, which reduces the effect of solid solution strengthening of elements such as Mo and W in the tempered martensite matrix.

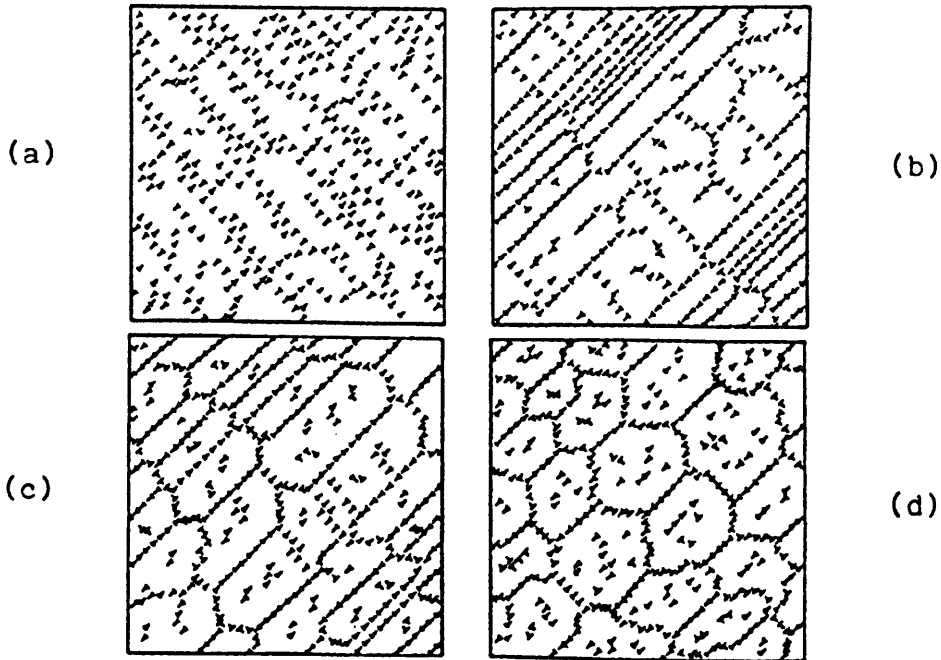


Figure 2.28: Schematic representation of the dislocation changes during creep in metals, illustrating the development of a subgrain boundary structure as creep continues. After Evans and Wilshire^[81].

Grain boundary misorientation has been shown to have a pronounced effect on diffusion and thus microstructure evolution. In an experiment involving the penetration of silver along (100) tilt boundaries in copper it was found that no preferential grain boundary penetration can be detected for $\theta \leq 10^\circ$ or $> 80^\circ$, however it is seen that for $\theta > 10^\circ$ the penetration increases to a maximum at approximately $\theta = 45^\circ$ ^[82] (Figure 2.29). As previously discussed, martensite has many different types of boundaries, which include prior austenite grain boundaries, block and packet boundaries, lath and also twin boundaries. The former tend to be high-angle randomly oriented grains whereas the latter are low angle sub-boundaries. It would thus be expected that the diffusion characteristics of the steel would change considerably as the microstructure evolves during prolonged creep deformation. Nakashima *et al*^[78] studied grain orientation in 9Cr-1Mo steels and found that small angle boundaries (10.5°) and near $\Sigma 11$ boundaries (49.5°) increased during high temperature deformation, whereas $\Sigma 3$ boundaries (70.5°) decreased. The driving force for subgrain growth was shown to be proportional to the energy of low angle sub-boundaries, thus it was concluded that the growth rate must be a function of subgrain misorientation^[74].

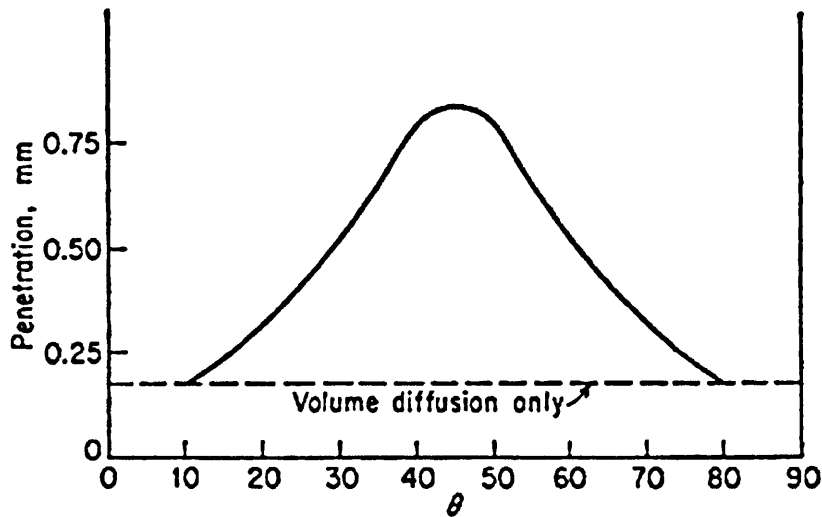


Figure 2.29: Penetration of silver along (100) tilt boundaries in copper after two weeks at 675°C. After Shewmon^[82].

Senicourt and Krahe^[83] studied antimony segregation in martensite and found that this element strongly segregated to high-angle packet boundaries, which are nuclei for the recrystallization process. It was proposed that impurity segregation reduced the mobility of these boundaries and hence retarded the recrystallization process. They also found that the segregation of this element is limited in low-angle lath boundaries in the lath martensite, which would result in lath wall migration becoming uninhibited.

2.4.2 Particle Size, Interparticle Spacing and Morphology

The most important strengthening mechanism in high chromium modified steels is precipitation strengthening^[84]. Evans and Wilshire^[81] commented that major improvements in creep resistance can be achieved by introducing a dispersion of fine precipitates, which provide effective obstacles to dislocation movement. It has been suggested by many authors that the average interparticle spacing is crucial in determining the creep strength of steel^[70,85], which is reasonable, as the Orowan stress of a material is dependent on the average interparticle spacing and particle size. The Orowan stress is given by equation 2.4:

$$\tau_{or} = \frac{0.81Gb \ln(d/b)}{2\pi(\lambda_c - d)(1-\nu)^{\frac{1}{2}}} \quad [2.4]$$

where G is the shear modulus, b is the Burger's vector, ν is Poisson's ratio, d is the average particle diameter, and λ_c is the average planar interparticle centre-to-centre spacing (IPS).

Buck and Garrison ^[85] and Dyson ^[60] have suggested that in the equation for secondary creep rate, in which power law creep is observed for particle-strengthened alloys (Equation 2.5), the σ_0 term coincides with the theoretical Orowan stress for particle dispersion. In this case, the secondary creep rate is dependent on the average interparticle spacing and particle size:

$$\dot{\epsilon} = A(\sigma_a - \sigma_b)^n \exp(-Q_c / RT) \quad [2.5]$$

where $\dot{\epsilon}$ is the secondary creep rate, A is a material dependent constant, σ_a is the applied stress, σ_b is the stress related to the resistance to dislocation glide from particles, n is the stress exponent, Q_c is the activation energy, T is the absolute temperature, and R is the universal gas constant.

Indeed, Dimmler *et al.* ^[86] found a correlation between calculated Orowan threshold and creep strength, where steels with higher Orowan threshold exhibit higher creep strength (Figure 2.30). The threshold values were calculated using precipitate size and volume fraction data from EFTEM images.

Foldyna *et al.* ^[84] address the fact that the formula for measuring mean interparticle spacing neglects the various shapes of particles, i.e. in a high Cr steel such as P91, the intergranular $M_{23}C_6$ particles are much larger than intragranular VN particles. This is because the growth and coarsening of intergranular $M_{23}C_6$ particles is controlled by grain boundary diffusion, whereas intragranular particles are controlled by volume diffusion, where the latter is generally much slower ^[87]. Therefore, the creep rupture strength and creep rate are controlled by the effective interparticle spacing of both of these particles, which can be established by:

$$1/L_{\text{eff}} = 1/L_{M_{23}C_6} + 1/L_{VN} \quad [2.6]$$

where L_{eff} , $L_{M_{23}C_6}$ and L_{VN} are the mean interparticle spacing for mean effective IPS, $M_{23}C_6$ and VN respectively. Spigarelli *et al.* ^[73] found that both fine intragranular MX precipitates and $M_{23}C_6$ particles coarsen after creep (Figure 2.31). Similar results have been reported elsewhere ^[89]. However, Czyrska-Filemonowicz *et al.* ^[71] have shown that the effect of strain induced coarsening of MX particles is relatively insignificant. Similar suggestions can be found elsewhere, where it was also shown that the coarsening of $M_{23}C_6$ carbides is accelerated by strain ^[88].

The coarsening rates of intergranular particles in martensitic steels is very much dependent on their location with respect to the various boundaries. Kaneko *et al.* [89] state that the diffusion rates along high angle boundaries such as random boundaries are higher than those along small angle boundaries. They also showed that most of the prior austenite grain boundaries are randomly oriented boundaries, whereas martensite lath boundaries are mainly low-angle boundaries, which means that carbides are expected to form and coarsen more easily on prior-austenite grain boundaries due to their faster diffusion paths (Figure 2.32).

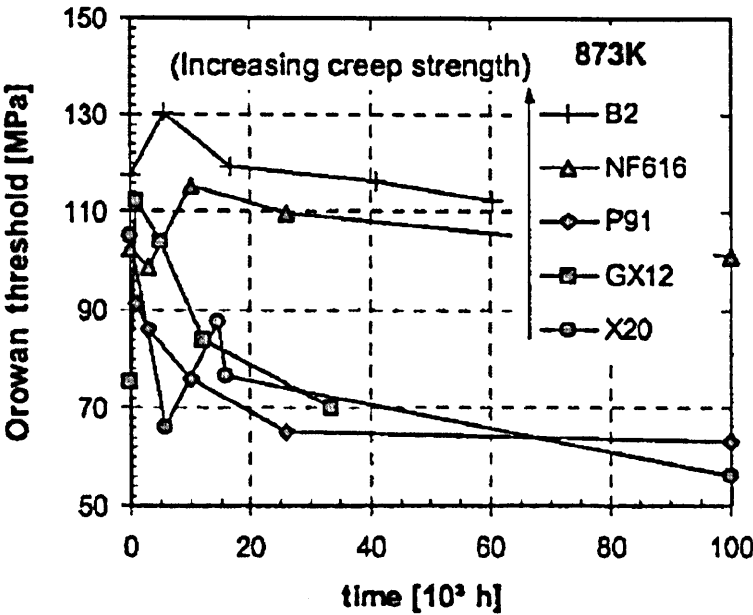


Figure 2.30: The evolution of the total back stress of precipitates of typical heat resistant steels held under creep exposure. After Dimmler *et al.* [86].

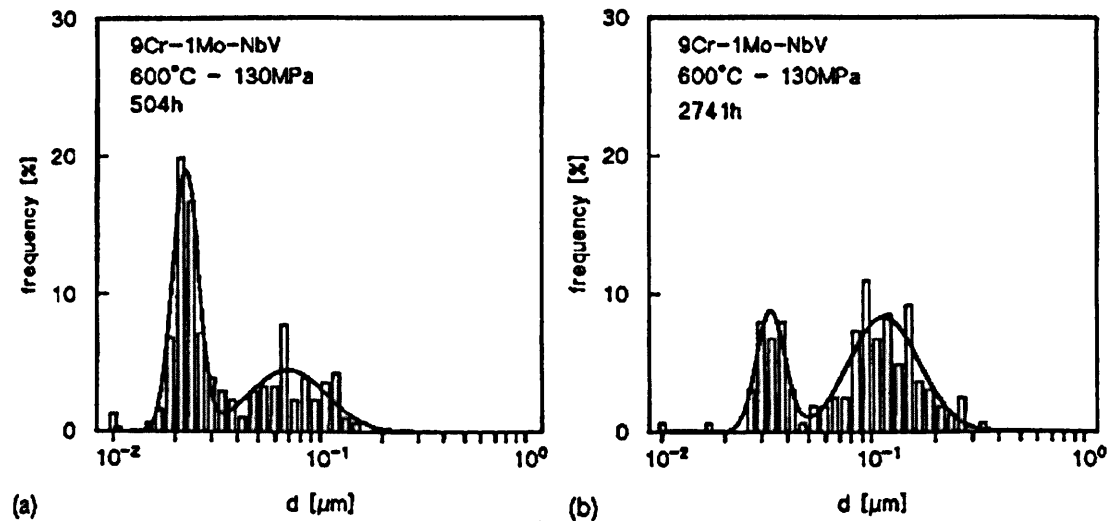


Figure 2.31: Typical bimodal distribution resulting from the precipitation of fine MX during creep, and from coarsening of both $M_{23}C_6$ and MX: a) 600°C – 130 MPa – 504 h; b) 600°C – 130 MPa – 2,741 h (rupture). After Spigarelli *et al.* [73].

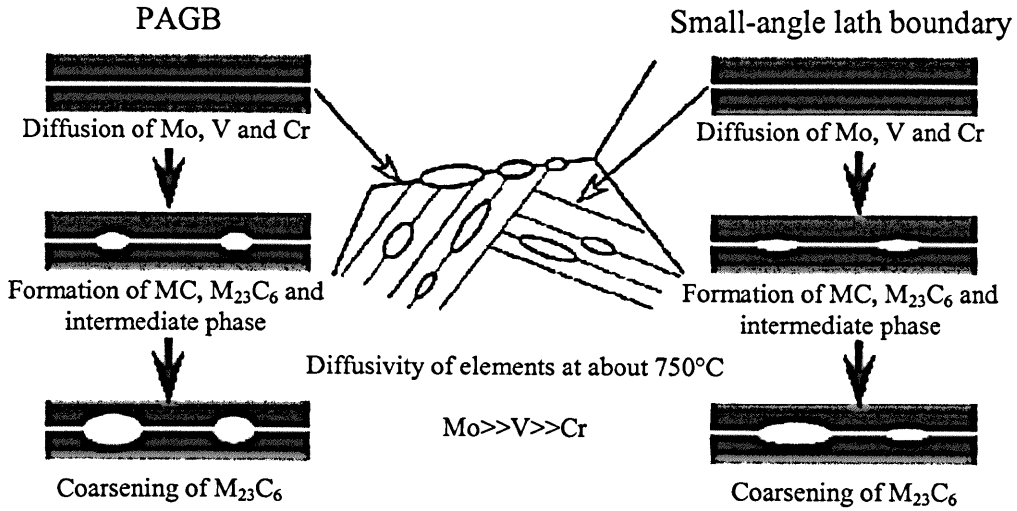


Figure 2.32: A schematic diagram of the formation of carbides at the different boundaries in a tempered martensitic microstructure, including at the prior austenite grain boundaries (PAGB) and small-angle lath boundaries. After Kaneko *et al.* [89].

Taneike *et al.* [35] studied the accelerated coarsening of MX carbonitrides during creep. Like many authors, they found that the effect of strain accelerates the coarsening rate of these particles. They reasoned that as the dislocation density becomes greater, the diffusion coefficient increases, hence particles should coarsen at a faster rate. However, it has been shown elsewhere [76] that the dislocation density decreases during creep, yet particle coarsening takes place more quickly in a stressed sample (creep) than in an unstressed sample (aging). Therefore, it has been suggested that the dislocation density cannot directly account for the high coarsening rates of MX particles experienced during creep [35]. An alternative theory has been proposed, whereby it is the moving dislocations, during creep deformation, that enhance diffusion [90], which is due to the fact that the probability of a solute atom interacting with dislocations is higher if the dislocation is moving (during creep deformation), as opposed to if the dislocation was static (during aging).

Strang and Vodarek [52] found that increasing the nickel content in 12CrMoVNb steel causes an increase in the coarsening rate of $M_{23}C_6$ precipitates. In a similar study, Faulkner *et al.* [87] calculated a relative effectiveness, P , to describe the effect of an element, E , on the precipitation kinetics in a Fe-11Cr ferritic steel with the following formula, where L_X is the average precipitate size:

$$P = \frac{L_{(X+E)} + L_X}{L_X} \times 100\% \quad [2.7]$$

when $P < 0$, the element of interest is beneficial in reducing precipitate growth rate whereas when $P > 0$, the element is harmful. They found that at concentrations higher than 0.4 wt.%, Ni is harmful, but increasing the Ni content up to 0.1 wt% was beneficial in reducing precipitate growth.

2.4.3 Summary of Microstructural Evolution in P91 Steel

9-12 wt.% Cr steels are susceptible to many microstructural processes causing the microstructure to constantly evolve during aging and creep in P91 steels. These include particle coarsening, grain migration, changes in the dislocation structure, and depletion of solid solution elements from the matrix, which all contribute to the gradual degradation of the mechanical properties of these materials in service.

In this section, it has been shown that there are contrasting views about which microstructural parameter is the most dominant. For example, some authors state that the dislocation structure is the most important parameter, whereas others consider that it is particle distribution which is more important.

2.5 Microstructure Modelling for Creep Life Prediction

In order to accurately predict the remaining creep life of ferritic heat resistant steels, it is essential that a creep equation should describe the relationship between microstructural parameters and creep rate, because creep rate has been demonstrated to be clearly affected by microstructure^[91]. Several methods have been developed which aim to predict the remanent lifetimes of materials in creep such as Larson-Miller parameter, theta projection method, Robinson's rule, Omega parameter and continuum damage mechanics (CDM), all of which have been clearly reviewed by Dyson^[60].

Previously, the main available method to assess the remnant life of materials working in conditions of high temperature creep was to employ empirical analyses based on the extrapolation of short-term creep data^[92]. This was typically done, for example, by using the Larson-Miller parameter which operates as a function of stress only and is functionally related

to temperature and time. However, as different materials are subjected to different combinations of structural change during service (which can influence creep performance), such as particle coarsening, phase changes and dislocation density changes, empirical data can only be made to fit an available database. In order to extrapolate to longer service periods these physical mechanisms must be integrated into the creep equations^[93]. This is even more important in the case of 9-12 wt.% Cr steels due to the complex interaction of many microstructural features.

Yin and Faulkner^[87] inserted precipitation and solute depletion data from a P92 steel composition from a precipitation model into the physically based continuum damage mechanics model due to Dyson^[60]. This method was shown to be reasonably effective at predicting the life of a P92 steel as the results from CDM modelling closely matched results from experimental creep tests (Figure. 2.33). Yang *et al*^[92] obtained a similar comparison on a T122 and a T92.

Yin and Faulkner^[87] also considered the effects of the coarsening of $M_{23}C_6$ and VN precipitates and depletion of W and Mo from the matrix due to the formation of Laves phase on the creep strain rate. However, this model does not consider the effects of other important microstructural parameters such as subgrain growth and does not differentiate between intralath and interlath precipitates.

Yang *et al.*^[92] compared results from experimental data against predicted values using Larson-Miller and physically based CDM analysis on two designs of blunt-notch test pieces of a T22 material. They found that the life predicted with CDM analysis was slightly conservative compared with actual test data, however, Larson-Miller analyses predicted a considerably shorter life.

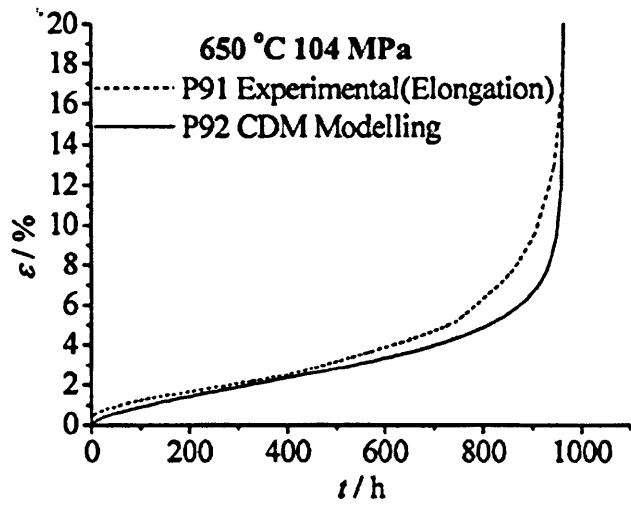


Figure 2.33: A comparison of a modelled creep curve of P92 using CDM with an experimental one of P91 at the same test conditions. After Yin and Faulkner ^[87].

2.6 Summary

The microstructure evolution and the effect of processing of power plant grade 9-12 wt.% Cr ferritic-martensitic steels under high temperature creep conditions have been reviewed in the present chapter.

It has been shown that the complexity of the microstructure is due to the large number of alloying additions, which induce the formation of several strengthening mechanisms. The high Cr content enables this class of alloys to become air-hardenable, and thus form martensite, which is very strong on account of the fine microstructure and high dislocation density, on cooling from the normalizing heat treatment. The subsequent tempering heat treatment promotes the precipitation of several phases, each having a different strengthening effect on the microstructure. For example, particles precipitating at the intergranular regions help pin grain boundaries and retard the recrystallization process, whereas intragranular precipitates are effective at inhibiting dislocation motion. The degree of strengthening from particles is strongly dependent on chemical composition and heat treatment.

The microstructure of 9-12 wt.% Cr power plant steels gradually changes during creep exposure, and this is manifested in the coarsening of precipitates, the formation of deleterious phases, and the recovery of the martensitic matrix. In general, it is evident that changes in the microstructure affect the creep strength, however, there is a distinct lack of availability of models that link such changes to the mechanical properties, and as such, be able to adequately

assess remaining creep life. Further details of microstructural modelling for creep life prediction are considered in Chapter 9 of this thesis.

Chapter 3

EXPERIMENTAL PROCEDURES

3.1 Introduction

This chapter describes the various experimental techniques that have been employed to investigate the microstructure evolution of the steel grade 91 (T/P91). Figure 3.1 is a general flow chart which illustrates the main experimental techniques employed in the present investigation. The top tier shows the different material conditions being examined. The middle tier shows the main experimental techniques employed, and the bottom tier shows the different microstructural features that were examined.

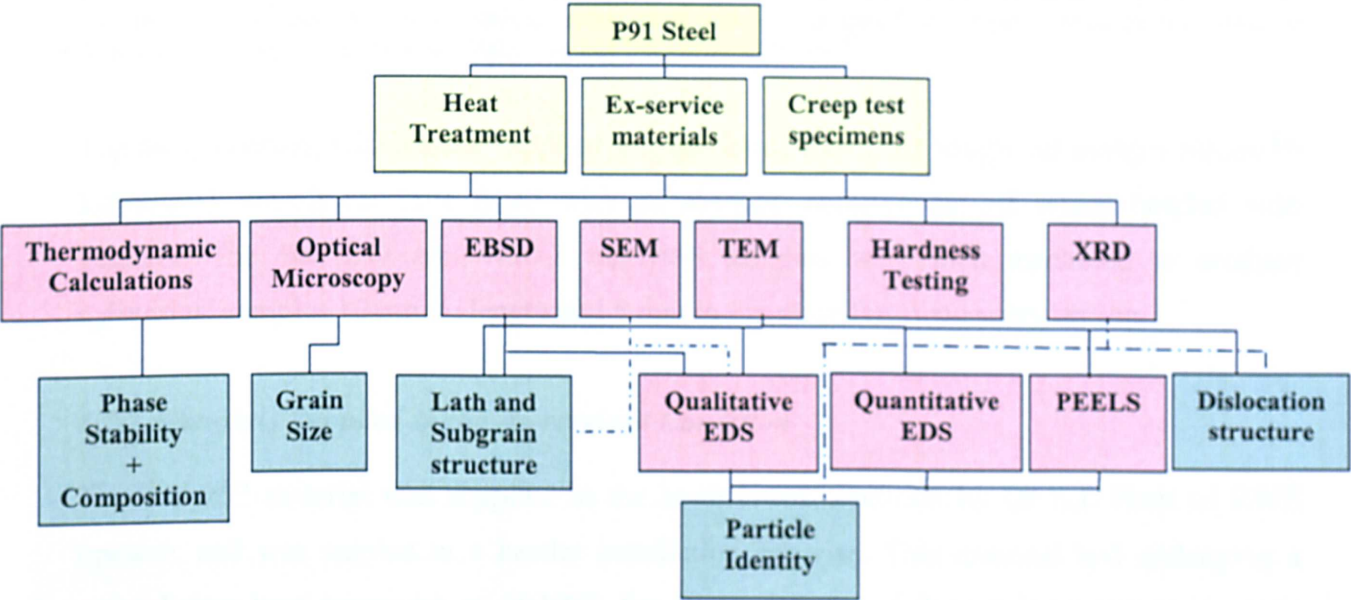


Figure 3.1: Flow chart illustrating the experimental programme for the P91 steel samples.

3.2 Materials

For the purpose of investigating the microstructure evolution of 9-12 wt.% chromium steels, grade 91 steel (9Cr-1Mo-V-Nb) or P91 was chosen as a suitable test material due to its vast commercial importance in advanced coal- and gas-fired power plant applications, such as boiler re-heater and super-heater tubing. Several P91 steel samples, with slight differences in the concentration of alloying elements, were used in the experiments carried out in this thesis in order to quantify the changes in the microstructure that occur under service conditions of prolonged elevated temperature creep exposure. An important aspect of this research is to

understand some of the effects that different bulk compositions of P91 have on key thermodynamic and kinetic characteristics, including the stability of different phases with respect to time and temperature. The materials used were kindly supplied by RWE npower and E.On UK, and their chemical compositions, which lie within the specified composition range for P91 steel, are shown in Table 3.1.

Material	Element wt% (Balance is Fe)											
	C	Si	Mn	P	S	Cr	Mo	Ni	Al	N	Nb	V
Bar 257*	0.12	0.25	0.47	0.013	0.009	8.24	0.96	0.17	0.027	0.03	0.08	0.18
W20-3*	0.09	0.33	0.44	0.008	0.005	8.66	0.94	0.09	0.003	0.04	0.06	0.25
U2B2**	0.14	0.27	0.44	0.010	0.008	8.22	0.92	0.11	0.026	0.039	0.1	0.2
Tee-piece**	0.105	0.3	0.52	0.02	0.004	8.55	0.91	-	0.036	0.038	0.08	0.25
Bottle 2**	0.097	0.24	0.38	0.011	0.01	8.18	0.93	0.12	0.036	0.038	0.11	0.21
Specified Composition Range	0.08-0.12	0.2-0.5	0.3-0.6	0.04 Max.	0.03 Max.	8.0-9.5	0.85-1.05	0.4 Max.	0.04 Max.	0.03-0.07	0.06-0.1	0.18-0.25

Table 3.1: Chemical compositions of the materials investigated. Materials supplied in the as-received condition are marked with *, and ex-service materials are marked with **. The specified composition range was obtained from a grade 91 tube manufacturer, Vallourec and Manesmann Tubes [8].

The steel samples, which were supplied in pipe form, were first rough-cut using a Struers™ Labotom-1 cut-off machine fitted with an alumina abrasive cut-off wheel bonded with bakelite. The Bar 257 and W20-3 materials samples were then machined to produce cylindrical samples 10 mm in length and 5 mm in diameter for dilatometry testing.

3.2.1 Materials Supplied in the As-received Condition

The Bar 257 material was supplied in the as-received condition by Dr S.J. Brett of RWE npower, and was surplus to a header installation exercise. This material had undergone a normalizing heat treatment at 1040°C for up to 6 hours followed by a tempering heat treatment at 760°C for 12 hours. The inner diameter of the pipe was 257 mm. Creep specimens of this same material were also supplied by the University of Nottingham (see section 3.2.3).

W20-3 was also supplied in the as-received condition by Dr D.J. Allen of E.On UK. The initial pre-service heat treatment comprised of normalizing for 1.5 hours at 1040°C, followed by air cooling and tempering at 760°C for 2.5 hours. This material can be considered to be a typical P91 steel composition.

3.2.2 Ex-Service Materials

The U2B2 material was supplied in an ex-service condition. This material had undergone 36,000 hours in service before failure at an operating temperature of 568°C at a nominal pressure of 160 bar. It originates from part of a T91 tube that had previously been machined from a thicker F91 forging^[94]. Dr. S.J. Brett of RWE npower, who kindly supplied this steel, reported that failure in this material occurred in the form of cracking, around half the circumference of the weld joining the F91 end of the transition piece to the P91 tubing of interest in this investigation^[94]. Further metallurgical investigation revealed that the failure mechanism was Type IV cracking at the outer edge of the heat affected zone, on the F91 side. This material would have undergone a similar pre-service heat treatment as the aforementioned as-received materials.

Bottle 2 was a part of a P91 section that had failed at approximately 30,000 hours service at 568°C. Tee-piece was part of a P91 section that had been sampled in service after 32,000 hours at the same temperature. A salient observation of the chemical composition of the Bar 257, U2B2, Bottle 2 and the Tee-piece materials show that they all contain the upper limit of allowable aluminium and carbon specified in the allowable composition range.

3.2.3 Materials Supplied After Accelerated Creep Testing

In the present investigation, P91 specimens that had undergone accelerated or short-term creep testing have been extensively characterized. Creep testing was performed at the University of Nottingham, and the specimens were fabricated from the Bar 257 material. The test conditions are given in Table 3.2. Creep tested weld specimens from the same material were also investigated. These were kindly supplied by the FOURCRACK collaboration. A key motive in their work was to establish whether differences in the mechanical properties of grade 91 steel parent metals affected the creep performance of the heat affected zone region. The mechanical properties of the Bar 257 material prior to creep testing were altered by subjecting the material to different pre-weld heat treatments, and these are shown in Table 3.3. The failure mode of each specimen was by Type IV cracking along the fully retransformed intercritical heat affect zone (ICHAZ) region. The creep test history of each specimen is shown in Table 3.4.

Temperature (°C)	Stress (MPa)	Final test duration (h)
650	60	2,217.2
	70	632
	82	281.5
	87	230.6
	93	82.4

Table 3.2: Creep test history of the Bar 257 material subjected to accelerated creep testing at the University of Nottingham.

Specimen	Condition prior to welding
A 204 HV	As-manufactured condition, normalized at 1040°C and tempered at 760°C for 12h
B 247 HV (strengthened)	Renormalized (from as-manufactured condition) at 1060°C and tempered at 760°C for 1h
C 184 HV (weakened)	Aged (from the as-manufactured condition) at 760°C for 24h.

Table 3.3: Heat treatment conditions of the three Bar 257 specimens prior to welding, post-weld heat-treatment and creep testing.

Specimen	Creep Test History				
	Final Test Duration (h)	Stress (MPa)	Temperature (°C)	Elongation (%)	Reduction of Area (%)
A	519	75	650	3.05	13.68
B	359	75	650	2.31	18.07
C	430	75	650	10.46	28.77

Table 3.4: Creep test history of the specimens from the FOURCRACK collaboration. Courtesy of Dr David Allen of E.On UK.

3.3 Heat Treatment

This section describes the different heat treatments applied to the grade 91 steels, Bar 257 and W20-3, in order to investigate the effect of varying heat treatment and aging parameters on the microstructural evolution of high Cr ferritic-martensitic power plant steels. Figure 3.2 is a schematic drawing of the different heat treatments employed in this investigation. Heat treatments consisted of three stages, normalizing, tempering and subsequent isothermal aging, and are described in the following sections.

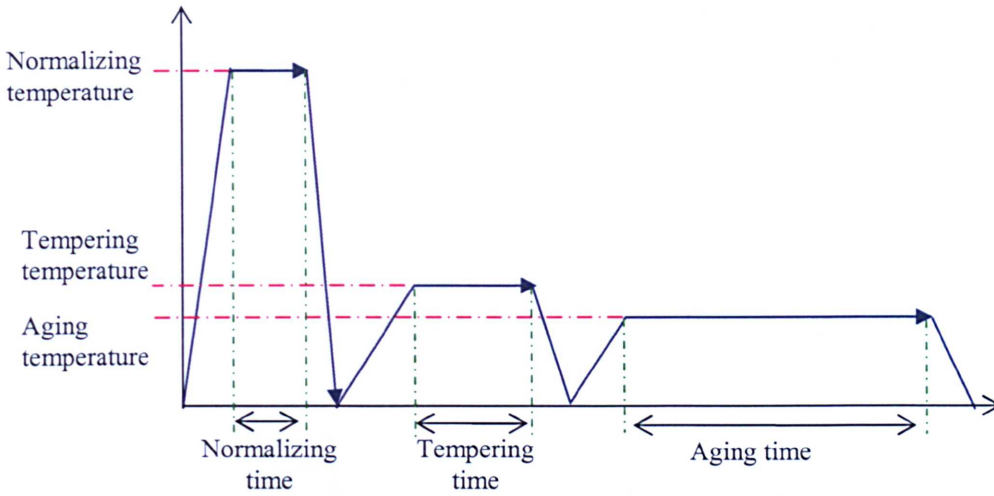


Figure 3.2: A schematic drawing of the different heat treatments applied in this investigation.

3.3.1 Normalizing

Specimens from the as-received materials, Bar 257 and W20/3, were subjected to different normalizing treatments using a Baehr-Thermoanalyse DIL805 dilatometer (Figure 3.3). Inside the dilatometer, the samples were mounted between an alumina probe connected to a linear variable differential transformer and an alumina support tube. Here, the material is induction heated using a high frequency generator. Normalizing treatments were performed in a vacuum environment, in order to avoid decarburization and oxidation of the sample surface during the heating cycle. Uniform heating is expected due to the specimens' cylindrical dimensions. After holding at the normalizing temperature, the specimens were subsequently cooled in a medium of helium gas, the supply of which was carefully controlled to alter the applied cooling rate.

The specimens were heated in the temperature range of 975 to 1100°C inclusive. In addition, they were held at each normalizing temperature for different times, 15, 30 minutes and 1 hour. The specimens were also cooled at different rates from the normalizing temperature, at 1 and 100°Cs⁻¹, in order to investigate the effect of cooling rate on the microstructure. Table 3.5 shows the identifications of the normalized samples together with their normalizing treatments. The data from the dilatometer were subsequently analysed using the equipment's WinTA 7.0 thermoanalysis software, which allows plots to be made of temperature versus change in length and other parameters such as time and deformation. The chosen temperature range corresponds to the peak temperatures experienced across the heat-affected zone (HAZ) line in a finite element analysis study of P91 steel by Yaghi *et al* ^[95] (Fig. 3.4), collaborators in this project.

Sample	Normalizing Temperature (°C)	Normalizing Time (mins)	Cooling rate (°Cs ⁻¹)
D1	975	15	1
D2	975	15	100
D3	1050	15	1
D4	1050	15	100
D5	1100	15	1
D6	1100	15	100

Table 3.5: Sample identification showing the normalizing temperatures and cooling rates used for the investigation.



Figure 3.3: Baehr-Thermoanalyse DIL805 dilatometer. From Baehr Thermoanalyse product website ^[96].

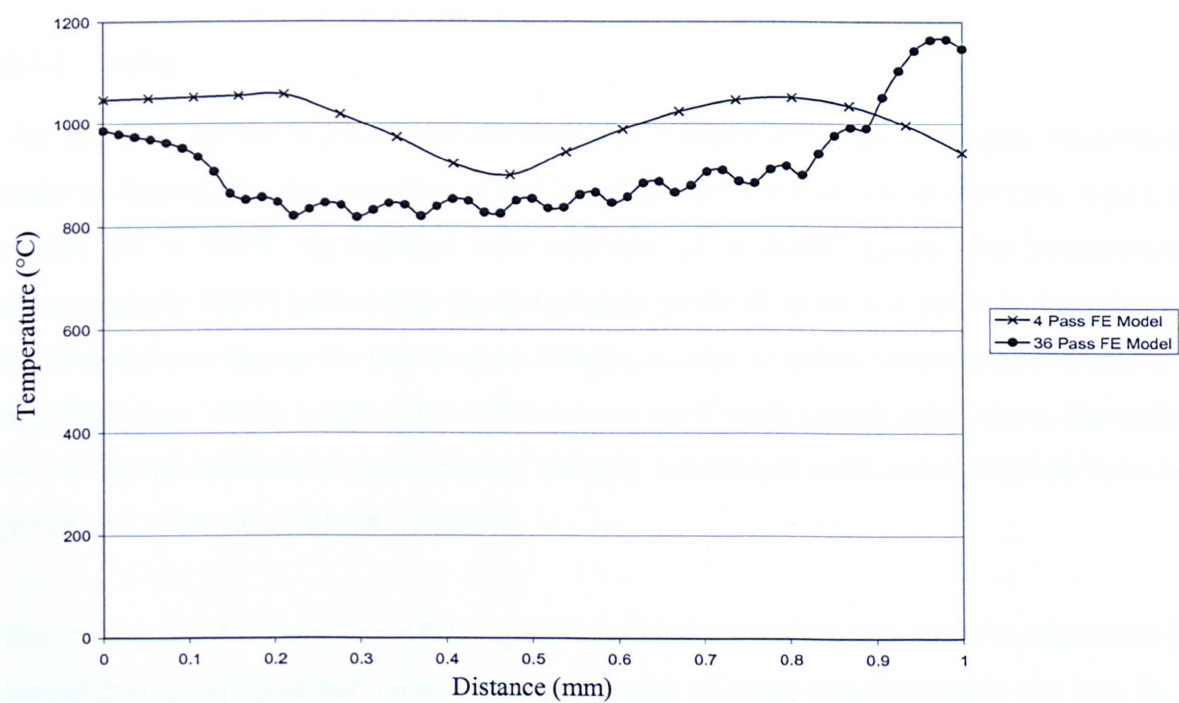


Figure 3.4: Peak temperatures (°C) along the HAZ line against normalised distance measured from the inside to the outside surface of the 4 pass and 36 pass FE models with R_i/T ratio of 4.37 and 7.5 respectively. After Yaghi *et al* ^[95].

3.3.2 Tempering

Following the normalizing and subsequent cooling treatment, the Bar 257 and W20-3 specimens were subjected to a standard stress-relief heat treatment at 750°C for 2 hours in an atmosphere of air. The samples were placed in ceramic boats and the tempering treatment was undertaken using a Carbolite™ 5 litre capacity chamber furnaces with a maximum operating temperature of 1300°C. The samples were air-cooled following the tempering treatment. Table 3.6 shows the identifications of the tempered samples along with their normalizing treatments.

Sample	Normalizing Temperature (°C)	Normalizing Time (mins)	Cooling rate (°Cs ⁻¹)	Tempering Temperature (°C)	Tempering Time (Hours)
T1	975	15	1	750	2
T2	975	15	100	750	2
T3	1050	15	1	750	2
T4	1050	15	100	750	2
T5	1100	15	1	750	2
T6	1100	15	100	750	2

Table 3.6: Sample identification showing the normalizing temperatures, cooling rates and tempering temperature used for the investigation.

3.3.2 Aging

The Bar 257 and the W20-3 materials were also subjected to long-term aging treatments in order to characterise the evolution of the initial pre-service martensitic structure. Aging was carried out at 650°C for different time intervals up to 10,000 hours. This temperature is approximately 100°C greater than the temperature grade 91 steels are typically operating at in service, and was chosen for two reasons. Firstly, in order to induce accelerated changes in the microstructure, which might otherwise not occur until much longer aging times. Secondly, a lot of data are available in the literature, whereby accelerated creep and aging tests have been performed in the range of 600 to 650°C.

Due to the small dimensions of the specimens, the precaution was taken to seal them in a borosilicate glass container under a partial pressure of argon (approximately 150 mm Hg) to prevent oxidation and decarburization during heat treatment. Table 3.7 shows the identifications of the aged samples along with their corresponding normalizing and tempering treatments.

Sample	Heat Treatment
A1.1	N 975°C 15mins, Cooled 1°C s ⁻¹ , T 750°C 2h, A 600°C 2,500h
A1.2	N 975°C 15mins, Cooled 1°C s ⁻¹ , T 750°C 2h, A 600°C 5,000h
A1.3	N 975°C 15mins, Cooled 1°C s ⁻¹ , T 750°C 2h A 600°C 10,000h
A2.1	N 975°C 15mins, Cooled 100°C s ⁻¹ , T 750°C 2h A 600°C 2,500h
A2.2	N 975°C 15mins, Cooled 100°C s ⁻¹ , T 750°C 2h A 600°C 5,000h
A2.3	N 975°C 15mins, Cooled 100°C s ⁻¹ , T 750°C 2h A 600°C 10,000h
A3.1	N 1050°C 15mins, Cooled 1°C s ⁻¹ , T 750°C 2h, A 600°C 2,500h
A3.2	N 1050°C 15mins, Cooled 1°C s ⁻¹ , T 750°C 2h, A 600°C 5,000h
A3.3	N 1050°C 15mins, Cooled 1°C s ⁻¹ , T 750°C 2h, A 600°C 10,000h
A4.1	N 1050°C 15mins, Cooled 100°C s ⁻¹ , T 750°C 2h, A 600°C 2,500h
A4.2	N 1050°C 15mins, Cooled 100°C s ⁻¹ , T 750°C 2h, A 600°C 5,000h
A4.3	N 1050°C 15mins, Cooled 100°C s ⁻¹ , T 750°C 2h, A 600°C 10,000h
A5.1	N 1100°C 15mins, Cooled 1°C s ⁻¹ , T 750°C 2h, A 600°C 2,500h
A5.2	N 1100°C 15mins, Cooled 1°C s ⁻¹ , T 750°C 2h, A 600°C 5,000h
A5.3	N 1100°C 15mins, Cooled 1°C s ⁻¹ , T 750°C 2h, A 600°C 10,000h
A6.1	N 1100°C 15mins, Cooled 100°C s ⁻¹ , T 750°C 2h, A 600°C 2,500h
A6.2	N 1100°C 15mins, Cooled 100°C s ⁻¹ , T 750°C 2h, A 600°C 5,000h
A6.3	N 1100°C 15mins, Cooled 100°C s ⁻¹ , T 750°C 2h, A 600°C 10,000h

Table 3.7: Sample identification showing the normalizing temperatures, cooling rates, tempering temperature, and aging times and temperature used for the investigation.

3.4 Thermodynamic Calculations

The software package ‘Metallurgical and Thermochemical Databank’ (MTDATA)^[97] version 4.73, developed by the National Physical Laboratory (UK), was used to carry out equilibrium thermodynamic calculations. The programme was used in conjunction with the NPL-supplied iron alloy specific database TC-FE^[98].

MTDATA is a thermodynamic modelling software package, the principle of which is that it uses mathematical models incorporated into the software that allows thermodynamic equilibrium in multi-component multiphase systems using, as a basis, critically assessed thermodynamic data. Therefore, it is possible to determine equilibrium conditions using alloy compositions and temperature ranges for which experimental data does not exist for a given system. Essentially, MTDATA calculates equilibria using a true Gibbs energy minimisation procedure of a system, thereby finding the equilibrium volume fraction and the composition of the phases that are present^[97].

The reliability of thermodynamic predictions is dependent on the data that are available for the components of interest and their interactions for any given system. The TC-FE database stores data in the form of assessed parameters for various models that describe the

thermodynamic properties of phases, which is accessed by the programme using an integral data management system. MTDATA has a principal calculation module called MULTIPHASE, which can solve equilibrium problems involving many phases and components, and will calculate the equilibrium state in terms of the distribution of components and species between the stable phases ^[99]. Figure 3.5 provides an overview of the different software modules used for data retrieval, assessment and calculation in the MTDATA software package.

Calculations of the equilibrium phase mass fractions have been performed on several steel compositions, shown in Table 3.1, over the temperature range of 500-1200°C at intervals of 20°C. The phases and elements that were allowed in the calculations are shown in Table 3.8. A miscibility gap of 2 was used to calculate the face-centred cubic (fcc) phases, which included austenite, and two possible variations of the MX precipitate, (V,Nb)(N,C) and (Nb,V)(C,N). All of the phases listed in Table 3.8 can be classified to be present or absent in the system by the user, however, the combination of the phases that are input will affect the results of the calculations.

The fact that such calculations only represent thermal equilibrium must be taken into consideration because this thermodynamic modelling software does not take into account the influence of time and the kinetics of reactions, which may affect the formation of a phase and the evolution of the alloy microstructure. This is of particular importance where complex, multi-stage heat treatments, such as those applied for high Cr power plant steels, are applied.

Steel	Allowed Elements	Allowed Phases
Bar 257, U2B2, W20/3	Fe, C, Si, Mn, Cr, Mo, Ni, Al, N, Nb, V	γ , α , M_3C , liquid, MX (fcc), $M_{23}C_6$, M_6C , M_7C_3 , AlN, Laves phase

Table 3.8: List of elements and phases that were allowed for thermodynamic calculations. Note: Two miscibility gaps were allowed for the fcc phase.

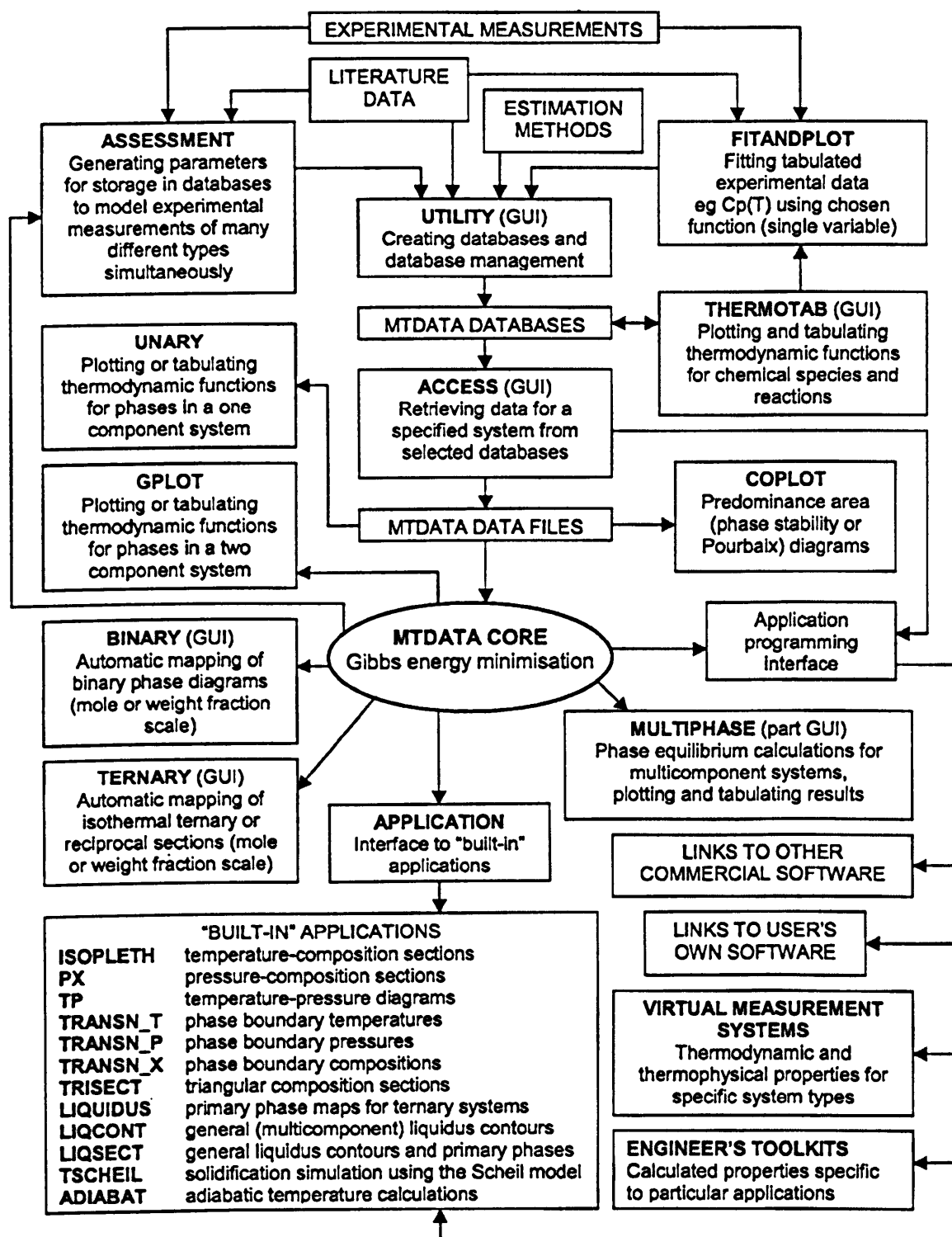


Figure 3.5: Structure overview of the MTDATA software package showing the different modules used for data retrieval, assessment and calculation. After Davies *et al* ^[99].

3.5 Optical Microscopy

Specimens were prepared for optical microscopy by firstly mounting them in electrically conducting Bakelite resin, wet grinding to 1200-grit using SiC paper, and then polishing on a diamond-paste impregnated porous neoprene polishing cloth in order to achieve a surface finish of 1 μm . Light etching in Vilella's reagent (1 g picric acid, 100 ml ethanol, 5 ml hydrochloric acid) was carried out to reveal the martensitic matrix and in particular to highlight prior-austenite grain and martensitic lath boundaries.

A Reichert-Jung MeF3 inverted metallurgical microscope in bright field mode was used for the characterization of the microstructure at up to 1000X magnification. This was coupled with a Fujitsu FUJIX HC-300Z digital camera and a FUJIX Photograb 300Z digital image capture system.

3.6 Metallography

The prior-austenite grain size of the different specimens was measured, from optical micrographs, using the mean linear intercept method ^[100-101]. Here, the grain size of a material is measured by determining the number of interceptions of grain boundaries along a test line of a finite and known length. The linear intercept grain size, L_1 , can be calculated using equation 3.1:

$$L_1 = \frac{\sum L}{M \sum x} \quad [3.1]$$

where M is the magnification, $\sum L$ is the total length of the n traverses, and $\sum x$ is total number of interceptions of the n traverses.

Grain boundary counts were taken along the full length of the transverse lines for all samples, and for practicality of measurement, the measuring magnification varied from $\times 50$ up to $\times 1000$ magnification depending on the magnification where each grain became distinguishable. In order to achieve statistically significant results, care was taken to space the test lines sufficiently far apart so that two adjacent lines do not cross the same grain.

For the determination of the virgin martensite lath widths, the width of a group of laths parallel to the lath length was measured, and then this value was divided by the number of laths, similar to Yardley ^[102]. Measurements were performed on SEM micrographs of the as-normalized specimens. More than 20 different areas per sample were analyzed, and nearly 400 laths were measured per specimen. The probable error estimate in the lath measurements was approximately $0.2 \pm 0.03 \mu\text{m}$.

3.7 Scanning Electron Microscopy

The equipment used was a LEO-1530VP Field Emission Gun Scanning Electron Microscope (FEGSEM) and was operated with an accelerating voltage of 20 kV. The field emission gun produces an electron beam with a much higher current density than a conventional SEM equipped with a thermionic gun ^[103], which in turn provides a higher achievable spatial resolution when imaging in secondary electron, In-Lens mode or indeed with electron backscatter diffraction.

Scanning electron microscopes normally have facilities for detecting secondary electrons and backscattered electrons. In scanning electron microscopy, the interaction between the irradiated electron beam and the atoms of the specimen surface produce various types of signals which are emitted and may be detected. These include secondary electrons, backscattered electrons, X-rays and cathodoluminescence. Secondary electrons have a relatively low energy, and thus provide the smallest interaction volume which allows for better spatial resolution in comparison to the other signals. Backscattered electrons, however, possess much higher energies and as a consequence produce a larger interaction volume and poorer spatial resolution. The advantage of imaging using a backscattered electron detector is that the signal is strongly dependent on atomic contrast differences along a specimen surface. Therefore, microstructural features with a high atomic number appear brighter and correspondingly low atomic number features appear darker. In this research, both detectors have been employed for imaging. The aperture selected for both imaging types was $30 \mu\text{m}$ in diameter.

3.8 Electron Backscatter Diffraction

EBSD has primarily been used in this research as a tool for the mapping of the crystallographic orientation of grade 91 steel.

In order to obtain a sufficiently high intensity of EBSD patterns, the specimen surface must be positioned so that it makes contact with the electron beam at an angle of 20° . Different scattering events take place when an electron beam strikes the specimen's surface. However, for the purposes of this investigation, backscattered electrons are used for the crystallographic analysis of steel specimens. When the beam interacts with a crystalline material, it is scattered inelastically and diffusely in all directions. Wherever the Bragg diffraction conditions are satisfied by atomic lattice plains in a crystal, two cones (known as Kossel cones) of diffracted electrons are produced and these are detected with a phosphor screen (Figure 3.6). A pair of conic sections, which appear as thin parallel bands, results in the creation of a Kikuchi band. It is these bands that provide key information about the crystal structure of the phase of interest. Such information includes the symmetry of the crystal lattice, which is reflected in an EBSD pattern. In addition, the width and intensity of the Kikuchi bands are directly related to the spacing of atoms in a crystal plane, and finally, the angles between the Kikuchi bands are directly related to the angles between atomic planes in the crystal lattice.

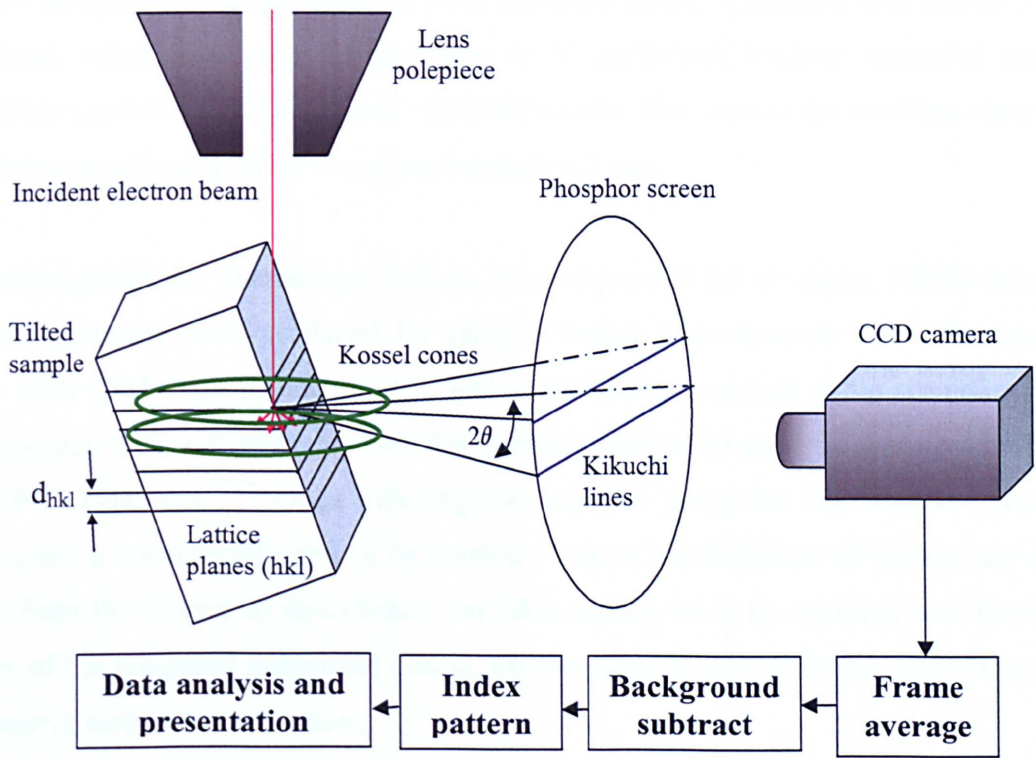


Figure 3.6: Schematic diagram of a typical EBSD installation. Adapted from Humphreys ^[104] and Schwartz ^[105].

3.8.1 Sample preparation for EBSD analysis

For EBSD analysis, samples were first polished from 6 μm to 1 μm using diamond paste. The EBSD technique involves shallow depths below a sample's surface, thus it is essential to remove all of the mechanical distortion that is produced during the previous metallographic treatments. In this case, the samples were subsequently polished using StruersTM OP-S, a suspension of colloidal silica with a 20 nm particle size, which removes areas affected by mechanical deformation. The polishing time for each sample was approximately 30 minutes, and was performed manually.

3.8.2 EBSD Analysis

EBSD analysis was carried out using an EDAX Pegasus system linked to the LEO 1530-VP FEGSEM operating at an accelerating voltage of 20 kV with the sample mounted onto a tilted holder at 70° with respect to the horizontal. The aperture size selected for EBSD was 30 μm . Full automatic indexing was performed by the system, which was controlled using the EDAX OIM Data Collection software [106], and is linked to the ICDD database [32] for crystallographic information.

The areas selected for indexing were typically 250 μm^2 , at $\times 5,000$ magnification which enabled the analysis of approximately 10 prior austenite grains. A suitable step size of 0.1 μm was selected, which enables a detailed scan to be performed without excessive analysis periods. This produced EBSD maps of $\sim 300,000$ pixels. The size of the smallest observable lath width measured using TEM was approximately 0.2 μm .

In this investigation the microscope settings were optimised for obtaining EBSD data. The best indexing results were produced by using a ferritic iron structure file TSL database, available with OIM Data Collection 4.6, which has a body centred cubic structure with a lattice parameter of $a = 0.2866$ nm. This file corresponded to the card number 04-0836 in the ICDD-JCPDS catalogue [32]. Good indexing was possible using this file because during the aging process, a considerable degree of recovery due to the diffusion of carbon and solute elements from the matrix to equilibrium carbides occurs, so it is expected that the lattice parameter of the tempered martensite matrix will be close to that of ferrite, especially given the low matrix carbon concentration.

In EBSD data analysis, the user may define the range in misorientation angle which are used to denote specific boundaries. For this investigation, grains were divided into two categories; low-angle boundaries with a misorientation between 2 and 10°, and high-angle boundaries with a misorientation of 10 to 180°. Increasing the boundary classification angle from 10 to 15° has a negligible effect on results, as the majority of measured low-angle boundaries had a misorientation of less than 10°. Similarly, the majority of measured high-angle boundaries had a misorientation greater than 50°. However, interest was mainly focussed on the total grain boundary length.

EDX data was acquired simultaneously with the EBSD scan which enabled chemical information to be collected. Particular interest was focussed on the following elements; Nb, Mo, Cr, Al, in order to establish if large precipitates were present in the scanned areas.

Analysis of the EBSD scans was performed using EDAX OIM analysis version 4.6 software [106]. The data acquired from EBSD experiments are very sensitive to a wide range of parameters associated with both specimen preparation, microscope settings and data analysis, thus great effort was used in this investigation to keep such parameters the same.

3.9 Transmission Electron Microscopy (TEM)

Two types of specimens were used for microstructural investigations of grade 91 steel, carbon extraction replicas and thin-foils. Transmission electron microscopy was performed using two instruments; a JEOL 2000FX TEM and a Philips Tecnai F20 field emission gun (FEGTEM). Both instruments were operated at an accelerating voltage of 200 kV. The main differences between the two microscopes are due to the electron sources used. The JEOL 2000FX uses a tungsten thermionic emitter, and this microscope was employed primarily for quantitative EDX analyses and general microstructure characterisation. The Tecnai F20 uses a field emission source, and is a hybrid TEM/STEM equipped with several analytical tools, including EDX, Parallel Electron Energy Loss Spectroscopy (PEELS), and a High Angle Annular Dark Field (HAADF) STEM detector. The operating modes of both microscopes are discussed separately below after a discussion of the specimen preparation techniques used in this research.

3.9.1 Specimen Preparation

3.9.1.1 Carbon Extraction Replicas

The carbon extraction replica is a useful technique for the characterization of second-phase particles. The main advantage of replicas over thin-foil samples is that any effects due to the iron matrix are eliminated, thus the chemical composition of the precipitate phases can be determined more accurately. Problems associated with working with a magnetic material (ferrite) in the TEM are also avoided. In addition, the examinable area may be larger than that for a thin-foil, which is limited by the regions that are electron transparent. Furthermore, carbon extraction replicas can preserve the relative positions and orientations of second-phase particles.

Carbon extraction replicas were produced by lightly etching the surface of polished and mounted specimens. Chemical etching was carried out by using Villela's reagent, which removes the matrix, but does not attack the particles of interest. Etching time was restricted to a short period of time of a few seconds, in order to expose and not remove the particles of interest. In addition, this etching procedure was carried out shortly before the carbon film was deposited so that the degree of contamination that could have arisen from airborne dust particles was kept to a minimum. A thin carbon film was then deposited onto the etched metal with a carbon vapourizer. This is basically a carbon arc source in a vacuum coating unit. The pressure of the coating chamber was approximately 10^{-5} torr. A suitable carbon coating thickness of approximately 20 to 30 nm, used in this investigation, was characterized by a dark brown colour.

Once the carbon had been deposited, the coated surface was scored into approximately 3 mm squares with a razor blade (the diameter of a copper mesh grid is 3 mm). To remove the replica from the surface, an electrolytic etch of 10% HCl in methanol was carried out, with a voltage of 1-3 V, and a current of 30-50 mA. The coated specimen was then rinsed in a beaker of pure methanol to remove the electrolyte. Finally the specimen was immersed in distilled water at a 45° angle, which removed the carbon film with the surface tension of water. Each replica was then collected with tweezers and deposited onto 400 mesh square copper grids. After drying, the replicas were ready for TEM examination. Figure 3.7 illustrates the preparation of carbon extraction replicas. It is possible that some of the particles are not extracted with this technique.

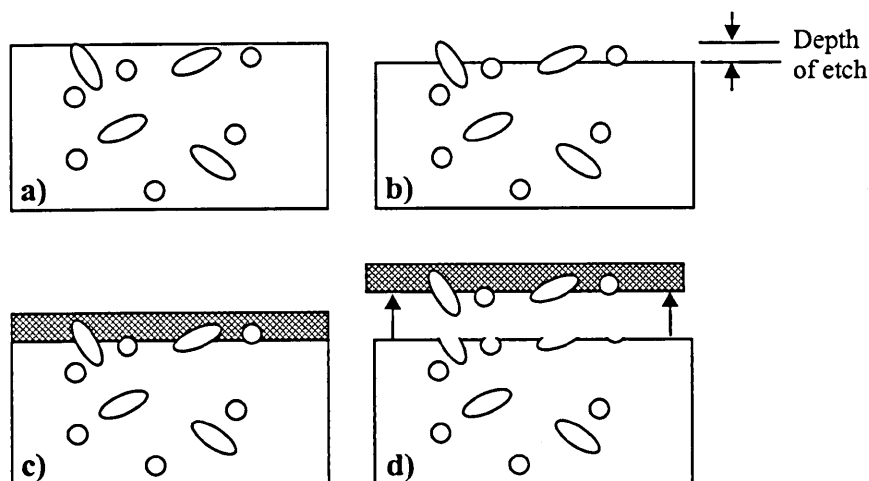


Figure 3.7: Schematic diagram illustrating the preparation of carbon extraction replicas. a) The two-phase (or more) specimen is b) etched and c) carbon coated. d) An additional electrolytic etch then lifts off the replica containing some second-phase particles.

3.8.1.2 Thin-foil Preparation

Thin discs were cut from the specimens of interest using a high speed precision cutting saw equipped with an alumina cut-off wheel. 3 mm discs were then cut from the larger discs using a spark erosion cutting machine. Subsequently, the discs were then mechanically ground by hand to a thickness smaller than 100 μm and then twin-jet electropolished to electron transparency, with the solution cooled to -40°C using liquid nitrogen. The solution used for the P91 specimens contained 10% perchloric acid and 90% methanol.

3.9.2 Microstructure Characterization with TEM

3.9.2.1 Imaging Modes Used

General microstructure characterisation was performed on carbon extraction replicas and thin foils in standard bright field mode in the JEOL 2000FX instrument. The Tecnai F20 instrument, when in STEM mode, can be operated such that images can be acquired in three modes; Bright Field (BF), Dark Field (DF) and HAADF. The latter was exceptionally advantageous for imaging precipitates, as it provides strong atomic number contrast.

3.9.2.2 Identification of Composition: Energy Dispersive X-ray Analysis (EDX)

Using Energy Dispersive X-ray Analysis (EDX), the chemical composition of precipitate particles can be measured. As an electron beam from the TEM strikes a precipitate, electrons become excited to a higher orbital. This causes characteristic X-rays to be emitted as electrons drop down from excited outer states to ground states. It is these characteristic X-rays that can

be used to identify different atoms. In the TEM, quantitative EDX analyses were performed on carbon replicas using Oxford Instruments Inca Link ISIS EDX system equipped with an ultra-thin polymer window, meaning that it is possible to detect light elements down to boron. One hundred particles were analysed on average for each specimen using an acquisition livetime of 50 seconds in order to ascertain the chemical composition. The detector deadtime was kept to below 20%.

3.9.2.3 Identification of Composition: Parallel Electron Energy Loss Spectroscopy (PEELS)

Parallel electron energy loss spectroscopy (PEELS) was performed using a Gatan DigiPEELS system attached to the Philips Tecnai F20 TEM. This technique was used in conjunction with EDX because PEELS is especially sensitive to low atomic number elements, such as nitrogen. The PEELS spectra were acquired in the imaging mode.

3.9.2.4 Identification of Structure: Electron Diffraction

Although composition measurement may provide useful data on precipitate particles, it will not unambiguously identify a phase. A more reliable technique is selected area diffraction carried out in the TEM. Here, an aperture (selected area) is chosen to isolate a particle. The electron diffraction pattern obtained from the precipitate particle is used to investigate its crystal structure. With knowledge of the crystal system, it is possible to match the obtained pattern with a particular phase. A schematic diagram of this technique is shown in Figure 3.8.

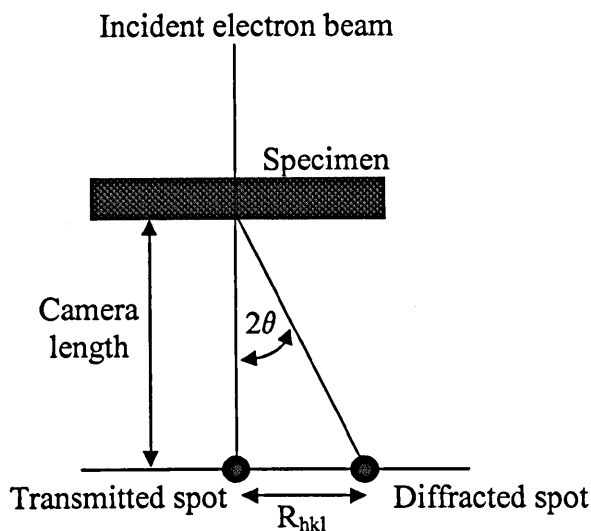


Figure 3.8: A schematic diagram of selected area diffraction pattern formation. The relationship between the camera length, distance on the diffraction and the Bragg angle is shown.

With selected area diffraction, the distance (R_{hkl}) between the transmitted spot and the diffracted spot in the pattern is related to the spacing (d_{hkl}) for the Bragg hkl indices, the camera length (L) and the wavelength associated with electrons of the appropriate energy, by the following equation:

$$R_{hkl}d_{hkl} = L\lambda \quad [3.2]$$

where $L\lambda$ is the camera constant. The wavelength of electrons is related to the accelerating voltage by the following relation:

$$\lambda = \sqrt{\frac{h}{2m_e eV}} \quad [3.3]$$

where V is the accelerating voltage, e is the charge on the electron, m_e is the electron mass, and h is Planck's constant. At an accelerating voltage of 200 kV, the electron wavelength is 0.025 Å.

3.10 Focussed Ion Beam

A dual beam focussed ion beam scanning electron microscope (FIBSEM) was used for additional microstructure characterisation, predominantly for ion beam imaging. The FIBSEM used in the present study was an fei Nova Nanolab 600 dual beam instrument.

The FIBSEM resembles a scanning electron microscope. However, in the present study, instead of using a focussed beam of electrons to image a sample, a focussed beam of gallium ions was used. Here, a gallium liquid metal ion source (LMIS) is placed into contact with a tungsten needle and is subsequently heated. This produces a large electric field as the gallium wets the tungsten, which causes ionization and field emission of the gallium atoms. The ions are then accelerated to an energy in the range of 5 to 50 kV, which are then focussed onto the specimen with the use of electrostatic lenses.

When the focussed gallium atoms strike the specimen, they will cause atoms to sputter from the specimen surface and the implantation of gallium atoms onto the surface. Therefore, unlike SEM imaging, FIB imaging is destructive to the specimen. However, the main benefit of ion beam imaging in the FIBSEM is the fact that it produces images with strong channelling contrast, which permits neighbouring grains, such as prior austenite grains,

packets and laths, to become easily distinguishable from each other. This effect can be seen in Figure 3.9, where the microstructural features of martensite can be seen with ion-beam imaging (Figure 3.9b), but not with secondary electron imaging (Figure 3.9a).

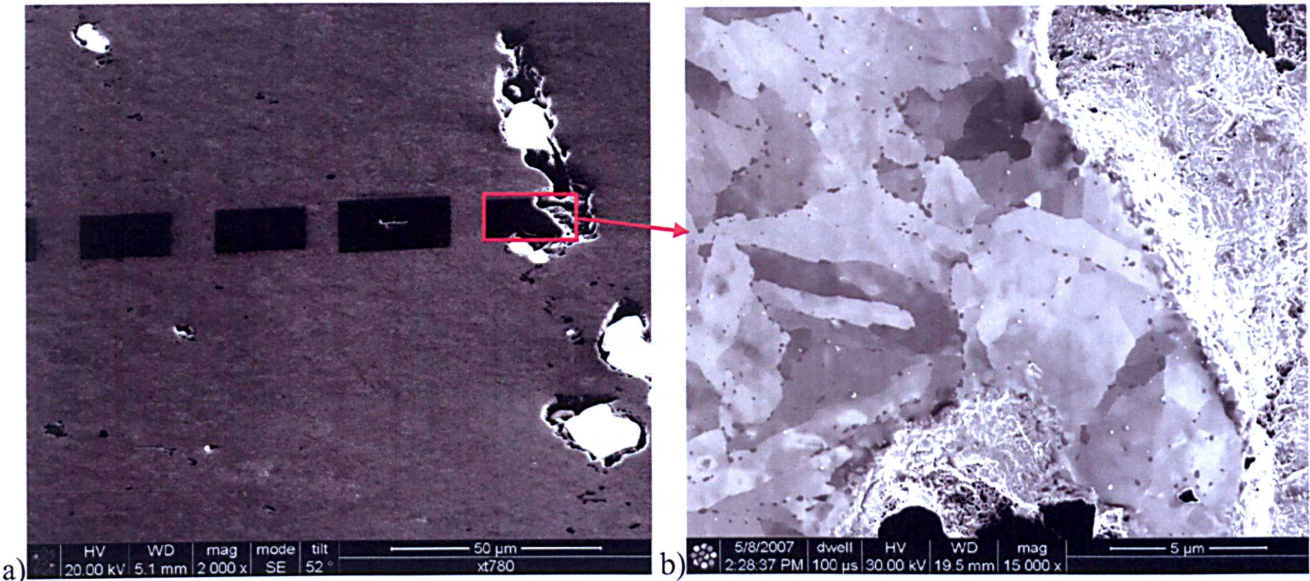


Figure 3.9: a) A secondary electron image and b) an ion-beam induced secondary electron of a grade 91 steel specimen showing creep cavitation after creep testing. The dark rectangles in a) represent the areas that were imaged with b) the ion beam. It can be seen that the ion-beam induced secondary electron image produced appreciable channelling contrast, such that the martensite laths and prior-austenite grain boundaries are easily distinguished.

For the characterization of grade 91 steel with the FIBSEM, specimens were prepared as for EBSD analysis (see section 3.8.1). The best imaging results were achieved using the following operational conditions at a magnification of $\times 15,000$; an accelerating voltage of 30 kV, a current setting of 50 pA, and a raster with a dwell time of 100 μs , giving a total scan time of 90 seconds.

3.11 X-Ray Diffraction

X-ray diffraction has also been employed to characterise the precipitate phases, from electrolytically extracted residues, and the matrix microstructure, from flat polished surfaces, of grade 91 steel. All analyses were performed using a Bruker AXS D8 X-ray diffractometer.

3.11.1 X-Ray Diffraction from Electrolytically Extracted Precipitates

X-ray diffraction on bulk steel specimens is unlikely to yield useful results when investigating minor phase precipitates, as these typically represent less than 1% of the volume of the material. This difficulty can easily be overcome by the electrolytic dissolution of the matrix phase, which leaves a residue of precipitate particles suitable for analysis with X-ray diffraction. The method for carbide extraction is described below.

An electrolytic cell was prepared using a beaker containing 250 ml of 10% HCl in methanol as shown in Figure 3.9. A cylindrical stainless steel plate was inserted into the solution and this is attached to a power supply unit using crocodile clips, where it acted as the cathode. Similarly, the specimen of interest was immersed in the solution and attached to the other lead of the power supply unit. Here, the specimen acted as the anode. A voltage of 1-3 V was applied to give a current density of 1-2 mA/mm², whereby the iron matrix dissolves whilst the carbide and nitride phases will sink to the bottom of the beaker and form a residue.

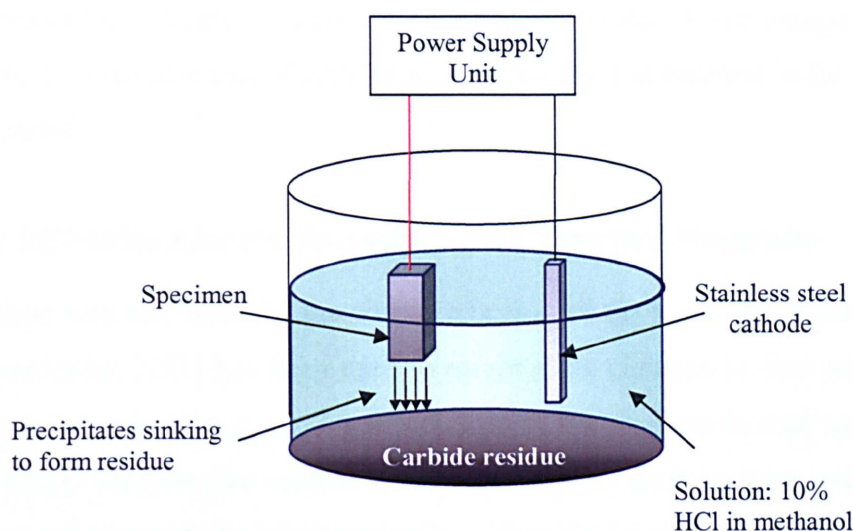


Figure 3.9: A schematic diagram of the electrolytical carbide extraction method. The specimen is the anode, and the iron matrix dissolves. The carbides sink to the bottom of the container where they form a residue.

After a period of approximately 3 hours when a sufficient quantity of carbides was obtained, the carbides were filtrated from the acid solution. In order to achieve this, a filter support is attached to a flask, which is connected to a water pump to achieve a partial pressure inside the flask. A glass microfibre filter paper, with a fine sub-micron mesh (0.02 μm), was then placed in between the filter support and a reservoir. This ensured that particles larger than 20 nm are retained. The reservoir was then filled with the solution from the extraction procedure, and

the residue from the extracted carbides deposited onto the filter paper. Finally, the filter paper containing the carbides was washed with methanol.

The filter containing the particle residue was then studied using 2θ X-ray diffractometer, whereby the data was plotted to a graph of the scattering angle (2θ) versus the intensity. The data was subsequently compared to the data available from the ICDD catalogue ^[32], which lists the various scattering angles and relative intensities for the phases of interest in this investigation. For phase identification, an angle range of 20 to 100° 2θ was used, with a step size of 0.02° 2θ and a dwell time of 30 seconds. The phases of interest were cubic Cr₂₃C₆ (ICDD card no. 35-0783), cubic NbC (ICDD card no. 38-1364), cubic VN (ICDD card no. 35-0768), cubic AlN (ICDD card no. 25-1495) and hexagonal AlN (ICDD card no. 25-1133).

This method has many advantageous attributes and should be used in combination with other identification techniques. The main advantage is that X-ray analysis can support TEM and other microstructural observations, as the amount of material investigated is far greater. In principle, quantitative information may be obtained. The main disadvantage is that particle information, such as particle size, distribution, morphology and location in the microstructure, cannot be obtained.

3.11.2 X-Ray Diffraction Line Profile Analysis from Tempered Martensite

X-ray diffraction was also used for the characterization of the matrix microstructure of grade 91 steel. In particular, XRD has been used to monitor the changes in line profile shape as a function of varying aging times and stress conditions, and was performed on the specimens prepared for EBSD analysis (see section 3.8.1), whereby flat surfaces were polished to a 1 μm finish and were subsequently polished manually with colloidal silica for 30 minutes.

The data was plotted to a graph of the scattering angle (2θ) versus the intensity and was subsequently compared to the ICDD card number (04-08360) for α -iron (ferrite), which list the various scattering angles and relative intensities for this particular phase. For phase identification, an angle range of 40 to 140° 2θ was used, with a step size of 0.02° 2θ and a dwell time of 30 seconds.

3.12 Hardness Testing

A Mitutoyo AVK-C2 Vickers hardness tester with a load of 10 kg was used to measure the hardness on all of the martensitic grade 91 steel samples. The load was applied for 10 seconds during testing on samples with a polished surface finish of 1 μm . At least 5 hardness measurements were taken from each sample and errors were calculated according to ISO 6507: (1/98) Metallic materials, Vickers hardness test. Equation 3.4 shows how mean hardness values were calculated and equation 3.5 shows how the standard deviation was calculated:

$$\bar{x} = \frac{\sum_{i=1}^n x_i}{n} \quad [3.4]$$

$$s_x = \sqrt{\frac{1}{n-1} \sum_{i=1}^n (x_i - \bar{x})^2} \quad [3.5]$$

where S_x is the standard deviation, x_i is the measured value of hardness, \bar{x} is the mean hardness, and n is the number of measurements.

3.13 Summary

The aim of this chapter was to discuss, as well as justify, the experimental techniques chosen in order to understand the microstructural evolution of high Cr power plant steels. From the literature review (Chapter 2), it was apparent that the evolution of these materials involves changes in several microstructural parameters, which can be broadly categorized into changes in the martensite matrix phase as well as changes in minor phase precipitates. Within each category particularly in the latter, both the size and chemical composition of microstructural features can vary considerably to the extent that no one technique can be used in isolation, hence the use of a broad range of techniques, including; optical, scanning and transmission electron microscopy, electron backscatter diffraction and X-ray diffraction, energy dispersive X-ray analysis and parallel electron energy loss spectroscopy.

Chapter 4

EFFECT OF INITIAL HEAT TREATMENTS ON THE MICROSTRUCTURE OF GRADE 91 STEEL

4.1 Introduction

It has been shown by previous workers ^[4,29,36,62] that high Cr steels are very sensitive to pre-service heat treatments which are applied in order to control microstructural features such as grain size, and to ensure that a fine distribution of small creep-resisting second-phase particles are formed, both of which are critical for the performance of power plant components. Conventional pre-service heat treatments consist of two stages; a normalizing treatment, performed between approximately 1050 and 1100°C followed by rapid cooling to martensite, and a subsequent tempering treatment, performed between 750 and 800°C. However, there are instances whereby the microstructure can be disrupted by additional abnormal heat treatments, for example, induced by the process of welding and/or renormalizing. The former gives rise to large temperature gradients, where the microstructure becomes renormalized to different peak temperatures, depending on the proximity of the base metal to the welded joint. The latter may be applied to improve the mechanical properties of a high Cr ferritic-martensitic component.

In this chapter, the effects of varying heat treatment parameters on the microstructure and hardness characteristics of grade 91 steel are described. Therefore, this chapter consists of four main areas of investigation. Firstly, the materials used in this experiment were characterized prior to the application of different initial heat treatments, i.e. in the as-received condition, to serve as a reference point to compare “real” materials to the conditions created in this chapter. Secondly, thermodynamic modelling has been performed to predict the equilibrium microstructure in the grade 91 steels investigated as a function of chemical composition. Thirdly, experimental details of the creation of starting microstructures using a dilatometer to simulate different normalizing conditions are discussed. Fourthly, the effect of varying heat treatment parameters on the microstructure are investigated using a range of different microscopy techniques, which include scanning and transmission electron microscopy, and electron backscatter diffraction. The effects of a post-normalizing tempering treatment on the initial microstructures are also discussed.

4.2 As-received Specimens

The grade 91 pipe materials used in this research were supplied in the normalized and tempered condition by RWE npower (Bar 257) and E.On UK (W20-3). The Bar 257 material is a forged F91 piece which was surplus to a header installation exercise. It had undergone a normalizing heat treatment at 1040°C for up to 6 hours, followed by air cooling to room temperature and then tempering at 760°C for 12 hours. This material had a mean hardness of 190 HV, which is considered comparatively low compared with typical grade 91 hardness values, regarded as acceptable above 200 HV prior to service. The W20-3 material had undergone a normalizing treatment at 1040°C for 1.5 hours, followed by air cooling to room temperature and tempering at 760°C for 2.5 hours. This material had a mean hardness of 208 HV.

4.2.1 Microstructure

Scanning electron micrographs of the two grade 91 materials in the as-received condition are presented in Figure 4.1. It is evident that the microstructure of the as-received specimens comprise of a tempered martensitic matrix, with the prior austenite grains, packet and lath boundaries clearly shown. The microstructure also contained fine intragranular (V,Nb)(N,C) MX precipitates and larger intergranular and interlath Cr-rich $M_{23}C_6$ precipitates; the latter are clearly shown in the images. In addition, the Bar 257 material contained a distribution of relatively large AlN particles, due to its high concentration of Al in comparison to the W20-3 material. The prior austenite grains in Bar 257 and W20-3 were measured by optical microscopy, and had a mean size of approximately 15 and 11 μm respectively.

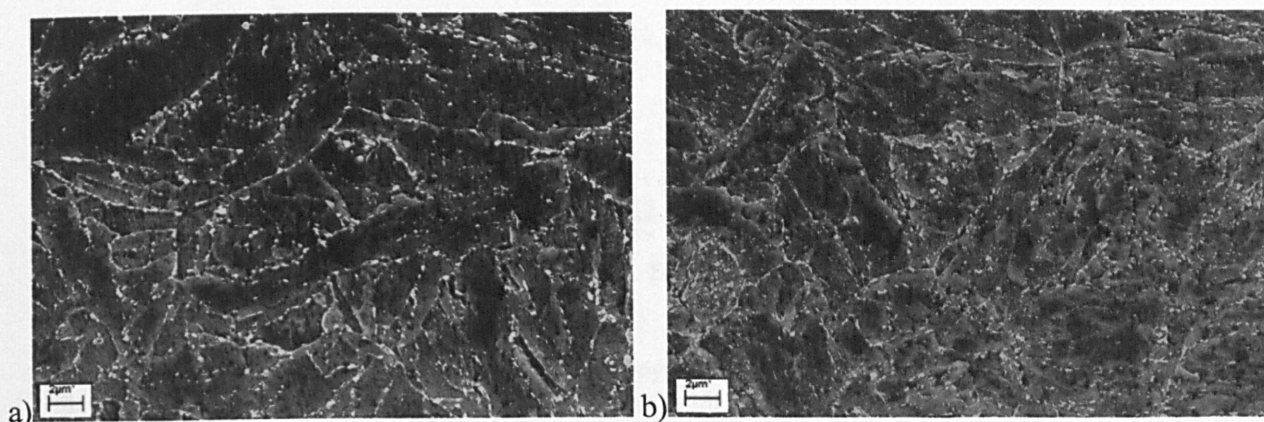


Figure 4.1: SEM In-lens images showing the tempered martensitic microstructure of a) Bar 257 and b) W20-3 materials in the as-received condition. The tempered martensite laths, the prior austenite grain boundaries, and the Cr-rich $M_{23}C_6$ particles decorating these boundaries are shown.

4.3 Equilibrium Predictions of the Phases in Grade 91 Steel

4.3.1 Overview of Predicted Phases

In an alloy which has been extensively aged or subjected to prolonged exposure under typical service conditions, the conditions of thermodynamic equilibrium are likely to be representative of the observed microstructure. Therefore, the equilibrium phases present in Bar 257 and W20-3 were predicted by thermodynamic calculations, performed using the software package MTDATA.

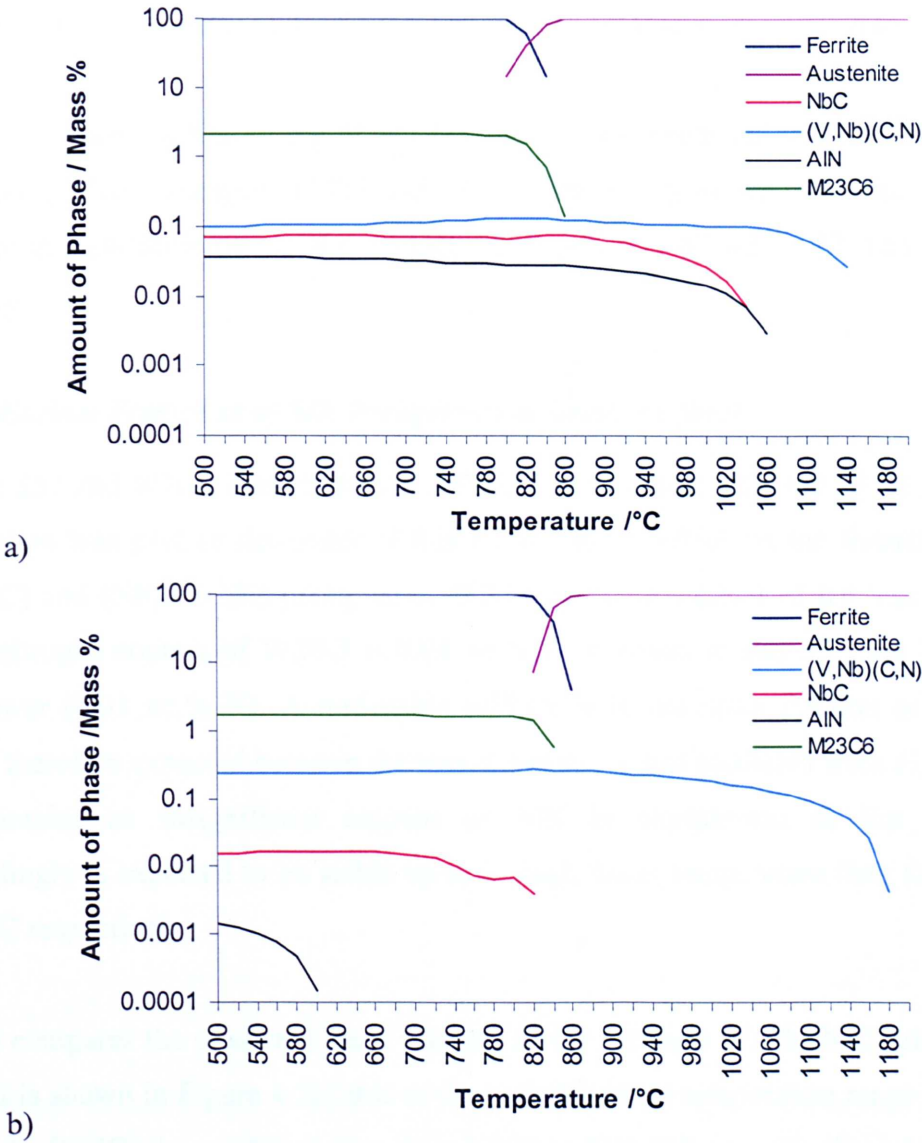


Figure 4.2: Phases predicted to be present at thermodynamic equilibrium in the grade 91 casts investigated, a) Bar 257 and b) W20-3. The calculations were performed with MTDATA.

Figure 4.2, a plot of predicted mass fraction of phase as a function of temperature for the two materials, shows that there are four types of second-phase particles that are in equilibrium in the two steel casts within the temperature ranges spanning the typical operating temperature of 568°C, up to 1200°C (much higher than the normalizing temperature), which are $M_{23}C_6$, AlN and two face-centred cubic MX precipitates, NbC and (V,Nb)(N,C). These four phases are shown to be stable at the service temperature and above, with the least stable carbide, $M_{23}C_6$, being predicted to be stable up to approximately 850°C. Indeed, the microstructure of the as-received materials, which have been tempered at 750°C, showed the presence of $M_{23}C_6$ precipitates (Figure 4.1). It is also shown that the (V,Nb)(C,N) precipitate is even stable at temperatures of up to 1180°C in the W20-3 material, and stable in Bar 257 up to ~1140°C.

The maximum mass fraction of the $M_{23}C_6$ precipitates was predicted to be higher in the Bar 257 than in the W20-3 material, 0.0214 and 0.017, respectively, which can be attributed to the higher carbon concentration in the former compared to W20-3; 0.12 and 0.09 wt.%, respectively.

4.3.2 Equilibrium Prediction of MX Precipitates in Grade 91 Steel

As the Bar 257 and W20-3 materials have different N:Al ratios, 1.11 and 13.33 respectively, close attention was paid to determine if this factor has an effect on the formation of AlN, (V,Nb)(N,C) and (Nb,V)(C,N) precipitates. W20-3 contains a factor of ten less Al than Bar 257. The nitrogen content of W20-3 is 0.04 wt.% N, whereas in Bar 257, the N content is slightly lower (0.03 wt.% N). A noticeable difference in the mass fraction of each minor phase was therefore expected between the two materials. It was predicted from Figure 4.2 that W20-3 contains an insignificant amount of AlN in comparison to Bar 257, which correspondingly is expected to be stable up to a much lower temperature than the latter, 620 and 1080°C respectively.

Figure 4.3 compares the predicted mass fraction of the AlN and (V,Nb)(N,C) phases in each material. It is shown in Figure 4.3a) that at the typical service temperature range for grade 91 steel, 500 to 600°C, the predicted amount of AlN in Bar 257 is approximately 0.037%, in comparison to W20-3, which is predicted to contain 0.002%. This means that if AlN, if present, would be difficult to detect in the W20-3 material by means of microstructural characterization. Interestingly, Figure 4.3b) shows that the MX phase (V,Nb)(N,C) is

predicted to be present in a significantly greater quantity in W20-3 (0.25%) than in Bar 257 (~0.13%).

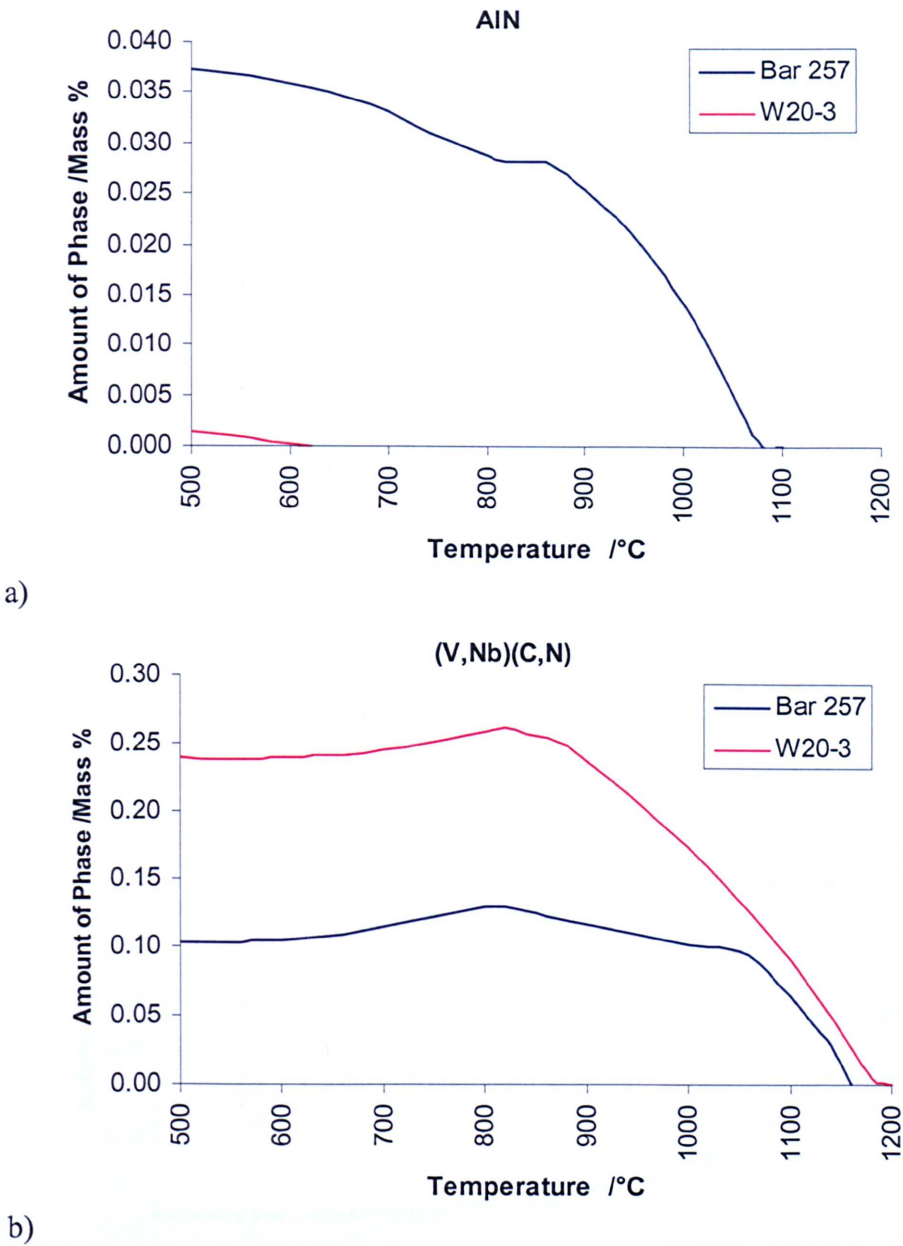


Figure 4.3: Mass fraction calculations showing the predicted amount of a) AlN and b) MX phases in each investigated material. The calculations were performed with MTDATA.

At lower temperatures in the (V,Nb)(N,C) phase, the two most stable elements are nitrogen and vanadium, implying that this phase consists predominantly of vanadium nitride (VN) (Figure 4.4). However, it is clearly shown that the niobium concentration gradually increases with increasing temperature, replacing the vanadium content in MX in both materials. In the Bar 257 material, Nb is predicted to become the dominant metallic element in MX at a

temperature of approximately 1070°C (Figure 4.4a)). The increase in Nb content in MX is not predicted to occur until even higher temperatures in the W20-3 material (Figure 4.4b)). This result indicates that the composition of the MX precipitates is sensitive to minor variations in the composition of the steel cast.

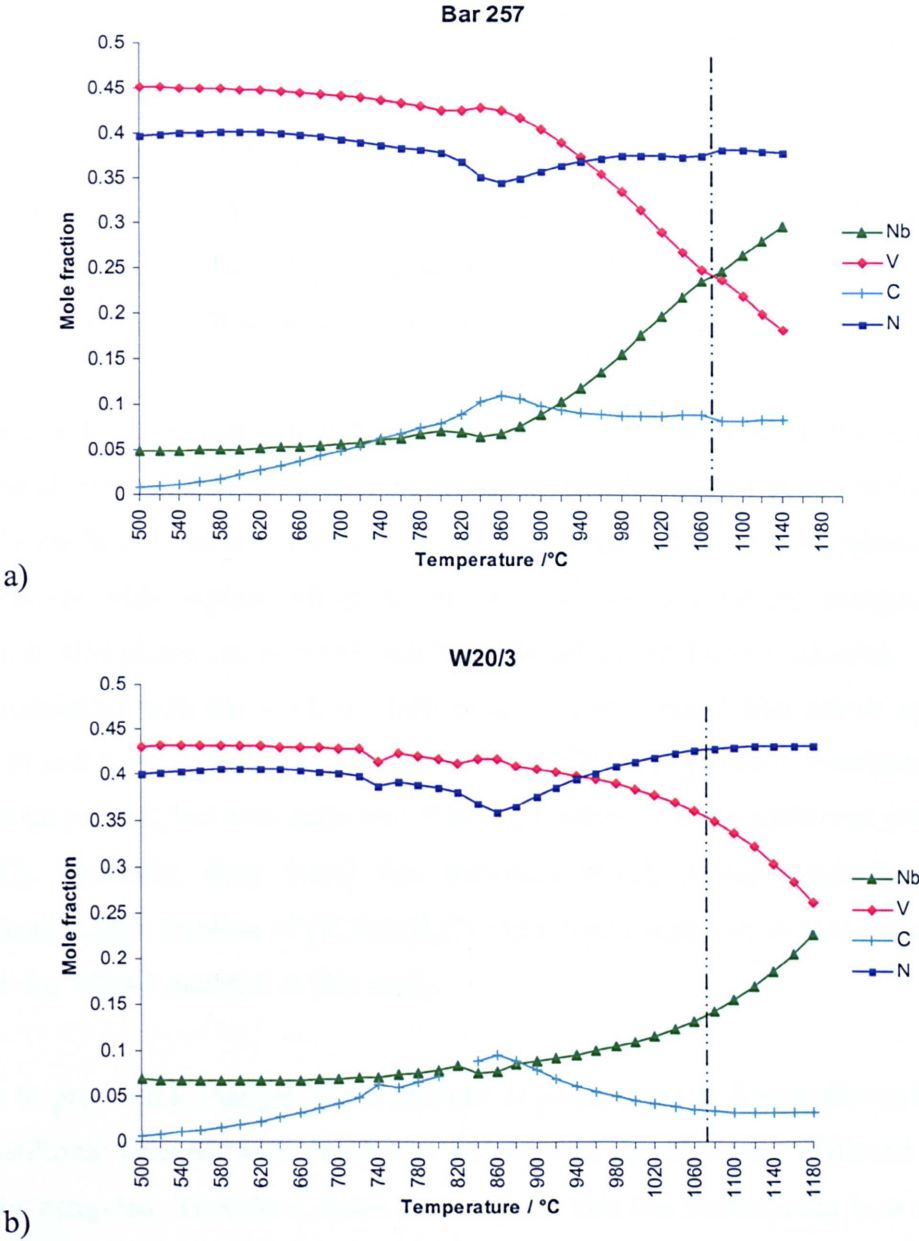


Figure 4.4: The calculated compositions of the (V,Nb)(C,N) phase present in the a) Bar 257 and b) W20-3 materials. The dotted black line represents the temperature at which Nb is expected to become the dominant metallic element in this phase in the Bar 257 material (~1070°C). The line is also shown in W20-3 at the same temperature, which illustrates that there are differences in the composition of MX precipitates between the two materials investigated.

4.3.3 Discussion of Equilibrium Predictions

Section 4.3.2 has shown that even though there are only minor variations in cast composition between the Bar 257 and W20-3 materials, the quantity, type, chemical composition and thermal stability of minor phase precipitates is predicted to vary significantly between the two casts.

Brett *et al.* ^[41] carried out similar predictions, where the percentage of minor phases was compared between the Bar 257 material and an ex-service alloy with a similar chemical composition, but with a high N:Al ratio of 5.7. Their calculations showed that in the material with a high N:Al ratio, the MX phase was predicted to be exclusively (V,Nb)(N,C), whereas the Bar 257 material MX was predicted to contain (V,Nb)(N,C), (Nb,V)(C,N) and AlN as the minor phases present, which is consistent with the findings presented in Figure 4.3.

It can therefore be seen that the N:Al ratio plays an important part in the predicted mass fraction, and identity, of the MX phase. It was shown that the mass fraction of this precipitate is greatest in the W20-3 sample, followed by Bar 257, which contain N:Al ratios of 13.33 and 1.11 respectively. This implies that more nitrogen was available for the precipitation of VN, hence more of this phase can be predicted to be found in the W20-3 material. These results are again consistent with the work of Brett *et al.* ^[41], who stated that above approximately 0.04 wt.% N and high Al levels (0.026 wt.% for Bar 257), significant quantities of AlN are predicted to be present, but with sufficient N being available for the additional precipitation of (V,Nb)(N,C). Similarly, they found that materials which contain high N and low Al concentrations, a high fraction of (V,Nb)(N,C) and a low fraction of AlN is expected, as was the case for the W20-3 material in this study.

In addition to promoting changes in the amount of phase present, it was shown in Figure 4.4 that compositional changes with respect to temperature are also very different between the two casts investigated. Therefore, these data suggest that the normalizing heat treatment, in addition to material composition, may influence the initial concentration of the different elements in this phase, which is considered important in determining the creep strength of these steels.

The findings from these calculations predict that the industrial specifications for normalizing heat treatments, which is carried out in the temperature range 1040-1080°C ^[4], do indeed succeed in dissolving most of the carbides in a grade 91 steel as $M_{23}C_6$ represents the largest proportion of second-phase precipitate in these steels, approximately two orders of magnitude greater than AlN and the other MX phases.

Normalizing within the temperature range of 1040-1080°C also predicts the complete dissolution of the NbC phase. The temperature at which AlN is predicted to fully dissolve (~1076°C) is very close to the maximum normalizing temperature (1080°C). These predictions thus imply that unless the maximum normalizing temperature is always applied, there may be traces of AlN particles present in the microstructure after quenching and tempering. The result, as indicated by thermodynamic equilibrium calculations, is that there would be less free nitrogen available for the precipitation of MX nitrides such as VN, resulting in a lower fraction of these particles precipitating. This scenario may be detrimental to the creep resisting properties of these steels. Realistically however, this would only apply to grade 91 materials with high concentrations of Al, as it has already been shown that in the W20-3 (with a low Al conc.), the AlN phase (if present) is predicted to dissolve at ~600°C. The actual magnitudes of the predicted dissolution temperatures require additional experimental verification.

4.3.4 Summary of Thermodynamic Equilibrium Predictions

Thermodynamic calculations provide a sound basis from which to construct an understanding of grade 91 steel. It has been shown that predictions can be made of the relative fraction of secondary phases, which in turn are likely to affect the creep strength of grade 91 steel. However, it should be noted that the predictions are based on thermodynamic equilibrium and therefore how fast the steel may reach this state is not taken into account, thus additional experimental work is necessary to investigate kinetic effects.

4.4 Creation of Starting Microstructures

Initial microstructures were produced by applying a normalizing heat treatment on the as-received Bar 257 and W20-3 materials. This was achieved by employing the use of a dilatometer, which facilitates the application of closely monitored and controlled heat treatments. For this investigation, a range of three different normalizing temperatures, 975, 1050 and 1100°C and two different cooling rates, 1 and 100°Cs⁻¹ were applied in order to study the effect of these heat treatment variables on the structure of grade 91 steel. The chosen temperature range corresponds to the peak temperatures experienced across the heat-affected zone (HAZ) line in a finite element analysis study of grade 91 steel by Yaghi *et al* [95]. The slower cooling rate was employed to account for the cooling behaviour that a thick section grade 91 might exhibit during air cooling from a normalizing temperature in the region of 1050°C. This might then mimic the cooling behaviour of an as-manufactured parent metal bar. The faster cooling rate employed was chosen to account for the rapid cooling behaviour exhibited by grade 91 steel during a typical multipass welding treatment, given the high thermal conductivity of this material.

4.4.1 Results from Dilatometry Experiments

From dilatometry testing, the martensite start temperature (M_s) can be determined from each of the heat treatments applied. Figures 4.5 and 4.6 show results obtained from dilatometry testing on the Bar 257 and the W20-3 material respectively. The M_s temperature was determined as the point on the change in length versus temperature curve that indicates the onset of the transformation of the martensite phase on cooling from the normalizing temperature. A summary of the results is presented in Table 4.1, from which it is evident that with increasing cooling rate, the M_s temperature decreases regardless of material and normalizing temperature. However, there seems to be no correlation between the M_s temperature and the normalizing temperature at a holding time of 15 minutes. Table 4.1 also suggests that chemical composition plays a significant role in the M_s temperature. Indeed, the M_s temperatures in the W20-3 specimens are somewhat lower than for the Bar 257 specimens. In addition, the drop in M_s temperature with increasing cooling rate is greater in the W20-3 material.

There are other interesting features in the graphs of change in length versus temperature. Further inspection of these graphs reveals that the shape of the cooling curve after the

martensite transformation had initiated is very different between the two cooling rates. In the rapidly cooled specimen the curve appeared to be smooth, whereas in the slower cooled samples there are peculiar 'kinks' in the curve, which would suggest some sort of additional transformation reaction occurring in this condition. To validate these results, dilatometry experiments were repeated, this time using extended times under normalizing conditions (30 minutes and 1 hour) in order to ensure the materials were not under-normalized (Figure 4.7). Table 4.2 shows the relationship between M_s and the time at normalizing temperature and cooling rate for the Bar 257 material. It can be seen that the M_s temperature decreases with longer holding times at 1050°C, and also that the M_s temperature is significantly lower at the faster cooling rate.

The kink does not appear to reduce as the normalizing time increases, which indicates that an additional process is occurring at the slower cooling rate, most probably considerable auto-tempering. Indeed, this feature on the cooling curve appears directly after the martensite start temperature. However, it is apparent that the maxima curve becomes smoother with increasing time at the normalizing temperature. It is also interesting to note that the bottom kink becomes larger and more noticeable with increasing normalizing temperature for both materials (Figures 4.5 and 4.6). This may indicate that a higher degree of auto-tempering is occurring, due to the increased availability of carbon from the dissolution of pre-existing carbides.

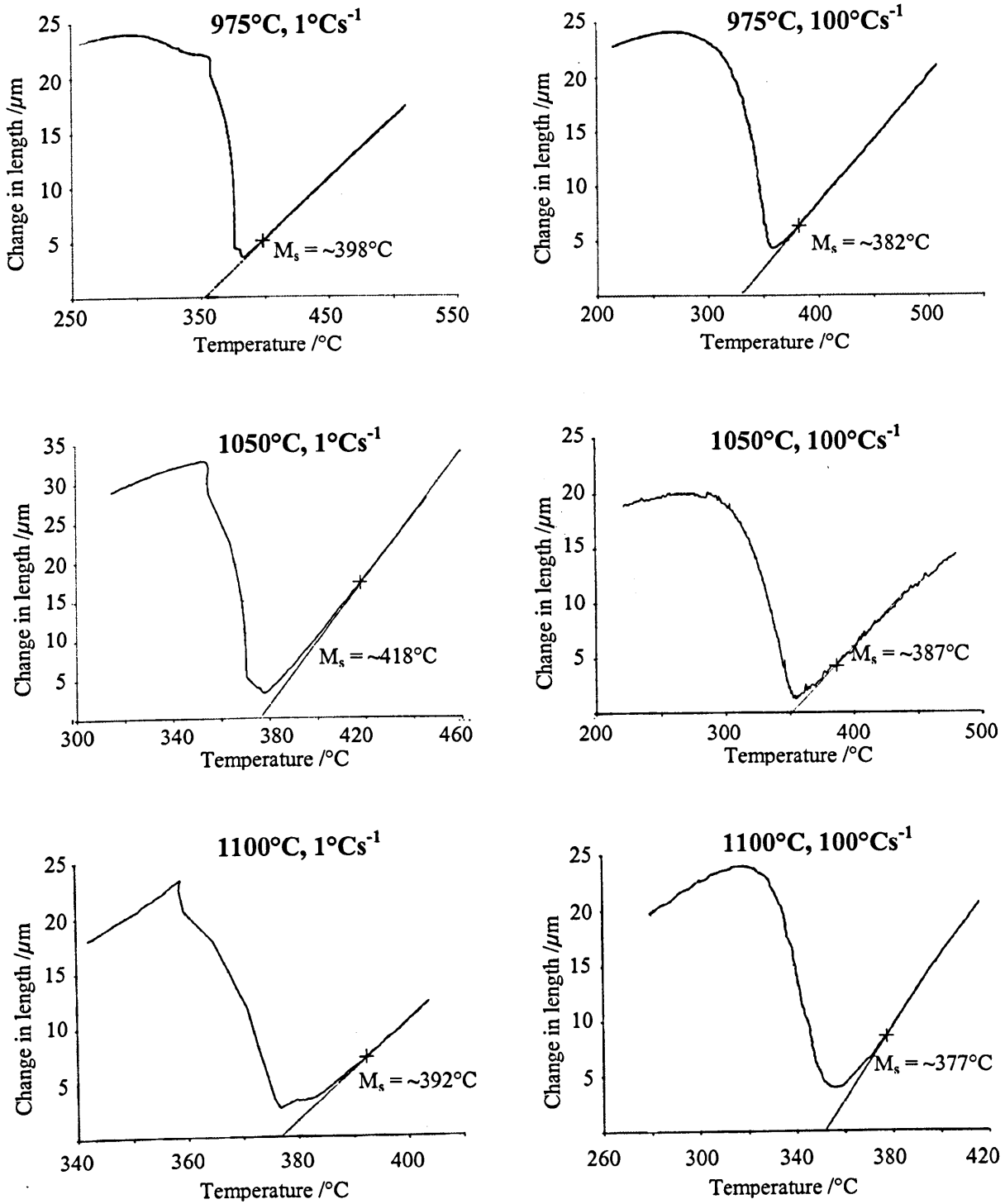


Figure 4.5: Dilatometry plots illustrating the change in length with respect to temperature on cooling of the Bar 257 specimens from the normalizing temperature: 975 $^{\circ}\text{C}$ (held for 15 minutes) cooled at a) 1 and b) 100 $^{\circ}\text{Cs}^{-1}$, 1050 $^{\circ}\text{C}$ (held for 15 minutes) cooled at c) 1 and d) 100 $^{\circ}\text{Cs}^{-1}$, and 1100 $^{\circ}\text{C}$ (held for 15 minutes) cooled at e) 1 and f) 100 $^{\circ}\text{Cs}^{-1}$. Indicated in the plots are the approximate martensite start temperatures (M_s).

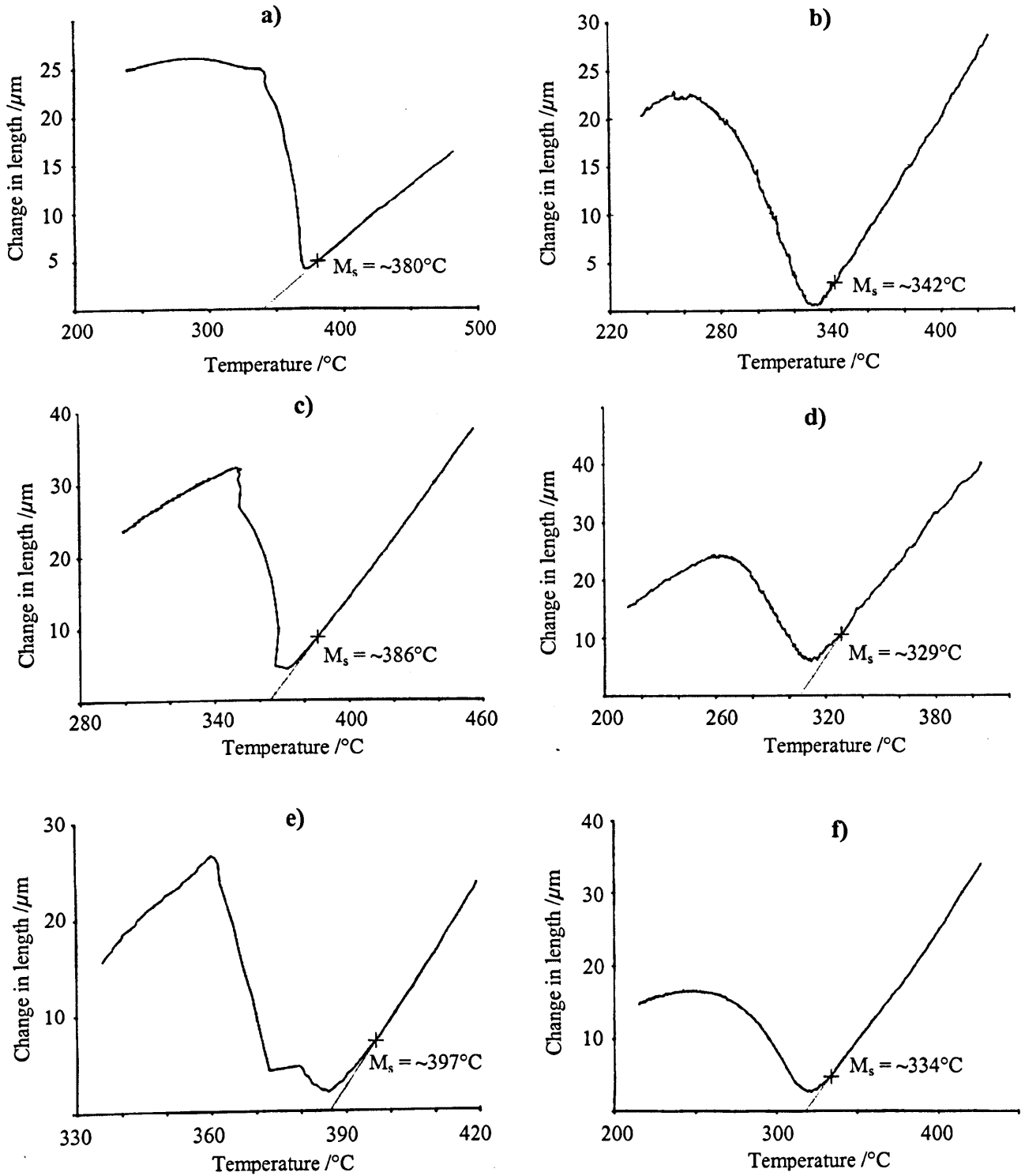


Figure 4.6: Dilatometry plots illustrating the change in length with respect to temperature on cooling of the W20-3 specimens from the normalizing temperature: 975°C (held for 15 minutes) cooled at a) 1 and b) 100°Cs⁻¹, 1050°C (held for 15 minutes) cooled at c) 1 and d) 100°Cs⁻¹, and 1100°C (held for 15 minutes) cooled at e) 1 and f) 100°Cs⁻¹. Indicated in the plots are the approximate martensite start temperatures (M_s).

Normalizing Temperature and Cooling Rate	M _s Temperature (°C)	
	W20-3	Bar 257
975°C, 1°Cs ⁻¹	380	398
975°C, 100°Cs ⁻¹	342	382
1050°C, 1°Cs ⁻¹	386	418
1050°C, 100°Cs ⁻¹	329	387
1100°C, 1°Cs ⁻¹	397	392
1100°C, 100°Cs ⁻¹	334	377

Table 4.1: Martensite start temperatures (M_s) measured from dilation experiments (from Figures 4.5 and 4.6) for both materials at the applied heat treatments.

Holding time at 1050°C (mins)	M _s temperature at a cooling rate of 1°Cs ⁻¹	M _s temperature at a cooling rate of 100°Cs ⁻¹
15	418	387
30	393	367
60	385	-

Table 4.2: Relationship between martensite start temperature (M_s) and time at normalizing temperature and cooling rate for the Bar 257 material.

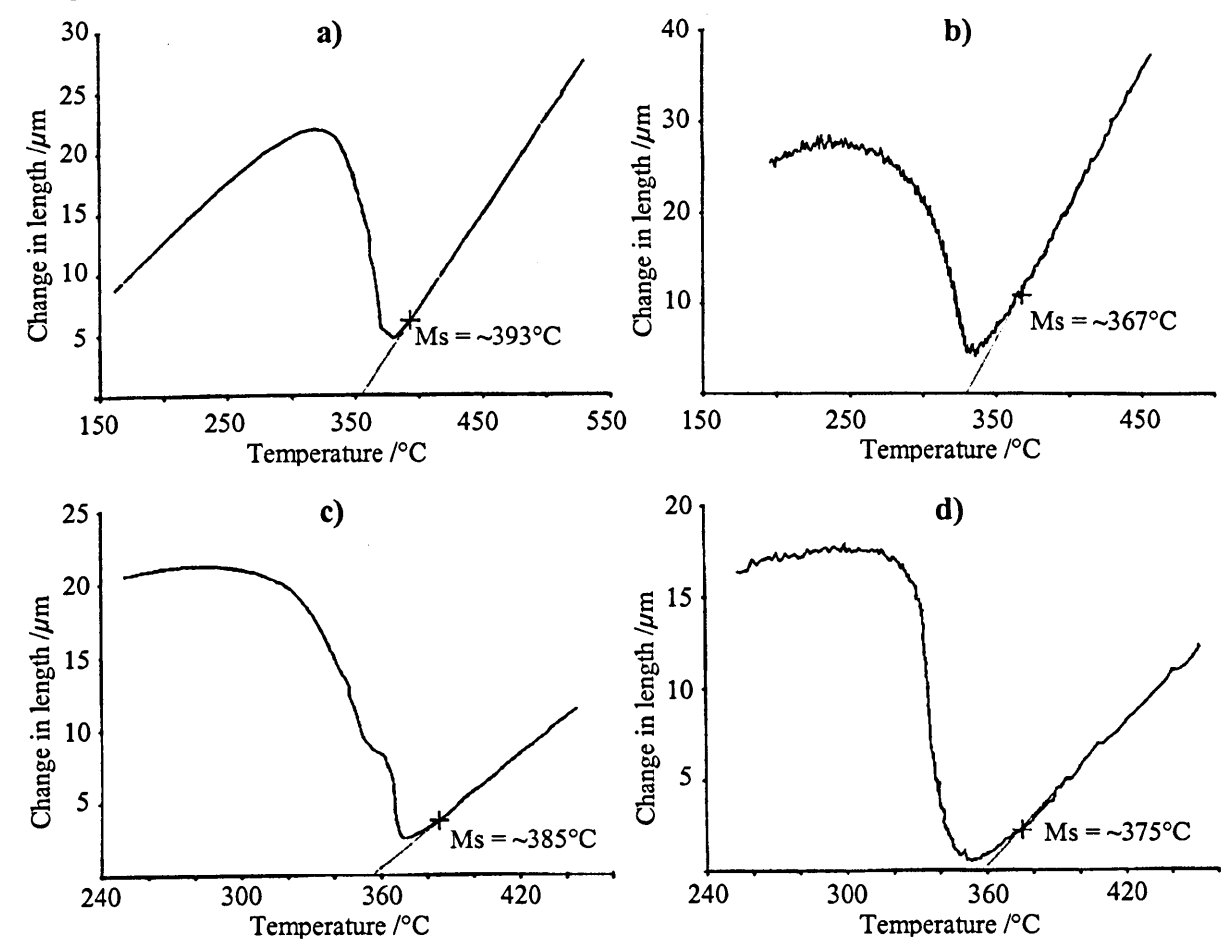


Figure 4.7: Dilatometry plots illustrating the change in length with respect to temperature on cooling of Bar 257 specimens from the applied normalizing temperature: a) Normalized at 1050°C for 30 mins and cooled at 1°Cs⁻¹, b) normalized at 1050°C for 30 mins and cooled at 100°Cs⁻¹, c) normalized at 1050°C for 1 hour and cooled at 1°Cs⁻¹ and d) normalized at 1050°C for 15 mins and cooled at 500°Cs⁻¹. Also indicated in the plots are the approximate martensite start temperatures (M_s).

4.4.2 Discussion of Dilatometry Results

It was shown in Table 4.1 that with increasing cooling rate, the M_s temperature decreases regardless of material and normalizing temperature. This result is consistent with that of Kim *et al* ^[107], who found that the martensite start temperature lowered from 340 to 318°C when the cooling rate increased from 2 to 10°C/min respectively in a X20CrMoV steel (normalizing temperature was unreported). These results are also consistent with the work of Berglund *et al* ^[108] who reported a decrease in the M_s temperature when increasing the cooling rate of a martensitic stainless steel (composition unreported) from 10°Cs⁻¹ to 100°Cs⁻¹. Pickering and Vassiliou ^[64] showed that the M_s temperature decreased systematically by increasing the normalizing temperature from 900 to 1100°C, which was correlated with the effect of undissolved carbides on the composition of the austenite in 9Cr-1Mo steel. Interestingly, although a similar temperature range was employed in this study, no correlation was evident between the normalizing temperature, holding for 15 minutes, and the subsequent M_s temperature on cooling. However, it was found that a gradual decrease in M_s temperature occurred with increasing the holding time from 15 to 60 minutes at 1050°C, indicating that a greater degree of particle dissolution, from Pickering and Vassiliou's hypothesis ^[64], had occurred. This result is indicative that the specimens held at 15 minutes may have been slightly under-normalized due perhaps to incomplete particle dissolution. Notwithstanding this, microstructural characterization is required to investigate the effects of the different normalizing treatments on the microstructure of these specimens to verify dilatometry results.

Skrotzki and Wiech ^[109] found that the M_s transformation temperature was higher in an Fe-Ni alloy that contained phosphorous as opposed to a binary Fe-Ni alloy, which was attributed to the fact that phosphorous strongly raises the thermodynamic equilibrium temperature at which ferrite and austenite have the same free energy. Indeed, the Bar 257 material contains a slightly higher P concentration (0.013 wt.%) than the W20-3 material (0.008 wt.%), which may explain the lower transformation temperatures in the latter. On the contrary, by applying the empirical Andrews ^[110] formula:

$$M_s (^{\circ}\text{C}) = 539 - 423 \times \text{wt.\% C} - 30.4 \times \text{wt.\% Mn} - 17.7 \times \text{wt.\% Ni} - 12.1 \times \text{wt.\% Cr} - 7.5 \times \text{wt.\% Mo}$$

for calculating the M_s temperature with respect to chemical composition it was shown that the Bar 257 material had a lower transformation temperature than the W20-3 material, 364.3 and 374.1°C respectively. Indeed, it is likely that the application of the empirical Andrews ^[110]

formula yields erroneous results when used for such comparisons, as it only considers a few select elements (C, Mn, Ni, Cr and Mo) and is heavily dependent on the carbon concentration, which is at the upper limit in the Bar 257 material for grade 91 steels, hence the lower predicted M_s values for this material.

Given that at the slow cooling rate the material is exposed to higher temperatures for longer time periods, it is expected that the extent of carbide dissolution will be greater than at the faster cooling rate. Therefore, this should have a similar effect to slightly increasing the normalizing temperature and cooling at the same fast rate. However, the fact that M_s temperature decreases with increasing cooling rate indicates that this phenomenon is governed by some other factor, such as prior austenite grain size, which will be discussed later on in this chapter.

4.5 Analysis of As-normalized Microstructures

One topic of particular interest was the study of the effect of cooling rate from the normalizing temperature on the microstructure of both materials, and the effect of initial microstructure on subsequent tempering and aging treatments. This type of study may yield commercially important results, as welded metals tend to experience different cooling rates from peak temperatures in different sections of the weld, for example, in the molten material, the heat affected zone and the parent metal. It is widely known that the different microstructures produced in each of these zones results in heterogeneous mechanical properties, which tend to give rise to weak sections in the weld; an obvious problem being Type IV cracking. Therefore, this study was performed in order to achieve a better understanding of how initial microstructures produced from varying heat treatments evolve, so that these data may be subsequently used for more accurate microstructure-based creep life predictions.

4.5.1 Martensitic Lath and Subgrain Structure

4.5.1.1 Results

Scanning electron microscopy was used to study the both the lath and subgrain structure of martensite, and the presence and characteristics of precipitates in all the materials subjected to different heat treatments.

Figure 4.8 shows the microstructures obtained in the Bar 257 specimens, which have experienced different normalizing temperatures and cooling rates. Visual inspection of these micrographs immediately reveals that there are clear distinctions between the samples cooled at different rates. The lath boundaries on the specimens that have been cooled at the slower rate (1°Cs^{-1}) tend to be a much lighter/whiter colour and they also appear to be slightly thicker. Retained austenite formation on the boundary regions is a possibility. However, according to Koistinen and Marburger ^[111] calculations ($V_m = 1 - \exp^{-\alpha(M_s - T)}$), the predicted volume fraction of retained austenite is $\sim 2\%$, which does not correspond to microstructural observations. Also, by definition, high Cr steels have a very high hardenability, thus in principle the same martensite structure should be present providing the cooling rate is not excessively slow as to produce a bainitic or mixed microstructure. In addition, it was shown from the dilatometry results that the M_s temperature reduces with increased cooling rate. However, this would predict a slightly higher fraction of retained austenite (if present) in the faster cooled samples, which from visual inspection is clearly not the case.

Figure 4.9 shows the microstructures obtained in the as-cooled W20-3 samples. It is clear that the differences between the lath structures cooled at the two different rates is much greater than those obtained in the Bar 257 samples. For example, the differences in the contrast and thickness of lath boundary regions between the two cooling rates is greater in the W20-3 material. In addition, there appears to be an appreciable reduction in auto-tempered precipitates in the fast cooled W20-3 specimen. which would suggest that chemical composition plays a significant role in the microstructure in the as-cooled condition. Indeed, the fact that the carbon content is in the lower limit in W20-3 must be considered, which may affect the precipitation kinetics of auto-tempered particles.

Transmission electron microscopy ascertained the lack of retained austenite in both materials after cooling at the slow and fast cooling rates. Instead, lath martensite with a high density of dislocations was observed (Figure 4.10).

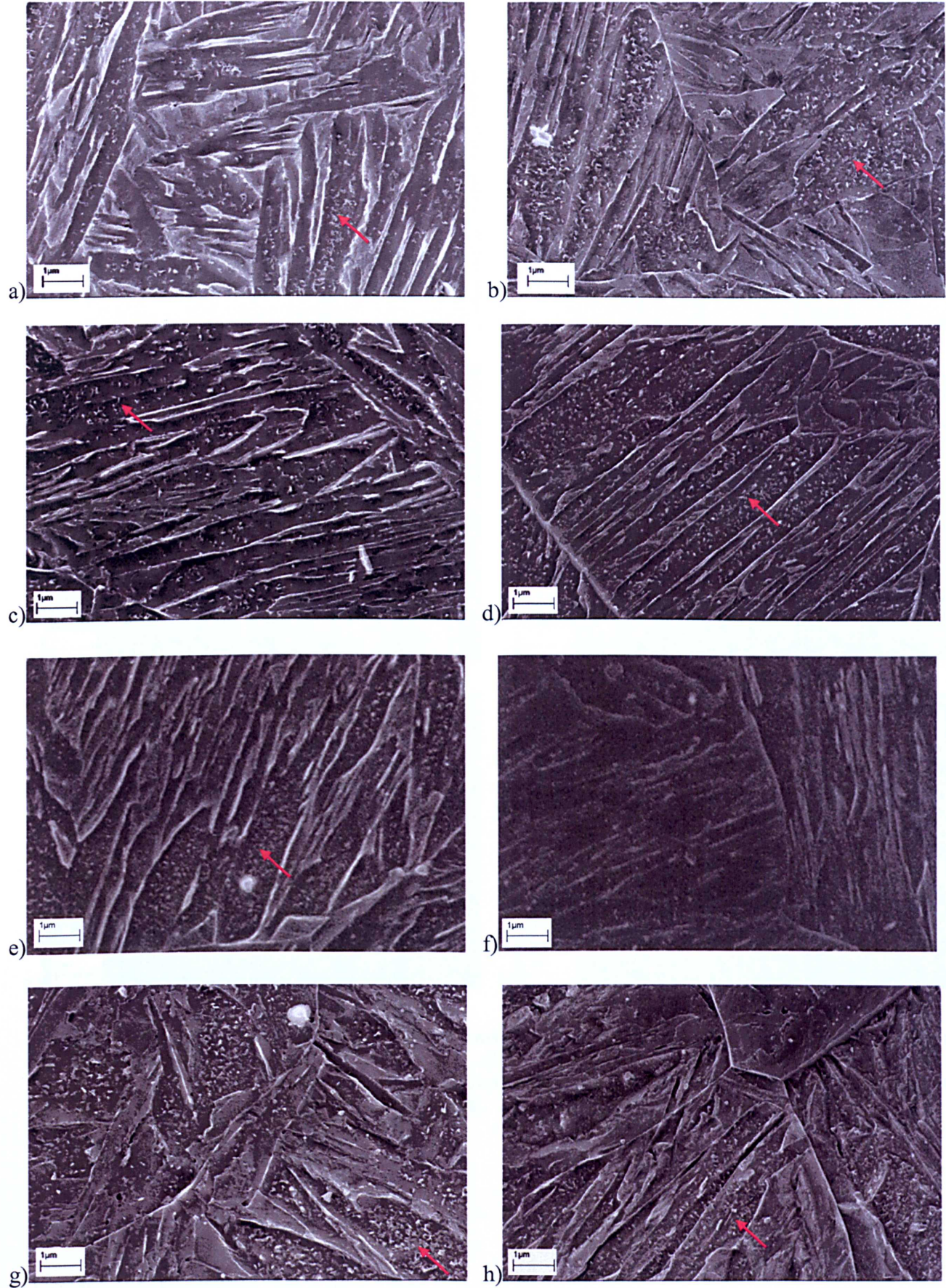


Figure 4.8: SEM images showing the martensitic lath structure of the as-cooled Bar 257 specimens: 975°C (held for 15 minutes) cooled at a) 1 and b) 100°Cs⁻¹, 1050°C (held for 15 minutes) cooled at c) 1 and d) 100°Cs⁻¹, 1050°C (held for 30 minutes) cooled at e) 1 and f) 100°Cs⁻¹, and 1100°C (held for 15 minutes) cooled at g) 1 and h) 100°Cs⁻¹. Auto-tempered particles were also detected in the intralath regions, indicated by a red arrow.

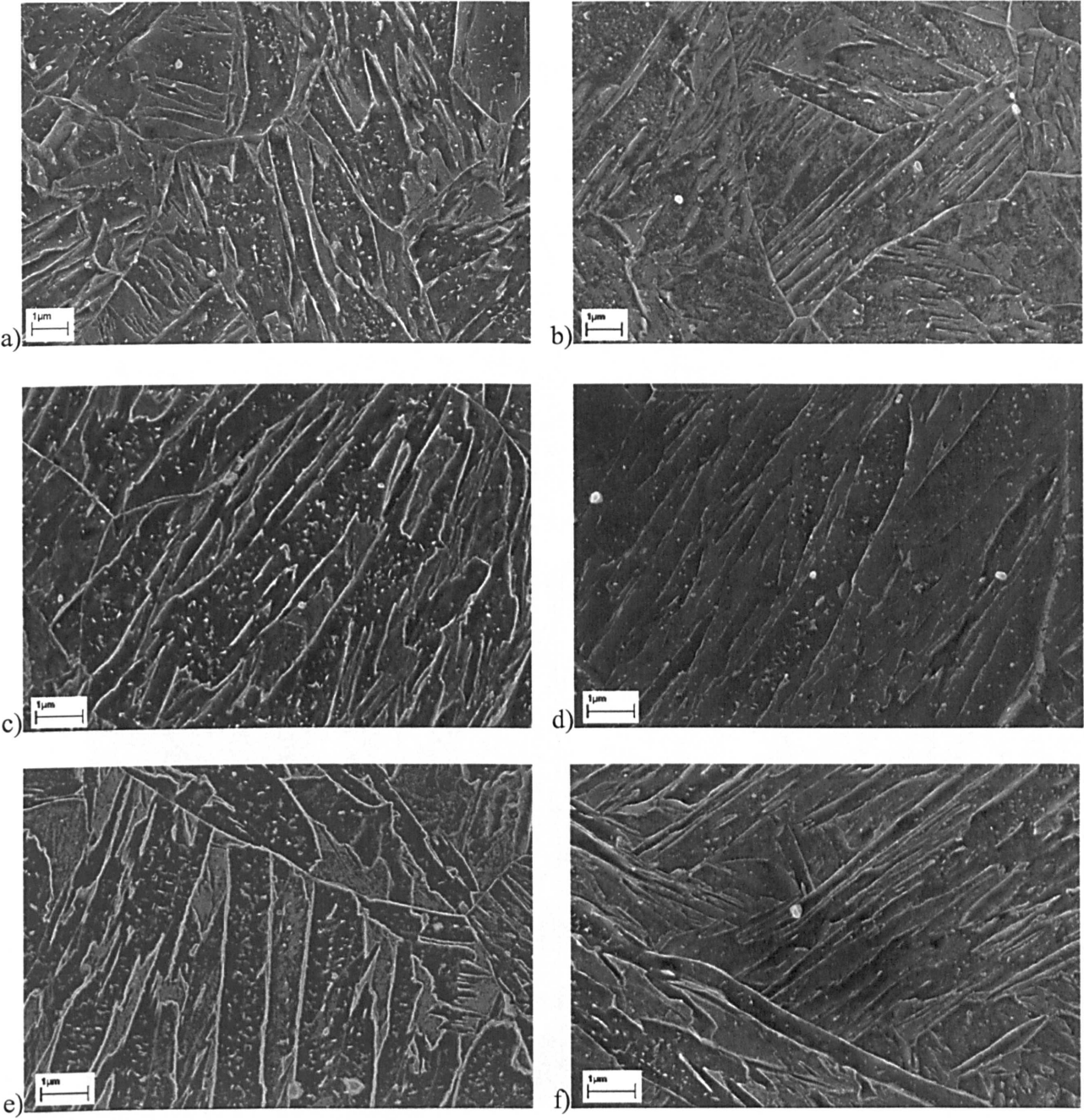


Figure 4.9: SEM In-lens images showing the martensitic lath structure of the as-cooled W20-3 specimens: 975°C (held for 15 minutes) cooled at a) 1 and b) 100°Cs⁻¹, 1050°C (held for 15 minutes) cooled at c) 1 and d) 100°Cs⁻¹, and 1100°C (held for 15 minutes) cooled at e) 1 and f) 100°Cs⁻¹. The presence of auto-tempered was also detected in the intralath regions of this material.

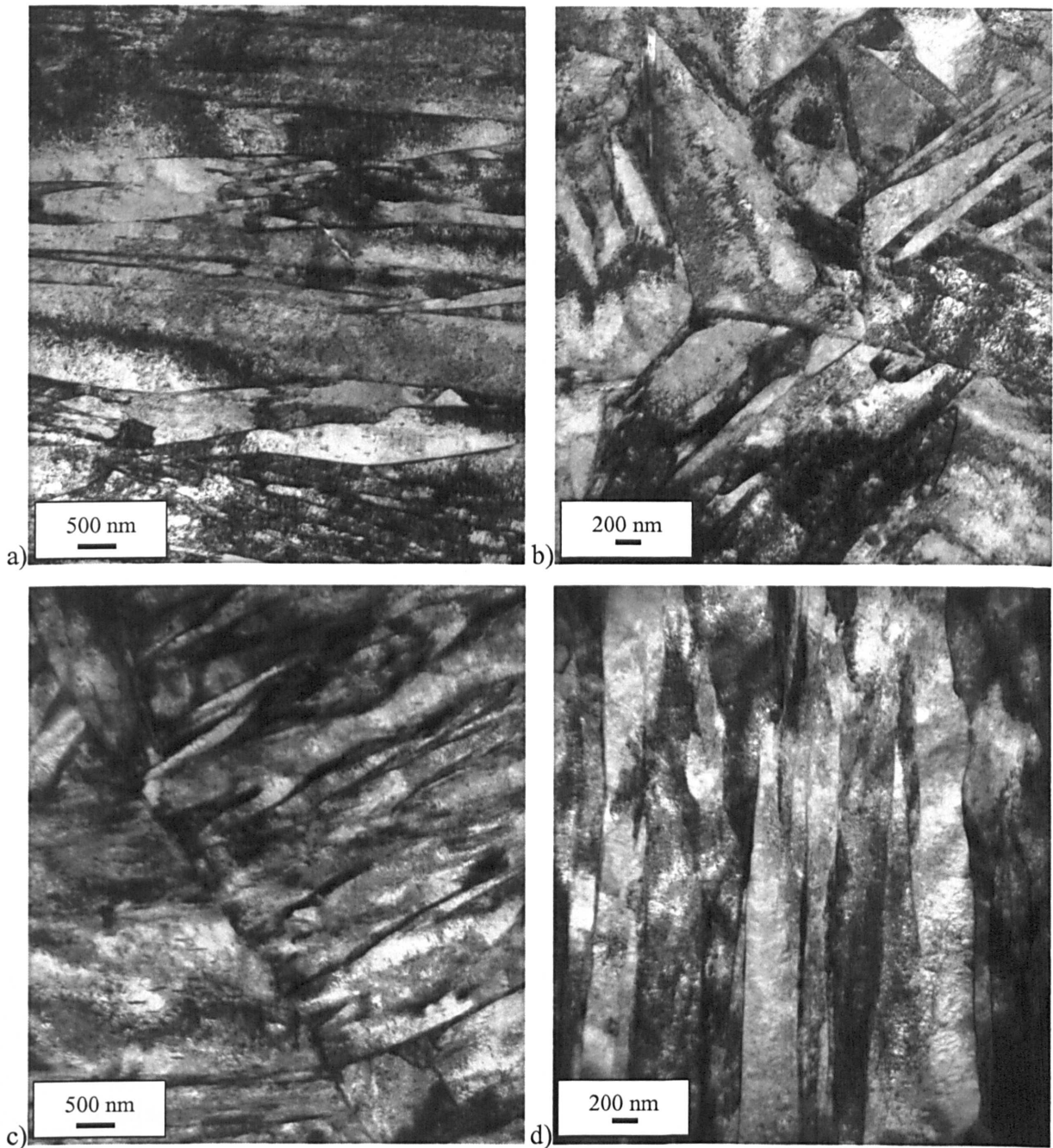


Figure 4.10: Bright field transmission electron micrographs of thin-foil specimens showing the lath martensite microstructure of as-cooled P91 materials that had experienced a normalizing heat treatment of 1100°C for 15 minutes; Bar 257 cooled at a) 1 and b) 100°Cs⁻¹, and W20-3 cooled at c) 1 and d) 100°Cs⁻¹.

Figures 4.11 a) and b) illustrate the effect that the applied normalizing treatments have had on both the prior austenite grain size (henceforth PAG) and on the martensitic lath width, respectively, of the Bar 257 and the W20-3 materials. In the first graph, it is evident that the mean PAG size increases with increasing normalizing temperature (Figure 4.11a)). It can also be seen that the grain growth is more severe in the Bar 257 specimen. Interestingly, there is a trend, for both materials, whereby the grain size of the faster cooled specimens, at each temperature, decreases slightly in comparison to the slower cooled specimens. It can also be

seen that in general the martensite lath width increases as PAG size increases in both materials. Figure 4.11b) shows that the martensite lath width increases with increasing normalizing temperature. Similarly to the effect on PAG size, the cooling rate also affects the martensite lath width, such that it decreases at the faster cooling rate. Interestingly, there appears to be $\sim 0.05 \mu\text{m}$ difference in the lath width between the each temperature step which in some cases is similar to the effect of varying the cooling rate. It is shown on the same graph that the higher the normalizing temperature, the greater the difference in mean lath width between the slow and fast cooled specimens.

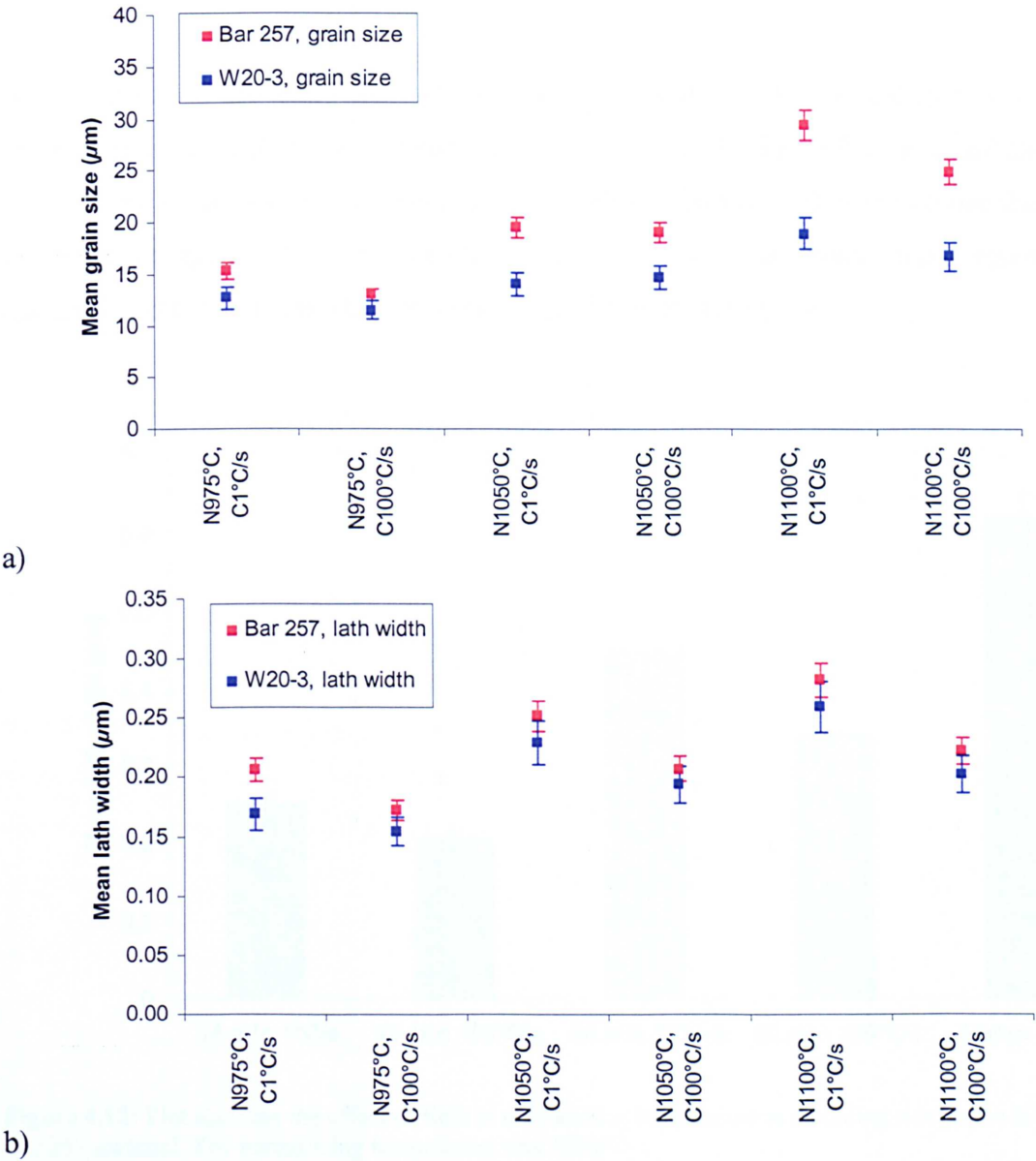


Figure 4.11: Plots showing the effect of normalizing temperature (N) and cooling rate (C) on a) the prior austenite grain size and b) the mean martensitic lath width of the Bar 257 and W20-3 materials. The time at the normalizing temperature was 15 minutes.

The effect of time at the normalizing temperature was also investigated, and the results are shown in Figure 4.12. Interestingly, it is shown that normalizing time also plays a significant role on the lath width of grade 91 steel. It can be seen that doubling the exposure time at a normalizing temperature of 1050°C from 15 minutes to 30 minutes doubles the mean lath width of the Bar 257 material, and also increasing the exposure time to 1 hour nearly triples the mean lath widths in comparison to samples heated for 15 minutes. The lath widths are considerably larger after heating for 30 minutes and 1 hour at 1050°C than they are after heating for 15 minutes at the higher temperature of 1100°C. Consistent with the results shown in Figure 4.11b), it can be seen that the lath width clearly decreases with increasing cooling rate from the normalizing temperature.

A comparison of the mean lath widths measured in the present investigation and some which are available in the literature are shown in Table 4.3. The values of as-normalized lath widths are consistent with those in the literature, and are somewhat smaller than those that have been tempered or aged, which is expected due to the fact that considerable recovery of the martensitic matrix occurs after the tempering of virgin martensite.

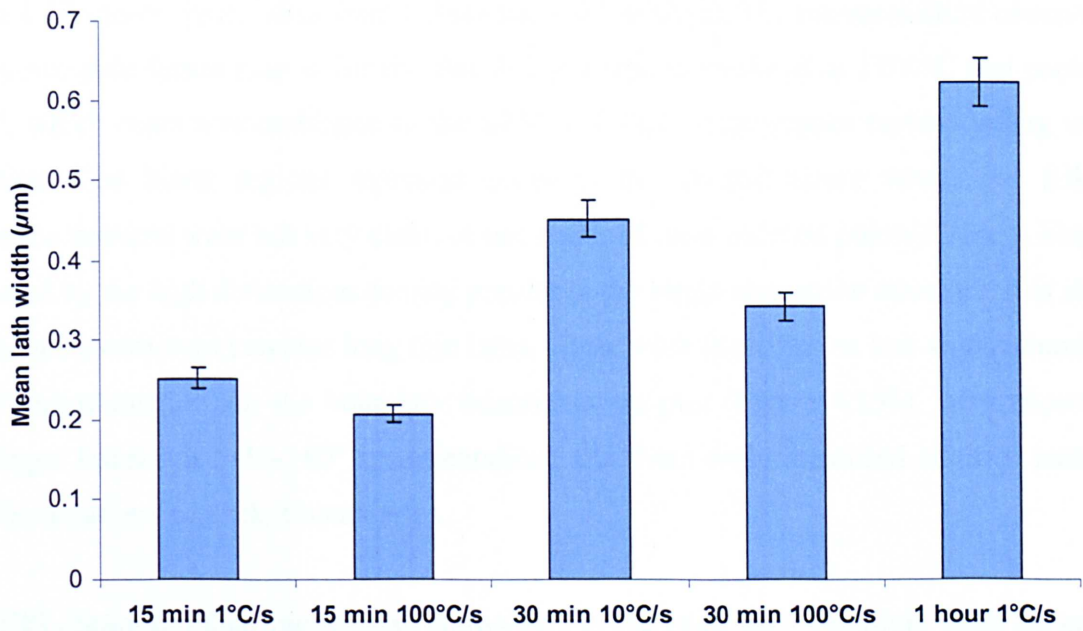


Figure 4.12: Plot showing the effect of time at normalizing temperature and cooling rate on the lath width of the Bar 257 material. The normalizing temperature was 1050°C.

Authors	Material	Condition	Dimensions (μm)
<i>Sanchez-Hanton</i>	grade 91	Cooled, 1°Cs^{-1}	0.17-0.28
<i>Sanchez-Hanton</i>	grade 91	Cooled, 100°Cs^{-1}	0.15-0.22
<i>Kim et al</i> ^[107]	10Cr ferritic steel	Air-cooled	0.28-0.43
<i>Sawada et al</i> ^[53]	9Cr ferritic steel	Air-cooled	<0.20
<i>Sklenicka et al</i> ^[112]	9Cr ferritic steel	Long term aged	0.31-0.76
<i>Ennis et al</i> ^[2]	grade 91	Tempered	0.40
<i>Sawada et al</i> ^[113]	grade 91	Tempered	0.53
<i>Czyrska-Filemonowicz et al</i> ^[71]	P92	Tempered	0.40

Table 4.3: Comparison of literature values of martensite lath widths and measurements performed in the present investigation.

Scanning electron microscopy has been seen to yield useful information about the microstructure of grade 91 steel. However, apart from illustrating the changes in the grain structure and providing an idea of the particle distribution, little other quantitative information about the grains themselves can be obtained. Electron backscatter diffraction (EBSD) or orientation imaging microscopy may yield useful data about the types of grain boundaries, the texture and the crystallographic nature of the material, which combined with traditional microscopy techniques can paint a better and more complete picture about the processes that are taking place in a material with regard to different applied temperature and stress treatments.

Figure 4.13 shows typical data from EBSD and EDS analysis. The microstructure observed in the inverse pole figure map is for the Bar 257 material normalized at 1100°C and cooled at 1°Cs^{-1} , which bears a resemblance to the SEM and TEM micrographs corresponding to this condition. The black regions represent areas in the microstructure where the Kikuchi diffraction patterns were not very clear, or not obtained (non-indexed points). This is likely to be caused by the high dislocation density present in the virgin martensite structure. It is shown that the microstructure contains long thin laths. These were identified as low-angle boundaries ($2\text{-}10^\circ$ misorientation) in the boundary misorientation plot (Figure 4.13b). Also shown are high-angle boundaries ($10\text{-}180^\circ$ misorientation) and these were identified as prior austenite grain boundaries and packet boundaries.

The EDS chromium distribution map shows that in the as-cooled condition, there appears to be an even distribution of Cr along the whole map area (Figure 4.13c). There are no areas enriched with Cr as the precipitation of M_{23}C_6 has not occurred at this stage. It has been shown that M_3C auto-tempered precipitates exist at this stage, however, these contain mostly Fe and were found to be very small, and indeed smaller than the spatial resolution of this

technique. The maps showing the distribution of Al and Nb show that there are a few small areas that are enriched with each element. This indicates the presence of particles that remained undissolved from the applied solution treatment, most probably NbC and AlN. It is interesting to note that there is one area (encircled in red) which contains a relatively high concentration of these two elements, which highlights the complexity of precipitate interactions in grade 91 steel.

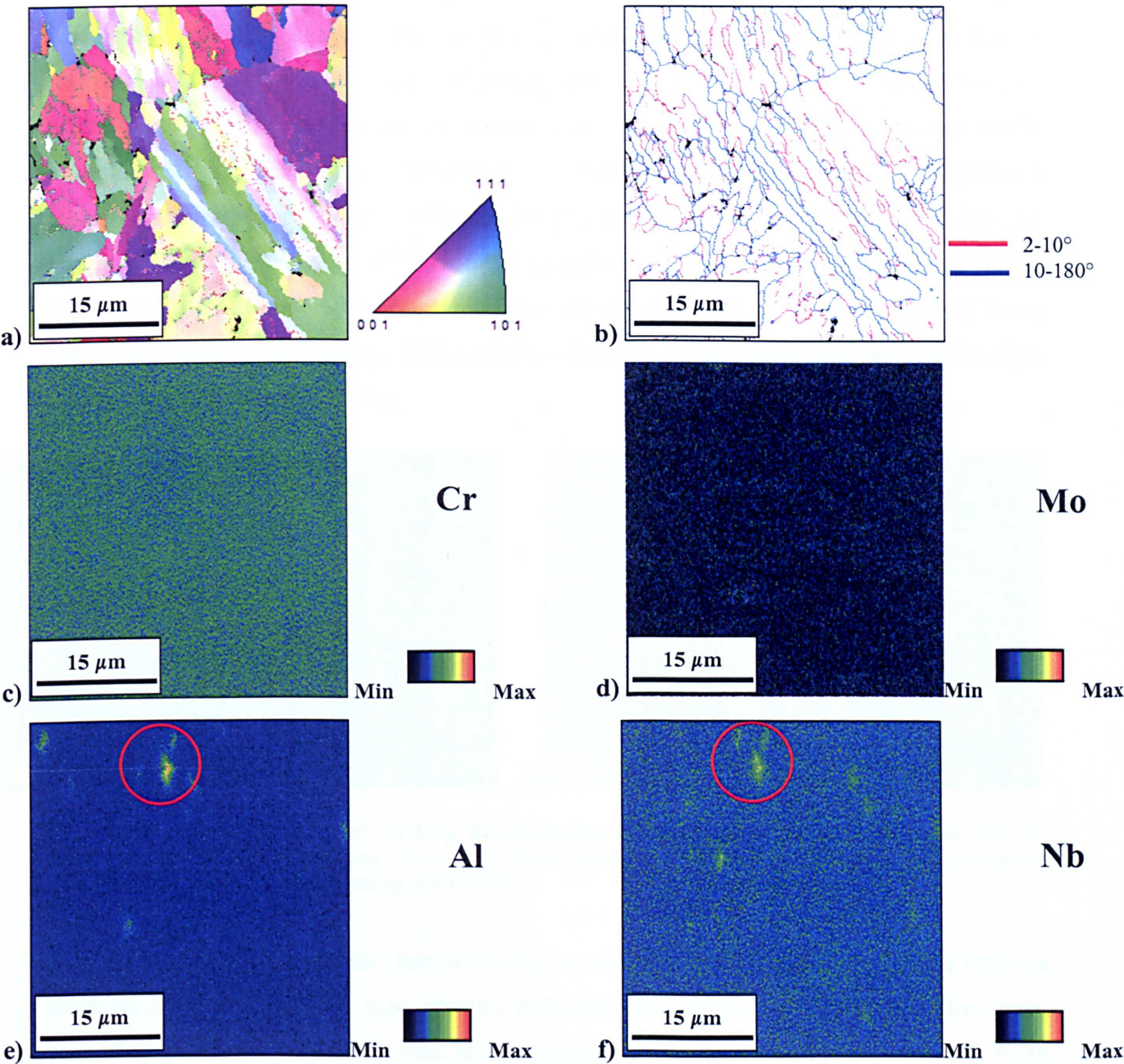


Figure 4.13: EBSD data from the Bar 257 specimen normalized at 1100°C for 15 minutes and cooled at a rate of 1°Cs⁻¹. a) Inverse pole Figure map, b) grain boundary misorientation map, and EDS maps showing the distribution of c) Cr, d) Mo, e) Al and f) Nb in the same area. The red circles indicate a zone where a large particle was detected, which contained Al and Nb.

4.5.1.2 Discussion

The findings from the microstructural analysis of the martensitic lath structure in the present section can be related to the dilatometry results in Section 4.4, which indicated a peculiarity during the transformation to martensite at the slower cooling rate. It was assumed earlier that the interruption in the cooling curve was due to the precipitation of some sort of auto-tempered carbide. It is evident that cooling at a rate of both 1 and $100^{\circ}\text{C s}^{-1}$ produces some intralath precipitates (Figures 4.8 and 4.9). Qualitative analysis suggests that there are fewer of these types of particles in the faster cooled specimens. Indeed, when cooling at an even faster rate of $500^{\circ}\text{C s}^{-1}$, the formation of these particles is virtually suppressed (Figure 4.14 b). Yamada *et al* [66] also found $(\text{Fe,Cr})_3\text{C}$ precipitates within the laths in a 9CrWCoVNb steel after air-cooling from the normalizing temperature, whereas Janovec *et al* [114] found similar particles after oil-quenching a 12% Cr steel. The differences in precipitation characteristics in the as-normalized condition may influence the precipitation of other phases upon further heat treatment. Indeed, Yamada *et al* [66] reported a suppression of M_{23}C_6 precipitation in quenched (fast cooled) and tempered steels, which they attributed to the diffusion Cr and W being suppressed during fast cooling, which would otherwise occur during exposure at the high-temperature region in air-cooling.

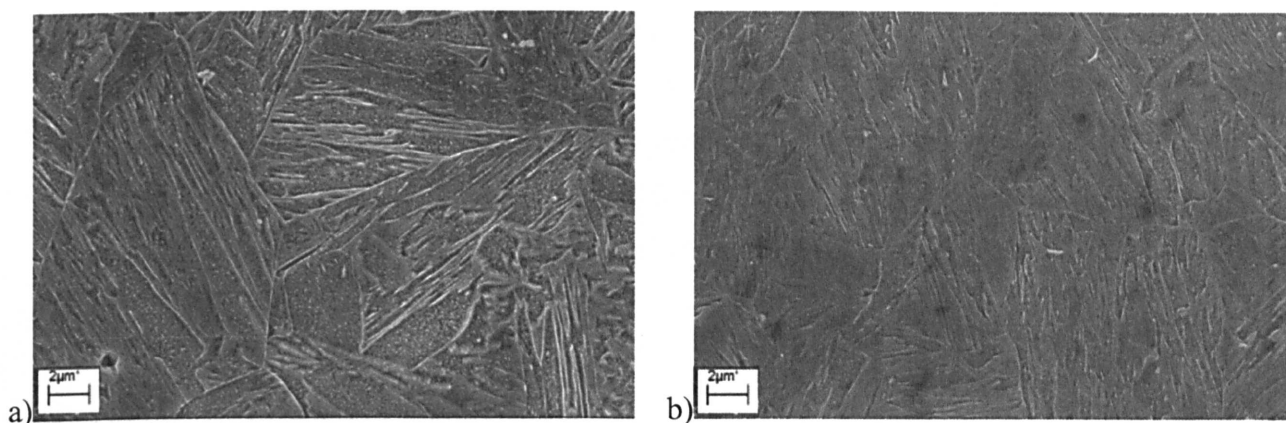


Figure 4.14: SEM In-lens images showing the martensitic lath structure of additional as-cooled Bar 257 specimens: a) Extended normalizing for 1 h and slow cooling at 1°C s^{-1} and b) short normalizing time (15 minutes) followed by very rapid cooling at $500^{\circ}\text{C s}^{-1}$.

The lack of boundary carbides observed in the as-normalized structures is consistent with the work of Janovec *et al* [114], who showed that grain boundaries were practically free from secondary phases, and that only thin M_3C carbides were present in the grain interiors. Work by Nutting [26] showed that these precipitates form in the laths as a result of auto-tempering.

It has been shown that the size of both prior-austenite grains (PAG) and martensite laths are sensitive to both the normalizing temperature and the cooling rate, such that higher normalizing temperatures increase the dimensions, and increasing the cooling rate decreases the dimensions of both microstructural parameters (Figures 4.11 a) and b). This finding is in good agreement with the work of Ennis *et al* ^[2], who found that the lath width generally increases with prior austenite grain size, which is a direct consequence of increasing normalizing temperature. Indeed, Raghavan ^[115] reasons that the grain size determines the size of the first martensite plate to form, which in most cases extends from boundary to boundary. Therefore, this seems a reasonable explanation to why an increase in lath dimensions with increasing normalizing temperature is observed.

Perhaps a more significant result is that the lath width shows a tendency to decrease as the cooling rate from a particular normalizing temperature is increased. In principle, the lath width being smaller in the faster cooled specimens can be attributed to the fact that the PAG sizes are generally smaller, as the faster cooled specimens experience less high-temperature exposure than the slow cooled specimens. However, it is clear that in both materials the lath widths of the specimen normalized at 1100°C and cooled at 100°Cs⁻¹ are much smaller than in the specimen normalized at 1050°C and cooled at 1°Cs⁻¹, even though the PAG size produced at the lower normalizing temperature is smaller (Figures 4.11 a) and b). Therefore, this is indicative of the fact that the cooling rate plays an important part in the dimensions of the martensitic laths and may therefore also play a role in microstructure evolution in these materials. Indeed, it is also evident that with increasing normalizing temperature, the cooling rate has a more profound effect on the lath width dimensions such that the differences in lath width are larger.

Another interesting feature of Figures 4.11 a) and b) is that both the PAG size and the lath width are consistently smaller in the W20-3 than the Bar 257 material. The smaller PAG size can be attributed to the higher predicted mass fraction of the stable MX phase in the W20-3 material at higher temperatures, which would have the effect of inhibiting grain growth by grain boundary pinning. This hypothesis is in good agreement with the work of Kim *et al* ^[107], who reported that PAG size and martensite lath width decreased with increasing N content in 10Cr ferritic steels, which was attributed to an increase in the content of NbX precipitates that remain undissolved at the applied normalizing treatment. Interestingly, Yamada *et al* ^[39] found that increasing the cooling rate suppressed the formation of NbC precipitates during

cooling. As a result, VN would not nucleate on these particles on tempering, which resulted in a finer distribution of precipitates. They attributed this finding to enhanced creep properties as a result of fast cooling, although the effects of lath width and grain size were not accounted for in their study.

4.5.2 Minor Phase Precipitation

It is evident from the previous section that changing normalizing parameters, such as normalizing temperature and cooling rate, strongly affect the matrix martensite microstructure of grade 91 steel. It was suggested that the microstructure was affected by the presence of minor phase precipitates, which remained undissolved from the normalizing treatment, or may have formed upon cooling. In the present section, the identity of such precipitates has been examined using transmission electron microscopy (TEM).

4.5.2.1 Results

The microstructure of the investigated normalized specimens all consisted of an abundance of intralath Fe- and Cr-rich cementite precipitates and also spherical Nb-rich MX particles scattered randomly in the microstructure. In addition, there was a clear absence of intergranular precipitates in all the specimens. Both fast and slow cooled Bar 257 specimens also contained Al-rich particles, which were scattered randomly throughout the microstructure. These particles were sometimes observed to be associated with Nb and V-rich MX particles. The minor phase precipitates have been primarily identified with EDS analysis in the TEM, however, some precipitates have also been characterized with selected area electron diffraction in the TEM.

Figures 4.15 shows the distribution of intragranular precipitates in the Bar 257 specimens normalized at 1050°C and cooled at 1°Cs⁻¹ and 100°Cs⁻¹ respectively. It can be seen that the intragranular precipitates in the slow cooled specimen (Figures 4.15 a) and b) are generally larger than those found at the faster cooling rate (Figures 4.15 c) and d). This effect was also evident at the other normalizing temperatures employed, 975 and 1100°C. Quantitative EDS analyses have shown that these auto-tempered precipitates typically contain a much higher concentration of Fe than Cr, 87 wt.% and 13 wt.% respectively.

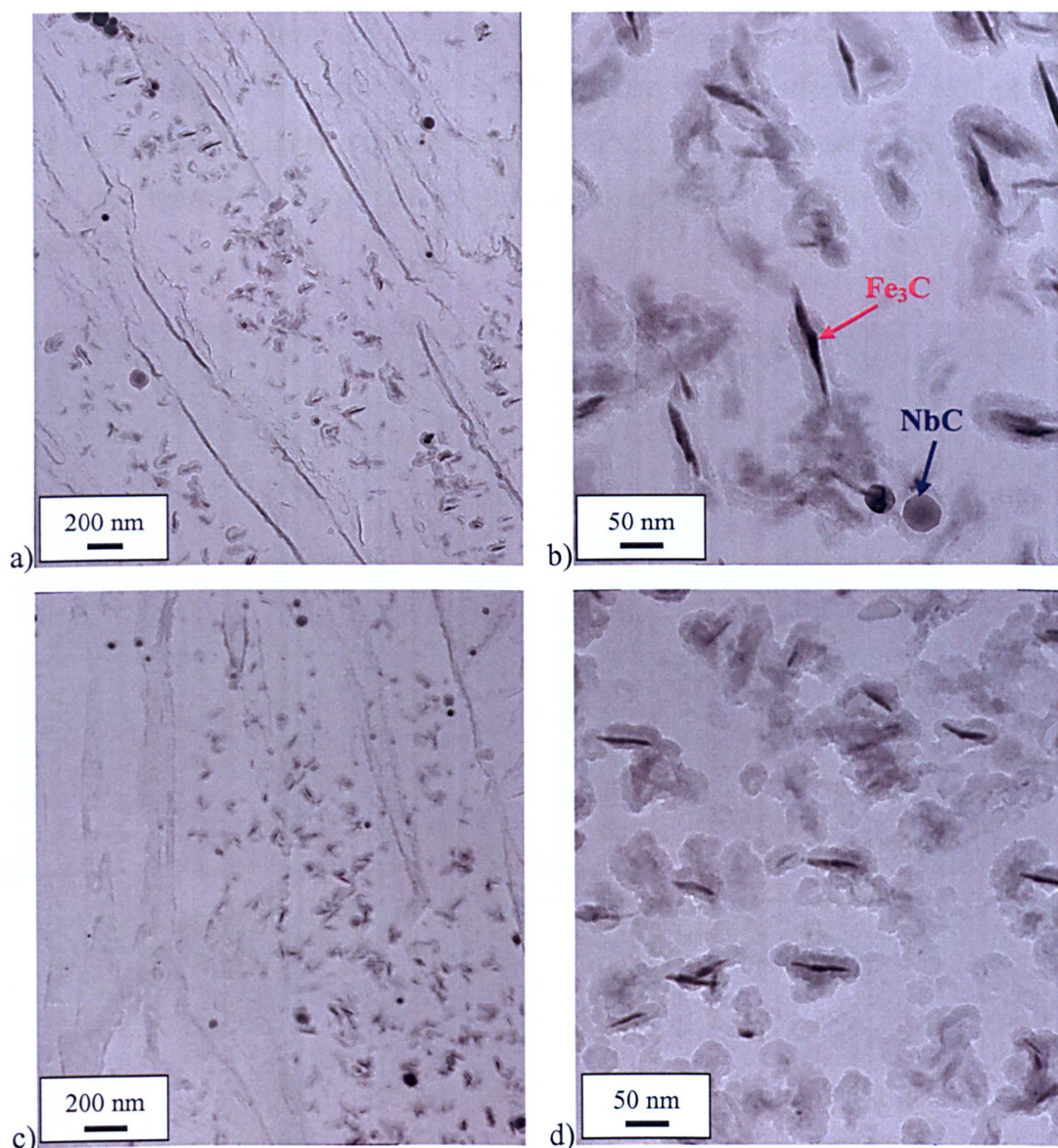


Figure 4.15: Bright field transmission electron micrographs of carbon extraction replicas of the Bar 257 material normalized at 1050°C and cooled at 1 (a) and b)) and 100°Cs⁻¹ (c) and d)) showing long needle-like auto-tempered cementite (Fe₃C) particles rich in Fe and Cr. a) and c) are low magnification images and b) and d) are higher magnification images.

Figure 4.16 shows the presence of AlN needle particles as well as spherical NbC particles in the Bar 257 sample normalized at 1050°C and cooled at the fast rate of 100°Cs⁻¹. The latter was predicted to be present, from thermodynamic calculations, in this material and were expected to dissolve at ~1070°C, so clearly a normalizing temperature of 1050°C for a relatively short time was insufficient to dissolve these particles. The EDX spectrum from the AlN particle reveals that the particle also contains traces of Nb and V (Figure 4.16c). Also shown in Figure 4.16b) is an AlN particle growing out of a large MnS particle. In most cases, the length of AlN particles across the longest axis exceeded 1 μm (Figure 4.16a).

Large (Nb,V)(C,N) particles were observed in all the specimens, and are shown for the fast cooled sample that was normalized at 1100°C (Figure 4.17). Indeed, this MX phase was predicted to dissolve at higher temperatures ($\sim 1140^\circ\text{C}$), and was predicted to predominantly consist of Nb. Figure 4.18 shows that in some cases, large AlN particles are associated with NbC particles.

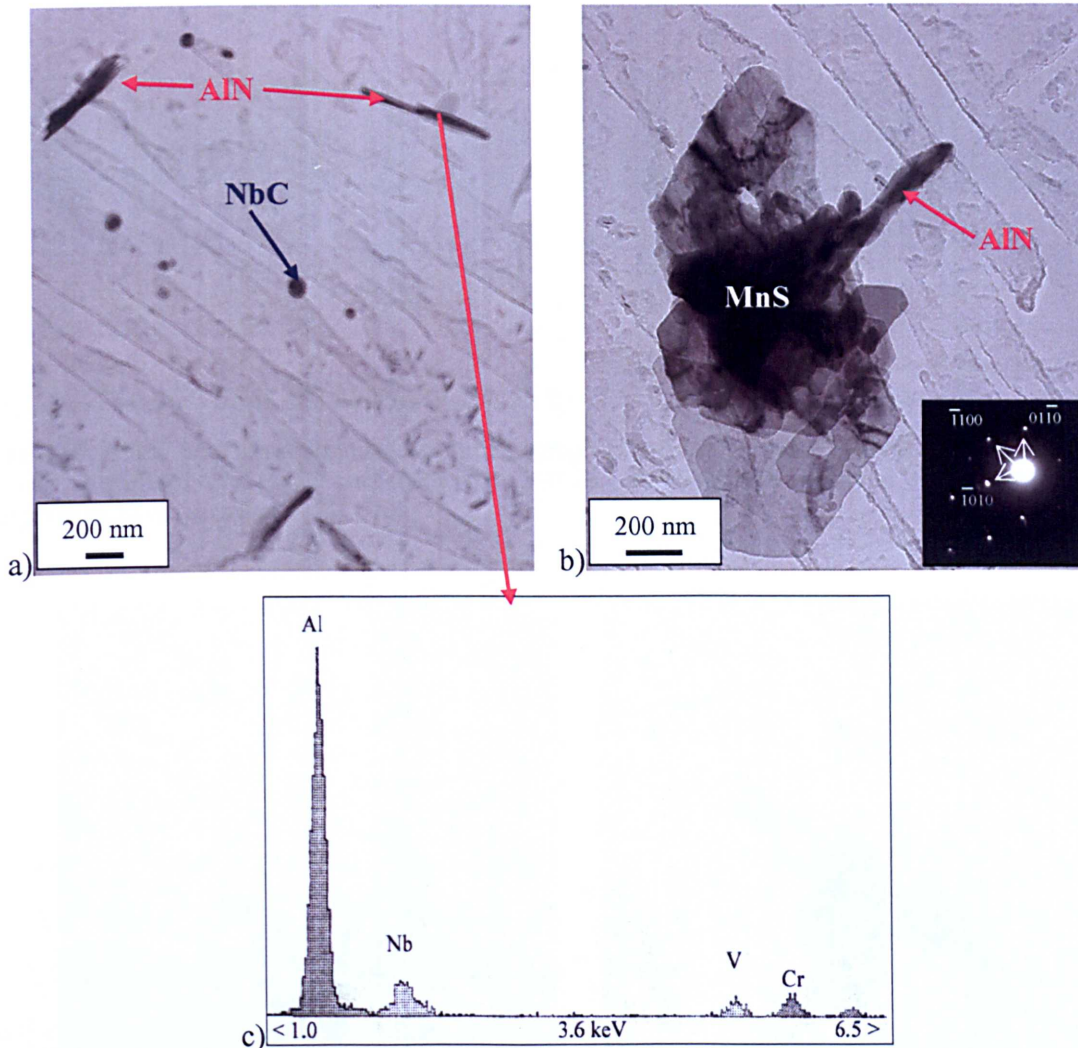


Figure 4.16: Bright field transmission electron micrographs of carbon extraction replicas of the Bar 257 material that was normalized at 1050°C and cooled at 100°C s^{-1} showing a) long needle-like AlN particles and spherical NbC particles. Also shown is b) an AlN particle growing out of an MnS inclusion, the electron diffraction pattern of the corresponding AlN particle (inset) shows a hexagonal crystal structure. c) The corresponding EDS spectra of one of the AlN particles from a).

The particles shown in Figure 4.18 are relatively large, which helps to explain the high counts of Al and Nb in the corresponding EDS maps shown in Figure 4.13 e) and f). In the present study, it has also been observed that the AlN and NbC particles tend to be present in areas that contain a relatively disperse distribution of cementite precipitates, which indicates that auto-

tempered precipitates do not tend to form on the particles that remained undissolved from the normalizing heat treatment.

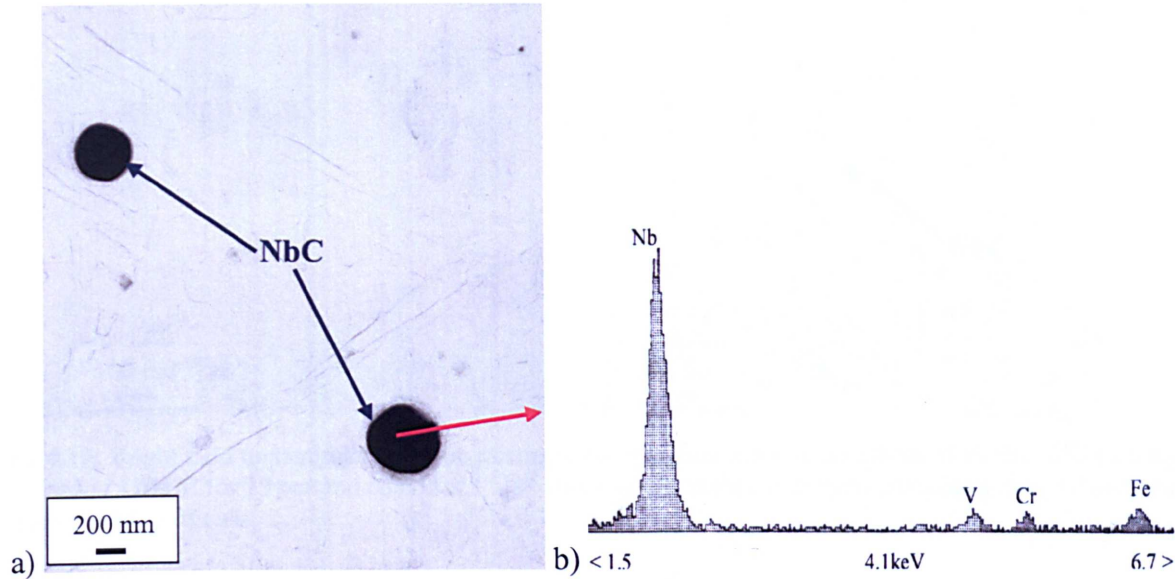


Figure 4.17: Bright field transmission electron micrograph of carbon extraction replicas of the Bar 257 material that was normalized at 1100°C and cooled at 100°Cs⁻¹ showing two spherical NbC particles and the corresponding EDS spectrum.

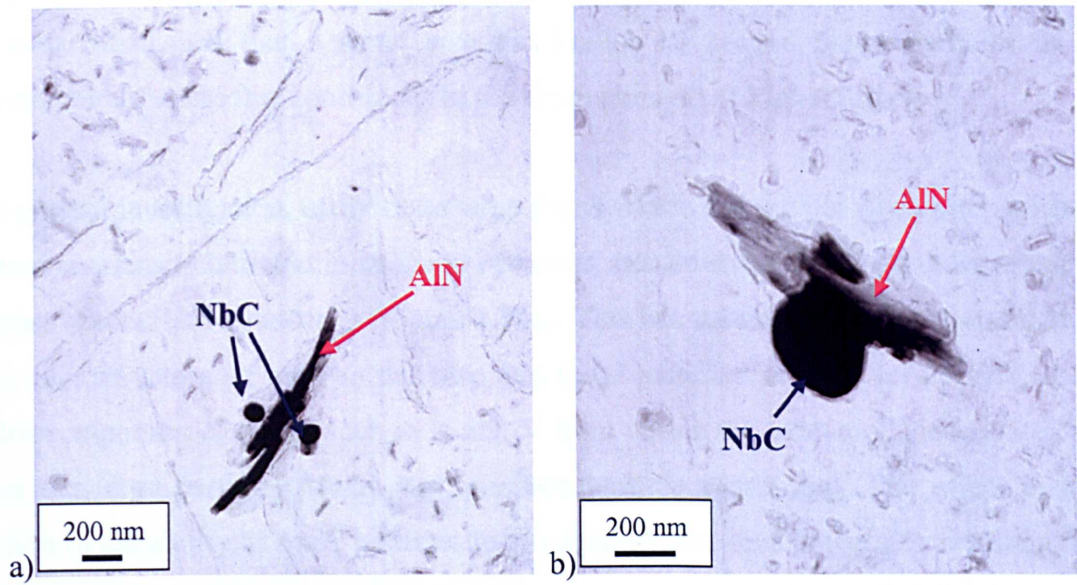


Figure 4.18: Bright field transmission electron micrographs of carbon extraction replicas of the Bar 257 material normalized at 1100°C and cooled at a) 1°Cs⁻¹ and b) 100°Cs⁻¹ showing large AlN needle particles in close proximity to spherical NbC particles.

Increasing the normalizing time to 1 hour at 1100°C did not show a significant variation in the identity of minor phases present in either material. This is shown in Figure 4.19, whereby an abundance of both cementite and NbC precipitates can be observed.

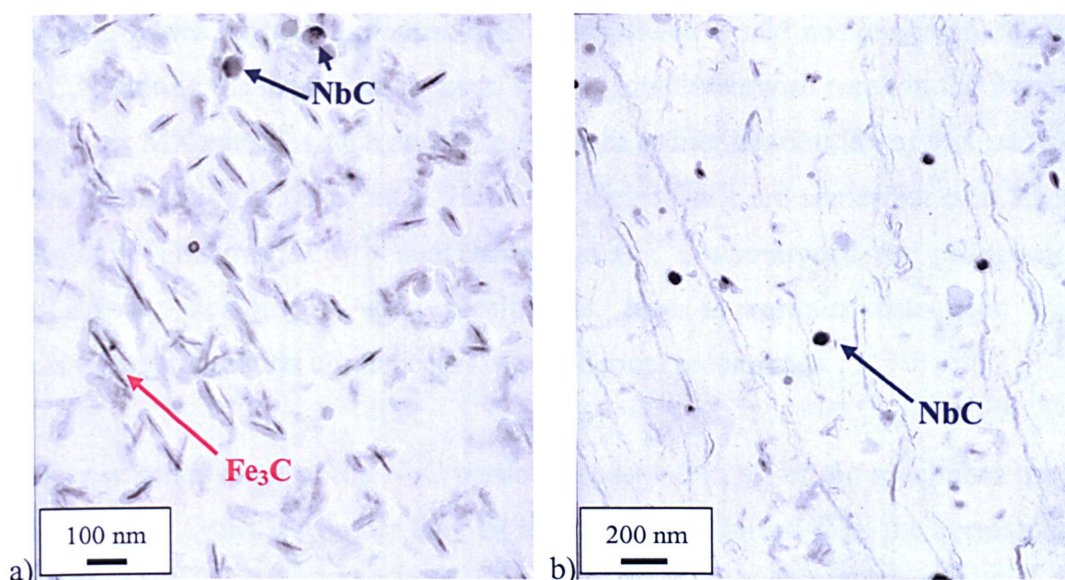


Figure 4.19: Bright field transmission electron micrographs of carbon extraction replicas of the Bar 257 material normalized at 1100°C for 1 hour and cooled at 1°Cs⁻¹ showing a) intralath cementite particles and b) a dispersion of spherical NbC particles.

4.5.2.1 Discussion

The presence of large precipitates in the as-normalized condition could be detrimental to the creep properties of grade 91 steel, and may explain the poor creep performance of Bar 257, as it is well established that a small size distribution of second phase particles is a key microstructural feature that contributes to the creep strength of high Cr steels.

In the present investigation, many cases were found where the particle sizes were greater than the mean martensite lath width. In many instances, needle-shaped AlN particles would often lie across several lath boundaries (Figure 4.16a). This has several implications on the stability of the microstructure. It may be the case that these particles act as a solute sink, and thus withdraw important elements such as N and V from within the laths to a concentrated region around the large particle, which may promote particle coarsening. The effect may be a reduction in the ability of small particles to pin dislocations, thus potentially resulting in poor creep strength properties.

Pertaining to the present discussion on the effect of initial heat treatment in this class of materials, Yamada *et al* ^[39] studied the effects of cooling rate on the creep properties of 9CrW steels and found that both creep rate and creep strain are lower in quenched and tempered steels than in air-cooled and tempered steels. The authors attributed these results to the suppression of the precipitation of Nb(C,N) particles, which occurred during the fastest

cooling cycle. It was argued, therefore, that VN particles would not preferentially nucleate onto Nb(C,N) during the tempering process, which would otherwise result in the formation of coarse complex MX particles such as V-wings, hence a finer distribution of MX particles can be achieved by cooling at faster rates. However, their results are somewhat contradictory to the findings of Tokuno *et al* ^[33,37] and Hamada *et al* ^[38], who argued that precipitates with complex shapes, including V-wing precipitates, tend to restrain dislocation climb in conditions where dislocation climb occurs over spherical precipitates.

It is unclear whether some of the NbC particles observed in all of the specimens precipitate during the cooling cycle or whether they all remained undissolved from the normalizing heat treatment. However, in the present study, qualitatively there is no indication that the volume fraction and size of (Nb,V)(C,N) precipitates varies significantly as a function of cooling rate. Therefore, the theory of Yamada *et al* ^[39] is difficult to prove.

It has been reported elsewhere that the precipitation of AlN in steel can also be suppressed by applying more rapid cooling rates ^[47]. However, this was not evident at the conditions investigated in the present study.

It was interesting to observe that in the majority of cases, the large needle-shaped AlN particles coexist independently of the NbC particles. However, a few examples exist when both of these particles form a duplex AlN-NbC particle (Figure 4.18). This is consistent with the work of Leap and Brown ^[51], who suggested that the number of Nb(C,N) precipitates found attached to AlN precipitates was restricted in a steel containing 0.2% C, 0.028% Al and 0.04% Nb. The authors' general conclusion was that in order for this duplex structure to form, the AlN precipitate must be oriented such that the interfacial energy between the two precipitates is lower than that of AlN and the matrix, whilst at the same time Nb(C,N) maintains an orientation relationship with the matrix.

The precipitation of MX and AlN particles during long-term aging are discussed in more detail in Chapter 5.

4.5.3 Effect of Normalizing Treatment on the Hardness

4.5.3.1 Results

The as-normalized specimens from both investigated materials have been subjected to Vickers hardness tests in order to assess the effect of varying initial heat treatments. Figure 4.20 shows the as-normalized hardness values of the Bar 257 and the W20-3 materials. It can be seen that the hardness of the faster cooled samples ($100^{\circ}\text{Cs}^{-1}$) is significantly greater than the slower cooled samples (1°Cs^{-1}). The hardness difference between the two cooling rates at all the normalizing temperatures is approximately 30 HV. It is also shown that the hardness tends to decrease as the normalizing temperature is increased. Another finding was that the hardness values of the Bar 257 material are somewhat higher than those in the W20-3 material.

Figure 4.21 illustrates that the normalized hardness values are significantly lower after normalizing at 30 minutes and 1 hour, than those shown in Figure 4.20, which were normalized for 15 minutes.

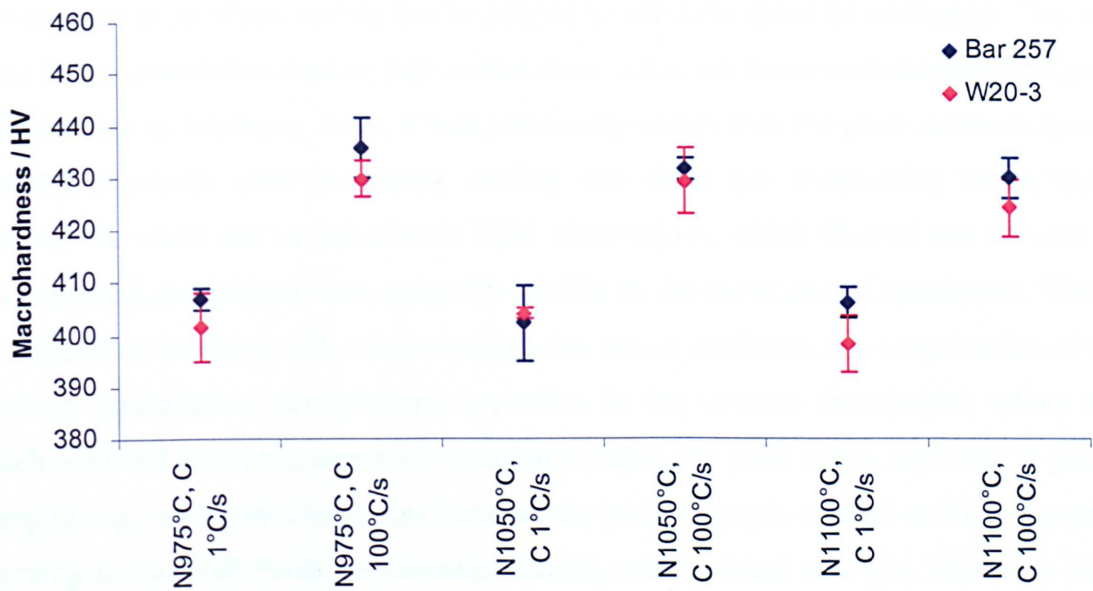


Figure 4.20: Macrohardness measurements as a function of normalizing temperature (N) and cooling rate (C) for the Bar 257 and W20-3 specimens normalized for 15 minutes at temperatures varying between 975 and 1100°C.

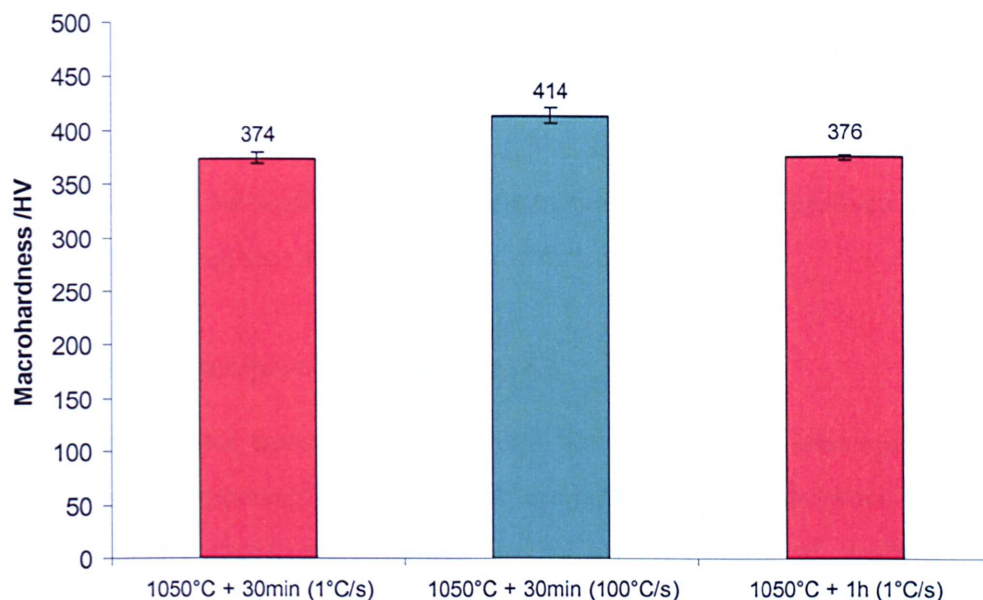


Figure 4.21: Macrohardness measurements as a function of normalizing temperature, normalizing time and cooling rate (shown in brackets) for the Bar 257 specimens.

4.5.3.2 Discussion

From the results of microstructure characterization on the as-normalized specimens, the discrepancies in hardness values can be related to the differences in martensitic lath widths, where it is expected that smaller lath widths observed in the faster cooled specimens give rise to an increase in hardness. Also, it was previously shown that the prior austenite grain size generally decreases with increasing cooling rate from the normalizing temperature. In addition, this result can be linked with TEM observations, which showed that the size of the auto tempered precipitates were generally smaller in the faster cooled specimens. Therefore, this increase in hardness with faster cooling rates can be attributed to a combination of factors including precipitation strengthening according to the Orowan mechanism, where a finer particle size and smaller interparticle spacing increase the yield stress, and also to grain size strengthening, where smaller grains increase the yield strength of steel at room temperature according to the Hall-Petch relationship. Indeed, the hardness was also shown to decrease slightly with increasing normalizing temperature at both cooling rates. Again, this is consistent with previous microscopy results, which showed that grain coarsening occurred at the higher treatment temperatures. Indeed, the hardness was also shown to decrease with increasing normalizing times.

The hardness values of the Bar 257 material were shown to be consistently higher than for the W20-3 material. This challenges the previous statement regarding grain strengthening as an inverse function of the square root of the grain diameter, as the degree of grain coarsening was greater in the Bar 257 material. However, the slightly higher values exhibited by this material may be due to the higher carbon concentration, which may produce a greater degree of lattice distortion during the martensitic transformation.

4.6 Analysis of the As-tempered Microstructures

A typical pre-service heat treatment comprises a normalizing heat treatment followed by a standard stress-relief tempering heat treatment, the latter is applied between 740 and 780°C, which produces some significant changes in the microstructure of grade 91 steel. The tempering process promotes the diffusion of carbon and other interstitial elements as part of the stress-relief process and at 750°C, the formation of chromium rich $M_{23}C_6$ precipitates was evident in the lath and grain boundaries of all of the specimens.

In the present section, the effects of tempering on the microstructure of the specimens previously normalized under varying conditions are discussed.

4.6.1 Minor Phase Precipitation Induced by Tempering

Figures 4.22 and 4.23 present low magnification scanning electron micrographs of the as-tempered microstructures of the Bar 257 and W20-3 materials respectively. These specimens had previously experienced different normalizing heat treatments. Although the prior austenite grains, lath and packet boundaries are clearly visible, the microstructure of all the specimens is dominated by the precipitation of $M_{23}C_6$ particles, which decorate the different boundaries. These particles have been identified with X-ray diffraction analysis, which was performed on bulk extracted carbides (Figure 4.24). This was possible due to the high fraction of $M_{23}C_6$ precipitates. On the other hand only small traces of NbC and AlN were present, due to the much lower volume fraction of these precipitates. Indeed, from microstructural characterization, there was little evidence of the precipitation of intragranular MX precipitates in either material after the applied tempering heat treatment. Attention was therefore focussed on the changes of $M_{23}C_6$ size distribution.

Due to the severity of the tempering heat treatment, it was very difficult to qualitatively distinguish the differences in the particle size distribution of the tempered specimens that had

experienced different normalizing treatments. Therefore, the particle size distribution of the $M_{23}C_6$ precipitates were measured using an automatic image analysis procedure, the methodology of which is discussed in the following section (4.6.1.1).

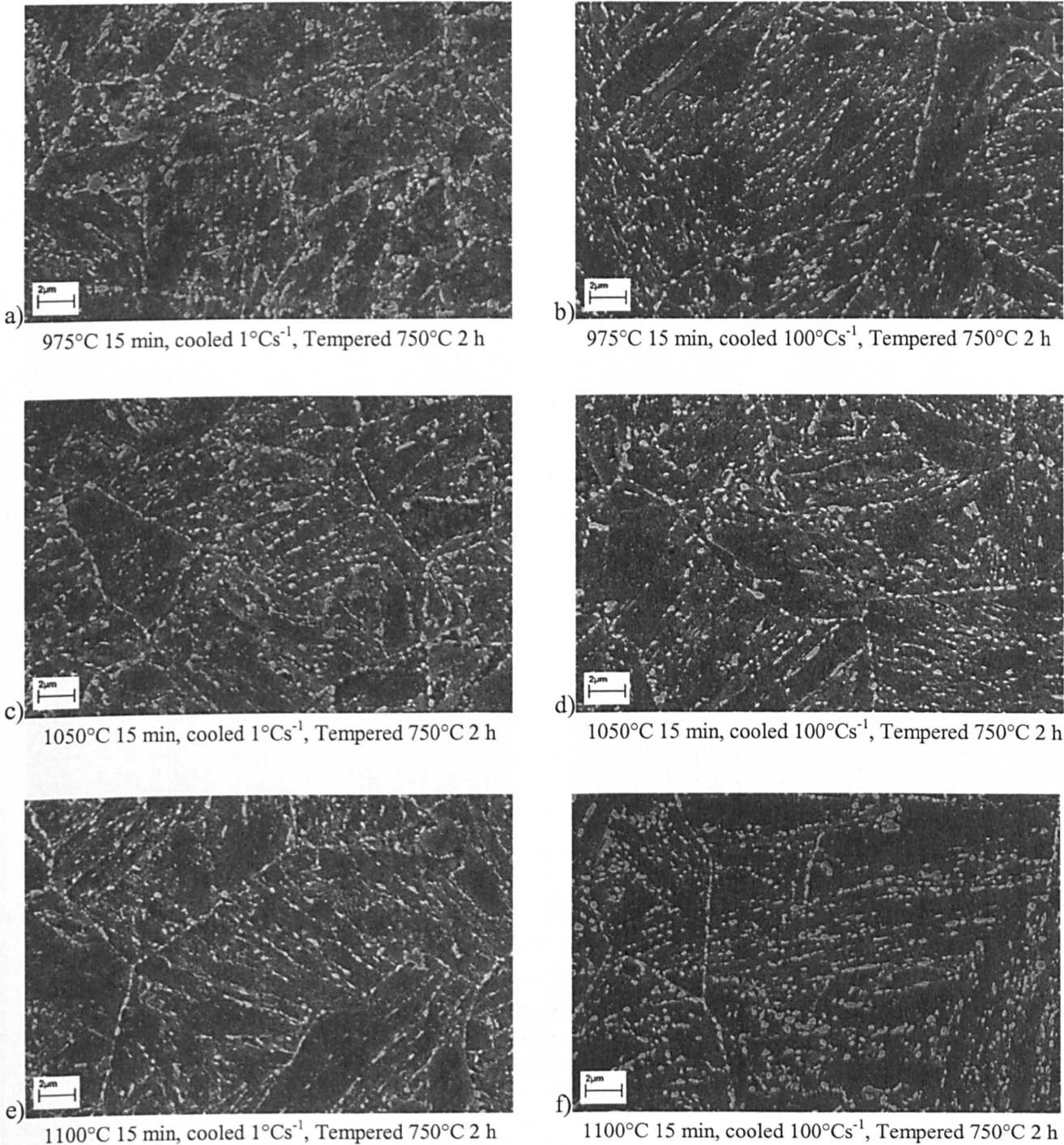


Figure 4.22: SEM In-lens images showing the martensitic lath structure and the distribution of $M_{23}C_6$ particles along the interlath regions in the Bar 257 specimens tempered at 750°C for 2 h. Annotated below the images are the normalizing temperatures and cooling cycles experienced prior to tempering.

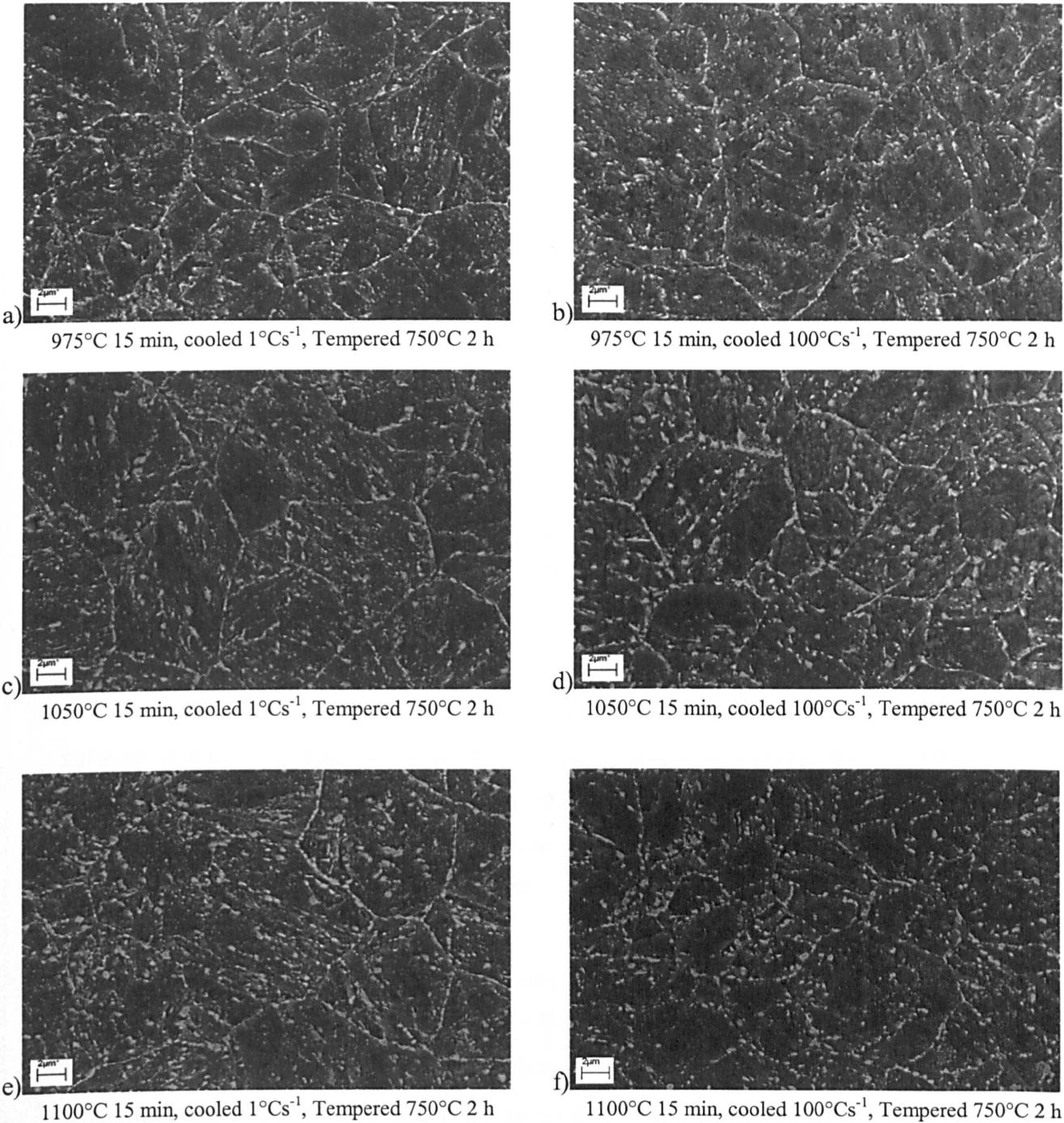


Figure 4.23: SEM In-lens images showing the martensitic lath structure and the distribution of $M_{23}C_6$ particles along the interlath regions in the W20-3 specimens tempered at 750°C for 2 h. Annotated below the images are the normalizing temperatures and cooling cycles experienced prior to tempering.

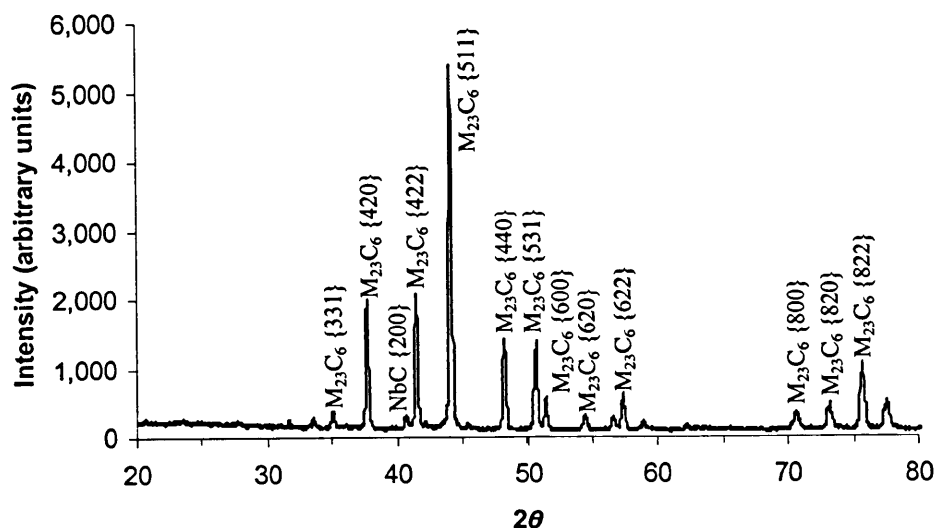


Figure 4.24: X-ray spectra of bulk extracted carbides from the specimen that was normalized at 1050°C for 30 minutes and cooled at 1°Cs⁻¹ and tempered at 750°C for 2 h. The peaks confirm the presence of predominantly $M_{23}C_6$ particles. NbC and AlN were also identified, however, the signal was very weak due to the much smaller volume fraction of these precipitates. The ICDD-JCPDS card numbers used for the identification of $M_{23}C_6$, NbC and AlN phases were 35-0783, 38-1364 and 34-0697 respectively.

4.6.1.1 The Particle Size Distribution of $M_{23}C_6$ Particles

For this study, SEM images of etched P91 samples were analysed using an image analysis software programme Image-pro plus 5.0^[116]. Digital images consisting of an area of 1024 by 768 pixels were used. Several measurement options are available using this software, a variety of which were evaluated such as maximum and minimum diameters, length, width, area, perimeter and aspect ratio, to name but a few.

SEM In-Lens images are ideal for automatic image analysis as the contrast between the particles and the matrix is achieved by differences in surface topography, as during the etching procedure, the matrix dissolves preferentially before the particles of interest, thus the latter have more height. The improved contrast in comparison to conventional secondary electron detection is due to the combination of short working distances (~3 mm) and improved secondary electron detection with a higher signal to noise ratio. Examples of particle measurements of ferritic-martensitic steels using the SEM can be found in the literature. For example, backscatter electron imaging has been used by Korcakova *et al*^[117] and Dimmler *et al*^[56] to quantify Laves phase in 9-12 wt.% Cr steels, where sufficient atomic contrast of this phase is possible due to the presence of Mo, which is a significantly heavier atom than the Fe and Cr-rich matrix. For the present study, however, this technique is not suitable for the measurement of $M_{23}C_6$ precipitates as backscatter electron imaging could not generate sufficient contrast between the matrix and precipitate, which both contain significant

quantities of Fe and Cr. Therefore, imaging using the In-Lens detector was considered favourable for this application.

Before the results from particle size analysis of $M_{23}C_6$ precipitates are presented, a brief review of the factors which may affect such results are first discussed.

Factors which may affect particle size analysis results from SEM

Particle size data may be influenced by particles which overlap, in which case two or more coalesced particles may only count as one when measured using an automatic imaging software. In principle, this should not be a detrimental factor so long as specimen surfaces are not over-etched.

Particles that make contact with each other will naturally decrease the interphase surface area per unit volume, and the number density of the particles present in the system whilst at the same time increase the mean particle size of the system^[118]. This phenomenon may occur as a result of nucleation of precipitates on pre-existing particles, and thus they need not be measured individually because the effective “obstacle” area should be considered as the sum of independent particles. Such treatment of the data would yield more reliable results when trying to interpret particle size and size distribution in terms of obstacles to dislocation and subgrain motion, which ultimately affect the degree of precipitation strengthening.

Of course, defects in the images may also produce contrast and care must be taken to remove any unwanted obvious flaws in the image so that they do not count as particles when measurements are taking place. This may include contaminants on the specimen surfaces which will produce contrast. Also, in order to achieve meaningful results, the operator must be confident that the image used for automatic analysis is relatively clear of defects and will represent the original microstructure that was observed in the microscope. Nonetheless, such defects are usually easy to detect and risks of uncertainty in measurement can be reduced by performing regular qualitative EDX analyses on the surface of interest.

Figure 4.25 shows a comparison between an SEM image of boundary $M_{23}C_6$ particles and the same image processing using an automatic image analysis software. A comparison between the two was made to judge whether the particle sizes are representative of the original image, or whether particle sizes were over- or underestimated. From Figure 4.25c) it can be seen that

there is a good agreement between the size of the precipitates in the original image and those after image processing with the analysis software.

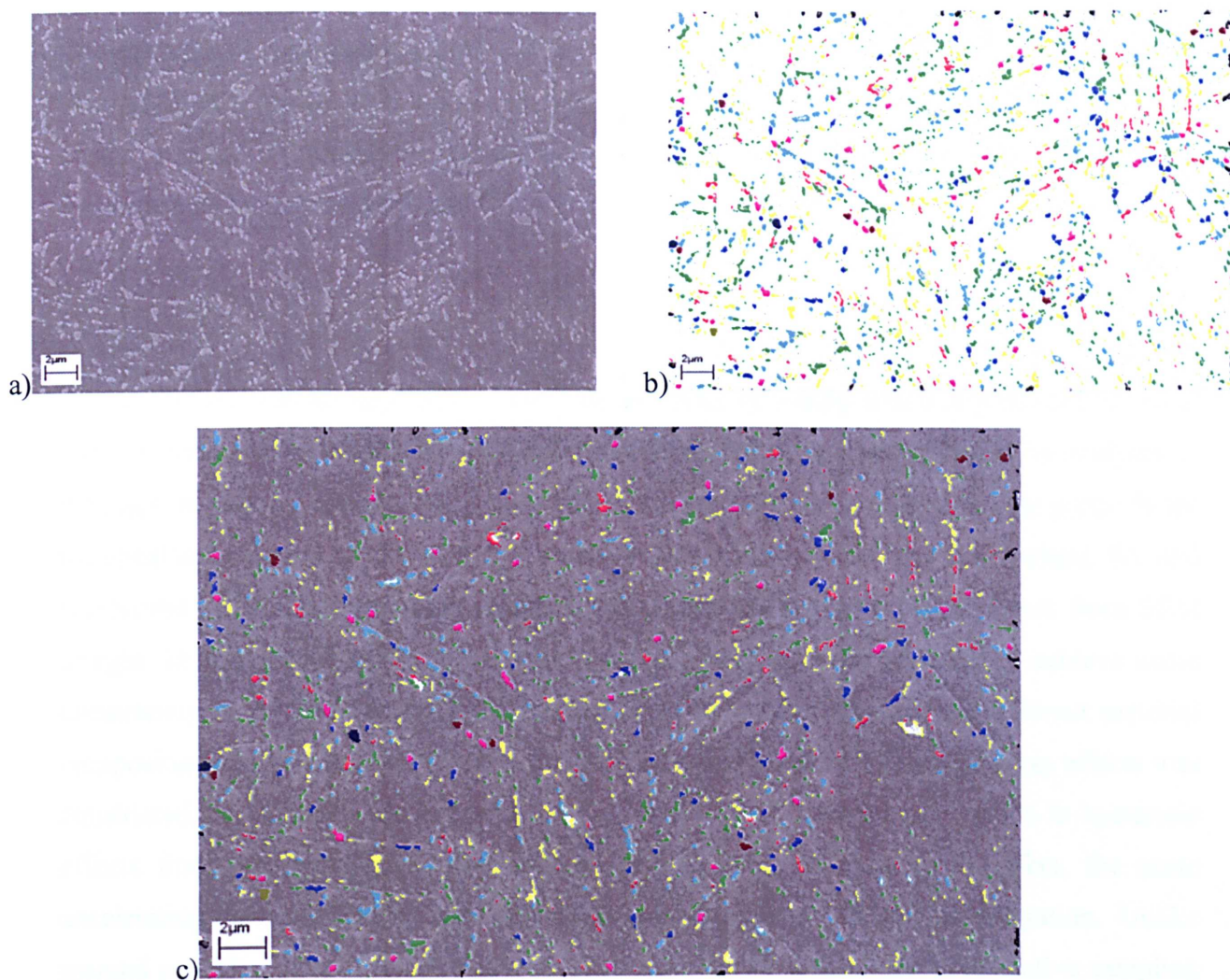


Figure 4.25: a) SEM image of grain boundary $M_{23}C_6$ precipitates in a tempered P91 steel specimen and b) the same image after size analysis. The different colours represent different size categories. c) shows the image analysis results superimposed onto the original SEM image.

An important issue with respect to accuracy is the number of pixels that can be assigned to any given particle. In other words, the greater the number of pixels that can be assigned to any given particle the more accurate the measurement is going to be. This could affect the results from particle characterisation when there is a bimodal distribution of precipitates and the size difference between two particle types is large. For this study, the smallest detectable particle size was 10 pixels, which means that any particles present in the image smaller than 50 nm diameter would remain unobserved and thus unaccounted for. In this study, it is assumed that the particles in a selected area are chosen randomly from the whole distribution of particles, such that the selected area accurately represents the whole material. This is only an assumption and it has been shown in previous studies that the $M_{23}C_6$ particle size distribution

can be very heterogeneous, with the example that particles along prior austenite grain boundaries are generally larger than those at lath boundaries ^[31,89].

The equivalent circle diameter ($d = 2 \sqrt{A / \pi}$) was used for the statistical analysis of particle size of $M_{23}C_6$ precipitates, similar to previous workers ^[32-34]. Korcakova *et al* ^[117] and Dimmler *et al* ^[56] corrected particle size measurements for truncation using the formula developed by DeHoff and Rhines ^[119]:

$$d_{corr} = \frac{4}{\pi} \overline{d_{obs}}$$

This correction was not applied for this study as a relatively deep etch was produced to reveal particle diameters which are close to their true value, which has been verified by analyses of particles in carbon extraction replicas. Also, this correction method assumes that particles are spherical and uniform in size, which is clearly not the case in these materials. Indeed, Wu and Sandström ^[120] did not apply correction factors to manual carbide measurements from SEM images. In this investigation, the etching time was kept constant in order to achieve some consistency in surface preparation. The fact that the etching response of different material compositions and thermal exposure will differ as a consequence of precipitation effects was considered. In addition, another factor which could affect particle size results is hysteresis effects from the scanning electron microscope. In order to reduce this effect, the same accelerating voltages and working distances were employed in this investigation. Unlike manual particle sizing of image features, there is a reduced risk of unrepresentative sampling as the number of measurements from an SEM image is quite high. A minimum of 2,000 particles were measured in each image.

4.6.1.2 Results of Particle Size Distribution of $M_{23}C_6$ Precipitates

Figure 4.26 compares the size distribution of $M_{23}C_6$ precipitates in the Bar 257 and W20-3 specimens, in the as-tempered condition. It is shown that the results are rather different between the two investigated materials. In the Bar 257 material, it can be seen that the size distributions of $M_{23}C_6$ precipitates are very similar in the specimens that have previously been normalized at 975 and 1050°C, the particles in the latter being slightly coarser (Figure 4.26a). A clear difference is observed in the specimens that had been normalized at 1100°C, such that they are considerably finer than those at the lower normalizing temperatures. It is also shown that the particles at this temperature are noticeably coarser at the faster cooling rate. This

trend is not evident at the lower normalizing temperatures. In the W20-3 material, however, it can be seen that the particle size distribution is very similar in all the specimens, which indicates that the precipitation of $M_{23}C_6$ in this material upon tempering is less sensitive to the previous normalizing heat treatment.

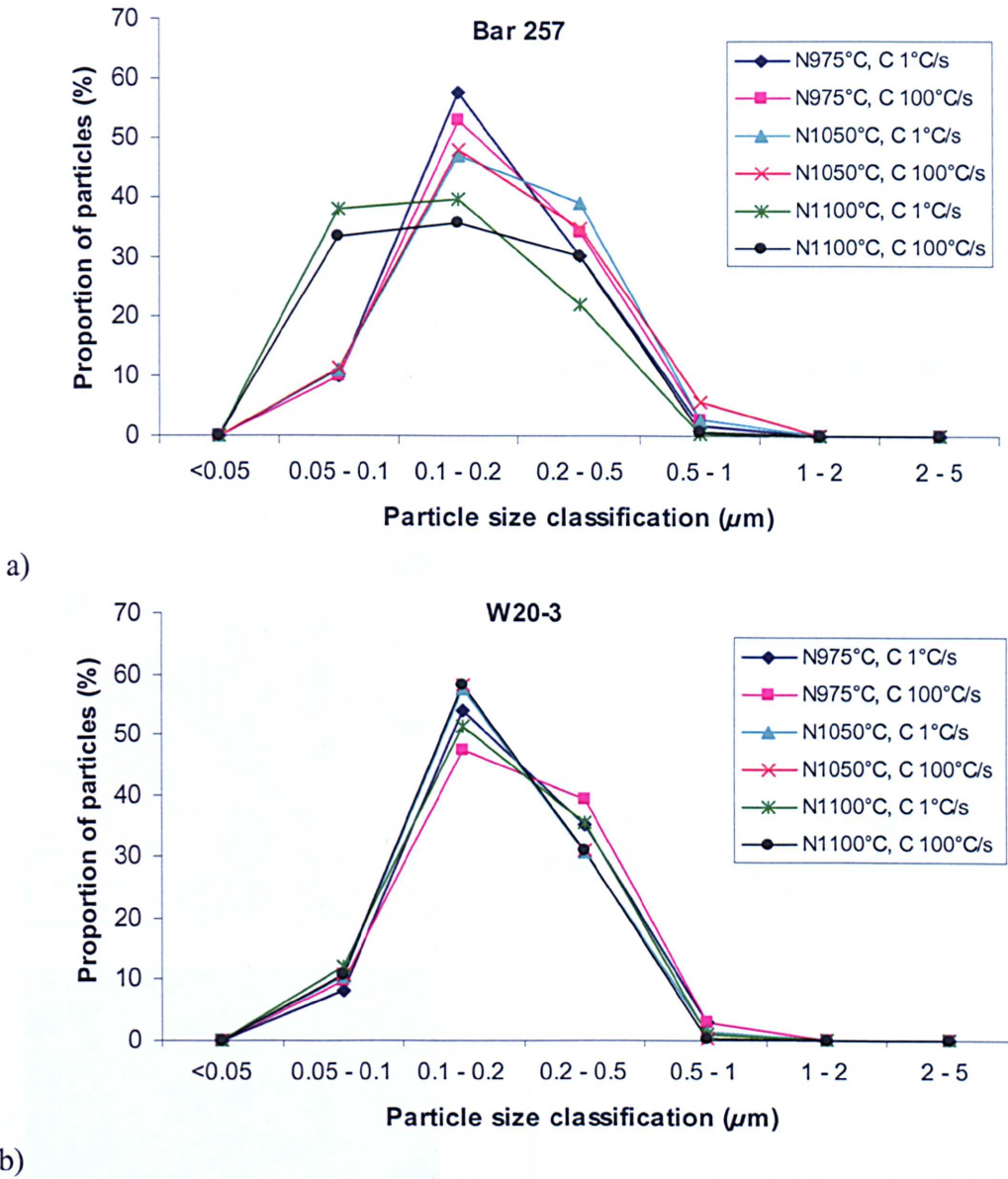


Figure 4.26: The particle size distribution of $M_{23}C_6$ precipitates in the as-tempered a) Bar 257 and b) W20-3 specimens that had previously undergone varying normalizing treatments.

4.6.1.3 The Effect of Aluminium Nitride on the Precipitation of $M_{23}C_6$

Figure 4.27 illustrates Cr-rich $M_{23}C_6$ particles, observed in the TEM, clustering around large pre-existing AlN precipitates that were present in the as-normalised condition. This phenomena has occurred in all of the as-tempered Bar 257 specimens.

It is well known that grain boundary $M_{23}C_6$ particles are essential for the creep resisting properties of grade 91 steel as they pin the boundaries and act as a resisting force against the process of recrystallization and grain growth.

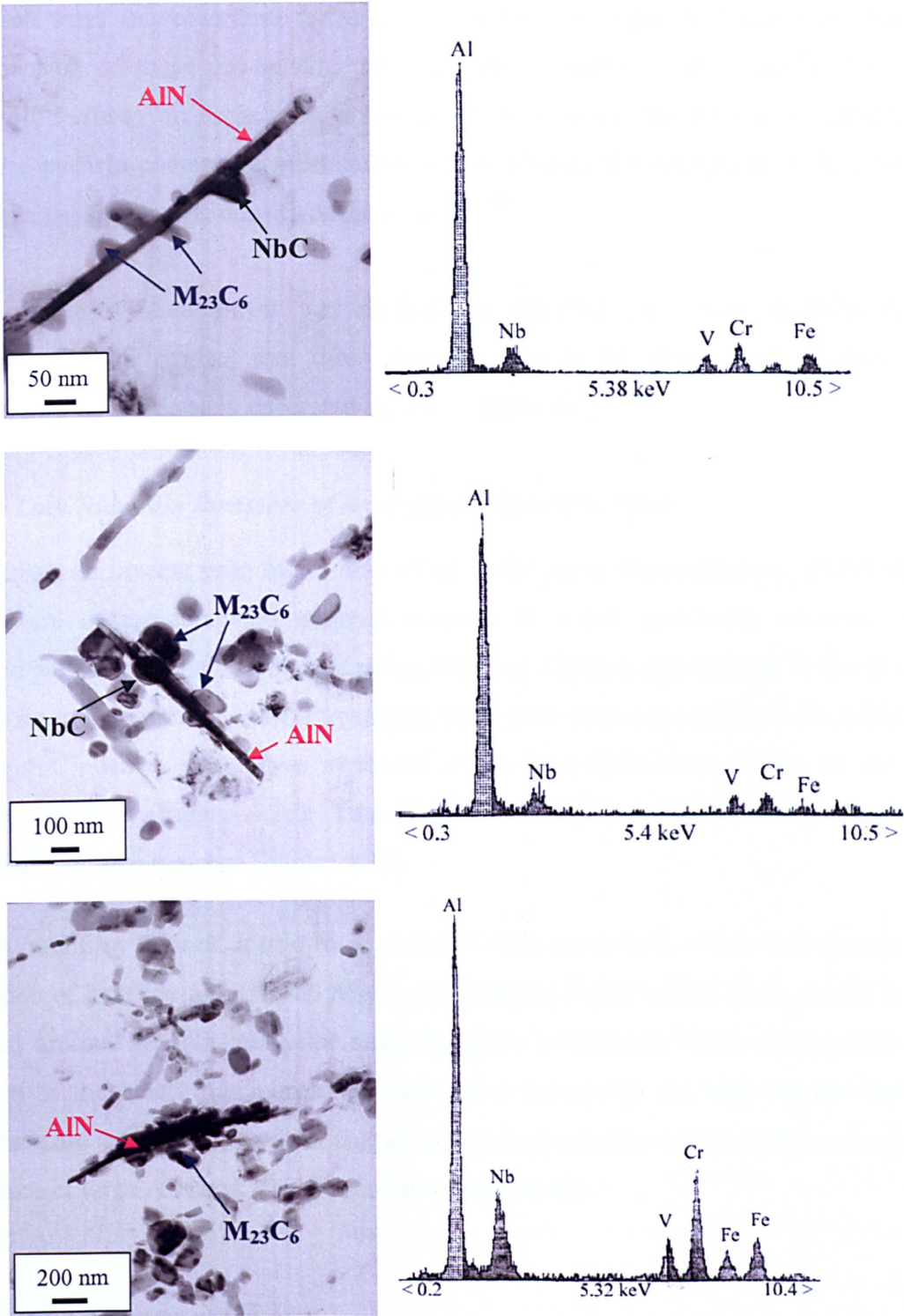


Figure 4.27: Bright field transmission electron micrographs of carbon extraction replicas of the Bar 257 material normalized at 1050°C for 15 minutes, cooled at 1°Cs⁻¹ and tempered at 750°C 2 h showing clustering of Cr-rich $M_{23}C_6$ precipitates onto large pre-existing needle shaped AlN particles. EDS spectra of the corresponding AlN precipitates are also shown.

In essence, the clustering of $M_{23}C_6$ and NbC particles around large pre-existing AlN particles may create an even larger particle size distribution and effectively increase the interparticle spacing. According to the Orowan mechanism, the greater the interparticle spacing, the more likely it will be that dislocations will find free paths to travel between particles. Therefore, large particle sizes may contribute to the poor creep strength of the steel. Given the relatively large dimension of these pre-existing particles, the probability that a newly precipitated particle will nucleate on these sites is increased. This would favour the occurrence of a coalescence particle coarsening mechanism, which reduces the interphase surface area per unit volume and the particle density of the system ^[118].

In the present investigation, it was difficult to ascertain the actual quantity of AlN precipitates, due to the fact that these particles tend to lie along prior austenite grain boundaries, which are densely decorated by $M_{23}C_6$ particles.

4.6.2 The Lath/Subgrain Structure of As-tempered Grade 91 Steel

Figure 4.28a), an inverse pole figure map of an as-tempered microstructure, shows that the microstructure of the tempered material consists of a lath martensite structure, which correspond well to the images obtained using scanning electron microscopy. In the as-cooled condition from the normalizing heat treatment, there were numerous points in the EBSD scan that were not indexed, which was attributed to the high dislocation density of the virgin martensite structure (Figure 4.13). This phenomena is not apparent in the as-tempered condition of the same material (Figure 4.28).

The grain boundary regions appear to be enriched with chromium, which corresponds to the precipitation of intergranular Cr-rich $M_{23}C_6$ precipitates (Figure 4.28c). Here, the Cr is finely distributed around the lath and prior austenite grain boundaries which corresponds to the emergence of the newly precipitated particles upon tempering. As with the previous EDS results, there are small regions which contain a high concentration of Al and Nb correspond to the presence of large AlN and NbC precipitates respectively.

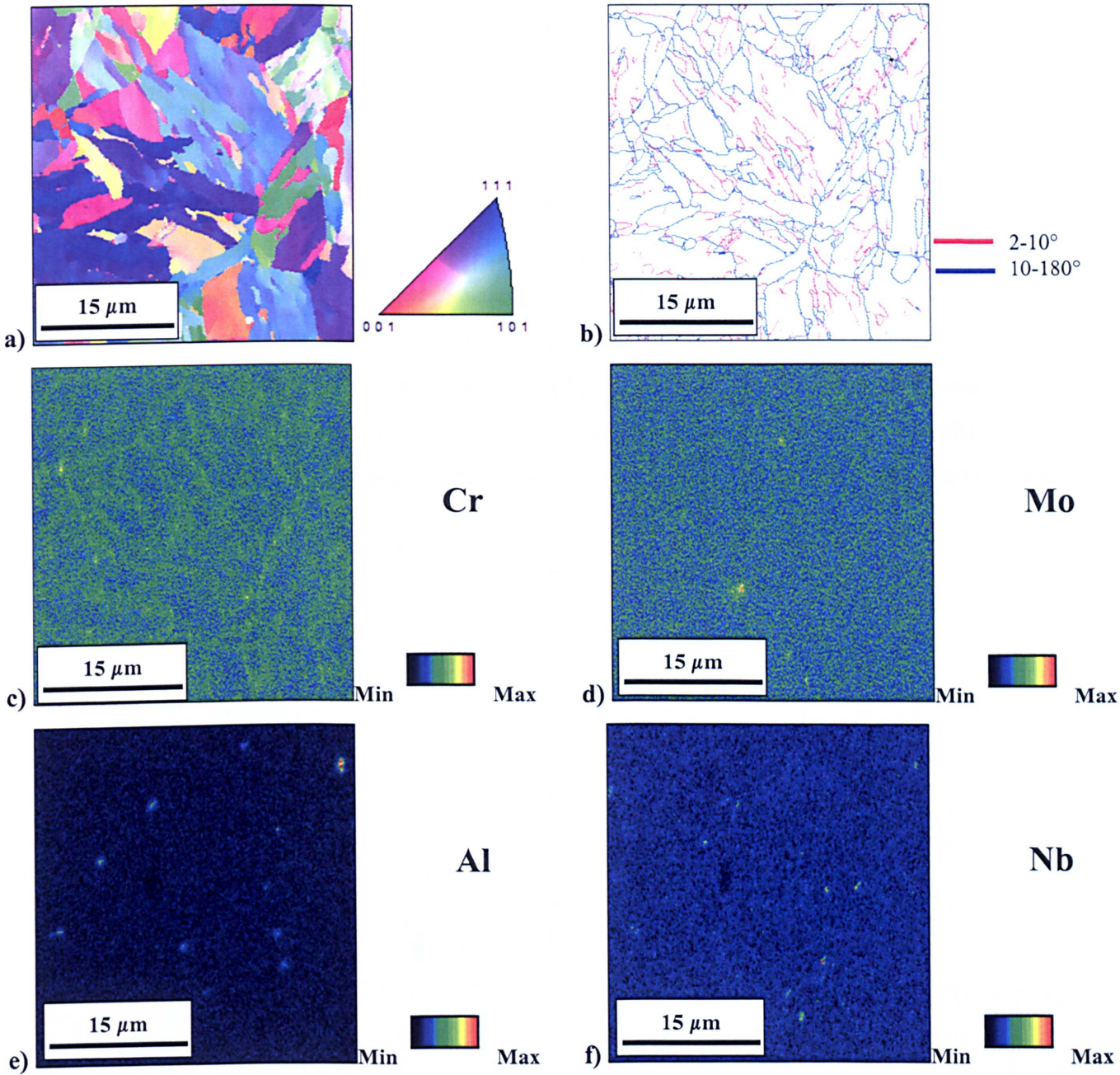


Figure 4.28: EBSD data from the Bar 257 specimen normalized at 1050°C for 15 minutes, cooled at a rate of 1°Cs^{-1} and subsequently tempered at 750°C for 2 h. a) Inverse pole figure map, b) grain boundary misorientation map, and EDS maps showing the distribution of c) Cr, d) Mo, e) Al and f) Nb in the same area.

4.6.3 Effect of Subsequent Tempering on the Hardness

Figure 4.29 shows the effect of the normalizing temperature and cooling rate on the as-tempered hardness values of the Bar 257 and the W20-3 materials. Interestingly, the results are very different to the as-normalized hardness values. Firstly, the hardness values appear to have dropped by approximately 200 HV, which indicates the severity of the tempering heat treatment. Secondly, the effect of normalizing temperature becomes more significant after tempering. In the as-normalized condition, it was shown that the hardness decreases slightly

with increasing normalizing temperature (Figure 4.20). However, after tempering, it is clearly evident that the hardness increases with an increase in normalizing temperature, the differences being greater after the application of the stress-relief treatment.

Figure 4.29 also shows that the hardness of the faster cooled specimens are greater than after slow cooling, a trend that was also observed in Figure 4.20. However, the differences between the two cooling rates after tempering becomes insignificant, in the order of 1 to 5 HV, in comparison to the as-normalized hardness, which showed a large difference of ~30 HV. Another similarity between the hardness characteristics of the two heat treatment stages was that the hardness of the Bar 257 material was found to be consistently higher than the W20-3 material. However, the disparity between the two materials is shown to be greater after tempering.

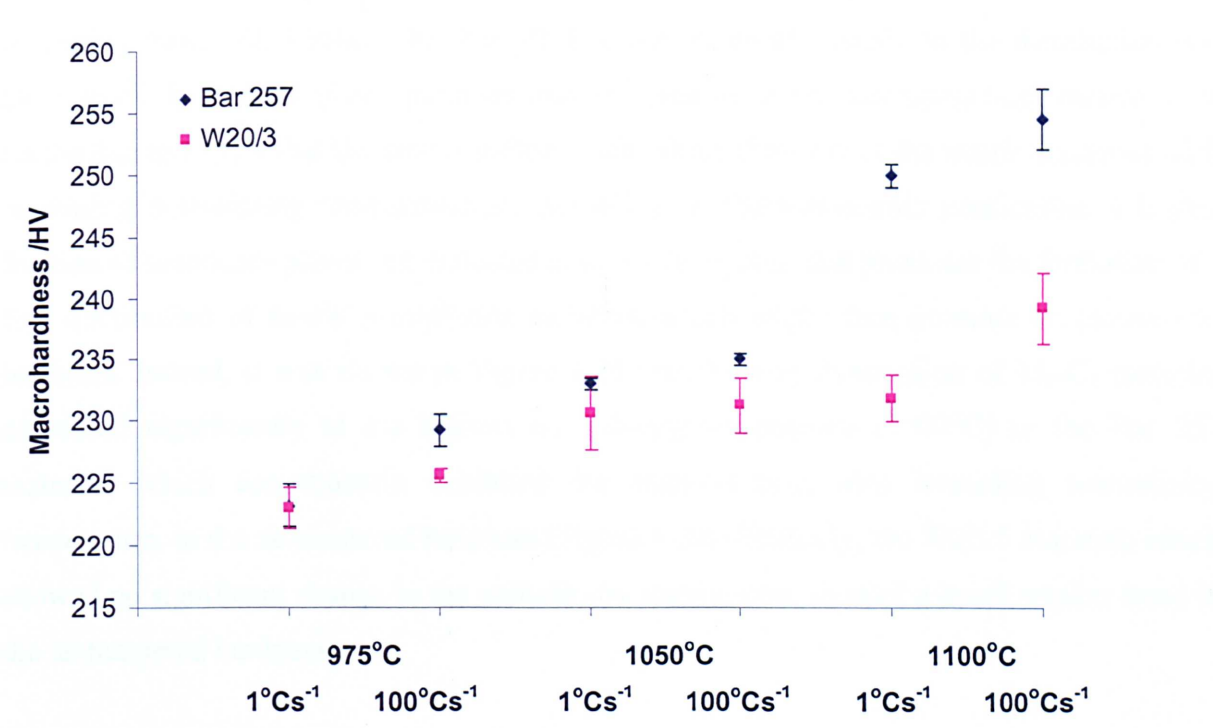


Figure 4.29: Macrohardness measurements as a function of normalizing temperature and cooling rate for the Bar 257 and W20-3 specimens normalized for 15 minutes and subsequently tempered at 750°C for 2 h.

4.6.4 Discussion on the Effect of Normalizing Condition on Subsequent Tempering

The tempering of P91 steel after the normalizing heat treatment results in drastic changes in the microstructure, whereby the most significant result was the precipitation of a large number of intergranular $M_{23}C_6$ carbides. Another significant finding was that the as-tempered hardness was shown to be very sensitive to both the normalizing heat treatment and to the bulk composition of the steel cast.

The fact that the as-tempered hardness increases with increasing normalizing temperature is particularly interesting. In section 4.5.3.2, it was suggested that the decrease in hardness with increasing normalizing temperature, in the as-normalized condition, was attributed to the corresponding increase in lath width and prior austenite grain size. The implication of the as-tempered hardness results is that, neither the martensite lath width, or indeed PAG size, are the major strengthening mechanism in these steels after the application of the stress relief tempering treatment. Instead, the strength becomes more dependent on the distribution and the size of the second phase particles that are present in the microstructure. Indeed, it is reasonable to expect that the concentration of dissolved elements in the matrix increases with increasing normalizing temperature as, according to thermodynamic predictions, a higher fraction of secondary phases are expected to dissolve. In turn, this promotes the formation of a fine distribution of newly precipitated particles, which might then promote an increase in hardness. Indeed, it was shown in Figure 4.26 that the size distribution of $M_{23}C_6$ particles decreased significantly at the highest normalizing temperature (1100°C) in the Bar 257 material, which consequently exhibited the sharpest rise, with increasing normalizing temperature, in the as-tempered hardness (Figure 4.29). Similarly, the W20-3 material, which showed no significant change in the particle size distribution, showed a much weaker trend in the as-tempered hardness.

In section 4.5.2, it was shown that the applied normalizing treatments did not succeed in dissolving all of the highly stable MX and AlN precipitates. These particles, which are present in the microstructure prior to tempering, are likely to have several effects on both the microstructure and mechanical properties of grade 91 steel. Firstly, pre-existing undissolved particles were shown to be relatively large as particles coarsen before they dissolve, which would tend to increase the mean particle size in the system. Secondly, undissolved precipitates will limit the amount of new precipitation that can occur, as solute atoms will be attached to the larger pre-existing particles. Thirdly, these precipitates were shown in section

4.6.1.3 to act as nucleation points on which new particles will preferentially precipitate. These factors may contribute to an overall increase in particle size and in turn a greater interparticle spacing, both of which are detrimental to the mechanical properties of high chromium power plant steels. Therefore, a reduction in the number density of these pre-existing particles, achievable by the application of higher normalizing temperatures and times, may improve the subsequent creep strength.

The results in the present study agree well with the work of Orr *et al* ^[29] on grade 91 steel, which also showed that the as-tempered hardness increases with an increase in normalizing temperature, and decreases with longer tempering times. Their reasoning for this increase in hardness was that an assessment of the solubility data for Nb (C,N), and VN in C-Mn type steels, revealed that the proportion of the available interstitial elements in steel 91 remain undissolved at 1050-1100°C. This explained their observations of a continuous increase in hardness with increasing normalizing temperature up to 1200°C.

Section 4.6.2 has shown that the matrix microstructure of the as-tempered microstructure is completely different to that in the as-normalized condition. This is due to the fact that many of the internal stresses, that were present as a result of the martensitic transformation, will have been removed due to the application of a severe stress relief tempering treatment. Amongst the recovery mechanisms, the annihilation of dislocations, and thus a decrease in the dislocation density is expected to occur in the material ^[77], which gave rise to an increase in the number of indexed points in the EBSD scan. This may have been responsible for the considerably large hardness drop of approximately 200 HV from the as-normalized condition. Another mechanism which may have affected the results is the loss in solid solution strengthening as elements are removed from the matrix to precipitate particles.

4.7 Summary of Initial Heat Treatments

This chapter has presented a study of the effect initial pre-service heat treatments. Changing normalizing parameters such as cooling rate and normalizing temperature have been shown to have a significant effect on the microstructure and hardness of grade 91 steel. Firstly, it has been shown that the virgin martensite lath widths decreased with faster cooling rate, and increased with increasing normalizing time and temperature. The lath width measurements were shown to be in good agreement with published literature data. Growth of the prior austenite grains was also observed to occur with increasing normalizing temperature, and it

was shown that grain growth occurred at a significantly faster rate in the weak grade 91 (Bar 257) cast. This was attributed to differences in the amount of secondary precipitates present in the two steel casts.

Secondly, cooling at the slower rate of 1°Cs^{-1} produced a lighter and somewhat thicker boundary region than cooling at the faster cooling rate. This became more evident in the W20-3 material. Thirdly, systematic trends in the values of martensite start temperature (M_s) were attributed to varying heat treatment parameters such as normalizing temperature, time at normalizing temperature and cooling rate. The strongest trend was the decrease in M_s with increasing cooling rate. The transformation temperature was also shown to be dependent on the chemical composition of the steel cast.

Hardness measurements were shown to be in good agreement with microstructural observations. EDS analysis from maps and from TEM examination confirmed the presence of the phases predicted by thermodynamic calculations described at the beginning of this chapter.

TEM examination of carbon extraction replicas showed that in addition to precipitating on lath and grain boundaries, $M_{23}C_6$ particles also tended to cluster around pre-existing AlN and NbC precipitates. The size distribution of $M_{23}C_6$ particles after tempering, as a function of varying normalizing parameters, was also examined. It was shown that the size distribution of these precipitates varied significantly between the investigated steel casts, such that the weaker Bar 257 material was more sensitive to changes in normalizing parameters.

Chapter 5

EFFECTS OF LONG-TERM AGING AND CREEP ON MINOR PHASE PRECIPITATION

5.1 Introduction

Minor variations in steel cast composition and varying pre-service heat treatment parameters, such as normalizing temperature and cooling rate, were shown in Chapter 4 to have a significant effect on the microstructure and hardness of grade 91 steel. This chapter is a continuation on the same theme, in which the effects of initial heat treatment on minor phase precipitation during thermal aging are discussed. The effects of other variables, such as accelerated creep testing and service exposure, on minor phase precipitation are also considered.

This chapter consists of three main areas of investigation. Firstly, the chemical composition and size of (V,Nb)X precipitates as a function of aging time in two P91 steel casts, with varying levels of V, Nb, Al, C and N, have been investigated. This was performed in order to establish whether substantial changes occur during exposure at relevant service temperatures, and thus determine whether such changes can be used as a method of assessing the condition, or thermal history, of high Cr ferritic-martensitic power plant steels. Secondly, the evolution of the particle size distribution of the larger $M_{23}C_6$ precipitates with respect to aging time has been investigated in order to determine whether the kinetics of particle coarsening are affected by minor composition variations. Finally, the precipitation of potentially deleterious phases, such as Laves phase and AlN , are also discussed. The results on the laboratory heat treated materials are also compared with the microstructure of ex-service and accelerated creep tested materials.

5.2 Materials

The grade 91 materials used in this research are of the same composition as the steels used in Chapter 4. The chemical composition of the investigated specimens, Bar 257 and W20-3, are shown in Table 3.1 (Chapter 3). The specimens used in this investigation have previously been subjected to various initial heat treatments described in the previous chapter. In order to examine the effects of different initial heat treatments on long-term aging, specimens that have been renormalized in the range of 975 to 1100°C and then re-tempered at 750°C for 2

hours were isothermally aged at 650°C for up to 10,000 hours in an argon atmosphere. In addition, several ex-service and creep tested grade 91 specimens have also been analysed.

5.3 Experimental Procedures

For transmission electron microscopy (TEM), carbon extraction replicas were used (see Chapter 3). Quantitative chemical composition measurements and imaging of particles were obtained using a JEOL JEM 2000FX instrument at 200 kV accelerating voltage in standard TEM mode with an Oxford Instruments Inca Link ISIS EDS system equipped with an ultra-thin window. One hundred particles were analysed for each specimen using an acquisition livetime of 50 seconds. Imaging for particle size analysis of MX precipitates was performed using a Philips Tecnai F20 FEGTEM instrument, operated in STEM mode with a High Angle Annular Dark Field (HAADF) detector in order to acquire images with strong atomic number contrast, which facilitates the automatic measurement of particle size distribution. Additional microanalyses of particle compositions were performed using a Gatan Digipeels parallel electron energy loss spectrometer (PEELS) instrument, which is fitted on the Tecnai F20.

5.4 Analysis of the Chemical Composition of MX Precipitates

The chemical composition of the MX carbonitrides was measured using EDS in order to understand how these particles evolve during exposure at high temperatures and also to ascertain any effects of different chemical composition of the bulk materials. The relative concentration distribution of V, Nb and Cr in MX with respect to different thermal treatments was interesting to examine, because it has been found that V(N,C) and Nb(C,N) are completely intersoluble ^[121,122]. Changes in chemical composition of such important creep resisting precipitates must be understood, as these may link to changes in both particle size and shape distribution, which may have a large influence in governing the creep behaviour of high chromium steels in service and also provide an indication of thermal history experienced by plant components. Indeed, a similar analysis method has been performed by Thomson ^[123] on other precipitates over a range of power plant steels.

5.4.1 Chemical Composition of MX in As-received Condition P91

Figure 5.1 shows the average concentration of the metallic elements Nb, V and Cr in the MX carbonitride precipitates in the Bar 257 and W20-3 materials in the as-received (normalized and tempered) condition. The chemical composition was determined using EDS in the TEM, which was performed on carbon extraction replicas. The measurements were performed on one hundred individual MX particles, which were randomly sampled. The mean concentration of the metallic elements in MX precipitates was considered because, as shown in Figure 5.2, the composition of the metallic elements can vary linearly to such an extent that it was difficult to distinguish between NbC and VN due to the fact that V and Nb are soluble in these phases respectively. The mean values thus give a good indication of the differences in particle compositions and types present in different samples.

It can be seen that the main difference between the compositions of MX precipitates in the two steel casts is that, in the Bar 257 material, the MX particles are primarily rich in Nb, whereas in W20-3 the majority of particles are rich in V (Figure 5.1). The measured compositions are shown to agree well with the predicted equilibrium values (from MTDATA calculations) shown in the same graph. An interesting observation can be seen, where the measured composition of precipitates exhibited relatively high concentrations of Cr, whereas this element was predicted to be present only in trace quantities under equilibrium conditions. Figure 5.2 shows the chemical composition distribution of the measured particles. Each point represents the composition of a single measured particle. It can be seen that the majority of particles measured in the Bar 257 material are clustered in the Nb-rich region, as the mean composition suggests. On the contrary, it can be seen that the majority of particles in the W20-3 material are in the V-rich region. However, it is evident that the dispersion in the fraction of Nb, V and Cr in MX precipitates is also greater in the W20-3 material.

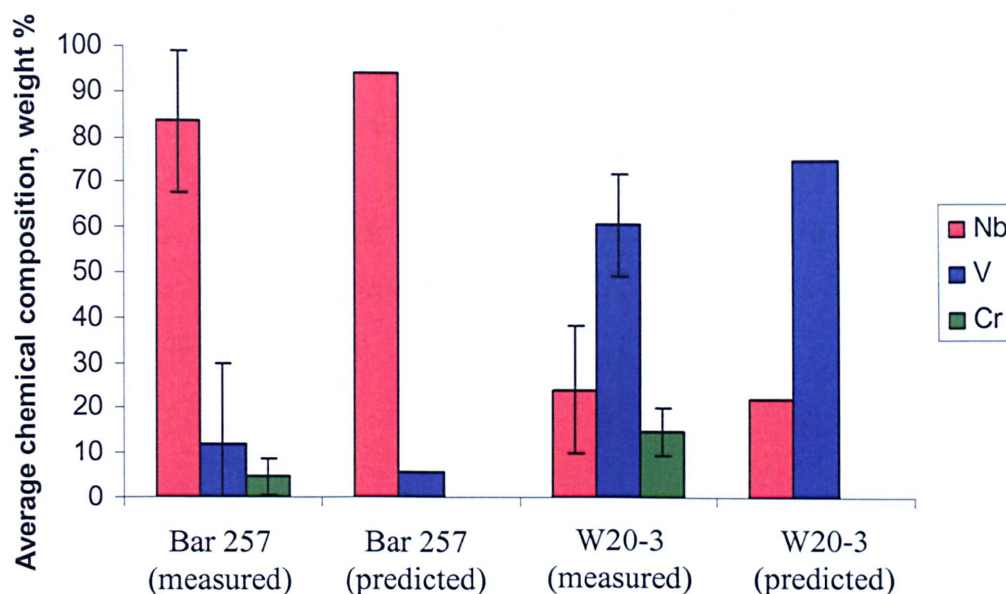


Figure 5.1: Plot showing the mean chemical composition of MX precipitates present in Bar 257 and W20-3 materials supplied in the as-received condition. The compositions were measured using EDS in the TEM on carbon extraction replicas. The equilibrium calculations were performed at 750°C, which corresponds to the pre-service tempering temperature experienced by these two grade 91 casts.

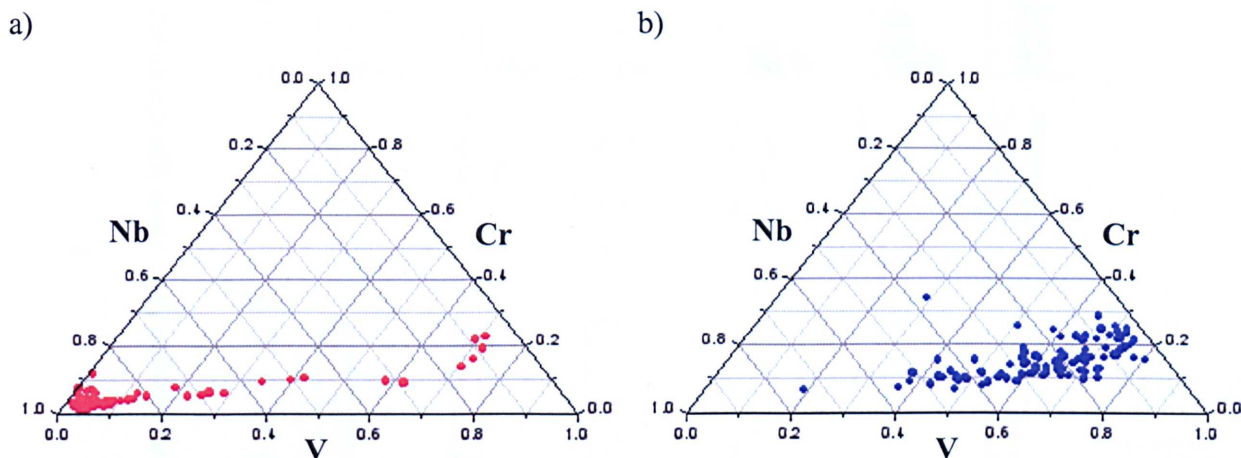


Figure 5.2: EDS measurements from individual MX precipitates comparing their V, Nb and Cr content in the a) Bar 257 and b) W20-3 materials in the as-received condition.

5.4.2 Chemical Composition of MX in As-normalized Specimens

5.4.2.1 Results

Quantitative microanalysis of MX precipitates in the as-normalized condition revealed that the vast majority of the MX particle population in both alloys were Nb-rich (Figure 5.3). It can be seen that, in the specimens which were rapidly cooled, there is a slight decrease in the Nb concentration in the MX precipitates, which corresponded to an increase in the V concentration in the same particles. In addition, the level of Cr concentration in MX appeared to be relatively unaffected by cooling rate, which is likely to be due to the low solubility of Cr

in Nb(C,N). Another interesting finding was that the Cr concentration in MX after renormalizing was found to be considerably lower than the measured Cr concentration in the as-received (normalized and tempered) condition, again due to its low solubility in this phase. For instance, in the W20-3 material, the Cr level dropped from ~15 wt.% in the as-received condition, to ~5 wt.% after renormalizing at 1100°C. A similar drop in Cr concentration was also observed in the Bar 257 material, from ~6 wt.% to ~3 wt.%, in the as-received at renormalized condition respectively.

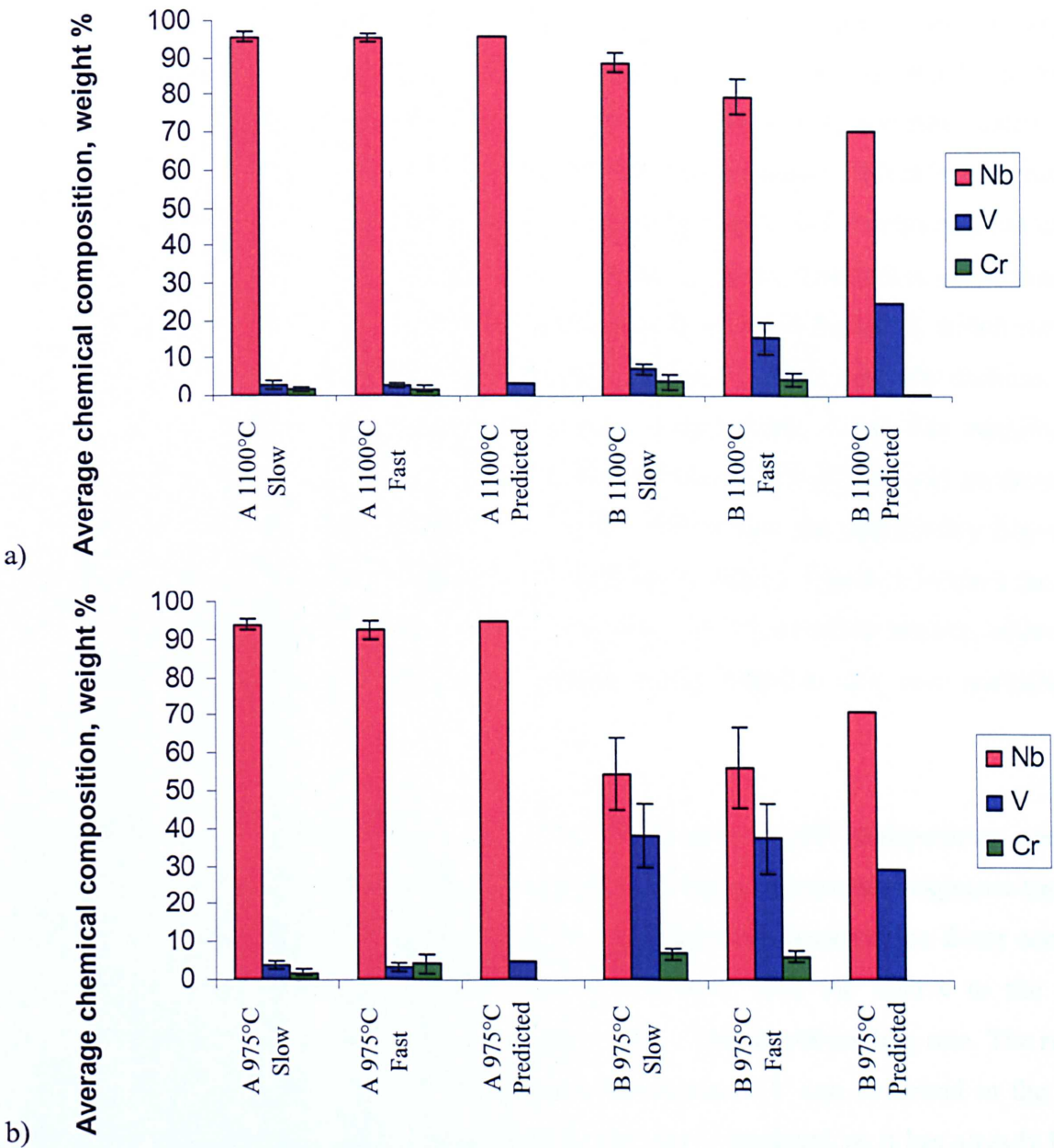


Figure 5.3: Plot showing the mean chemical composition of MX precipitates present in the as-normalized condition at temperatures of a) 1100°C and b) 975°C in the Bar 257 (A) and W20-3 (B) materials subjected to different cooling rates. The chemical composition was determined from EDS measurements in the TEM from carbon extraction replicas. Also shown are the predicted equilibrium compositions of these precipitates at the two normalizing temperatures.

The overall drop in Nb and corresponding increase in V content as a function of cooling rate was more evident in W20-3, which suggests, from composition measurements of the as-received materials, that the particle compositions are strongly dependent on the chemical composition of the material in addition to heat treatment.

5.4.2.2 Discussion

According to Shanmugan *et al* ^[124], “Thermodynamically, titanium and niobium form the least soluble (highly stable) carbonitrides” in microalloyed steels, which would result in only a small concentration of this element in the austenitic temperature range. They also argued ^[124] that the solubility of vanadium nitride is considerably higher, so much so that a significantly higher amount of vanadium would be left in solution in the iron matrix as a result of the higher solubility of this phase. The fact that the solubility of Nb is lower than that of V in MX is pertinent to the present findings. In principle, the relative concentration of the most slowly diffusing element (Nb) continues to increase up to the dissolution temperature of these precipitates. This was previously demonstrated in Figure 4.4 (Chapter 4), which showed the predicted chemical composition of MX between 500 and 1180°C, whereby niobium was found to replace vanadium at increasingly higher temperatures. From this equilibrium calculation, it was also shown that a concentration increase of Nb in MX was predicted to occur at higher temperatures in W20-3 than in Bar 257, hence the appreciably higher V concentration at the normalizing temperature in the former. Indeed, Figure 5.3 shows that the chemical compositions of MX in Bar 257 at 975°C and 1100°C are rather similar, whereas a large difference between the Nb and V content exists between the two normalizing temperatures in W20-3.

The apparent susceptibility of W20-3 to sensitive changes in MX composition can be rationalized by two rather conflicting hypotheses, the first being that the total exposure time at high temperatures during the normalizing treatment is somewhat shorter at the faster cooling rate. Therefore, less time was available for Nb to diffuse from the matrix to the MX precipitates during the renormalizing heat treatment than at the slower cooling rate. The result of cooling at the faster rate was that a higher concentration of V can be found in the MX precipitates. This effect is somewhat magnified in the W20-3 material, as it has already been shown that MX particles in W20-3 were expected to contain a higher V concentration throughout the temperature range of interest, according to thermodynamic predictions. However, this effect is not evident at the lowest normalizing temperature (975°C)

investigated. The second argument is that a close observation of Figure 5.3 shows that the fast cooled specimen has a mean composition that is more representative of the equilibrium value, which implies that exposure time differences between the two cooling rates are actually insignificant. Therefore, less time was available for minor compositional adjustments, due to changing equilibrium compositions at different temperatures, to occur upon cooling. As such it is expected that the faster cooled specimen resembles the predicted equilibrium composition at the normalizing temperature.

In fact, neither argument accounts for the most important observation, which is that at the slower cooling rate, the V concentration is significantly lower than the equilibrium value. This is discussed further in section 5.5.

From these results, it can be seen that the effect of thermal cycling is to considerably change particle compositions, to the extent that they are ultimately dependent upon the peak temperature and cooling rate. It is postulated that subjecting P91 steel (or other high Cr ferritic-martensitic steels) to a variation of these parameters, as would be expected in a typical welding cycle, would give rise to a highly localized inhomogeneous distribution of MX compositions across a specimen area, prior to the application of a stress relief or post weld heat treatment. The effects of different initial heat treatments on MX composition have also been shown to be sensitive to minor variations in material composition.

5.4.3 Chemical Composition of MX in Aged Specimens

Following a post-normalizing tempering treatment at 750°C for 2 hours, a dispersion of intragranular MX precipitates was present in the microstructure of all the investigated P91 steel specimens, in addition to intergranular and interlath $M_{23}C_6$ precipitates. The effects of prolonged high temperature exposure, from different initial heat treatments, on the composition of these particles, were examined and are presented henceforth.

Figure 5.4 a) shows the mean concentration measured using EDS in the TEM of Nb, V and Cr in MX in the aged Bar 257 specimens. It is shown that, at the slow cooling rate, a significant enrichment of Nb in MX precipitates occurs after 5,000 h aging. After 10,000 h aging however, the V concentration slightly increases, albeit within experimental error. However, this trend is also evident in the fast cooled specimens, which may be an indication of secondary precipitation of VN particles. Nevertheless, the majority of MX precipitates in this

material remain rich in Nb, consistent with thermodynamic predictions and composition measurements of the as-received condition (Figure 5.1). This may be attributable to both the presence of AlN in the as-normalized condition, and the slightly lower V concentration in this material.

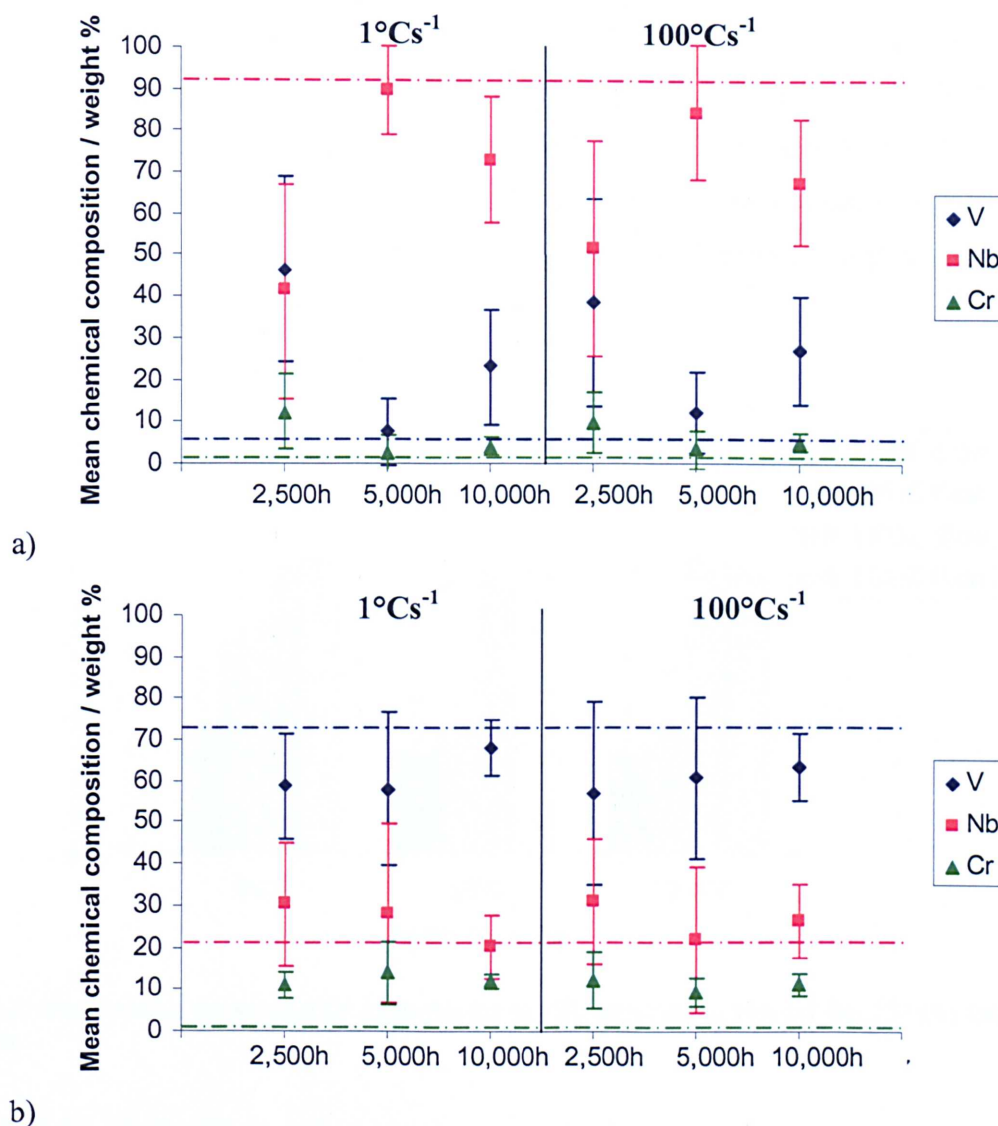


Figure 5.4: Mean chemical composition, normalized for the metal constituent, derived by EDS analyses of MX precipitates present in the a) Bar 257 and b) W20-3 materials cooled at different rates from the normalizing temperature and subsequently aged at 650°C for up to 10,000 h. Measurements were performed using EDS in the TEM on carbon extraction replicas. The dotted lines represent the equilibrium compositions of this phase, which were calculated using MTDATA.

In contrast, W20-3 is shown to have a more stable composition of MX with a mean composition of predominantly V-rich particles, indicating a higher compositional stability of these precipitates in this material (Figure 5.4b). With increasing aging times, the V content is shown to gradually increase at the expense of Nb, which is indicative that the mean compositions of these particles are striving to reach their equilibrium value. This appears to

occur at a nominally faster rate in the slow cooled specimen, although this change is within experimental error.

Further analyses of the particle compositions show that the mean concentration of Cr in MX is much higher in W20-3 than in Bar 257 (Figure 5.5). It was also found that the decrease in Cr with respect to aging time is much slower in the former, which may be due to the fact that there is a higher fraction of VN, in which Cr is more soluble, in this material. Thermodynamic calculations performed using the software package MTDATA have shown that the predicted level of Cr in solution in ferrite between 500°C and the A_{c1} temperature is higher in W20-3, which is feasible as a result of the nominally higher Cr concentration and a lower predicted mass fraction of $M_{23}C_6$ precipitates.

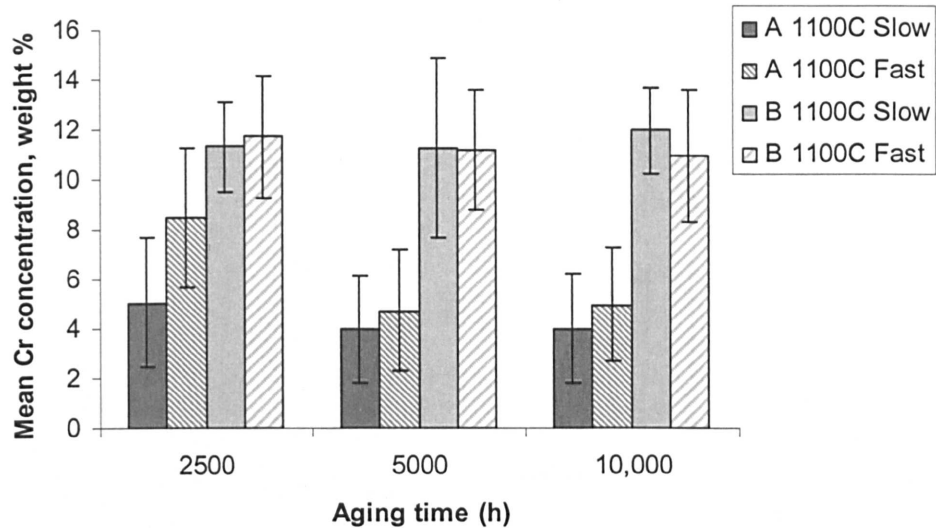


Figure 5.5: Plot showing the average Cr concentration in MX versus aging time for Bar 257 (A) and W20-3 (B) specimens.

It can be seen from the chemical composition distribution plots that with increased aging times the composition distribution of MX precipitates partitions, to such an extent that there are two distinct particle types, in this case either Nb-rich or V-rich precipitates, where at an earlier aging stage the composition distribution of the metallic elements in MX precipitates was linear (Figures 5.6 and 5.7). This effect is shown to be more prominent in Bar 257 (Figure 5.6).

In W20-3 however, there appears to be a reduction in the fraction of Nb-rich MX particles present and this effect is greatest in the fast cooled specimen after 10,000 h aging, due

perhaps to significant secondary precipitation of VN (Figure 5.7). In the slow cooled specimens, the effect of two phase separation between Nb(C,N) and V(N,C) was not yet apparent even after 10,000 h aging, again indicating that the compositional stability of MX precipitates is much higher in both this material and condition.

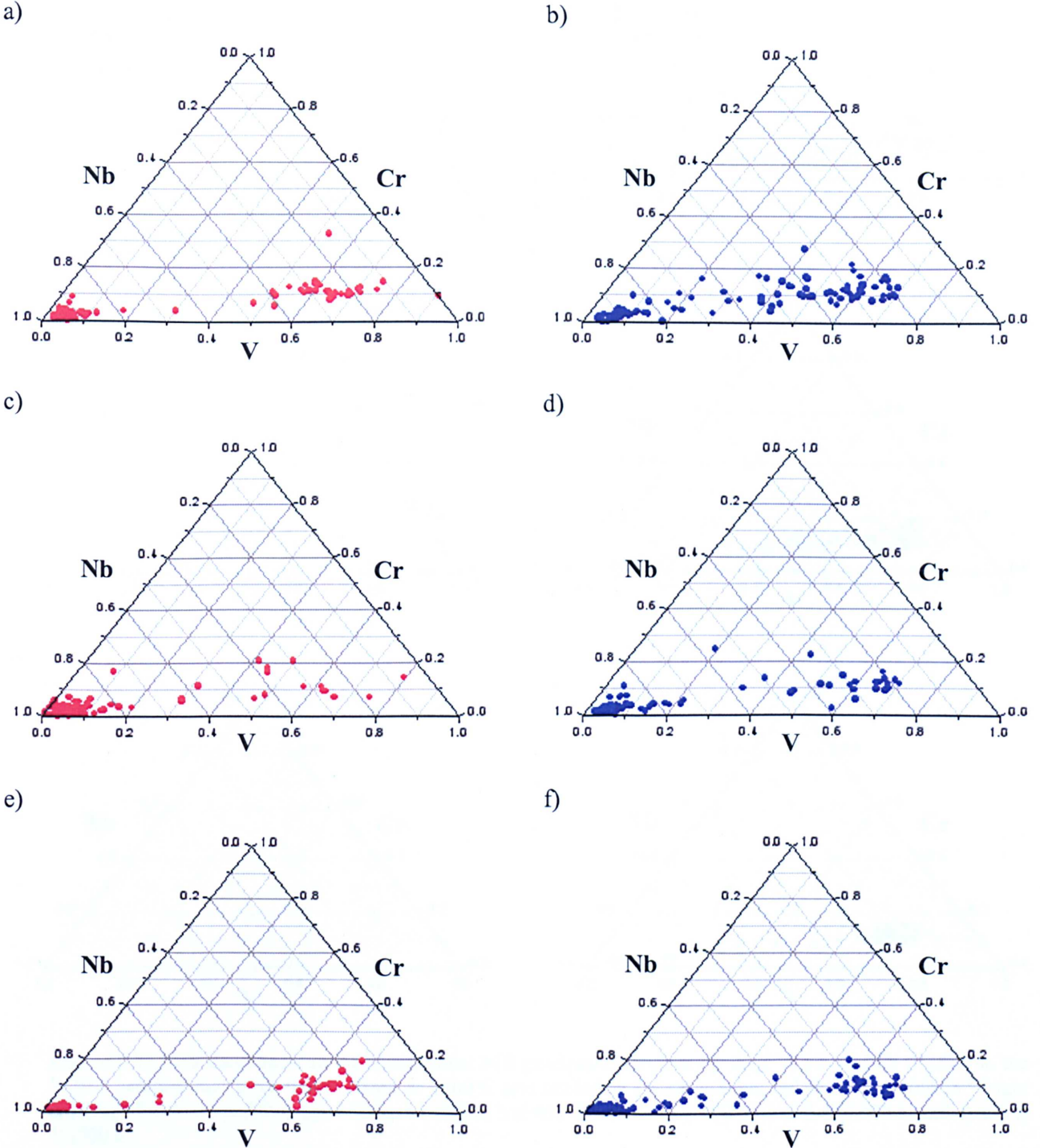


Figure 5.6: EDS measurements from individual MX precipitates comparing their V, Nb and Cr fraction in the Bar 257 samples that were renormalized at 1100°C and cooled at 1 (left column, red dots) and 100°Cs⁻¹ (right column, blue dots), and then aged for up to 10,000 h at 650°C; a) and b) 2,500 h, c) and d) 5,000 h, and e) and f) 10,000 h.

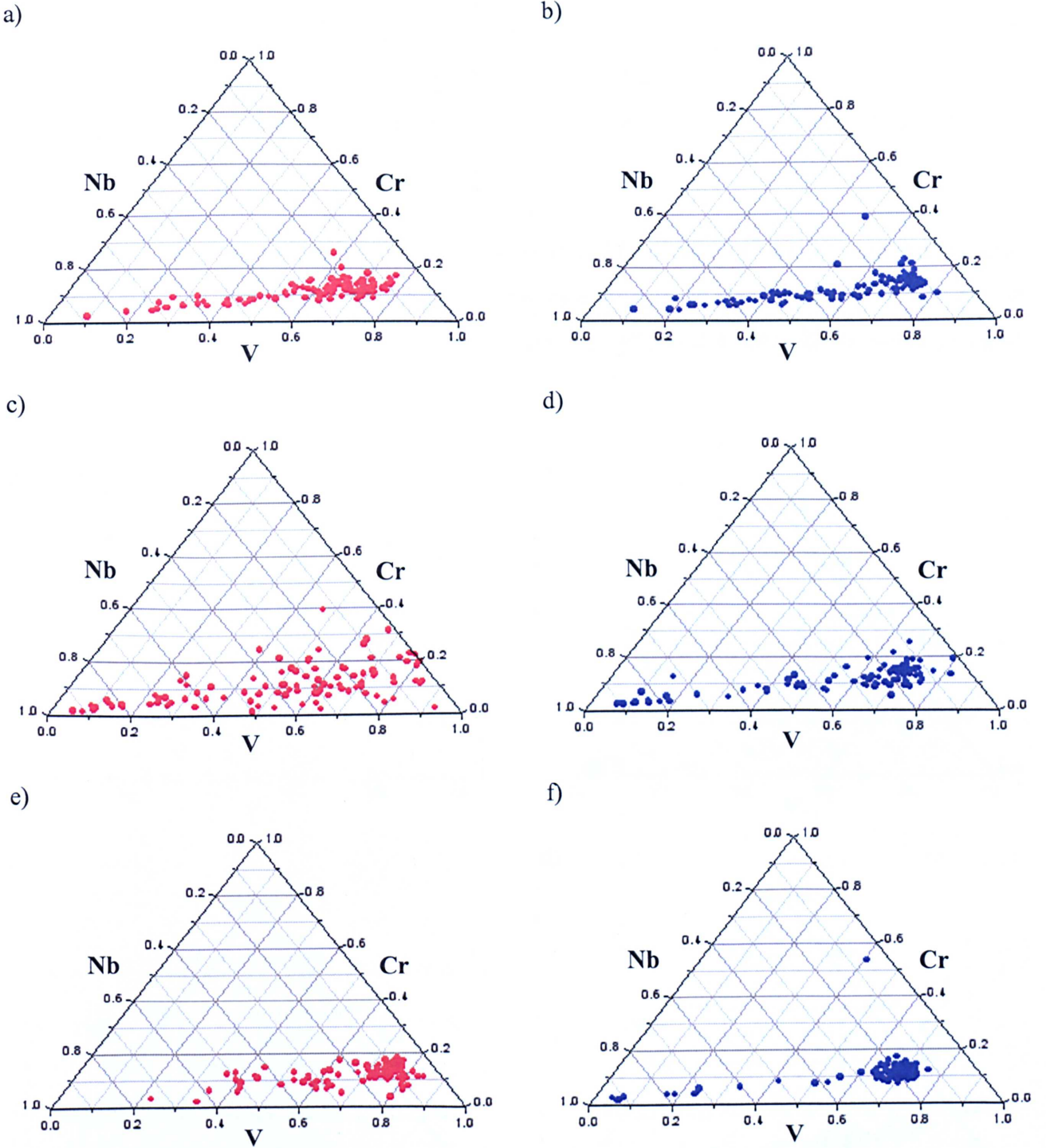


Figure 5.7: EDS measurements from individual MX precipitates comparing their V, Nb and Cr fraction in the W20-3 samples that were renormalized at 1100°C and cooled at 1 (left column, red dots) and 100°Cs⁻¹ (right column, blue dots), and then aged for up to 10,000 h at 650°C; a) and b) 2,500 h, c) and d) 5,000 h, and e) and f) 10,000 h.

The significant difference in composition distribution between the two cooling rates in W20-3 is highlighted by the fact that the concentration distribution of Cr in MX is much wider at the slow cooling rate, especially in the V-rich precipitates in which Cr is soluble. After aging for 10,000 h, it is clear that the majority of MX precipitates are rich in V. In a similar study, Suzuki *et al* ^[121] reported two-phase separation of MX to occur in P91 steel after tempering at 765°C for 30 minutes.

Figure 5.8 shows the chemical composition distribution of MX in Bar 257 and W20-3 after aging from the lowest renormalizing temperature employed in this study (975°C). It can be seen that two-phase separation has occurred in the former after only 2,500 hours aging at 650°C.

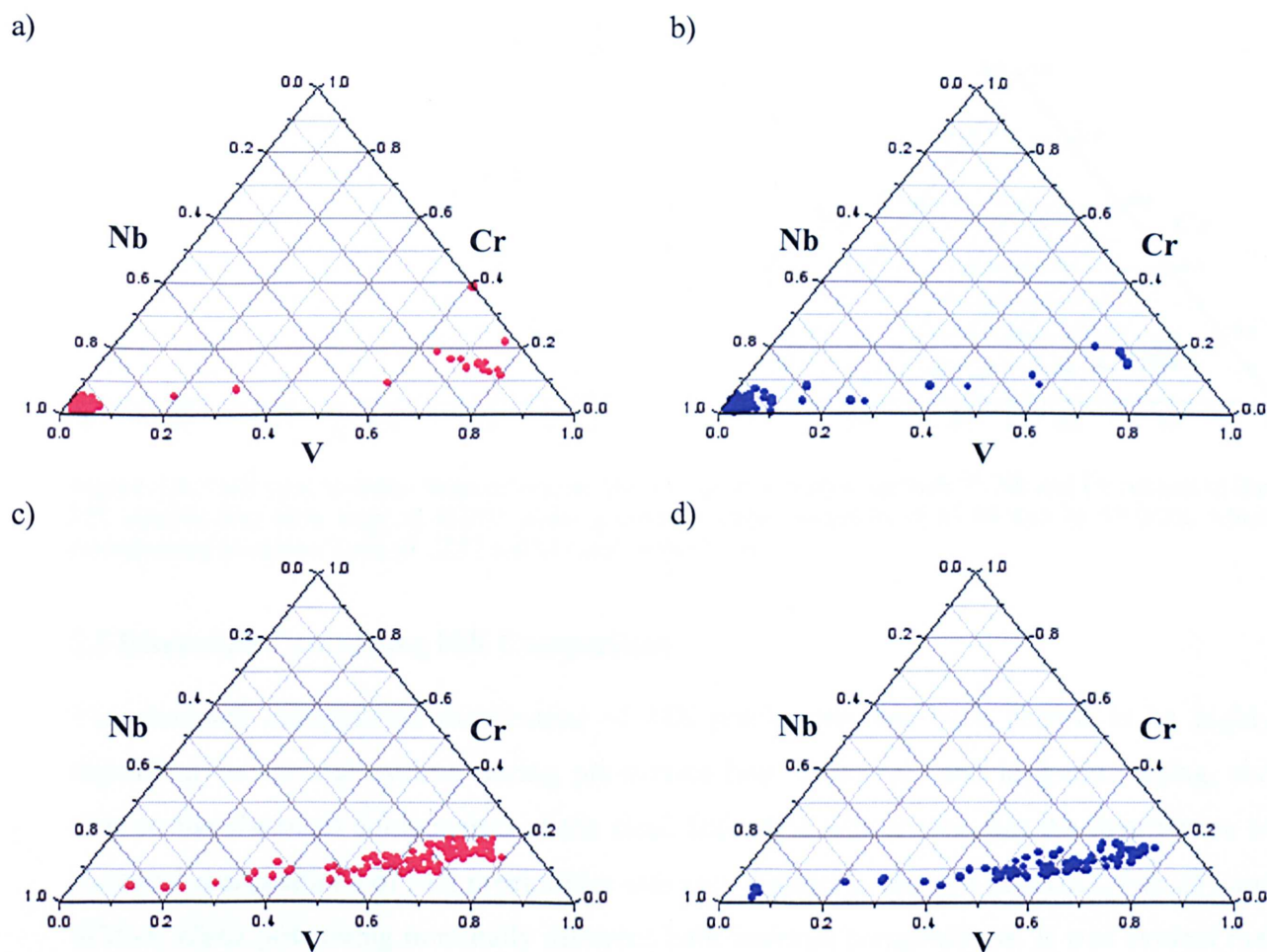


Figure 5.8: EDS measurements from individual MX precipitates comparing their V, Nb and Cr fraction in Bar 257 (a) and b)) and W20-3 (c) and d)) samples that were renormalized at 975°C and cooled at 1 (left column, red dots) and 100°Cs⁻¹ (right column, blue dots), and then aged for 2,500 h at 650°C.

5.4.4 Chemical Composition of MX in Accelerated Creep Test Specimens

The chemical composition distribution of MX precipitates in accelerated creep test specimens of the Bar 257 material, were also investigated. Figure 5.9 shows the composition of MX particles in the gauge (stressed) portion of the creep specimens subjected to the lowest and highest applied stresses. It can be seen that the effect of two-phase separation is more evident at the lower stress (60 MPa), which is unsurprising as the rupture time was far greater in this specimen, 2,217.2 hours, in comparison to 82.4 hours at an applied stress of 93 MPa. The specimen subjected to a stress of 60 MPa somewhat resembles the same material that was aged at the same temperature for 2,500 hours. Therefore, the effects of applied stress in these samples were found not to have a strong influence on the changes in chemical composition of MX precipitates.

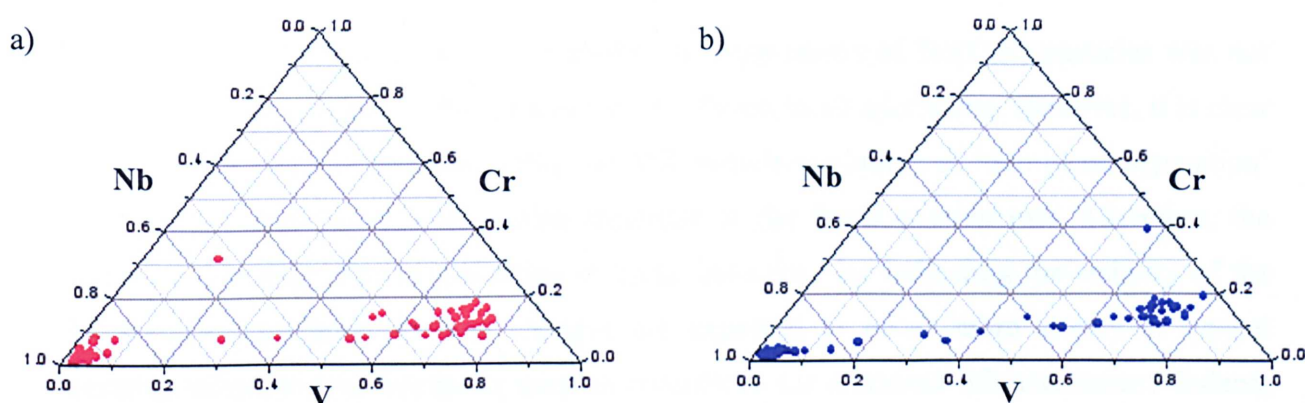


Figure 5.9: EDS measurements from individual MX precipitates comparing their V, Nb and Cr content in Bar 257 samples that were crept at 650°C under a constant stress condition of a) 60 and b) 93 MPa, which corresponded to rupture times of 2,217 and 82 hours respectively.

5.5 Discussion Concerning MX Composition

The chemical composition distribution of MX precipitates has been shown to be highly dependent on thermal cycling during pre-service heat treatments and long-term aging, and also on the chemical composition of the steel. Indeed, it was shown that the distribution of chemical compositions of MX precipitates was very distinct in the two materials, Bar 257 and W20-3, albeit possessing nominally different bulk material compositions. It was evident that ‘two-phase separation’ occurred in Bar 257 into NbC and VN after a relatively short aging time of 2,500 h, whereas W20-3 maintained a linear composition distribution of Nb and V in MX precipitates to longer aging times.

The cooling rate from the normalizing temperature was found to have a significant effect on the chemical composition distribution of MX particles. Yamada *et al* ^[39] studied the effects of cooling rate on the creep properties of 9CrW steels and found that both creep rate and creep strain are lower in quenched and tempered steels than for air-cooled and tempered steels. This was attributed to the rapid formation of Nb(C,N) during cooling becoming suppressed at the faster cooling rate and, as a result, this precipitate did not become a preferential nucleation site for fine VN *per se*, which would otherwise result in a coarse complex MX particle, such as 'V-wings'. Therefore, their argument was that a finer distribution of MX particles is achieved by cooling at faster rates. The implication of the work of Yamada *et al* ^[39] is that the cooling rate from the normalizing temperature, or from a welding operation, can affect the precipitation characteristics of MX, which may, in turn, influence the creep strength of high Cr ferritic-martensitic steels, such as P91.

At the cooling rates employed in this study, the suppression of Nb(C,N) particles was not observed (Chapter 4), and V-wing particles were found in all specimens. However, it is clear that cooling rate has an important effect on MX particle evolution, as 'two-phase separation' of MX was somewhat slower in both materials at the faster cooling rate. Therefore, the separation rate may give an indication of creep behaviour by indicating the stability of the MX particle population and, as changes are expected to occur more slowly at typical operating temperatures, this factor may be considered for remanent life assessment. Indeed, the MX particles in Bar 257, which is known to be weak in creep, separate at a faster rate than in the more conventional W20-3 material.

From the findings in this study, it is possible that the Al concentration, or more specifically N:Al ratio, may have a direct effect on the composition differences achieved by cooling at different rates. In the case of Bar 257, which has approximately a tenfold higher Al concentration than W20-3, the formation of nitride precipitates is effectively a competition between AlN, V(N,C) and Nb(C,N). The fact that Al₄C₃ was not found in either material implies that either excess Al forms AlN, or it is left in solution. On the other hand, V and Nb readily form carbides. Prior to the application of the normalizing treatments, Bar 257 in the as-received condition contained large AlN precipitates. Considering that the enrichment of Nb in MX precipitates was found to occur at high temperatures due to the low solubility of Nb in steel in comparison to V, it is reasonable to assume that V and N go into solution during normalizing as NbC is more stable than NbN at typical normalizing temperatures. Therefore,

on renormalizing Al may aid the Nb enrichment process by readily bonding with N, which is removed from MX to form AlN. Indeed, the concentration of Al and N in Bar 257 are close to stoichiometric, which may explain the relatively low VN fraction in this cast in comparison to W20-3.

The shortfall in VN precipitation in Bar 257 is of interest as it implies that the majority of MX precipitates are Nb(C,N), notwithstanding the bulk concentration of Nb (0.08 wt.%) is less than half that of V (0.18 wt.%). Correspondingly, most of the V must be in solution in the Fe matrix. Therefore, the total amount of MX precipitates in Bar 257 must be less than that of W20-3. Indeed, thermodynamic calculations showed the mass fraction of MX precipitate values to be approximately 0.1 and 0.25 wt.% in Bar 257 and W20-3 respectively. Vanadium is known to form carbides and according to Zajac *et al* ^[126], VN has a lower solubility in comparison to vanadium carbides (VC) or low nitrogen V(C,N), which suggests that the latter phases will coarsen more rapidly as solubility is a rate controlling factor in the coarsening process of precipitated particles.

Zajac *et al* ^[125] suggested that the morphology of VN in micro-alloyed steels was governed by not only the N content, but also the ratio of V:N, to such an extent that when this ratio is high (high V), VN precipitates coarsen rapidly. Similarly, Strid and Easterling ^[126] reasoned that an increase in N tends to refine the particle size distribution, whereas an increase in the portion of nitride-forming elements results in a coarser particle size distribution. They also suggested that both Al and Nb tend to promote particle coarsening unless extra N is present in the steel. These hypotheses are consistent with the present findings, as the concentration of both these elements is greater in the faster coarsening Bar 257 material (see section 5.6).

In addition to decreasing the cooling rate, it was also found that ‘two-phase separation’ occurs more rapidly as the normalizing temperature decreases. The concentration of Nb in MX increases up to the peak temperature. However, it is postulated that at the lower temperature, MX particle coarsening is occurring instead of particle dissolution, to such an extent that enrichment of V and Nb is occurring in (V,Nb)(N,C) and (Nb,V)(C,N) respectively. As a result, there would be a reduction of carbonitride forming elements in solution in the matrix, thus, on subsequent re-tempering, there would be less newly precipitated particles, which would cause a reduction in precipitates with a random concentration of Nb and V. This may lead to a decrease in the mechanical properties due to the higher probability of attaining a

large interparticle spacing, which would decrease the desired pinning of dislocations and subgrain boundaries. Indeed, the as-tempered hardness values were shown in Chapter 4 to decrease with decreasing normalizing temperature.

The high initial concentration of Cr in MX after short aging times may occur as Cr is readily available due to its relatively high concentration in the ferrite matrix, in contrast to the other metallic carbonitride formers V and Nb. Therefore, Cr enrichment can be explained by the fact that V and Nb have to diffuse over longer distances due to their relatively low concentration.

Studies performed by Andren *et al* ^[127] on MX precipitates in 18/12 austenitic stainless steels showed that MX precipitates after short aging times were both largely sub-stoichiometric and had a relatively high Cr concentration, which substituted for the metallic (M) elements Nb and V. They suggested that the substitution of M elements by Cr was driven by a reduction in lattice parameter of MX, to such an extent that the lattice mismatch between these precipitates and the austenitic matrix would also reduce, thus reducing the effects of stress generation, which are caused by accommodating a flow of vacancies necessary for the growth of MX. However, the authors indicated that stoichiometric carbides have a lower free energy and, as a result, they grow at the expense of sub-stoichiometric ones.

The stoichiometric compositions between the metallic elements and carbon and nitrogen have not been investigated in this study. However, several MX precipitates were analysed using parallel electron energy loss spectroscopy (PEELS) and it was found that the majority of V-rich MX precipitates were shown to exhibit a large N peak in the spectra (Figure 5.10). Nb-rich particles tended to show an indistinguishable N peak. In this study, it is clear that the mean concentration of Cr in MX precipitates decreases with increasing aging times. The gradual mean reduction in Cr concentration was found to be relatively slow. In addition, it was shown that the reduction in Cr concentration occurred significantly faster in the weak Bar 257 cast, consistent with results which illustrated the partitioning of the composition of MX precipitates. Accordingly, the decrease in the Cr concentration in MX precipitates, a change which is expected to occur slowly during the operational lifetime of grade 91 components, may be used as an indicative measure of the condition of power plant components.

The present results showed that aging at 650°C up to relatively short times from different starting microstructures significantly changes the distribution of chemical compositions in these precipitates. However, it is expected that, due to the fact that ordered carbides and nitrides possess very low diffusivities, changes in composition of MX should be slow at typical operating temperatures of approximately 568°C.

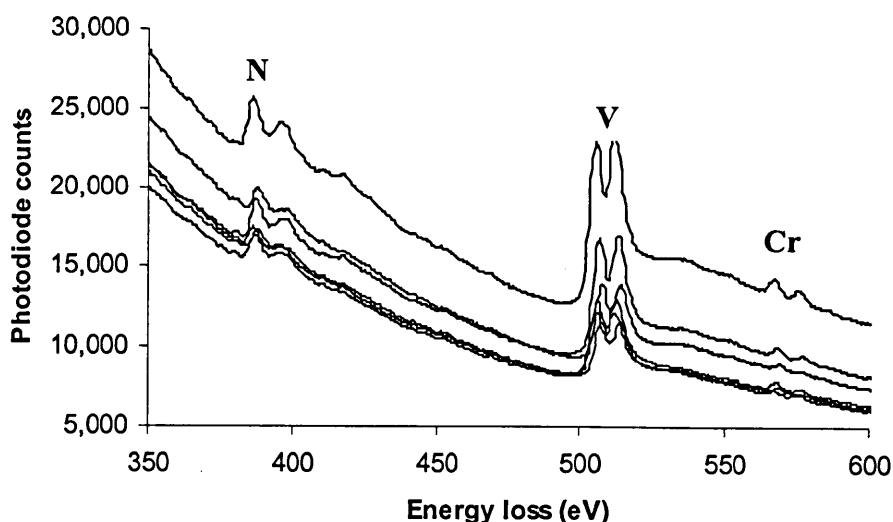


Figure 5.10: Parallel electron energy loss (PEELS) spectra of 6 V-rich MX precipitates showing the presence of a large N peak.

5.6 Particle Size Analysis of Minor Phase Precipitates

It is generally accepted that precipitation strengthening is one of the most, if not the most, important strengthening mechanism in P91 steel. The stability of the microstructure is dependent on a fine dispersion of small precipitates which act as grain boundary pinning points and also pin dislocations in the matrix to retard the motion of dislocations, and hence the process of recovery. Many studies of precipitates in P91 have reported data from particle size measurements, but most of these are based on manual measurements on a limited number of particles. In an effort to link microstructural features to the creep properties and remaining lifetimes, a need exists to accurately determine precipitate size, given the influence of precipitates on the strength of power plant steels. Indeed, Thomson ^[123] identified that carbide coarsening could potentially be used as a microstructural parameter for the assessment of remanent creep life prediction in high chromium steels. However, in order to achieve this milestone, a necessarily large quantity of data must be collected in order for the results to accurately represent the distribution of particle sizes present in a material. At the same time, there are other constraints involved when collecting this data, the main one being cost, not to

mention ease of acquisition and repeatability in order to yield accurate results. The former requires short analysis times, and the latter a minimisation of human error in measurement.

Image analysis software relies on contrast differences in an image that allows certain features to be distinguishable from others, e.g. grains and grain boundaries, and also particles and the matrix must have sufficient contrast in order to separate the two components. The results of detailed particle size analysis of the different precipitate phases in grade 91 steel are discussed in the following sections.

5.6.1 Particle Size Distribution of MX Precipitates

In addition to the measurement of compositional variations of MX precipitates, the particle size distribution of these precipitates was also investigated. To achieve this, carbon extraction replicas were examined using a high angular annular dark field detector (HAADF) in STEM mode in the Tecnai F20 FEGTEM. This detector allows different particle types to be identified, as atomic number contrast images can be produced using this technique (Figure 5.11). The modus operandi has been discussed in Chapter 3. For this investigation, 20 random 1024×1024 pixel images at a magnification of $\times 14,000$, which was suitably high to allow MX precipitates to be visible, yet low enough to analyse a large area, were acquired from the TEM and subsequently analysed with an automatic image analysis software ^[116]. A minimum of 500 particles were measured from each specimen.

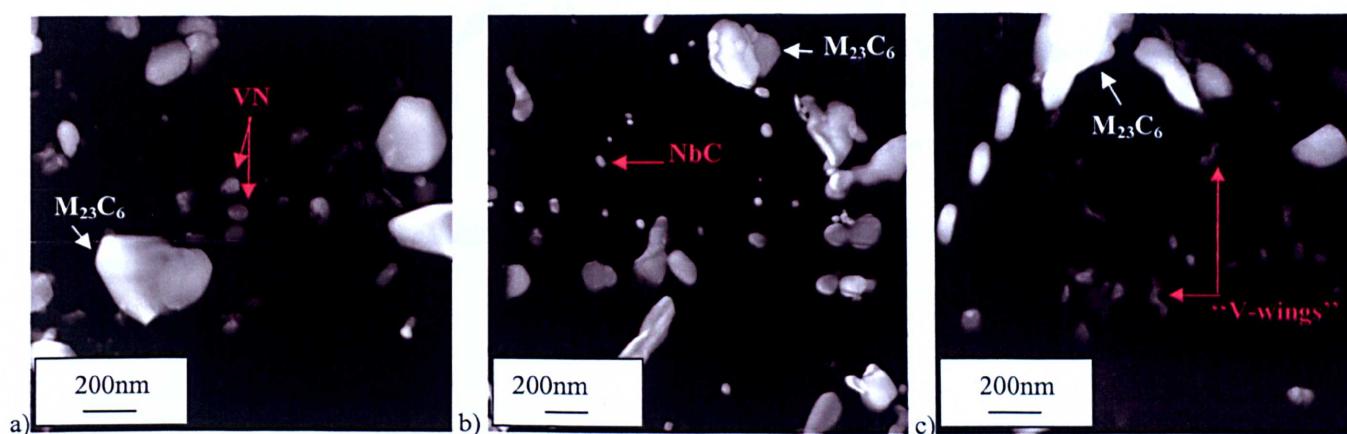


Figure 5.11: HAADF STEM images of carbon extraction replicas of aged P91 steel showing intragranular a) VN, b) small spherical NbC, and c) 'V-wing' precipitates.

Results are presented in Figure 5.12 and 5.13, which show the measured particle size distribution in the W20-3 and Bar 257 materials respectively, at different isothermal aging intervals. In W20-3, there was a distinct difference in the size distribution of MX precipitates with respect to cooling rate from the normalizing temperature. In the slow cooled specimen, the majority of the measured particles lie in the size range between 50 and 100 nm, whereas at the fast cooling rate the majority of the particles lie in the 20 to 50 nm size range. This is consistent with the findings from Yamada *et al* [39], which have been previously discussed. It is interesting to note that progressive coarsening of MX precipitates is evident with increasing aging time, as shown by the fact that the size distribution curve steadily widens. Nonetheless, the peak of the size distribution curve does not appear to shift, which indicates good high temperature stability with respect to particle size of these precipitates in this steel cast.

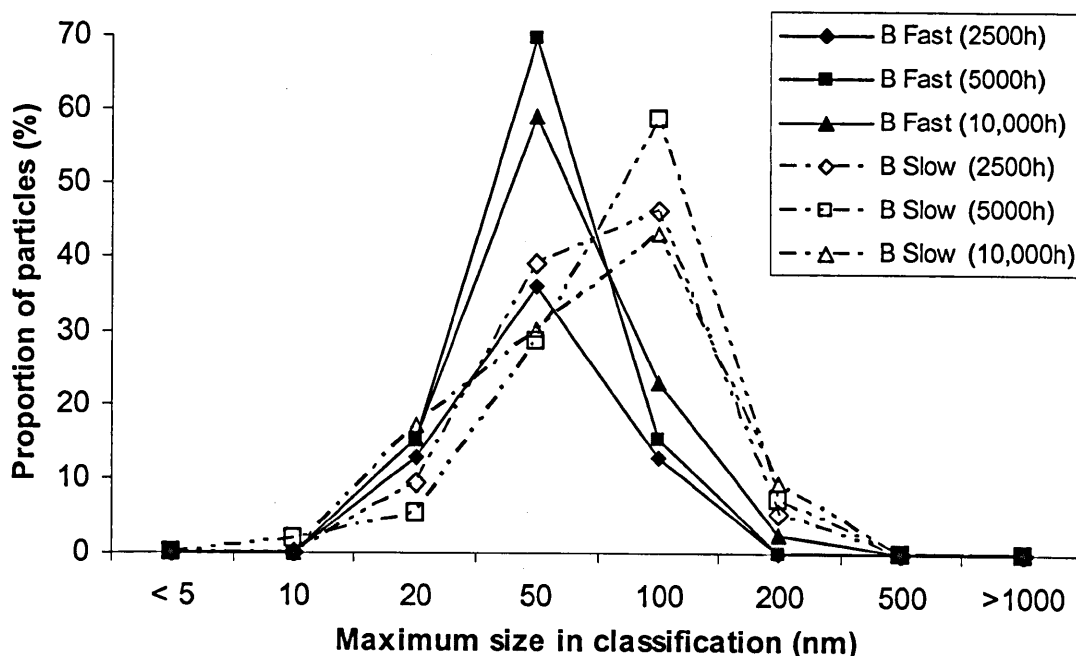


Figure 5.12: Plot showing the particle size distribution of MX in W20-3 (B) as a function of time at an aging temperature of 650°C.

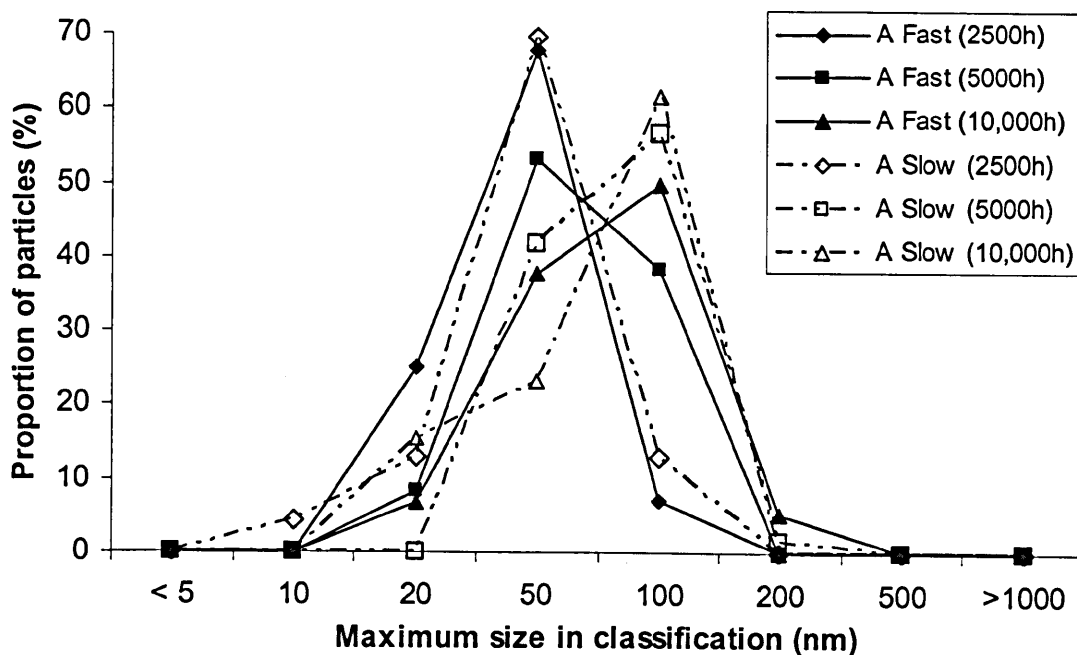


Figure 5.13: Plot showing the particle size distribution of MX in Bar 257 (A) as a function of time at an aging temperature of 650°C.

In Bar 257, a difference in particle size distribution is also observed between the different cooling rates from the normalizing temperature (Figure 5.13). In both the fast and slow cooling rates, the size distribution curve peak lies in the size range of 20 to 50 nm after aging for 2,500 hours. In the slow cooled specimen, the peak of the curve shifts to the 50 to 100 nm size range after 5,000 hours aging and remains there after 10,000 hours aging. Peak broadening is evident between these two aging times. In the fast cooled specimen, particle coarsening appears to occur at a somewhat slower rate, where the peak of the size distribution curve does not shift to the larger size range until 10,000 h aging. However, a higher fraction of relatively large MX precipitates (100 to 200 nm) is present in this specimen than at the slower cooling rate. The results from Figures 5.12 and 5.13, therefore, show that the changes in the particle size with respect to aging time occur more rapidly in the Bar 257 material than in the W20-3 material, which is consistent with the results from the chemical composition analysis of MX particles in both materials whereby changes were found to occur more rapidly in Bar 257.

5.6.2 Particle Size Distribution of $M_{23}C_6$ Precipitates

In this section, the effects of long-term aging and creep on the coarsening behaviour of grain boundary $M_{23}C_6$ precipitates are discussed. The particle size distribution of $M_{23}C_6$ precipitates was determined from SEM In-lens images, which were subsequently analyzed with the automatic image analysis software Image Pro Plus ^[116]. The methodology for particle size analysis has been described in section 4.6.1.1 (Chapter 4).

5.6.2.1 As-received Materials

Figure 5.14 compares the size distribution of $M_{23}C_6$ precipitates in Bar 257 and W20-3 in the as-received condition. It can be seen that the Bar 257 material exhibits a slightly coarser size distribution than the W20-3 material. This is attributable to various factors, such as differences in the pre-service heat treatment and carbon concentration between the two materials. Indeed, Bar 257 has a higher carbon concentration than W20-3, 0.12 and 0.09 wt.% C respectively, and had also been subjected to a longer tempering duration, 12 and 2 hours respectively. The microstructure of the as-received materials, showing the dispersion of $M_{23}C_6$ precipitates, was illustrated in Figure 4.1 (Chapter 4).

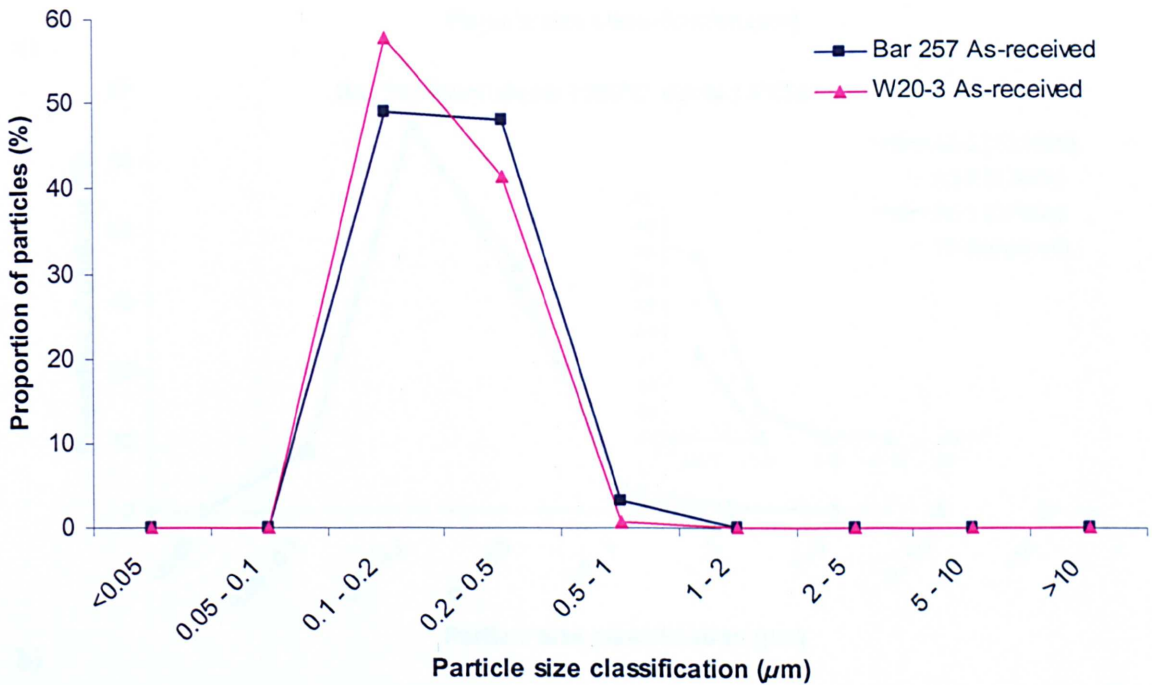


Figure 5.14: Plot of the particle size distribution (equivalent circular diameter) of $M_{23}C_6$ precipitates in the materials supplied in the as-received condition. The particles were measured from SEM In-lens images using an automatic image analysis software, whereby more than 2000 particle sizes were measured.

5.6.2.2 Long-term Aged Specimens

Figure 5.15 compares the size distribution of $M_{23}C_6$ precipitates in the Bar 257 material, which had previously been normalized at 1100°C for 15 minutes, cooled at different rates and tempered at 750°C for 2 hours, as a function of subsequent aging time at 650°C. It can be seen that there is a large increase in the $M_{23}C_6$ particle size distribution from the as-tempered condition to aging for 2,500 h. A similar scenario is observed for both fast and slow cooling rates. However, the degree of particle coarsening from 2,500 to 10,000 hours aging was somewhat greater in the fast cooled (100°Cs^{-1}) specimens.

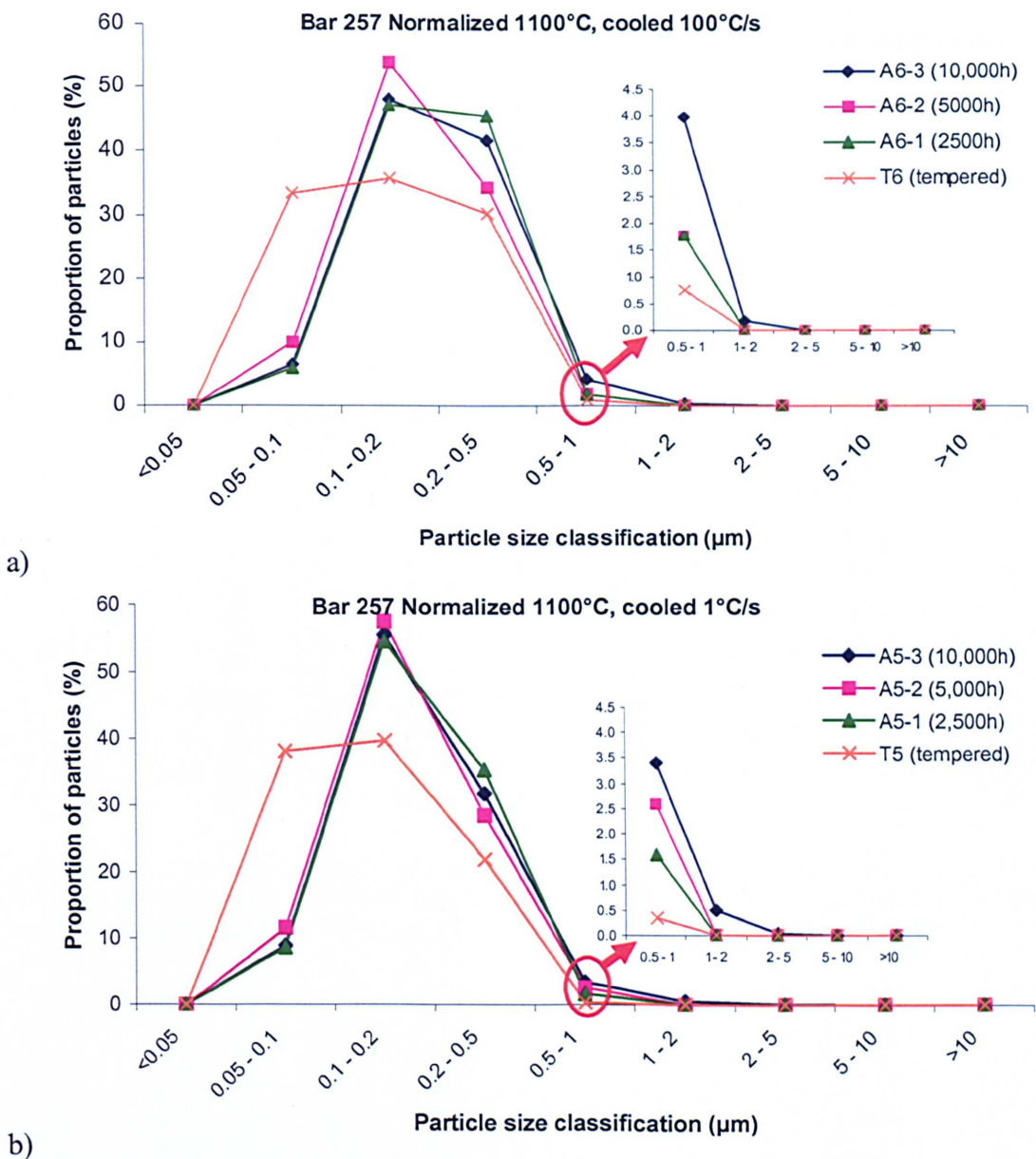


Figure 5.15: Plots showing the particle size distribution of $M_{23}C_6$ precipitates in Bar 257 specimens as a function of time at an aging temperature of 650°C. The specimens had previously been normalized at 1100°C for 15 minutes and cooled at a rate of a) 100 and b) 1°Cs^{-1} , and subsequently tempered at 750°C for 2 hours. The particles were measured from SEM In-lens images using an automatic image analysis software, whereby more than 2,000 particle sizes were measured.

Figure 5.16 compares the size distribution of $M_{23}C_6$ precipitates in the W20-3 material, which had previously been normalized at the same conditions as Bar 257. Remarkably, it can be seen that the particle size distribution remains stable from the as-tempered condition to after 10,000 h aging, as opposed to the Bar 257 material. Figures 5.17 to 5.22 show the microstructure of the Bar 257 and W20-3 specimens that were aged for varying time periods from different initial heat treatment conditions. The presence of coarse $M_{23}C_6$ carbides can be seen in all Bar 257 specimens that were aged for 10,000 hours. Figure 5.23 compares the microstructure evolution of both materials with respect to aging time.

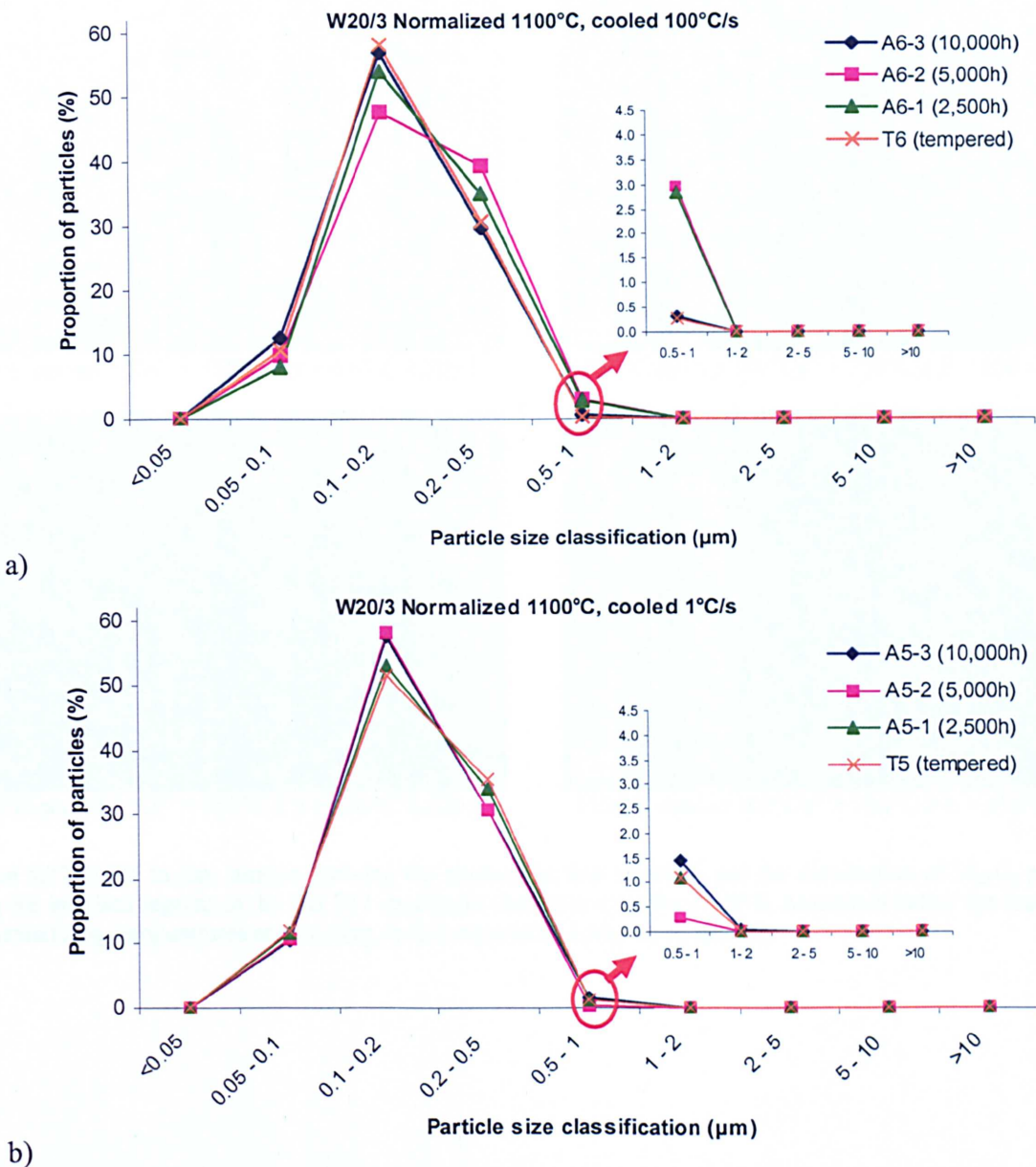


Figure 5.16: Plots showing the particle size distribution of $M_{23}C_6$ precipitates in the W20-3 specimens as a function of time at an aging temperature of 650°C. The specimens had previously been normalized at 1100°C for 15 minutes and cooled at a rate of a) 100 and b) 1°Cs⁻¹, and subsequently tempered at 750°C for 2 hours. The particles were measured from SEM In-lens images using an automatic image analysis software, whereby more than 2000 particle sizes were measured.

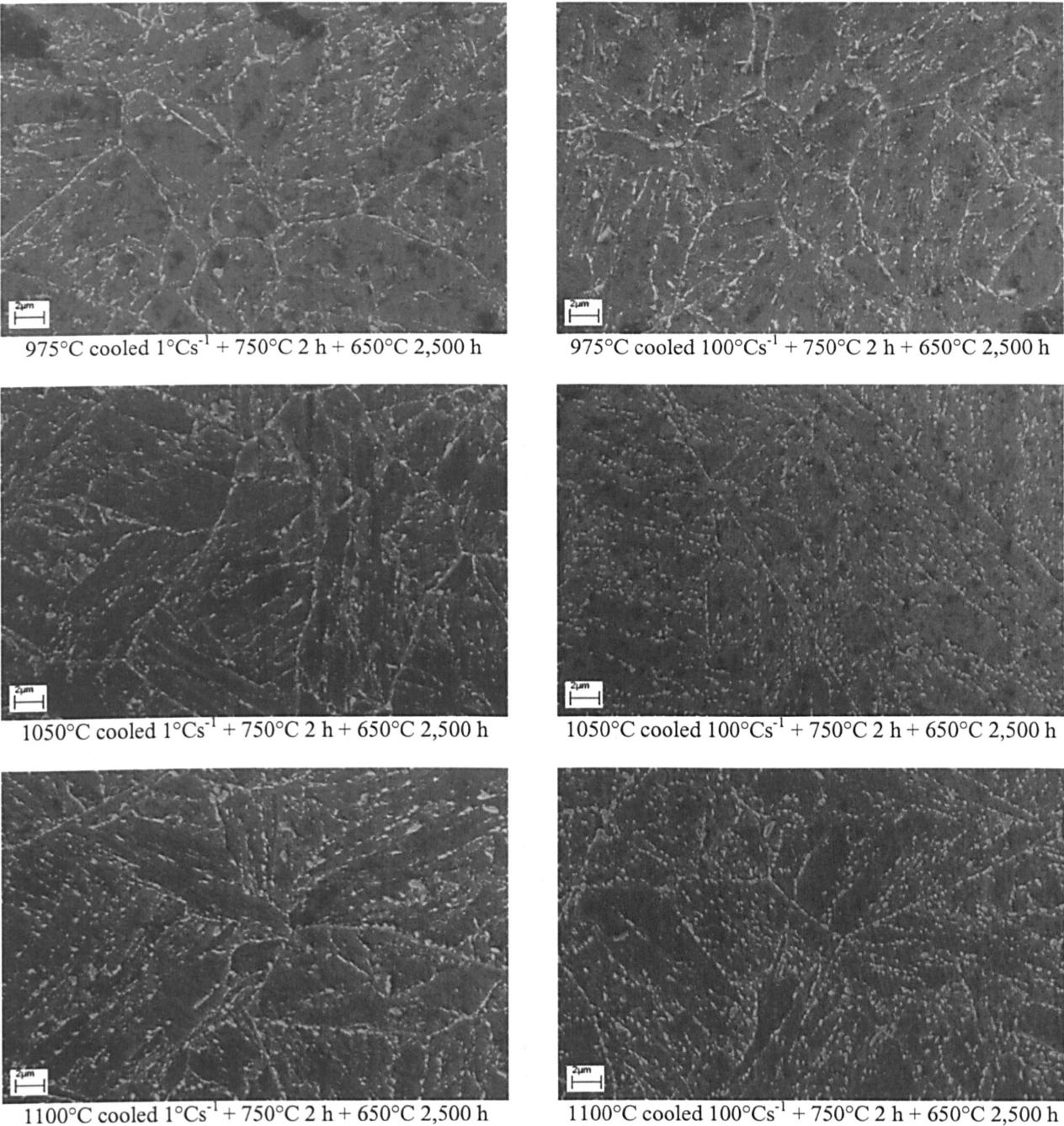
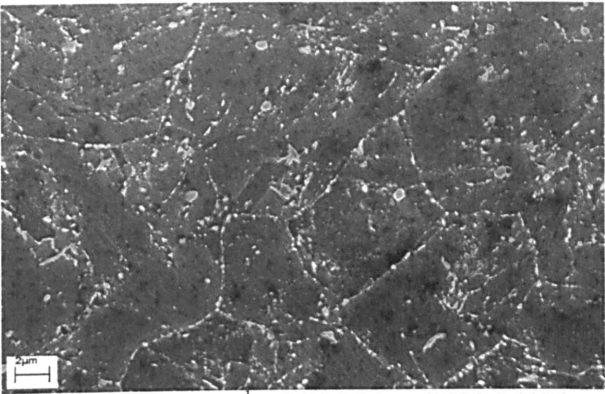
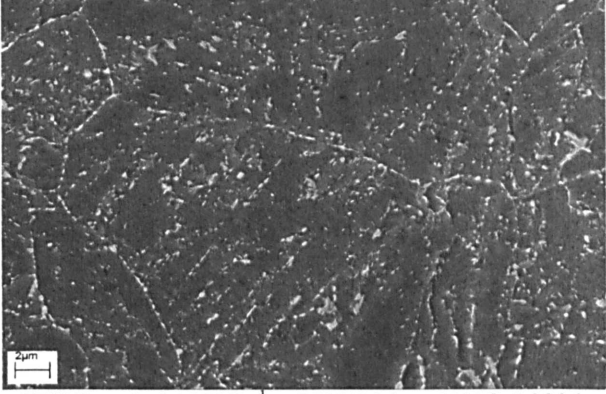


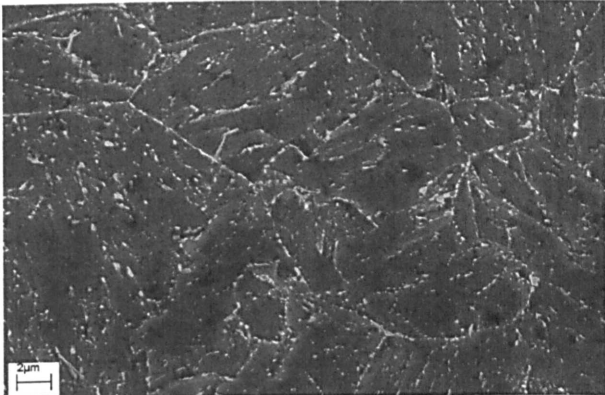
Figure 5.17: SEM In-lens images showing the martensitic lath structure and the distribution of $M_{23}C_6$ particles along the interlath regions in the Bar 257 specimens that were aged for 2,500 h. Annotated below the images are the normalizing temperatures and cooling cycles experienced prior to tempering.



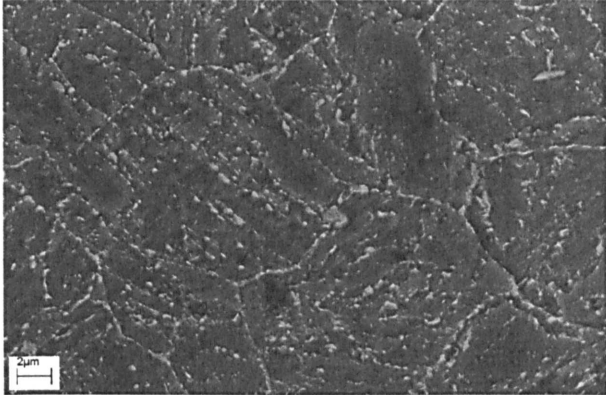
975°C cooled 1°Cs^{-1} + 750°C 2 h + 650°C 5,000 h



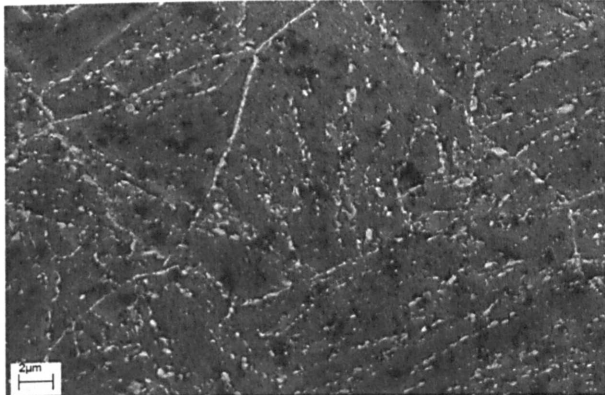
975°C cooled $100^{\circ}\text{Cs}^{-1}$ + 750°C 2 h + 650°C 5,000 h



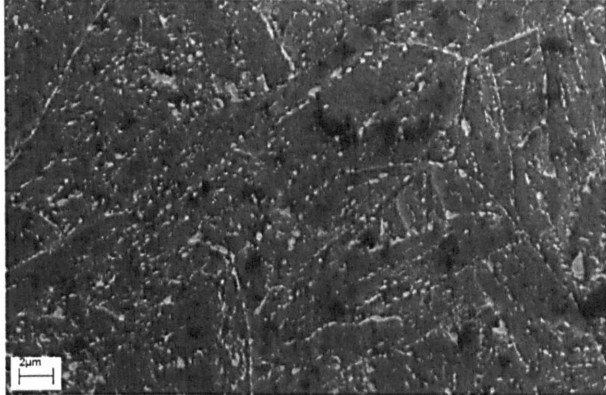
1050°C cooled 1°Cs^{-1} + 750°C 2 h + 650°C 5,000 h



1050°C cooled $100^{\circ}\text{Cs}^{-1}$ + 750°C 2 h + 650°C 5,000 h



1100°C cooled 1°Cs^{-1} + 750°C 2 h + 650°C 5,000 h



1100°C cooled $100^{\circ}\text{Cs}^{-1}$ + 750°C 2 h + 650°C 5,000 h

Figure 5.18: SEM In-lens images showing the martensitic lath structure and the distribution of M_{23}C_6 particles along the interlath regions in the Bar 257 specimens that were aged for 5,000 h. Annotated below the images are the normalizing temperatures and cooling cycles experienced prior to tempering.

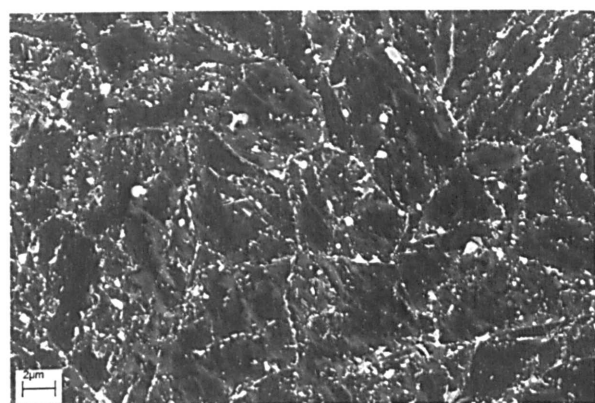
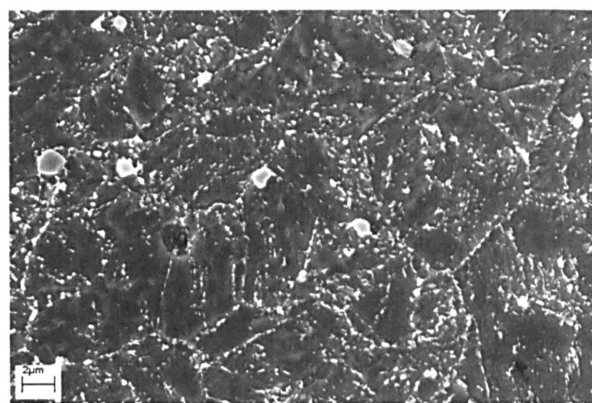
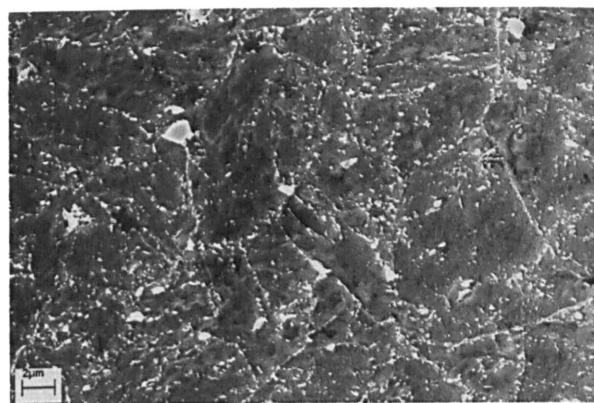
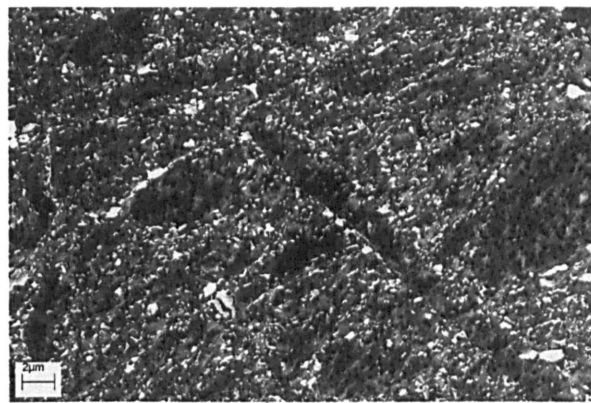
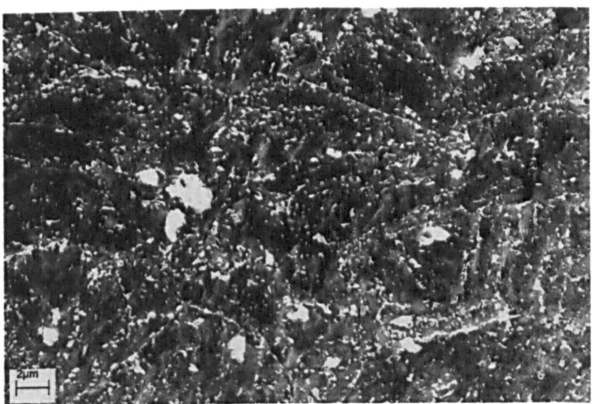
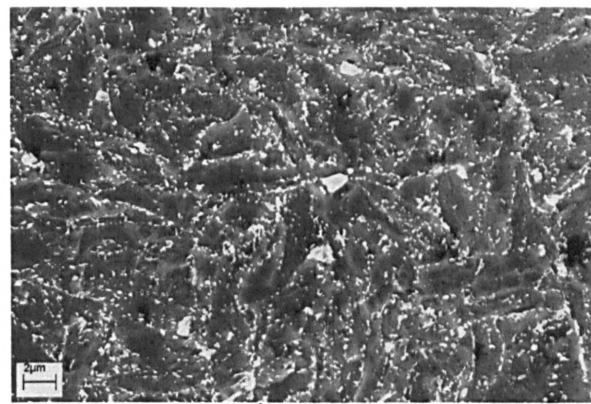
975°C cooled 1°Cs⁻¹ + 750°C 2 h + 650°C 10,000 h975°C cooled 100°Cs⁻¹ + 750°C 2 h + 650°C 10,000 h1050°C cooled 1°Cs⁻¹ + 750°C 2 h + 650°C 10,000 h1050°C cooled 100°Cs⁻¹ + 750°C 2 h + 650°C 10,000 h1100°C cooled 1°Cs⁻¹ + 750°C 2 h + 650°C 10,000 h1100°C cooled 100°Cs⁻¹ + 750°C 2 h + 650°C 10,000 h

Figure 5.19: SEM In-lens images showing the martensitic lath structure and the distribution of $M_{23}C_6$ particles along the interlath regions in the Bar 257 specimens that were aged for 10,000 h. Annotated below the images are the normalizing temperatures and cooling cycles experienced prior to tempering.

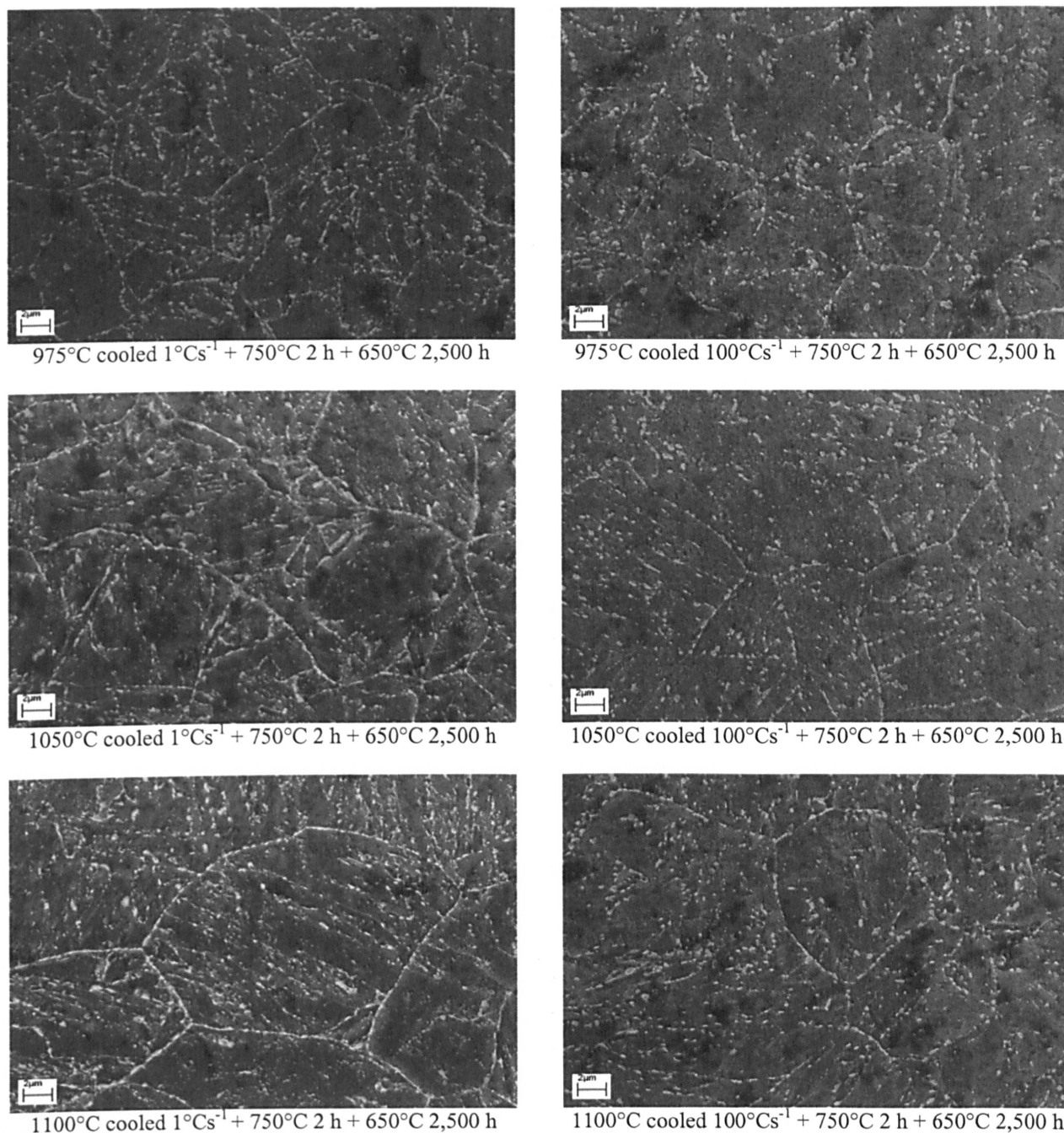


Figure 5.20: SEM In-lens images showing the martensitic lath structure and the distribution of M_{23}C_6 particles along the interlath regions in the W20-3 specimens that were aged for 2,500 h. Annotated below the images are the normalizing temperatures and cooling cycles experienced prior to tempering.

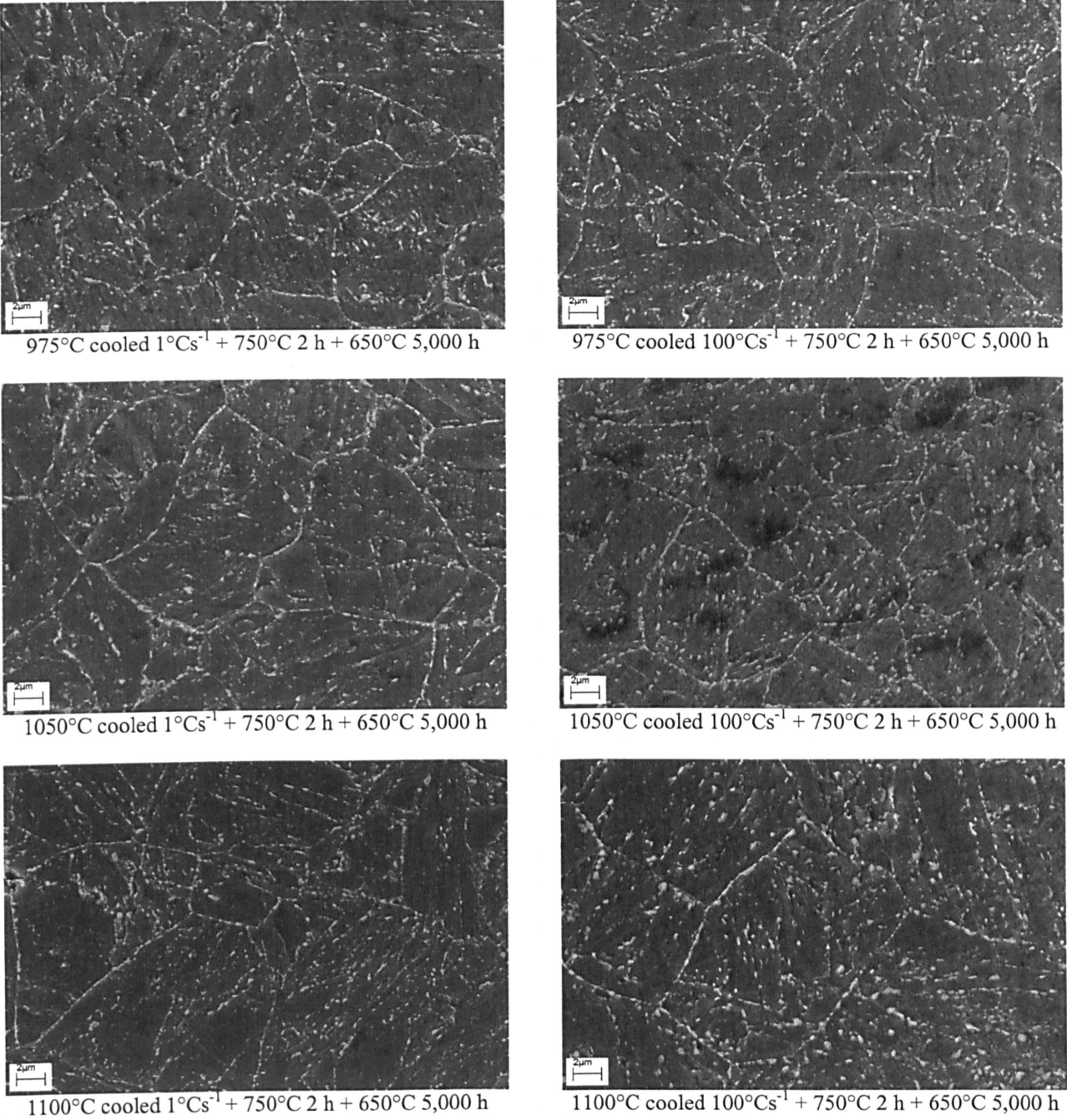
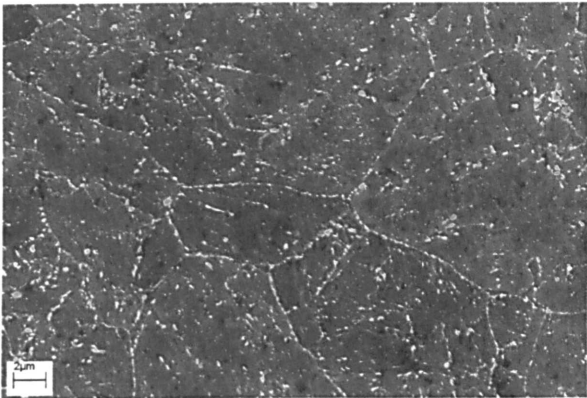
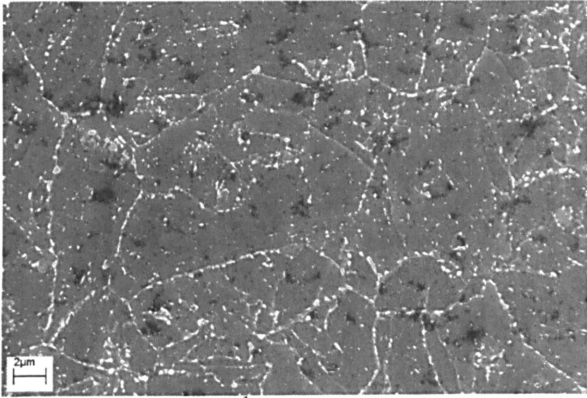


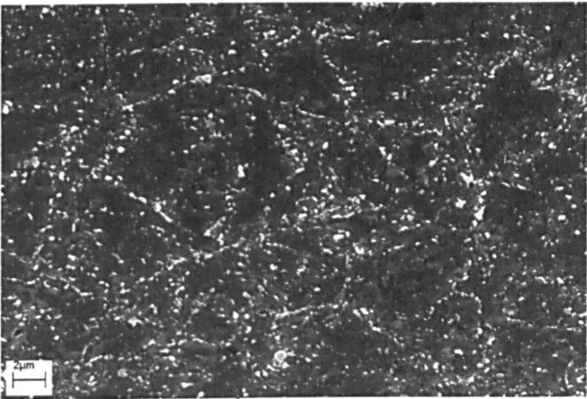
Figure 5.21: SEM In-lens images showing the martensitic lath structure and the distribution of M_{23}C_6 particles along the interlath regions in the W20-3 specimens that were aged for 5,000 h. Annotated below the images are the normalizing temperatures and cooling cycles experienced prior to tempering.



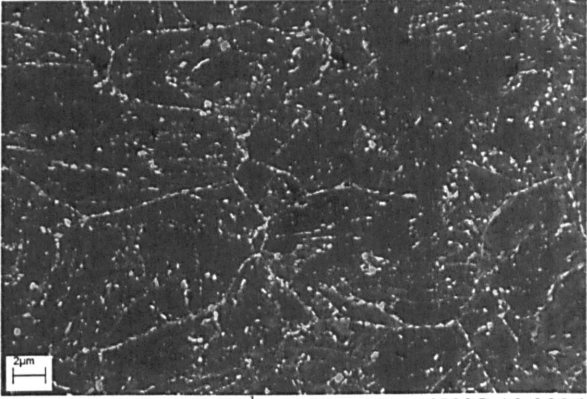
975°C cooled 1°Cs^{-1} + 750°C 2 h + 650°C 10,000 h



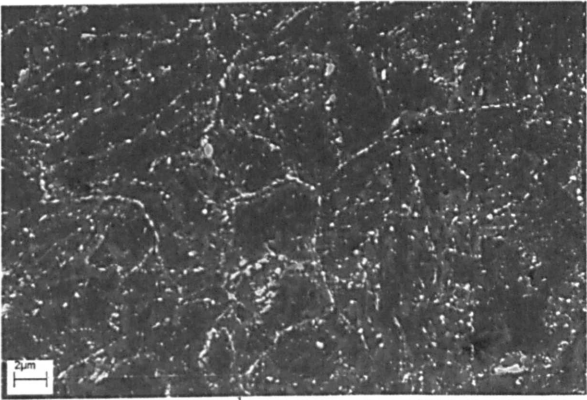
975°C cooled $100^{\circ}\text{Cs}^{-1}$ + 750°C 2 h + 650°C 10,000 h



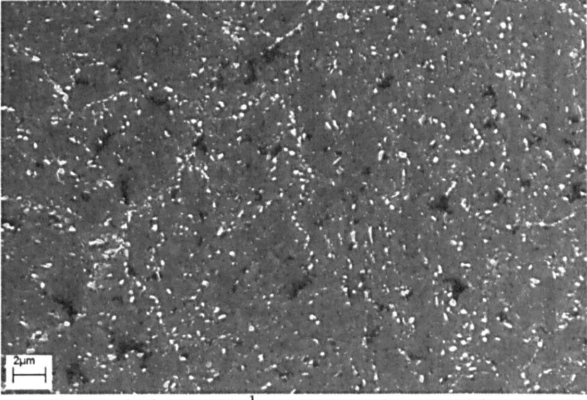
1050°C cooled 1°Cs^{-1} + 750°C 2 h + 650°C 10,000 h



1050°C cooled $100^{\circ}\text{Cs}^{-1}$ + 750°C 2 h + 650°C 10,000 h



1100°C cooled 1°Cs^{-1} + 750°C 2 h + 650°C 10,000 h



1100°C cooled $100^{\circ}\text{Cs}^{-1}$ + 750°C 2 h + 650°C 10,000 h

Figure 5.22: SEM In-lens images showing the martensitic lath structure and the distribution of M_{23}C_6 particles along the interlath regions in the W20-3 specimens that were aged for 10,000 h. Annotated below the images are the normalizing temperatures and cooling cycles experienced prior to tempering.

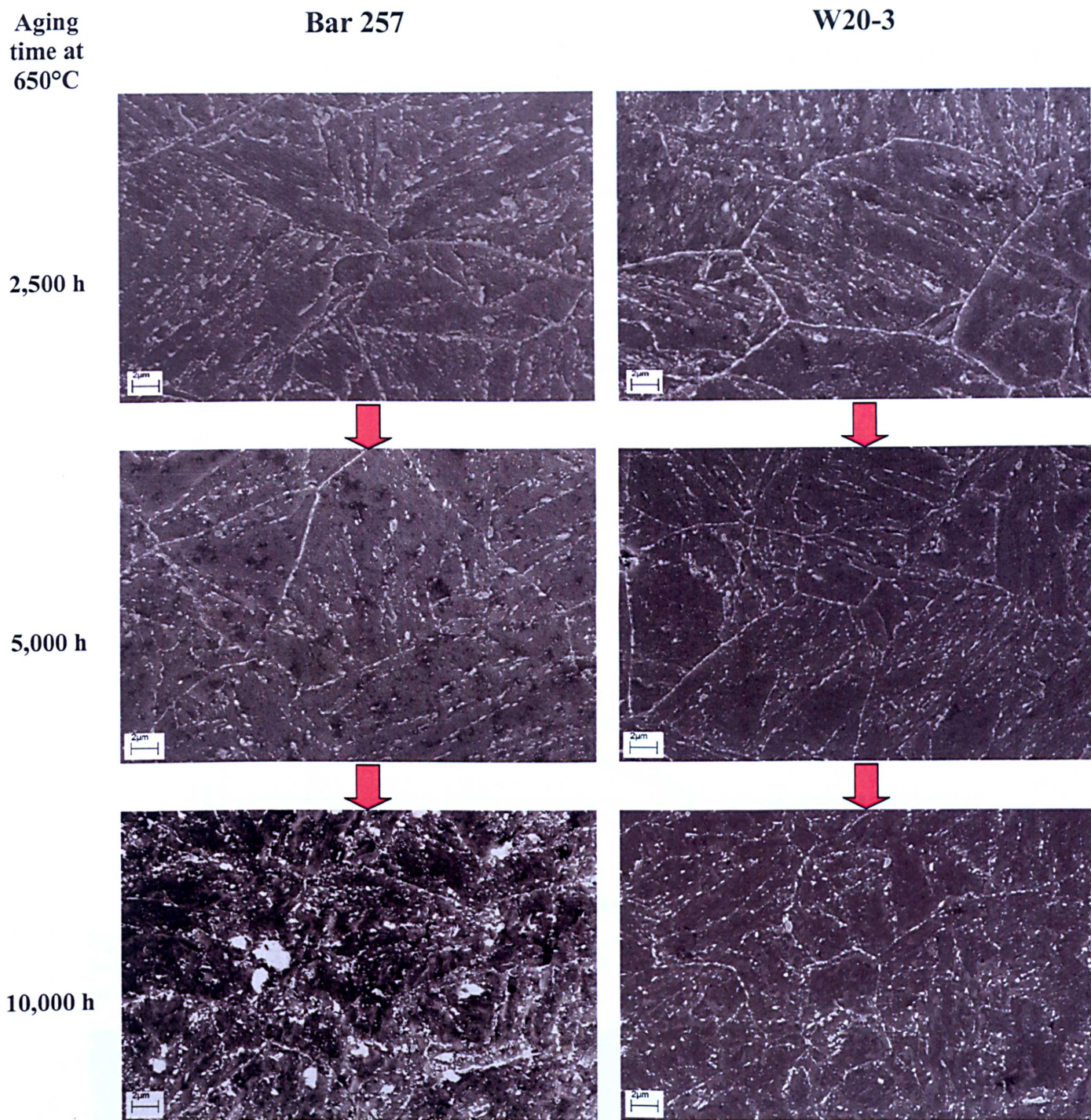


Figure 5.23: SEM In-lens images comparing the size distribution of the Bar 257 and W20-3 materials with respect to aging time, up to 10,000 h, at 650°C. Both materials had previously undergone a heat treatment that consisted of normalizing at 1100°C for 15 minutes and cooled to room temperature at a rate of 1°Cs⁻¹, and they were subsequently tempered at 750°C for 2 h.

5.6.2.3 Creep Specimens

Figure 5.24 shows the particle size distribution of Bar 257 creep specimens, taken from the gauge (stressed) section, that have experienced different applied stresses. It can be seen that there is a systematic increase in particle coarsening with a decrease in applied stress, which can be explained by the fact that at the lower stress (60 MPa) the time to rupture was considerably greater than at the highest stress (93 MPa), 2,217 and 82 hours respectively. Therefore, coarsening can be explained by increased time at temperature. SEM images of Bar 257 creep specimens qualitatively illustrate this effect in Figure 5.25. The creep specimens exhibited a much coarser particle size distribution than the long-term aged specimens.

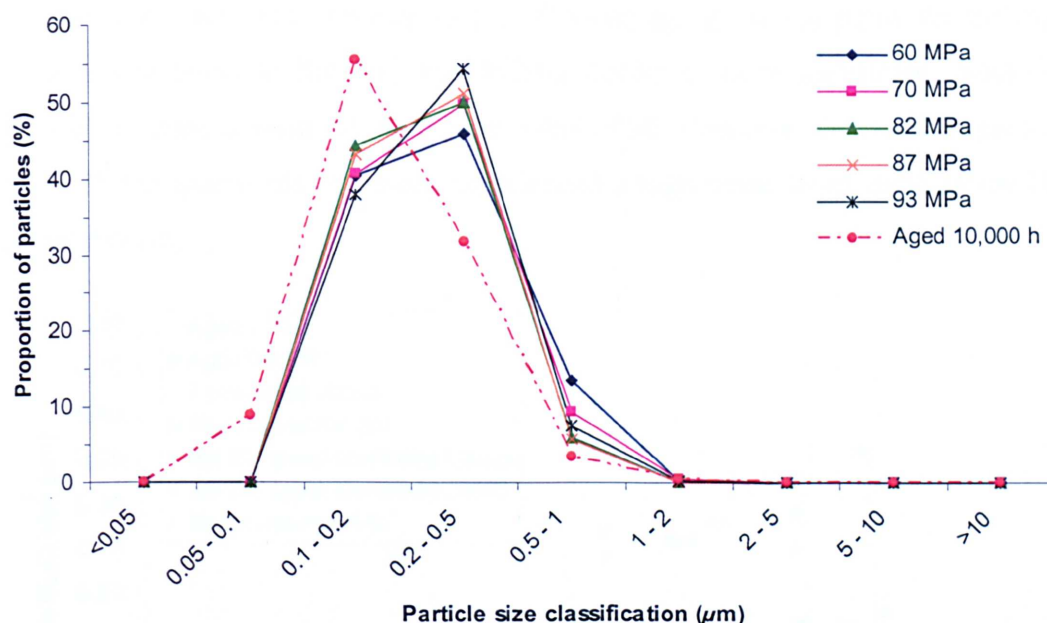


Figure 5.24: The particle size distribution of $M_{23}C_6$ precipitates in Bar 257 creep specimens subjected to various loading conditions at 650°C. For comparison, the size distribution curve of the coarsest long-term isothermally aged Bar 257 specimen (10,000 h at 650°C) is also shown.

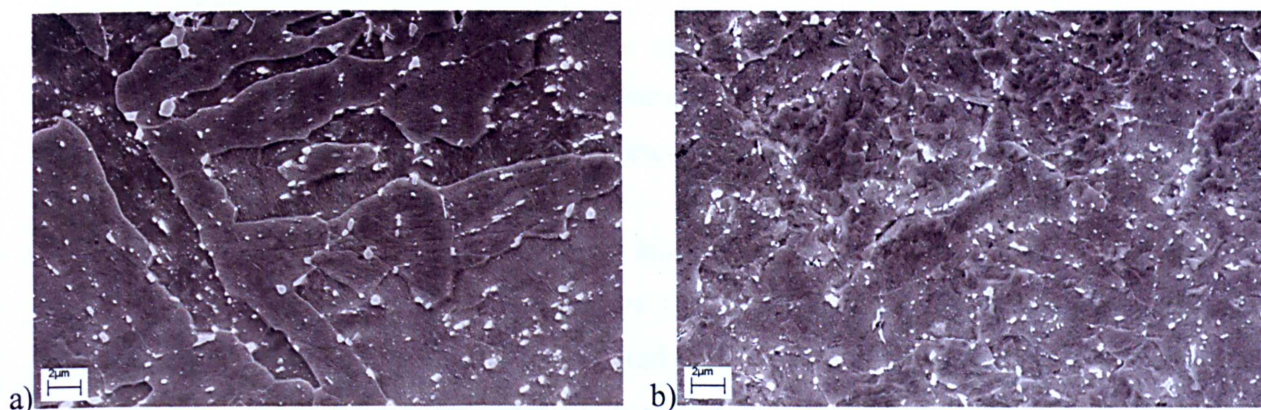


Figure 5.25: SEM In-lens images showing the microstructure of Bar 257 creep specimens that were subjected to creep stresses of a) 60 MPa and b) 93 MPa. The final test durations, determined as the time to failure, of a) and b) were 2,217 and 82 hours respectively. The temperature at which the creep test was performed was 650°C.

It is evident that the particle size distributions of the creep specimens are significantly coarser than the isothermally aged specimens, even though the latter have experienced considerably longer times at temperature. This indicates that strain accelerates the particle coarsening process. However, the stress levels experienced by the creep specimens are considerably higher than those which a component might experience during typical service operating conditions.

5.6.2.4 Comparison of $M_{23}C_6$ Particle Size

Figure 5.26 compares the mean $M_{23}C_6$ particle size as a function Larson-Miller^[60] parameter for all of the investigated P91 specimens. It can be seen that the mean particle size of long-term aged specimens remains stable up to 10,000 hours aging. At this point, the difference in mean particle size between Bar 257 and W20-3 becomes more significant. Note that the Larson-Miller constant is assigned the typical value of 20. However, this value expected to be greater than 20 for specimens that have experienced a high stress level, such as the Bar 257 creep test specimens.

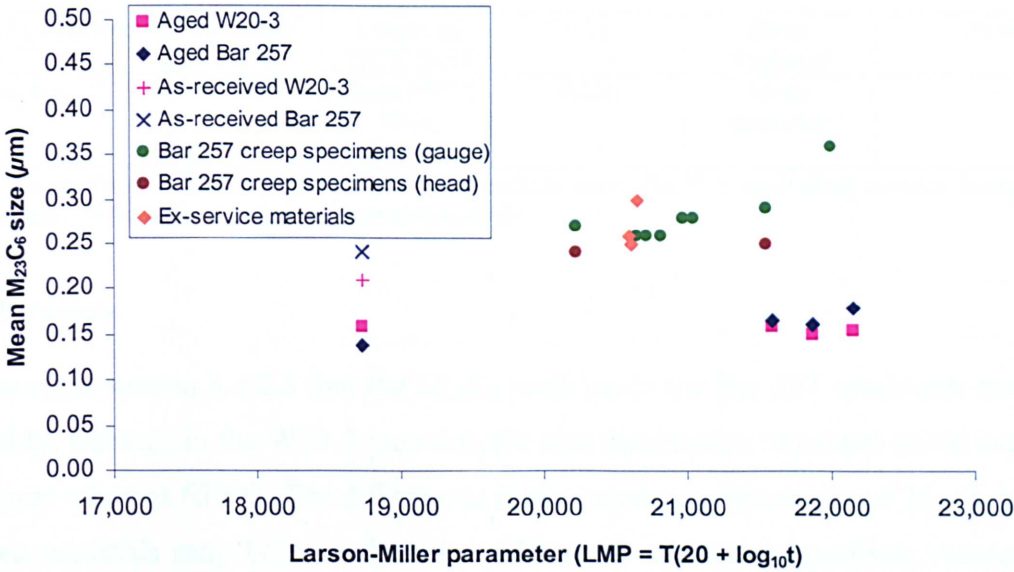


Figure 5.26: Plot comparing mean $M_{23}C_6$ size as a function of Larson-Miller parameter for various investigated P91 materials.

Table 5.1 compares values of $M_{23}C_6$ particle sizes obtained in this study with a selection of values from the existing literature. It is evident that the different values presented agree well with each other. However, it must be considered that the number of measurements performed in this study is often at least an order of magnitude greater than those reported. This may significantly affect results of creep life prediction when inputting values into appropriate formulae. Caution must be exercised when interpreting particle size data from images as the

presence of a very large particle will increase the mean value. The great advantage of this technique is that it can measure various particle parameters, thus making it a versatile analytical tool.

Authors	Material	Condition	Dimensions (μm)	Parameter Measured	No. of Measurements
Sanchez-Hanton	P91	Aged 650°C 2 - 10,000 h	0.151-0.176	ECD	>2,000
Sanchez-Hanton	P91	Crept 650°C 60-93 MPa	0.25-0.35	ECD	>2,000
Saroja, Vijayalakshmi & Raghunathan ^[128]	9Cr-1Mo	Aged 650°C 2,000h	0.150	Mean diameter	-
Jones, Hills & Polonis ^[27]	P91	Tempered 760°C 1h	0.25-0.5	Mean diameter	-
Eggeler ^[31]	12CrMoV	Crept 600°C 109,380h 62MPa	0.15-0.24	Max. and min. diameter	46
Gustafson & Andren ^[129]	P92	Aged 650°C 26,000h	0.153	ECD*	114
Hattestrand & Andren ^[72]	P92	Crept 650°C 10,000 h	0.150	ECD*	-
Wu & Sandtrom ^[120]	12CrMoV	Aged 620°C 2,000h	0.215	ECD	~100
Bjarbo & Hattestrand ^[130]	12CrMoV NbW	Tempered 750°C 5min	0.22	Mean diameter	30-60
Nakajima et al ^[131]	T91	Crept 650°C 738h, 85MPa	0.156	Mean diameter	-

Table 5.1: Comparison of literature values of M_{23}C_6 particle sizes. (ECD = equivalent circular diameter, * = corrected values, - = number of measurements unspecified).

5.6.2.5 Discussion

It was shown in section 5.6.2.3 that the M_{23}C_6 particles in the Bar 257 specimens coarsened considerably, whereas in the W20-3 material, the size distribution remained stable even after 10,000 hours aging at 650°C. The differences in the coarsening behaviour of M_{23}C_6 particles in the two materials may be related to the differences in cast composition. According to Marshall^[132] who investigated austenitic power plant steels, N retards both the formation and coarsening rates of M_{23}C_6 because N reduces the diffusivity of Cr and C in austenite. Indeed, the N content is much higher in the W20-3 material. Thermodynamic calculations also showed that the amount of N available in solution in ferrite is higher in W20-3 than in Bar 257 when all the phases are in equilibrium. In addition, it was also found that the amount of Ni is higher in Bar 257, which may be relevant to particle size distribution differences, as Ni is believed to increase the coarsening rate of M_{23}C_6 in high Cr ferritic-martensitic steels^[22,52]. The chemical composition of M_{23}C_6 precipitates was not investigated in the present study; as

previous workers have established that precipitation kinetics of $M_{23}C_6$ occur very rapidly in these materials, due to the high Cr content in the class of alloys of interest and, therefore, any composition changes are likely to be small throughout the service life.

The accelerated coarsening of $M_{23}C_6$ precipitates produced in the Bar 257 material that had been cooled at the fastest rate from the previous normalizing heat treatment can be correlated with the matrix microstructure. Indeed, Mukherjee *et al* ^[133] found that in the martensitic structure, which contains both a fine grain size and a fine dislocation substructure, a considerable increase in carbide coarsening rate was produced compared to a ferrite matrix. The martensite lath width was shown to vary considerably with changes in cooling rate in Chapter 4, where a decrease in the mean lath width corresponded to increased cooling rates from the normalizing temperature. From this hypothesis, grain boundary carbide coarsening can be expected to occur more rapidly in the fast cooled specimens, as a finer microstructure gives rise to an increase in the number of fast diffusion paths, i.e. a higher pipe diffusion flux. However, this trend is not evident in the W20-3 material, which possessed the smallest mean lath and prior austenite grain size values. Therefore, coarsening of $M_{23}C_6$ precipitates is more likely to be influenced by the recovery of the microstructure upon aging, rather than by initial microstructure.

5.6.3 Particle Size Distribution of AlN and Laves Phase

Quantification of AlN and Laves phase precipitates was performed using SEM operated in backscattered electron mode, in a manner similar to Korcakova *et al* ^[117] and Dimmler *et al* ^[56]. AlN precipitates were found in all investigated grade 91 materials with the exception of W20-3. Laves phase particles, on the other hand, were only found in the ex-service materials, Tee-piece and Bottle 2. These were also found in the microstructure of the ex-service U2B2 material, albeit in a very small quantity, which made accurate measurement difficult. Figure 5.27 shows a series of backscattered electron SEM images of various grade 91 specimens. Laves phase precipitates are shown as large bright precipitates in the microstructures of the Tee-piece and Bottle 2 materials, whereas AlN can be identified as dark needle-shaped features in all the investigated materials, with the exception of W20-3.

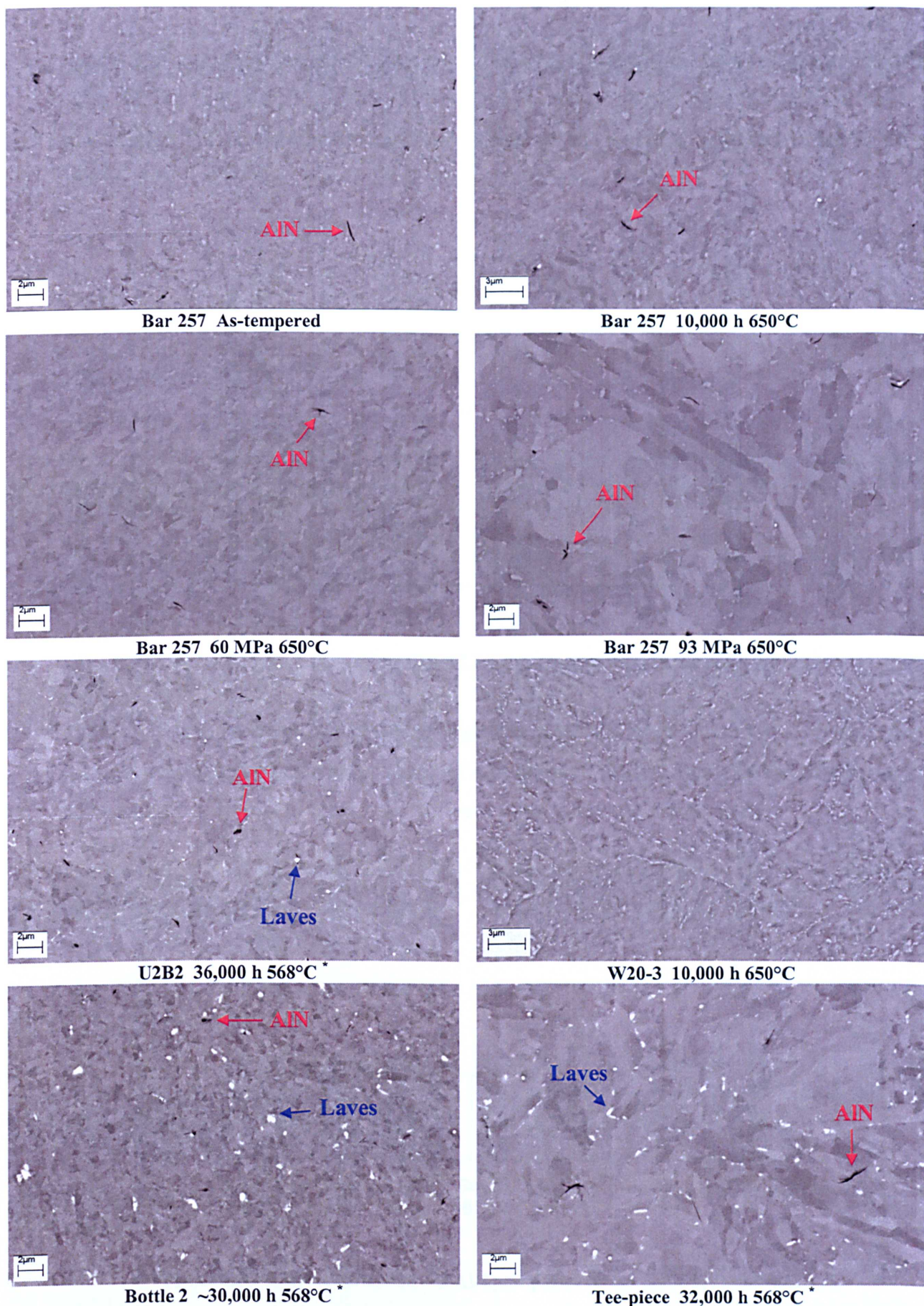


Figure 5.27: Backscattered electron SEM images of various grade 91 materials investigated in this study. Annotated below the images are material, aging temperature and time. The dark particles correspond to AlN precipitates, whereas the bright white particles have been identified as Laves Phase, the latter where only found in ex-service materials (*).

Figure 5.28 compares the mean size of Laves phase precipitates, measured automatically using the Image Pro + programme ^[116], in the ex-service Tee-piece and Bottle 2 materials. It can be seen that the mean size is slightly larger in the Bottle 2 material, which failed in service, than in the Tee-piece material, which was sampled in service.

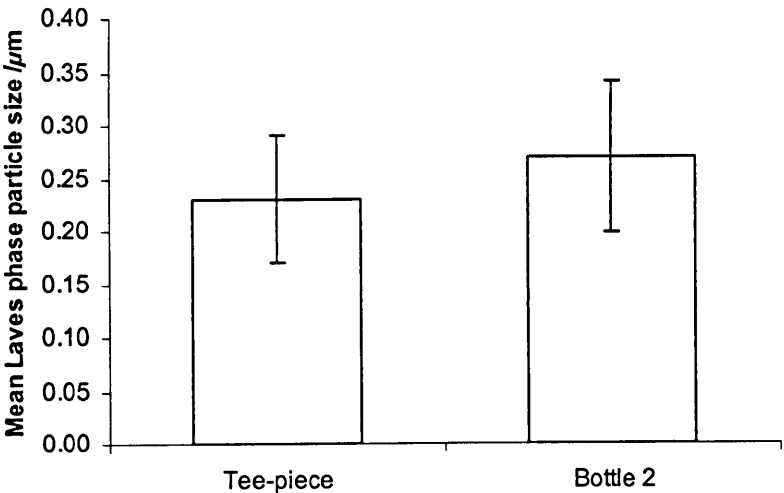


Figure 5.28: Average particle size of Laves phase precipitates in ex-service materials.

Figure 5.29 compares the size of AlN precipitates in several investigated P91 steel specimens. It can be seen that the mean particle size of AlN needles does not vary significantly in the Bar 257 specimens that have experienced different aging and creep conditions.

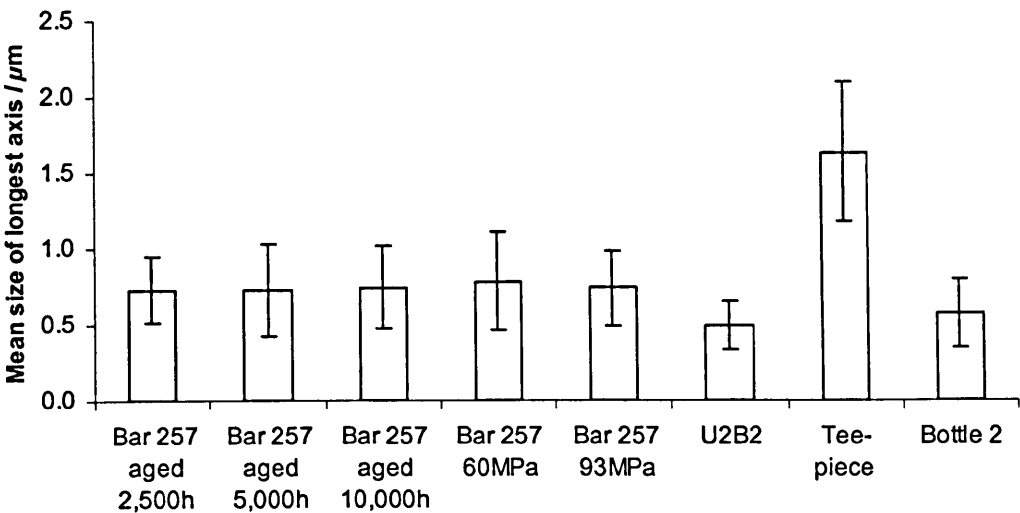


Figure 5.29: Average particle size of AlN precipitates in various investigated materials.

The fact that the AlN particle size does not vary much is indicative of several key concepts. Firstly, it appears that renormalizing at 1100°C has not altered the AlN precipitate size from the as-received condition, hence the size of these particles in the crept condition (from the as-received condition) are similar to the renormalized and aged specimens. Secondly, the fact that the sizes of the AlN particles effectively remain the same after prolonged aging at 650°C is indicative of the lack of additional precipitation and particle coarsening processes of AlN occurring in this material. And finally, it is evident that under accelerated creep conditions of considerably higher applied stresses to those typically experienced in service, the effects of particle coarsening are not evident, thus the AlN particle size appears to be relatively insensitive to the effects of strain accelerated coarsening.

5.7 Summary

It was shown in this investigation that the relative amounts of the three metallic elements (V, Nb and Cr) in MX precipitates in high Cr power plant steels are a function of both the pre-service heat treatment and aging time. The main observed change was the gradual partitioning of the composition of MX precipitates from a linear composition distribution of V and Nb in MX into two distinct particle compositions, VN and NbC, with increasing aging times. In addition, the mean Cr concentration in MX was found to gradually decrease with an increase in high temperature exposure. Intuitively, such changes are anticipated to occur rather slowly due to the slow diffusivity in highly ordered carbide and nitride structures. Interestingly, the change in chemical composition of MX occurred somewhat more rapidly in a known weak cast in comparison to a conventional P91 steel cast. Therefore, the chemical composition variation of MX may be used to monitor the condition of power plant components, and thus be used to make an informed judgement on the remanent lifetime of critical plant components. In addition, it was suggested that the presence of AlN particles in these steels disrupts the stability of MX precipitates, as coarsening and two-phase separation appear to accelerate in high Al containing ferritic-martensitic steels.

The coarsening of $M_{23}C_6$ precipitates with increased aging times appeared to occur at an accelerated rate in the weak Bar 257 cast in comparison to the more conventional W20-3 P91 cast, which was shown to exhibit a more stable particle size distribution. This is indicative that the weakening of Bar 257 is not solely attributed to variations in MX particle identity. The size and volume fraction of AlN particles were found to be insensitive to varying heat treatment, aging and creep conditions.

The following chapter is a continuation on the theme of microstructural evolution, in which the changes in the matrix structure of grade 91 steel, under the same aging and creep conditions as the samples examined in this chapter, have been investigated.

Chapter 6

EFFECTS OF LONG-TERM AGING AND CREEP ON THE MATRIX MICROSTRUCTURE

6.1 Introduction

The previous chapter has illustrated the importance of minor phase precipitates on the creep strength of grade 91 steel. The effects of initial heat treatment, long term aging and creep on the chemical composition and size of these precipitates were discussed.

In addition to the important role of minor phase precipitation, the creep behaviour of ferritic-martensitic power plant steel is also very much dependent on the matrix microstructure. It was evident from the literature review in Chapter 2 that the matrix microstructure of ferritic-martensitic steels undergoes considerable changes with respect to aging time and simulated creep conditions. Therefore, in order to fully understand how the matrix microstructure evolves, it is necessary to monitor and quantify the changes that occur initially in samples with known thermal histories. Investigations have, therefore, been undertaken to compare the matrix microstructure development of grade 91 steel specimens with contrasting creep behaviour. Two such methods may rely on the use of electron backscatter diffraction (EBSD) in the scanning electron microscope and X-ray diffraction line profile analysis.

In this chapter, an attempt is made to quantify changes in the matrix microstructure, in specimens with different precipitation behaviour, under varying thermal aging and creep loading conditions. This is a non-trivial task, because many parameters, all of which influence the creep properties of P91 steel, must be accounted for, thus, two main areas of investigation are presented. Firstly, the grain and subgrain structure of grade 91 steel has been extensively characterised with the use of electron backscatter diffraction in the scanning electron microscope. This entailed the quantification of various microstructure parameters, in particular the grain boundary misorientation angles, the total boundary line length and subgrain size distribution. Secondly, X-ray diffraction line profile analysis has been carried out in an attempt to quantify changes in the dislocation density under the same conditions. Transmission electron

microscopy on thin-foil specimens was used to verify results from EBSD and XRD where necessary.

6.2 EBSD for the Assessment of Material Microstructure

The martensitic microstructure of grade 91 steel is very important for the creep strength of power plant components. The microstructure is very fine with a high dislocation density, which makes it very effective at inhibiting dislocation motion at typical operating stresses. However, martensite is a non-equilibrium phase and prolonged exposure to high temperatures will eventually lead to progressive recovery of the microstructure, whereby damage is induced by softening or deterioration of mechanical properties, most notably creep strength and hardness.

It is important to consider the effects of long-term high temperature exposure on the recovery of the matrix microstructure and attempt to quantify such changes in order to inform models that determine creep life. The main experimental technique employed in this section is electron backscatter diffraction (EBSD), which is ideally suited to this investigation as it can provide good grain orientation data from reasonable sampling areas, which is an important prerequisite for any quantitative study.

With EBSD, several parameters may be scrutinised in an attempt to quantify microstructural change. For example, the number fraction of boundaries with a specific misorientation angle can be quantified using this technique. Jazaeri and Humphreys^[134] showed that monitoring the high-angle grain boundary content of Al alloys is a reliable and rapid method of quantifying recrystallization. Another method of determining the degree of recrystallization using the EBSD technique was proposed by Tarasiuk *et al*^[135], who discussed that the image quality index can be considered to be linked to the work hardening state of materials. This latter method is based on the premise that surface preparation can be considered the same for all investigated regions and also that there is only one main process which is responsible for the changes of the quality index. However, in the case of high Cr power plant steels there are potentially many microstructural features which may affect image quality. These include differences in dislocation density, the formation of fine scale dislocation structures, and changes in lattice parameter as a result of the diffusion of interstitial and solute atoms from the matrix to second phase particles, to name the most important. In addition, these results may also be affected by other external variables that can easily be resolved, such as scratches and contamination.

Another example whereby EBSD has been shown to yield useful data was proposed by Wilson and Spanos ^[136], who presented a few examples where image (pattern) quality maps of steel samples were better than conventional secondary electron SEM images at resolving grain boundaries. Indeed, one of the current limitations of the EBSD technique is the angular precision that can be obtained, which means that grains with a boundary misorientation of less than 2° are very difficult to characterize accurately, hence certain features may be indistinguishable in boundary plots. Therefore, image quality maps can yield useful data because small dislocation structures will result in poor indexing of a region, and will thus appear as a feature on the map.

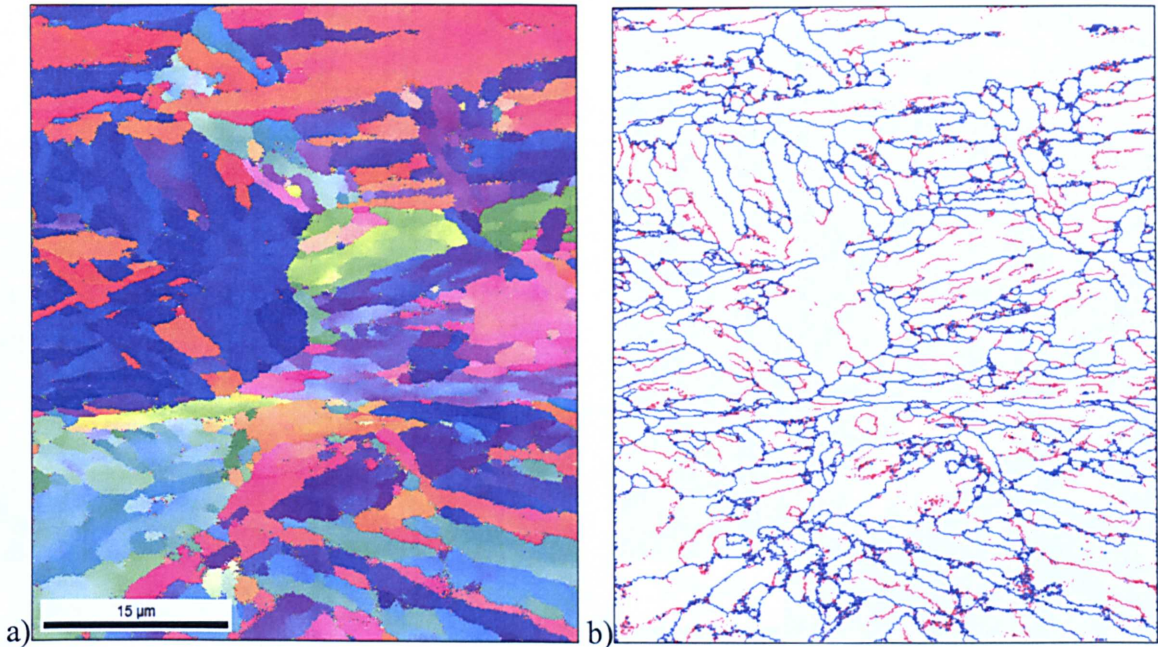
EBSD information may also be supplemented by energy dispersive X-ray spectroscopy (EDS) data, which can be collected simultaneously. This allows the user to qualitatively identify the presence of secondary phases with compositions different from the matrix. At this stage however, it must be taken into consideration that the spatial resolution of the EDS is lower than EBSD, especially when investigating low atomic number elements, thus there is little hope of identifying small submicron MX precipitates using this technique at present. In this investigation, therefore, the microscope settings were optimised for obtaining EBSD data.

The data obtained from EBSD experiments is very sensitive to a wide range of parameters associated with specimen preparation, microscope settings and data analysis. Therefore, great effort was used in this investigation to keep such parameters the same. The methods of specimen preparation, data acquisition and analysis are described in detail in Chapter 3.

6.2.1 The Microstructure of As-received P91 Steel

All of the investigated materials exhibited a characteristic tempered martensite microstructure in addition to a dispersion of intergranular and interlath $M_{23}C_6$ precipitates, and small intralath (V,Nb)(N,C) carbonitride precipitates, which has been discussed in the previous chapters. The Bar 257 material, which has been shown to exhibit a larger grain size in comparison to W20-3, is also shown to have a larger grain size with the use of EBSD (Figure 6.1). A typical tempered martensite lath microstructure is illustrated in the inverse pole figure maps shown in Figure 6.1b) and d). Figure 6.2 shows thin-foil TEM micrographs of the same materials, which confirm the presence of tempered martensite laths, in which a high density of dislocations can be seen in the intralath regions.

Bar 257



W20-3

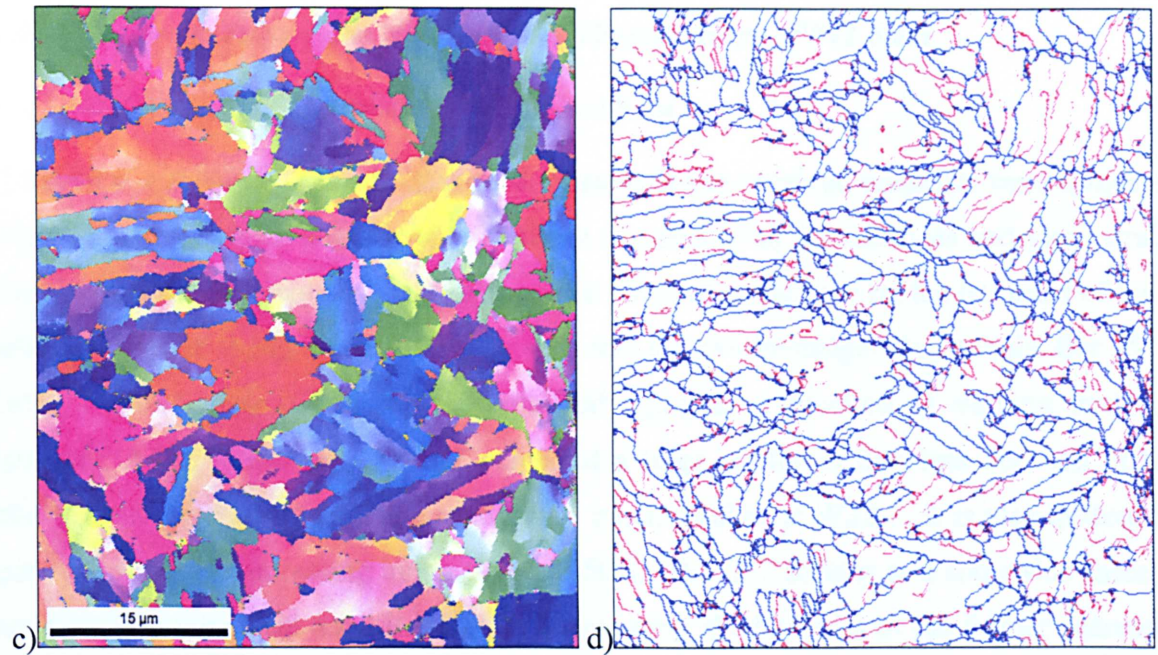


Figure 6.1: Inverse pole figure maps a) and c), and boundary angle maps b) and d) illustrating the microstructure of the Bar 257 and W20-3 materials in the as-received (pre-service) condition, respectively. The unit triangle shows the crystallographic poles aligned with the specimen surface normal direction.

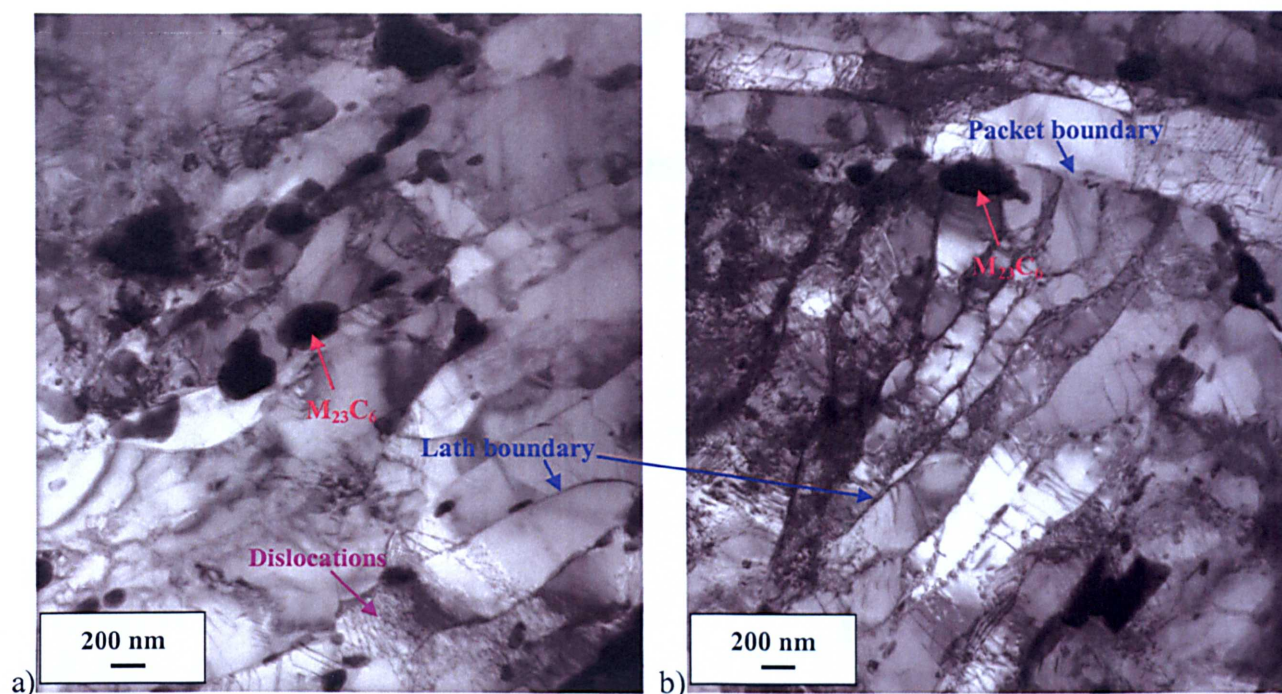


Figure 6.2: Thin foil TEM micrographs of the lath structure of a) the Bar 257 and b) the W20-3 materials in the as-received condition.

6.2.2 The Effect of Long-Term Aging on the Microstructure of P91 Steel

6.2.2.1 The Effect of Long-term Aging on the Hardness

In Chapter 4, a methodology was described whereby the as-received materials were subjected to different heat treatments in order to investigate the effects on the hardness and microstructure evolution upon subsequent long-term aging. The effect of aging time on the hardness of the P91 steels is illustrated in Figure 6.3. It can be seen that the two investigated materials, Bar 257 and W20-3, respond quite differently to prolonged aging as a function of varying initial heat treatments. After tempering, Bar 257 exhibited a large scatter in hardness between different initial heat treatments, whereas the scatter was much smaller in W20-3. It is also evident from Figure 6.3 that with increasing aging time at 650°C, Bar 257 softens at a somewhat faster rate than W20-3, to the extent that after 10,000 hours aging, the hardness of the former decreases to below 200 HV.

Another important feature shown in Figure 6.3 is that, with prolonged time at the aging temperature, the difference in hardness between specimens subjected to different initial heat treatments decreases. On the basis of these results, specimens from both materials at one initial heat treatment condition, (normalized at 1100°C cooled at 1°Cs⁻¹ and tempered at 750°C for 2 h) and at several stages of aging were characterised using EBSD in an attempt to quantify

microstructure evolution, and thus account for the changes in mechanical properties. These results are presented in the following section.

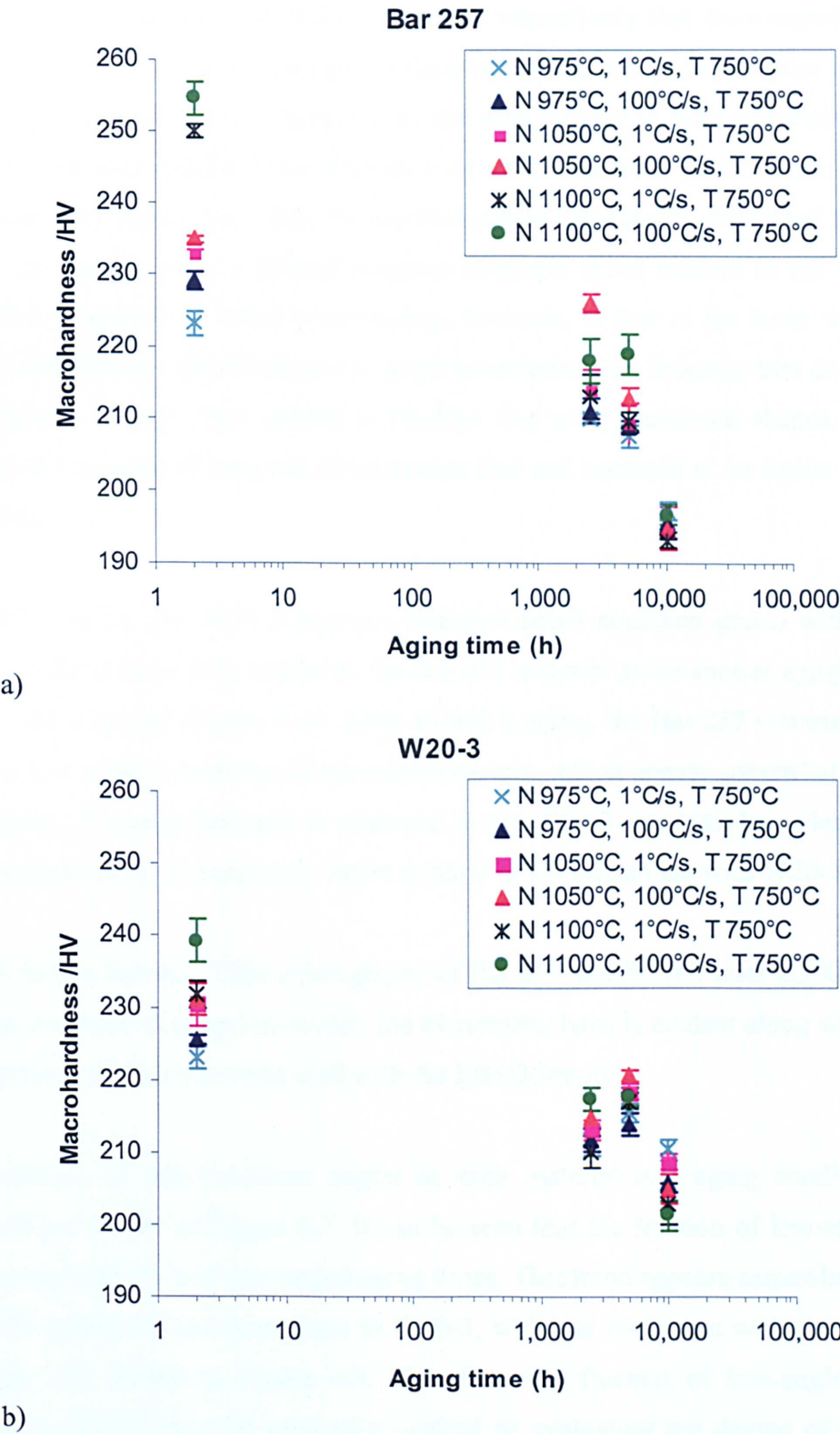


Figure 6.3: Plots showing the effect of aging time at 650°C on the hardness of a) the Bar 257 and b) the W20-3 materials subjected to different pre-service heat treatments. (N = normalizing temperature an T= tempering temperature).

6.2.2.2 EBSD Analyses of Long-term Aged Microstructures

Figures 6.4 and 6.5 show the microstructures, both in inverse pole figure maps and rotation angle maps, of the Bar 257 and W20-3 materials respectively that have experienced different aging times at 650°C. It can be seen that in the as-tempered condition, the prior austenite grains, martensitic packets and the martensitic laths are well defined in both materials. After 2,500 h the Bar 257 material exhibited the formation of small equiaxed grains within the martensite laths (Figure 6.4). Apart from this, the microstructure very much resembled the as-tempered condition. In contrast, such a defined subgrain structure is not evident in the W20-3 material after 2,500 h (Figure 6.5). What is interesting, however, is that in the latter there are regions within the laths that are identified as low angle boundaries (red features) that do not assume the shape of grains. Instead, they appear as random fine scale undefined shapes, which may be interpreted as the onset of subgrain development that had occurred at an earlier time in the Bar 257 material.

After 5,000 h aging, the W20-3 material exhibited small equiaxed grains within the original martensitic laths (Figure 6.5), similar to the Bar 257 material at the shorter aging time, although to a much lesser degree (Figure 6.4). After 10,000 h aging, the Bar 257 material shows a large increase in low angle boundaries in the microstructure, which appear somewhat finer than after 2,500 h aging. A similar scenario is observed in the W20-3 material. It is clear therefore that microstructural change is happening faster in Bar 275 in comparison with W20-3.

Figure 6.6 shows thin-foil TEM micrographs of Bar 257 and W20-3 after 2,500 h aging. In the former, the presence of subgrains within the martensitic laths is evident along with the presence of dislocations, which correspond well with the EBSD results.

The distribution of misorientation angles in each material and aging condition have been plotted, and are shown in Figure 6.7. It can be seen that the fraction of low-angle boundaries increases progressively with prolonged aging times. This trend appears somewhat accelerated in the Bar 257 specimens in comparison to W20-3, which is consistent with the faster softening rate of Bar 257 shown in Figure 6.3. Therefore, the fraction of low-angle boundaries as determined by EBSD may be used as a method of evaluating the degree of recovery of the microstructure of high Cr steel power plant components.

There are, however, some problems associated with using the boundary angle distribution graph. For example, there are features which can affect the shape the distribution curve. The main factor being the poorer statistics of the high angle prior austenite grain boundaries due to their random nature and low number of grains sampled within the EBSD scan area sizes employed in this investigation, which of course are a compromise between the highest resolution settings and reasonable analysis times.

An alternative and simplified method of interpreting boundary angle data is to compare the ratio of low-angle ($2-10^\circ$) to high-angle ($10-180^\circ$) boundaries, as illustrated in Figure 6.8. It is shown here that this ratio increases with prolonged aging time and, in good agreement with Figure 6.7, this increase occurs more rapidly in the Bar 257 material.

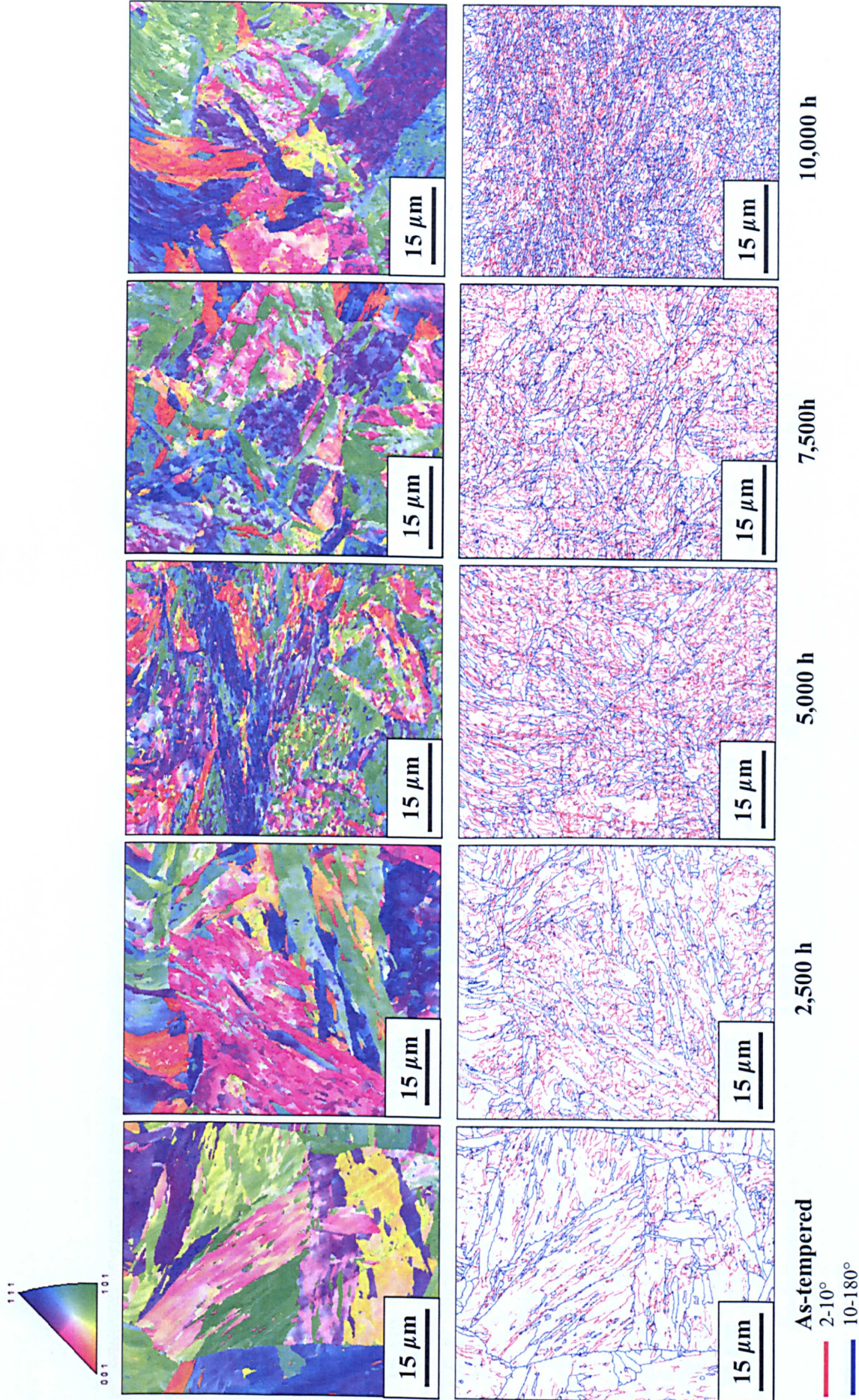


Figure 6.4: Inverse pole figure maps (top) and rotation angle maps illustrating the microstructure evolution of the Bar 257 material from the as-tempered condition (far left) to 10,000 h isothermal aging (far right).

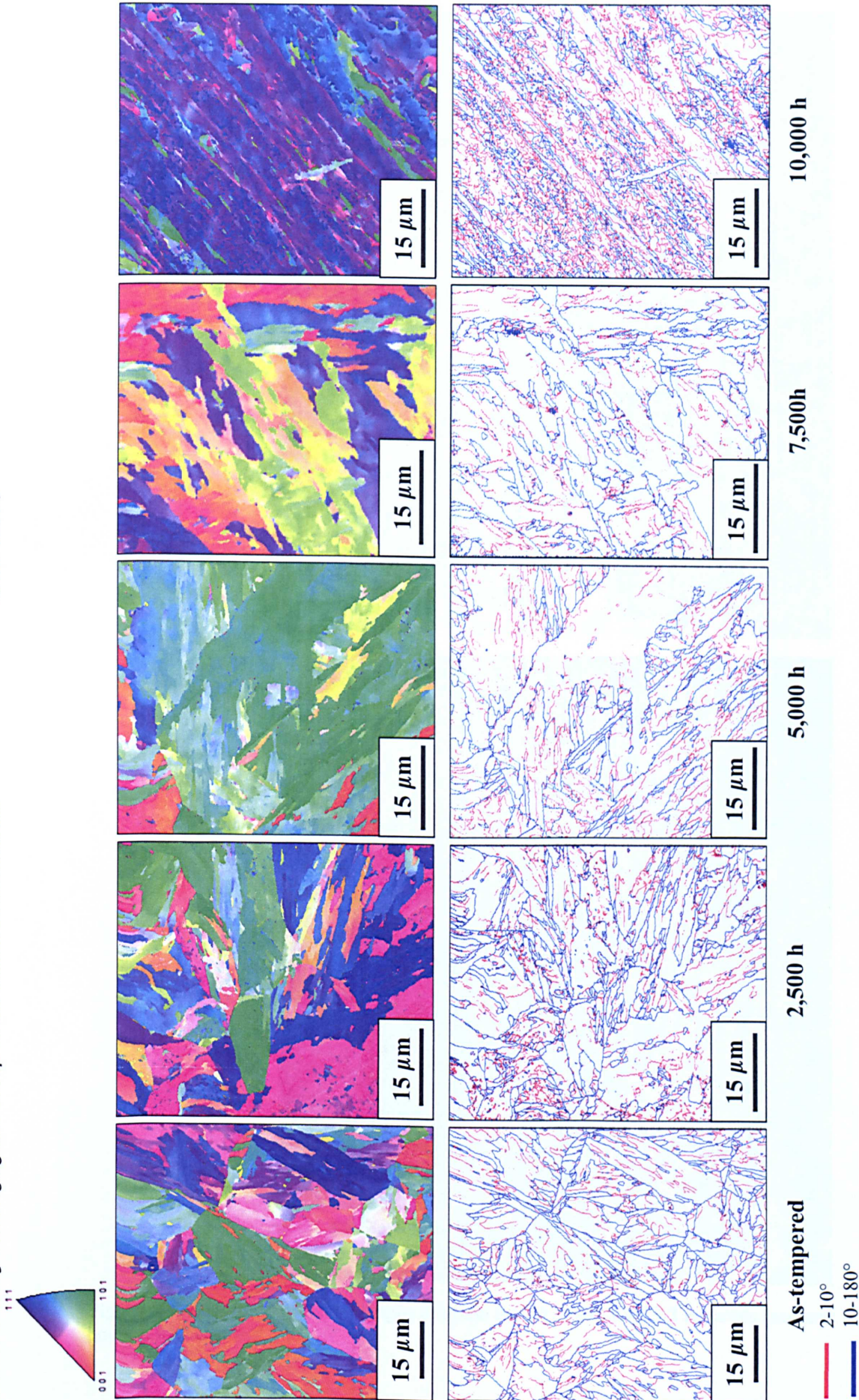


Figure 6.5: Inverse pole figure maps (top) and rotation angle maps illustrating the microstructure evolution of the W20-3 material from the as-tempered condition (far left) to 10,000 h isothermal aging (far right).

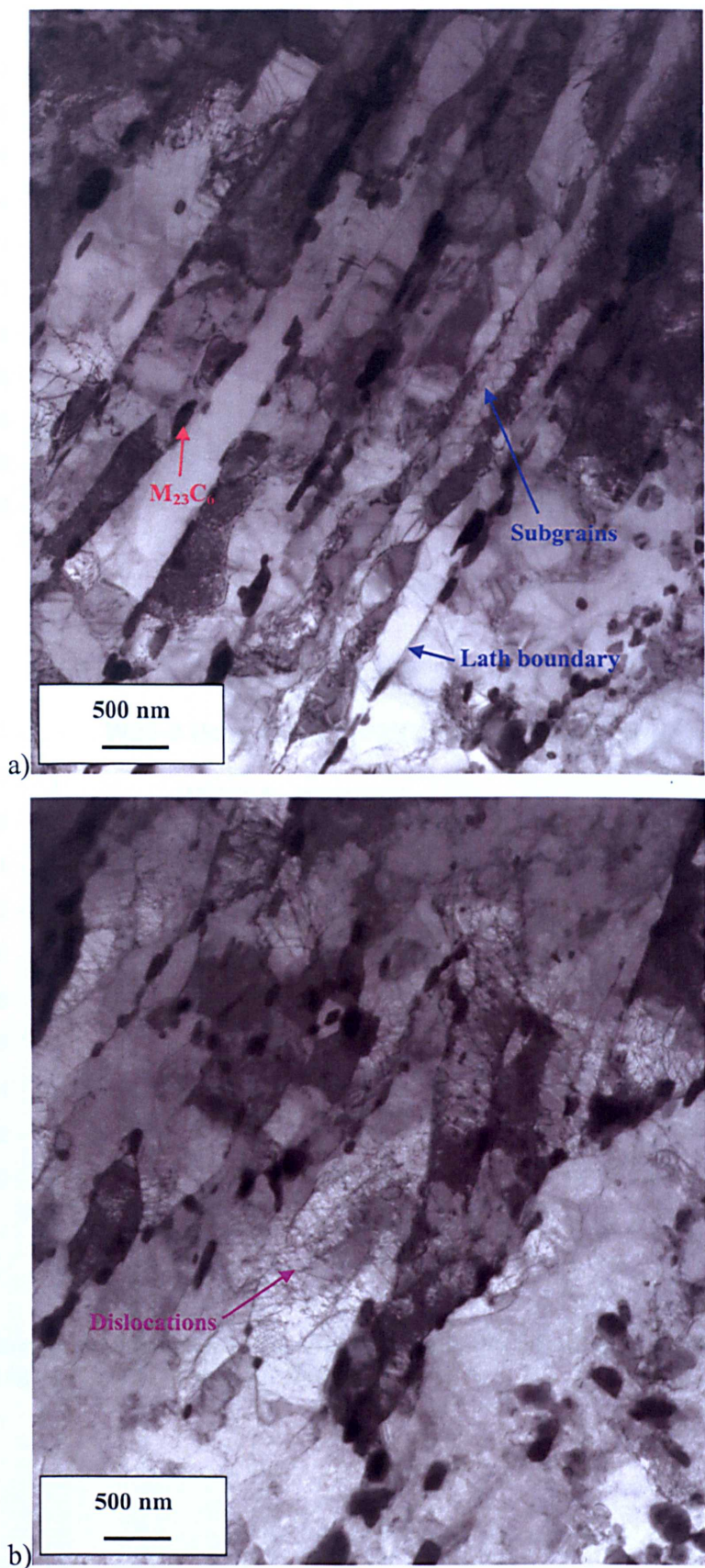


Figure 6.6: Thin-foil TEM micrographs of a) the Bar 257 and b) W20-3 materials that have been aged for 2,500 hours at 650°C.

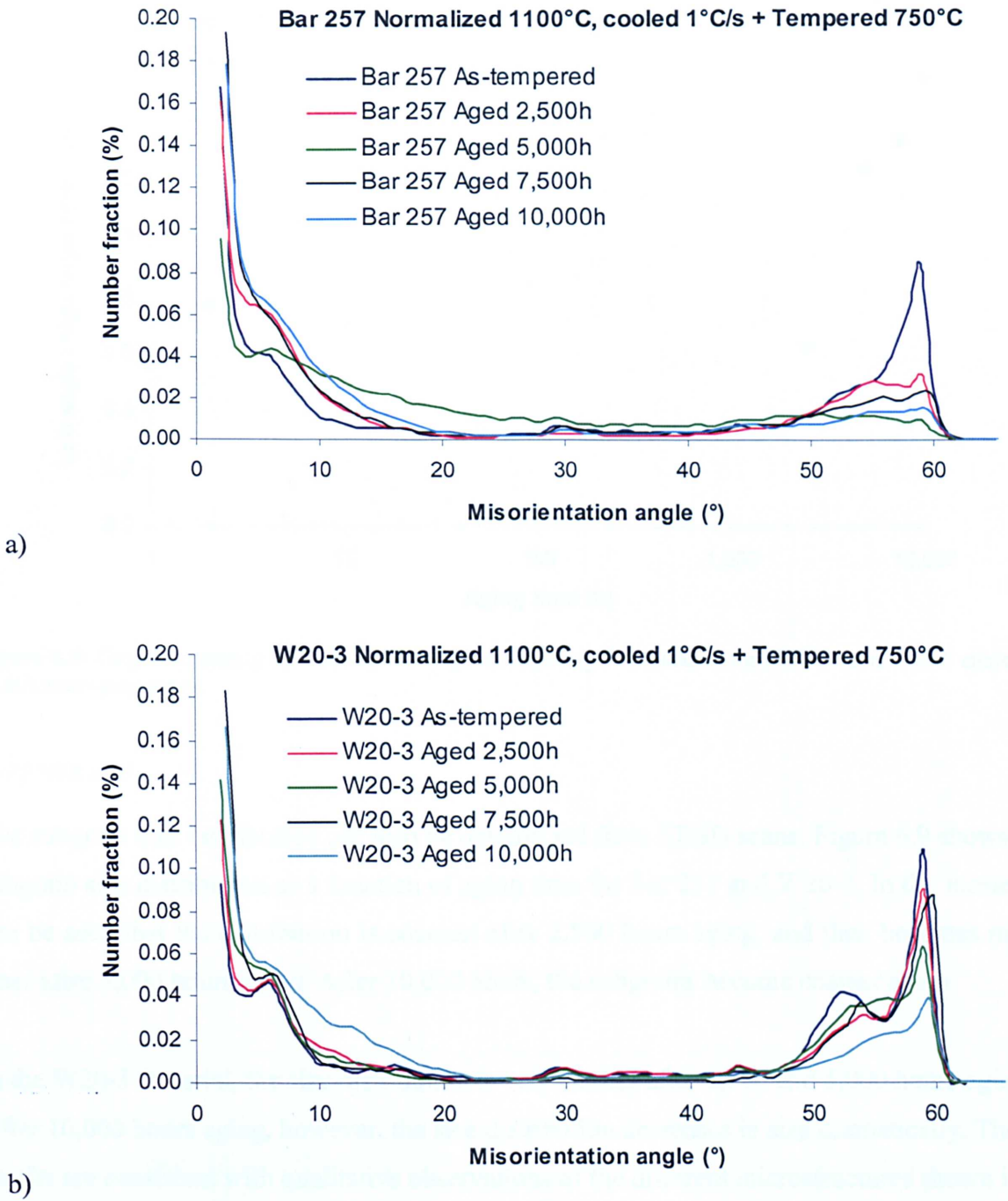


Figure 6.7: Plots showing the distribution of misorientation angles for the a) Bar 257 and b) W20-3 specimens subjected to thermal aging at 650°C for different times.

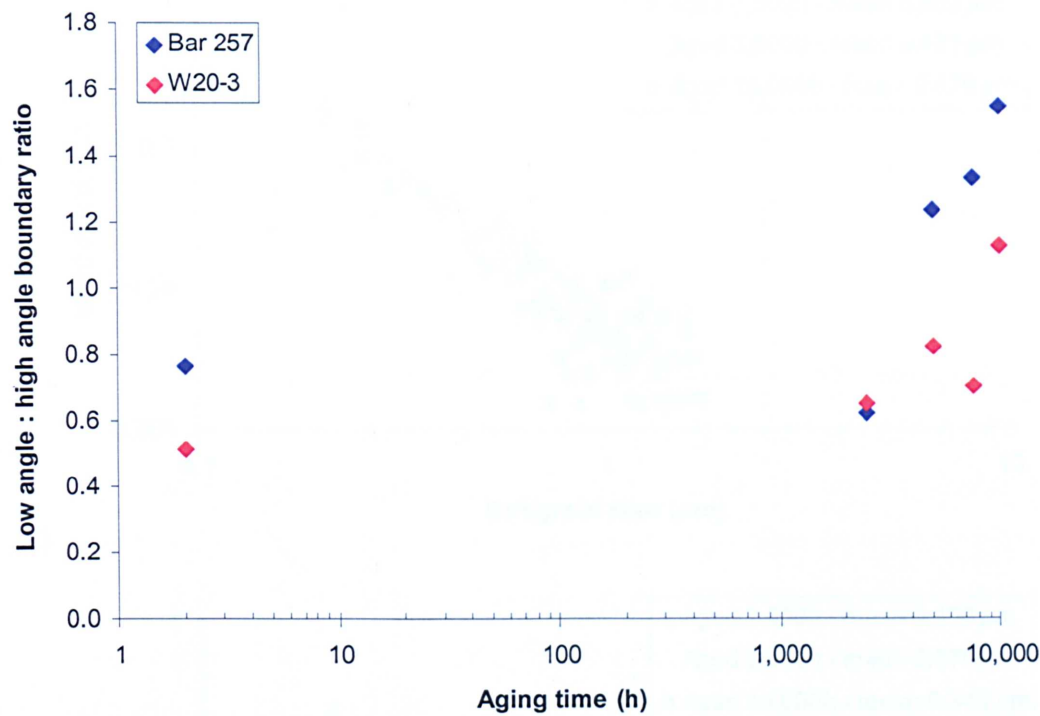


Figure 6.8: Graph illustrating the ratio of low-angle to high-angle boundaries for Bar 257 and W20-3 subjected to different aging times.

Subgrain size

The subgrain size distribution can also be determined from EBSD scans. Figure 6.9 shows the subgrain size distribution as a function of aging time for Bar 257 and W20-3. In the former, it can be seen that the distribution is coarsest after 2,500 hours aging, and then becomes much finer after 5,000 hours aging. After 10,000 hours, the subgrains become coarser again.

In the W20-3 material, the size distribution is very similar after 2,500 and 5,000 hours aging. After 10,000 hours aging, however, the size distribution decreases in size dramatically. These results are consistent with qualitative observations of the different microstructures shown in Figures 6.4 and 6.5.

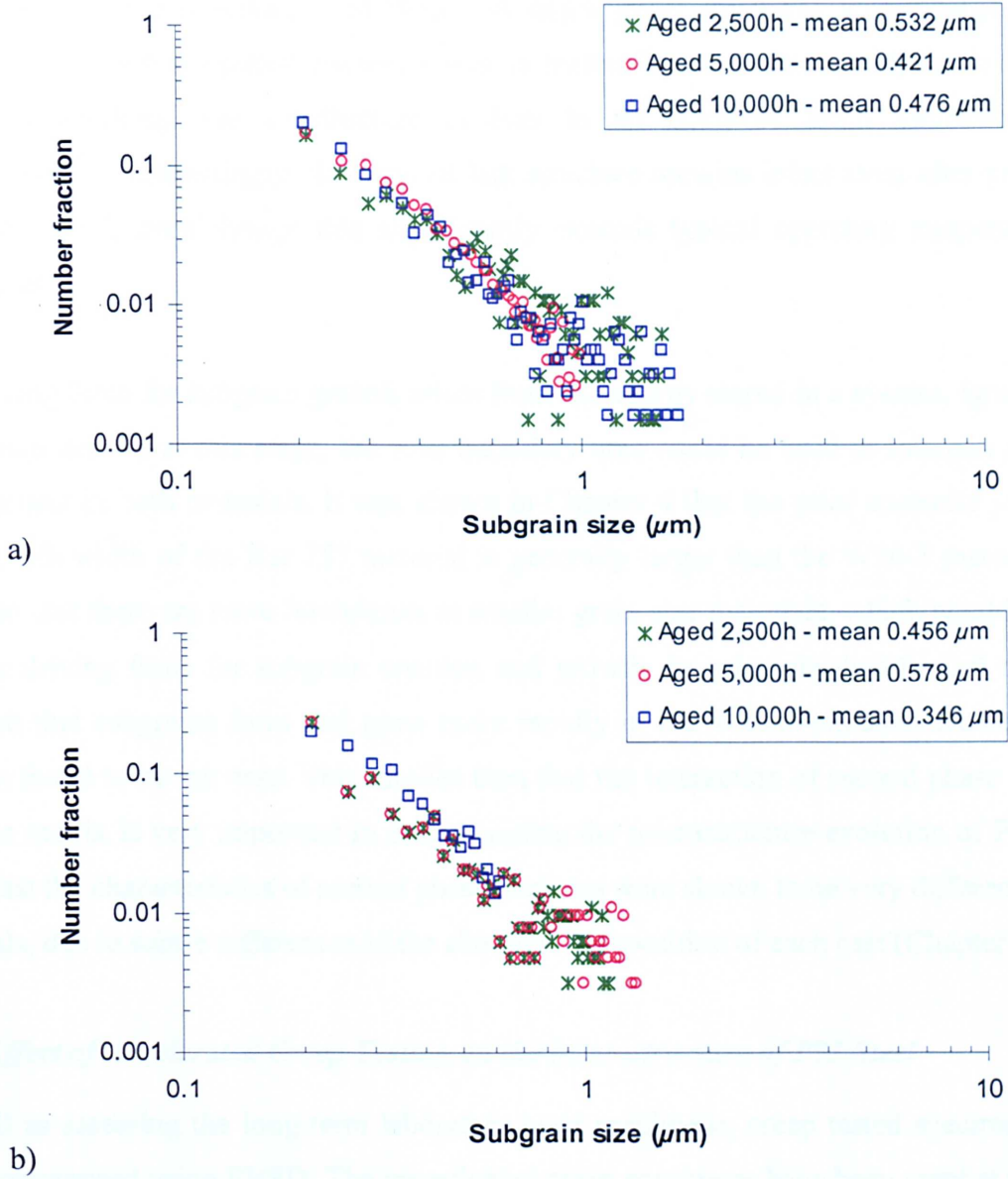


Figure 6.9: The subgrain size distribution in the aged a) Bar 257 and b) W20-3 materials subjected to different aging times at 650°C .

6.2.2.3 Discussion on the Effect of Long-term Aging on the Microstructure Evolution

It is reasonable to assume that at the shorter aging times, smaller grains than those observed may not have been accounted for due to the step size employed in this investigation. It is also very likely that the majority of dislocations had not rearranged to lower energy configurations due to short aging times. Evans and Wilshire^[81] - quoting Takeuchi and Argon^[137] - discussed that as the creep process takes place at high temperatures, the creation and motion of dislocations results in work hardening, whilst recovery processes such as climb and cross-slip are occurring simultaneously, which permit dislocations to either be annihilated or to rearrange themselves into low energy configurations, such as subgrains. This is a plausible

explanation for the observation of these low-angle grain structures within larger grains. Indeed, it has been suggested elsewhere that in materials which undergo dynamic recovery during hot-working, the substructure evolves to an equiaxed grain structure during deformation ^[15]. Interestingly, the original lath structure remains intact even after prolonged aging at 650°C, even though this significantly exceeds typical operating temperatures in power plant.

The driving force for subgrain growth arises from the energy stored in a system. Ignoring the dislocation density at this stage, the total boundary area could be used to interpret subgrain development in both materials. It was shown in Chapter 4 that the prior austenite grain size and the lath width of the Bar 257 material is generally larger than the W20-3 material. It is expected that there are more boundaries in smaller grain size materials, which would provide a larger driving force for subgrain creation and growth. In principle therefore, it might be expected that subgrains form and grow more rapidly in the W20-3 material. However, this was not found to be the case. This implies then that the interaction of second phase particles with the matrix is very important in understanding the microstructure evolution of P91 steel, given that the characteristics of second phase particles were shown to be very different in both materials, due to subtle differences in the chemical composition of each cast (Chapter 5).

6.2.3 Effect of Accelerated Creep Testing on the Microstructure of P91 Steel

As well as assessing the long-term laboratory aged specimens, creep tested specimens were also characterised using EBSD. The investigated creep specimens have been crept at the same temperature (650°C) as the laboratory aged specimens. In addition to experiencing conditions of high temperature exposure, high Cr ferritic-martensitic steels are also subjected to high pressure conditions which cause these materials to creep. Often, the creep behaviour is determined by performing accelerated creep tests, whereby the test temperatures and/or stresses significantly exceed the design criteria specified for these materials to operate under normal conditions. This scenario is far from ideal, however, given the long design lives, it is often the only practical solution to assess the creep behaviour. It is thus of great importance to link the creep behaviour of power plant steel components to the microstructure, and many studies have been undertaken on this topic using more conventional microscopy techniques such as TEM ^[15,69,139]. The advantages of EBSD have already been introduced earlier in this

chapter, thus a study of accelerated creep test specimens is attempted here using this technique.

6.2.3.1 The Effect of Creep Stress on the Hardness of P91

Accelerated creep tested P91 specimens, which were manufactured from the Bar 257 material were characterised using EBSD. The creep tests were performed at the University of Nottingham. The specimens were tested to failure at a temperature of 650°C and at varying constant stress values, ranging from 60 to 93 MPa. Accordingly, the test duration ranged from 2,270 h at the low stress to 82.4 h at the highest stress condition. Figure 6.10 shows the effect of applied creep stress on the rupture time of the investigated creep specimens and Figure 6.11 shows the hardness differences between the head (unstressed) and gauge (stressed) regions of the investigated creep specimens. In the latter, it is evident that strain contributes to accelerated softening of these materials. The differences in the matrix microstructure evolution between the head and gauge regions are discussed in the following section.

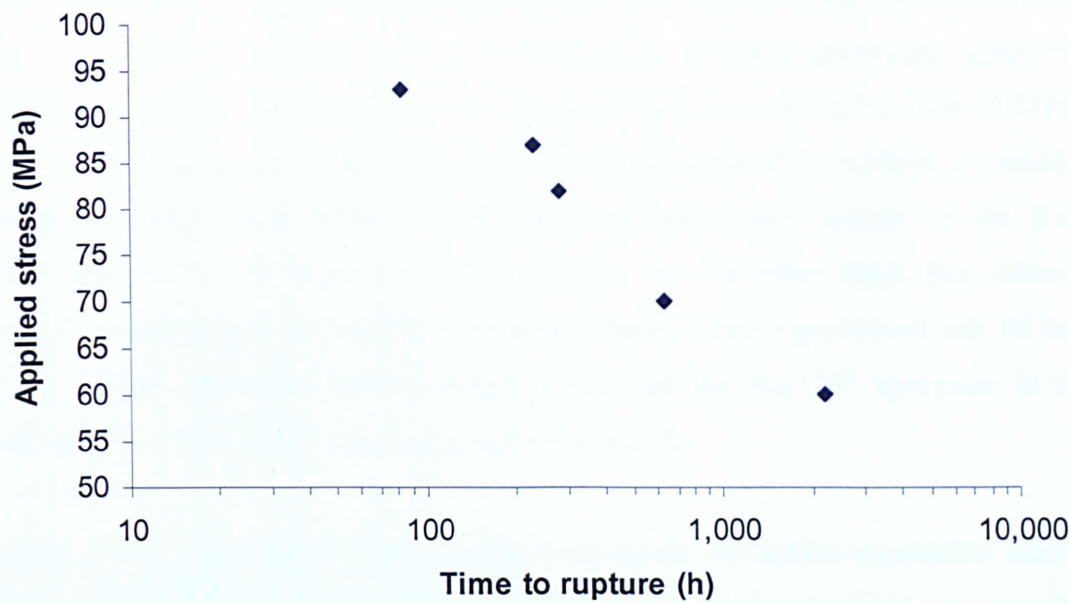


Figure 6.10: Plot illustrating the stress versus the rupture time of the Bar 257 specimens subjected to accelerated creep testing. The test temperature was 650°C. The creep tests were performed at the University of Nottingham.

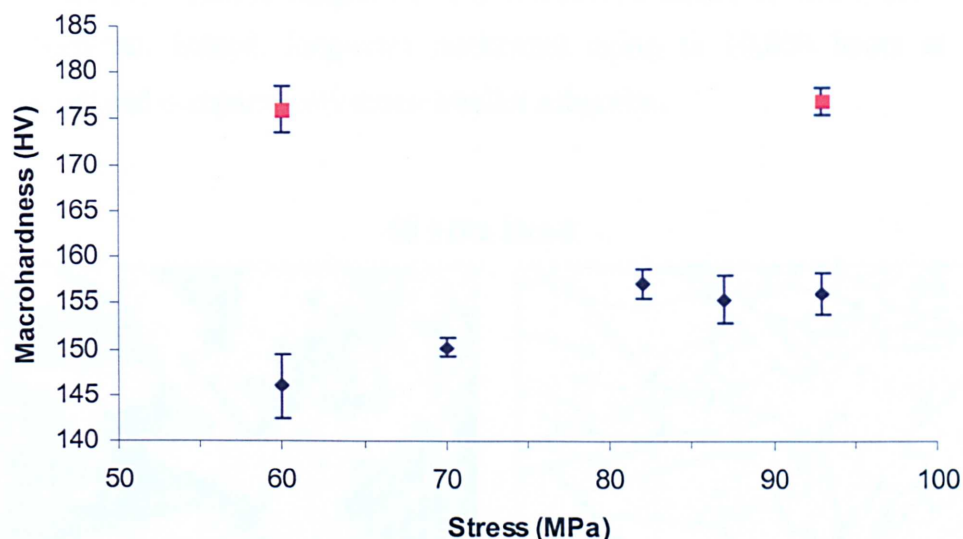


Figure 6.11: Plot illustrating the stress versus the macrohardness of the Bar 257 specimens subjected to accelerated creep testing at 650°C. The red symbols indicate the hardness of the unstrained (head) portion and the blue symbols represent the (strained) gauge portion.

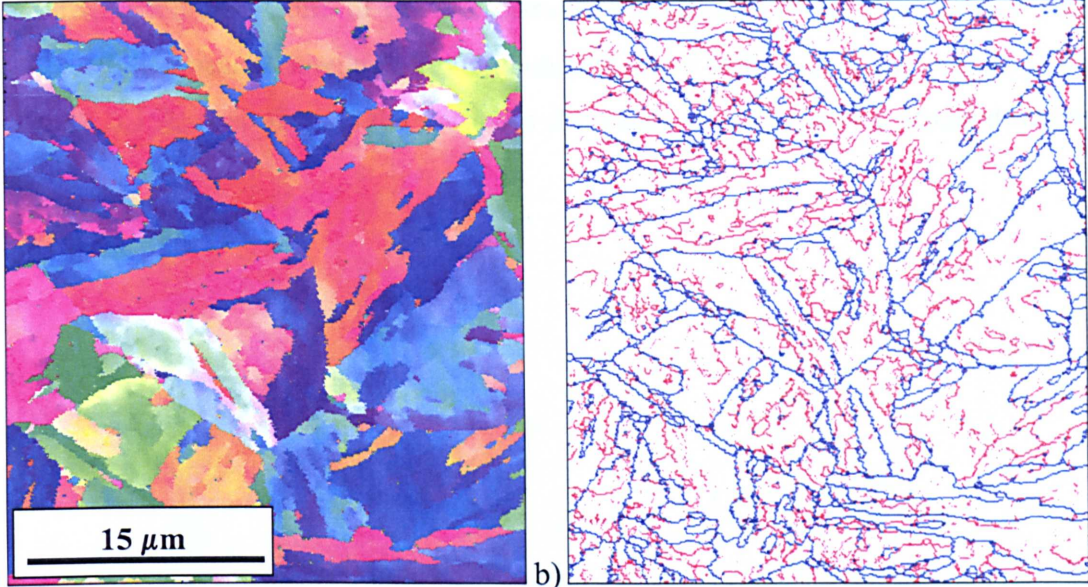
6.2.3.2 EBSD Analyses of Accelerated Creep Tested Microstructures

The microstructure of the investigated head portions of two of the creep specimens are shown in Figure 6.12. It can be seen that the microstructure of these specimens unsurprisingly resemble the long-term aged Bar 257 specimens described in section 6.2.2. The 60 MPa head sample, which experienced approximately 2,200 hours at 650°C, exhibits a considerable amount of low-angle substructure within the martensitic laths, similar to the Bar 257 specimen aged for 2,500 hours (see section 6.2.2). On the other hand, this substructure development is not evident in the 93 MPa head specimen, which experienced only 80 hours at 650°C. The latter specimen correspondingly resembled the Bar 257 specimen in the as-manufactured, or as-tempered condition (see section 6.2.1).

The effect of a high degree of strain at high temperature on ferritic-martensitic steels is to drastically alter the microstructure to such an extent that it is unrecognisable compared to the as-manufactured condition. This effect is illustrated in Figure 6.13, where the microstructures of the gauge portion of several Bar 257 creep specimens are shown. A heterogeneous distribution of grain sizes is observable in these micrographs, which contain grains that are clearly larger and more equiaxed than the laths present in the head (unstressed) portion of the creep specimens. These are visible within the prior austenite grains and have been identified as high-angle boundaries, although there are also grains with a similar shape identified as low

angle boundaries. These results suggest that considerable strain accelerated coarsening of subgrains has occurred. Indeed, long-term isothermal aging to 10,000 hours at the same temperature produced comparatively much smaller subgrains.

60 MPa Head



93 MPa Head

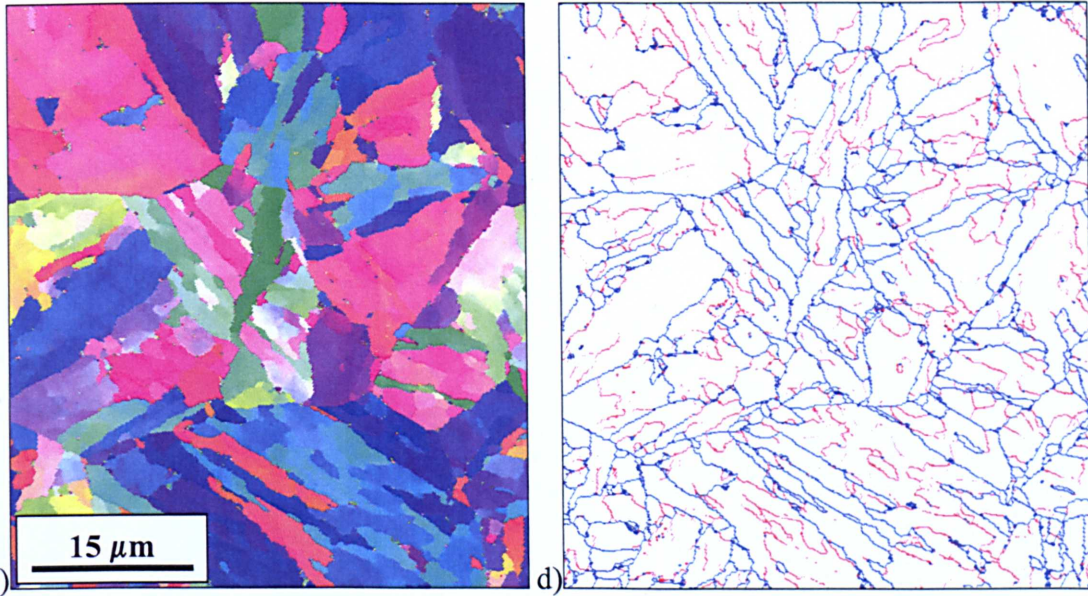


Figure 6.12: Inverse pole figure maps a) and c), and rotation angle maps b) and d) illustrating the microstructure of the head (unstressed) portion of the Bar 257 material crept at 650°C at 60 and 93 MPa respectively. The times to failure for both conditions were 2,217 and 82 hours respectively.

Figure 6.14 shows a thin-foil micrograph of a typical microstructure from the gauge section of an investigated creep specimen. Large equiaxed grains are observed with some grains exhibiting a heterogeneous dislocation substructure, which is consistent with the findings obtained using EBSD.

The main distinguishing feature of the microstructures produced at different applied stresses is the systematic increase in low:high-angle boundary ratios with respect to increasing applied stress (Figure 6.15), even though the hardness decreases with decreasing stress down to 60 MPa.

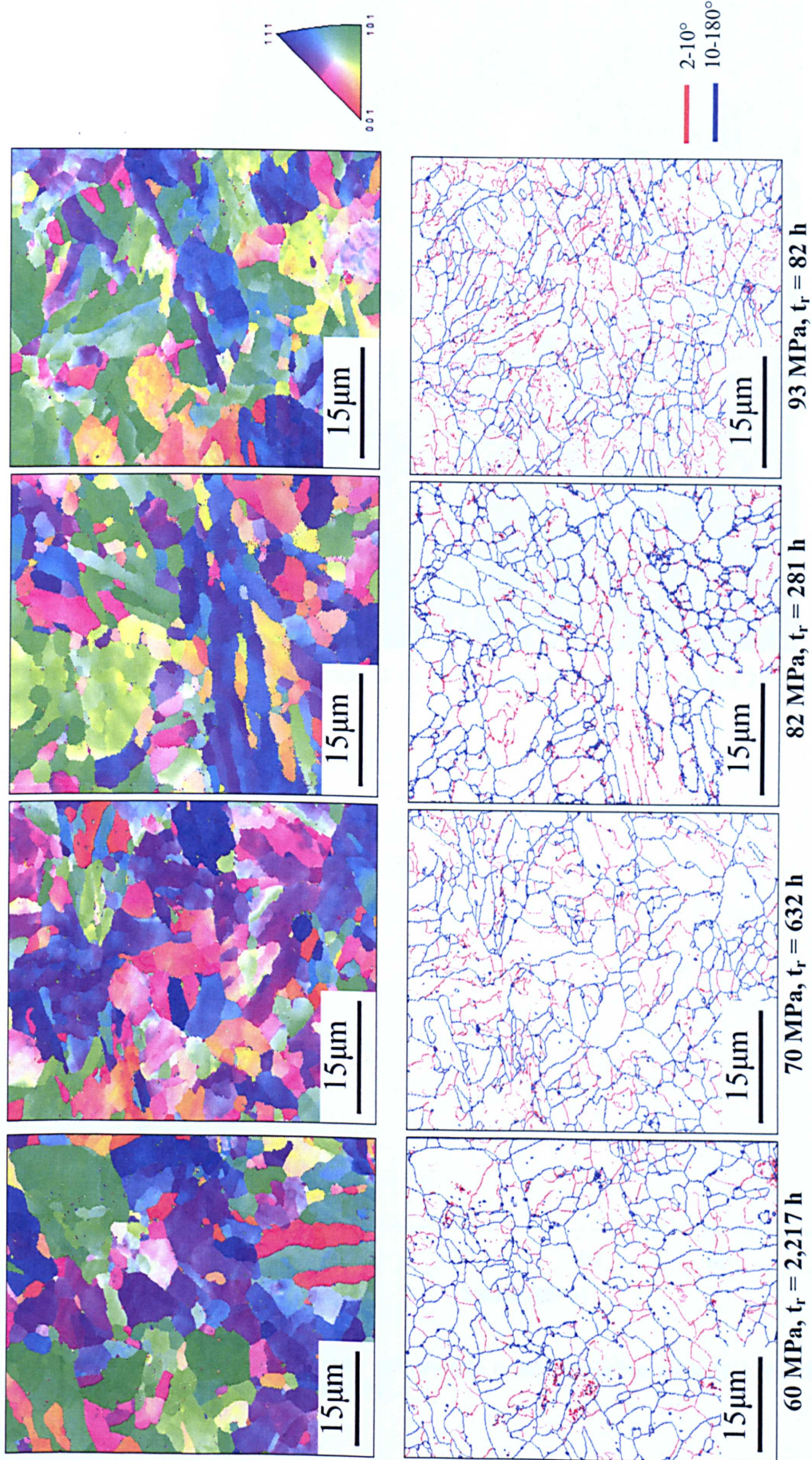


Figure 6.13: Inverse pole figure maps (top) and rotation angle maps illustrating the microstructure of the gauge (stressed) regions of the Bar 257 material subjected to accelerated creep tests to failure under different stresses ranging from 60 (far left) to 93 MPa (far right) at 650°C. t_r = time to rupture.

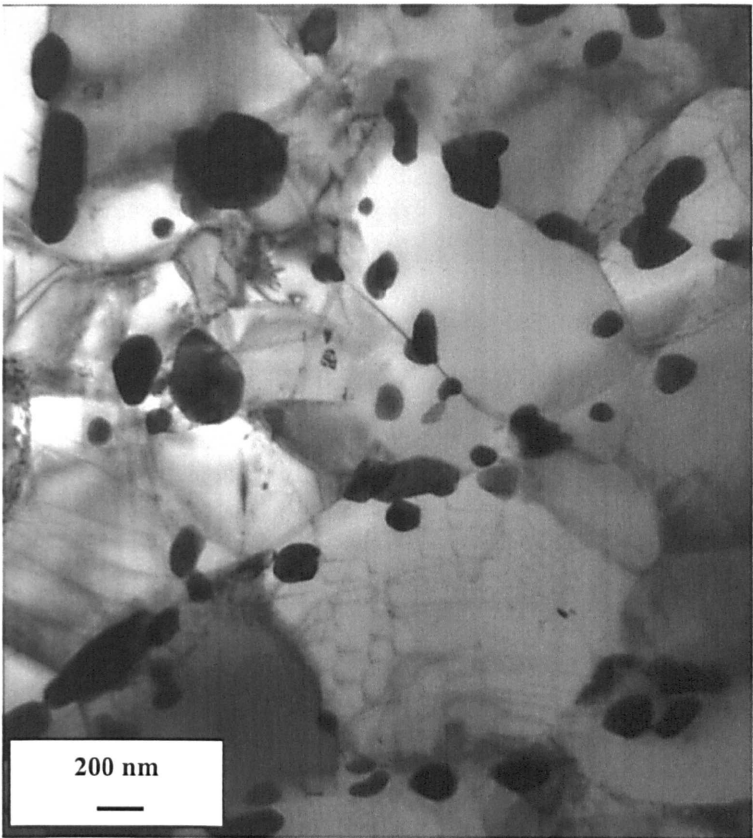


Figure 6.14: Thin-foil TEM micrograph of the gauge (stressed) section of the Bar 257 material stressed at 87 MPa at 650°C.

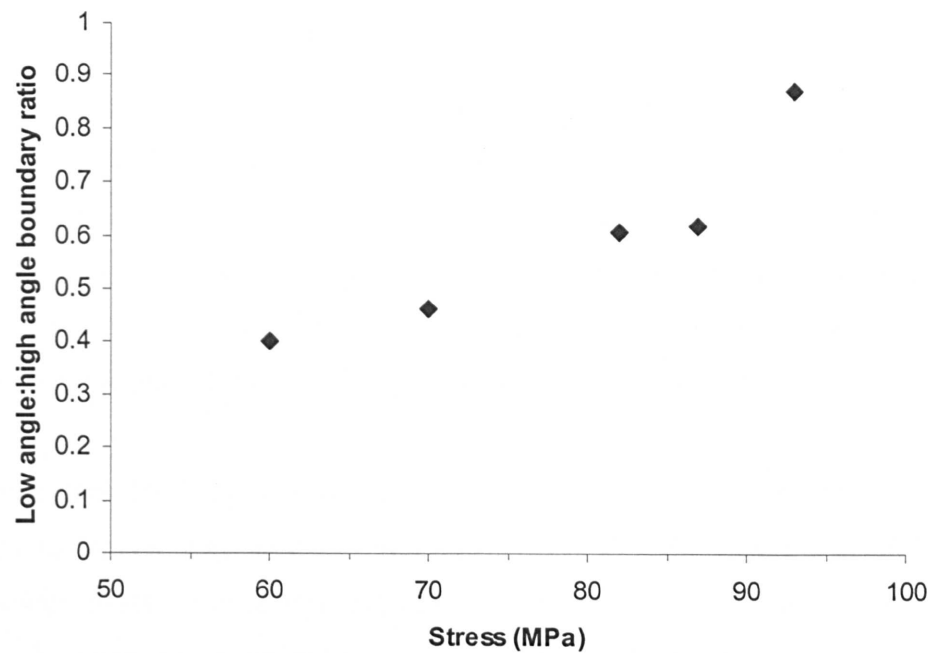


Figure 6.15: Graph illustrating the ratio of low-angle to high-angle boundaries for Bar 257 creep specimens subjected to different creep stresses at 650°C.

6.2.3.3 Discussion of the Effect of Creep Testing on the Microstructure Evolution

During accelerated creep testing, the mechanism responsible for microstructural change is more severe than recovery; this was shown by the fact that the microstructures of these specimens are more indicative of the mechanism of recrystallization. The fact that a trend exists between the ratio of low:high-angle boundaries and the applied stress, is probably less relevant than the relationship between this ratio and the test exposure time. This point can be rationalised if the stress range of 60 to 93 MPa is considered to be sufficiently high to not further influence the microstructure. Therefore, if only the time at test temperature is considered, it is evident that increasing the time produces a lower low:high-angle boundary ratio, or a higher fraction of high-angle boundaries. It must also be noted that there is a considerably larger amount of low-angle substructure within the equiaxed grains in the 93 MPa specimen than the 60 MPa specimen, which may also explain the higher hardness in the former. This observation, according to Jazaeri and Humphries ^[134], can be used as a measure of the degree of recrystallization. Therefore, according to their hypothesis, the degree of recrystallization clearly decreases with increasing stress, or more accurately, with decreasing creep exposure times.

6.2.4 Boundary Length as a Method of Assessing Material Microstructure

One parameter, which may be quantified using the EBSD technique, is the total grain boundary line length in a given area. Simplistically, a grain boundary in conventional metallography symbolises a line which separates two grains. However, in EBSD, a grain boundary refers to a line segment which separates two points in a scan. As the orientation at two points which is separated by a line segment is known, the misorientations associated by the segment can be calculated. The misorientation is simply referred to as the bringing of a crystal lattice of one grain into coincidence with a neighbouring grain.

The grain boundary line length per unit area was measured in each specimen in order to assess whether this parameter may be quantified and used to describe microstructural changes in high Cr power plant components subjected to different thermal exposure and loading conditions. A range of misorientation angles has been considered to denote specific boundaries. For this investigation, interest was mainly focussed on the total grain boundary line length.

Figure 6.16 shows that the total grain boundary length per unit area increases in Bar 257 and W20-3 with respect to an increase in aging time. It is also shown that the total boundary length is consistently somewhat longer in the Bar 257 material at all the aging times examined. The data for the creep specimen subjected to a stress of 93 MPa showed that in the unstressed head region, the boundary length is similar to that of the as-tempered condition, which is sensible as the durations of the creep tests were a relatively low 82 and 2,200 hours at 650°C. Interestingly, the boundary lines lengths were much lower in the stressed region, which corresponds to the presence of large equiaxed grains, thus strain has been shown to play a very important part in microstructure evolution in P91, bearing in mind that the strain levels experienced by this specimen, which failed in a ductile manner, far exceeds what a normal material will experience in service. In addition, it is also shown that there is a stage at which the boundary line length dramatically increases with increasing aging time. For example, this sharp increase occurs in the range from 2,500 to 5,000 hours in Bar 257, whereas it occurs in the range of 5,000 to 10,000 hours in W20-3. This is indicative of the poorer creep properties of Bar 257.

Figure 6.17 shows that the boundary line length increases with increasing applied stress during creep testing, which was shown to be inversely related to failure time. This was earlier related to the degree of recrystallization, which was shown to increase with increasing time to failure, or more accurately, exposure time.

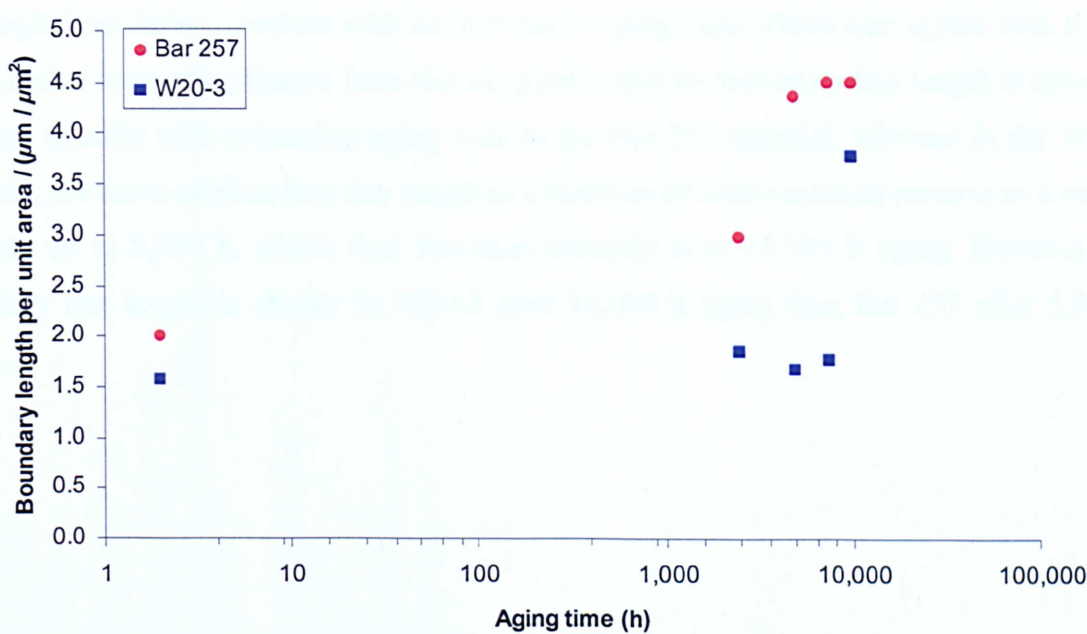


Figure 6.16: Plot showing the effect of aging time at 650°C on the grain boundary line length of isothermally aged P91 steel specimens.

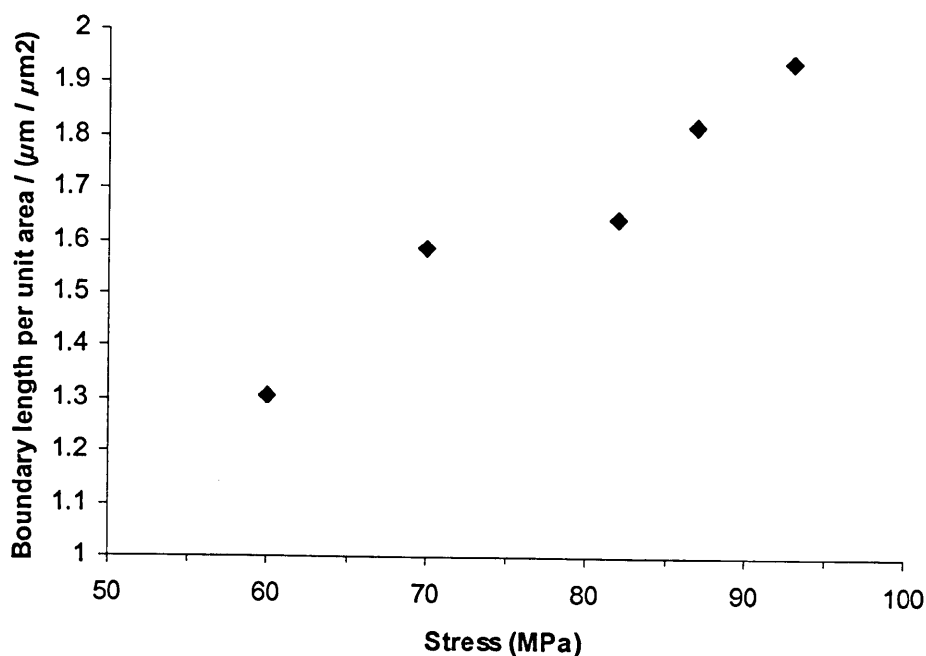


Figure 6.17: Plot showing the effect of creep stress on the boundary length of creep tested Bar 257 P91 steel specimens. The test temperature was 650°C and the creep stresses ranged from 60 to 93 MPa.

Another method of interpreting the change in microstructure is to plot a boundary density chart, which is essentially the integral of the distribution of grain boundary misorientations, and illustrates the boundary line length per unit area as a function of misorientation angle. Figure 6.18 shows, in agreement with Figure 6.16, that the boundary length increases in both Bar 257 and W20-3 as a function of aging time. In addition, it also shows that the density of low-angle boundaries increases with an increase in aging time, which also agrees with Figure 6.8. Another interesting feature from this diagram is that the boundary line length is shown to increase steadily with increasing aging time in the Bar 257 material, whereas in the W20-3 material, the curve of boundary line length as a function of misorientation remains in a similar position up to 5,000 h, which then increases abruptly after 10,000 h aging. However, the boundary line length is shorter in W20-3 after 10,000 h aging than Bar 257 after 5,000 h aging.

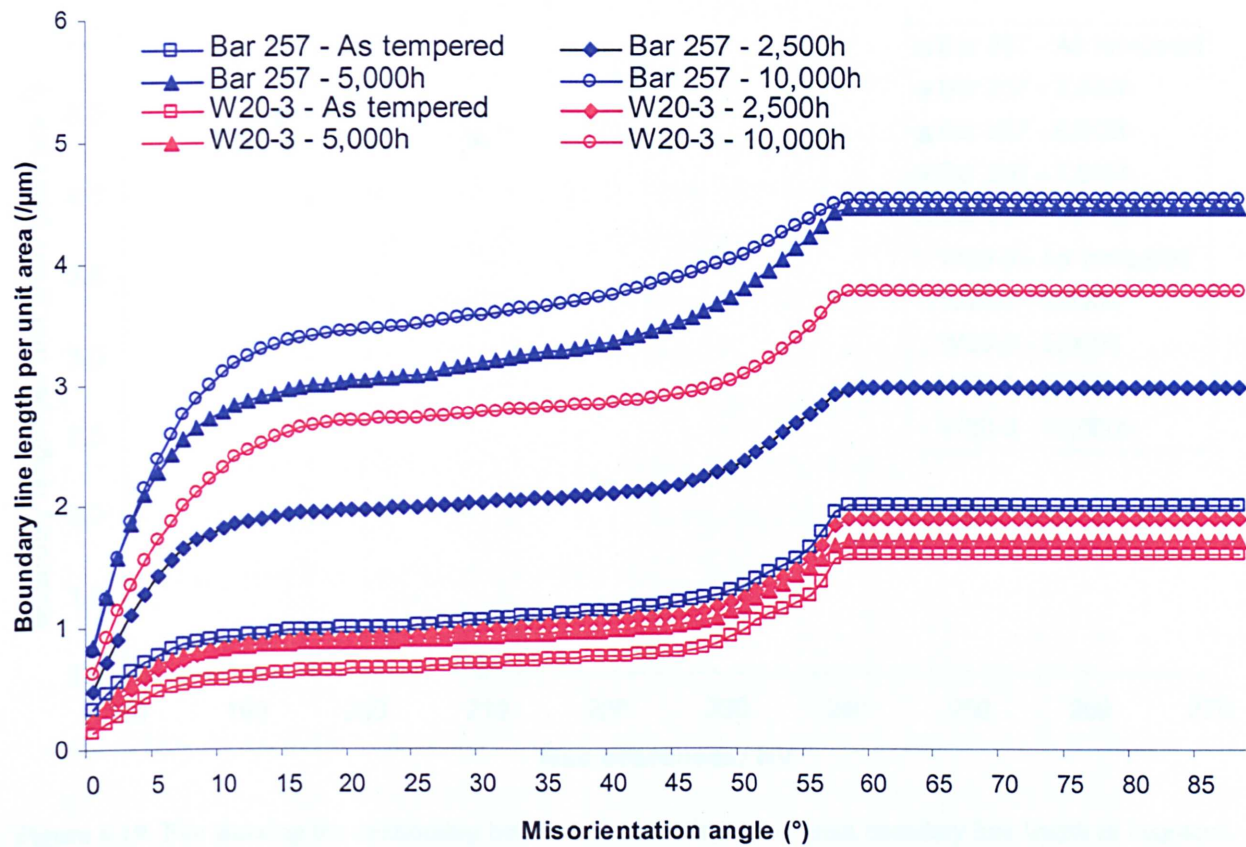


Figure 6.18: Plot showing the boundary line length as a function of misorientation angle.

Figure 6.19 shows that there is a good correlation between hardness and grain boundary length where the hardness of P91 steel decreases with increasing boundary length per unit area and this trend is evident for both materials. This shows that boundary length may be used as an indicator for gradual softening of P91 steel in service. A weaker trend between hardness and applied stress can be observed, where the boundary line length is shown to somewhat increase with increasing stress (Figure 6.20). This phenomena was rationalised in section 6.2.3.2.

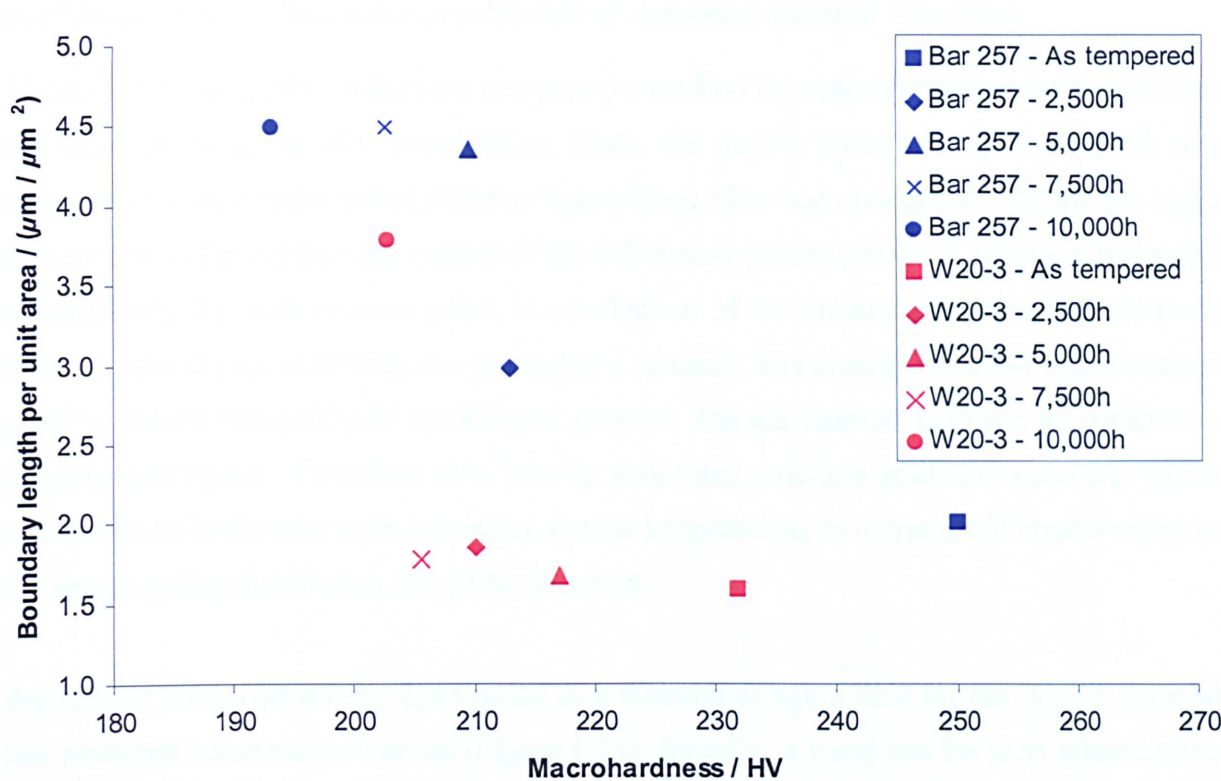


Figure 6.19: Plot showing the relationship between macrohardness and grain boundary line length in long-term aged P91 steel specimens. The aging temperature was 650°C.

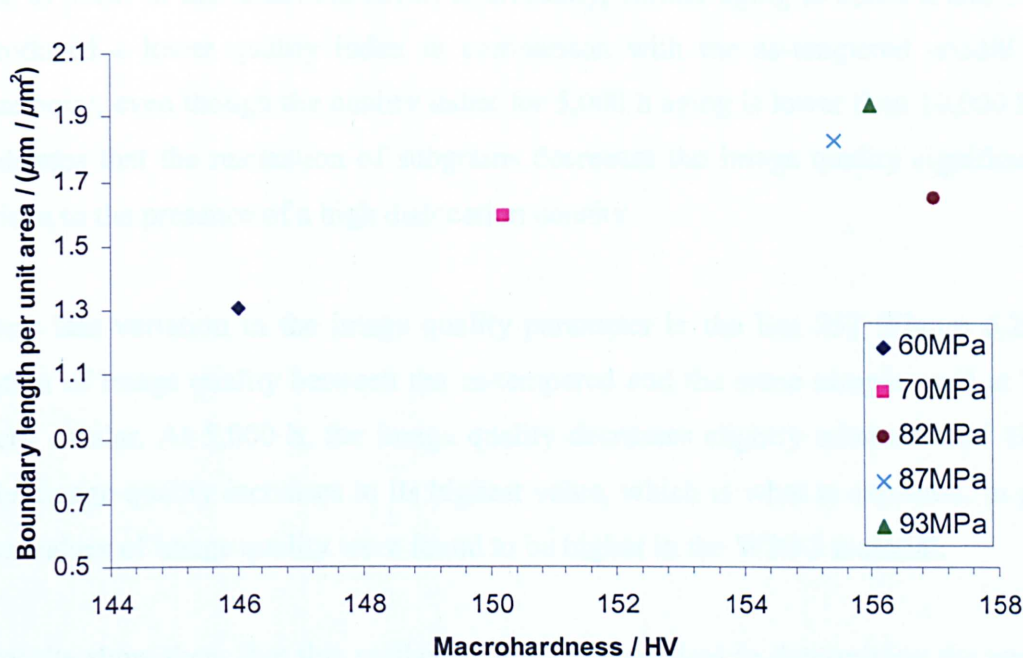


Figure 6.20: Plot showing the relationship between macrohardness and boundary length in P91 steel specimens subjected to accelerated creep specimens. The creep test temperature was 650°C.

6.2.5 Image Quality Parameter as a Method of Assessing Material Condition

The use of image quality index as a comparative method for assessing the material condition has been evaluated in this investigation. Here, the quality index distribution of the two materials that have experienced different aging times have been compared. The simple logic behind this method is that the quality of the diffraction pattern obtained, which is measured automatically for each indexed point, is a reflection of the amount of lattice imperfections such as dislocations, vacancies, etc. present in a material. The presence of these imperfections tends to reduce the quality of the Kikuchi patterns that are indexed to create an orientation imaging micrograph. Therefore, as a heavily dislocated structure gradually recovers, which was shown to be the case with increasing time at temperature, an incremental improvement in the image quality distribution should be observed.

Analysis of the image quality distribution as a function of aging time for the W20-3 material has produced inconclusive results (Figure 6.21). Initially, a trend can be seen whereby the image quality parameter clearly increases, indicating an improvement in image quality, when comparing the as-tempered condition to 2,500 h aging, where considerable recovery is expected to occur in the latter. However, equivocally, further aging to 5,000 h and 10,000 h have produced a lower quality index in comparison with the as-tempered condition as a reference point, even though the quality index for 5,000 h aging is lower than 10,000 h aging. This indicates that the nucleation of subgrains decreases the image quality significantly, in comparison to the presence of a high dislocation density.

There was less variation in the image quality parameter in the Bar 257 (Figure 6.22). The distribution of image quality between the as-tempered and the same sample aged at 2,500 h were very similar. At 5,000 h, the image quality decreases slightly whereas after 10,000 h aging the image quality increases to its highest value, which is what is expected. In general, the mean values of image quality were found to be higher in the W20-3 material.

These results show then, that this method is not very practical in determining the amount of recovery experienced in P91 steel subjected to different aging treatments, even though it has successfully been applied to determine the degree of cold working and recrystallization in other simpler materials, such as copper and brass ^[135], which consequently contain fewer microstructural parameters that affect the recovery mechanism.

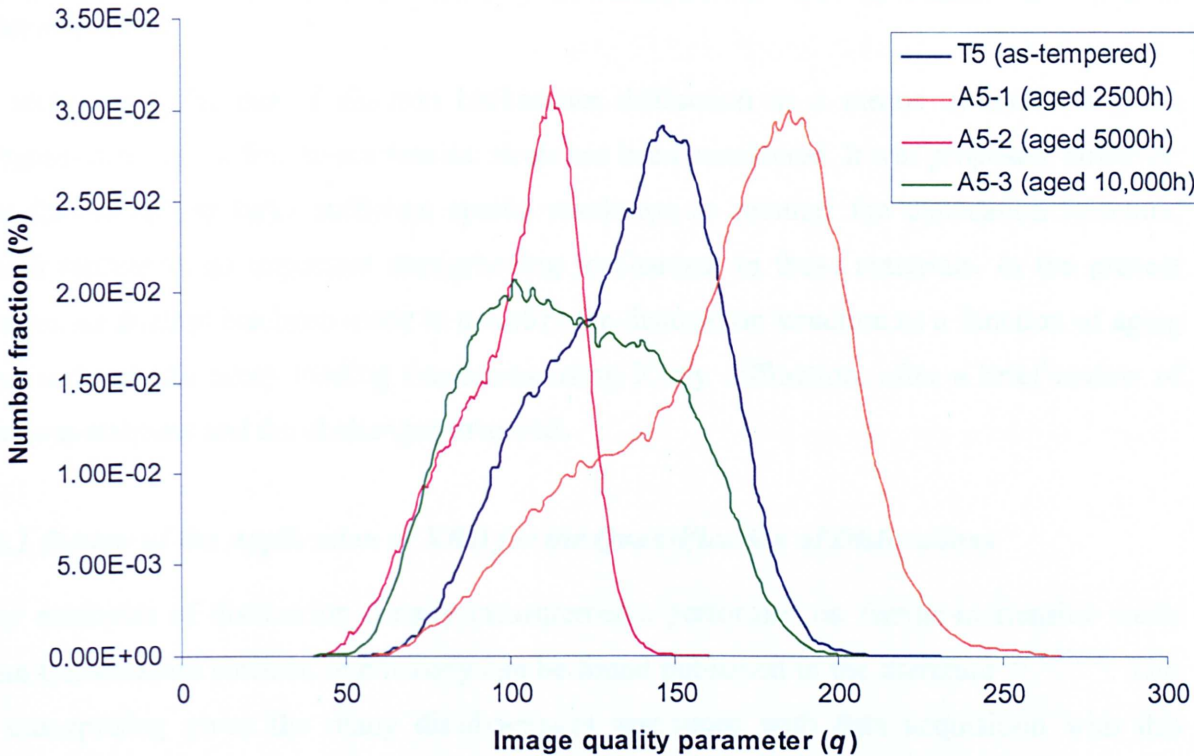


Figure 6.21: Plot showing the distribution of image quality parameter with respect to aging time at 650°C in the W20-3 material. Aging treatments were performed for up to 10,000 h.

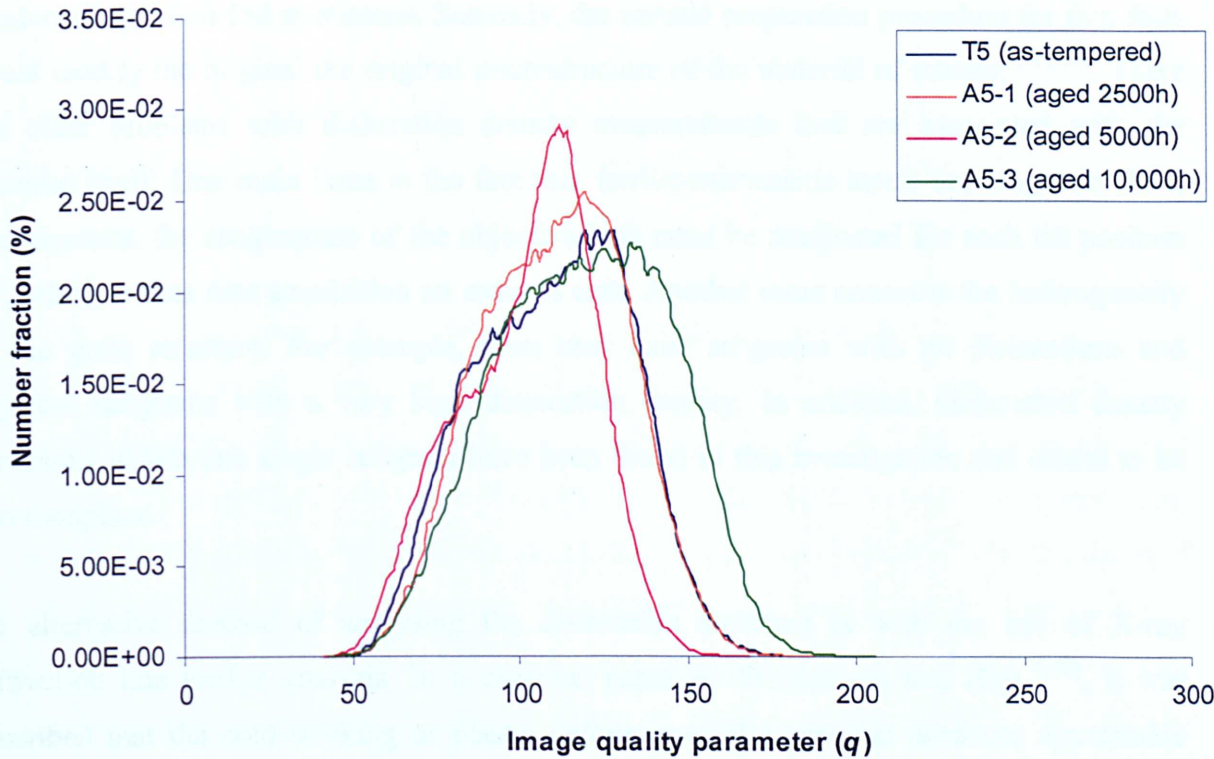


Figure 6.22: Plot showing the distribution of image quality parameter with respect to aging time at 650°C in the Bar 257 material. Aging treatments were performed for up to 10,000 h.

6.3 X-Ray Diffraction (XRD) Line Profile Analysis for the Assessment of Material Microstructure

In section 6.2, the use of electron backscatter diffraction as a means of monitoring the subgrain structure in ferritic-martensitic steels has been considered. It was proposed, however, that this technique lacks sufficient spatial resolution to monitor the dislocation structure, which represents an important strengthening mechanism in these materials. In the present section, an attempt has been made to quantify the dislocation structure as a function of aging time and varying creep loading conditions using X-ray diffraction, after a brief review of previous attempts and the challenges involved.

6.3.1 Review of the Application of XRD for the Quantification of Dislocations

Few examples of dislocation density measurements performed on ferritic-martensitic steels from transmission electron microscopy can be found published in the literature [2,76,77,78]. This is unsurprising given the many disadvantages associated with data acquisition with this technique. These have been highlighted by Pešićka *et al* [76], however a short account is presented here. Firstly, dislocation densities can only be evaluated from small regions in one TEM micrograph, which is also limited by the size of electron transparent areas that can be produced with thin-foil specimens. Secondly, the sample preparation procedure for thin foils could modify the original the original microstructure of the material of interest [76,139]. There are other problems with dislocation density measurements that are associated with the material itself. One main issue is the fact that ferritic-martensitic steels are magnetic. As a consequence, the astigmatism of the objective lens must be readjusted for each tilt position [76], which makes data acquisition an arduous task. Another issue concerns the heterogeneity of the grain structure. For example, there may exist subgrains with no dislocations and adjacent subgrains with a very high dislocation density. In addition, dislocation density variations within one single subgrain have been found in this investigation and others to be commonplace.

An alternative method of analysing the dislocation structure is with the use of X-ray diffraction line profile analysis. In a classical paper by Williamson and Hall [140], it was described that the cold working or plastic deformation of a material produces appreciable changes in the intensity distribution of diffracted X-rays, the most important being changes in the line shape and in integrated intensity. Several authors have thus found that lattice defects such as dislocations, point defects, and the presence of second-phase particles and inclusions

cause X-ray diffraction peaks to be broadened in many materials, as these induce stress fields in the microstructure by displacing atoms from their ideal lattice positions. Of these defects, Kužel^[141] argued that dislocations are the main reasons for strain broadening.

Indeed, XRD may overcome several problems associated with the measurement of dislocations in the TEM, with the most obvious advantage being the fact that information from significantly larger material volumes can be obtained. Other advantages include more straightforward and less ambiguous measurement. In addition, specimen preparation is somewhat simpler, which will limit the amount of damage induced in comparison to thin-foil preparation (see Chapter 3).

Only recently, XRD measurements have been used to quantify the microstructure of high Cr ferritic-martensitic steels, in particular P91 steel. Yajiang *et al*^[142] have calculated d-spacings from a tempered P91 steel weld in the base metal and weld metal regions and subsequently compared their values with the d-spacings published in the ICDD-JCPDS cards of α -Fe and Fe-Cr. The comparison produced a very good match, in the base metal and weld metal, to the ICDD-JCPDS card for Fe-Cr (ICDD card no. 34-396) in the main reflectors.

More recently, Tamura *et al*^[41] have measured changes in the breadth of the 110 peak in P91 steel as a function of tempering temperature, from 740 to 800°C, and times up to 500 hours. Interestingly, they found that the peak breadth decreased with increasing tempering times, which was attributed to recovery of the microstructure.

Arguably, the most comprehensive investigation in which XRD has been used to characterise P91 and similar materials, has been performed by Pešićka *et al*^[76]. Here, they systematically compared dislocation density measurements on P91 from TEM and XRD experiments, and the authors found that there was a good correlation between the two. From these initial, yet promising, results published in the literature, XRD line profile analysis has been employed in the present investigation in an attempt to complement results from EBSD in order to gain a better understanding of changes in the matrix microstructure as a function of varying long-term aging and creep parameters, with the view of applying numerical data into possible future microstructure-based models for creep deformation.

6.3.2 Some Considerations for Dislocation Density Measurements with XRD

The study of dislocation densities in complex multicomponent and multiphase materials such as high Cr ferritic-martensitic steel is by far a non-trivial task. The possibility of applying this technique to characterize these industrially important materials has been explored in this investigation. At this stage the results must be treated as indicative rather than an accurate representation of dislocation density. This is due to many factors, ranging from material related factors to the difficulties in data interpretation, which must be considered. A brief discussion of such issues is provided below.

A simple drawback of the characterisation of dislocations with XRD for the materials of interest is the fact that only average values of dislocations are yielded, provided an experimentally reasonable confidence in this technique can be asserted. The apparent heterogeneity of the distribution of dislocations, which increases with prolonged aging or creep exposure, is thus unaccounted for. Pešićka *et al* ^[76] expressed a similar concern. At present, however, as no attempt has been given to explain the impact of such microstructural heterogeneities on the creep behaviour of these materials, the evolution of average dislocation density values may suffice, in addition to mean subgrain size, to account for the microstructure evolution.

Kužel ^[141], and Kamminga and Seijbel ^[146], have also expressed concern about the fact that dislocations are treated as being straight, infinitely long, and are distributed in an ideal way, which may fail to adequately describe a strongly inhomogeneous, as in ferritic-martensitic steels, distribution of dislocations.

The rationalisation of XRD line broadening data with regards to dislocations in tempered ferritic-martensitic steels is further complicated by the distinction between two types of dislocations; free dislocations (ρ_f) and grain boundary dislocations (ρ_b), which are related to the total dislocation density (ρ_{tot}) in a material by the following simple relationship:

$$\rho_{tot} = \rho_b + \rho_f \quad [6.1]$$

To quote Pešićka *et al* ^[76], who refers to Straub *et al* ^[147]: ‘the total dislocation density is only 10% larger than those dislocations that make up grain boundaries.’ Therefore, in the event dislocations in grain boundaries cause line broadening, significant errors can be expected

when trying to rationalise the density of free dislocations. However, a favourable circumstance which allows the boundary dislocations to be separated from free dislocations in XRD analysis is the fact that low-angle boundaries – shown to increase in fraction with prolonged aging – have, unlike free dislocations, no long-range stress field ^[148]. This is an important consideration, as it is long-range stress fields that are required to rationalise line broadening ^[76,147].

The effect of stacking faults on the line broadening was deemed negligible by Pešićka *et al* ^[77], and was not considered in the present investigation. Although Ribarik *et al* ^[149] argued that stacking faults may contribute to broadening, they also reasoned that most often they are outnumbered by the density of the dislocations, which is a dominant feature in the microstructure of ferritic-martensitic steels.

6.3.3 XRD Analysis of the As-received P91 Steel Specimens

Figure 6.23 shows that there are appreciable differences between the XRD line intensity profiles of the two as-manufactured materials, Bar 257 and W20-3. Although the mean prior austenite grain sizes were similar for the two materials (15 and 11 μm), the hardness differences were much greater, 204 and 220 HV for Bar 257 and W20-3 respectively. This can be attributed to a variation in the severity of the pre-service tempering treatment, both of which were performed at 760°C. Nonetheless, the duration of each was 12 and 2.5 hours respectively. Therefore, from Figure 6.23, a qualitative expectation of material behaviour can be observed. To clarify, the material that has received the shortest pre-service tempering, W20-3, shows slightly broader and less intense peaks than Bar 257, where the peaks are expected to be sharper as the dislocation decreases during increased tempering times. These results are consistent with the findings of Tamura *et al* ^[40] and Pešićka *et al* ^[76].

Figure 6.24 shows the XRD profile associated with the 211 reflection of the as-manufactured materials. As expected, the Bar 257 material exhibits a sharper profile and also the two maxima, which correspond to $\text{CuK}_{\alpha 1}$ and $\text{CuK}_{\alpha 2}$ radiation, seem more pronounced.

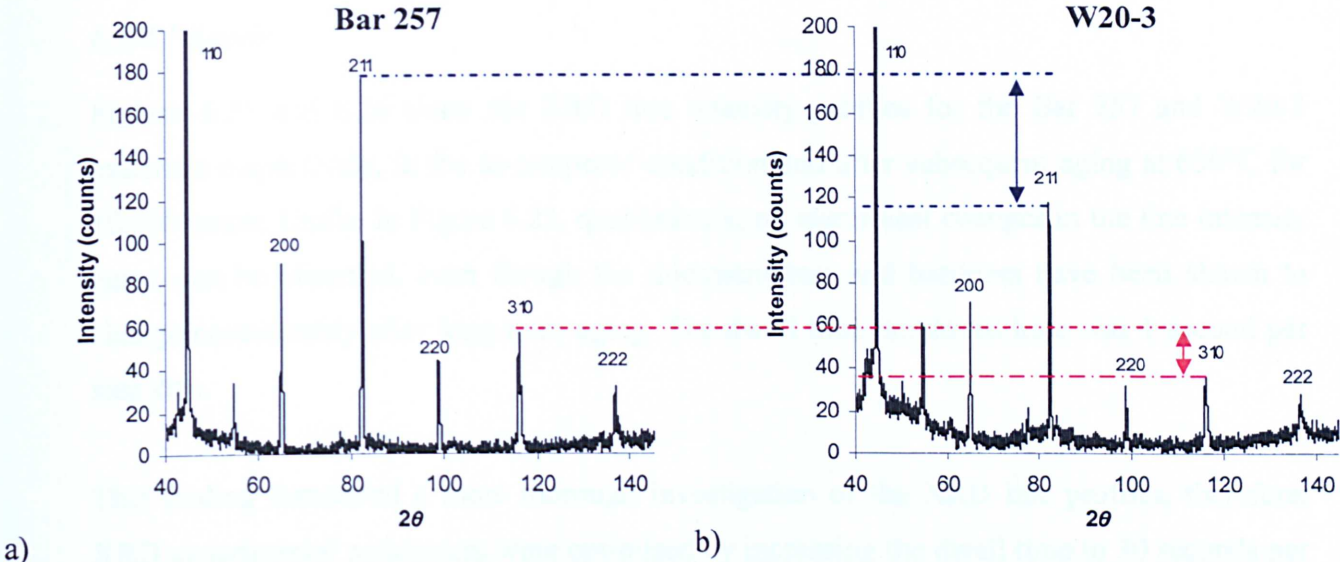


Figure 6.23: XRD line profiles of a) the W20-3 and b) the Bar 257 materials which were examined in the as-received (pre-service) condition. The XRD scan was performed at a 2θ angle range of 40 to 145° , with a 2θ step size of 0.02° and a dwell time of 1 second. The peaks correspond to the reflectors of the bcc ferrite iron crystal structure (ICDD card no. 04-0832). The blue dotted lines indicate the differences in peak height for the 211 reflector between the two materials, and similarly, the red lines indicate the peak height differences for the 310 reflector. Note: in both plots the 110 peak is truncated.

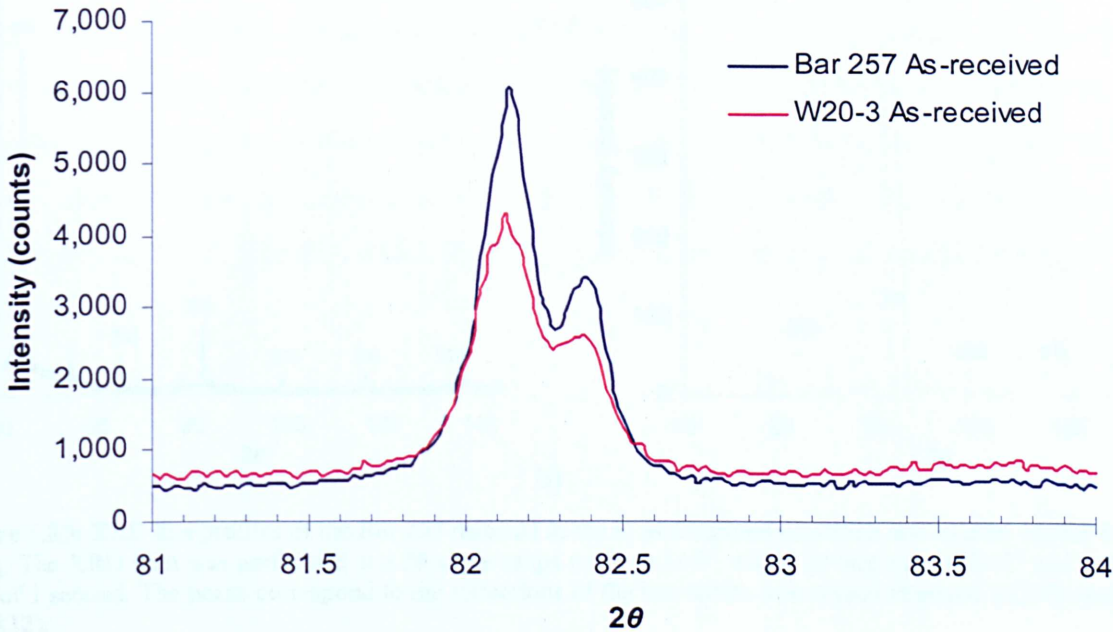


Figure 6.24: XRD line profiles showing the differences in the 211 between the two investigated as-manufactured materials. The 2θ step size was 0.02° and the dwell time was 30 seconds.

6.3.4 XRD Line Profile Analysis of Long-Term Aged Materials

6.3.4.1 Results

Figures 6.25 and 6.26 show the XRD line intensity profiles for the Bar 257 and W20-3 materials respectively, in the as-tempered condition and after subsequent aging at 650°C for 10,000 hours. Unlike in Figure 6.23, qualitatively, no significant changes in the line intensity curve can be observed, even though the microstructure and hardness have been shown to change considerably after long-term aging. The dwell time employed here was 1 second per step size.

This finding demanded a more thorough investigation of the XRD line profiles, therefore, XRD experimental parameters were optimised by increasing the dwell time to 30 seconds per step in order to increase the signal to noise ratio and obtain higher counts, which allow a quantitative analysis of the different reflectors in P91 steel to be made. These results are shown in Figures 6.27 and 6.28 for Bar 257 and W20-3 respectively.

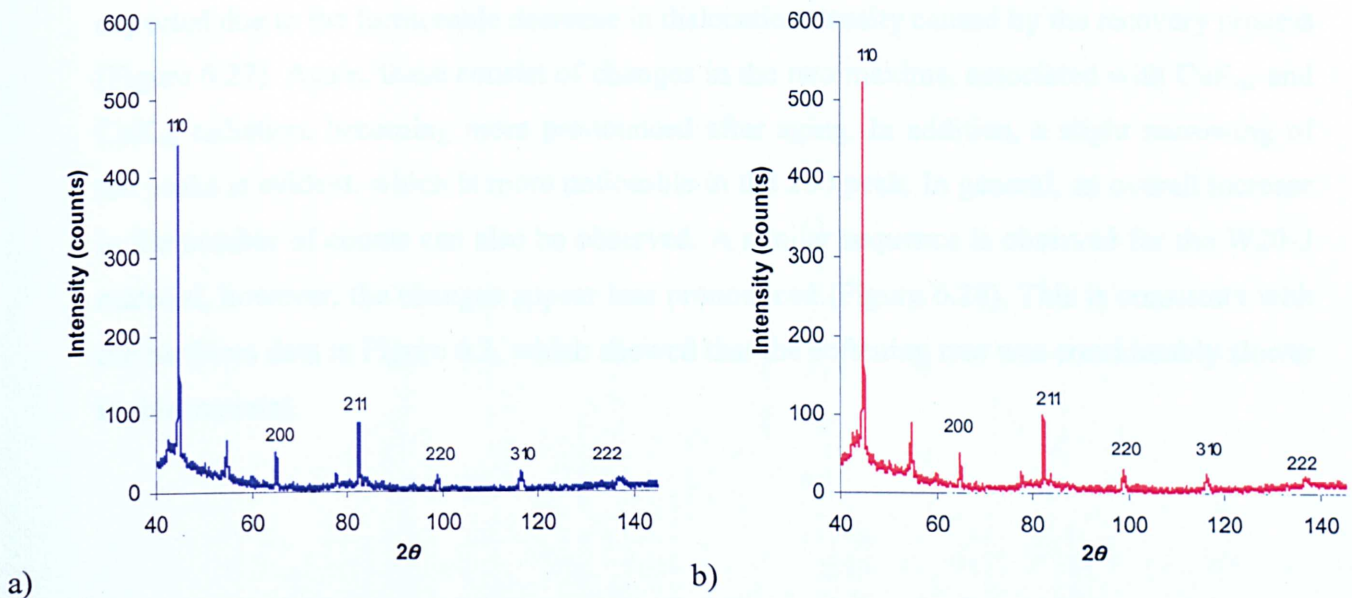


Figure 6.25: XRD line profiles of the Bar 257 material in the a) as-tempered condition and b) after 10,000 hours aging. The XRD scan was performed at a 2θ angle range of 40 to 145°, with a 2θ step size of 0.02° and a dwell time of 1 second. The peaks correspond to the reflections of the bcc ferrite iron crystal structure (ICDD card no. 04-0832).

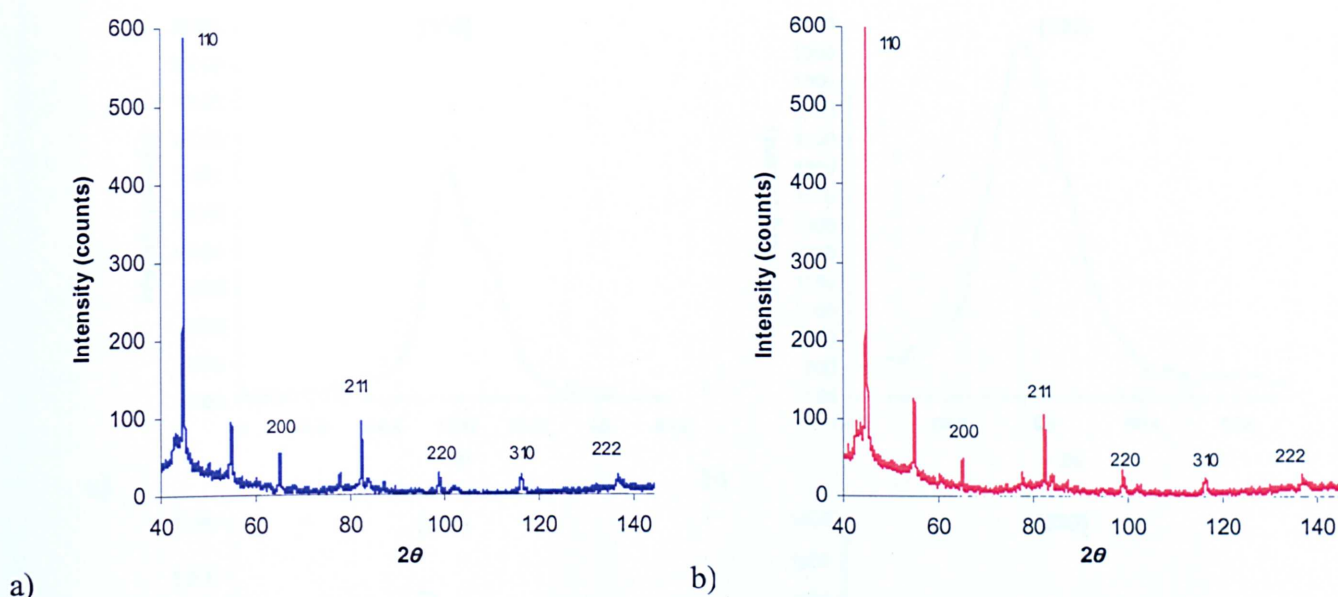


Figure 6.26: XRD line profiles of the W20-3 material in the a) as-tempered condition and b) after 10,000 hours aging. The XRD scan was performed at a 2θ angle range of 40 to 145° , with a 2θ step size of 0.02° and a dwell time of 1 second. The peaks correspond to the reflections of the bcc ferrite iron crystal structure (ICDD card no. 04-0832).

After 10,000 hours aging, the Bar 257 material exhibits changes in the peak profiles, which is expected due to the foreseeable decrease in dislocation density caused by the recovery process (Figure 6.27). Again, these consist of changes in the two maxima, associated with $\text{CuK}_{\alpha 1}$ and $\text{CuK}_{\alpha 2}$ radiation, becoming more pronounced after aging. In addition, a slight narrowing of the peaks is evident, which is more noticeable in the 200 peak. In general, an overall increase in the number of counts can also be observed. A similar sequence is observed for the W20-3 material, however, the changes appear less pronounced (Figure 6.28). This is consistent with the hardness data in Figure 6.3, which showed that the softening rate was considerably slower in this material.

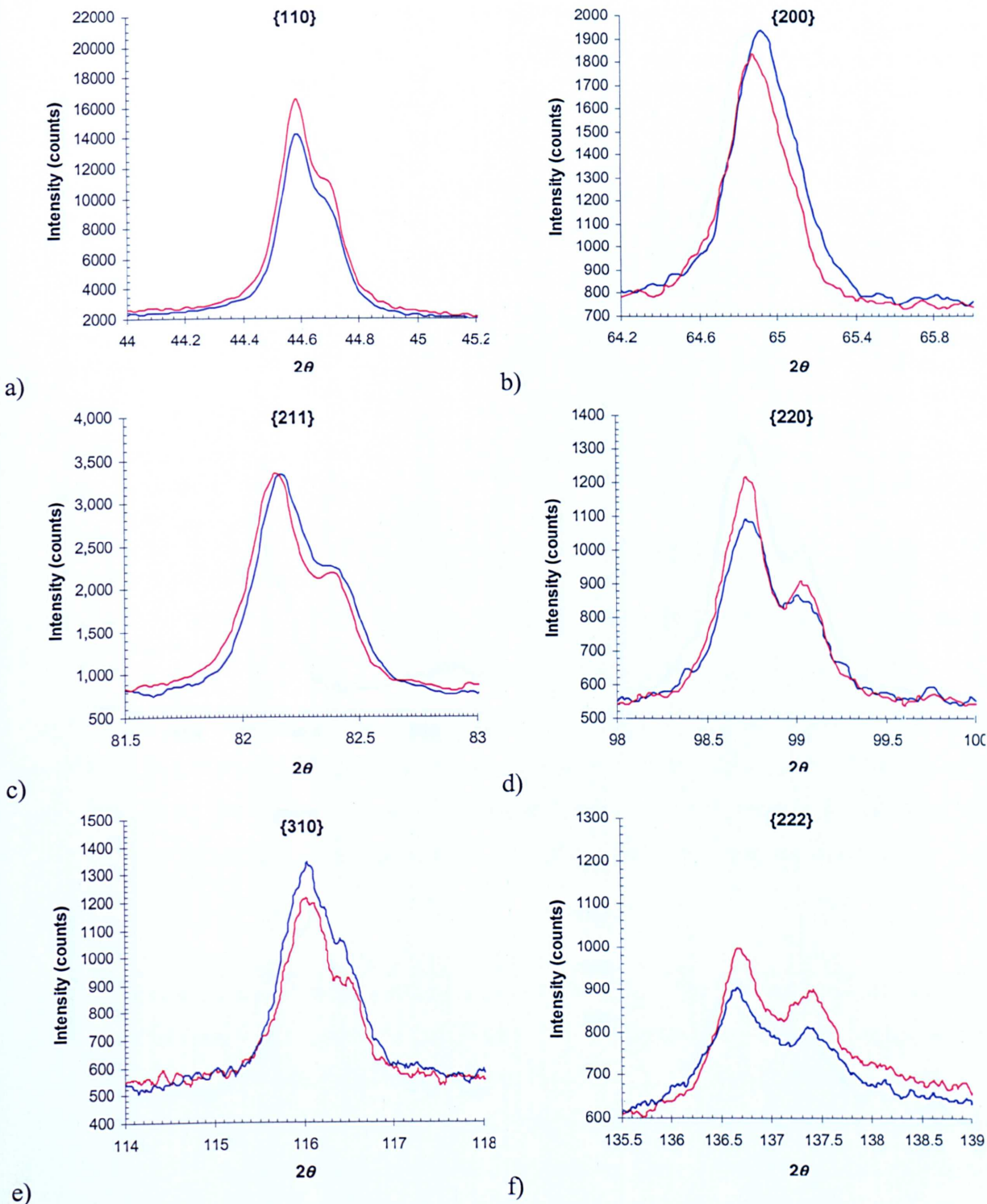


Figure 6.27: XRD line profiles of P91 Bar 257 samples in the as-tempered condition (blue) and after aging at 650°C for 10,000 hours (red). Each scan represents the following peaks; a) 110, b) 200, c) 211, d) 220, e) 310. The 2θ step size for each reflector was 0.02° and the dwell time was 30 seconds.

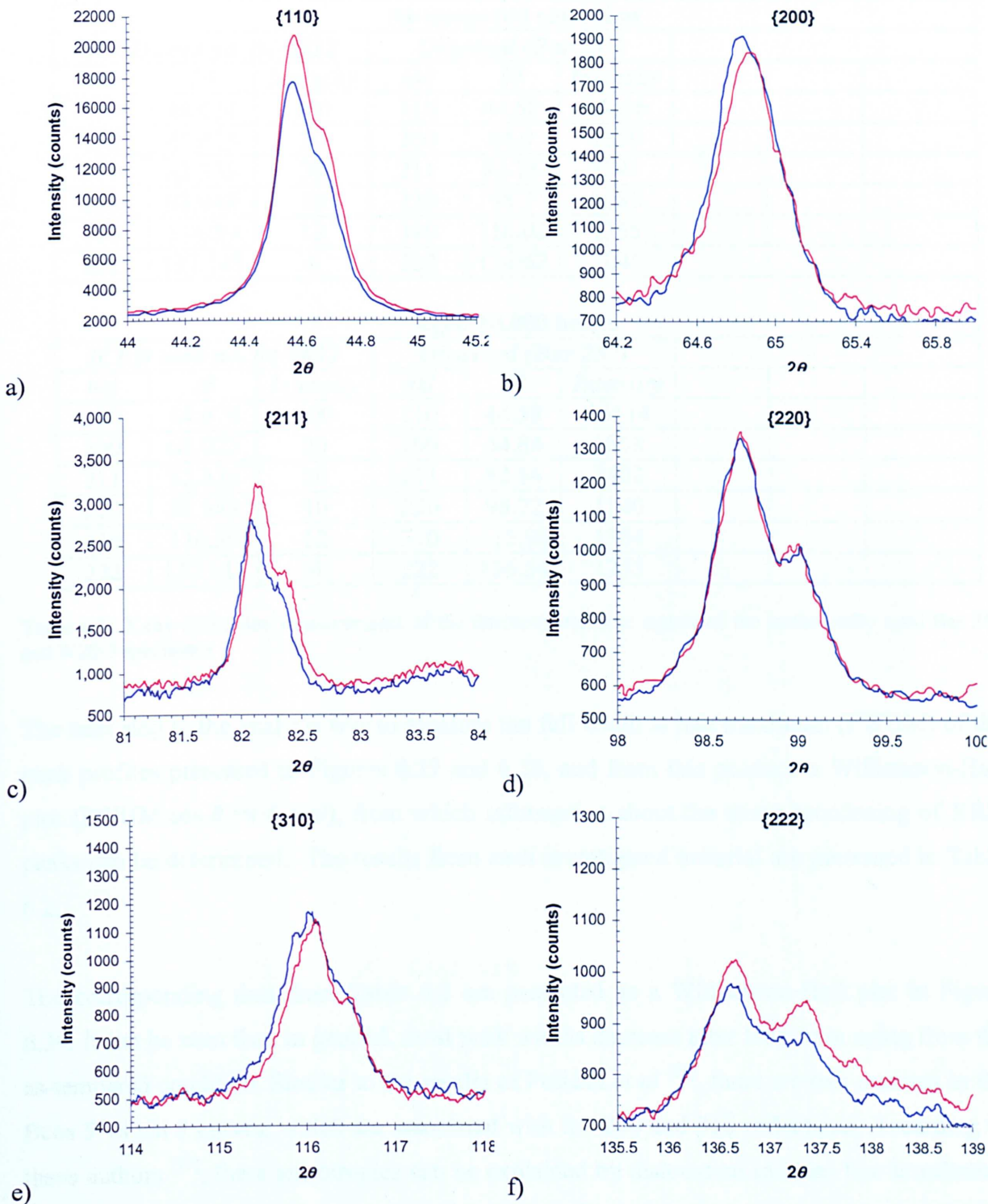


Figure 6.28: XRD line profiles of P91 W20-3 samples in the as-tempered condition (blue) and after aging at 650°C for 10,000 hours (red). Each scan represents the following peaks; a) 110, b) 200, c) 211, d) 220, e) 310. The 2θ step size for each reflector was 0.02° and the dwell time was 30 seconds.

As-tempered condition								
ICDD card no. 04-0832			Observed (Bar 257)			Observed (W20-3)		
<i>hkl</i>	2θ	Intensity	<i>hkl</i>	2θ	Intensity	<i>hkl</i>	2θ	Intensity
110	44.674	100	110	44.58	14256	110	44.58	17565
200	65.023	20	200	64.9	1859	200	64.8	1912
211	82.335	30	211	82.18	3341	211	82.08	2801
220	98.948	10	220	98.7	1088	220	98.58	1237
310	116.39	12	310	116.02	1355	310	116	1320
222	137.143	6	222	136.62	1046	222	136.58	1017
Aged 10,000 hours								
ICDD card no. 04-0832			Observed (Bar 257)			Observed (W20-3)		
<i>hkl</i>	2θ	Intensity	<i>hkl</i>	2θ	Intensity	<i>hkl</i>	2θ	Intensity
110	44.674	100	110	44.58	16514	110	44.58	20670
200	65.023	20	200	64.84	1858	200	64.88	1845
211	82.335	30	211	82.14	3402	211	82.12	3224
220	98.948	10	220	98.72	1340	220	98.72	1392
310	116.39	12	310	115.98	1354	310	116.1	1300
222	137.143	6	222	136.54	1255	222	136.54	1149

Table 6.1: X-ray diffraction measurements of the ferritic-martensitic matrix of the isothermally aged Bar 257 and W20-3 specimens

The next step in the analysis was to measure the full width at half maximum (FWHM) of the peak profiles presented in Figures 6.27 and 6.28, and from this produce a Williamson-Hall plot ($\text{FWHM} \cdot \cos \theta$ vs $4 \cdot \sin \theta$), from which information about the strain broadening of XRD peaks can be determined. The results from each investigated material are presented in Table 6.2.

The corresponding data from Table 6.2 are presented as a Williamson-Hall plot in Figure 6.29. It can be seen that, in general, most peak widths decrease after long-term aging from the as-tempered condition. Similar to the results of Pešićka *et al* ^[76], there are two maxima in the $\text{Bcos } \theta$ vs $\sin \theta$ curves, which are associated with the 200 and 310 reflections. According to these authors ^[77], these anisotropies can be explained by dislocation induced line broadening and the corresponding orientation (contrast) factors for the most common slip systems in the bcc structure. Indeed, Dragomir *et al* ^[139] further explain that the anisotropic X-ray line broadening effect can be detected due to the fact that neither the full width at half maximum (FWHM) nor the integral breadths are monotonic functions of the dislocation vector, thus, asymmetric X-ray line shapes are caused by heterogeneous dislocation densities of one sign, within dislocation walls or sub-boundaries. Thus, from Figure 6.29 there is a limited trend

towards a decrease in strain anisotropy with increasing time at temperature for both materials. However, this is more evident in the Bar 257 material.

Material and condition	$\{hkl\}$	FWHM ($2\theta/\text{degrees}$)	FWHM.cos θ (radians)
<i>Bar 257</i> <i>As-tempered</i> <i>(750°C 2h)</i>	110	0.21	0.00339
	200	0.37	0.00545
	211	0.4	0.00526
	220	0.54	0.00614
	310	1.06	0.00979
	222	1.34	0.00863
<i>Bar 257</i> <i>Long-term</i> <i>aged</i> <i>(650°C</i> <i>10,000h)</i>	110	0.21	0.00339
	200	0.37	0.00545
	211	0.28	0.00368
	220	0.3	0.00341
	310	1.03	0.00951
	222	1.2	0.00785
<i>W20-3</i> <i>As-tempered</i> <i>(750°C 2h)</i>	110	0.22	0.00355
	200	0.39	0.00574
	211	0.43	0.00566
	220	0.37	0.00421
	310	0.88	0.00813
	222	1.22	0.00786
<i>W20-3</i> <i>Long-term</i> <i>aged</i> <i>(650°C 10,000h)</i>	110	0.22	0.00355
	200	0.37	0.00545
	211	0.38	0.00499
	220	0.35	0.00398
	310	0.82	0.00767
	222	1.19	0.00773

Table 6.2: Values of full width at half maximum determined from X-ray line profile analysis performed on the investigated Bar 257 and W20-3 materials.

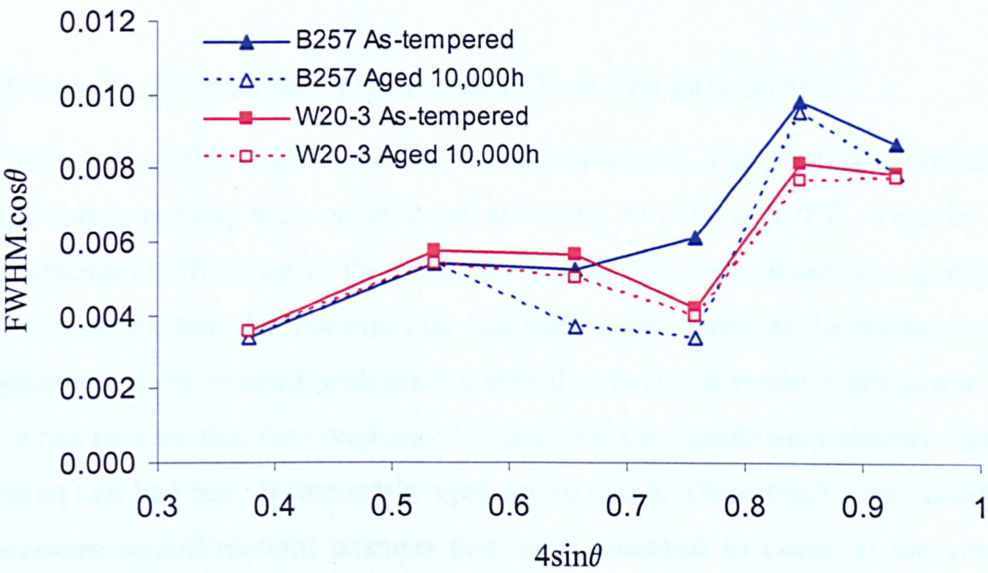


Figure 6.29: Williamson–Hall plots for the Bar 257 and W20-3 materials. The figure shows four series of XRD peak widths as a function of $\sin \theta$.

6.3.4.2 Discussion

Early work published by Mazur^[143] and Hall^[144] suggested that if a graph of $B\cos\theta$ against $\sin\theta$ is made, a horizontal straight line will be obtained if the specimen has a small crystallite size but no strain; whereas a straight line passing through the origin will be obtained if there are strains but the crystal size is large. The same authors hypothesized that if broadening is due to both effects, and if the line breadth is the sum of the breadths due to the two effects separately, then a straight line will still be obtained. Thus, the crystal size can be calculated from the intercept on the $B\cos\theta$ axis, and the mean strain can be found from the slope. However, Stokes (in Peiser *et al*^[145]) suggested that in general the strains are not additive, and a straight line will not be obtained, but the departure from a straight line relation is unlikely to be very marked, especially if the broadening is due to one factor.

From the aforementioned hypothesis of Stokes (in Peiser *et al*^[145]), it is possible that the XRD line profile broadening of the investigated materials, as shown in Figure 6.29, could be due to the effects of both crystallite size and strain, given the disparity of the $B\cos\theta$ vs $\sin\theta$ curve to a straight line relationship, which provides an uncertainty in data analysis. On the contrary, Pešićka *et al*^[76] asserted that subgrains were generally larger than $0.1\ \mu\text{m}$, which they argued, negates the influence of crystallite size broadening. Since the subgrain diameters measured in the present study exceed this minimum value, the possibility of deriving values of dislocation density from XRD measurements warrants the effort to apply this technique to high Cr ferritic-martensitic steels.

6.3.5 XRD Line Profile Analysis of Accelerated Creep Test Specimens

Figure 6.30 shows the XRD line profiles associated with the 211 and 310 peaks obtained from the Bar 257 specimens that were creep tested at 60 and 93 MPa at 650°C . It can be seen that there is a noticeable difference in the peak profile shape between these two specimens. For example, it is shown that the material that had been creep tested at the higher stress has a much sharper and more defined peak profile than the specimen tested at the lower stress. In addition, it can be seen that the creep tested specimens are significantly sharper than the Bar 257 specimen that had been isothermally aged for 10,000 h. These results are consistent with the more severe microstructural changes that were observed to occur in the creep tested specimens. Table 6.3 shows the measured values of the peak breadths.

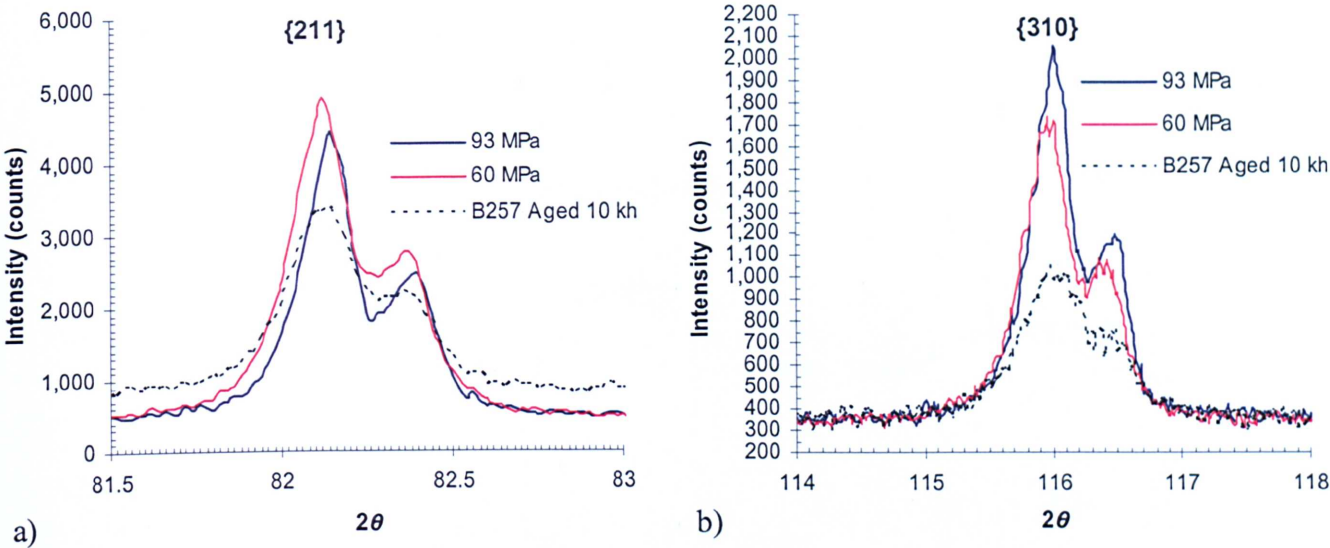


Figure 6.30: XRD line profiles of the a) 211 and b) 310 reflectors of the P91 Bar 257 samples that were creep tested at 650°C at 60 and 93 MPa . Also shown for comparison are the XRD data for the Bar 257 material that was isothermally aged for 10,000 h at 650°C. The 2θ step size for each reflector was 0.02° and the dwell time was 30 seconds.

Material and condition	{hkl}	FWHM (2θ/degrees)	FWHM.cos θ (radians)
<i>Bar 257 Crept (650°C 60 MPa)</i>	110	0.19	0.00306732
	200	0.34	0.00500771
	211	0.21	0.00276278
	220	0.23	0.00261323
	310	0.4	0.00369315
	222	0.58	0.00373527
<i>Bar 257 Crept (650°C 93 MPa)</i>	110	0.12	0.00193726
	200	0.23	0.00338753
	211	0.175	0.00230228
	220	0.19	0.00215873
	310	0.35	0.00323138
	222	0.44	0.00283363

Table 6.3: Values of full width at half maximum determined from X-ray line profile analysis performed on the investigated Bar 257 creep specimens.

It can be seen from Figure 6.30 that the peak breadths are considerably narrower in the accelerated creep tested specimens than those in the long-term aged P91 specimens shown in Figure 6.29. As with the previous graph, the presence of two maxima, which correspond to the 200 and 310 reflections, can be detected. Interestingly, all peak widths were narrower in the 93 MPa specimen, even though this condition exhibited the highest hardness value in the gauge region. However, the profiles of the investigated creep tested specimens were very similar, which reflects the extensive damage incurred by the application of high stresses and strains.

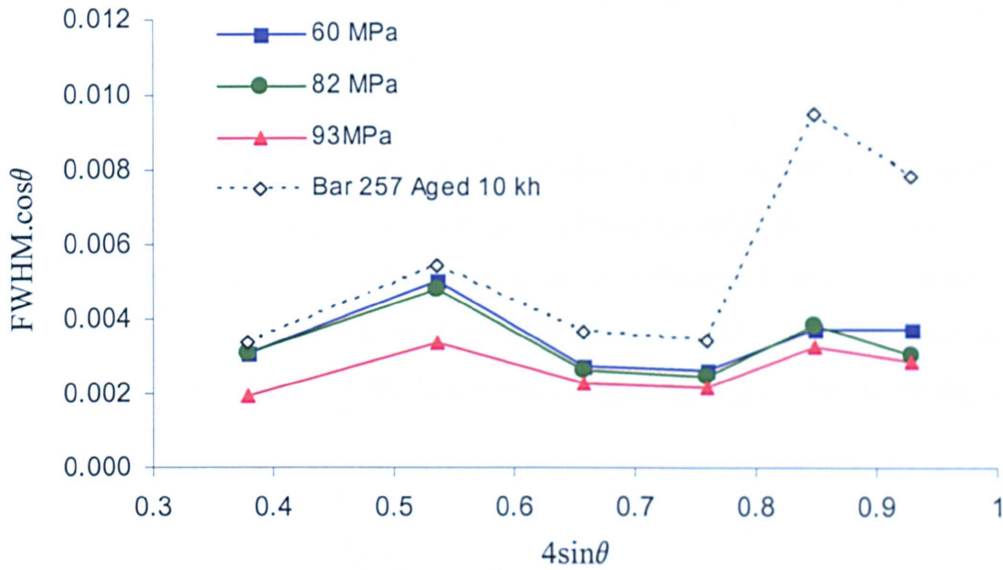


Figure 6.31: Williamson–Hall plots for the Bar 257 subjected to different stresses during creep testing at 650°C. The figure shows four series of XRD peak widths B (in reciprocal space units) as a function of $\sin \theta$. Also shown for comparison are the results from the Bar 257 material that had been isothermally aged for 10,000 h at 650°C.

The results from XRD analysis on the accelerated creep tested specimens are in reasonable agreement with microstructural characterisation and hardness analysis results, whereby the poorer mechanical properties of the creep tested materials can be associated with a dramatic decrease in dislocation density due to a significant decrease in strain anisotropy, as well as particle size distribution and subgrain growth, both of which have been extensively investigated earlier.

6.3.6 XRD Analysis of Dislocation Densities in P91 Steel

In order to derive values of dislocation density from XRD line profile analysis, Pešićka *et al* [77] used a simplified procedure by Kužel *et al* [141], whereby the peak breadth, β , is related to the dislocation density, ρ , by the following equation:

$$\beta = \frac{k}{D} + b_0 \cdot W(g) + B_0 \cdot \sqrt{\rho} \cdot \sqrt{\langle \chi \rangle} \cdot \frac{\sin \theta}{\lambda} + O^2 \quad [6.2]$$

where k is the Scherrer constant, D is the mean domain size, b_0 is a factor accounting for the effect of stacking faults, $W(g)$ is an orientation dependent factor, $B_0 = A_0 \cdot b \cdot \sqrt{2 \cdot \ln P}$ (where: $A_0 \sim 1$, b is the Burgers vector and P accounts for the correlation between dislocations), χ is the

contrast factor, O^2 denotes higher order terms and λ and θ have their usual meanings of wavelength and diffraction angle respectively.

The main difficulty encountered in the present study, by applying the above equation, was that several parameters are unknown and as such difficult to quantify. In a later paper, Kužel^[141] published a similar equation, which excluded the effects of domain (crystallite) size, stacking faults and orientation, terms neglected by Pešićka *et al*^[76] as they were deemed to make no significant contribution to the line broadening, which gave the following simplified relationship:

$$\beta = b\sqrt{\rho}\sqrt{\chi}\sqrt{\frac{\ln P}{2}}A\frac{\sin\theta}{\lambda} \quad [6.3]$$

In the same publication^[141], P , which is the factor related to the correlation in dislocation arrangement, can be estimated to equal 3 for a Cauchy profile shape, which gave the best approximation to the data obtained in the present investigation. A significant concern, according to Kužel^[141], is that the calculation of P is very complicated as it is dependent on other factors that are unknown, a discussion of which is not attempted here.

The Burgers vector line length, b , was assumed to be 2.5\AA , which is the approximate value for a bcc ferrite crystal structure.

In order to determine the contrast factor, χ , the equation in the Kužel paper^[141] was rearranged to obtain this value, which required *a priori* knowledge of the dislocation density that was provided in the paper by Pešićka *et al*^[76]. This value was found to be very small ($\sim 10^{-19}$) and also found to vary slightly according to material condition and crystallographic reflector. However, it was not found to affect the calculated results significantly. For the present investigation, values of $\chi = 3.11 \times 10^{-19}$ and 2.31×10^{-19} were used for the 200 and 310 reflections respectively, which correspond to dislocation induced line broadening^[141]. This factor, Kužel^[141] describes, determines the hkl-dependence of the diffraction parameter, which is determined by the elastic characteristics of the material and by the orientation of the defects with respect to the diffraction vector and crystallographic axes.

Parameter	Value
$\beta_{\{200\}}$	From Table 6.2
$\beta_{\{310\}}$	From Table 6.2
$\chi_{\{200\}}$	3.11×10^{-19}
$\chi_{\{310\}}$	2.31×10^{-19}
P	3
λ	$1.5418 \times 10^{-10} \text{ m}$

Table 6.4: Values used for the parameters from equation 6.2 in order to calculate the dislocation density from X-ray line profile analysis.

6.3.6.1 Results

From equation 6.3 and the values of the various parameters shown in Table 6.3, the dislocation densities of long-term aged and crept specimens have been derived and these are shown in Table 6.4. In the as-tempered condition, the Bar 257 material is shown to have a higher dislocation density than W20-3, which is consistent with the hardness results from Figure 6.3, where the as-tempered hardness value of the specimens that had previously been normalized at 1100°C for 15 minutes was higher in Bar 257 (250 HV) than in W20-3 (232 HV).

It can be seen that long-term aging promotes a decrease in dislocation density from the as-tempered condition to aging for 10,000 hours. In the Bar 257 material the dislocation density is shown to decrease from 3.15 to $3.01 \times 10^{14} \text{ m}^{-2}$. Interestingly, the decrease in dislocation density after aging was more pronounced in the W20-3 material, from 2.65 to $2.37 \times 10^{14} \text{ m}^{-2}$ after aging for 10,000 h, even though the hardness drop from the as-tempered condition was lower in the W20-3 material than the Bar 257 material, ~32 and ~55 HV respectively.

It is also shown, from Table 6.4, that the application of creep strain promotes a much stronger decrease in dislocation density compared to stress free aging. For example, the values of dislocation density were considerably smaller after short-term creep testing, than after stress free aging for 10,000 hours at the same temperature. There was also a big difference between the dislocation density values of the specimens that were crept at 60 and 93 MPa, 1.25 and $0.66 \times 10^{14} \text{ m}^{-2}$ respectively, indicating that increasing the applied creep stress decreases dislocation density at a faster rate.

In general, the results presented in Table 6.5 are in good agreement with data that are available in the literature for the dislocation density of high Cr tempered ferritic-martensitic power plant steels.

Material and Condition	Mean Subgrain Diameter, w (10^{-6}m)	Dislocation density, ρ_f (10^{14}m^{-2})
P91 (W20-3) tempered 750°C 2 h	0.649	2.65
P91 (W20-3) aged 650°C 10,000 h	0.346	2.37
P91 (B257) tempered 750°C 2 h	0.517	3.15
P91 (B257) aged 650°C 10,000 h	0.476	3.01
P91 (B257) creep tested 60 MPa 650°C/2,200 h	1.32	1.25
P91 (B257) creep tested 93 MPa 650°C/84 h	1.46	0.66
*P91 annealed 1050°C 1 h, water quenched	-	4.2
*P91 (as above) + tempered 750°C 1 h	-	0.79
*P91 (as above) + tempered 750°C 100 h	-	0.06
*X20 annealed 1050°C 1 h, water quenched	0.341	9.4 (9.26)
*X20 (as above) + tempered 750°C 1 h	0.373	0.86 (0.98)
*X20 (as above) + tempered 750°C 100h	0.428	0.09
+P92 normalized 1070°C, tempered 715°C 2 h	0.37	(9.0)
+P92 normalized 1070°C, tempered 775°C 2 h	0.42	(7.5)
+P92 normalized 1070°C, tempered 835°C 2 h	0.5	(2.3)
+P92 normalized 1070°C, tempered 775°C 2 h, creep tested 600°C/1,500 h	0.7	(5.3)
+P92 normalized 1070°C, tempered 775°C 2 h, creep tested 600°C/33,000 h	1.5	(1.5)

Table 6.5: Comparison of subgrain diameters and dislocation densities for a range of high Cr tempered ferritic-martensitic steels and heat treatment conditions between those obtained in the investigation and some values found in the literature. The numbers in brackets represent dislocation densities determined by TEM measurements. * from the Pešićka paper ^[77], + from the Ennis paper ^[2].

6.3.6.2 Discussion

XRD line profile analysis has been used to determine the dislocation density of P91 samples that have been isothermally aged for long periods and creep tested. The results presented in Table 6.5 are consistent with dislocation density values published in the literature for similar materials. An interesting finding was that, in the creep tested specimens, the lowest value of dislocation density corresponded to the material which exhibits the largest mean subgrain size. This result agrees well with the work of Ennis *et al* ^[2], who showed that there is a relationship between the subgrain size and the dislocation density in P92 steel that was creep tested at 600°C, whereby the larger subgrain sizes observed after longer creep testing periods correspond to a lower dislocation density. Cerjak *et al* ^[3] published similar findings for the 12% Cr cast G-X12CrMoVWNbN. However, such a trend was not evident for the long-term aged materials investigated in this study. Here it is shown that, although the dislocation density decreases, the subgrain size has also shown a slight decrease after 10,000 hours aging in both the Bar 257 and W20-3 materials. This is because the mean subgrain size decreased

due to the onset of subgrain formation after aging to 10,000 hours, which was earlier attributed to the rearrangement of dislocations into a lower energy configuration. It is thus expected that further aging will, henceforth, agree better with the hypotheses in the literature.

6.4 Summary

The evolution of the matrix microstructure of grade 91 steel subjected to varying thermal aging and creep conditions have been discussed. Two techniques, EBSD and XRD, have been shown to be particularly valuable in studying, and quantifying, various microstructural parameters which can describe the microstructural degradation of the matrix in ferritic-martensitic high Cr steels.

EBSD has been shown to be a powerful tool for quantifying microstructural change. The microstructural evolution during long-term aging consists of gradual subgrain nucleation and growth within tempered martensite laths. The lath structure was stable at aging times up to 10,000 h at 650°C. This process, in addition to being evident on visual inspection of EBSD maps, was quantified in terms of both the increase in total grain boundary line length and also the increase in the ratio of low to high-angle boundaries as a function of prolonged high temperature exposure. These results have been validated by comparing a standard P91 composition (W20-3) with a known weak cast (Bar 257), and it has been shown that the latter has both a longer grain boundary line length and a higher low to high-angle boundary ratio over the range of aging times investigated.

XRD, to a lesser extent, has also been shown to yield useful information on the dislocation density of tempered martensitic-ferritic steels. As expected, increased aging time was accompanied by a subsequent decrease in dislocation density. Creep strain accumulation, in corroboration with published data, was shown to promote an accelerated decrease in dislocation density. Although the values of dislocation density obtained with XRD are consistent with literature values from TEM analysis, there remain concerns about the accuracy of the derivation of dislocation parameters from line broadening. Nonetheless, the combination of XRD line profile analysis and EBSD have shown to yield fruitful quantitative descriptions of the matrix structure in P91 steel.

Chapter 7

MICROSTRUCTURE OF EX-SERVICE MATERIALS

7.1 Introduction

The effects of thermal aging and creep on the microstructural evolution of minor phase precipitates and the matrix microstructure in P91 under thermal conditions, whereby accelerated microstructure change is expected to occur, have been discussed in detail in Chapters 5 and 6.

Pertinent to the theme of remanent lifetime assessment of grade 91 steel based on an understanding of microstructure, it is vitally important to verify whether accelerated creep and aging tests produce microstructures that are representative of “real” microstructures, formed under typical plant operating conditions. Such an understanding is invaluable in order to make an informed judgement on the remaining creep life as a function of microstructure. Given the relatively recent deployment of such materials for critical high temperature components, there is a distinct lack of microstructural data from ex-service materials out to significant service times available in the literature. Therefore, in order to address this issue, several ex-service P91 specimens were examined after cyclic operation in power plant. The specimens originated from various P91 components that had been exposed in service for similar periods of time. The components resided in regions where conditions of high temperature creep prevail, whose origins have been described in Chapter 3.

In this chapter, both the minor phase precipitation and the matrix microstructure of ex-service materials have been investigated. For experimental consistency, the materials investigated in this chapter have been characterized using the same analytical techniques used in the preceding chapters.

7.2 Materials and Experimental Techniques

The component identities, including the exposure time, post-service hardness and creep strain rate are shown in Table 7.1. The chemical composition of each of the investigated materials was shown in Table 3.1 in Chapter 3. It is interesting to note that the creep strain rate is an order of magnitude lower in the Tee-piece material than the U2B2 and Bottle 2 specimens after service exposure, indicating a lower creep strength in the latter two materials, even

though the three materials have been exposed to similar operating times and conditions. The results from the impression creep tests give a strong indication that the microstructure evolution of the ex-service materials may be radically different on subsequent high temperature exposure under the same conditions. On this basis, each ex-service specimen was subsequently subjected to an additional re-aging heat treatment of 750°C for 100 hours in a conventional chamber furnace in order to promote considerable additional microstructural degradation to facilitate the comparison of the rate of microstructural change between each material. The materials investigated in this chapter have, therefore, been examined in the ex-service condition and after the re-aging heat treatment.

Specimen	Component and condition	Exposure time at 568°C (h) [†]	Hardness (HV)	Mean prior-austenite grain size (μm)	Minimum creep strain rate at 600°C/155MPa impression test [*]
Bottle 2	Transition Bottle	30,000	179	17 ± 5	$1.61 \times 10^{-3} \text{ hr}^{-1}$
Tee-piece	Superheater tee-piece	32,000	183	32 ± 12	$2.87\text{-}6.13 \times 10^{-4} \text{ hr}^{-1}$
MAES	Heat exchanger pipe	56,000	201	12 ± 4	-
U2B2	Header endplate	36,000	175	24 ± 9	$1.2 \times 10^{-3} \text{ hr}^{-1}$

Table 7.1: Summary of the ex-service specimens investigated in this chapter. * Impression creep test results from Brett ^[41]. [†] This temperature represents a nominal value of the steam temperature, which is subject to minor fluctuations due to adjustments in plant operating conditions.

7.3 Results from Microstructural Characterization

7.3.1 Thermodynamic Modelling of Minor Phase Precipitates

Prior to the microstructural characterisation of minor phase precipitates, a preliminary understanding of the characteristics of such precipitates was achieved by performing equilibrium thermodynamic calculations using the chemical composition data of the ex-service materials. Thermodynamic data for the MAES material is not presented here, as the cast composition of this material was not available. Figure 7.1 shows results for the predicted mass fraction of the M_{23}C_6 , AlN and (V,Nb)(N,C) precipitates in the investigated ex-service specimens. It can be seen that there is an appreciably higher predicted fraction of M_{23}C_6 precipitates in the U2B2 material, due mainly to the much higher carbon concentration (0.14 wt.%) in comparison to the Tee-piece (0.105 wt.%) and Bottle 2 materials (0.097 wt.%).

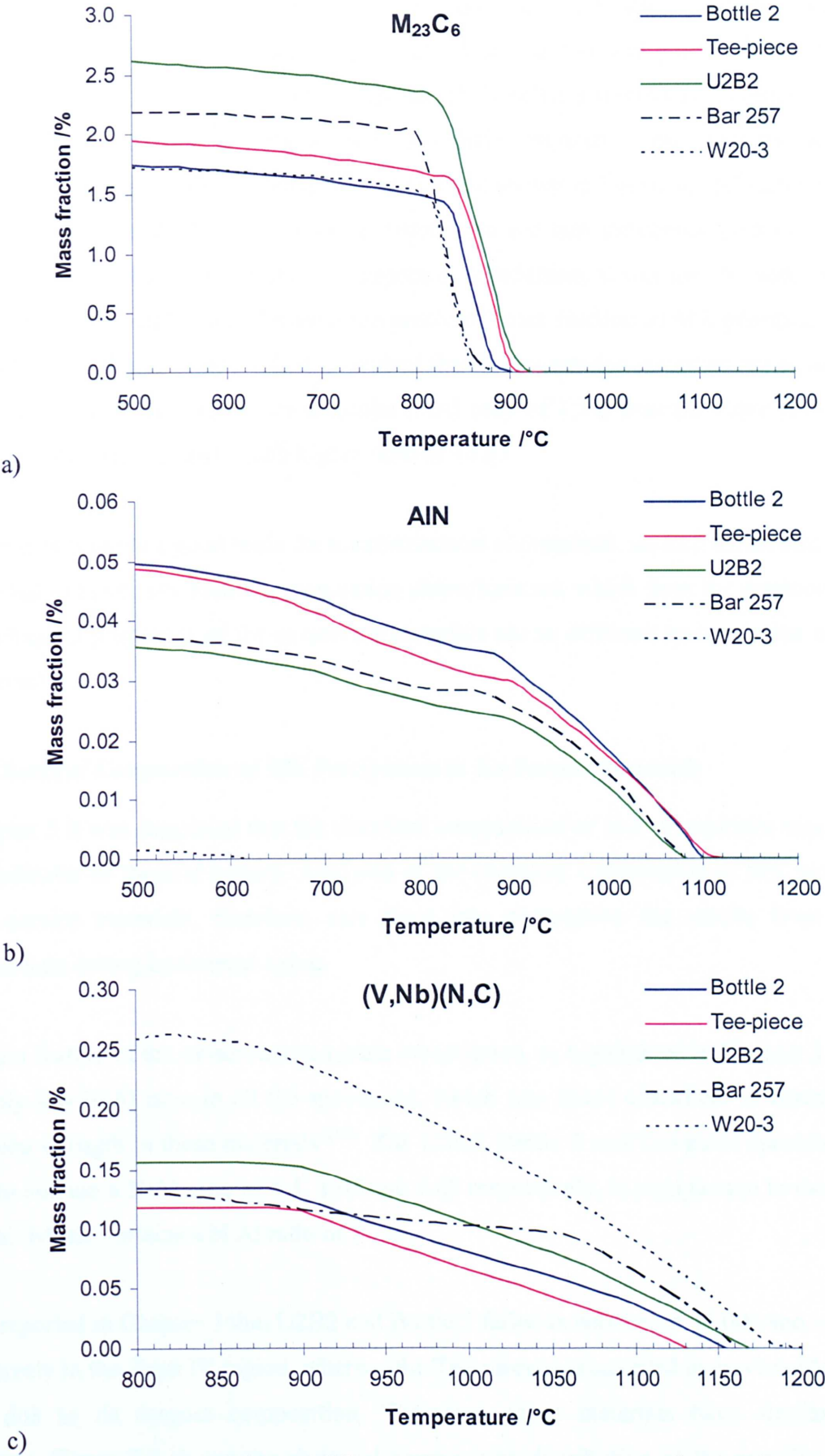


Figure 7.1: Mass fraction calculations of different minor phase precipitates predicted to be present in the investigated ex-service specimens; a) $M_{23}C_6$, b) AlN and c) $(V,Nb)(N,C)$. Also shown for comparison are the data from the ‘as-received’ Bar 257 and W20-3 materials

The Bottle 2 and Tee-piece specimens have an identical N:Al ratio of 1.055, whereas the U2B2 specimen had a slightly larger ratio of 1.5. Close attention was paid to determine if this factor has an effect on the formation of AlN and (V,Nb)(N,C) precipitates. Figure 7.1 shows that the predicted fraction of AlN is lower in U2B2 compared to the other two materials, although the differences are not as significant as those shown in Figure 4.3 (Chapter 4), which is expected because the N:Al ratio value differences are less pronounced between the ex-service specimens than those previously reported. In addition, it can also be seen that there were no significant differences between the predicted mass fraction of MX precipitates in the three specimens. From Figure 7.1, it is evident that the ex-service materials are most similar to the Bar 257 material, which has a similar N:Al ratio of 1.11, than the more conventional W20-3 material, which has a much higher ratio of 13.33.

These results provide a good basis for microstructural comparison, as each ex-service material is expected to have very similar precipitation characteristics, which begs the question of why the mechanical properties of the ex-service materials are so different under similar operating conditions?

7.3.2 Chemical Composition of MX Precipitates in Ex-Service Materials

In Chapter 5 it was suggested that the chemical composition of MX precipitates may be used as an indicator of thermal history. Analyses of the chemical composition of MX particles in the ex-service materials, therefore, can place into perspective the results from particle compositions during isothermal aging.

The main feature of the ex-service materials investigated, as highlighted in Chapter 3, was the relatively low N:Al ratio in all the specimens, which was found elsewhere to correlate with low creep strength in these materials ^[41]. The U2B2, Bottle 2 and Tee-piece specimens were found to contain a N:Al ratio of 1.5, 1.05 and 1.05 respectively, in comparison to the Bar 257 material, which contains a N:Al ratio of 1.11.

It was reported in Chapter 3 that U2B2 and Bottle 2 failed in service, at 36,000 and ~30,000 h respectively in the Type IV region, whereas the Tee-piece was sampled in service after 32,000 hours due to its suspect composition. Therefore, these materials have similar service exposures. Figure 7.2 shows the chemical composition distribution of the metallic elements Nb, V and Cr in the MX carbonitride precipitates, measured with EDS in the TEM, of the ex-

service materials investigated. Each point represents the composition of a single measured particle. It can be seen that large differences in the chemical composition distribution of MX particles were found between the investigated ex-service specimens. These findings can be rationalized as follows.

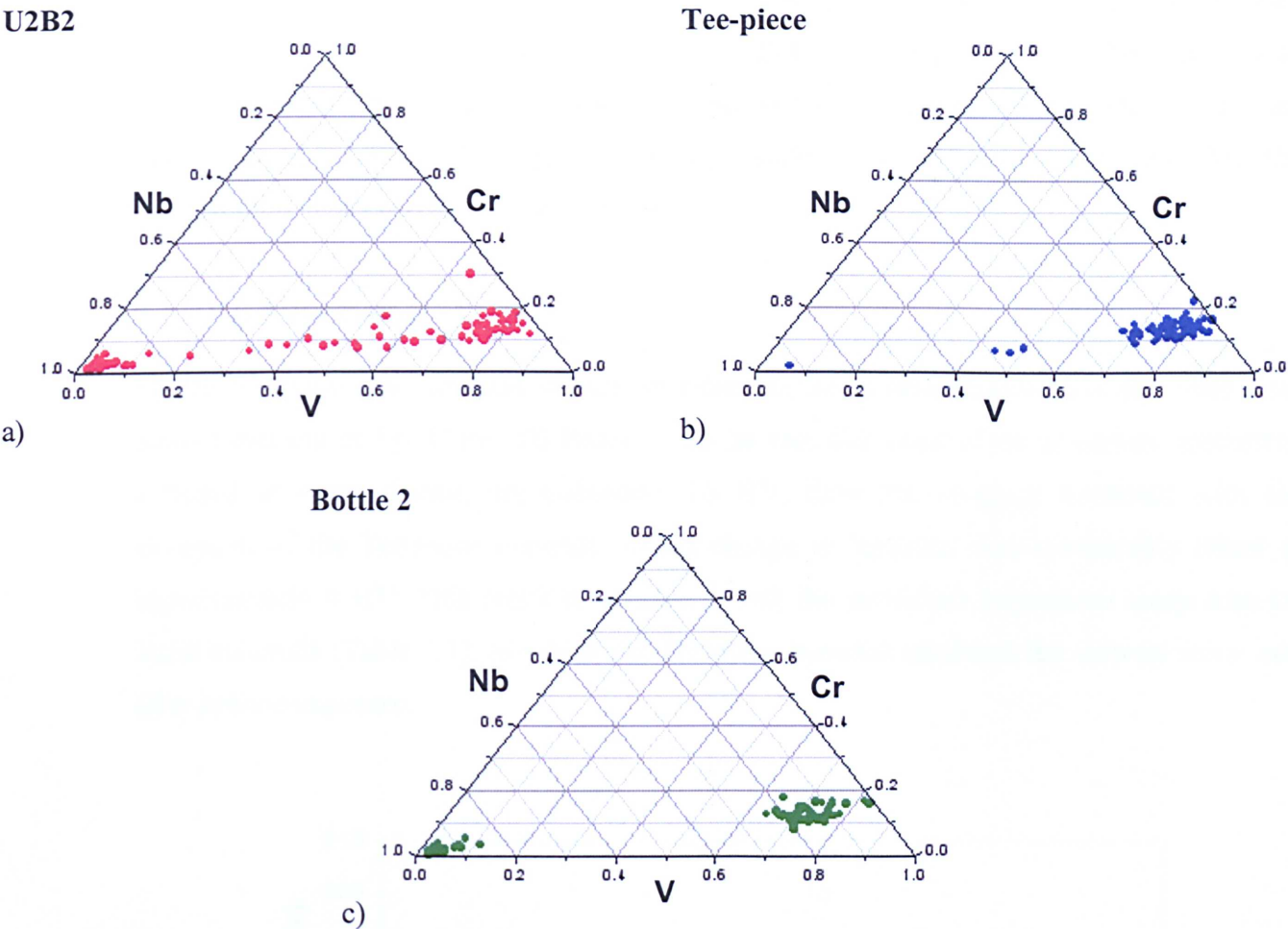


Figure 7.2: EDS measurements from individual MX precipitates comparing their V, Nb and Cr content in the ex-service materials investigated. All materials were exposed to a service temperature of $\sim 568^{\circ}\text{C}$; a) U2B2, b) Tee-piece and c) Bottle 2.

The U2B2 material, with the highest N:Al ratio, exhibited a linear composition distribution of MX precipitates and some early evidence of two-phase separation occurring (Figure 7.2a). The Tee-piece material, with the same lower N:Al ratio as Bottle 2, comprised almost exclusively of V-rich MX (Figure 7.12b). On the other hand, strong evidence of two-phase separation was found to occur in Bottle 2 (Figure 7.12c), even though this material has an identical N:Al ratio to Tee-piece.

On the basis of results from the analysis of the chemical composition of the MX precipitates in the long-term aging experiments from Chapter 5, it is logical to suggest that U2B2, which has the highest N:Al ratio and lowest predicted AlN content, exhibits the highest compositional stability of MX precipitates in the examined ex-service materials. Similarly, it is also reasonable to predicate the accelerated ‘two-phase separation’ in Tee-piece and Bottle 2, in comparison to U2B2. The differences between the content of Nb-rich MX precipitates in the latter two materials are attributable to the differences in Nb and V content, 0.08 and 0.25 wt.% in Tee-piece, and 0.11 and 0.21 wt.% in Bottle 2 respectively. Assuming that these materials exhibited a linear composition distribution of V and Nb in MX in the as-manufactured condition, it is clear that minor variations in bulk composition can affect the precipitation behaviour of P91 components.

7.3.3 Hardness Testing

Figure 7.3 shows the hardness of each specimen in the ex-service condition and after a re-aging treatment at 750°C for 100 hours. It can be seen that most of the ex-service specimens softened to some degree, approximately 10 HV, after the re-aging treatment with the exception of the Tee-piece material, whose change in hardness was comparably minor at approximately 4 HV. This result is consistent with the published impression creep data for these materials (Table 7.1), in which the Tee-piece material exhibited the slowest strain rate after service exposure.

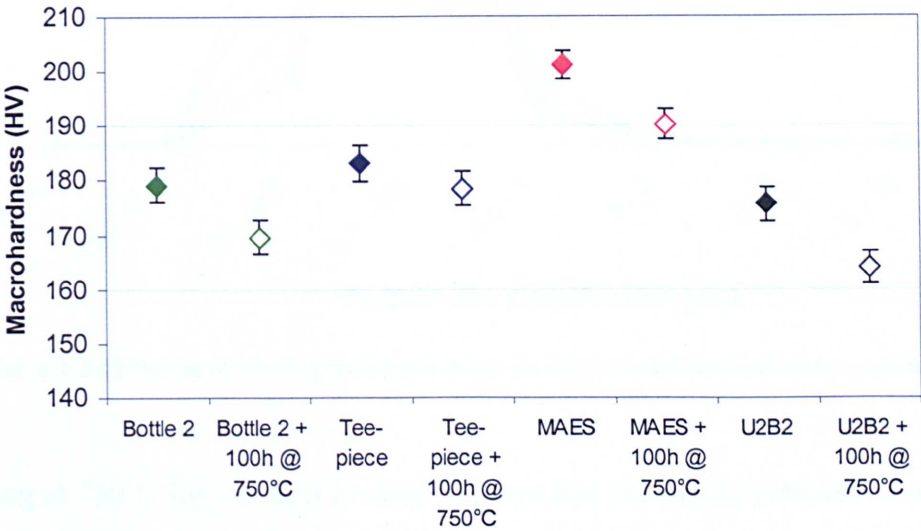


Figure 7.3: Plot comparing the macrohardness of the investigated materials in the ex-service condition and after a re-aging heat treatment at 750°C for 100 hours.

7.3.4 $M_{23}C_6$ Size Distribution

Figure 7.4 shows a comparison of the $M_{23}C_6$ particle size distribution both in the ex-service condition and after re-aging for 100 h at 750°C. In the ex-service condition, it can be seen that the material with the smallest $M_{23}C_6$ particle sizes is MAES, followed by Bottle 2, Tee-piece and U2B2 in order of increasing particle size. From the particle size results in Chapter 5, it was shown that the majority of $M_{23}C_6$ particles were present in the 0.1 to 0.2 μm size range in the long-term isothermally aged Bar 257 and W20-3 samples. Two ex-service materials (before re-aging), MAES and Bottle 2, also exhibited the majority of these particles in this size range, whereas the majority of particles were in the 0.2 to 0.5 μm size range in the Tee-piece and U2B2 materials, similar to the accelerated creep tested specimens in Chapter 5. However, it must be noted that the number of particles in the larger size range, 0.5 to 1 μm , in the ex-service specimens is less than the number found in the accelerated creep test specimens, even after the re-aging of the former.

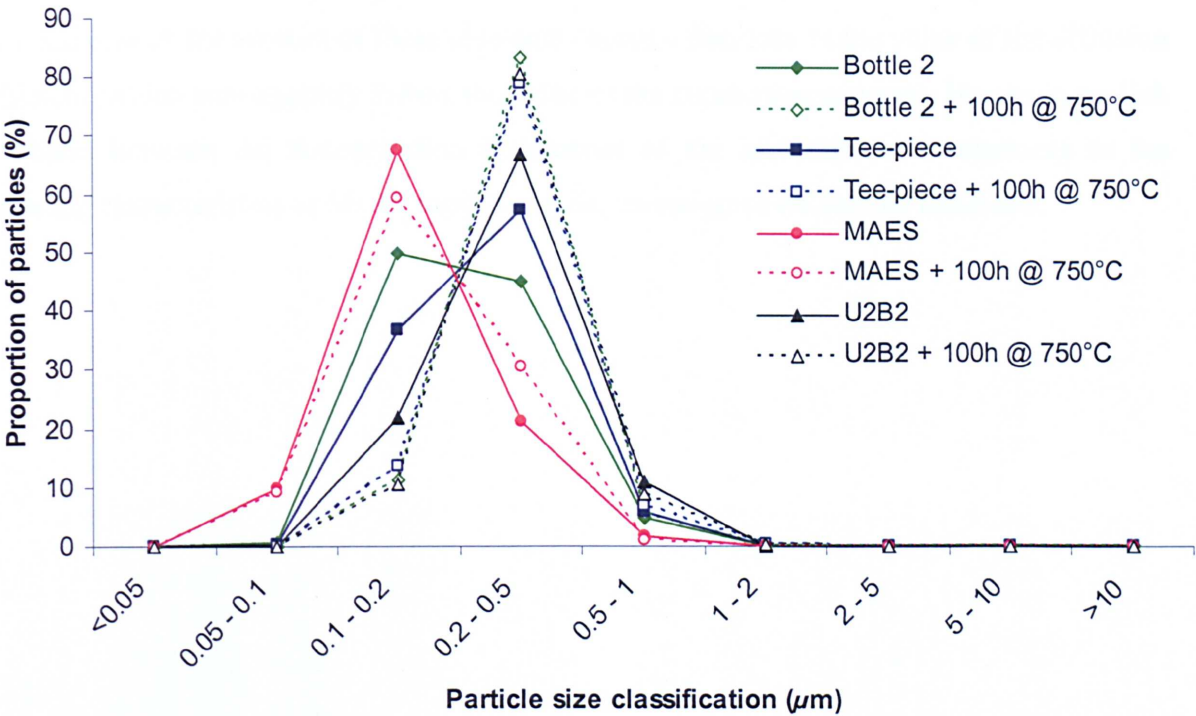


Figure 7.4: The size distribution of $M_{23}C_6$ precipitates in the ex-service condition and after re-aging at 750°C for 100 hours.

After re-aging at 750°C for 100 h, it is clearly shown that the $M_{23}C_6$ particles have coarsened considerably from the ex-service condition, the degree of which appear to be different between the investigated ex-service materials. Bottle 2 was shown to have experienced the most coarsening from its initial ex-service condition, followed by Tee-piece, U2B2 and the

MAES material. This can partially explain the decrease in hardness after re-aging. Indeed, the MAES material, with the smallest particle size distribution in comparison to the other materials before and after aging, exhibited a superior hardness level to the other materials at both conditions.

The results from the effects of long-term isothermal aging on the coarsening behaviour of $M_{23}C_6$ particles presented in Chapter 5 are somewhat comparable to the coarsening behaviour of these particles under typical plant conditions, although the ex-service specimens are expected to have experienced small strain levels in plant conditions. The rate of particle coarsening was shown in Chapter 5 to be influenced by chemical composition of the casts, similar to the present results. SEM images, which clearly show the change in $M_{23}C_6$ size and distribution of the ex-service materials, are presented in Figure 7.5. Several workers have identified different elements, the inclusion of which promote an acceleration in the coarsening rate, with the Ostwald ripening mechanism, of $M_{23}C_6$ precipitates. These elements include Mo (Hald and Straub ^[150]), Ni (Strang and Vodarek ^[22]) and Mn (Hayashi *et al* ^[151]). It was argued that a decrease in the amount of these elements causes a decrease in the value of the diffusion coefficient, which subsequently lowers the value of the coarsening constant. However, no link was found between the concentration differences of the aforementioned elements to the coarsening characteristics of $M_{23}C_6$ particles in the investigated ex-service materials.

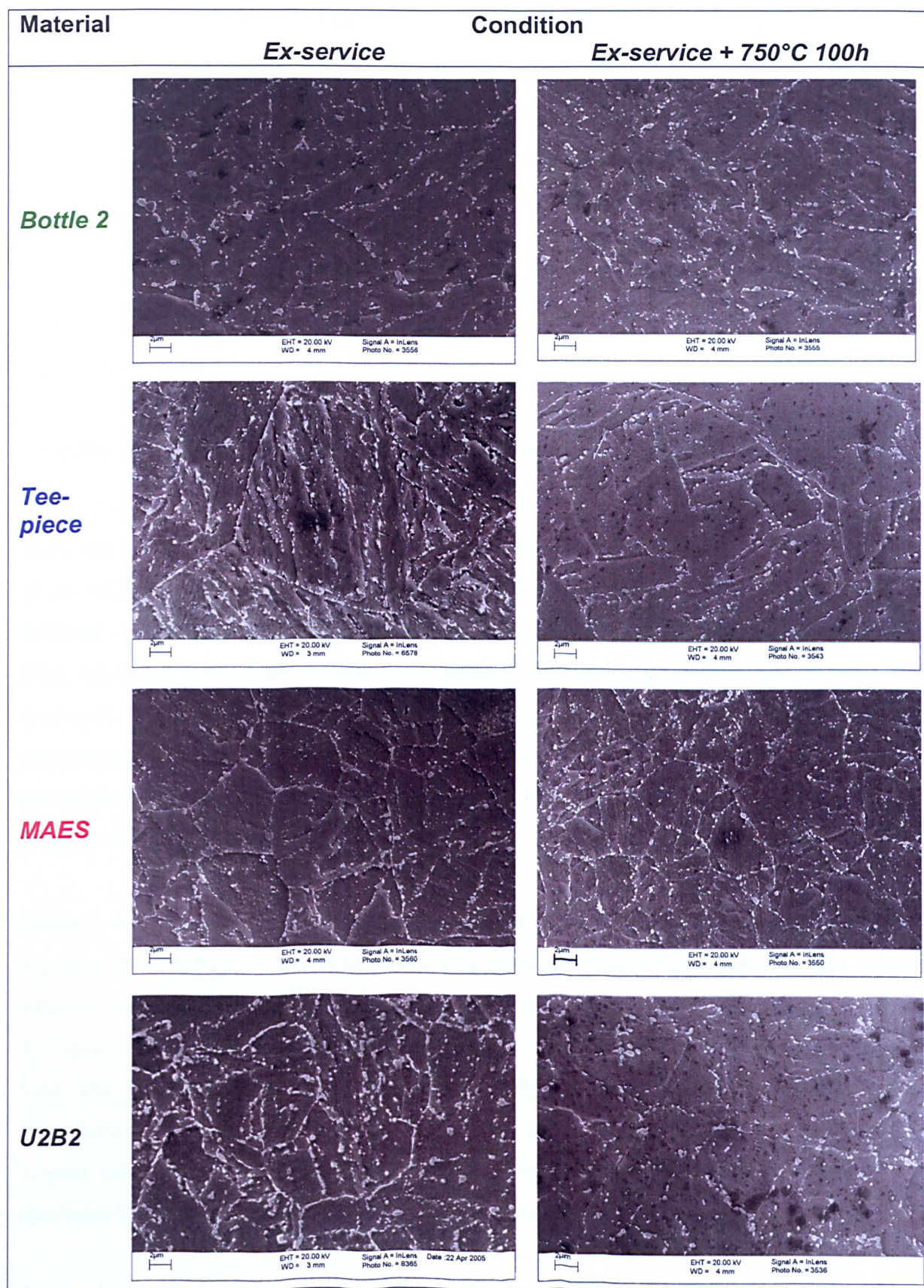


Figure 7.5: SEM In-lens images showing the martensitic lath structure and the distribution of $M_{23}C_6$ particles of the investigated ex-service specimens before and after re-aging at 750°C for 100 hours.

7.3.5 Precipitation of Laves Phase

The precipitation of Laves phase in the ex-service materials was studied in Chapter 5. From Figures 5.27 and 5.28, it was shown that the specimens with the most severe Laves phase precipitation and coarsening were Tee-piece and Bottle 2. Interestingly, this coincides with the complete two-phase separation in these specimens, which is indicative that significant changes in particle composition have occurred from the as-received condition up to ~30,000 hours in service. Correspondingly the U2B2 material, which exhibited a linear composition distribution of Nb and V in MX precipitates, gave evidence of the initial stages of Laves phase precipitation.

7.3.6 The Effect of Service Exposure on the Subgrain Structure of P91

Figure 7.6 shows the matrix microstructure, both in inverse pole figure maps and rotation angle maps, from EBSD analysis, of the investigated ex-service materials. It can be seen that, albeit with similar operating conditions and exposure times, the microstructures of the different ex-service specimens vary considerably. U2B2, which had the lowest hardness (184 HV), exhibited a structure whereby the original martensite laths have been almost fully destroyed. In place, the presence of large equiaxed grains can be observed, mostly with a low misorientation angle. This microstructure was found to be very similar to those exhibited by the accelerated creep test specimens (Chapter 6, Figure 6.12), albeit with a much smaller subgrain size in the former (Figure 7.6).

Bottle 2, with the intermediate hardness value (190 HV), was similar to the U2B2 material, whereby the presence of equiaxed grains was detected (Figure 7.6). However, the subgrain structure was much finer in the former. This material bore the closest resemblance to the Bar 257 specimen that had been isothermally aged for 10,000 hours at 650°C (Chapter 6, Figure 6.4). The Tee-piece specimen exhibited practically no substructure and resembled an as-manufactured (as-tempered) microstructure. The MAES material, which experienced the longest time in service (56,000 h), exhibited a microstructure that resembled the Bar 257 specimen that was isothermally aged for 2,500 h at 650°C.

Figure 7.7 exhibits the microstructures of the same ex-service materials after re-aging at 750°C for 100 hours. It is clearly shown that the most radical changes in microstructure after the re-aging treatment occurred in the Tee-piece and MAES materials. In the former, a high degree of low-angle substructure formation is evident within the martensite laths. This

scenario is comparable to the long-term aged Bar 257 material (Figure 6.4), whereby the formation of low-angle equiaxed grains were shown to be present after 2,500 hours aging from the as-tempered condition, which coincidentally exhibited a similar microstructure to Tee-piece in the ex-service condition. Correspondingly, the re-aging of the MAES material simulated the aging of the Bar 257 from 2,500 to 10,000 hours at 650°C, whereby in the latter, the lath structure appeared to be completely destroyed and replaced by a very fine size distribution of equiaxed subgrains. The two weakest materials, U2B2 and Bottle 2, showed hardly any change (qualitatively) in matrix microstructure.

Figure 7.8 shows thin-foil TEM micrographs affirming the tempered martensite lath microstructure of the Tee-piece material, and the equiaxed subgrain microstructure of U2B2, in the ex-service condition.

The distribution of misorientation angles in the investigated ex-service materials before and after re-aging are shown in Figure 7.9. It can be seen that the fraction of high-angle boundaries decreases after the re-aging heat treatment in all materials. These results are also consistent with the EBSD results from the long-term aged Bar 257 and W20-3 specimens (Chapter 6, Figure 6.7). Interestingly, the Tee-piece material, which exhibited an as-manufactured tempered martensite microstructure, exhibited the most significant increase in low-angle boundaries after the re-aging heat treatment.

Figure 7.10 shows the boundary density chart corresponding to the investigated ex-service materials. In the Tee-piece specimen, an appreciable increase in boundary line length is observed, which is attributable to the observed formation of a low-angle boundary structure after re-aging. The MAES material also exhibits an increase in grain boundary line length, however, to a much lesser degree. In good agreement with qualitative examination of the EBSD maps, the Bottle 2 material exhibited hardly any change in line length, even after being re-aged. However, the U2B2 material actually exhibited a decrease in boundary line length, which may indicate the growth of subgrains.

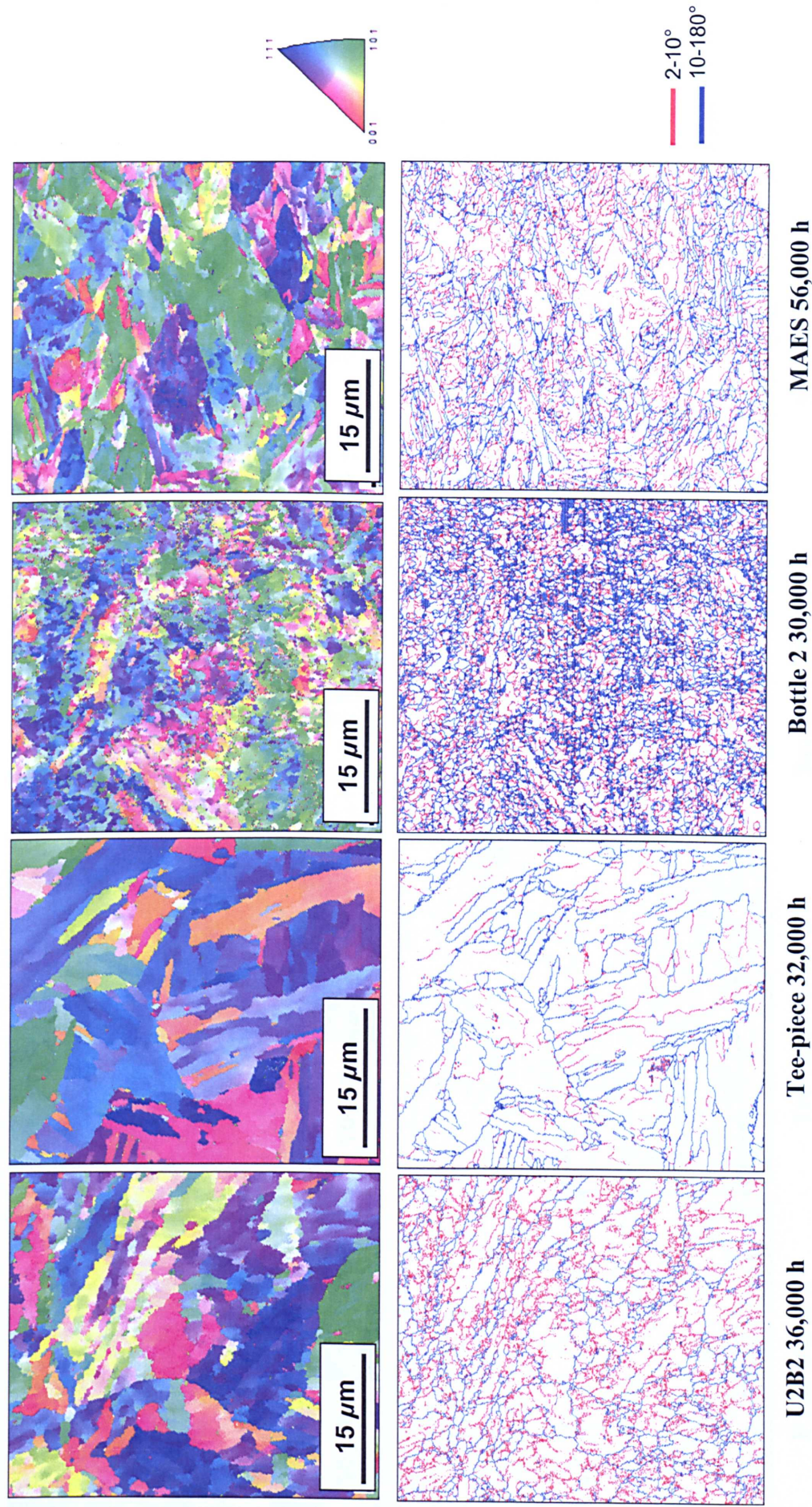


Figure 7.6: Inverse pole figure maps (top) and rotation angle maps illustrating the microstructure of the investigated ex-service materials.

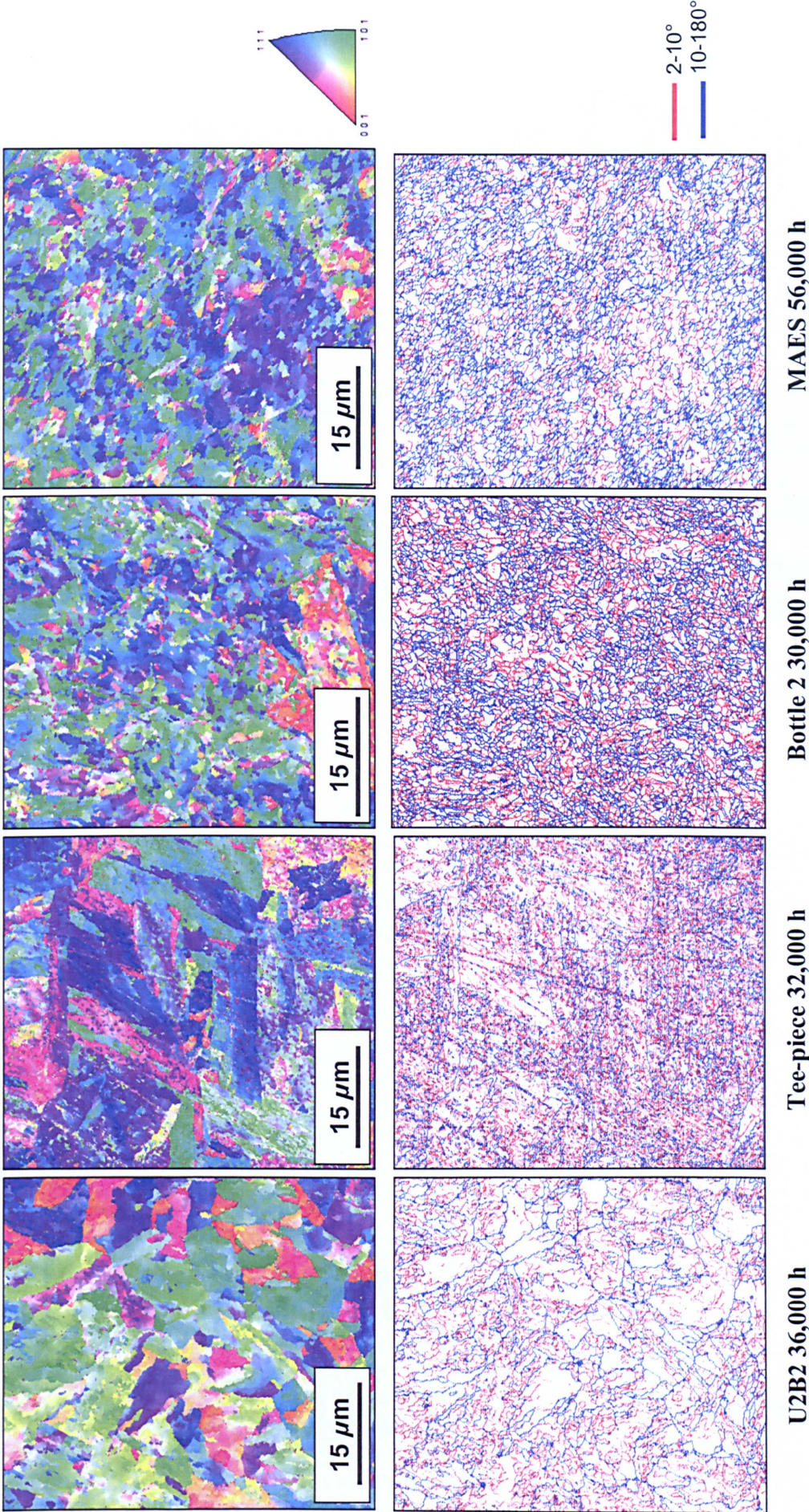


Figure 7.7: Inverse pole figure maps (top) and rotation angle maps illustrating the microstructure of the investigated ex-service materials after re-aging at 750°C for 100 hours.

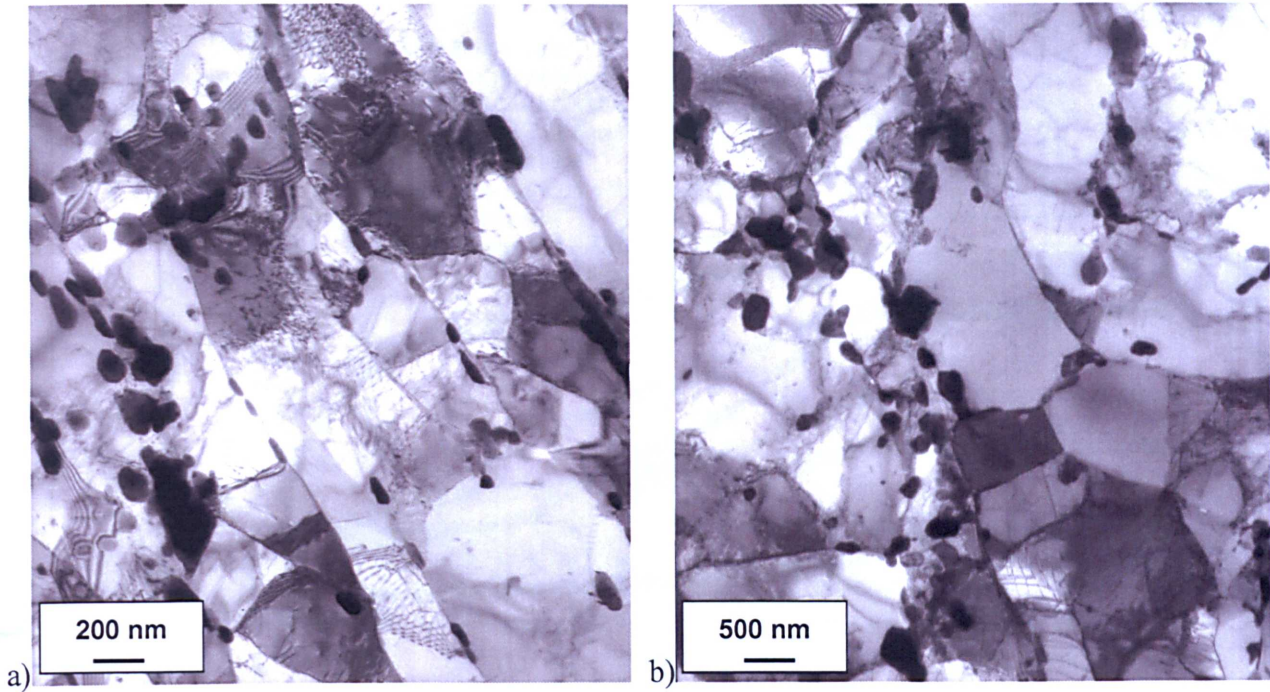


Figure 7.8: Thin-foil TEM micrographs of the a) Tee-piece and b) U2B2 materials in the ex-service condition. In the Tee-piece material, the microstructure consisted of lath martensite, whereas the U2B2 material exhibited a more equiaxed grain microstructure.

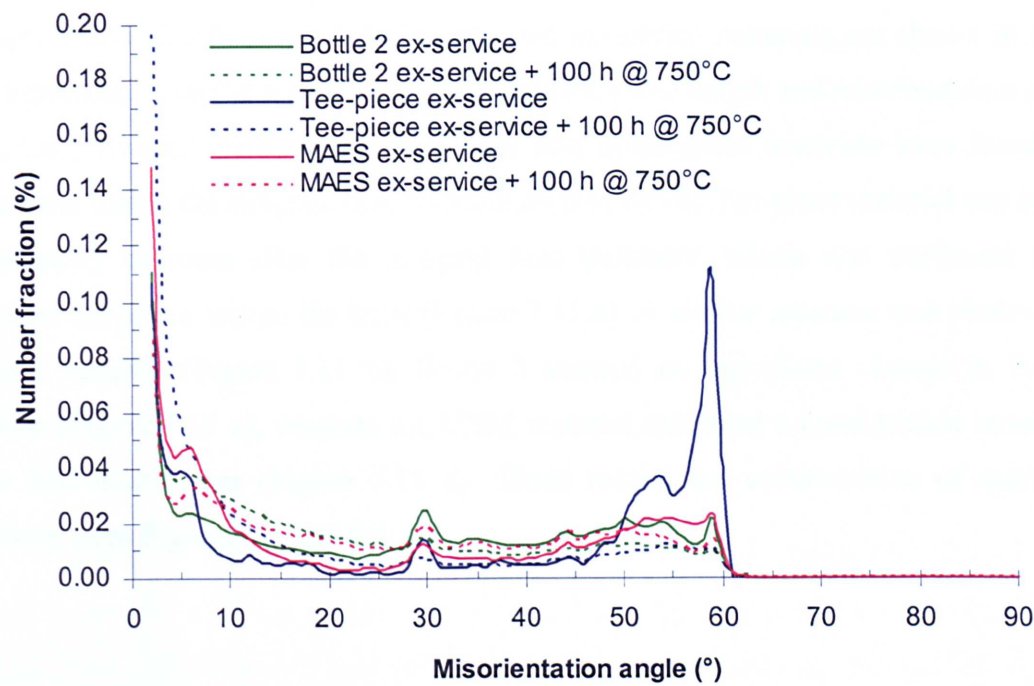


Figure 7.9: Plot showing the distribution of misorientation angles for the investigated ex-service specimens before and after re-aging at 750°C for 100 hours.

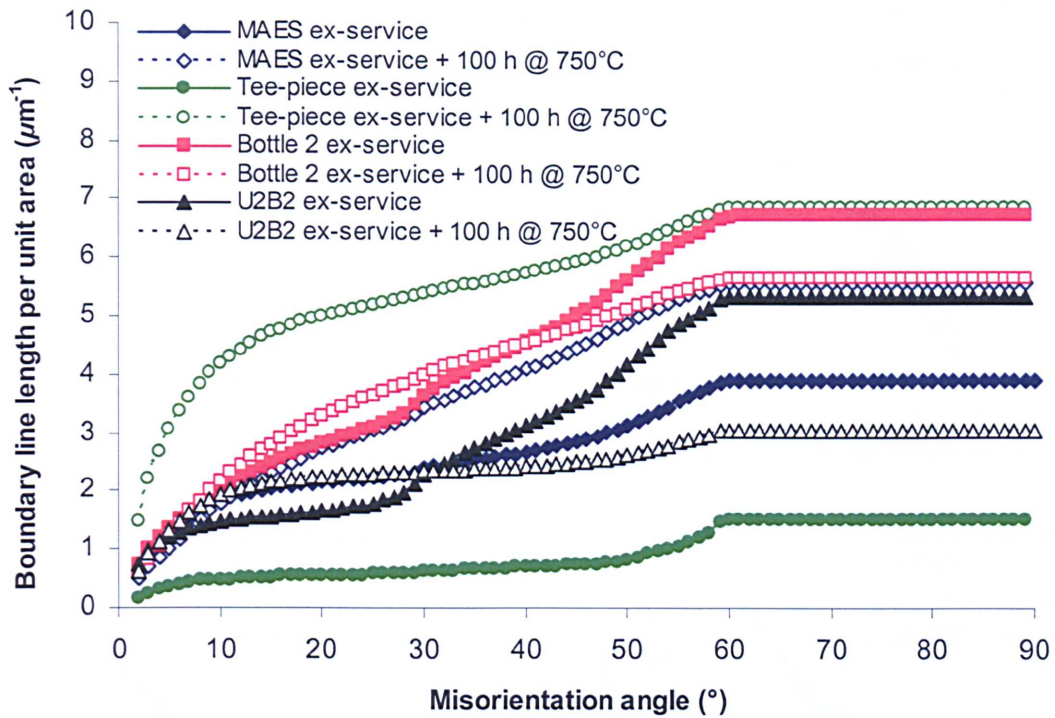


Figure 7.10: Plot showing the boundary line length as a function of misorientation angle for the investigated ex-service materials and after re-aging at 750°C for 100 hours.

7.3.7 Subgrain Size

The subgrain size distributions of the investigated ex-service materials are shown in Figure 7.11. In agreement with the results from grain boundary line length and misorientation profile analysis, the following differences between the four investigated materials were found. The subgrain sizes within the subgrain size distribution plot for the Tee-piece material can be seen to considerably decrease after the re-aging heat treatment, which was attributed to the formation of subgrains within the laths (Figure 7.11 a). A similar scenario was observed for the MAES material (Figure 7.11 b). Bottle 2 showed no significant change in the size distribution (Figure 7.11 c), whereas the U2B2 material exhibited a considerable increase in subgrain size distribution (Figure 7.11 d). These results are corroborative of qualitative observations from Figures 7.6 and 7.7.

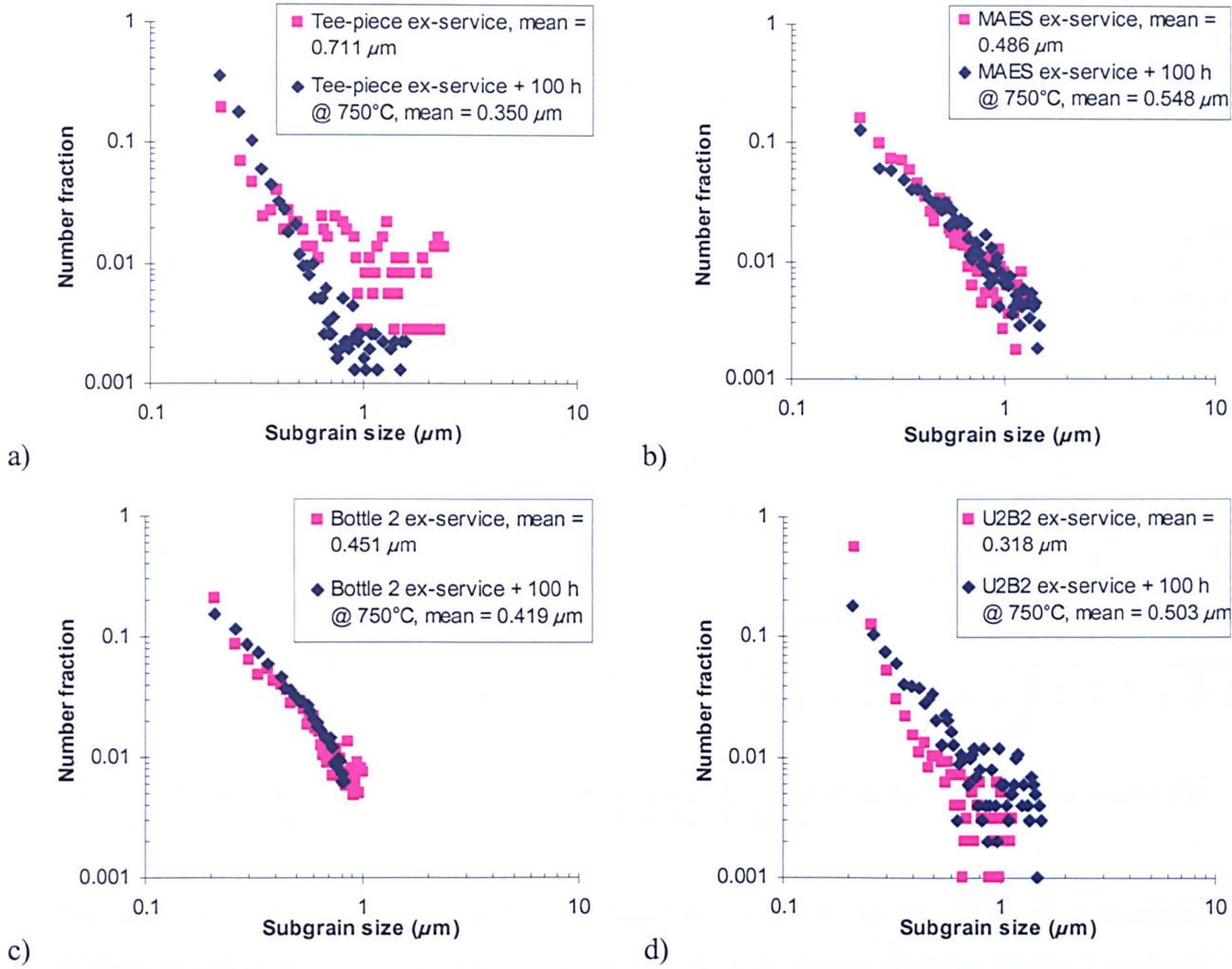


Figure 7.11: The subgrain size distribution in the investigated ex-service materials before and after re-aging at 750°C for 100 h; a) Tee-piece, b) MAES, c) Bottle 2 and d) U2B2.

7.3.8 The Effect of Service Exposure on the Dislocation Structure of P91

In the previous chapter, XRD was used to provide additional information on the microstructure of P91 to EBSD, whereby this technique has been shown to be sensitive to changes in dislocation density.

Figure 7.12 shows the XRD line profiles of the {211} peak in the ex-service materials. It can be seen that there are differences between the XRD line intensity profiles of the different ex-service materials, despite being exposed to similar service conditions. The results from this figure are in agreement with the hardness results from Figure 7.3. For instance, the material that exhibited the highest hardness value, MAES, exhibits the broadest XRD peak, whilst the softest material, U2B2, exhibits the sharpest peak (Figure 7.12a)). It is also shown that the diffracted peaks sharpen upon the re-aging of the investigated materials (Figure 7.12b)).

These findings prompted the attempt to characterize the dislocation density of the ex-service materials and in turn compare these values to those obtained from long-term aged specimens in Chapter 6.

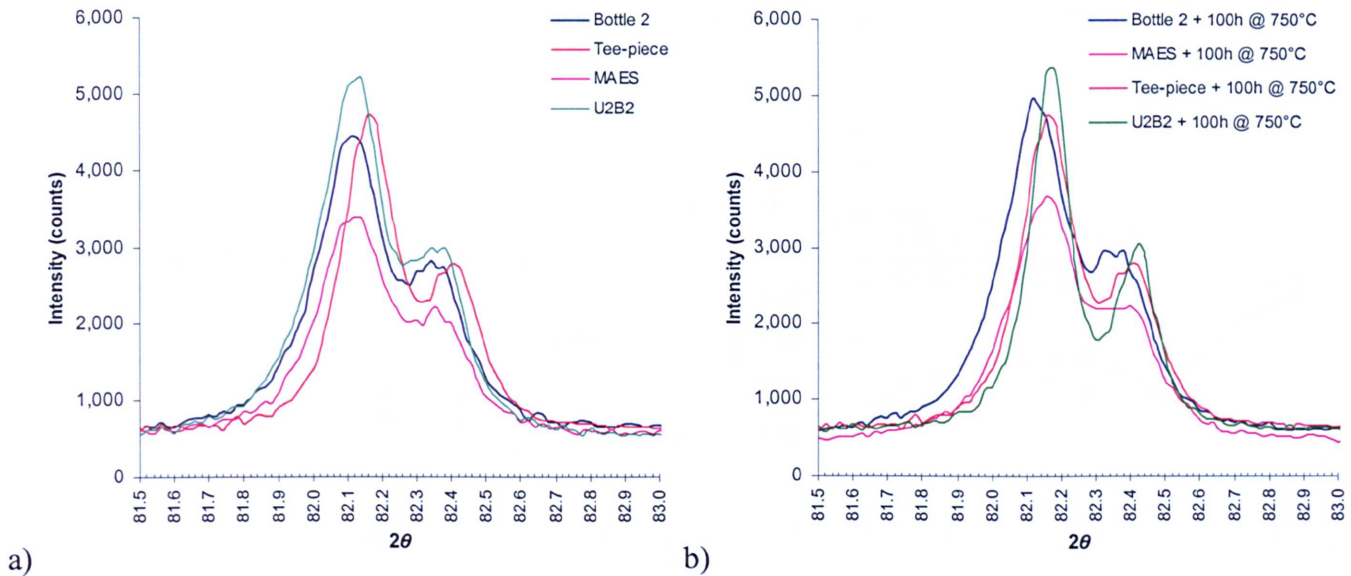


Figure 7.12: XRD line profiles showing the evolution of the {211} peak of a) the investigated ex-service P91 materials, and b) the same materials after re-aging at 750°C for 100 hours.

The data for integral peak breadth as a function of $\sin \theta$, in the form of a modified Williamson-Hall plot, are presented in Figure 7.13. It is shown that the Bottle 2 material exhibits a noticeable difference to such an extent that the integral peak breadths are narrower after re-aging, as could be expected. Similarly, albeit more significantly, the U2B2 material also exhibits a decrease in peak breadth and a decrease in strain anisotropy after re-aging. Indeed, the line profile shape resembles those obtained from the accelerated creep tested specimens, which also exhibited similar microstructures (see Chapter 6, Figure 6.30). In contrast, such changes were not observable in the MAES and Tee-piece materials, both of which were shown to resemble long-term aged microstructures, which can be expected, as long-term aging at 650°C did not produce a significant difference in profile shape either (see Chapter 6, Figure 6.29).

The values of dislocation density in the ex-service specimens were derived from the present XRD line profile results and are shown in Table 7.2. It can be seen that the values of dislocation density are rather similar for all the investigated ex-service materials, and that these values generally decrease after severe re-aging. The largest decrease in dislocation

density occurred in the U2B2 material, followed by Bottle 2, MAES and Tee-piece respectively, which affirm the results from hardness testing. Interestingly, although the Tee-piece and MAES specimens exhibited a similar tempered martensitic-ferritic microstructures to some of the long-term aged specimens in Chapter 6, the dislocation values were somewhat lower. This may be due to the effects of strain enhanced recovery, which promote the rapid decrease in dislocation density^[76,77].

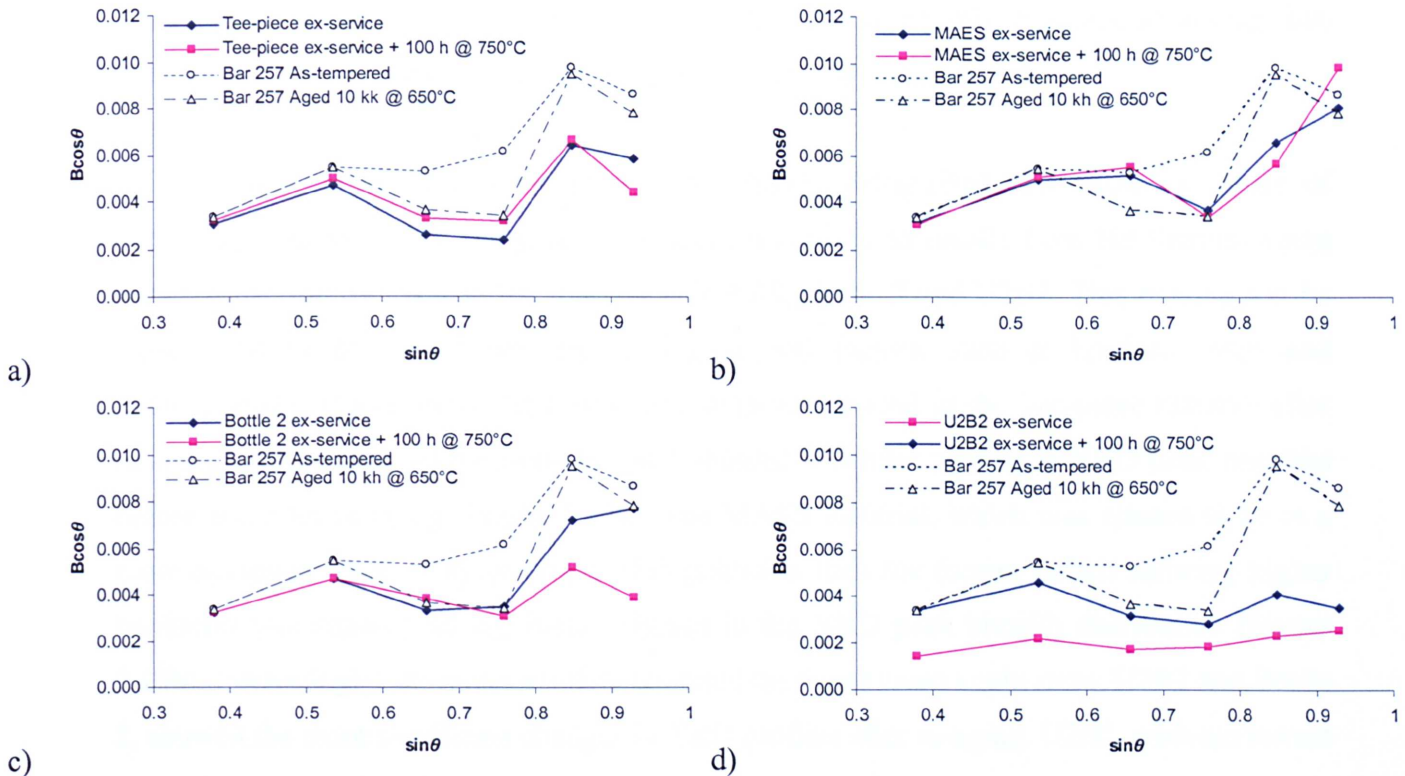


Figure 7.13: Williamson–Hall plots for the ex-service materials and after subsequent re-aging at 750°C for 100 hours. The figure shows four series of XRD peak widths B (in reciprocal space units) as a function of $\sin \theta$; a) Tee-piece, b) MAES, c) Bottle 2 and d) U2B2.

Material and Condition	Mean Subgrain Diameter, w (10^{-6}m)	Dislocation density, ρ_f (10^{14}m^{-2})
Bottle 2 568°C/30,000h	0.451	1.94
Bottle 2 568°C/30,000h + 750°C 100 h	0.419	1.42
Tee-piece 568°C/32,000h	0.711	1.77
Tee-piece 568°C/32,000h + 750°C 100 h	0.351	1.81
MAES 568°C/56,000h	0.486	1.89
MAES 568°C/56,000h + 750°C 100 h	0.548	1.66
U2B2 568°C/36,000h	0.318	1.15
U2B2 568°C/36,000h + 750°C 100 h	0.503	0.29

Table 7.2: Dislocation densities determined by XRD for the investigated ex-service P91 materials.

7.4 Discussion Concerning the Microstructure of Ex-service Materials

Throughout the results section of this chapter, many parallels have been drawn between the microstructures of the ex-service materials and those of the long-term aged specimens presented in Chapters 5 and 6. This comparison, then, has proven to be satisfactory as it may allow the remanent lifetimes of ex-service materials, particularly sampled plant components, to be ranked according to the condition of the microstructure. Ideally, such an appraisal must be complemented with comprehensive data from mechanical testing, which unfortunately was not available for this investigation. However, although not entirely rigorous, an attempt has been made to link microstructure evolution with simple hardness testing.

On this basis, if the microstructure can be crudely categorized and ranked in order of decreasing remaining life (longest to shortest), according to results from the thermal aging experiments, the results may be; Tee-piece, MAES, Bottle 2 and U2B2. This ranking can be rationalized as follows. When considering several factors, such as hardness drop and microstructure, it was shown that very little change occurred in the Tee-piece material after re-aging. Indeed, the Williamson-Hall plot showed a similar profile of XRD peak breadths before and after re-aging (Figure 7.13a). The MAES material, which was classed to be at a more advanced stage of microstructural degradation than the former (albeit showing higher hardness) also showed no significant change in the XRD peak breadth distribution (Figure 7.13b). Interestingly, the materials that exhibited the faster creep strain rates, U2B2 and Bottle 2, showed the more significant changes in XRD profiles after re-aging. U2B2, with the lowest hardness, showed the most dramatic changes (Figure 7.13d).

From the results of microstructural characterization presented throughout this and the previous chapters, it should be possible to rank P91 components in plant in terms of microstructural degradation, provided conditions allow for small amounts of material sampling. The ultimate goal would then be to incorporate microstructural data, which is descriptive of the degree of degradation, into suitable models in order to assess the remaining lifetime of power plant components in service.

7.5 Summary

The microstructure of P91 components that have experienced typical plant operating conditions have been extensively characterized by applying the same analysis criteria discussed in the preceding chapters. The fruitful outcome of this experiment was that striking similarities between the microstructures of the ex-service materials and the long-term aged materials were found, which enabled the former to be ranked according to the level of microstructure evolution undergone by the latter. Similarly, the experiments provided the opportunity to validate the microstructures produced under accelerated thermal aging conditions, with those obtained under “real” operating conditions.

Chapter 8

MICROSTRUCTURAL CHARACTERIZATION OF P91 STEEL WELDS

8.1 Introduction

The microstructure of the original as-manufactured material, which is designed for specific service conditions, may be altered by additional heat treatment and welding procedures applied in power plant. Welded joints may reduce component integrity, and many studies have been performed to ascertain the effects of various welding parameters, such as post-weld heat treatment, interpass temperature and preheating, and material parameters such as chemical composition, on the creep performance of high Cr power plant steel components. However, at present the effects of the condition of the parent (base) metal microstructure on the creep behaviour of welded high temperature pipework remains unclear.

To quote Bhadeshia: ‘...It is amazing that we dare to do this (welding) with engineering components.’ His reasoning was that ‘welding is perhaps the most complex of fabrication processes, embodying virtually every metallurgical phenomenon...not only are the properties of the weldment expected to be different from those components to be joined, but the flow of heat into the solid components causes metallurgical changes which can make or break the joint in the critical heat affected zone adjacent to the fusion boundary’ ^[4]. Indeed, a fairly recent phenomenon causing the nucleation and propagation of creep voids in the fine-grained heat affected zone of high Cr ferritic steels, currently recognized as Type IV cracking, has become a worldwide problem to solve ^[152]. Brett *et al* ^[94] reported an important example of untimely failure of grade 91 power plant component, by Type IV cracking, which occurred during regular service operation. In response to the occurrence of such untimely failures in power plant, Allen and Fleming ^[153] suggested that the available creep data from the parent components ‘may not be the most important consideration in high temperature materials selection.’

Chapters 5 and 6 showed that different initial heat treatments applied to P91 steel affect several microstructural features, in particular the precipitation characteristics of minor phases, the matrix microstructure and also the mechanical properties. In a previous publication by Allen *et al* ^[154], Bar 257 (P91) specimens were creep tested after welding was performed on

parent metal specimens that had undergone three radically different heat treatments. One of the materials had a characteristic tempered martensitic 'as-received' microstructure, which is the result of conventional industrial heat treatment. Another specimen had been renormalized and tempered, which led to a significant degree of strengthening over the as-received specimen. The final specimen had been severely aged prior to welding, which caused significant weakening of the parent material over the as-received specimen. Their study showed that there was a complex relationship between the parent metal properties and the heat affected zone (HAZ) properties. These results are indicative of the fact that the microstructure of the parent material, which is influenced by varying heat treatment, affect the performance of joined high Cr ferritic steel components. As part of the present investigation's aim to link the creep behaviour of P91 steel to its microstructure, it was decided to extensively characterise the aforementioned specimens using the variety of analytical electron microscopy techniques described in the previous chapters in order to account for the varying creep performance of different pre-weld conditions, given the increasing concerns for Type IV failures in these materials.

8.2 Experimental Procedure

One grade 91 (9Cr-1Mo-V-Nb) steel cast was investigated in this study, the chemical composition of this material was shown in Table 3.1 (Chapter 3). This material, also known as Bar 257, was of particular interest due to its relatively high Al concentration, which gave rise to a low N:Al ratio of 1.11. This has been attributed elsewhere for the poor creep rupture properties of this material ^[41,154,155]. The specimens were kindly supplied in the creep tested condition by E.On UK.

Table 8.1 describes the material condition prior to welding, post-weld heat-treatment (PWHT) and creep testing. Welding was undertaken using a manual metal arc weld metal and each specimen was subjected to a post-weld heat treatment (PWHT) of 760°C for 3 h, except specimen B, which was aged for 1 h. Creep testing was undertaken at 650°C at a nominal stress value of 75 MPa until failure. The failure mode of each specimen was by Type IV cracking along the fully retransformed fine grained heat affect zone (HAZ) region. The creep test history of each specimen is shown in Table 8.1, and the cracks in the Type IV region are also shown. The pre-aged specimen exhibited considerable necking in comparison to the as-manufactured and the renormalized and tempered specimens.


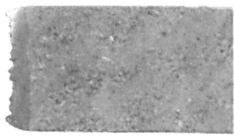
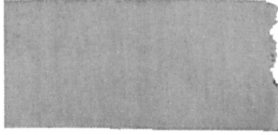

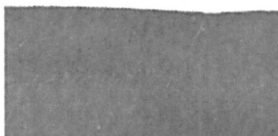
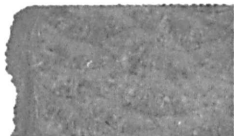
Specimen	Condition prior to welding	Parent Metal	Weld Metal
A 204 HV	As-manufactured condition, normalized at 1040°C and tempered at 760°C for 12 h.		
B 247 HV (strengthened)	Renormalized (from as-manufactured condition) at 1060°C and tempered at 760°C for 1 h.		
C 184 HV (weakened)	Aged (from the as-manufactured condition) at 760°C for 24 h.		

Table 8.1: Heat treatment conditions of the three specimens tested prior to welding, post-weld heat-treatment and creep testing. Macrographs of the specimens after creep testing are also shown.

Specimen	Creep Test History		
	Final Test Duration (h)	Elongation (%)	Reduction of Area (%)
A	519	3.05	13.68
B	359	2.31	18.07
C	430	10.46	28.77

Table 8.1: Creep test history of the specimens.

8.3 Results from the Microstructural Characterization of P91 Steel Welds

8.3.1 The Matrix Microstructure

Figure 8.1 shows optical micrographs of the parent metal microstructures after creep testing, all of which comprised of a tempered martensite matrix with $M_{23}C_6$ carbides decorating the interlath and intergranular regions. There was no clear distinction between the as-manufactured (A) and renormalized (B) parent metal microstructures, aside from a slightly smaller prior austenite grain size in the latter (Figures 8.1a) and b). The microstructure of the pre-aged specimen could be distinguished from the previous two specimens by a coarser lath and precipitate distribution (Figure 8.1c). Figure 8.2 shows the HAZ microstructures where Type IV failure occurred. These consisted of a fine equiaxed grain structure, which replaced the typical lath martensite microstructure associated with the parent metal, and was found to vary considerably with different starting microstructures. For example, in the pre-aged HAZ, the particles appear coarser and more sparsely distributed than in the as-manufactured and renormalized specimens. This is indicative of the fact that the Type IV region must have experienced a temperature in excess of the equilibrium transformation temperature of ferrite

and austenite (A_{c1}), which for grade 91 steel is approximately 850°C [8]. The consequence of heating to such a temperature resulted in the lath martensite phase becoming destroyed in this region. Interestingly, the fact that the HAZ microstructures of the different pre-weld conditions are different gives an indication that, during the welding process, some of the effects of prior parent material heat treatment may “survive” the HAZ retransformation process.

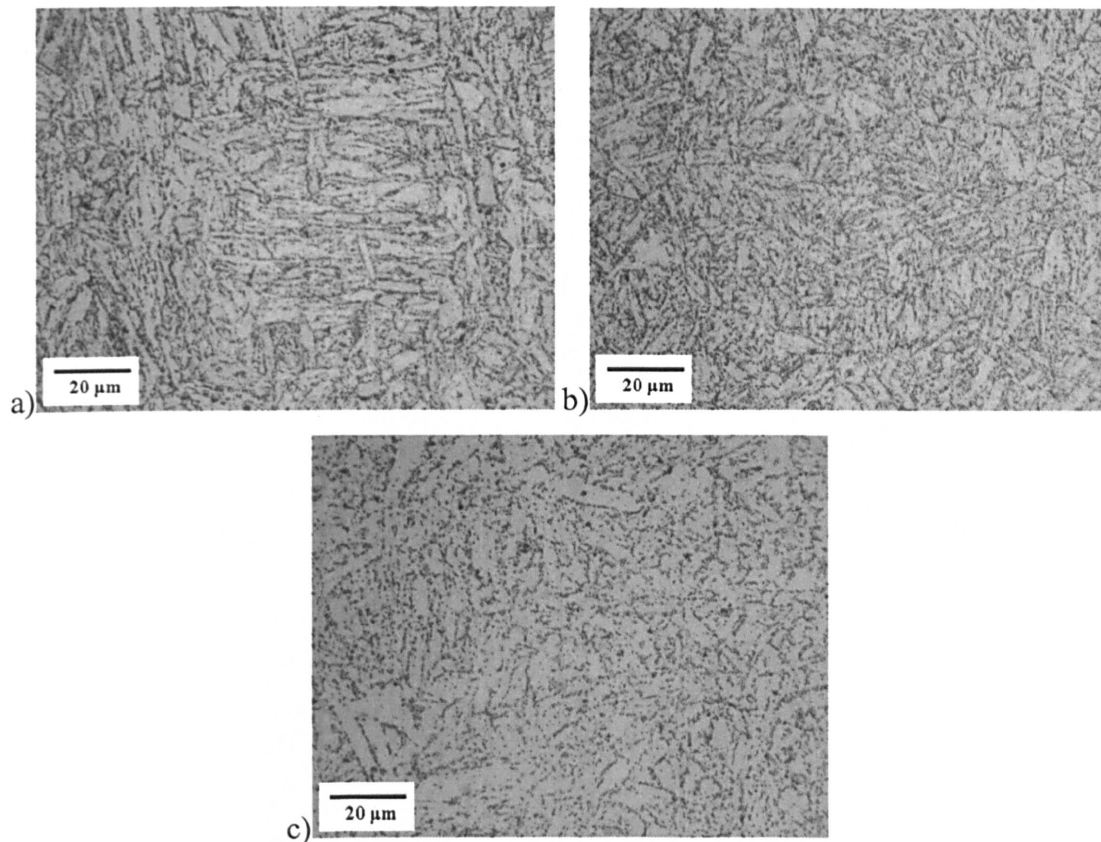


Figure 8.1: Optical micrographs illustrating the microstructure in the parent metal microstructure of a) the as-manufactured, b) the renormalized and tempered and c) the pre-aged specimens after creep testing.

The matrix microstructure of the creep tested specimens in the parent metal and Type IV HAZ regions were further characterized using electron backscatter diffraction (EBSD) in the scanning electron microscope. EBSD was used primarily to identify the characteristic features of the grain structure in the different zones of each specimen after creep testing.

Figure 8.3 shows the matrix microstructure, both in inverse pole figure maps and rotation angle maps, from EBSD analysis, of the investigated P91 weld specimens. The parent metal region of specimen A resembles the optical micrograph in Figure 8.1, whereby a fine tempered martensite lath microstructure is observed, and was also found to resemble its corresponding microstructure prior to creep testing in the as-manufactured (prior to welding

and creep testing) condition (Figure 6.1, Chapter 6). The HAZ region of the same specimen is composed of an equiaxed distribution of high-angle grains with a boundary misorientation of greater than 10° . Interestingly, a small substructure composed of low-angle boundary grains exist within some of these large grains, which resemble a metallic grain structure that has undergone dynamic recrystallization. This same feature was observed in the HAZ region of specimen C. Watanabe *et al* ^[152] also found that the Type IV region consisted of a fine grained structure, and they observed that this region consisted of a low dislocation density in comparison to the parent material.

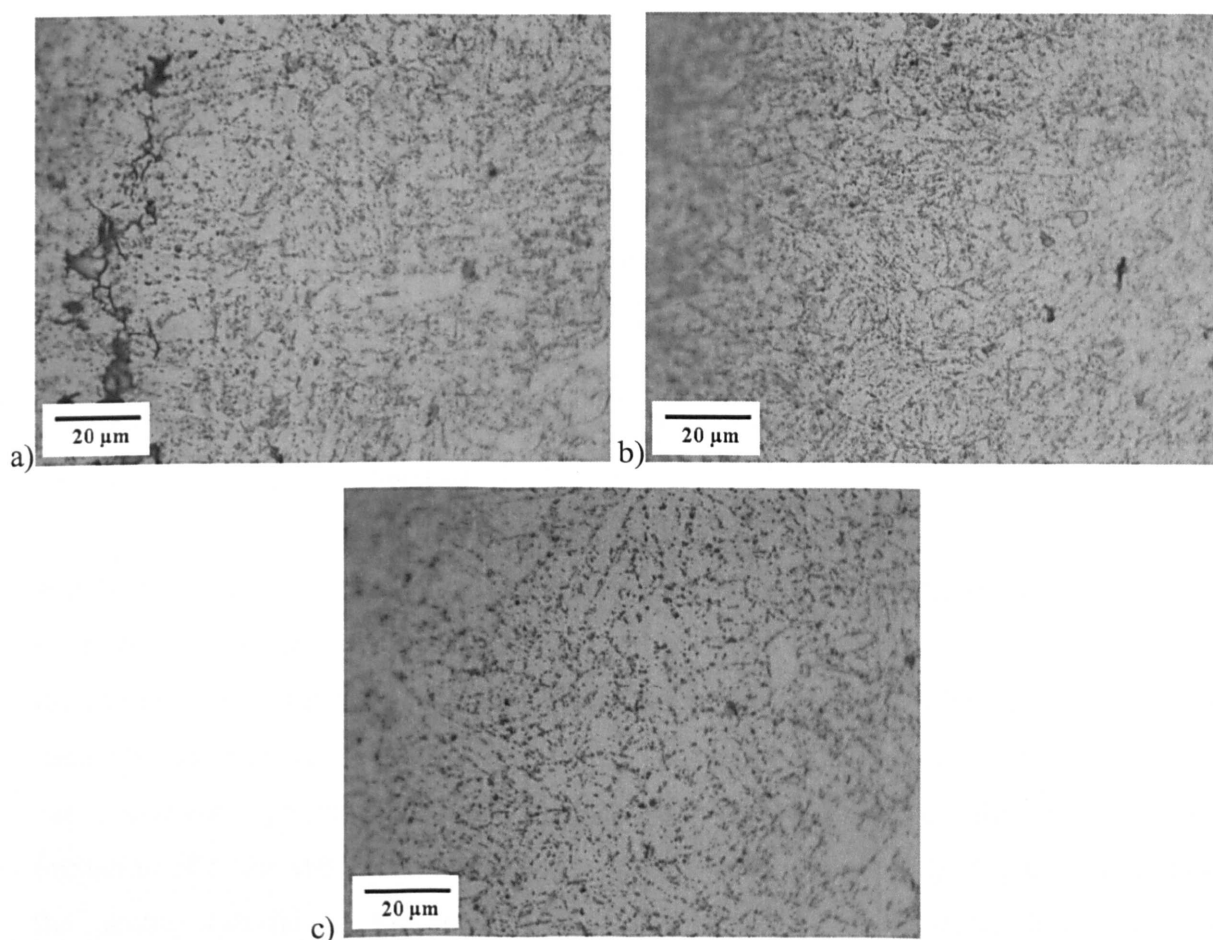


Figure 8.2: Optical micrographs showing the HAZ microstructure on the parent metal side near the Type IV crack region after creep testing in a) the as-manufactured, b) the renormalized and tempered, and c) the pre-aged materials.

Although the parent metal region of specimens A and B were shown to exhibit a similar lath martensite microstructure using standard optical and scanning electron microscopy, EBSD has shown that the renormalized specimen has a finer lath structure and a higher density of low-angle boundaries within the laths in comparison to specimen A (as-manufactured condition). This is due to the fact that this specimen has been tempered less severely than specimen A. Therefore, a higher dislocation density can be expected in this material, which is reflected by

the considerable hardness increase exhibited in this specimen. The parent metal region of specimen C was very similar to its corresponding HAZ microstructure, the main difference being a slightly smaller equiaxed grain size in the former.

To supplement EBSD data, a focussed ion beam (FIB/FEGSEM) instrument has been employed to produce site specific ion-beam induced secondary electron images of the microstructures of the HAZ and parent metal regions. The main advantage of this technique over conventional secondary electron images is that they induce strong channelling (h.k.l) contrast, providing high resolution, qualitative information of the grain structure. Figures 8.4, 8.5 and 8.6 show a series of micrographs taken across the interface of the Type IV region and the parent metal region in the as-manufactured (A), renormalized (B) and pre-aged (C) creep specimens, respectively each taken at the same magnification.

In specimen (A), a fine equiaxed microstructure is observed in the Type IV HAZ region (Figure 8.4). Interestingly, the microstructure at the parent metal region is also very fine, with equiaxed grains within the martensitic laths, due to the recovery of the original lath martensite microstructure. This behaviour was also typically observed in the Bar 257 material after long-term isothermal aging (Chapter 6).

A different scenario is observed in the renormalized specimen (B). Although a fine equiaxed microstructure is observable in the Type IV region, this substructure abruptly disappears as the distance from the crack towards the parent metal increases, when the microstructure suddenly becomes lath martensite (Figure 8.5). In the parent metal region, the lath martensite has a different appearance from that in specimen (A), as there is very little evidence of the formation of a fine sub-structure. This is indicative of the fact that the degree of recovery in the parent material of the renormalized specimen was considerably lower than that experienced in the as-manufactured specimen. The pre-aged specimen (C) also exhibited a different microstructural profile from the as-manufactured specimen (Figure 8.6). Here, coarse equiaxed grains near the cracked region steadily change to a very coarse lath martensite microstructure in the parent metal region. It can be seen that the severe pre-aging heat treatment produced considerable microstructural damage in comparison to the as-manufactured condition, as the microstructures exhibited in specimen (C) very much resemble the accelerated creep tested specimens investigated in Chapter 6.

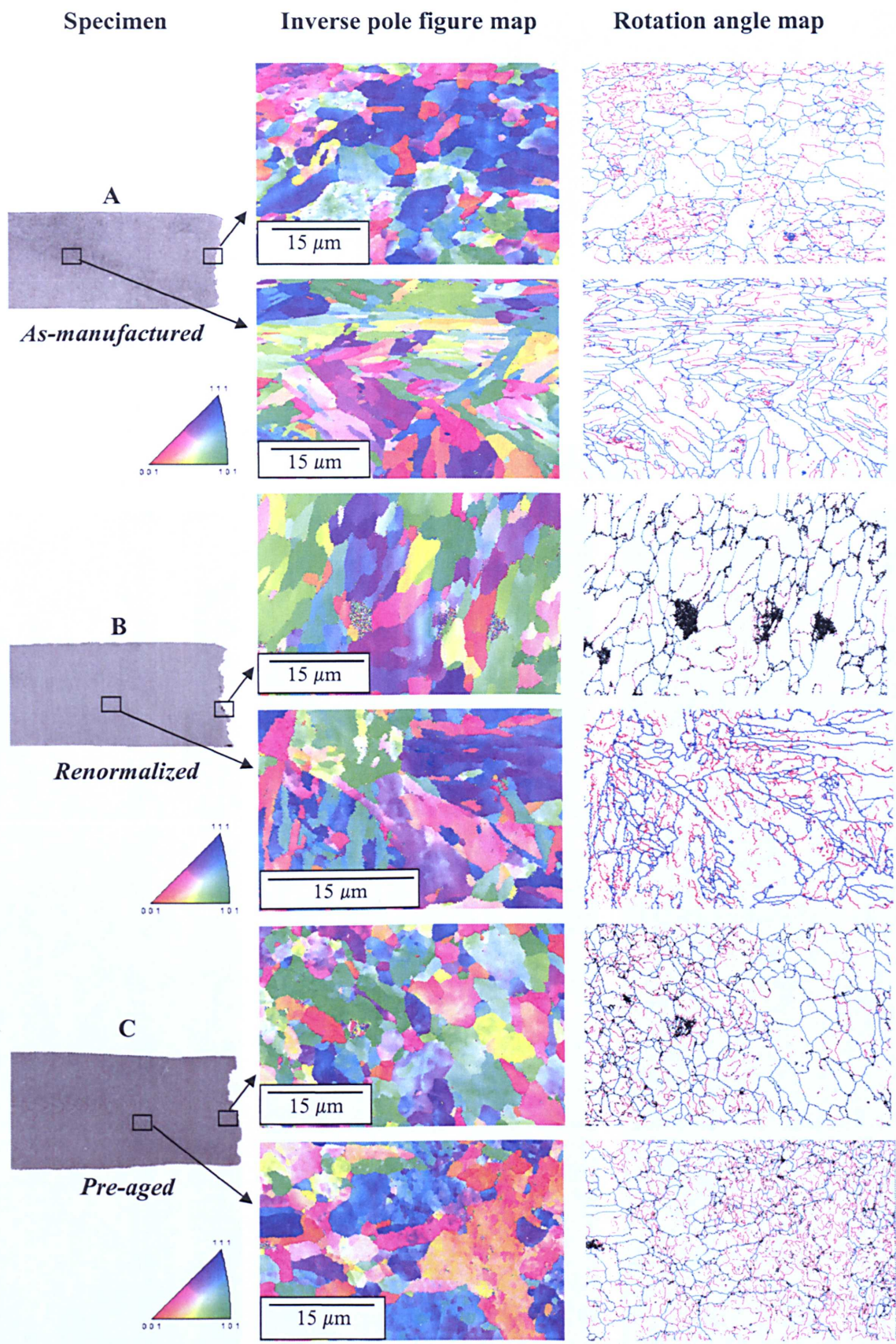


Figure 8.3: Electron backscatter images showing inverse pole figure maps and rotation angle maps of specific HAZ and parent metal regions of all the investigated specimens. The blue lines in the rotation angle maps represent high-angle grain boundaries (10-180°) and red lines indicate low-angle grain boundaries (2-10°). Black regions indicate creep cavitation damage.

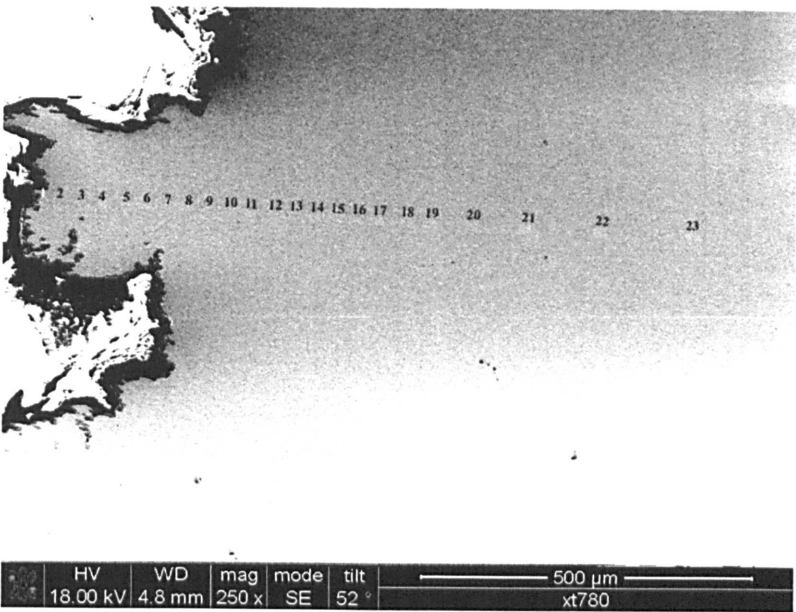


Figure 8.4: Ion beam induced secondary electron images of the creep specimen (after rupture) with the parent metal supplied in the as-manufactured condition (A). The image on the right is a secondary electron image showing the position of the ion beam images below from the Type IV crack (position 1) progressively towards the parent metal region.

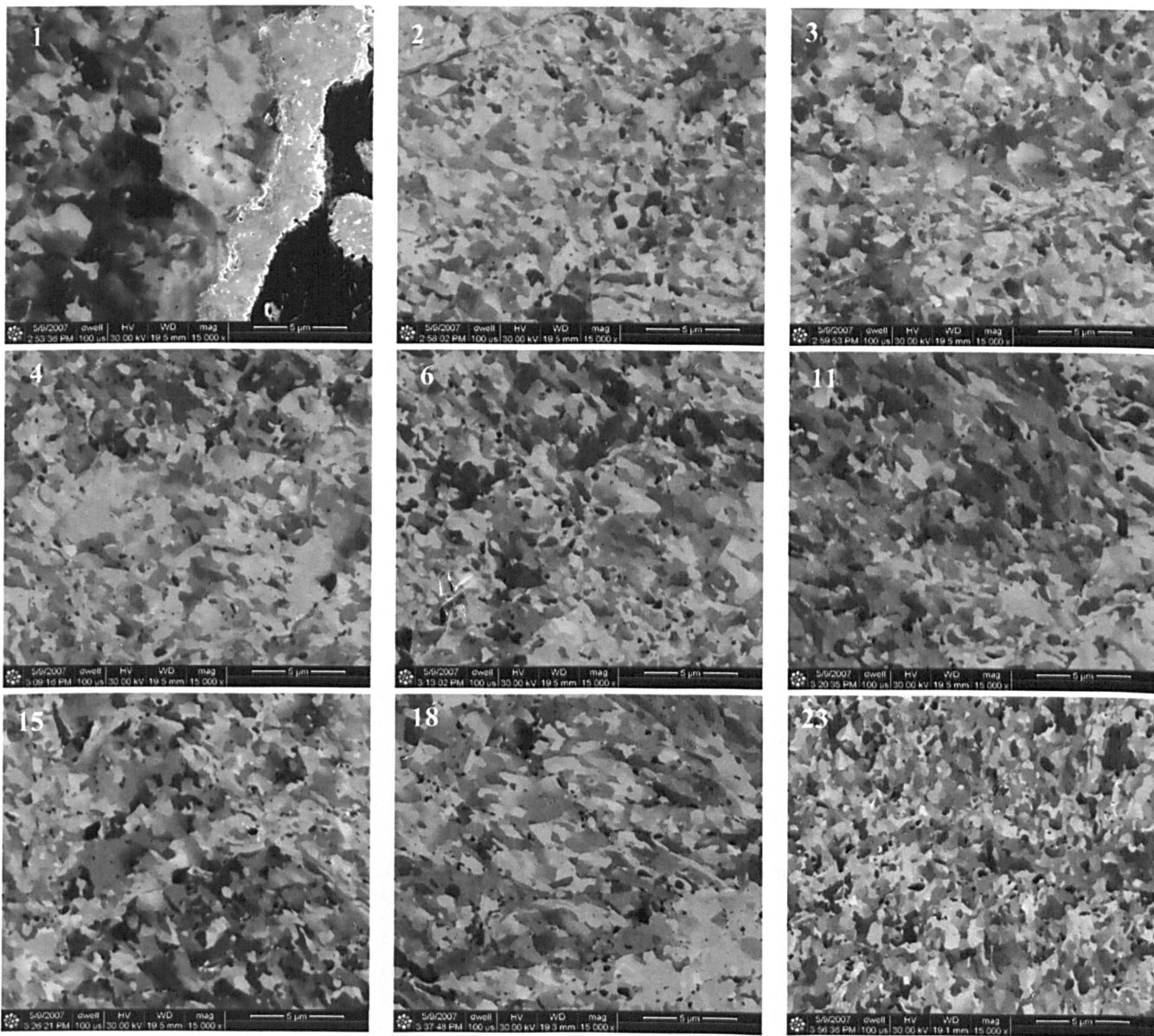


Figure 8.5: Ion beam induced secondary electron images of the creep specimen (after rupture) with the parent metal supplied in the renormalized condition (B). The image on the right is a secondary electron image showing the position of the ion beam images below from the Type IV crack (position 1) progressively towards the parent metal region.

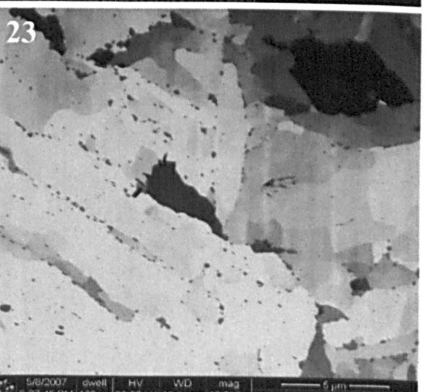
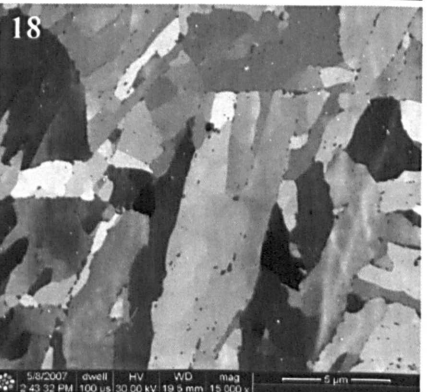
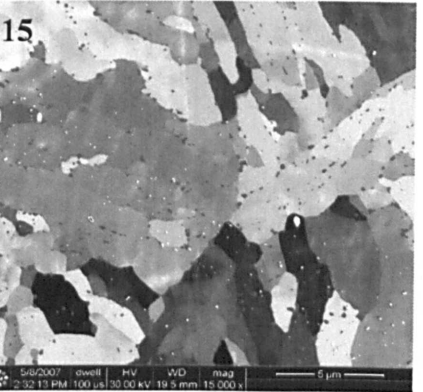
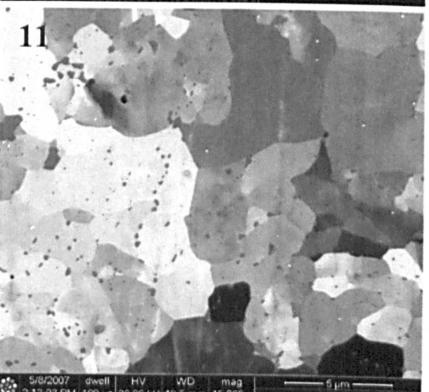
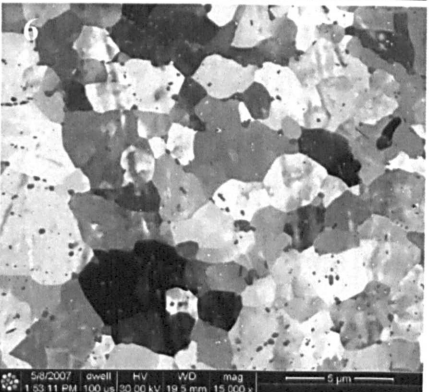
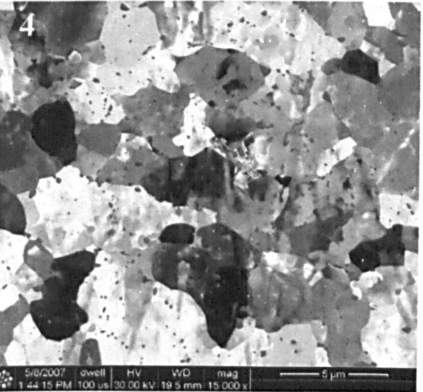
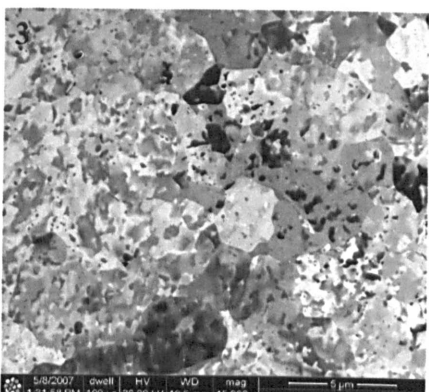
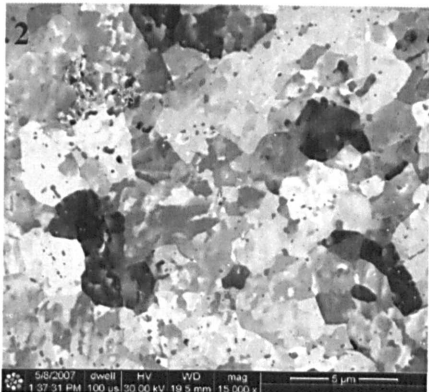
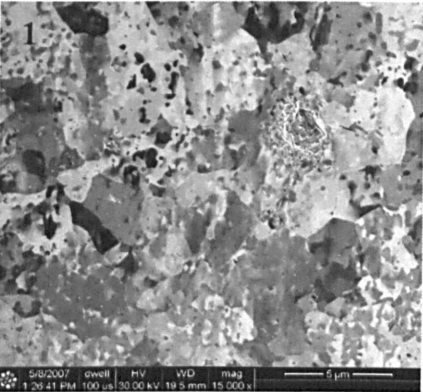
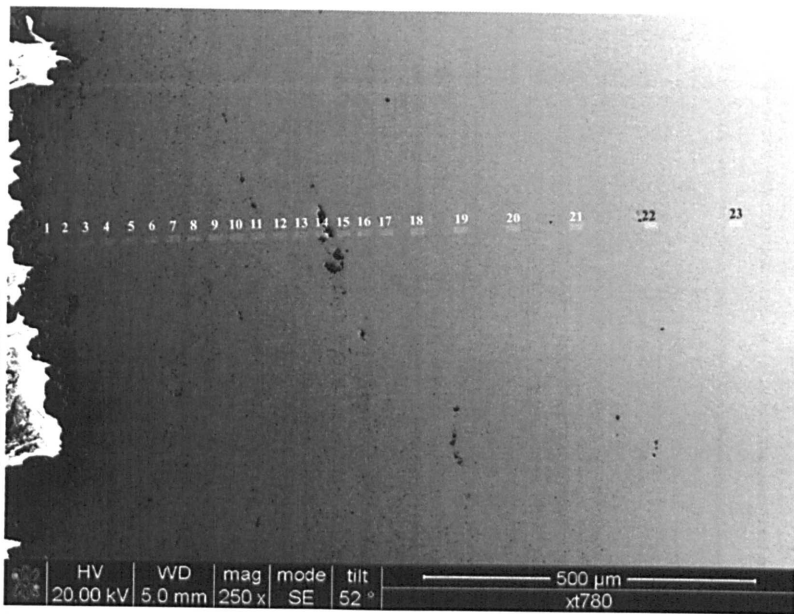


Figure 8.6: Ion beam induced secondary electron images of the creep specimen (after rupture) with the parent metal supplied in the pre-aged condition (C). The image on the right is a secondary electron image showing the position of the ion beam images below from the Type IV crack (position 1) progressively towards the parent metal region.

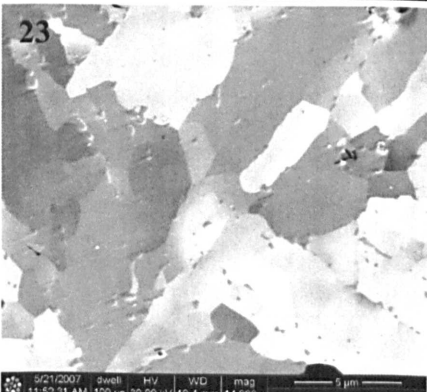
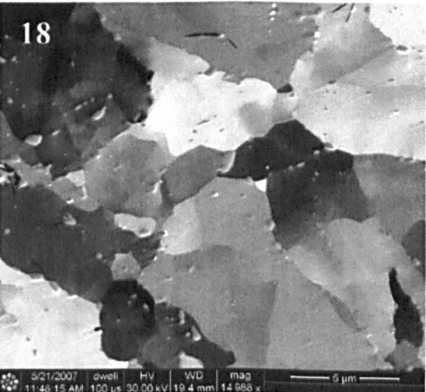
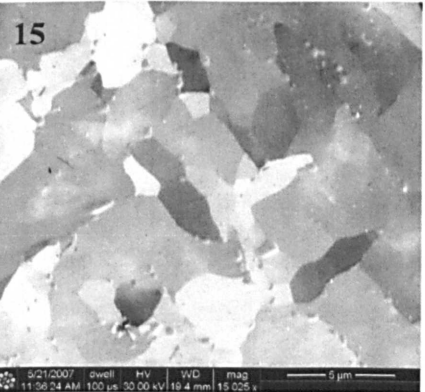
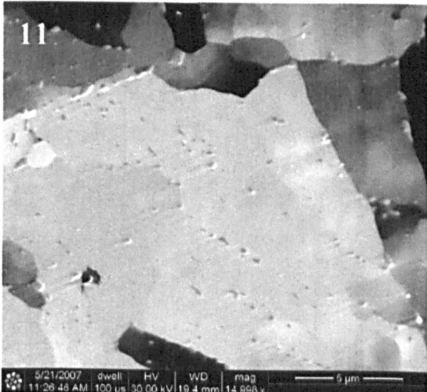
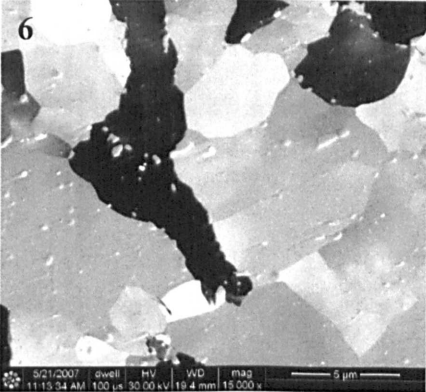
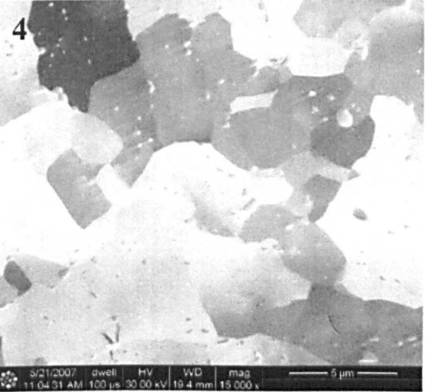
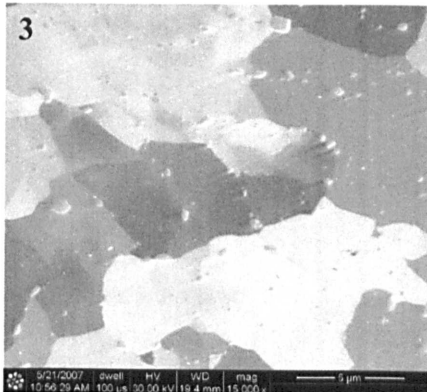
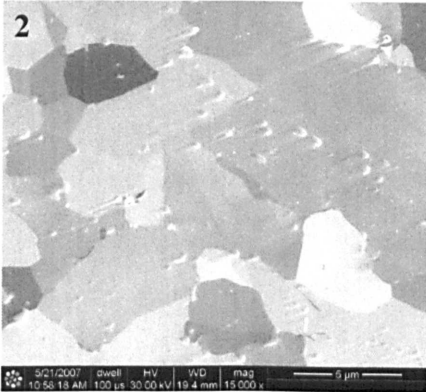
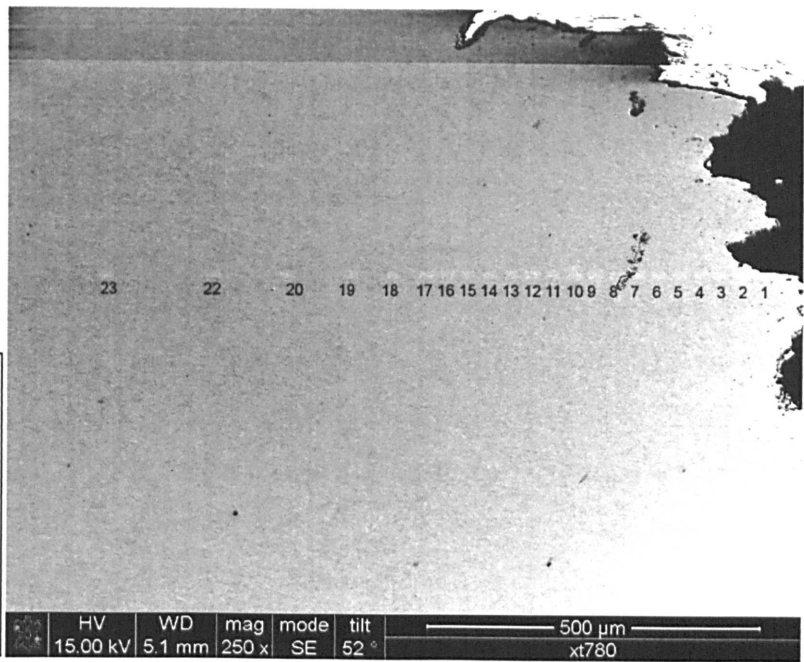


Figure 8.7 shows the hardness profile, taken from the Type IV crack region towards the parent metal region, of the investigated cross-weld creep specimens. Interestingly, the largest mismatch in hardness value between the parent metal and HAZ region is found in the renormalized specimen, where the hardness decreased from ~180 HV in the parent metal to ~150 HV in the Type IV HAZ region. This result is in agreement with Figure 8.5, which showed that this condition also produced the largest microstructural differences between the two regions. In the as-manufactured specimen, the hardness dropped from ~165 HV to ~145 HV, and in the pre-aged specimen, the hardness dropped from ~150 HV to ~145 HV, in the parent metal and Type IV HAZ regions respectively. Consistent with the results from previous investigators, the minimum hardness values of welded joints were found to occur at the location in the vicinity of the HAZ adjacent to the base metal ^[153,158,159].

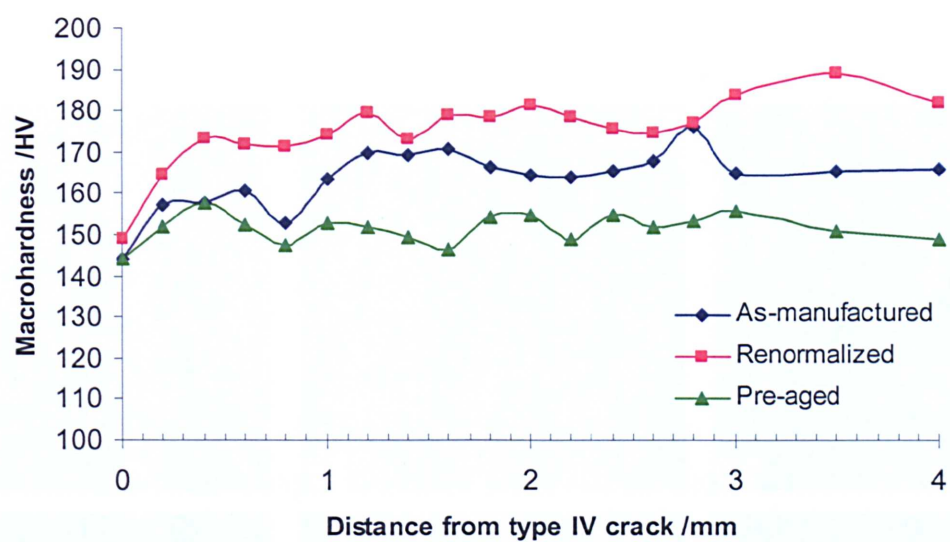


Figure 8.7: Plot showing the variations in macrohardness from the Type IV crack region towards the parent metal.

8.3.2 $M_{23}C_6$ Precipitate Size Distribution

Figure 8.8 shows the distribution of $M_{23}C_6$ precipitates in both the HAZ region near the Type IV cracks and the parent metal region of each specimen. It is clearly shown that the parent metal microstructures after creep testing in specimens A and B (Figure 8.8 a) and b)) are completely different to the HAZ microstructures (Figures 8.8 d) and e)). However, the parent metal microstructure in the aged material somewhat resembles the corresponding HAZ region (Figures 8.8 c) and f)), in corroboration with EBSD and ion-beam induced secondary electron imaging results. Figure 8.9 shows the $M_{23}C_6$ particle size distribution in the each specimen. The mean size of $M_{23}C_6$ precipitates in the parent metal region of specimen A, B and C were

172 ± 3 nm, 163 ± 4 nm and $180 \text{ nm} \pm 4$ nm respectively. These were found to be generally smaller than those in the HAZ region, which were 182 ± 4 nm, 168 ± 3 nm and $189 \text{ nm} \pm 6$ nm respectively. These results corroborate with the findings of Shinozaki *et al* ^[158], Watanabe *et al* ^[153] and Matsui *et al* ^[159], who showed that the coarsening process of $M_{23}C_6$ precipitates was more severe in the Type IV region. It is curious that the size of these precipitates in the parent metal correspond to those in the HAZ. For example, they are smallest in the renormalized and tempered material and largest in the pre-aged material. The material condition that exhibited the largest difference in the size distribution of $M_{23}C_6$ precipitates between the different regions was the as-manufactured specimen. As this material exhibited the longest time to rupture, it is unlikely that the coarsening of $M_{23}C_6$ precipitates was the major HAZ weakening factor, which provided the differences in rupture life between the three specimens.

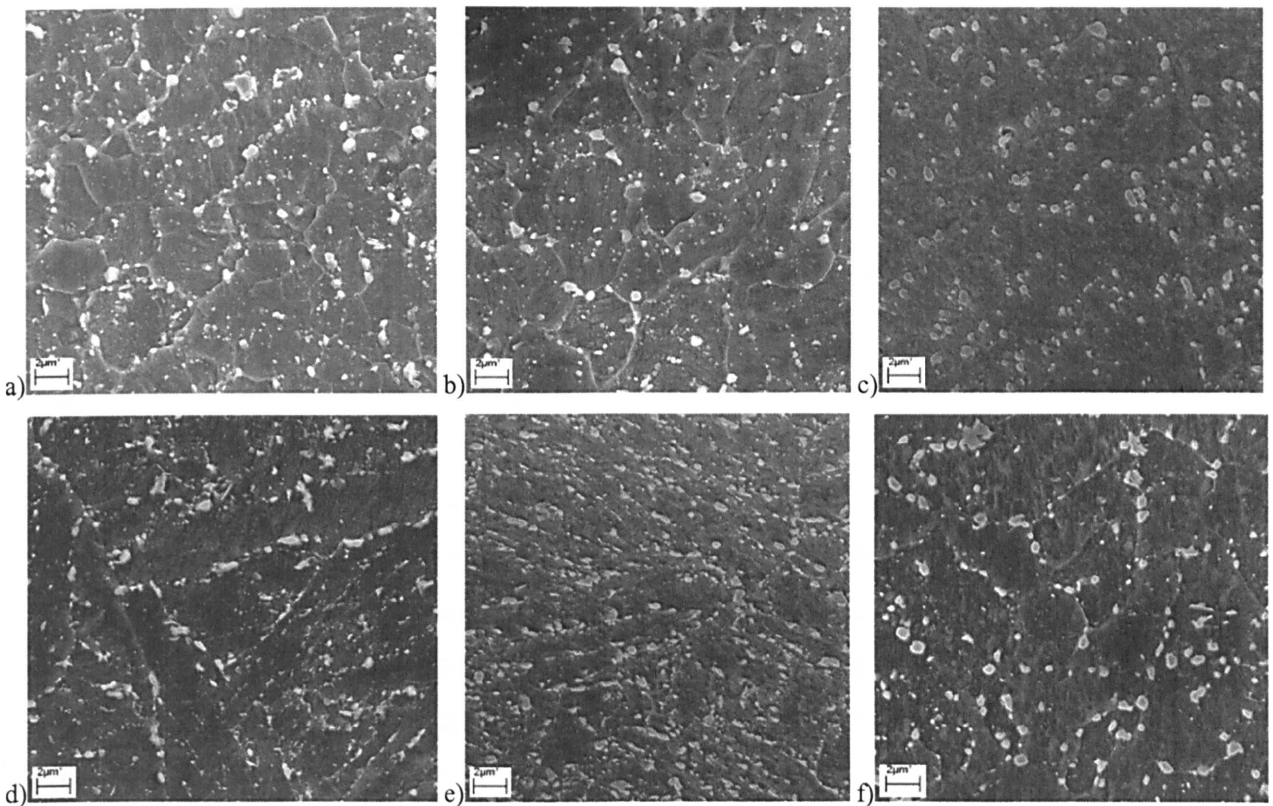


Figure 8.8: Scanning electron micrographs showing the HAZ microstructure on the parent metal side near the Type IV crack region after creep testing in a) the as-manufactured, b) the renormalized and tempered, and c) the pre-aged materials. Micrographs d), e) and f) show the parent metal microstructure corresponding to a), b) and c) respectively.

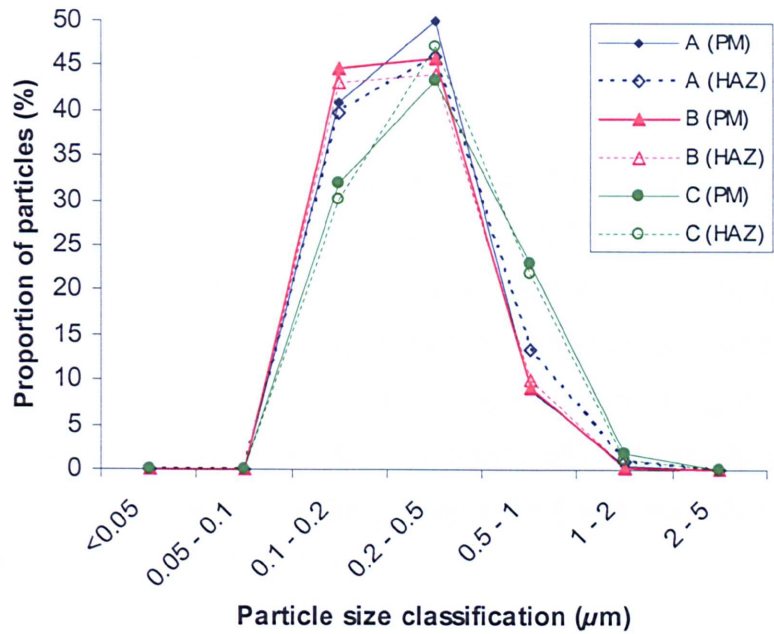


Figure 8.9: The size distribution of $M_{23}C_6$ precipitates in the parent metal (PM) and HAZ regions of the different specimens.

8.3.3 Chemical Composition of MX Precipitates

Similar to Chapters 5 and 7, the chemical composition distribution of MX precipitates, which were shown to be sensitive to changes in heat treatment and thus provide an indication of thermal history, were investigated in the present study in order to compare differences between the Type IV region and the parent metal after creep testing.

Figure 8.10 shows the chemical composition distribution of the metallic elements Nb, V and Cr in the MX carbonitride precipitates, measured with EDS in the TEM, of the parent metal and Type IV HAZ regions of the welded specimens. The results show that in both parent metal and the HAZ region of the as-manufactured (A) specimen, the composition of MX precipitates varies greatly, to such an extent that there is a linear composition distribution of Nb and V in MX particles (Figure 8.10), similar to the Bar 257 specimen that was aged at 650°C for 2,500 hours in Chapter 5 Figure 5.6b). In the pre-aged (C) specimen, some partitioning of MX particles into two distinct particle types, NbC and VN, was found to occur, which corroborates well with the compositions of the long-term aged and creep tested Bar 257 specimens (Chapter 5). This partitioning of MX particles is also evident in the renormalized and tempered (B) material. Interestingly, the composition distribution exhibited in the parent material reflects the composition of MX precipitates in the HAZ for each pre-weld heat treatment condition. This suggests that the additional heat input experienced in the fine

grained Type IV region during the welding process was not severe enough to alter the chemical composition of MX precipitates.

Figure 8.11 presents TEM micrographs of carbon extraction replicas of the Type IV HAZ regions of the welded specimens showing both $M_{23}C_6$ and MX precipitates. Qualitative TEM observation of the various regions showed a large differences in the quantity of MX precipitates in each specimen. It can be seen that there is an abundance of fine intragranular MX precipitates in the HAZ region of the as-manufactured material (Figure 8.11a). This was also found to be the case to a lesser degree in the renormalized HAZ (Figure 8.11b). However, the number density of MX precipitates in the pre-aged HAZ was dramatically lower than in the aforementioned conditions (Figure 8.11 c).

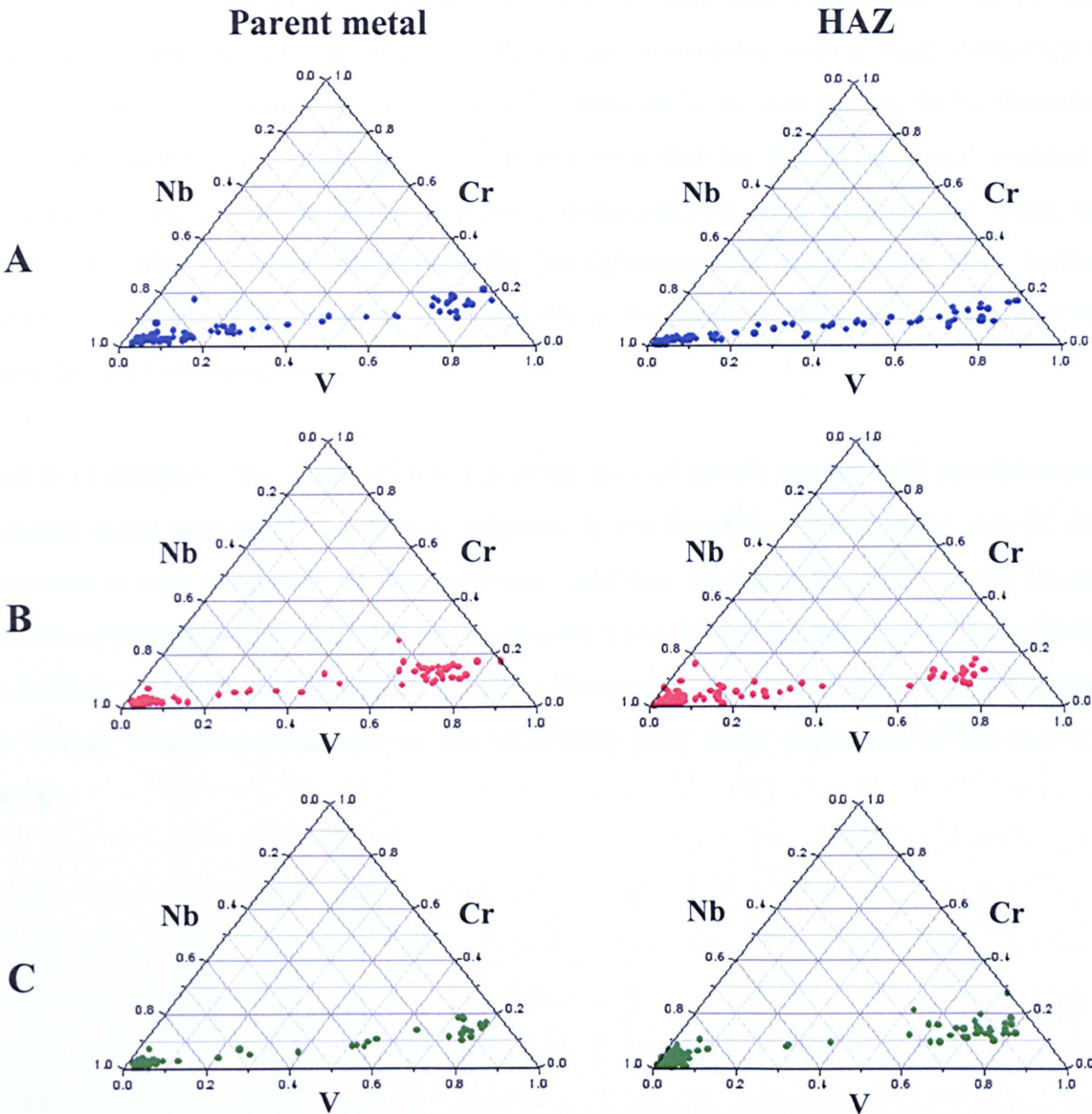


Figure 8.10: EDS measurements from individual MX precipitates comparing their V, Nb and Cr content in the parent metal and HAZ region of the three creep tested cross-weld P91 specimens, which have experience different heat treatments prior to creep testing; A) as-received, B) renormalized and tempered and C) pre-aged.

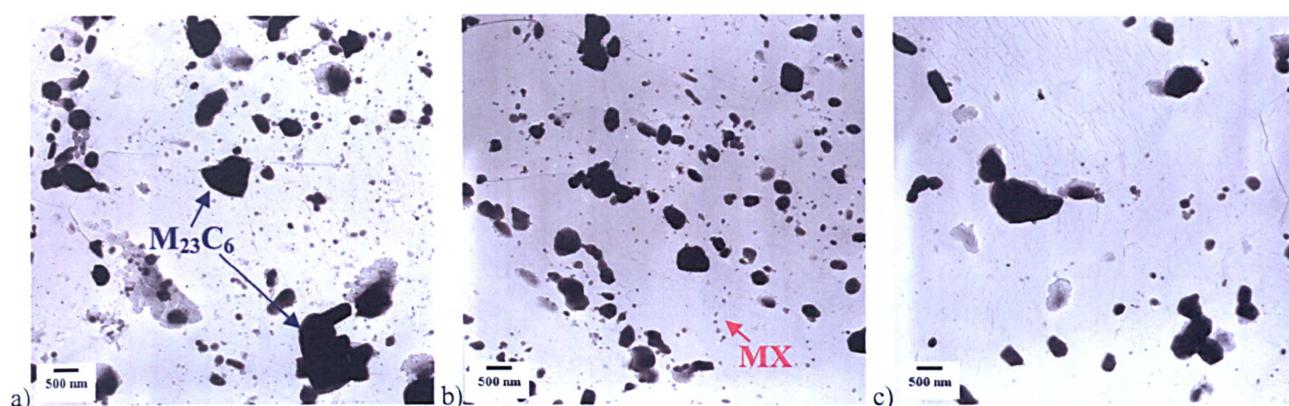


Figure 8.11: Transmission electron micrographs of carbon extraction replicas showing coarse intergranular $M_{23}C_6$ and fine intragranular MX precipitates the HAZ region of the a) as-manufactured, b) renormalized and c) pre-aged specimens after creep testing.

8.3.4 Aluminium Nitride

Scanning electron microscopy using a backscattered electron detector was employed in order to achieve atomic number contrast imaging. This enables particles with a large difference in atomic number to the matrix, for example AlN particles in an iron matrix, to be identified easily. From previous investigations ^[41,157], it was clear that the Bar 257 material contains a significant fraction of AlN particles. Therefore, these particles were characterised using this technique in order to establish whether AlN has influenced the results from creep testing. Figure 8.12 shows needle-shaped AlN precipitates in the parent metal and HAZ region of the as-manufactured (A) specimen.

Figure 8.13 compares the length of the maximum axis of needle shaped AlN precipitates in the parent metal section of the three specimens. It can be seen that the mean size of AlN precipitates is very similar in all the specimens, and that the mean length along the longest axis of these precipitates averaged at approximately $1\ \mu\text{m}$. Given the outcome of these results, it is unlikely that AlN particles have directly affected the outcome of the creep test results, even though they may contribute to the inherently poor creep properties of the Bar 257 material.

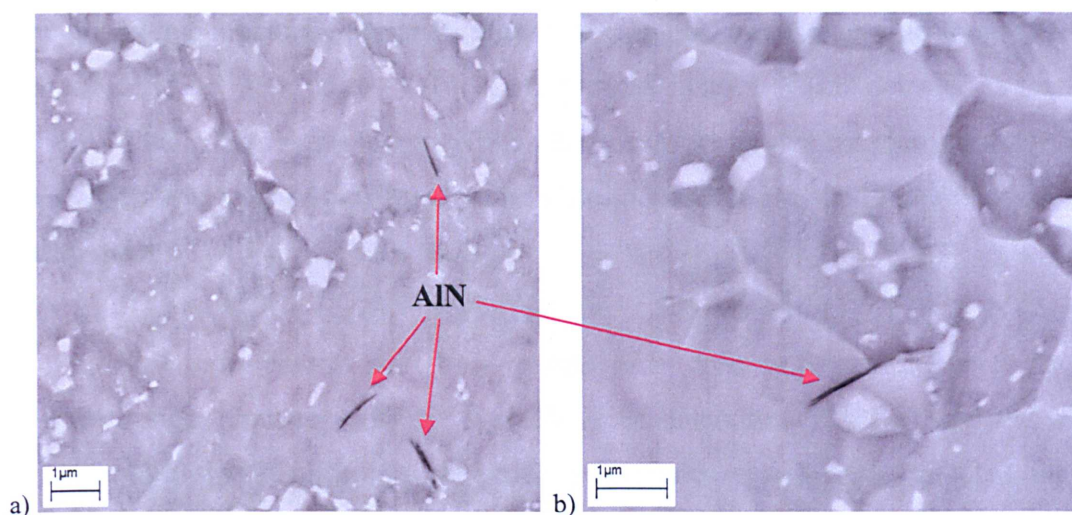


Figure 8.12: Backscattered electron images showing dark needle shaped AlN precipitates in a) the parent metal and b) the HAZ microstructure of the specimen in the as-manufactured condition prior to welding and creep testing.

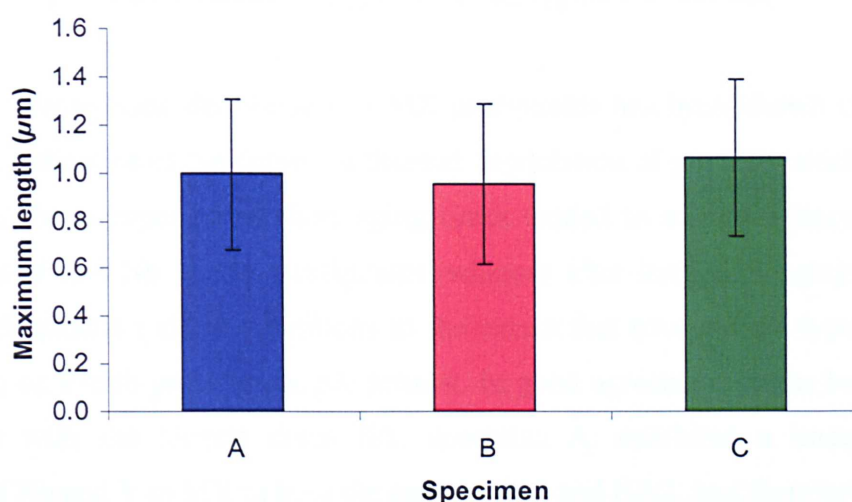


Figure 8.13: Plot comparing the maximum length of needle shaped AlN precipitates in the parent metal section of both the as-received and the aged specimens after creep testing.

8.4 Discussion Concerning the Effect of Heat Treatment on the Creep Strength of P91 Steel Welds

The aim of this study was to investigate whether there was a microstructural correlation between the parent metal and the HAZ microstructure, which may give rise to the weakening of the latter. There was found to be a large variation in the microstructure of the three grade 91 weldments that had experienced different heat treatments prior to creep testing, which resulted in small variations in Type IV creep life. The “strengthened” specimen B, with a mean hardness value approximately 40 HV higher than the as-manufactured bar, was found to have the shortest Type IV creep life. Parallel tests to about 2,000 hours duration ^[156] confirm the general trends, with the welds in both the pre-aged and the renormalized and tempered materials consistently showing modest reductions in HAZ rupture life as compared with

welds in the as-manufactured material. However, a much more extensive longer term test programme would be required to establish whether the history effects detected in tests up to 2,000 hours will still be observable once plant have been in service for many years. Also, the specimen with clearly the largest $M_{23}C_6$ size distribution, the pre-aged material, was not the weakest material.

Several microstructural features have been quantified in order to determine which parameter has had the strongest influence on the Type IV creep behaviour. Firstly, there was no clear evidence that the size distribution of $M_{23}C_6$ precipitates significantly affected the creep performance of the three weldments. This is because the only specimen that showed a variation in size distribution between the parent metal and HAZ region was the strongest as-manufactured bar, where some coarsening in the HAZ region was evident.

The chemical composition distribution of MX precipitates has been shown in the previous chapters to be indicative of the degree of thermal degradation of grade 91 steel. For example, specimens that have experienced short aging times tended to exhibit a linear composition distribution of V and Nb in MX precipitates, whereas after long-term aging or creep, this composition distribution clearly partitions to the extent that two particle types, in this case either Nb-rich or V-rich precipitates, are present. In good agreement, it has been shown that the specimen with the longest creep life, specimen A, exhibited a linear composition distribution of Nb and V in MX in both the parent metal and HAZ, and therefore is a plausible explanation for the apparent weakening of the HAZ in the renormalized specimen, which showed evidence of the partitioning of the particle types. Therefore, it can be hypothesized that the renormalizing treatment from the as-manufactured condition was severe enough to accelerate the changes in chemical composition of MX precipitates, which would normally occur after long-term aging and creep under typical service operating conditions. The high parent metal hardness value of the renormalized specimen is in fact misleading, as this high value can be attributed to the newly produced martensitic microstructure and the shorter tempering time, which is expected to contain a higher dislocation density in comparison to the as-manufactured bar.

The pre-aged condition produced a completely different parent metal microstructure, which comprised of equiaxed grains (Figures 8.3 and 8.6) and a coarse distribution of $M_{23}C_6$ precipitates (Figure 8.9). This is indicative that considerable material recovery, and in particular a notable reduction in the number density of MX precipitates (Figure 8.10c), had taken place during the aging process prior to creep testing. The effect of this pre-aging heat treatment on the mechanical properties was to reduce parent material strength, but at the same time improve ductility. It is not clear whether the HAZ was similarly affected, but it may be that the moderately good creep performance of the weld in the pre-aged material is related to the balance between HAZ ductility and strength properties.

In agreement with the work of Allen *et al* ^[154], these detailed microstructural investigations provide evidence to suggest that the effects of prior parent material heat treatment, in particular the characteristics of second-phase particles, do indeed “survive” the HAZ retransformation process with the consequence of altering the creep performance of welded grade 91 steel components.

Of greater importance, however, were the combined results from ion-beam induced SEM imaging and hardness testing (Figures 8.4 to 8.7). Here, it was shown that the largest disparities between the microstructure and mechanical properties of the Type IV and parent metal regions occurred in the renormalized specimen (Figure 8.5), which consequently performed the worst in creep. A rationale for the results from creep testing could be that as the Type IV failure is an interface, albeit a relatively diffuse one ^[156], any creep strength difference between the Type IV zone material and the adjacent parent material may potentially enhance Type IV cavitation by increasing the local level of triaxial stress ^[158,159]. Increasing triaxility, Bhadeshia *et al* ^[160] argued, ‘reduces creep deformation rates, but increases creep cavitation, which is almost certainly a contributory factor in the so called Type IV cracking’. Assuming the intrinsic Type IV strength is similar in the three specimens – the hardness at the HAZ were very similar in the three specimens - this mismatch, and hence the stress level, will increase as the parent metal strength increases ^[159].

However, as the mismatch in hardness and microstructure is smallest in the pre-aged material, this hypothesis would expect this condition to exhibit superior creep properties. Thus, it is possible that another mechanism, which acts in the opposite direction, interferes with the aforementioned logic, hence the expected results, where the order of decreasing creep rupture life (from highest to lowest) would be pre-aged > as-received > renormalized, were not obtained. In Allen and Fleming's paper ^[153], it was shown that P91 similar welds with a P91 weld metal, P91 dissimilar welds with a stronger Inconel 182 weld metal, and P91 dissimilar welds with an even stronger Inconel 625 weld metal produced Type IV failures with similar lives, albeit a slight improvement in the HAZ creep life was evident in the latter. Their results, therefore, suggest that 'the effects of creep mismatch between the ferritic weld metal, HAZ and parent material are evidently small' ^[153] and that 'it helps to have a strong parent, which provides constraint, reducing creep deformation in the adjacent narrow HAZ' ^[161]. Evidently, in order to clarify the actual effects of parent metal microstructure on the consequential HAZ creep life under typical service condition, more tests need to be performed.

8.5 Summary

The effect of pre-weld heat treatment on the microstructure of welded grade 91 creep specimens has been investigated using a variety of analytical electron microscopy techniques. Several microstructural parameters have been quantified, and in particular it has been shown that the chemical composition distribution of MX carbonitride and the size distribution of $M_{23}C_6$ precipitates in the HAZ region are very similar to those found in the parent metal region. These results are indicative of the fact that the effects of prior parent material heat treatment, which give rise to microstructural variations in particle size and composition, "survive" the HAZ retransformation and this may ultimately affect the creep performance of welded grade 91 steel.

It was also found that a strengthened parent material with a high hardness value, which had been renormalized prior to welding and creep testing, had an adverse effect on the creep properties of grade 91 steel. This was rationalized on the basis that the mismatch in strength between the parent metal and the Type IV region was greatest in this specimen, which resulted in the enhancement of Type IV cavitation by increasing the local level of triaxial stress. Indeed, this is attributable to both microstructural characterization from site specific ion-beam induced secondary electron images from a FIB-FEGSEM instrument and hardness testing, which showed that the differences in the microstructure and mechanical properties

between the Type IV HAZ region and the adjacent parent metal was the greatest in the “strengthened” material.

Chapter 9

A MODEL FOR THE PREDICTION OF CREEP STRENGTH IN GRADE 91 STEEL

9.1 Introduction

It is well known that complex engineering alloys that are used for high temperature power plant applications, where creep performance is the main design criteria, experience different combinations of structural change during their creep lives. These changes, which were quantitatively investigated in the previous chapters, include particle coarsening, subgrain coarsening, changes in the dislocation structure, phase changes and solute depletion from the matrix, in addition to cavitation and cracking. The complexity of trying to account for this combination of structural changes lies in the fact that all of these changes may occur simultaneously, although the likelihood is that only one or two dominant mechanisms may operate at any one time. Subsequent changes in the microstructure, as a function of time, temperature and creep strain, cause the gradual deterioration in mechanical properties which ultimately constitute a loss of structural integrity of high temperature plant components. An important achievement for the power generation industry, therefore, would be the ability to reliably predict the remanent life of critical components with the use of a creep-life predictive model which incorporates microstructural data. Indeed, Tamura *et al.* ^[91] suggested that “a creep equation should describe the relation between creep rate and microstructural parameters, because creep rate is clearly affected by microstructure”. One such method to achieve this milestone may rely on Physically Based Continuum Damage Mechanics (CDM) creep modelling. Recently, Dyson ^[60] and McLean and Dyson ^[93] have reviewed the feasibility of CDM, and have shown that it provides a “unifying framework for some seemingly diverse methods of predicting design and remanent lifetimes”, particularly the creep life.

Essentially, the purpose of CDM is to attempt to predict the effect of microscale defects, such as microstructural damage (e.g. particle coarsening), and damage at the macroscale, such as creep strain, by making assumptions about the nature of the damage and its effect on the macroscale properties. To achieve this, CDM consists of coupled rate equations, for the various damage parameters, which can then be integrated using specific boundary conditions

appropriate to the component operating conditions, e.g. constant load and temperature, for creep life prediction ^[60].

Throughout this thesis, many different microstructural parameters have been quantified and shown to change as a function of both aging time and applied stress. These parameters are summarized in Table 9.1. The changes in microstructural parameters have been shown to correlate with changes in the mechanical properties of grade 91 steel and may, therefore, consequently represent ‘damage’ at the macroscale, e.g. loss in hardness, increase in creep strain etc. Therefore, possible methods of incorporating the microstructural ‘damage’ parameters, specific to modern high Cr ferritic-martensitic steels into the CDM model which, in turn, may facilitate subsequent incorporation into a finite element analysis for creep-rupture life prediction are discussed in this chapter, with specific reference to the results from microstructural characterization work discussed in the previous chapters.

Minor Phase Precipitation	Matrix Microstructure
M ₂₃ C ₆ size	Subgrain size
MX size	Dislocation density
MX composition	Boundary line length
Volume fraction of precipitates	

Table 9.1: Summary of the microstructural features that have been quantified in this thesis and that have been shown to be sensitive to aging time, applied stress and cast composition.

9.2 Physically Based Continuum Damage Mechanics (CDM) Modelling

Equations for determining the creep strain rate at a specific time, or to calculate the evolution of creep strain rate, have been suggested in the literature with slight variations, depending on whether they have been extracted from Dyson [9.1] ^[60] or McLean and Dyson [9.2] ^[93]:

$$\dot{\varepsilon} = \frac{\dot{\varepsilon}_0}{(1 - D_d)(1 - D_s)} \sinh \left(\frac{\sigma(1 - H)}{\sigma_0(1 - D_p)(1 - D_N)} \right) \quad [9.1]$$

$$\dot{\varepsilon} = \dot{\varepsilon}_0 \frac{(1 + D_d)}{(1 - D_s)} \sinh \left(\frac{\sigma(1 - H)}{\sigma_0(1 - D_p)(1 - D_N)} \right) \quad [9.2]$$

The ‘ D ’ terms represent a particular damage parameter which can be distinguished, according to the specific mechanism, by the subscript. For example, D_d represents damage caused by the multiplication of mobile dislocations, D_s accounts for the depletion of solid-solution strengthening elements, D_p represents particle coarsening and D_N represents creep-constrained cavity nucleation controlled damage. The two ‘composite’ parameters, $\dot{\epsilon}_0$ and σ_0 , which are related to the creep strain rate and creep stress respectively, are shown by equations 9.3 and 9.4 to contain several microstructural terms:

$$\dot{\epsilon}_0 = k' \rho_m \phi_p^{1/2} (1 - \phi_p) (1 - \phi_p^{1/2}) \cdot c_j D_m \quad [9.3]$$

$$\sigma_0 = \frac{kTF(\phi_p)\sigma_{Orowan}}{Gb^3} \quad [9.4]$$

where ρ_m is the mobile dislocation density, ϕ_p is the particle volume fraction, c_j is the jog density, D_m is the matrix diffusivity or self-diffusion coefficient, k' is a constant of the order of unity, G is the shear modulus, σ_{Orowan} is the Orowan stress for particle bypass, and $F(\phi_p)$ is predicted to increase from unity during primary creep, due to the stress redistribution around particles, to reach a maximum value of $F(\phi_p) = 1 + 2\phi_p$ at the minimum creep rate.

Dyson ^[60] used equation 9.5 instead of 9.3 in order to compare experimentally determined creep data from Inconel 738LC, a directionally solidified nickel-base superalloy, to CDM predictions of minimum creep rate as a function of varying stress and temperature. Likewise, he substituted equation 9.4 for equation 9.6, which has been developed on the basis that the volume fraction of γ' progressively decreases with increasing temperature.

$$\dot{\epsilon}_0 = \ddot{\epsilon}_0 \exp\left[-\frac{Q_{d/j}}{RT}\right] \quad [9.5]$$

$$\sigma_0 = \sigma_{0,m} \left[1 - \exp\left(-\frac{\Delta H}{RT_s} \left(\frac{T_s}{T} - 1\right)\right) \right] \quad [9.6]$$

where $Q_{d/j}$ is the combined activation energy for diffusion and jog formation, $\sigma_{0,m}$ is the maximum value of σ_0 (at $T = 0$), ΔH is the enthalpy of solution, and T_s is the solvus

temperature of γ' when $\sigma_0 = 0$. Yin and Faulkner^[162,163] have also applied equations 9.5 and 9.6 in order to model the creep strain rate of P92 steel in spite of the fact that these equations were developed to account for the decrease in the volume fraction of γ' as a function of temperature. However, it should be noted that high Cr ferritic-martensitic steels, like P91 and P92, are designed to operate at a narrow temperature range where the volume fraction of precipitates is expected to remain constant.

The parameters needed to use equations 9.3 and 9.4 are listed in Table 9.2. Note that no values of jog density (or jog concentration) were found in the literature for high Cr ferritic-martensitic steels.

Parameters needed to determine 'composite' parameters	Values
Mobile dislocation density, ρ_m	Steady state dislocation density, ρ_∞ , From equation [9.14]
Particle volume fraction, ϕ_p	Measured, or predicted from thermodynamic equilibrium software (MTDATA)
Burgers vector, b	$\sim 2.5 \times 10^{-10}$ m
Shear modulus, G	~ 64 GPa, From Maruyama <i>et al</i> [183]
Orowan stress for particle bypass, σ_{or}	Equation [9.20]
Self-diffusion coefficient, D_m , $D_m = D_0 \exp[-Q/RT]$	$D_0 = 0.5 \times 10^{-4} \text{ m}^2 \text{ s}^{-1}$, self-diffusion of iron in ferrite, From Fridberg <i>et al</i> ^[186]

Table 9.2: The parameters required to solve equations 9.3 and 9.4 and some examples of values that can be inserted into the equations.

In the following sections, the main microstructural 'damage' parameters for high Cr ferritic-martensitic steels, particle coarsening (D_p) and dislocation substructure (D_d), will be discussed and an attempt will be made to compare existing models, which describe these microstructural parameters, with the data from microstructural characterization work from the previous chapters. The effects of creep-constrained cavity nucleation controlled damage (D_N) and the depletion of solid-solution strengthening elements (D_s) are not considered in this investigation, due to the fact that cavitation is not expected to occur until the latter stages of creep, and that the precipitate volume fractions are shown in section 9.2.3 to remain stable up to very long aging times, and therefore it is expected that the solid solution strengthening elements do not change significantly.

9.2.1 Primary Creep

The CDM model, [9.1] and [9.2], uses a dimensionless parameter, H , in order to model the effects of primary creep, which is given by equation 9.7. The evolution of H is given by equation 9.8:

$$H = \frac{\sigma_i}{\sigma} \quad [9.7]$$

$$\dot{H} = \frac{h'}{\sigma} \left[1 - \frac{H}{H^*} \right] \dot{\varepsilon} \quad [9.8]$$

where σ_i is an internal back stress, which is generated by the redistribution of stress within ‘hard’ regions of the microstructure, such as particles and subgrains, during the accumulation of inelastic strain, and σ is the uniaxial stress. The estimation of the value of σ_i is somewhat arbitrary because, at present, there are no accurate descriptions available for this parameter. However, as an indication, Dyson ^[60] states that H can represent values from zero to a material dependent maximum, H^* (<1). h' equals $E\phi$, where E is Young’s modulus and ϕ is the volume fraction of all phases giving rise to the stress redistribution, which may include minor phase precipitates, subgrains and free dislocations. Indeed, Tamura *et al.* ^[91] highlighted that the “equivalent stress to the internal stress is sometimes called athermal stress, threshold stress (σ_{th}), frictional stress, or back stress”, where σ_{th} can be “assumed to be an Orowan stress”. This parameter, however, changes during creep, thus Tamura *et al.* ^[91] suggested that “creep equations concerning internal stress have not yet been complete”. The parameters needed to use equations 9.7 and 9.8 are listed in Table 9.3.

Parameters needed to model primary creep	Values
Young’s Modulus, E	~162 GPa at 650°C, From Haarman <i>et al</i> ^[8]
Particle volume fraction, ϕ_p	Measured, or predicted from thermodynamic equilibrium software (MTDATA)
h' ($=E\phi$)	40 GPa From Yin and Faulkner ^[162,163]
H^*	0.4, From Yin and Faulkner ^[162,163]
Uniaxial stress, σ	Applied stress

Table 9.3: The parameters required to solve equations 9.7 and 9.8, and some examples of values that can be inserted into the equations.

9.2.2 ‘Damage’ Due to the Dislocation Substructure

9.2.2.1 Review of Dislocation and Subgrain Evolution Parameters

The damage due to the ‘multiplication’ of dislocations, D_d , from the Dyson^[60] and McLean and Dyson^[93] papers, is given by equation 9.9, and the evolution of this parameter is given by equation 9.10:

$$D_d = 1 - \frac{\rho_0}{\rho_t} \quad [9.9]$$

$$\dot{D}_d = C(1 - D_d)^2 \dot{\varepsilon} \quad [9.10]$$

where ρ_0 and ρ_t are the initial values of dislocation density and after time t , respectively, and C is a material constant, for which a value of 100 was used by Yin and Faulkner^[162,163]. Equation 9.9 was formed on the presumption that dislocations are carriers of, rather than obstacles to, plastic deformation, according to the following equation, where an increase in the density of free dislocations (ρ_f) represents an increase in the strain rate ($\dot{\varepsilon}_0$):

$$\dot{\varepsilon}_0 = \rho_f b v \quad [9.11]$$

where b is the Burgers vector and v is the average velocity of dislocations. In high Cr power plant steels, however, it is expected that the initial value of dislocation density is at a maximum value in the as-received condition, which progressively decreases to a steady state value with prolonged aging time or exposure to creep conditions. In this investigation, a drop in the value of dislocation density was observed to occur from the as-tempered condition ($3.15 \times 10^{14} \text{ m}^{-2}$ in Bar 257 and $2.65 \times 10^{14} \text{ m}^{-2}$ in W20-3) to 10,000 hours isothermal aging ($3.01 \times 10^{14} \text{ m}^{-2}$ in Bar 257 and $2.37 \times 10^{14} \text{ m}^{-2}$ in W20-3) in both materials. In addition, Pesicka *et al*^[77], in response to the McLean and Dyson paper^[93], argued that their results, from a 12% Cr steel creep tested at 650°C at 120 MPa, suggested that the increase in creep rate (with respect to exposure time) was not due to an increase in dislocation density “as it is sometimes assumed in phenomenological micro mechanical models”. Instead, they found that the dislocation density remained constant during steady-state (secondary) creep.

An alternative description of the evolution of dislocation density has been developed by Straub ^[180], who found experimentally that the development in dislocation density (and subgrain size) in 9-12 wt.% Cr steel can be described mainly as a function of creep strain (ϵ):

$$\log x = \log x_{\infty} + \log(x_0 / x_{\infty}) \exp\left(-\frac{\epsilon}{k_{\log x}}\right) \quad [9.12]$$

where x is either subgrain size, ω , or the spacing between free dislocations in the subgrains, $\rho_f^{-0.5}$ (ρ_f is the density of free dislocations), x_0 is the initial value, x is the value after creep exposure, and $k_{\log x}$ is a rate constant dependent on the creep stress and takes a value of 0.12 for subgrain development. With increasing strain, the values of subgrain size and dislocation spacing approach steady state values, which are dependent on the applied stress σ , and are determined by:

$$\omega_{\infty} = 10 \frac{Gb}{\sigma} \quad [9.13]$$

$$\begin{aligned} \rho_{f,\infty}^{-0.5} &= 3.9 \frac{Gb}{\sigma} \\ \rho_{f,\infty} &= \left(\frac{\sigma}{0.5MGB} \right)^2 \end{aligned} \quad [9.14]$$

where G is the shear modulus and b is the Burgers vector line length. A significant assumption of the steady state dislocation density and subgrain values is that they are independent of material and initial states of the dislocation substructure. Nevertheless, several authors have shown that values of experimental data from subgrain size measurement of crept high Cr steel specimens are comparable with the equations 9.12-9.13 (Spigarelli *et al.* ^[174], Qin *et al.* ^[69], Polcik *et al.* ^[181], Qin ^[182], Maruyama *et al.* ^[183]).

The parameters which are needed to model the ‘damage’ due to dislocations are listed in Table 9.4. These values have been used to compare model results of steady state dislocation density and subgrain size to measured values from specimens that have undergone different aging and creep loading conditions, the results of which are presented in the following section.

Parameters needed to model 'damage' due to dislocations	Values
Shear Modulus, E	~64 GPa (From Maruyama <i>et al</i> ^[183])
Burgers vector, b	2.5×10^{-10} m
Taylor factor, M	3
Uniaxial stress, σ	Applied stress
Initial dislocation density, ρ_0	Measured using EBSD or TEM
Initial subgrain size, ω_0	Measured using XRD or TEM

Table 9.4: The parameters required to solve equations 9.12, 9.13 and 9.14 and some examples of values that can be inserted into the equations.

When considering the separate effects high temperature exposure and creep strain, Qin *et al.* ^[69] suggested that the coarsening of subgrains is “negligible” during annealing, whereas they found that, on the contrary, subgrains coarsen strongly during creep. They applied equation 9.12 and found a good agreement between measured and modelled subgrain sizes, from which they deduced, quoting Blum and Gotz ^[184], that “one can in principle use the subgrain size as a sensor for strain and residual lifetime”.

On the importance of the separate effects of the dislocation substructure and minor phase precipitates on the creep strength of high Cr ferritic-martensitic steels, Maruyama *et al.* ^[183] argued that the dislocation substructure produces greater values of athermal yield stress (or the Orowan threshold stress) than particles. Therefore, they concluded that the dislocation substructure is the major obstacle to plastic deformation (creep strain) in these class of alloys. However, Spigarelli *et al.* ^[174] argued that, if ω_∞ and ρ_∞ are unique functions of stress, the differences in dislocation density or subgrain size cannot explain the difference in creep strength of different variations of high Cr power plant steels. On this basis, they suggested that subgrain strengthening is not the main creep strengthening mechanism. In the following section, therefore, the effects of the changes in the dislocation density and subgrain size as a function of aging time and creep stress, which were measured in Chapter 6, on the hardness will be investigated, and these results will be compared to model results from equations 9.13 and 9.14 in order to evaluate the ‘damage’ due to dislocations.

9.2.2.2 Comparison Between Experimental and Modelled Subgrain Size and Dislocation Density Results

Figures 9.1 and 9.2 compare the experimentally determined values of subgrain size and dislocation density against the predicted steady state values determined from equations 9.13 and 9.14 respectively. In Figure 9.1, it can be seen that the measured subgrain sizes are inversely related to the hardness, which implies that the growth of subgrains can be used as a parameter that causes ‘damage’ to the microstructure. It can also be seen that the calculated steady state values of subgrain size (ω_{∞}) are very similar, albeit slightly overestimated, to the measured values of subgrain size for the creep tested specimens. From Figure 9.1 and equation 9.13, the steady state grain size is expected to increase with decreasing uniaxial creep stress. For example, ω_{∞} was predicted to be 2.667 and 1.721 μm in the Bar 257 specimens that were creep tested at 60 and 93 MPa respectively.

Figure 9.2 shows that a trend exists between dislocation density and hardness, where a decrease in the dislocation produces a decrease in hardness. It is also shown that the calculated steady state values of dislocation density, ρ_{∞} from equation 9.14, are considerably smaller than the measured dislocation density values of the Bar 257 creep specimens that have been creep tested at 60 and 93 MPa. These values were measured from x-ray line profile analysis (see section 6.3.4). The ρ_{∞} values are also considerably smaller than the range of values, $1\text{--}10 \times 10^{14} \text{m}^{-2}$, which are commonly reported in the literature for high Cr ferritic-martensitic steels. Most of the literature values correspond to measurements performed from transmission electron micrographs on thin-foil specimens. Also shown in Figure 9.2 is the fact that, according to equation 9.14, the steady state dislocation density, ρ_{∞} , is expected to decrease with decreasing creep stress. This does not correspond to the measured dislocation density values from the creep tested Bar 257 specimens, which show a decrease in dislocation density with increasing uniaxial stress. However, the measured results may be slightly misleading as the rupture times varied significantly between the 60 and 93 MPa specimens, 2,217 and 82 hours respectively at 650°C.

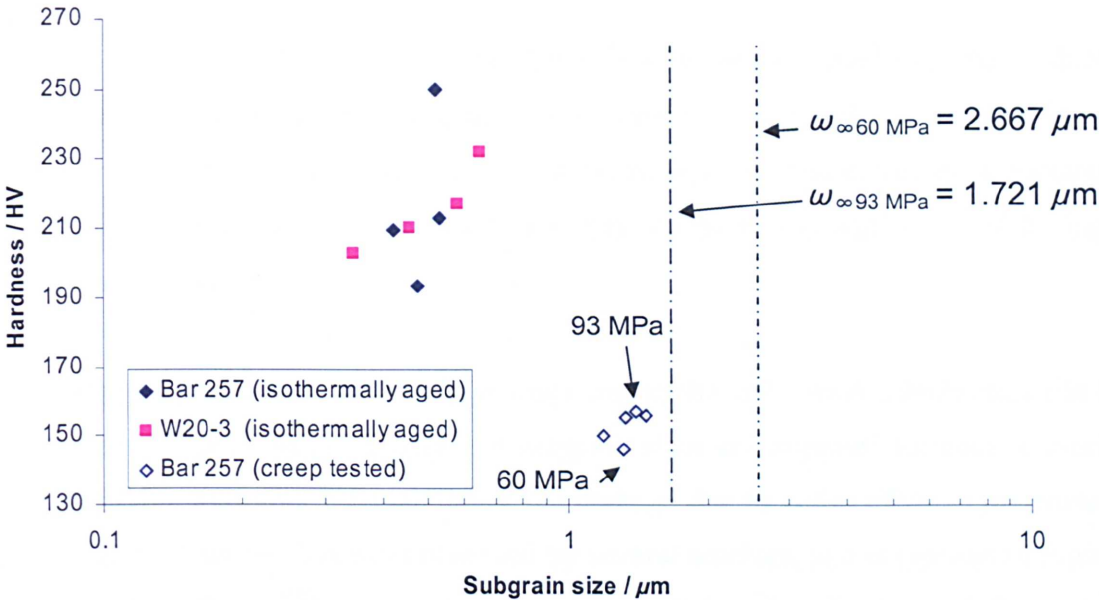


Figure 9.1: Plot showing the effect of subgrain size on the hardness of grade 91 components. The temperature at which isothermal aging and creep testing was carried out was 650°C. The steady state values of the subgrain sizes as a function of creep stress, ω_∞ were calculated from equation 9.13.

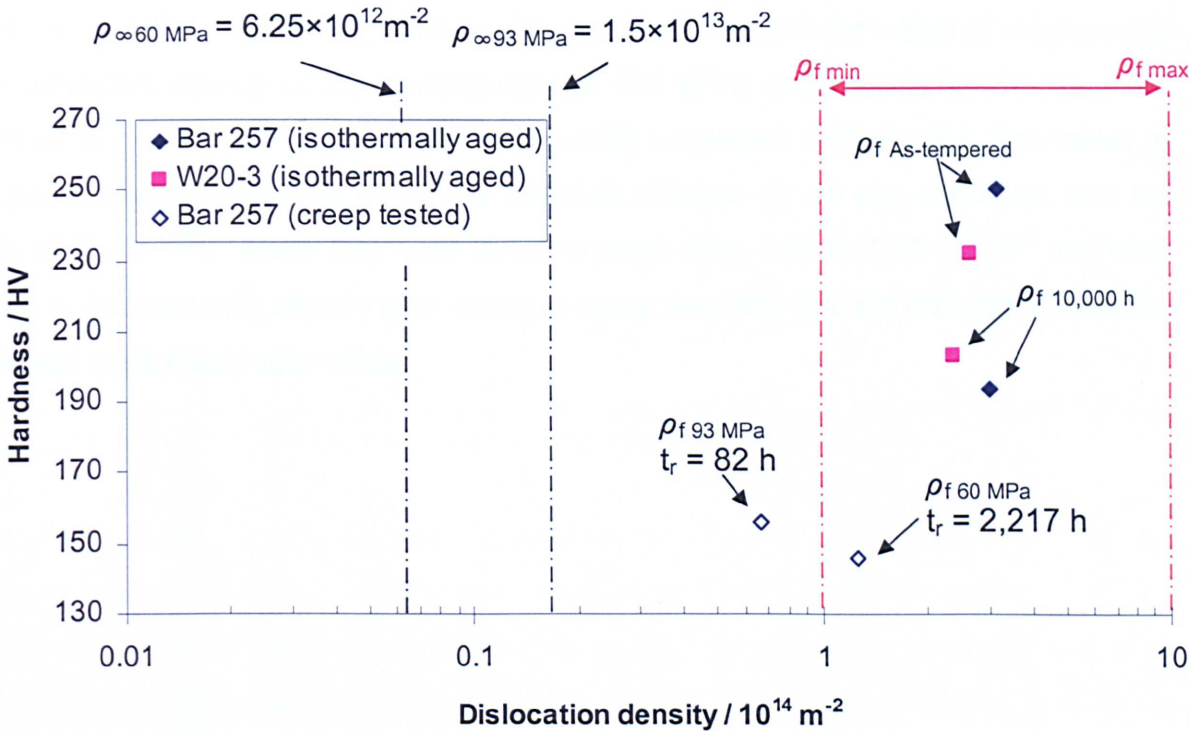


Figure 9.2: Plot showing the effect of free dislocation density, ρ_f , on the hardness of grade 91 components. The temperature at which isothermal aging and creep testing was carried out was 650°C. t_r is the time to rupture. The steady state values of the dislocation densities as a function of creep stress, ρ_∞ which are represented by the black dashed lines, were calculated from equation 9.14. The red dashed lines represent the typical range, from the literature, of dislocation density values in high Cr ferritic-martensitic steels that have experienced different creep loading conditions.

9.2.2.3 Discussion Concerning the 'Damage' Due to the Dislocation Substructure

A comparison between the hardness and the subgrain size has indicated that the hardness generally decreases with increasing subgrain size (Figure 9.1). Similarly, a decrease in the density of free dislocations also correlated with a hardness drop. Therefore, the subsequent evolution of these two microstructural parameters may represent 'damage' incurred by high Cr ferritic-martensitic steels.

The complexity of trying to account for the damage due to the dislocation substructure lies in the fact that both the dislocation density and subgrain sizes are expected to reach a steady state value, implying that after a certain point the damage due to either of these parameters becomes negligible. This fact has been observed by several workers, and is typified in Figure 9.3 from the work of Ennis ^[185], in which the evolution of the subgrain size and dislocation density of P92 steel, which had been crept at 600 and 650°C, is clearly shown. In this investigation, he measured the dislocation density and the subgrain size from measurements in the TEM. Ennis ^[185] showed that after creep testing 3,000 h at 650°C a stable structure was achieved, in which the dislocation density and subgrain size reached steady state values of $\sim 2 \times 10^{14} \text{m}^{-2}$ and $2 \mu\text{m}$ respectively. These values are consistent with the values of subgrain size and dislocation density of the investigated Bar 257 (P91) creep tested specimens, $0.66\text{--}1.25 \times 10^{14} \text{m}^{-2}$ and $1.32\text{--}1.46 \mu\text{m}$, respectively, which are plotted in Figure 9.4. The values of the dislocation density of the ex-service materials (Chapter 7) are also consistent with the work of Ennis ^[185], where they were found to range from 1.15 to $1.94 \times 10^{14} \text{m}^{-2}$ and were shown to decrease only slightly after severe re-aging, implying that the dislocation densities do indeed reach steady state values.

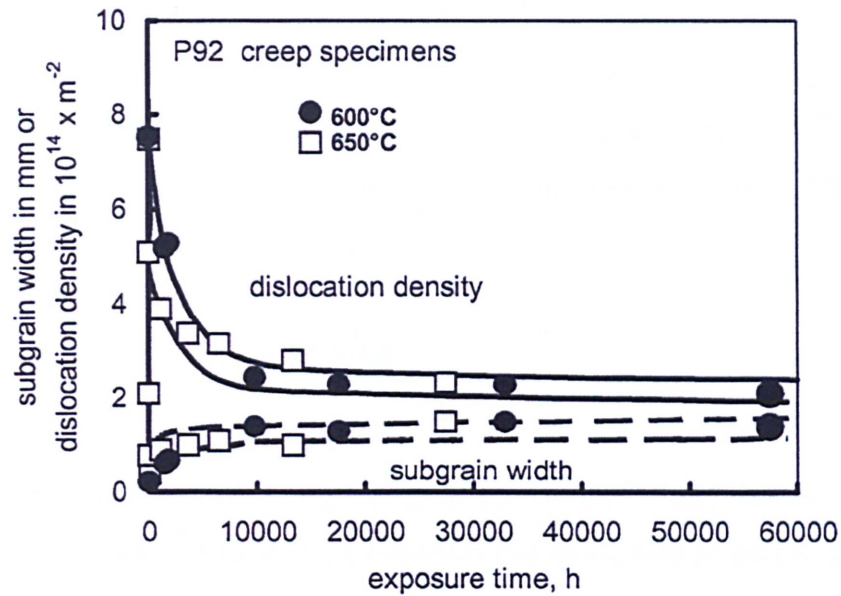


Figure 9.3: Plot showing the changes in dislocation density and subgrain width as a function of exposure time for P92 creep specimens at 600 and 650°C. After Ennis ^[185]. Note: the actual subgrain dimensions were measured in μm , not mm.

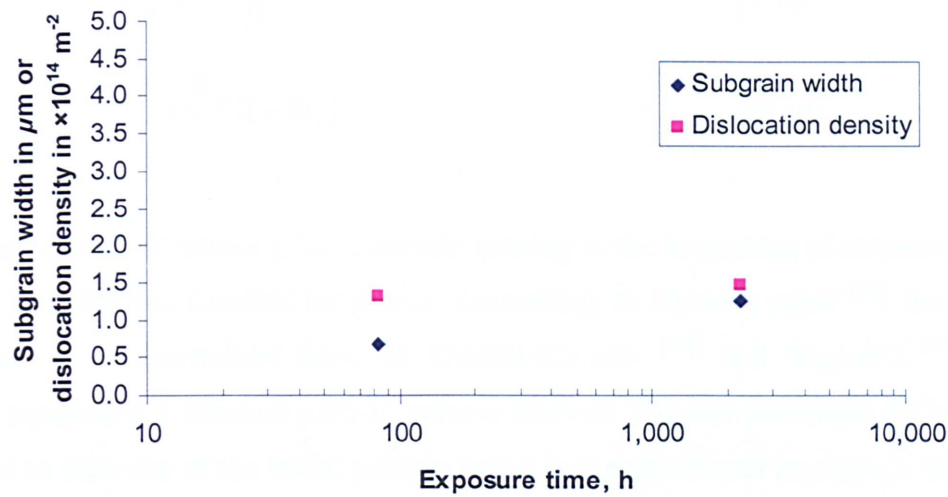


Figure 9.4: Plot showing the changes in dislocation density and subgrain width in the investigated Bar 257 creep specimens as a function of exposure time. The creep tests were performed at 650°C.

Both the dislocation density and subgrain size have been shown in the literature to affect the creep properties of high Cr ferritic-martensitic steels. For example, Maruyama *et al* ^[183] argued that a higher dislocation density and smaller subgrain size improved the creep resistance of these materials, after they showed that, in a creep test performed at 650°C at 98 MPa, a 11Cr-2W-0.3MoCuVNb steel with an initial dislocation density of $1.5 \times 10^{14} \text{ m}^{-2}$, achieved 1% strain at 10% of the rupture life. This was compared to a similar steel with an initial dislocation density of $7.7 \times 10^{14} \text{ m}^{-2}$, which achieved 1% strain at 70% of the creep rupture life. The main challenge of trying to incorporate a dislocation ‘damage’ parameter

into the Dyson model is that, at present, differences in the dislocation density or subgrain size, which have been shown by previous workers to affect the creep properties, cannot easily be used to explain the difference in creep strength of steels of the same family^[174], or differences in the creep strength of the same class of alloys which have experienced different pre-service heat treatments.

9.2.3 'Damage' Due to Particle Coarsening

9.2.3.1 Review of Particle Coarsening Equations

The damage due to particle coarsening, D_p , from the Dyson^[60] and McLean and Dyson^[93] papers, is given by equation 9.15, and the evolution rate of D_p with respect to time is given by equation 9.16:

$$D_p = 1 - \frac{P_0}{P_t} \quad [9.15]$$

$$\dot{D}_p = \frac{K_p}{3} (1 - D_p)^4 \quad [9.16]$$

where P_0 and P_t are the values of interparticle spacing at the beginning of coarsening and at time t , and K_p is the rate constant for particle coarsening. In Dyson's paper^[60], the evolution of D_p is said to be determined from the Lifshitz-Slyozov^[164] and Wagner's^[165] (LSW) coarsening equation at a constant particle volume fraction. The rate parameter K_p is inversely proportional to the cube of the initial particle radius and proportional to $\exp[-Q_c/RT]$, where Q_c is the sum of the activation energy for diffusion and the enthalpy of solution of the rate controlling element in the matrix. Dyson^[60] suggested that the damage caused by particle coarsening requires two further parameters, a constant, K_p' , and an activation energy parameter Q_p :

$$K_p = K_p' \exp\left(-\frac{Q_p}{RT}\right) \quad [9.17]$$

$$\begin{aligned} \frac{1}{r^3} - \frac{1}{r_0^3} &= \frac{8}{9} \frac{\gamma \cdot \Omega D C_0}{RT} t \\ \frac{1}{r^3} - \frac{1}{r_0^3} &= K t \end{aligned} \quad [9.18]$$

The coarsening constant, K , is determined by the matrix diffusivity D , interfacial energy γ , equilibrium solute concentration C_0 and the molar volume of the precipitate Ω . Yin and Faulkner^[162,163] mentioned that K_p (in [9.16]) is determined by both K (in [9.18]) and the initial particle radius \bar{r}_0 . However, neither these authors nor Dyson^[60] offered an explanation of how K_p and K_p' (in [9.17]) are actually determined, and do not clarify whether K can be substituted for K_p in equation 9.16.

Yin and Faulkner^[162,163] argued that the obvious limitation to the LSW coarsening model is that it is only applicable to intragranular particles, and thus, it cannot account for the effects of the grain boundary diffusion, as well as the volume diffusion controlled coarsening of $M_{23}C_6$ precipitates. To address this issue, they developed a Monte Carlo approach, in which they suggested that more information can be acquired about the microstructural evolution of these steels, such as particle size distribution and interparticle spacing, which they argued was the limitation of the approaches by Robson and Bhadeshia^[166,167] and the DICTRA^[168] software method.

However, in a later paper, Bhadeshia and Sourmail^[169] observed that the Yin and Faulkner approach^[162,163] also contains several fundamental limitations. Firstly, multicomponent diffusion is neglected, to such an extent that the theory only accounts for Cr diffusion. Secondly, the effects of capillarity were calculated without allowing for multicomponent effects. In addition, Yin and Faulkner's^[162,163] treatment of interparticle spacing is somewhat simplified, as it is assumed that the combined interparticle spacing of intragranular VN and grain boundary $M_{23}C_6$ precipitates is given by:

$$P(t) = \left[\frac{V}{N(t) + N_{GB}(t)} \right]^{1/3} \quad [9.19]$$

where V is the volume of the simulation cell, $N(t)$ is the number of VN particles in the cell, and $N_{GB}(t)$ is the number of grain boundary particles. This approach, which is intended to relate interparticle spacing to the damage caused by particle coarsening, may introduce errors in the results as there is no discrimination between the two particle types which may, in turn, contribute to strengthening by completely different mechanisms, i.e. grain boundary pinning and dislocation trapping. In addition, given the extreme heterogeneity of the dispersion of

particles, particularly intragranular MX precipitates; due in large part to the very small volume fraction of the strengthening precipitates, it is perhaps optimistic to make assumptions about the uniformity of the microstructure, hence, the lack of reported values of interparticle spacing for high Cr steels in the literature. The inclusion of interparticle spacing as a major strengthening mechanism may be better suited to describe single crystal Ni-superalloy substrates, which contain a very large fraction of coherent strengthening particles. It is possible that a more general parameter is required to describe the effects of precipitation strengthening in high Cr steels, particularly when the main parameter considered is the Orowan stress. Indeed, the Orowan stress equation may also take the form ^[61]:

$$\sigma_{Orowan} = 3.32Gb \frac{\sqrt{f_p}}{d_p} \quad [9.20]$$

where f_p is the precipitate volume fraction and d_p is the mean precipitate diameter, G is the shear modulus, and b is the Burgers vector. Good physical models are available, which can predict both of these parameters for high Cr steels with reasonable accuracy. These are discussed below.

Robson and Bhadeshia ^[166,167] developed a model to simulate the kinetics of carbide precipitation reactions in high Cr steels which occur over long periods of time at temperature as a function of chemical composition. One of the key features of this model is that it is capable of handling several simultaneous precipitation reactions, to the effect that different precipitate phases can influence each other. The model, adapted from the classical Johnson-Mehl-Avrami theory which describes the rate at which a phase precipitates during solid state transformation, requires thermodynamic data (readily obtainable from MTDATA), such as the equilibrium volume fraction of precipitate, the equilibrium concentration of the rate controlling species in the precipitate and in the matrix, along with some assumptions on the value of nucleation site density and the interfacial energy of the nucleus of the different precipitate types.

The evolution of the size of precipitates in power plant components can be modelled according to the LSW equation [9.18]. An important consideration for equation 9.18 is that the coarsening rate is for a binary alloy system. Hald and Korcakova ^[61] discussed that, recently, extensions to multicomponent systems have been obtained by Umantsev and Olson

[170] and Ågren *et al.* [168], where the latter produced a formula in a multi-component system of β precipitate particles in a α matrix:

$$K_p = \frac{8}{9} \frac{\gamma V_m^\beta}{\sum_{i=1}^c \frac{(x_i^\beta - x_i^{\alpha/\beta})^2}{x_i^{\alpha/\beta} D_i / RT}} \quad [9.21]$$

where γ is the interfacial energy, V_m^β is the molar volume of the precipitate phase, D_i is the diffusion coefficient of element i in the matrix, x_i^β is the mole fraction of element i in the precipitate and $x_i^{\alpha/\beta}$ is the mole fraction of element i in the precipitate/matrix interface. Again volume diffusion is assumed, whereas the supply of the solute elements in high Cr steel can also include grain boundary and dislocation pipe diffusion. However, Hald and Korcakova [61] found that, on comparing the coarsening model [9.21] to measured particle sizes, the former could be fitted to the latter by an adjustment of the value of the interfacial energy γ . It was postulated that, in general, the expected value of γ ranges between 0.1-1 J/m², such that lower values correspond to coherent particle/matrix interfaces, and the higher values correspond to incoherent interfaces. Therefore, it can be postulated that lower values are more representative of intragranular precipitates, and higher values by particles in regions with much lower order, such as grain boundaries. Accordingly, Hald [171] found good agreement with experimental data by adjusting the interfacial energy values in P92 steel to 0.5 J/m² for MX, 0.8 J/m² for Laves and 1 J/m² for M₂₃C₆, all at a temperature of 650°C.

Furthermore, Abe [172], citing Takayama *et al.* [173], states that the grain boundary diffusion controlled Ostwald ripening of carbides can be given by:

$$\bar{r}^4 - \bar{r}_0^4 = K_4 t$$

$$K_4 = \left(\frac{3}{4}\right)^3 \left(\frac{2\sigma V \delta D_{gbM}}{RT}\right) \left\{ \frac{K_{gb}}{(u_{pM} - u_M)^2} \right\} \quad [9.22]$$

where σ is the interfacial energy, δ is the thickness of the grain boundary, D_{gbM} is the grain boundary diffusion coefficient of M atom, V is the molar volume of the carbides, u_M and u_{pM} are the concentration of M in the matrix and carbides, and K_{gb} is the segregation parameter. However, Abe [172], when trying to account for the coarsening behaviour of M₂₃C₆ in 9Cr-W

steel, concluded that “the volume diffusion controlled process is mainly in the coarsening of $M_{23}C_6$ carbides during creep”. He added that equation 9.22 overestimated the coarsening rate, and concluded that a better approximation to experimental results was obtainable from equation 9.18.

In addition to the grain boundary diffusion assisted coarsening of precipitates, Spigarelli *et al.* ^[174] suggested that “when the dislocation density is high, pipe diffusion of alloying elements along dislocation cores could increase the coarsening rate of the precipitates”. To address this issue, they employed a phenomenological approach in order to determine the stress dependence of particle coarsening. Here, the activation energy for the process of coarsening was assumed to be a function of stress:

$$\Delta H_c = \Delta H_{0c} + G(T, \sigma) \quad [9.23]$$

where ΔH_0 is the activation energy of the process which controls the coarsening at zero stress (isothermal aging), and $G(T, \sigma)$ is a generic temperature and stress dependent parameter determined by:

$$G(T, \sigma) = -k(\sigma / E)^p \quad [9.24]$$

where k and p are temperature dependent parameters. The coarsening constant, which includes the stress dependency of coarsening, can thus be given by:

$$K = K_0 \exp[k(\sigma / E)^p] \quad [9.25]$$

$$K_0 = \frac{8D_0\gamma_c V_m^2}{9RT} \exp\left(-\frac{\Delta H_{0c}}{RT}\right)$$

Spigarelli *et al.* ^[174] used values of k and p of 1.8×10^{11} and 3.3 respectively for $M_{23}C_6$ precipitates, and 7.0×10^6 and 1.8 respectively for MX precipitates, at a temperature of 600°C. Although empirical, Spigarelli *et al.* ^[174] argued that the description is consistent with their

observed increase of the coarsening coefficient with stress, as high dislocation densities may accelerate the precipitate coarsening rate by promoting diffusion around dislocation cores.

9.2.3.2 Comparison Between Experimental and Modelled Particle Coarsening Results

Precipitation of Minor Phase Particles

The Robson and Bhadeshia ^[166,167] model has been applied in this research in order to estimate the volume fraction of MX and M₂₃C₆ precipitates, as a function of time, in the Bar 257 and W20-3 P91 steel casts in the present investigation. The predicted values have been compared to measured values of volume fraction. The volume fractions of precipitates were determined experimentally from High Angular Annular Dark Field (HAADF) images taken on carbon extraction replicas from the FEGSTEM. The volume fraction, v_f , was subsequently calculated from the mean equivalent circular particle diameter, d , and the number of particles per unit area, N_a , which were obtained from the images using an image analysis software package ^[117]:

$$v_f = \frac{4}{3} \pi \left(\frac{d}{2} \right)^3 N_v$$

$$N_a = N_v d$$
[9.26]

where N_v is the number of particles per unit volume. The Robson and Bhadeshia model essentially reads thermodynamic data, in this case from MTDATA, and from a pre-established database, such as TCFE. The purpose of the Robson-Bhadeshia model ^[166,167] purpose is to calculate the evolution of volume fraction with time for up to six precipitates forming simultaneously, accounting for the competition of solute elements. This model was therefore used predict the constituents of the microstructure of P91 steel as a function of time at temperature, and cast composition.

The inputs used for the Robson-Bhadeshia model were obtained from MTDATA calculations performed for the Bar 257 and W20-3 compositions and these are shown in Table 9.5. These inputs include the mean composition of species (X_B), the mole fraction of the rate controlling elements in the precipitate phase (X_C) and composition of species in the ferrite matrix (X_A), all of which were simple to obtain. The model implies that the density of each phase and the matrix are similar, which is a reasonable approximation, therefore, the volume fraction (V_{MAX}

and V_{EQ}) can be calculated by using the amount of phase divided by the total mass of the system predicted by MTDATA. In order to calculate the maximum volume fraction of a precipitate phase in the system (V_{MAX}), equilibrium calculations were performed considering only one phase of interest, i.e. $M_{23}C_6$, VN, cementite *or* Laves phase, plus ferrite. To calculate the equilibrium volume fraction of each precipitate, equilibrium calculations were performed with all the possible phases included in the calculation, i.e. $M_{23}C_6$, VN, cementite *and* Laves phase, plus ferrite.

Other parameters, such as the interfacial energy and the nucleation site density of precipitate phases were obtained from Robson ^[175], and are shown in Table 9.6. Consistent with the results from long-term aging and creep testing in this study, the calculation was performed at 650°C. The results are shown in Figure 9.5.

Material	Cementite (Fe_3C)										
	$X_{B,Cr}$	$X_{C,Cr}$	$X_{A,Cr}$	$X_{B,Mo}$	$X_{C,Mo}$	$X_{A,Mo}$	$X_{B,V}$	$X_{C,V}$	$X_{A,V}$	V_{MAX}	V_{EQ}
Bar 257	0.0824	0.6916	0.082	0.0096	0.0028	0.0095	0.0018	0.0203	0.0017	0.017	0
W20-3	0.0866	0.6635	0.0865	0.0094	0.0009	0.0094	0.0025	0.0041	0.0024	0.027	0
	$M_{23}C_6$										
	$X_{B,Cr}$	$X_{C,Cr}$	$X_{A,Cr}$	$X_{B,Mo}$	$X_{C,Mo}$	$X_{A,Mo}$	$X_{B,V}$	$X_{C,V}$	$X_{A,V}$	V_{MAX}	V_{EQ}
Bar 257	0.0824	0.5742	0.0795	0.0096	0.0928	0.0091	0.0018	0	0.0018	0.023	0.022
W20-3	0.0866	0.6131	0.0843	0.0094	0.1031	0.0089	0.0025	0	0.0025	0.038	0.018
	Laves										
	$X_{B,Cr}$	$X_{C,Cr}$	$X_{A,Cr}$	$X_{B,Mo}$	$X_{C,Mo}$	$X_{A,Mo}$	$X_{B,V}$	$X_{C,V}$	$X_{A,V}$	V_{MAX}	V_{EQ}
Bar 257	0.0824	0.0124	0.0823	0.0096	0.192	0.0091	0.0018	0	0.0018	0.0007	0
W20-3	0.0866	0.0198	0.0866	0.0094	0.2652	0.0081	0.0025	0	0.0025	0.0006	0
	MX										
	$X_{B,Cr}$	$X_{C,Cr}$	$X_{A,Cr}$	$X_{B,Mo}$	$X_{C,Mo}$	$X_{A,Mo}$	$X_{B,V}$	$X_{C,V}$	$X_{A,V}$	V_{MAX}	V_{EQ}
Bar 257	0.0824	0.0086	0.0823	0.0096	0.0131	0.0095	0.0018	0.2456	0.0010	0.008	0.0010
W20-3	0.0866	0.0004	0.0866	0.0094	0.0001	0.0093	0.0025	0.542	0.0016	0.0027	0.0016

Table 9.5: Table showing values of the mean composition of species (X_B), the mole fraction of species in the precipitate phase (X_C), the composition of species in the ferrite matrix (X_A), all mole fractions, and the maximum (V_{MAX}) and mean (V_{EQ}) volume fractions of the precipitate phases in the Bar 257 and W20-3 materials, all of which have been calculated using MTDATA. These values were input into the Robson and Bhadeshia ^[166,167] model to predict the volume fraction of precipitates as a function of time.

Particle Identity	Interfacial Energy (Jm ⁻²)	Nucleation site density (m ⁻³)	Phase Type (0 – cementite 1 – needle 2 – spherical)
<i>Cementite (Fe₃C)</i>	0	1	0
<i>M₂₃C₆</i>	0.269	4.92×10 ⁻⁷	2
<i>Laves</i>	0.331	4.92×10 ⁻¹⁴	2
<i>MX</i>	0.26	9.84×10 ⁻⁹	1

Table 9.6: Values for interfacial energy, nucleation site density and particle type for each phase, that were used as inputs to the Robson and Bhadeshia model. After Robson ^[175].

In Figure 9.5, it can be seen that three phases are predicted to precipitate, which are M₃C, M₂₃C₆ and MX. Laves phase was not predicted to form at 650°C as it was not present in equilibrium with the other precipitates in the MTDATA calculations. Indeed, Laves phase was not detected in the investigated long-term aged Bar 257 and W20-3 specimens. In both materials M₃C is shown to be present initially, however, it is predicted to dissolve rapidly, after approximately 20 minutes, at the expense of the precipitation of M₂₃C₆. The MX phase is predicted to precipitate slightly later. These results are consistent with findings in Chapter 4, where auto-tempered particles, likely to be iron carbide, were shown to be present in the as-normalized condition and absent after a subsequent tempering treatment at 750°C. After aging for one hour, the microstructure is predicted to consist of M₂₃C₆ and MX, and after ~10 hours, the equilibrium volume fractions of M₂₃C₆ and MX are reached (Figure 9.5). It can also be seen that there is generally a good agreement between the modelled and the measured results of precipitate volume fraction. The results show that the volume fraction of M₂₃C₆ is highest in the Bar 257 material, and that the volume fraction of MX is highest in the W20-3 material. Evidently, there is some scatter present in the measured results, and these are attributable to experimental errors, which were discussed in Chapter 5.

Figure 9.5 predicts that the volume fraction of precipitate phases is expected to remain stable up to very long times at 650°C. Therefore, it is anticipated that the most important mechanism in which the evolution of minor phase particles may cause ‘damage’ to the creep properties of Grade 91 steel is particle coarsening (of the larger M₂₃C₆ particles), where the mean particle size increases with a constant particle volume fraction.

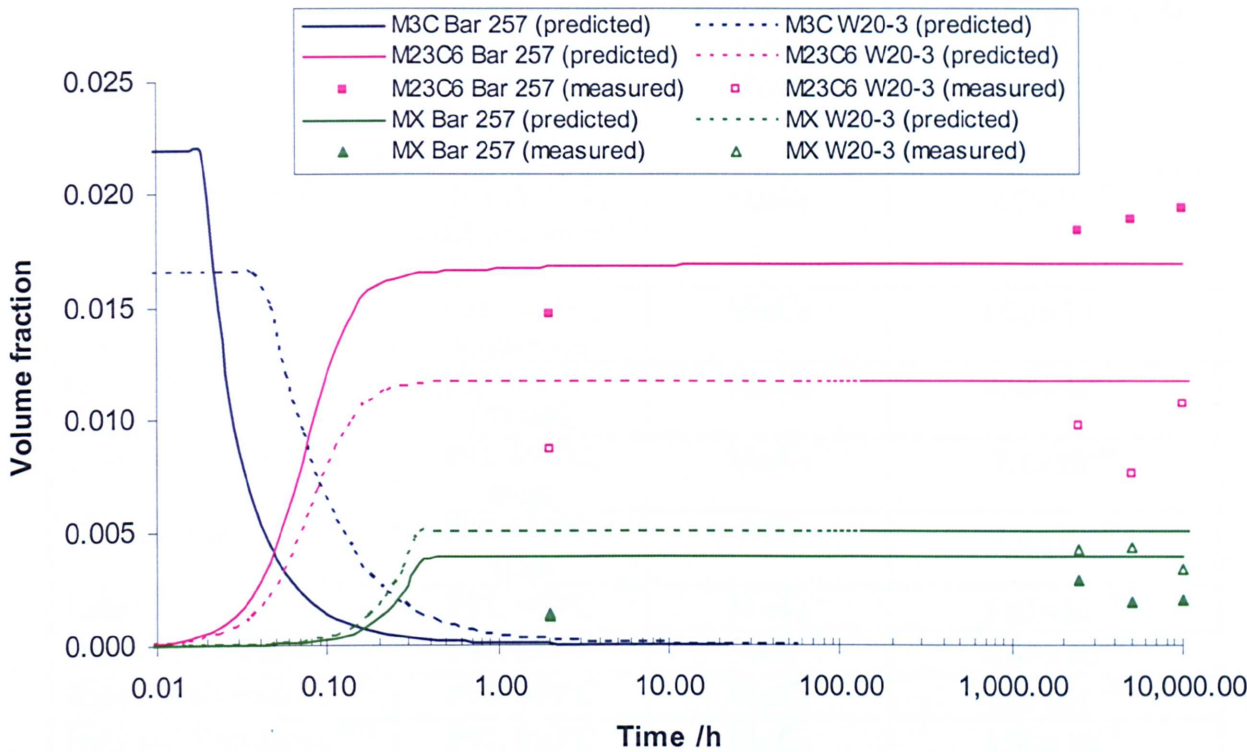


Figure 9.5: Evolution of the volume fraction of precipitate at 650°C with time in the Bar 257 and W20-3 materials. The lines represent predicted results according to the Robson-Bhadeshia model ^[166,167] and the points represent measured volume fractions. The inputs for the model were obtained from Tables 9.5 and 9.6.

Particle Coarsening

Several workers have published different values of the coarsening constant, K , to account for the coarsening behaviour of MX and $M_{23}C_6$ particles in a variety of high Cr ferritic-martensitic power plant steels (Table 9.7). These have been compared with the results of particle measurements from the previous chapters in Figure 9.6. Here, equation 9.12 was rearranged to solve for the particle radius r at time t , the values of initial particle radius r_0 were assumed to be representative of the measured values of mean particle radius in the as-tempered condition. The different curves on the plot represent the different values of coarsening constant that were found in the literature for $M_{23}C_6$ and MX particles as a function of cast composition, aging time and stress, and these are shown in Table 9.7.

Reference	Material and temperature	Precipitate type	Coarsening rate, K , m^3s^{-1}
Strang and Vodarek ^[22]	12CrMoVNb, low Ni content, 600°C, crept	M_{23}C_6	3.1×10^{-30}
Strang and Vodarek ^[22]	12CrMoVNb, high Ni content, 600°C, crept	M_{23}C_6	8.7×10^{-30}
Orlova <i>et al.</i> ^[5]	P91, 600°C, unstressed	M_{23}C_6	1.00×10^{-29}
Orlova <i>et al.</i> ^[5]	P91, 600°C, 175MPa	M_{23}C_6	4.98×10^{-28}
Yoshizawa <i>et al.</i> ^[176]	P91, 650°C, crept	M_{23}C_6	7.1×10^{-28}
Sawada <i>et al.</i> ^[177]	P92, 650°C, crept	MX	4.8×10^{-30}
Hald ^[171]	P91, 600°C	M_{23}C_6	1.03×10^{-29}
Hald and Korcakova ^[61]	P92, 650°C	MX	6.55×10^{-32}
Hald and Korcakova ^[61]	P91, 600°C	M_{23}C_6	7.67×10^{-30}
Hald and Korcakova ^[61]	P91, 650°C	M_{23}C_6	5.98×10^{-29}

Table 9.7: List of the Ostwald ripening coarsening rates, K , published in the literature for M_{23}C_6 and MX precipitates in a variety of high Cr ferritic steel casts and conditions.

Several key findings are evident from the examination of Figure 9.6. The most significant is that the measured MX and M_{23}C_6 particle sizes agree well with the model predictions. It can be seen that the predicted mean size of MX particles does not increase significantly, even after exposure for up to 30 years, whereas the coarsening rate of M_{23}C_6 precipitates increases dramatically after the equivalent exposure of around 10,000 hours at 650°C, which is indicative, in accordance with previous authors, of the fact that the ‘damage’ due coarsening will be dominated by M_{23}C_6 . It would appear, from Figure 9.6, that the particle coarsening model which exhibited the closest match to experimental findings of M_{23}C_6 size was from Hald and Korcakova [6.1], who used equation 9.21. In this model, they assumed that the interfacial energy for M_{23}C_6 particles, γ , had a value of 1 Jm^{-2} . This model also showed a good approximation to the measured MX particle sizes, in which they used a γ value of 0.5 Jm^{-2} . Interestingly, there was a large degree of scatter between predicted and measured size of M_{23}C_6 precipitates in the accelerated creep specimens, which were found to be the coarsest. This is unsurprising as the LSW equation does not incorporate a term to account for stress.

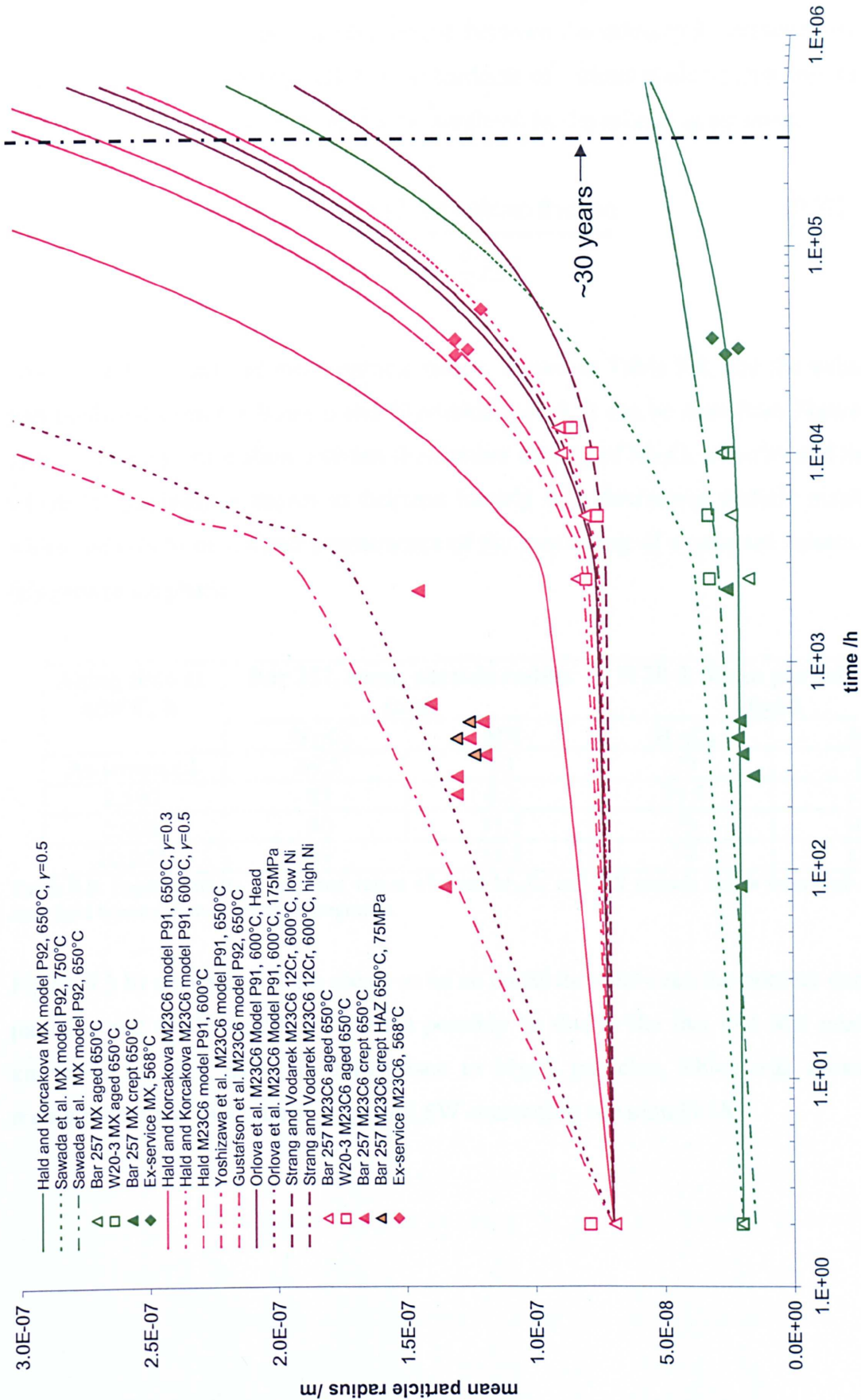


Figure 9.6: Plot showing a comparison of mean particle sizes of $M_{23}C_6$ and MX precipitates measured in this report versus predicted particle sizes according to the LSW equation [9.18] as a function of aging time. Each curve represents a different value of coarsening constant (K), determined by previous workers, which depends on cast composition, particle type, aging time and temperature, and creep loading conditions, and these are shown in the plot legend.

Figures 9.7 a) and b) show the relationship between the calculated number density of $M_{23}C_6$ and MX precipitates respectively and the hardness of various grade 91 specimens investigated in this thesis. The number density can be predicted by the following equation:

Number density =
$$\frac{\text{Predicted volume fraction}}{\frac{4}{3}\pi r^3}$$

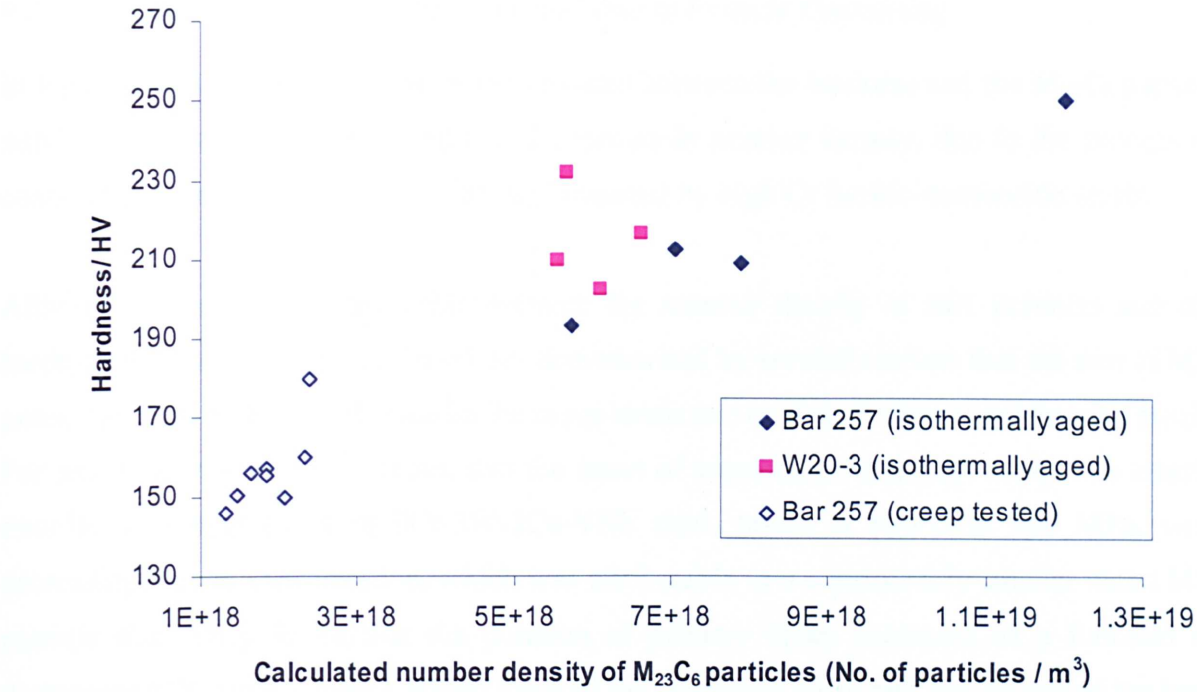
[9.27]

where r is the measured mean particle radius, shown in Table 9.8, and the volume fraction was predicted from the Robson and Bhadeshia model. It can be seen from Figure 9.7 a) that there is a strong correlation between the number density of $M_{23}C_6$ particles and the hardness, where the hardness is shown to decrease linearly with decreasing particle number density, which appears to be a direct consequence of the coarsening of a constant volume fraction of this precipitate phase.

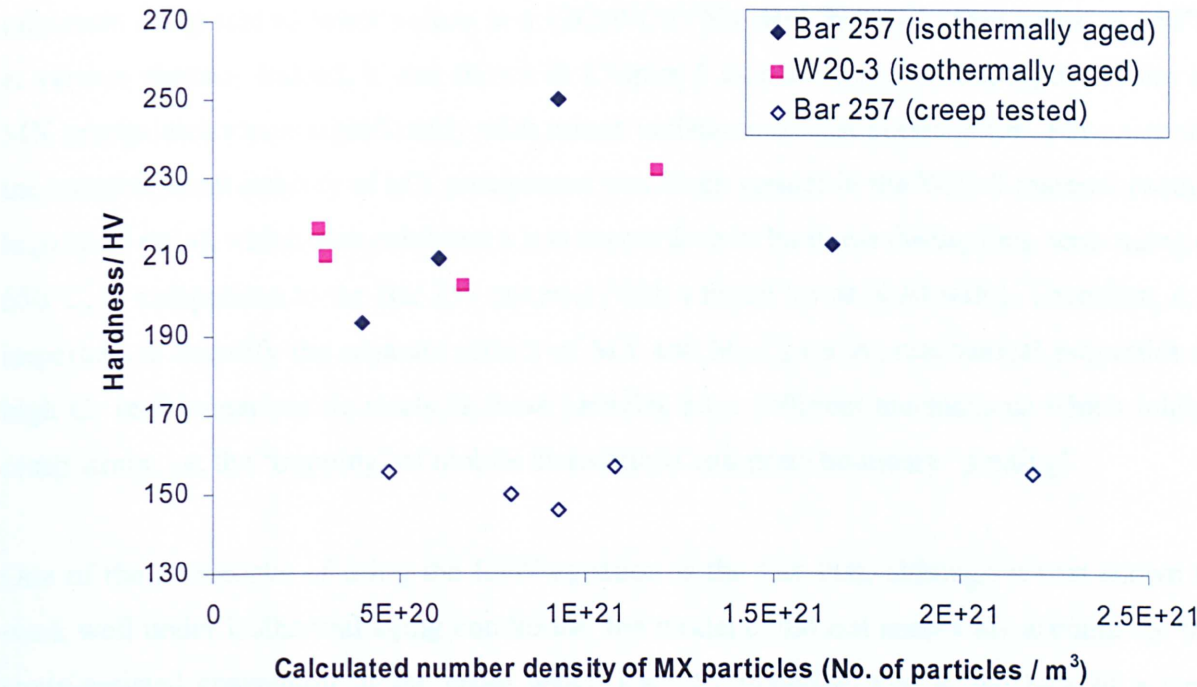
Aging time at 650°C, h	Bar 257, mean particle radius (nm)		W20-3, Mean particle radius (nm)	
	$M_{23}C_6$	MX	$M_{23}C_6$	MX
As-tempered	69.5	10	79	13
2,500	83	8.2	79.5	15.8
5,000	80	11.5	75	16.1
10,000	89	13.2	77	12.1

Table 9.8: Experimentally determined values of mean $M_{23}C_6$ and MX particle radius from high angle annular dark field transmission electron micrographs.

Figure 9.3 b) shows that there seems to be no correlation between the number density of MX particles and the hardness. This could possibly be due to the fact that MX precipitates are known to be very stable, in comparison to $M_{23}C_6$ particles, which was shown by direct measurement and modelling using the LSW coarsening equation [9.18].



a)



b)

Figure 9.7: Plots showing the effect of number density of precipitates on the hardness of grade 91 materials; a) $M_{23}C_6$ and b) MX.

9.2.3.3 Discussion Concerning the 'Damage' Due to Particle Coarsening

In Figure 9.7 a) it was shown that a trend existed between the hardness and the $M_{23}C_6$ particle number density, to such an extent that a decrease in number density, due to the process of coarsening, increases the level of 'damage' incurred by high Cr ferritic-martensitic steels.

Although no trend was observable between the number density of MX particles and the hardness in this investigation, it has been demonstrated by several workers that the size of MX precipitates has a strong influence on the creep strain rate of high Cr ferritic-martensitic steels. For example, Abe *et al* ^[178] found that the onset of acceleration (tertiary) creep was clearly retarded to longer times in 9Cr-3W-3Co-VNb steel, tested at 650°C at 160 MPa, with decreasing carbon concentration, which was attributable to a considerably smaller mean MX particle size. They found that the duration of primary creep increased as a function of decreasing MX particle radius, which lowered the minimum creep rate and increased the time to creep rupture. In addition, Knezevic *et al* ^[179] found that the increased addition of MX-forming elements reduced the creep rate in the primary creep regime and shifted the strain for minimum creep rate to lower values in a 12CrWCoVNb steel that was creep tested at 650°C at various stresses. Indeed, it was shown in Chapter 5 that the composition, type and size of MX precipitates varies significantly with minor variations in cast composition. For example, the compositional stability of MX precipitates was much greater in the W20-3 material (with a high N:Al ratio), which also exhibited a less severe drop in hardness during long-term aging at 650°C, in comparison to the Bar 257 material (with a much lower N:Al ratio). Therefore, it is important to quantify the separate effects of MX and $M_{23}C_6$ on the mechanical properties of high Cr ferritic-martensitic steels as these particles have different mechanisms which inhibit creep strain, i.e. the 'trapping' of mobile dislocations and grain boundary 'pinning'.

One of the drawbacks of using the LSW equation is the fact that, although it was shown to work well under isothermal aging conditions, the model could not accurately account for the strain-assisted coarsening of the creep tested Bar 257 materials due to the lack of a term incorporating the effect of strain. However, given the low design strain rates experienced by power plant components, Bhadeshia ^[4] quoted "approximately 2% elongation over 30 years", this may not be the most important consideration. Indeed, the size of $M_{23}C_6$ precipitates in the ex-service specimens, which have been employed as high temperature pressure vessels, are shown to agree well with the modelled results, even though the effects of strain were not accounted for.

There is still room for improvement with regards to precipitation and coarsening theory. Bhadeshia and Sourmail ^[169] argued that the “coarsening kinetics do not require an explicit treatment but follow naturally from the precipitation theory which for each phase includes the capillarity effect” and, therefore, “the separation of precipitation and coarsening is artificial”. The greatest challenge, suggested by the same authors ^[4,169], is the development of a proven theory which covers multiphase coarsening. At present, however, it has been shown that the combination of the Robson and Bhadeshia model, as well as the LSW model, agree well with the experimental data from this thesis and, therefore, may be adequate descriptors of ‘damage’ due to particle coarsening.

9.3 Summary

In this chapter, the experimental data obtained from the microstructural characterization of Grade 91 components, from earlier chapters, were used to validate existing microstructural evolution models which may be fed into a physically based continuum damage mechanics (CDM) creep model in order to assess the remaining creep life of high Cr ferritic-martensitic steels. At present, a physically-based CDM model accounting for the effect of the recovery of the matrix structure is incomplete due to the lack of good models that account for both the decrease in dislocation density and the increase in grain size a function of time, temperature and strain specific to these materials. However, microstructure evolution modelling, using the Robson and Bhadeshia simultaneous precipitation model and the Lifshitz-Slyozov and Wagner particle coarsening equation, were in good agreement with experimental measurements in predicting the volume fraction, type and size of minor phase precipitates in Grade 91 steel. These models, therefore, may be used to describe the ‘damage’ due to particle coarsening.

Chapter 10

CONCLUSIONS AND FURTHER WORK

The main objective of this research was to develop a complete understanding of the microstructural evolution of high-Cr ferritic-martensitic steels as a function of varying pre-service heat treatment, long-term aging and creep conditions and, in turn, assess the different strategies that may be involved in order to predict the remanent operational lifetime of these components that are widely used in the power generation industry.

In Chapter 4, it has been shown that varying initial heat treatment parameters, such as normalizing temperature and cooling rate, have a significant effect on the microstructure and hardness of Grade 91 steel. This was attributable to significant variations in the prior-austenite grain size, martensitic lath width, and the amount of precipitate, both undissolved MX and auto-tempered cementite, present in the as-normalized microstructure. Significant differences were observed between the microstructures of two Grade 91 casts with minor composition differences. The microstructure of one cast, with known poor creep properties and a high Al content, was shown to be more sensitive to varying heat treatments in comparison to a more conventional Grade 91 cast, to such an extent that both grain coarsening and larger lath widths occurred much more rapidly with increasing normalizing temperature in the former. The differences in sensitivity between the two casts were also evident after a stress-relief tempering heat treatment, where it was shown that the size distribution of the intergranular $M_{23}C_6$ carbides varied substantially in the 'weak' material as a function of varying normalizing heat treatments. For example, it was clearly shown that these particles were much coarser at lower normalizing temperatures. On the other hand, the size distribution of $M_{23}C_6$ carbides in the 'conventional' cast remained stable, to such an extent that the size distribution profiles of $M_{23}C_6$ carbides was very similar at all the normalizing temperatures investigated.

After subsequent long-term aging, up to 10,000 h at 650°C, the microstructures of the two steel casts evolved rather differently. Chemical analysis of the metallic elements V, Nb and Cr in MX precipitates, using energy dispersive X-ray spectroscopy, showed that the relative amounts of these elements varied significantly as a function of pre-service heat treatment and aging time. The main observed change was the gradual partitioning of the composition of MX precipitates, from a linear composition distribution of V and Nb in (V,Nb)(N,C), into two

distinct particle compositions, VN and NbC, with increasing aging times. The mean Cr concentration in MX was also found to decrease with increasing aging time. It was postulated that such changes in the composition of MX carbides occur rather slowly, therefore, the chemical composition changes in MX may be used to make an informed judgment on the thermal history of Grade 91 components. Consistently, these changes were shown to occur more rapidly in the 'weak' cast. In addition, the size distribution of MX and $M_{23}C_6$ were determined as a function of aging time, which showed that particle coarsening of the two carbide types was more severe in the 'weak' material in comparison to the 'conventional' cast, the latter exhibiting a stable size distribution up to 10,000 hours aging.

The evolution of the tempered martensitic matrix microstructure was also investigated, using two potentially powerful microstructural characterization tools, electron backscatter diffraction (EBSD) for the characterization of the subgrain structure, and X-ray line profile analysis for the quantification of the free dislocation density. The microstructural evolution during long-term aging consists of the gradual formation and growth of subgrains within tempered martensite laths. This process, in addition to being evident from visual inspection of EBSD maps, was quantified in terms of both the increase in total grain boundary line length and also in the increase in the ratio of low to high-angle boundaries as a function of high temperature exposure. Again, the 'weak' cast was compared to the 'conventional' cast, and it was found that the former exhibited a longer grain boundary line length and a higher low to high-angle ratio over the range of aging times investigated, indicating a more rapid recovery of the matrix microstructure. The differences in the recovery rate were attributed to the large differences in the minor phase precipitation characteristics between the two casts, which was examined in Chapter 5.

The microstructures of ex-service Grade 91 components that have experienced typical power plant operating conditions have also been extensively characterized. The fruitful outcome of this experiment was that striking similarities between the microstructures of the ex-service materials and the long-term aged materials were found, which enabled the ex-service materials to be ranked according to the level of microstructure evolution undergone by the long-term aged specimens. Similarly, the experiments provided the opportunity to validate the microstructures produced under accelerated thermal aging conditions, with those obtained under 'real' operating conditions.

Finally, the experimental data obtained from the microstructural characterization of Grade 91 components were used to validate existing microstructural evolution models, which may be fed into a physically based continuum damage mechanics (CDM) creep model in order to assess the remaining creep life of high Cr ferritic-martensitic steels. Microstructure evolution modeling of minor phase precipitates as a function of aging time and cast compositions, which was performed using the Robson and Bhadeshia simultaneous precipitation model and the Lifshitz-Slyozov and Wagner particle coarsening equation, were in good agreement with experimental measurements obtained in this research in predicting the volume fraction, type and size of minor phase precipitates in Grade 91 steel. At present, however, a physically based CDM model accounting for the effect of both particle coarsening and the recovery of the matrix structure is incomplete due to the lack of good models which account for both the decrease in dislocation density and the increase in grain size a function of time, temperature and strain.

This work has highlighted several areas where further work may be of both practical and theoretical interest. It would be desirable to carry out more X-ray diffraction work and link the values of dislocation density determined from both this technique and from transmission electron microscopy on thin-foil specimens, in order to validate the results from X-ray diffraction. This requires generating many samples which have been creep tested under different temperature and loading conditions. Therefore, if XRD can reliably determine the dislocation density, given its potential for good statistics on account of large examinable areas, this would facilitate the process of developing a model which describes the evolution of this microstructural parameter as a function of time, temperature and strain, in order to complete a theoretical framework for predicting creep life due to microstructural evolution.

It is becoming a well accepted view that Type IV cracking in the heat affected zone may be the life-limiting failure mechanism in high Cr ferritic-martensitic steels. The microstructures of creep tested cross-weld specimens Grade 91 specimens were investigated in Chapter 8, and it was shown that prior heat treatment of the parent (base) material can influence the creep strength of welded Grade 91 components by affecting the strength of the Type IV heat affected zone (HAZ). From a practical viewpoint, since the problem is associated with a completely different microstructure in the HAZ compared to the parent material, it would be interesting to carry out further work to investigate the effects of novel post-weld heat treatments in order to improve both the

microstructure and mechanical properties of the HAZ region. It would also be interesting to investigate the effect of varying cast compositions on the creep properties of welded specimens and, therefore, establish which alloying additions have the greatest effect on the Type IV creep strength. This would involve detailed microstructural characterisation using the advanced techniques described in this thesis, including ion beam imaging, particle size distribution and composition determination and electron backscatter diffraction, across the different regions within the HAZ microstructure. Results from these experiments may provide a better insight on how to reduce the damaging affects of Type IV cracking and extend the life of existing high Cr ferritic-martensitic steel components in conventional fossil-fired power plant.

References

- [1] Kimura, K., Kushima, H. and Abe, F., Degradation Behaviour of T91 Steel During Long-term Creep, in *Case Histories on Integrity and Failures in Industry: Proceedings of the Symposium on Integrity and Failures in Industry*, 1st October 1999, Milan, Italy, Eds. V. Bicego, A. Nitta, J. W. H. Price and R. Viswanathan, p. 381-387 (1999)
- [2] Ennis, P.J., Zielińska-Lipiec, A. and Czyrska-Filemonowicz, A., Quantitative Comparison of the Microstructures of High Chromium Steels for Advanced Power Stations, in *Microstructural Stability of Creep Resistant Alloys for High Temperature Plant Applications*, Eds. A. Strang, J. Cawley and G.W. Greenwood, p. 135-145 (1998)
- [3] Cerjak, H., Hofer, P. and Schaffernak, B., Microstructural Aspects on the Creep Behaviour of Advanced Power Plant Steels, *Key Engineering Materials*, 171-174, p. 453-460 (2000)
- [4] Bhadeshia, H.K.D.H., Royal Society Charles Algernon Parsons Memorial Lecture: Design of Heat Resistant Alloys for the Energy Industries, in *Proceedings of the Fifth International Charles Parsons Turbine Conference*, 3-7 July 2000, Cambridge, UK, Eds. A. Strang *et al*, Institute of Materials, p. 3-40 (2000)
- [5] Orlova, A., Bursik, J., Kucharova, K. and Sklenicka, V., Evolution of Microstructure in P91-Type Steel in High Temperature Creep, *Microstructural Stability of Creep Resistant Alloys for High Temperature Plant Applications*, Eds. A. Strang, J. Cawley and G.W. Greenwood, p. 89-107 (1998)
- [6] Kiameh, P., Power Generation Handbook: Selection, Applications, Operation and Maintenance, McGraw-Hill Handbooks (2003)
- [7] Vanstone, R.W., Advanced ('700°C') Pulverised Fuel Power Plant, in *Proceedings of the Fifth International Charles Parsons Turbine Conference*, 3-7 July 2000, Cambridge, UK, Eds. A. Strang *et al*, Institute of Materials, p. 91-97 (2000)
- [8] Haarmann, K., Vaillant, J.C., Bendick, W., Arbab, A., The T91/P91 Book, Vallourec and Mannesmann Tubes (1999)
- [9] Orr, J. and Burton, D., Development, Current and Future Use of Steel 91, *Ironmaking and Steelmaking*, 20, p. 335 (1993)
- [10] Askeland, D.R., The Science and Engineering of Materials, 3rd ed., Stanley Thornes Press (1996)
- [11] Porter, D.A. and Easterling K.E., Chapter 6: Diffusionless Transformations, in *Phase Transformations in Metals and Alloys*, 2nd ed., Nelson Thornes Press (1992)
- [12] Sanderson, S.J., Mechanical Properties and Metallurgy of 9%Cr -1%Mo Steels, in *Ferritic Steels for High Temperature Applications*, American Society for Metals, p. 85-99 (1983)

- [13] Honeycombe, R.W.K and Bhadeshia, H.D.K.H, Steels: Microstructure and Properties, 2nd ed., Butterworth-Heinemann (1995)
- [14] Speich, G.R., Ferrous Martensitic Structures, in *Metals Handbook*, Vol. 9, 9th ed., *Metallography and Microstructures*, American Society for Metals, p. 668-672 (1985)
- [15] Cerri, E., Evangelista, E., Spigarelli, S., and Bianchi, P., Evolution of Microstructure in a Modified 9Cr-1Mo Steel During Short Term Creep, *Materials Science and Engineering A*, 245, p. 285-192 (1998)
- [16] Speich, G.R. and Leslis, W.C., "Tempering of Steel", *Metallurgical Transactions*, 3, p. 1043 -1054 (1972)
- [17] Speich, G.R., Tempering of Low-Carbon Martensite, *Transactions of the Metallurgical Society of AIME*, 245, p. 2553-2563 (1969)
- [18] Thomson, R.C. and Miller, M.K., An Atom Probe Study of Carbon Distribution in Martensite in 2 ¼Cr1Mo Steel, *Scripta Metallurgica et Materialia*, 32 (2), p 149-154 (1995)
- [19] Rasche, C., Bendick, W., and Orr, J., Physical Properties, Transformation Behaviour, and Microstructure of Grade T91, British Steel Technical Document, p. 1-13 (1992)
- [20] Newell, H.D., Properties of the 9% Chromium Steel (An Intermediate Alloy) in *Metal Progress*, February 1936, p. 51-55 (1936)
- [21] Zajac, S., Ferrite Grain Refinement and Precipitation Strengthening in V-Microalloyed Steels, in *Proceedings of the 43rd Mechanical Working and Steel Processing Conference*, 28-31st October 2001, Charlotte NC USA, Ed. D.L. Kanagy, Iron & Steel Society, p. 499-508 (2001)
- [22] Strang, A., and Vodarek, V., Microstructural Degradation of Martensitic 12%Cr Power Plant Steels During Prolonged High Temperature Creep Exposure, in *Proceedings of the 6th Liege Conference on Materials for Advanced Power Engineering 1998*, Liege, Belgium, Eds. J. Lecomte-Beckers *et al.*, Trans Tech Publications, p. 605-614 (1998)
- [23] Kuo, K., Carbides in Chromium, Molybdenum and Tungsten Steels, *Journal of the Iron and Steel Institute*, p. 363-375 (1953)
- [24] Yakel, H.L., Crystal Structures of Stable and Metastable Iron-Containing Carbides, *International Metals Reviews*, 30 (1), p. 17-40 (1985)
- [25] Andrews, K.W., Dyson, D.J. and Keown, S.R., "Interpretation of Electron Diffraction Patterns", Hilger and Watts Ltd. (1967)
- [26] Nutting, J. in *Proceedings of the Advanced Heat Resistant Steel for Power Generation Conference*, 19-27th April 1998, San Sebastian, Spain, Eds. R. Viswanathan and J. Nutting, The Institute of Materials, UK, p. 12 (1998)
- [27] Jones, W.B., Hills, C.R. and Polonis, D.H., Microstructural Evolution of Modified 9Cr-1Mo Steel, *Metallurgical Transactions A*, 22, p. 1049-1058 (1991)

- [28] Beech, J. and Warrington, D.H., M_7C_3 to $M_{23}C_6$ Transformation in Chromium Containing Alloys, *Journal of the Iron and Steel Institute*, 204, p. 460-467 (1966)
- [29] Orr, J., Burton, D. and Rasche, C., Sensitivity of Microstructure and Mechanical Properties of Steel 91 to Initial Heat Treatments, *Ironmaking and Steelmaking*, 20, p. 415-422 (1993)
- [30] Foldyna, V., Jakobova, A., Vodarek, V. and Kubon, Z., Chromium Modified Steels-Metallurgical Understanding, in *Proceedings of the 5th Liege International Conference on Materials for Advanced Power Engineering*, 3-6 October 1994, Liege, Belgium, Eds. D. Coutouradis *et al*, Kluwer Academic Publishers Group, p. 453-464 (1994)
- [31] Eggeler, G., "The Effect of Long-Term Creep on Particle Coarsening in Tempered Martensite Ferritic Steels", *Acta Metallurgica*, 37, p. 3225-3234 (1989)
- [32] The International Centre for Diffraction Data, Joint Committee on Powder Diffraction Standards
- [33] Tokuno, K., Hamada, K., Uemori, R., Takeda, T., and Itoh, K., Role of Complex Carbonitride of Niobium and Vanadium in Creep Strength of 9% Cr Ferritic Steels, *Scripta Metallurgica et Materialia*, 25, p. 1763-1768 (1991)
- [34] Zajac, S., Siwecki, T., Hutchinson, W.B. and Lagneborg, R., The Role of Carbon in Enhancing Precipitation Strengthening of V-Microalloyed Steels, in *Proceedings of the International Conference on Microalloying in Steels*, 7-9 September 1998, San Sebastian, Spain, Eds. J. M. Rodríguez-Ibabe *et al*, (1998)
- [35] Taneike, M., Kondo, M. and Morimoto, T., Accelerated Coarsening of MX Carbonitrides in 12% Cr Steels During Creep Deformation, *ISIJ International*, 41, p. 111-115 (2001)
- [36] Orr, J. and Di Gianfrancesco, A., Effect of Compositional Variations on Properties of Steel 91, *Ironmaking and Steelmaking*, 20, p. 424-430 (1993)
- [37] Tokuno, K., Hamada, K. and Takeda, T., Dispersion Strengthening High-Cr Steels by Forming "V-Wings", *Journal of the Minerals, Metals and Materials Society*, 44, p. 25-28 (1992)
- [38] Hamada, K., Tokuno, K., Tomita, Y., Mabuchi, H. and Okamoto, K., Effects of Precipitate Shape on High Temperature Strength of Modified 9Cr-1 Mo Steels, *ISIJ International*, 35, p. 86-91 (1995)
- [39] Yamada, K., Igarashi, M., Muneki, S. and Abe, F., Creep Properties Affected by Morphology of MX in High-Cr Ferritic Steels, *ISIJ International*, 41, p. 116-120 (2001)
- [40] Tamura, M., Iida, T., Kusuyama, H., Shinozuka, K. and Esaka, H., Re-Dissolution of VN During Tempering in High Chromium Heat Resistant Martensitic Steel, *ISIJ International*, 44, p. 153-161 (2004)
- [41] Brett, S.J., Bates, J.S. and Thomson, R.C., Aluminium Nitride Precipitation in Low Strength Grade 91 Steels, in *EPRI Conference Proceedings of the Fourth International*

Conference on Advances in Materials Technology for Fossil Power Plants, 25th October, Hilton Head, USA, p. 1157-1171 (2004)

- [42] Naoi, H., Ohgami, M., Liu, X. and Fujita, T., "Effects of Aluminum Content on the Mechanical Properties of a 9Cr-0.5Mo-1.8W Steel", *Metallurgical and Materials Transactions A*, 28, p. 1195-1203 (1997)
- [43] De Ardo, A.J., Gray, J.M. and Meyer, L: in "Niobium 81", Ed.. H. Stuart, Metallurgical society of AIME, Warrendale, PA, USA, p. 684-759 (1984)
- [44] Kubon, Z. and Foldyna, V., The Effect of Nb, V, N and Al on the Creep Rupture Strength of 9-12% Cr Steel, *Steel Research*, 66, p. 389-393 (1995)
- [45] Michel, J.P. and Jonas, J.J., Precipitation Kinetics and Solute Strengthening in High Temperature Austenites Containing Al and N, *Acta Metallurgica*, 29, p 513-526 (1981)
- [46] Cheng, L.M., Hawbolt, E.B. and Meadowcroft, T.R., "Dissolution and Coarsening of Aluminium Nitride Precipitates in Low Carbon Steel- Distribution, Size and Morphology", *Canadian Metallurgical Quarterly*, 39, p. 73-86 (2000)
- [47] Wilson, F.G. and Gladman, T., Aluminium Nitride in Steel, *International Materials Reviews*, 33, 5, p. 221-288 (1988)
- [48] Yamanaka, K. and Ohmori, Y., Precipitation of AlN in Austenite and Hardenability of Boron Treated Steels, *Transactions ISIJ*, 18, p. 404-411 (1978)
- [49] Edwards, R.H., Barbaro, F.J. and Gunn, K.W., Stress Cracking in Cr-Mo-V Steels, *Metals Forum*, 5, 2, p. 119-129 (1982)
- [50] Hall, D. and Bennett, G.H.J., Inhibition of Austenitic Grain Growth by Aluminium Nitride, *Journal of the Iron and Steel Institute*, p. 309-314 (1967)
- [51] Leap, M.J. and Brown, E.L., Crystallography of Duplex AlN-Nb(C,N) Precipitates in 0.2%C Steel, *Scripta Materialia*, 47, p. 793-797 (2002)
- [52] Strang, A and Vodarek, V., Microstructural Stability of Creep Resistant Martensitic 12% Cr Steels, in *Microstructural Stability of Creep Resistant Alloys for High Temperature Plant Applications*, Eds. A. Strang, J. Cawley and G.W. Greenwood, p. 117-135 (1998)
- [53] Sawada, K., Taneike, M., Kimura, K. and Abe, F., Effect of Nitrogen Content on Microstructural Aspects and Creep Behaviour in Extremely Low carbon 9Cr Heat-resistant Steel, *ISIJ International*, 44, 7, p 1243-1249 (2004)
- [54] Jack, D.H. and Jack K.H., Structure of Z-Phase NbCrN, *Journal of the Iron and Steel Institute*, (1972)
- [55] Strang, A. and Vodarek, V., Z-Phase Formation in Martensitic 12CrMoVNb Steel, *Materials Science and Technology*, 12, p. 552-556 (1996)

- [56] Dimmler, G., Weinert, P., Kozeschnika, E. and Cerjak, H., Quantification of the Laves phase in advanced 9–12% Cr steels using a standard SEM, *Materials Characterization*, 51, p. 341–352 (2003)
- [57] Sawada, K., Takeda, M., Maruyama, K., Ishii, R., Yamada, M., Nagae, Y. and Komine, R., Effect of W on Recovery of Lath Structure During Creep of High Chromium Martensitic Steels, *Materials Science and Engineering A*, 267, p.19–25 (1999)
- [58] Vanstone, R. W., Microstructure and Creep Mechanisms in Advanced 9-12% Chromium Creep Resisting Steels- A Collaborative Investigation in COST 501/3 WP11, in *Materials for Advanced Power Engineering, Part 1*, Kluwer Academic Publishers Group, p. 465-4673 (1994)
- [59] Ryu, S.H., Kim, M.S., Lee, Y.S., Kim, J.T., Yu, J. and Lee, B.J., The Effects of Carbon and Austenite Stabilizing Elements (Co, Cu, Ni and Mn) on the Microstructural Changes and Creep Rupture Strength in 9-12% Ferritic Heat Resistant Steels, in *EPRI Conference Proceedings of the Fourth International Conference on Advances in Materials Technology for Fossil Power Plants*, 25th October, Hilton Head, USA, p. 1310-1324 (2004)
- [60] Dyson, B., Use of CDM in Materials Modelling and Component Creep Life Prediction, *Journal of Pressure Vessel Technology*, 122, p 281-296 (2000)
- [61] Hald, J. and Korcakova, L., Precipitate Stability in Creep Resistant Ferritic Steels – Experimental Investigations and Modelling, *ISIJ International*, 43, 3, p. 420-427 (2003)
- [62] Orr, J. and Burton, D., Improving the Elevated Temperature Strength of Steel 91, in *Materials for Advanced Power Engineering, Part I*, Kluwer Academic Publishers Group, p. 263-280 (1994)
- [63] Llewellyn, D.T., Steels: Metallurgy and Applications, 2nd ed, Butterworth-Heinemann (1994)
- [64] Pickering, F.B. and Vassiliou, A.D., Effect of Austenitizing Temperature on Constitution, Transformation and Tempering of 9Cr-1Mo Steel, *Metals Technology*, p. 409-413 (1980)
- [65] Borggreen, K., Some Effects of the Solution Heat Treatment Temperature on the Properties of Grade P91, in *Proceedings of the International Conference on Plant Condition and Life Management, Baltica III*, 6-8th June 1995, Espoo, Finland, Eds. S. Hietanen and P. Auerkari, p. 417-432 (1995)
- [66] Yamada, K., Igarashi, M., Muneki, S. and Abe, F., Effect of Heat Treatment on Precipitation Kinetics in High-Cr Ferritic Steels, *ISIJ International*, 42, 7, p. 779–784 (2002)
- [67] Bursik, J., and Merk, N., Quantitative Microstructural Assessment of P91 Ferritic Steel After Long-Term Creep at High Temperature, in *Proceedings of the ASI Conference on the Mechanical Behaviour of Materials at High temperature*, 12-22nd September 1995, Sesimbra, Portugal, Eds. C. Moura Branco, R. Ritchie and V. Sklenicka, p. 696-701 (1996)

- [68] Orlova, A., Bursik, J., Kucharova, K. and Sklenicka, V., Microstructural Development During High Temperature Creep of 9% Cr Steel, *Materials Science and Engineering A*, 245, p. 39–48 (1998)
- [69] Qin, Y., Gotz, G. and Blum, W., Subgrain Structure During Annealing and Creep of the Cast Martensitic Cr-Steel G-X12CrMoWVNbN 10-1-1, *Materials Science and Engineering A*, 341, p. 211-215 (2003)
- [70] Abe, F., Nakazawa, H., Araki, H., and Noda, T., The Role of Microstructural Instability on Creep Behaviour of a Martensitic 9Cr-2W Steel, *Metallurgical Transactions A*, 23, p. 469-477 (1992)
- [71] Czyrska-Filemonowicz, A., Spidarek-Hahn, K., Bryla, K., Firganek, H., Zielinska-Lipiec, A. and Ennis, P.J., Transmission Electron Microscopy and Boron Trace Autoradiography Investigation of Precipitates in Creep Deformed 9% Chromium Steels, in *EPRI Conference Proceedings of the Fourth International Conference on Advances in Materials Technology for Fossil Power Plants*, 25th October, Hilton Head, USA, p. 1325-1338 (2004)
- [72] Hattestrand, M. and Andren, H., Influence of Strain on Precipitation Reactions During Creep of an Advanced 9% Chromium Steel, *Acta Materialia*, 49, 12, p. 2123-2128 (2001)
- [73] Spigarelli, S., Cerri, E., Evangelista, E. and Bontempi, P., Microstructure and Creep of a T91 steel, in *Proceedings of the Advanced Heat Resistant Steel for Power Generation Conference*, 19-27th April San Sebastian, Spain, Eds. R. Viswanathan and J. Nutting, (1998)
- [74] Humphreys, F.J. and Hatherly, M., Recrystallization and Related Annealing Phenomena, Pergamon Press (1995)
- [75] Sawada, K., Taneike, M., Kimura, K. and Abe, F., *In Situ* Observation of Recovery of Lath Structure in 9% Chromium Creep Resistant Steel, *Materials Science and Technology*, 19, p. 739-742 (2003)
- [76] Pešićka, J., Kuzel, R., Dronhofer, A. and Eggeler, G., The Evolution of Dislocation Density During Heat Treatment and Creep of Tempered Martensite Ferritic Steels, *Acta Materialia*, 51, p. 4847–4862 (2003)
- [77] Pešićka, J., Dronhofer, A. and Eggeler, G., Free Dislocations and Boundary Dislocations In Tempered Martensite Ferritic Steels, *Materials Science and Engineering A*, 387-389, p. 176-180 (2004)
- [78] Nakashima, H., Abe, H., Terada, D., Yoshida, F. and Hayakawa, H., EBSP Analysis of Modified 9Cr-1Mo Martensitic Steel, *ISIJ International*, 41, p. 97-100 (2001)
- [79] Kunz, L., Lukas, P. and Sklenicka, V., Creep/Fatigue Behaviour of an Advanced 9%Cr Steel, in *Materials for Advanced Power Engineering, Part 1*, Eds. D. Coutsouradis *et al*, Kluwer academic publishers, p. 445-452 (1994)
- [80] Speich, G.R., Tempering of Ferrous Martensites, in *Martensite: A Tribute to Morris Cohen*, Eds. G.B. Olson and W.S. Owen, ASM International, p. 243-270 (1992)

- [81] Evans, R.W., and Wilshire, B., Introduction to Creep, Institute of Materials, London (1993)
- [82] Shewmon, P.G., Diffusion in Solids, 1st Ed, McGraw-Hill Books, p. 172-173 (1963)
- [83] Senicourt, D. and Krahe, P.R., The Influence of Antimony on the High-Temperature Tempering of Low Carbon Martensites Containing Manganese, in *Electron Microscopy and Structure of Materials*, Ed. G. Thomas., University of California Press, p. 808 (1972)
- [84] Foldyna, V., Purmensky, J. and Kubon, Z., Development of Advanced Chromium Steels With Respect to Microstructure and Structural Stability, *ISIJ International*, 41, Supplement, p. 81-85 (2001)
- [85] Buck, R.F. and Garrison, W.M., Effect of Precipitate Dispersion on Secondary Creep Rate in Martensitic Stainless Steels, in *Proceedings of the International Symposium on High Performance Steels for Structural Applications*, 30 October 1995, Cleveland, Ohio, USA (1995)
- [86] Dimmler, G., Weinert, P. and Cerjak, H., Analysis of Steady State Creep Behaviour of 9-12% Chromium Ferritic-Martensitic Steels, *Materials Science and Technology*, 20, p. 1525-1530 (2004)
- [87] Faulkner, R.G. and Yin, Y.F., Microstructural Modelling for Creep Strength Prediction in Ferritic Steels, in *EPRI Conference Proceedings of the Fourth International Conference on Advances in Materials Technology for Fossil Power Plants*, 25th October, Hilton Head, USA, p. 890-903 (2004)
- [88] Hattestrand, M. and Andren, H.O., Evaluation of Particle Size Distributions of Precipitates in a 9% Chromium Steel Using Energy Filtered Transmission Electron Microscopy, *Micron*, 32, p.789-797 (2001)
- [89] Kaneko, K., Matsumura, S., Sadakata, A., Fujita, K., Moona, W., Ozaki, S., Nishimura, N. and Tomokiyo, Y., Characterization of Carbides at Different Boundaries of 9Cr-Steel, *Materials Science and Engineering A*, 374, p. 82-89 (2004)
- [90] Cohen, M., *Bulletin of the Japan Institute of Metals*, 9, p. 271 (1980)
- [91] Tamura, M., Sakasegawa, H., Kato, Y., Kohyama, A., Esaka, H. and Shinozuka, K., Relation Between Creep Rupture Strength and Substructure of Heat Resistant Steel, *ISIJ International*, 42, 2, p. 1444-1451 (2002)
- [92] Yang, J., Hsiao, J.S., Fong, M. and Gibbons, T.B., The Application of Physically Based CDM Modelling in Prediction of Materials Properties and Component Lifetime, *Journal of Pressure Vessel Technology*, 126, p. 369-375 (2004)
- [93] McLean, M. and Dyson, B.F., Modelling the Effects of Damage and Microstructural Evolution on the Creep Behaviour of Engineering Alloys, *Journal of Engineering Materials Technology*, 122, p. 273-278 (2000)

- [94] Brett, S.J., Allen, D.J., and Pacey, J., Failure of a Modified 9Cr Header Endplate, in *Proceedings of the International Symposium on Case Histories on Integrity and Failures in Industry*, 28th September – 1st October 1999, Milan, Italy, p. 873-883 (1999)
- [95] Yaghi, A.H., Hyde, T.H. Becker, A.A., Williams, J.A. and Sun, W., Residual Stress Simulation in Welded Sections of P91 Pipes, *Submitted to IFAMPT*, 15 March (2005)
- [96] Baehr Thermoanalyse product website; www.baehr-thermo.de/uk/produkte (2005)
- [97] National Physical Laboratory (NPL). MTDATA, www.npl.co.uk/npl/cmmt/mtdata/ (2004)
- [98] Sundman, B., TCFe Database supplied by TCAB for use with MTDATA, Available from Thermo-Calc Software AB, Stockholm (2001)
- [99] Davies, R.H., Dinsdale, A.T., Gisby, J.A., Robinson, J.A.J. and Martin, S.M., MTDATA – Thermodynamic and Phase Equilibrium Software from the National Physical Laboratory
- [100] Higginson, R.L. and Sellars, C.M., Worked Examples in Quantitative Metallography, Institute of Materials, Minerals and Mining, p. 32-41 (2003)
- [101] Underwood, E.E., Quantitative Metallography, in *Metals Handbook, Volume 9, Metallography and Microstructures*, 9th ed., American Society for Metals, p. 123-132 (1985)
- [102] Yardley, V., Magnetic Detection of Microstructural Change in Power Plant Steels, University of Cambridge PhD Dissertation (2003)
- [103] Goodhew, P.J. and Humphreys, F.J., Electron Microscopy and Analysis, 2nd Edition, Taylor and Francis, London (1992)
- [104] Humphries, F.J., Review: Grain and Subgrain Characterisation by Electron Backscatter Diffraction, *Journal of Materials Science*, 36, p. 3833-3854 (2001)
- [105] Schwartz, A.J., Kumar, M. and Adams, B.L., Electron Backscatter Diffraction in Materials Science, New York: Kluwer Academic/Plenum, (2000)
- [106] OIM Data Collection version 4.6, EDAX, computer software (2006)
- [107] Kim, B.S., Lee S.H., Jung, N.G. and Kim, D.S., Tempering Effect of X20CrMoV12.1 Boiler Tube Steels for Power Plant, in *EPRI Conference Proceedings of the Fourth International Conference on Advances in Materials Technology for Fossil Power Plants*, 25th October, Hilton Head, USA, p 1325-1338 (2004)
- [108] Berlung, D., Alberg, H. and Runnemalm, H., Simulation of Welding and Stress Relief Heat Treatment of an Aero Engine Component, *Finite Elements in Analysis and Design*, 39, p. 865-881 (2003)
- [109] Skrotzki, B. and Wiech, U., Influence of Austenite Strength on Martensite Start Temperature M_s , *Steel Research*, 64, 10, p. 509-512 (1993)

- [110] Andrews, K.W., Empirical Formulae for the Calculation of Some Transformation Temperatures, *Journal of the Iron and Steel Institute*, 203, p. 721-727 (1965)
- [111] Koistinen, D.P. and Marburger, R.E., A General Equation Prescribing the Extent of the Austenite-Martensite Transformation in Pure Iron-Carbon Alloys and Plain Carbon Steels, *Acta Metallurgica*, 7, p. 59-60 (1959)
- [112] Sklenicka, V., Kucharova, K., Dhouly, A. and Krejci, J., Creep Behaviour and Microstructure of a 9% Cr Steel, in *Materials for Advanced Power Engineering, Part 1*, Eds. D. Coutouradis *et al.*, Kluwer academic publishers, p. 435-444 (1994)
- [113] Sawada, K., Takeda, M., Maruyama, K., Ishii, R., Yamada, M., Nagae, Y. and Komine, R., Effect of W on Recovery of Lath Structure During Creep of High Chromium Martensitic Steels, *Materials Science and Engineering A*, 267, p.19-25 (1999)
- [114] Janovec, J., Svoboda, M. and Blach, J., Evolution of Secondary Phases During Quenching and Tempering 12%Cr Steel, *Materials Science and Engineering A*, 249, p. 184-189 (1998)
- [115] Raghavan, V., Kinetics of Martensitic Transformations, in *Martensite: A Tribute to Morris Cohen*, Eds. G.B. Olson and W.S. Owen, ASM International, p 197-225 (1992)
- [116] Image Pro Plus 5.0.0.39 for Windows 2000/XP Professional, Media Cybernetics, Computer software
- [117] Korcakova, L., Hald, J. and Somers, M.A.J., Quantification of Laves Phase Particle Size in 9CrW Steel, *Materials Characterization*, 47, p. 111 – 117 (2001)
- [118] Courtney, T.H., Kinetics and Mechanisms of Coarsening, in *Proceedings of the Solid to Solid Phase Transformations Conference*, 10-14th August 1981, Pittsburg, USA, p 1057-1076 (1982)
- [119] DeHoff, R.T. and Rhines, F.N., Quantitative Microscopy, New York: McGraw-Hill, (1968)
- [120] Wu, R. and Sandstrom, R., Carbide Coarsening During Creep in 12 Percent CrMoV Steel, *Journal of Materials Engineering and Technology*, p 485-492 (1996)
- [121] Suzuki, K., Kumai, S., Toda, Y., Kushima, H. and Kimura, K., Two-phase Separation of Primary MX Carbonitride During Tempering in Creep Resistant 9Cr1MoVNb Steel, *ISIJ International*, 43, p. 1089-1094 (2003)
- [122] Inoue, K., Ishikawa, N., Ohnuma, H., Ohtani, H. and Ishida, K., Calculation of Phase Equilibria Between Austenite and (Nb,Ti,V)(C,N) in Microalloyed Steels, *ISIJ International*, 41, p. 175-182 (2001)
- [123] Thomson, R.C., Carbide Composition Changes in Power Plant Steels as a Method of Remanent Creep Life Prediction, University of Cambridge PhD Dissertation (1992)
- [124] Shanmugam, S., Tanniru, M., Misra, R.D.K., Panda, D. and Jansto, S., Precipitation in V Bearing Microalloyed Steel Containing Low Concentrations of Ti and Nb, *Materials Science and Technology*, 21, p. 883-892 (2005)

- [125] Zajac, S., Siwecki, T., and Korchynsky, Importance of Nitrogen for Precipitation Phenomena in V-Microalloyed Steels, in *Proceedings of the International Symposium on Low-Carbon Steels for the 90's*, 17-21 October 1993, Pittsburgh, USA, Eds. R. Asfahani and G. Tither, p. 139-149 (1993)
- [126] Strid, J. and Easterling, K.E., On the Chemistry and Stability of Complex Carbides and Nitrides in Microalloyed Steels, *Acta Metallurgica*, 33, 11, p.2057-2074 (1985)
- [127] Andren, H.O., Henjered, A. and Norden, H., Composition of MC Precipitates in a Titanium Stabilized Austenitic Stainless Steel, *Journal of Materials Science*, 15, p. 2365-2368 (1980)
- [128] Saroja, S., Vijayalakshmi, M. and Raghunathan, V.S., Effect of Prolonged Exposures of 9Cr-1Mo-0.07C Steel to Elevated Temperatures, *Materials Transactions, Journal of the Institute of Materials*, 34, p. 901-906 (1993)
- [129] Gustafson, A. and Hattestrand, M., Coarsening of Precipitates in an Advanced Creep Resistant 9% Chromium Steel – Quantitative Microscopy and Simulations, *Submitted to Metallurgical and Materials Transactions A*. in Hattestrand, H., *Precipitation Reactions at High Temperatures in 9-12% Chromium Steels*, Chalmers Gotesborg University PhD Dissertation (2000)
- [130] Bjarbo, A. and Hattestrand, M., Complex Carbide Growth, Dissolution and Coarsening in a Modified 12 Pct Chromium Steel – An Experimental and Theoretical Study, *Metallurgical and Materials Transactions A*, 31, p. 1-9 (2000)
- [131] Nakajima, T., Spigarelli, S., Evangelista, E. and Endo, T., Strain Enhanced Growth of Precipitates During Creep of T91, *Materials Transactions*, 44, 9, p. 1802-1808 (2003)
- [132] Marshall, P., *Austenitic Stainless Steels: Microstructure and Mechanical Properties*, Elsevier, London (1984)
- [133] Mukherjee, T., Stumpf, W.E., Sellars, C.M. and Tegart, W.J., Kinetics of Coarsening of Carbides in Chromium Steels at 700°C, *Journal of the Iron and Steel Institute*, p. 621-631 (1969)
- [134] Jazaeri, H. and Humphreys, F.J., Quantifying Recrystallization by Electron Backscatter Diffraction, *Journal of Microscopy*, 213, p. 241–246 (2004)
- [135] Tarasiuk, J., Gerber, Ph. and Bacroix, B., Estimation of Recrystallised Volume Fraction from EBSD Data, *Acta Materialia*, 50, p. 1467-1477 (2002)
- [136] Wilson, A.W. and Spanos, G., Application of Orientation Imaging Microscopy to Study Phase Transformations in Steels, *Materials Characterization*, 46, p. 407-418 (2001)
- [137] Takeuchi, S. and Argon, A.S., Steady-State Creep of Single-Phase Crystalline Matter at High-Temperature, *Journal of Materials Science*, 11, p.1542-1566 (1976)
- [138] Straub, S., Polcik, P., Henes, D. and Blum, W., Simulation of the Long-Term Cyclic Creep Behaviour of a Low Alloyed Ferritic Chromium Steel, *Materials Science and Engineering A*, 234-236, 30, p. 1037-1040 (1997)

- [139] Dragomir, I.C. and Ungár, T., Contrast Factors of Dislocations in the Hexagonal Crystal System, *Journal of Applied Crystallography*, 35, p.556-564 (2002)
- [140] Williamson, G.K. and Hall, W.H., X-Ray Line Broadening from Filed Aluminium and Wolfram, *Acta Metallurgica*, 1, p. 22-31 (1953)
- [141] Kužel, R., Dislocation Line Broadening, *Zeitschrift für Kristallographie Supplement*, 22, p. 75-80 (2006)
- [142] Yajiang, L., Juan, W., Bing, Z. and Tao, F., XRD and TEM Analysis of Microstructure in the Welding Zone of 9Cr-1Mo-V-Nb Heat-resisting Steel, *Bulletin of Materials Science*, 25, p. 213-217 (2002)
- [143] Mazur, J., Grain Size of Martensite After Treatment at Very Low Temperatures, *Nature*, 164, p. 358 (1949)
- [144] Hall, W.H., X-Ray Line Broadening in Metals, *Proceeding of the Physics Society A*, 62, p. 741-743 (1949)
- [145] Peiser, H.S., Rooksby, H.P. and Wilson, A.J.C., X-Ray Diffraction by Polycrystalline Materials, Chapman and Hall Ltd, London (1960)
- [146] Kamminga, J.D. and Seijbel, L.J., Diffraction Line Broadening Analysis if Broadening is Caused by Both Dislocations and Limited Crystallite Size, *Journal of Research of the National Institute of Standards and Technology*, 109, p. 65-74 (2004)
- [147] Straub, S., Blum, W., Borbely, T. and Ungár, S., in *Proceedings of the 4th European Conference on Advances in Materials and Processing, Symposium F — Materials and Process Control*, 25-28 September 1995, Padua/Venice, Italy, p. 57 (1995)
- [148] Hull, D. and Bacon, D.J., Introduction to Dislocations, 4th Edition, Butterworth-Heinemann (2002)
- [149] Ribárik, G., Ungár, T. and Gubicza, J., MWP-fit: A Program for Multiple Whole-Profile Fitting of Diffraction Peak Profiles by *ab initio* Theoretical Functions, *Journal of Applied Crystallography*, 34, p. 669-676 (2001)
- [150] Hald, J., Straub, S. and Foldyna, V., Microstructural Stability of 9-12%CrMo(W)VNbN Steels, in *Proceedings of the 6th Liege Conference on Materials for Advanced Power Engineering*, 5-7 October 1998, Liege, Belgium, Eds. J. Lecomte-Beckers *et al.*, p.155-170 (1998)
- [151] Hayashi, K., Kojima, T. and Minami, Y., Development of 12% Cr Heat Resistant Steel Plate (TEMPALLOY F-12M) for USC Boiler, in *Proceedings of the 6th Liege Conference on Materials for Advanced Power Engineering*, 5-7 October 1998, Liege, Belgium, Eds. J. Lecomte-Beckers *et al.*, p. 411-420 (1998)
- [152] Watanabe, T., Tabuchi, M., Yamazaki, M., Hongo, H. and Tanabe, T., Creep Damage Evaluation of 9Cr-1Mo-V-Nb Steel Welded Joints Showing Type IV Fracture, *International Journal of Pressure Vessels and Piping*, 83, p. 63-71 (2005)

- [153] Allen, D.J. and Fleming, A., Creep Performance of Similar and Dissimilar E911 Steel Weldments for Advanced High Temperature Plant, in *Proceedings of the Fifth International Charles Parsons Turbine Conference*, Cambridge 3-7 July 2000, Eds. A. Strang *et al*, p. 276-290 (2000)
- [154] Allen, D.J., Harvey, B. and Brett, S.J., "FOURCRACK" – An Investigation of the Creep Performance of Advanced High Alloy Steel Welds, in *Proceedings of the ECCC Creep Conference*, London UK 12-14th September 2005, Eds. I.A. Shibli *et al*, p. 772-781 (2005)
- [155] Brett, S.J., Identification of Weak Thick Section Modified 9Cr Forgings in Service, in *EPRI Conference Proceedings of the Third International Conference on Advances in Materials Technology for Fossil Power Plants*, 4-6th April, Swansea, UK, (2001)
- [156] Shinozaki, K., Li, D.J., Huroki, H., Harada, H. and Ohishi, K., Analysis of Degradation of Creep Strength in Heat-affected Zone of Weldment of High Cr Heat-resisting Steels Based on Void Observation, *ISIJ International*, 42, p. 1578-1584 (2002)
- [157] Matsui, M., Tabuchi, M., Watanabe, T., Kubo, K., Kinugawa, J. and Abe, F., Degradation of Creep Strength in Welded joint of 9% Cr Steel, *ISIJ International*, 41, p. 126-130 (2001)
- [158] Albert, S.K., Matsui, M., Hongo, H., Watanabe, T., Kubo, K. and Tabuchi, M., Creep Rupture Properties of HAZs of a High Cr Ferritic Steel Simulated by a Weld Simulator, *International Journal of Pressure Vessels and Piping*, 81, p. 221-234 (2004)
- [159] Internal Communication with Dr S.J. Brett of RWE npower (2/1/2007)
- [160] Bhadeshia, H.K.D.H., Strang, A. and Gooch, D.J., Ferritic Power Plant Steels: Remanent Life Assessment and Approach to Equilibrium, *International Materials Reviews*, 43, p. 45-69 (1998)
- [161] Internal Communication with D.J. Allen (2/1/2007)
- [162] Yin, Y. and Faulkner, R.G., Modelling Precipitation Kinetics and Creep in Power Plant Ferritic Steels, in *Engineering Issues in Turbine Machinery, Power Plant and Renewables: Proceedings of the Sixth International Charles Parsons Turbine Conference*, 16-18 September 2003, Dublin Ireland, Edited by Strang, A. *et al.*, Institute of Materials, p. 457-471 (2003)
- [163] Yin, Y. and Faulkner, R.G., Creep Damage and Grain Boundary Precipitation in Power Plant Metals, *Materials Science and Technology*, 21, p. 1239-1246 (2005)
- [164] Lifshitz, I.M. and Slyozov, V.V., The Kinetics of Precipitation from Supersaturated Solid Solutions, *Journal of Physics and Chemistry of Solids*, 19, p. 35-50 (1961)
- [165] Wagner, C., Theorie der Alterung Yon Niederschlagen durch Umlosen., *Zeitschrift fur Elektrochemie*, 65, p. 581 (1961)
- [166] Robson, J.D. and Bhadeshia, H.K.D.H., Modelling Precipitation Sequences in Power Plant Steels Part 1- Kinetic Theory, *Materials Science and Technology*, 13, p. 631-639 (1997)

- [167] Robson, J.D. and Bhadeshia, H.K.D.H., Modelling Precipitation Sequences in Power Plant Steels Part 2- Application of Kinetic Theory, *Materials Science and Technology*, 13, p. 640-644 (1997)
- [168] Ågren, J., Clavaguera-Mora, M.T., Golcheski, J., Inden, G., Kumar, H. and Sigli, Applications of Computational Thermodynamics, *Calphad*, 24, p. 42 (2000)
- [169] Bhadeshia, H.K.D.H. and Sourmail, T., Design of Creep-resistant Steels: Success & Failure of Models, Japan Society for the Promotion of Science, Committee on Heat-Resisting Materials and Alloys, 44, p. 299-314 (2003)
- [170] Umantsev, A. and Olson, G.B., Ostwald Ripening in Multicomponent Alloys, *Scripta Metallurgica et Materialia*, 29, p. 1135-1140 (1993)
- [171] Hald, J., Thermodynamic Modelling of the Microstructure of High Cr Ferritic Creep Resistant Steam Pipe Steels, in Modelling of Microstructural Evolution in Creep Resistant Materials, Edited by Strang, A. and McLean, M., Institute of Materials, London, p. 1-9 (1999)
- [172] Abe, F., Coarsening Behavior of Lath and its Effect on Creep Rates in Tempered Martensitic 9Cr-W Steels, *Materials Science and Engineering A*, 387-389, p. 565-569 (2004)
- [173] Takayama, T., Wey, M.Y. and Nishizawa, T., Grain Growth in Dual-Phase Steel, *Tetsu-to-Hagane*, 68, p. 1016-1023 (1982)
- [174] Spigarelli, S., Cerri, E., Bianchi, P. and Evangelista, E., Interpretation of Creep Behaviour of a 9Cr-Mo-Nb-V-N (T91) Steel Using Threshold Stress Concept, *Materials Science and Technology*, 15, p. 1433-1440 (1999)
- [175] Robson, J.D., Modelling of Carbide and Lave Phase Precipitation in 9-12 wt% Chromium Steels, University of Cambridge PhD Dissertation (1996)
- [176] Yoshizawa, M., Igarashi, M. and Nishizawa, T., Effect of Tungsten on the Ostwald Ripening of $M_{23}C_6$ Carbides in Martensitic Heat Resistant Steel, *Tetsu to Hagane*, 91, p. 272-277 (2005)
- [177] Sawada, K., Kubo, K. and Abe, F., Contribution of Coarsening of MX Carbonitrides to Creep Strength Degradation in High Chromium Ferritic Steel, *Materials Science and Technology*, 19, p. 732-738 (2003)
- [178] Abe, F., Horiuchi, T., Taneike, K. and Sawada, M., Stabilization of Martensitic Microstructure in Advanced 9Cr Steel During Creep at High Temperature, *Materials Science and Engineering A*, 378, p. 299-309 (2004)
- [179] Knezevic V., Sauthoff, G., Vilk, J., Inden, G., Schneider, A., Agamennone, R., Blum, W., Wang, Y., Scholz, A., Berger, C., Ehlers, J. and Singheiser, L., Martensitic/Ferritic Super Heat-Resistant 650°C Steels—Design and Testing of Model Alloys, *ISIJ International*, 42, p. 1505-1514 (2002)

- [180] Straub, S., Verformungsverhalten und Mikrostruktur Warmfester Martensitischen 12%-Chromstähle, *Fortschritt-Berichte VDIO, reihe 5*, No. 405, VDI Verlag, Dusseldorf (1995)
- [181] Polcik, P., Sailer, T., Blum, W., Straub, S., Bursik, J. and Orlova, A., On the Microstructural Development of the Tempered Martensitic Cr-steel P 91 During Long-term Creep – a Comparison of Data, *Materials Science and Engineering A*, 260, p. 252-259 (1999)
- [182] Qin, Y., Microstructure Evolution of the Cast Martensitic Steel G-X12CrMoWVNbN 10-1-1 During Creep at 823 K, *Materials Science and Engineering A*, 357, p. 1-6 (2003)
- [183] Maruyama, K., Sawada, K. and Koike, J., Strengthening Mechanisms of Creep Resistant Tempered Martensitic Steel, *ISIJ International*, 41, p.641-653 (2001)
- [184] Blum, W. and Gotz, G., Evolution of Dislocation Structure in Martensitic Steels: The Subgrain Size as a Sensor for Creep Strain and Residual Creep Life, *Steel Research*, 70, p. 274 (1999)
- [185] Ennis, P.J, Creep Strengthening Mechanisms in 9-12% Cr Steels, in *EPRI Conference Proceedings of the Fourth International Conference on Advances in Materials Technology for Fossil Power Plants*, 25th October, Hilton Head, USA, p. 1120-1133 (2004)
- [186] Fridberg, J., Torndahl, L.E. and Hillert, M., Diffusion in Iron, *Jernkontorets Ann.*, 153, p. 263-276 (1969)